IDŐJÁRÁS

QUARTERLY JOURNAL
OF THE HUNGARIAN METEOROLOGICAL SERVICE

CONTENTS

Ákos Horváth, Ferenc Ács and *András T. Seres:* Thunderstorm climatology analyses in Hungary using radar observations 1

Ferenc Dombai: Attempts to enhance the localization accuracy and to monitor the reliability of the SAFIR HMS lightning localization system 15

Béla Gombos: Modeling water temperature of Hungarian rice fields 33

S.M. Robaa: On the estimation of UV-B radiation over Egypt 45

Book review 61

****

http://www.met.hu/Journal-Idojaras.php

VOL. 112 * NO. 1 * JANUARY - MARCH 2008

IDŐJÁRÁS

Quarterly Journal of the Hungarian Meteorological Service

Editor-in-Chief
LÁSZLÓ BOZÓ

Executive Editor
MARGIT ANTAL

EDITORIAL BOARD

AMBRÓZY, P. (Budapest, Hungary)
ANTAL, E. (Budapest, Hungary)
BARTHOLY, J. (Budapest, Hungary)
BATCHVAROVA, E. (Sofia, Bulgaria)
BRIMBLECOMBE, P. (Norwich, U.K.)
CZELNAI, R. (Dörgicse, Hungary)
DÉVÉNYI, D. (Boulder, CO, U.S.A.)
DUNKEL, Z. (Budapest, Hungary)
FISHER, B. (Reading, U.K.)
GELEYN, J.-Fr. (Toulouse, France)
GERESDI, I. (Pécs, Hungary)
GÖTZ, G. (Budapest, Hungary)
HANTEL, M. (Vienna, Austria)
HASZPRA, L. (Budapest, Hungary)
HORÁNYI, A. (Budapest, Hungary)
HORVÁTH, Á. (Siófok, Hungary)
HORVÁTH, L. (Budapest, Hungary)
HUNKÁR, M. (Keszthely, Hungary)
MAJOR, G. (Budapest, Hungary)
MÉSZÁROS, E. (Veszprém, Hungary)
MIKA, J. (Budapest, Hungary)
MERSICH, I. (Budapest, Hungary)
MÖLLER, D. (Berlin, Germany)
NEUWIRTH, F. (Vienna, Austria)
PAP, J.M. (Greenbelt, MD, U.S.A.)
PINTO, J. (R. Triangle Park, NC, U.S.A)
PRÁGER, T. (Budapest, Hungary)
PROBÁLD, F. (Budapest, Hungary)
RADNÓTI, G. (Budapest, Hungary)
S. BURÁNSZKY, M. (Budapest, Hungary)
SZALAI, S. (Budapest, Hungary)
SZEIDL, L. (Budapest, Hungary)
TAR, K. (Debrecen, Hungary)
TÄNCZER, T. (Budapest, Hungary)
TOTH, Z. (Camp Springs, MD, U.S.A.)
VALI, G. (Laramie, WY, U.S.A.)
VARGA-HASZONITS, Z. (Moson-magyaróvár, Hungary)
WEIDINGER, T. (Budapest, Hungary)

Editorial Office: Gilice tér 39, H-1182 Budapest, Hungary
P.O. Box 39, H-1675 Budapest, Hungary
E-mail: bozo.l@met.hu or *antal.e@met.hu*
Fax: (36-1) 346-4809

Covered in the abstract and citation database SCOPUS®

Subscription by

mail: IDŐJÁRÁS, P.O. Box 39, H-1675 Budapest, Hungary;
E-mail: kenderesy.k@met.hu or *antal.e@met.hu*

IDŐJÁRÁS

Quarterly Journal of the Hungarian Meteorological Service
Vol. 112, No. 1, January–March 2008, pp. 1–13

Thunderstorm climatology analyses in Hungary using radar observations

Ákos Horváth[1]•, Ferenc Ács[2] and András T. Seres[2]

[1]*Hungarian Meteorological Service,*
Vitorlás u. 17, H-8600 Siófok, Hungary; E-mail: horvath.a@met.hu

[2]*Department of Meteorology, Eötvös Loránd University,*
P.O. Box 32, H-1518 Budapest, Hungary

(Manuscript received in final form November 30, 2007)

Abstract—This paper presents the results of an objective analysis, which deals with thunderstorm-climatology. The aim of this study is twofold: firstly, to describe the space and time distribution of severe thunderstorms in Hungary using radar data in the five-year period of 2003–2007, and secondly, to analyze the relationship between severe thunderstorms and macrosynoptic circulation types. We have applied *Péczely's* (1957) synoptic circulation types. The core of the examination is the modified TITAN (Thunderstorm Identification, Tracking, Analysis, and Nowcasting)-method (*Dixon* and *Wiener*, 1993), where thunderstorms are represented with ellipses (thunderstorm-ellipses). Severe and highly severe thunderstorm-ellipses and stormy days are defined. Most of the severe and highly severe stormy days were associated with typical synoptic situations: prefrontal warm sectors of active cyclones, cold fronts, and anticyclone edges. The detected thunderstorm-ellipses had maxima in the south-west, north, and east parts of Hungary. The results of this examination may be important for forecasting severe thunderstorms, so damage and loss can be reduced.

Key-words: thunderstorms, radar, TITAN-method, climatology, Hungary, Péczely-classification

1. Introduction

The information society of today has a growing demand for weather forecasts; interest in the examination of severe thunderstorms has grown rapidly. The climatological aspects of these phenomena have become more common worldwide. In these studies, we have used visual observations and

• Corresponding author

measurements (*Manohar* and *Kesarkar*, 2003), satellite images (*Banta* and *Schaaf*, 1987), lightning tracking systems (*Watson et al.*, 1994; *Shwehdi*, 2005), soundings (*Craven* and *Brook*s, 2004), weather and climate models (*Ziegler et al.*, 1997; *Schär et al.*, 1999), and meteorological radar data. In this study, an approach based on radar data has been presented.

Radar data-based thunderstorm climatology studies appeared for the first time in the USA in the 1950s (*Braham*, 1958). These investigations refer to different regions of the United States (*Myers*, 1964; *Kuo* and *Orville*, 1972; *Henz*, 1974; *Falconer*, 1984; *Croft* and *Shulman*, 1989; *Geerts*, 1997; *MacKeen* and *Zhang*, 1999). Nevertheless, in recent decades there have also been studies referring to South America (*Paiva Pereira* and *Rutledge*, 2003), Canada (*Brimelow et al.*, 2004), Australia (*Steiner* and *Houze*, 1996), and Europe (*Jaeneke*, 2001; *Rigo* and *Liasat*, 2002).

The first study in Hungary considering thunderstorms from a climatological point of view was carried out by *Héjas* (1898; 1909) and *Raum* (1910). Héjas examined the relationship between atmospheric pressure systems and the distribution in space of thunderstorms. This investigation is based on visual observations and measurements. Many studies dealing with different aspects of thunderstorm climatology appeared in the 1960s (*Adámy* and *Máhr*, 1963; *Ozorai*, 1965; *Götz* and *Pápainé*, 1966, 1967). Götz and Pápainé examined the distribution of thunderstorms in both the summer and winter seasons using data from a 10-year period. All these studies used data obtained by visual observations. In recent years, there have also been studies (*Horváth* and *Geresdi*, 2000; *Bodolainé* and *Tänczer*, 2005; *Horváth et al.*, 2007), which consider thunderstorms from dynamical and synoptical points of view. In these Hungarian studies, there were no radar data-based analyses.

The aim of this study is twofold: firstly, to describe the space/time distribution of severe thunderstorms in Hungary using radar data in the 5-year period of 2003–2007, and secondly, to analyze the relationship between severe thunderstorms and synoptic circulation patterns. *Péczely's* (1957) classification for synoptic patterns has been applied. The analysis reveals which locations are most endangered by thunderstorms and which synoptic patterns are beneficial to severe convective weather. In the first part of the study radar measurements and the localization method (TITAN-method) of thunderstorms are described. The TITAN-method was applied to detect severe and highly severe thunderstorms and their space/time distribution. The relationship was made between Péczely synoptic classes and objectively detected severe thunderstorms.

2. Methodology

2.1. Radar measurements

We used the radar network of the Hungarian Meteorological Service (HMS). Hungary is covered by three radars: the western, the central, and the eastern

radar. In 2003 only two radars provided observations: the western MRL-5 type, in Szentgotthárd-Farkasfa and the central Doppler type in Budapest-Pestszentlőrinc. The eastern, which is located in Nyíregyháza-Napkor, was not in continuous operation because of modernization work being carried out, therefore, there was no reliable information from the north-eastern parts of Hungary in this year. In 2004–2007 Doppler radar measurements covered the whole region (the western radar also changed to Doppler instrumentation and was moved to Pogányvár). All 3 radars operate on the C band (5 cm).

In this study only Doppler radar reflectivity was used. During the measurement procedure the Doppler wind was also applied for noise filtering and quality upgrading, and the composite fields resulted from the upgraded, filtered and smoothed data from the 3 radars. Composite image resolution is $2\,\text{km} \times 2$ km in space and 15 minutes in time. To additionally reduce measurement noise, the median-filter method was also used before beginning the analysis.

2.2. The core of the methodology: The modified TITAN-method

TITAN-method was developed by *Dixon* and *Wiener* (1993). In this study we used the first part of this system: the thunderstorm identification. Using the method, irregular-shaped thunderstorms can be characterized by regular ellipses. The main point of identification is as follows: the parameters of the ellipses are determined by the covariance matrix of the isolated, irregular-shaped cluster on the image using the condition that the area of the cluster has to be equal to the area of the ellipse. The center of a cluster is defined by

$$\overline{x} = \frac{1}{n}\sum_{i=1}^{n} x_i\,, \qquad \overline{y} = \frac{1}{n}\sum_{i=1}^{n} y_i\,, \tag{1}$$

where x and y indicate the longitude and latitude of the relevant pixels (pixels which have reflectivity higher than a threshold value). The covariance of the cluster is

$$A = \text{cov}_{xy} = \begin{bmatrix} d & e \\ e & f \end{bmatrix}, \tag{2}$$

where d is the deviation from the center of the x coordinate

$$d = \frac{1}{n-1}\sum_{i=1}^{n}(x_i - \overline{x})^2. \tag{3}$$

f is the deviation from the center of the y coordinate

$$f = \frac{1}{n-1}\sum_{i=1}^{n}(y_i - \overline{y})^2, \tag{4}$$

while e is

$$e = \frac{1}{n-1}\sum_{i=1}^{n}(x_i - \overline{x})(y_i - \overline{y}). \tag{5}$$

The parameters of the ellipse can be estimated by calculating the eigenvector and eigenvalue of this covariance matrix. These parameters are as follows: the coordinates of the center, the length of the minor and the major axes, and the orientation angle (the angle between the major axis and the x axis). With these parameters, the focus points and the equation of the ellipse can be easily determined, and so the ellipse can be visualized (*Fig. 1*).

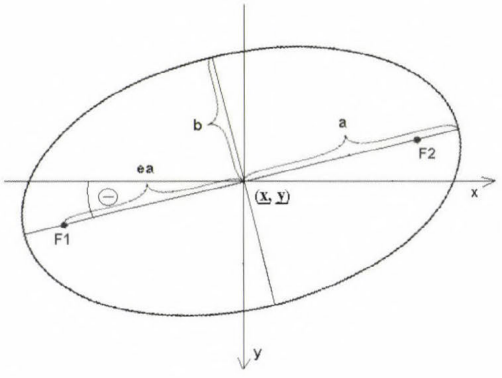


Fig. 1. Characteristics of the thunderstorm-ellipse: $\underline{x}$ and $\underline{y}$ are the coordinates of the centre, a is the half of the major axis, b is the half of the minor axis, *F1* and *F2* are the focus points, Θ is the orientation angle.

These "estimated ellipses" are called *thunderstorm-ellipses*. In carrying out the analysis, the noises were reduced. Two types of thresholds: *the area* ($N_{minlimit}$) and *the value threshold* ($P_{minlimit}$) are defined. The area threshold determines the minimum area of a cluster. In our examination $N_{minlimit}$ is set to be 5 radar pixels (20 km^2). The value threshold specifies that the values of all the individual pixels of the cluster (in our case 5 pixels) have to reach this limit. In our examination $P_{minlimit}$ is set to 45 (so-called severe thunderstorm-ellipses) or 50 dBZ (so-called highly severe thunderstorm-ellipses). Using these thresholds, small and weak objects are eliminated. *Fig. 2* shows the ellipses. The original radar image is presented in *Fig. 2a* for May 18, 2005, 14:45 UTC, while the thunderstorm-ellipses are presented in *Fig. 2b*, where $N_{minlimit}$ is 5 radar pixels (20 km^2) and $P_{minlimit}$ is 45 dBZ. In this case two isolated convective systems went through Hungary. These systems produced numerous serious convective

phenomena: for example a supercell near Lake Balaton (to the west of the Danube) and near Hortobágy. The latter caused a tornado not far from Hosszúpályi (*Horváth*, 2005).

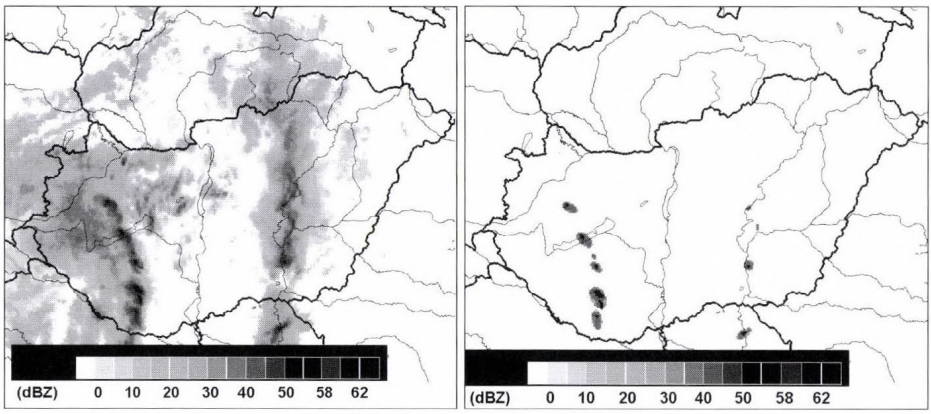


Fig. 2. Radar echo pictures of the thunderstorms observed on May 18, 2005, 14:45 UTC. Left: original picture, right: picture where thunderstorms are represented by ellipses.

3. Results

3.1. Severe and highly severe stormy days and thunderstorm seasons

A day is denoted as a *severe or a highly severe stormy day* when at least one detected severe ($P_{minlimit}$ = 45 dBZ) or highly severe ($P_{minlimit}$ = 50 dBZ) thunderstorm ellipse can be found on radar images, and at least one thunderstorm was visually observed by the Hungarian synoptic station network. Visual observations were taken from the *Időjárási Napijelentés* (2003–2007) of the Hungarian Meteorological Service. Using these data the time distribution of stormy days (*Fig. 3*) can be determined, and the number of these days can be counted for each year (*Table 1*).

The most severe stormy days were in 2006, while the most highly severe days occurred in 2007. Note that in 2007, the last three months (October, November, and December) were not processed, therefore, this short period is not presented. 2003 is also shown, but this year is not representative because of the missing reliable radar measurements in the eastern parts of Hungary. From *Fig. 3* it is obvious that in 2003 and 2005 severe and highly severe stormy days appeared mostly in July. In 2004 and 2007, severe and highly severe stormy days appeared mostly in June, while in 2006 these days occurred mostly in August. It is obvious that most severe and highly severe stormy days and thunderstorm-ellipses appeared between April and September, therefore this period is denoted as a *thunderstorm season*.

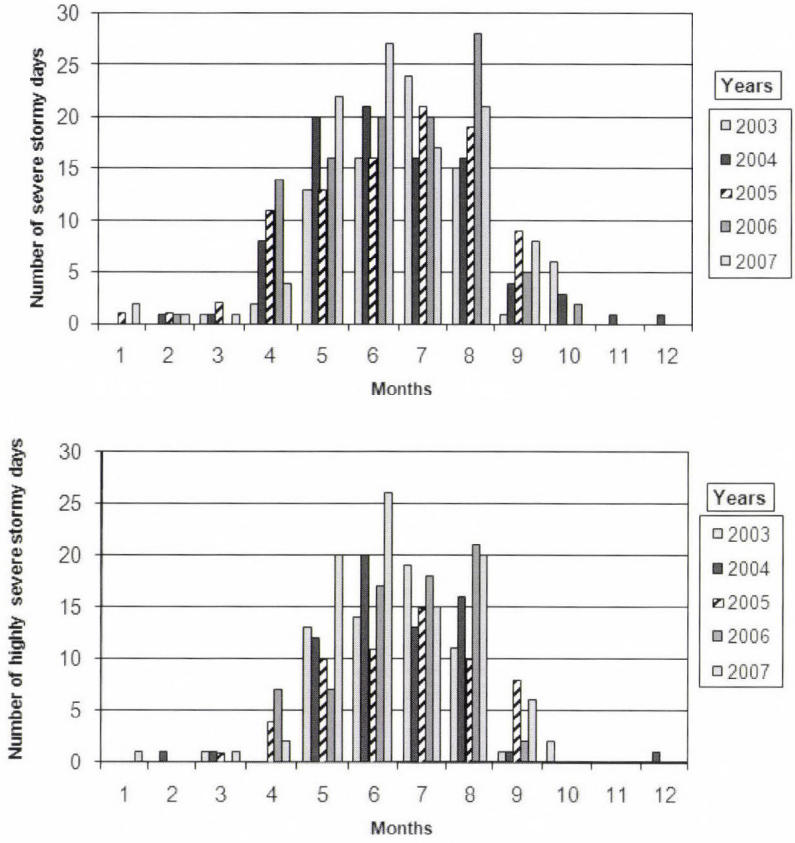


Fig. 3. Annual course of (up) severe and (down) highly severe stormy days in the years 2003, 2004 2005, 2006, and 2007. Note that in 2007 only the 9-month period from January to September was processed.

Table 1. Number of the severe and highly severe stormy days in the years 2003–2007

Years	**Number of severe stormy days** ($P_{minlimit}$ = 45 dBz)	**Number of highly severe stormy days** ($P_{minlimit}$ = 50 dBz)
2003	78	61
2004	92	65
2005	93	59
2006	106	72
2007	103	91

3.2. *Spatial distribution of thunderstorm ellipses*

The spatial distribution of thunderstorms is analyzed by constructing *thunderstorm statistic maps*. The maps show the spatial distribution of severe and highly severe thunderstorm ellipses. Note that these calculated values are not equal to the number of the thunderstorms (they are proportional to it, however), because a severe thunderstorm may occur on subsequent radar images. Thunderstorm statistic maps were made for all of the five years from 2003 to 2007 by using the abovementioned different pixel limits ($P_{minlimit} = 45$ or $P_{minlimit} = 50$) for Hungary. The maps were made only for the thunderstorm season period. (In the winter period, there were only a few thunderstorm-ellipses and the measurement noises were high.)

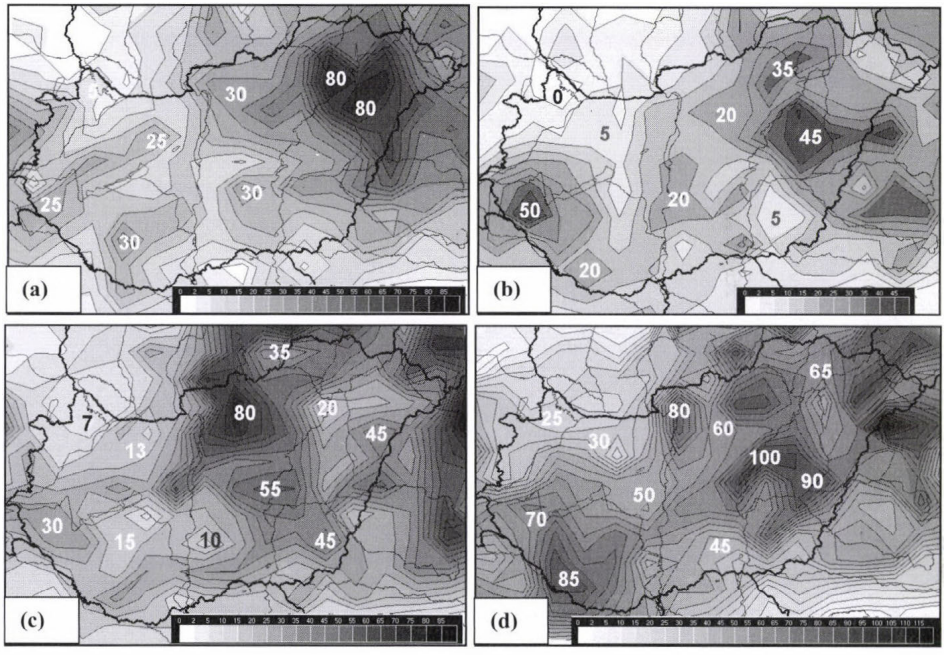


Fig. 4. Spatial distribution of severe (at least 45 dBZ) thunderstorm-ellipses in the thunderstorm season of (a) 2004, (b) 2005, (c) 2006, and (d) 2007. The resolution is 30 km × 30 km. These images were visualized by the HAWK system (Hungarian Advanced Workstation).

In 2003, the maxima of severe or highly severe thunderstorms were in the middle parts of Hungary and in the western-central regions to the west of the Danube (not shown). In 2004 the area density maximum is located in the east, north-east part of Hungary. Less severe thunderstorms occurred to the west of the Danube or in the southern regions of the country (*Figs. 4a* and *5a*). In 2005 most of the severe and highly severe thunderstorm-ellipses were located in the

south-west and north-east regions of Hungary, while only a few severe convective objects appeared in the north-west, central, and south-east parts of the country (*Figs. 4b* and *5b*). In 2006 the maxima were in the central-northern parts of Hungary, while less severe and highly severe thunderstorm-ellipses occurred to the west of the Danube (especially in the north-western parts) and in the southern regions (*Figs. 4c* and *5c*). In 2007 most of the severe and highly severe thunderstorm-ellipses were located in the central-eastern and south-western regions of Hungary (*Figs. 4d* and *5d*).

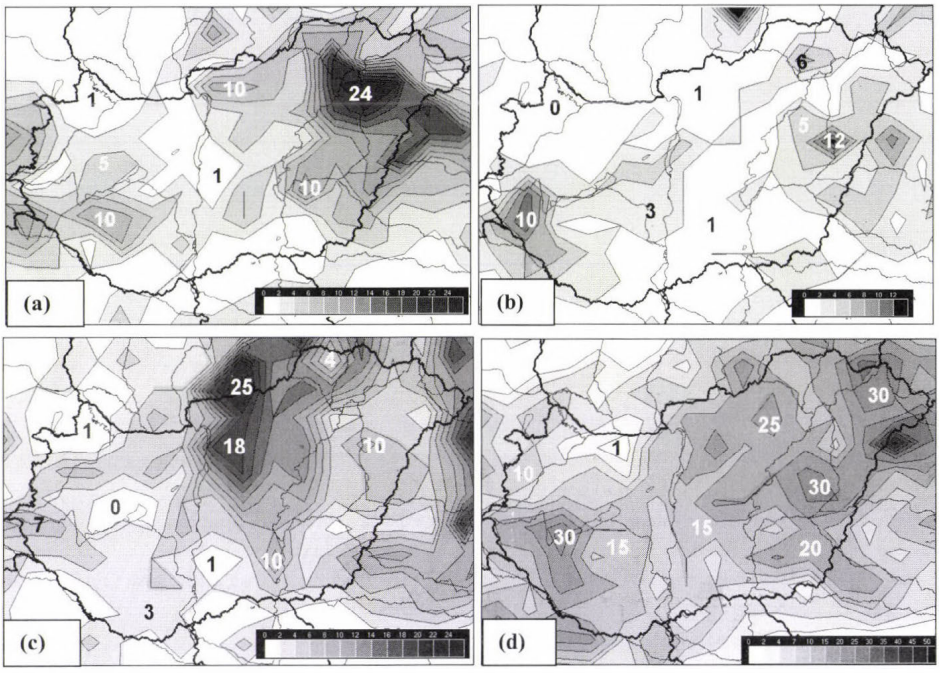


Fig. 5. Spatial distribution of severe (at least 50 dBZ) thunderstorm-ellipses in the thunderstorm season of (a) 2004, (b) 2005, (c) 2006, and (d) 2007. The resolution is 30 km × 30 km. These images were visualized by the HAWK system (Hungarian Advanced Workstation).

3.3. Frequency distribution of severe and highly severe stormy days according to Péczely's synoptic circulation types

The relation between stormy days and the synoptic patterns were analyzed by investigating the frequency distribution of severe and highly severe stormy days according to *Péczely's* (1957) synoptic circulation types. The Péczely classification was created to describe the weather patterns especially for Central Europe. Synoptic circulation types were diagnosed from the maps of the published daily weather reports.

Severe and highly severe stormy days in all the years appeared most frequently in the circulation types 4, 1, 6, and 9. Type 11 was quite frequent in 2004 and the type 13 appeared more frequently in 2005. The frequency of appearance of the other types was much smaller (*Fig. 7*). In the circulation type 4, Hungary is in advance of the cold front or in the warm sector (so called pre-frontal situation), which belongs to western/northern cyclones. The type 6 also represents a pre-frontal situation, but in this case the cold front belongs to a Mediterranean cyclone. The type 1 represents situations when the weather of the Carpathian Basin is controlled by a cold front which belongs to a northern cyclone. Type 9 is associated with a western anticyclone, when Hungary is located on the eastern edge of the anticyclone. Type 11 is associated with an anticyclone above Scandinavia, when our region is located on the edge of this anticyclone. On many occasions types 9 and 11 can also be post-frontal, when a western or northern anticyclone develops behind the cold front. The type 13 is associated with cyclones/shallow cyclones above the Carpathian Basin.

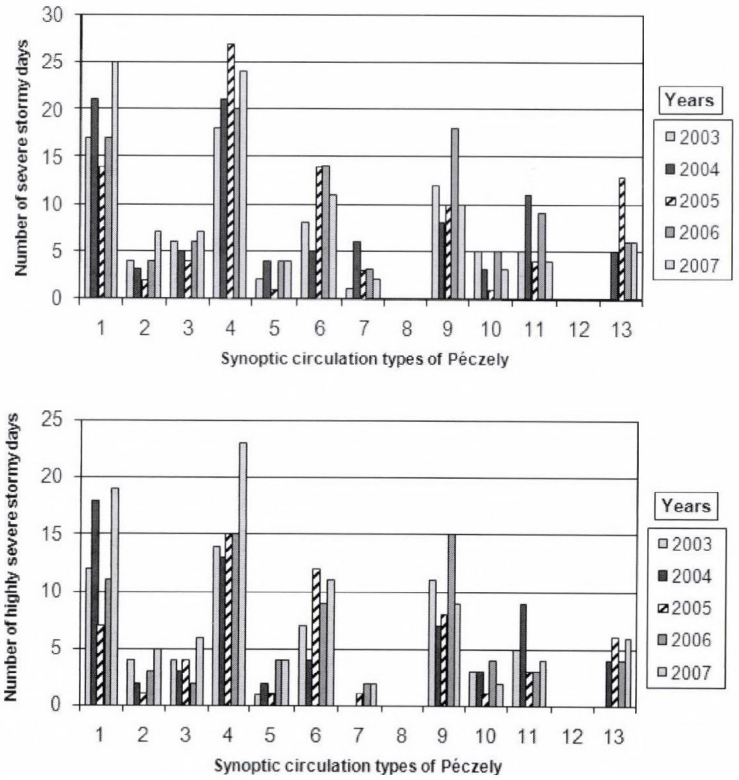


Fig. 6. Frequency distribution of (up) severe and (down) highly severe stormy days according to Péczely's synoptic circulation types in the years 2003, 2004, 2005, 2006, and 2007.

3.4. *Frequency distribution of the detected thunderstorm-ellipses according to Péczely's synoptic circulation types*

To determine the frequency distribution, the number of detected thunderstorm-ellipses of the stormy days has to be counted. Two main groups of *severe stormy days* can be defined: *days with few* and *days with many ellipses* (the number of the detected thunderstorm-ellipses does not exceed or does exceed 50). The frequency distribution of these two different types of severe stormy days is presented in *Fig. 7*. In all examined years, severe stormy days with few thunderstorm-ellipses appeared most frequently in the synoptic circulation types 4, 1, and 9. In one or two years, type 6 (in 2006), type 11 (in 2004 and 2006), and type 13 (in 2005) were frequent (*Fig. 7a*). Considering days with many severe thunderstorms, in 2003 the highest frequency distributions appeared in the circulation types 1 and 4. In 2004 the types 1 and 4, in 2005 the types 4 and 6, in 2006 the types 4 and 9, and in 2007 the types 1, 4, and 6 possessed the highest frequency distributions (*Fig. 7b*).

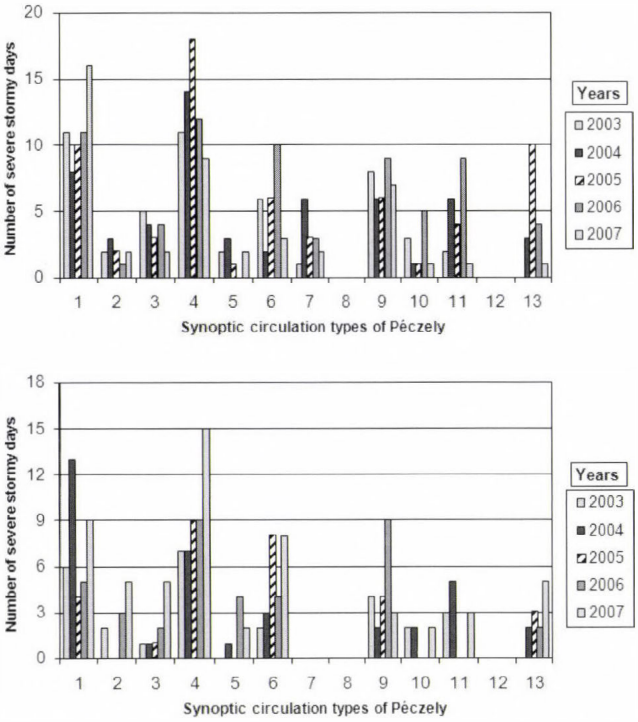


Fig. 7. Frequency distribution of severe stormy days with (up) few (the number of thunderstorm-ellipses does not exceed 50) and (down) many (the number of thunderstorm-ellipses exceeds 50) thunderstorm-ellipses according to Péczely's synoptic circulation types in the years 2003, 2004, 2005, 2006, and 2007.

Analogously to severe stormy days, two main groups of *highly severe stormy days* can be defined: *days with few* and *days with many ellipses* (the number of the detected thunderstorm-ellipses does not exceed or does exceed 50) (*Fig. 8*). Highly severe stormy days with few ellipses appeared most frequently in the synoptic circulation types 1, 4, and 9. The appearance was also quite frequent in synoptic circulation types 6 (mainly in 2005), 3 (in 2004 and 2005), and 11 (especially in 2004) (*Fig. 8a*). Except for the years 2004 and 2005, the most highly severe stormy days with many thunderstorm-ellipses were caused by the synoptic circulation type 4. In 2004, the type 1 was the most frequent. In 2005, there were no highly severe stormy days with many ellipses. Highly severe stormy days with many ellipses appeared also, but with lower frequency, in the circulation types 2, 3, 5, 6, 9, and 13 (*Fig. 8b*). Note the high number of highly severe stormy days in 2007! The type 2 is associated with an anticyclone above the British Isles, the 3 with cold fronts of a Mediterranean cyclone, and the 5 with the edge of an eastern anticyclone.

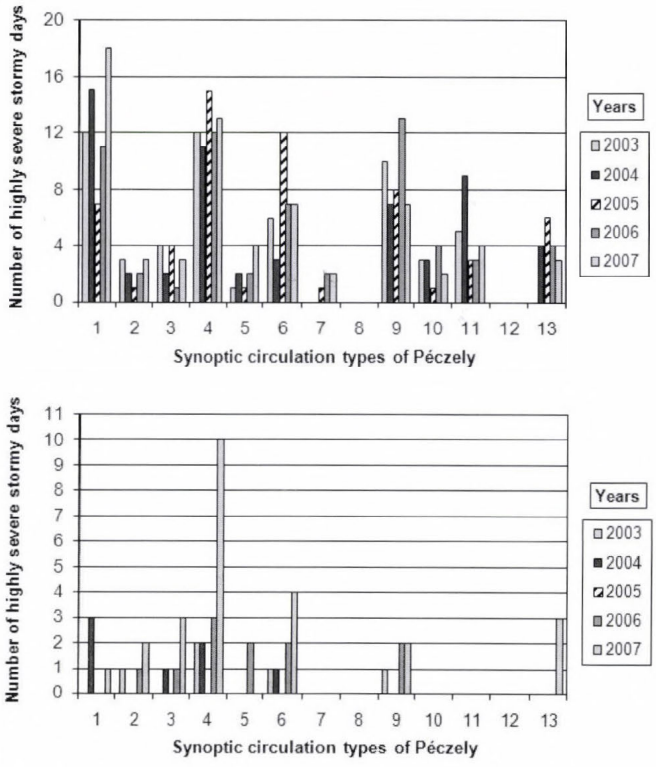


Fig. 8. Frequency distribution of highly severe stormy days with (up) few (the number of thunderstorm-ellipses does not exceed 50) and (down) many (thunderstorm-ellipses exceeds 50) thunderstorm-ellipses according to Péczely's synoptic circulation types in the years 2003, 2004, 2005, 2006, and 2007.

4. Conclusions

This paper presents the results of an objective analysis which dealt with thunderstorm-climatology. The aims were to describe the space and time distribution of severe thunderstorms in Hungary and analyze the relationship between severe thunderstorms and synoptic circulation patterns for the five-year period 2003–2007.

The main results of the examination are as follows:

- The time distribution of stormy days was slightly different in each year. In 2004 and 2007 the stormiest days appeared in June, in 2003 and 2005 July had the stormiest days, while in 2006 August was the stormiest month. In the examined period, 2007 had the highest number of highly severe stormy days.
- Maxima of severe or highly severe thunderstorms/thunderstorm-ellipses were located in the south-western, in the northern central, and in the north-eastern parts of Hungary. The territory least at risk is the north-western region of the country.
- Most of the severe and highly severe stormy days and detected thunderstorms-ellipses are associated with various types of cold fronts and anticyclone-edges (Péczely-types 4, 1, 9, and 6 in order of frequency).
- The most dangerous situation of highly severe stormy days with many ellipses can be clearly linked to the type 4, which represents an open warm sector of an active cyclone.

In the future, this objective examination can be carried out for a longer period, since radar-measurements began in Hungary in the 1990s. Note that the radar measurements contain noise (and not all noise could be eliminated during this research), so in the near future a noise-filtering method should be developed.

Acknowledgements—The authors are grateful for the radar data provided by the Hungarian Meteorological Service. This research was supported by the Jedlik Ányos Program 2005, identification number: OM-00103/2005.

References

Adámy, L. and *Máhr, J.*, 1963: Some statistical data of the thunderstorm climatology in Nyíregyháza and Szeged (in Hungarian). *Időjárás 67,* 226-232.

Banta, R.M. and *Schaaf, C.B.*, 1987: Thunderstorm genesis zones in the Colorado Rocky Mountains as determined by traceback of geosynchronous satellite images. *Mon. Weather Rev. 115*, 463-476.

Bodolainé, J.E. and *Tänczer, T.*, 2007: Mesoscale convective complexes. In *Atmospheric Convection* (in Hungarian) (ed.: *Á. Horváth*). Országos Meteorológiai Szolgálat, Budapest, 35-45.

Braham, R.R., 1958: Cumulus cloud precipitation as revealed by radar-Arizona 1955. *J. Meteorol. 15*, 75-83.

Brimelow, J.C., Reuter, W.G., Bellon, A., and *Hudak, D.*, 2004: A radar-based methodology for preparing a severe thunderstorm climatology in Central Alberta. *Atmos.-Ocean. 42,* 13-22.

Craven, J.P. and *Brooks, H.E.*, 2004: Baseline climatology of sounding derived parameters associated with deep, moist convection. *Nat. Wea. Digest 28,*13-24.

Croft, P.J. and *Shulman, M.D.*, 1989: A five-year radar climatology of convective precipitation for New Jersey. *Int. J. Climatol. 9*, 581-600.

Dixon, M. and *Wiener, G.*, 1993: TITAN: Thunderstorm Identification, Tracking, Analysis and Nowcasting – A radar-based methodology. *J. Atmos. Ocean. Tech. 10,* 785-797.

Falconer, P.D., 1984: A radar-based climatology of thunderstorm days across New York State. *J. Appl. Meteorol. 23,* 1115-1120.

Geerts, B., 1997: Mesoscale convective systems in the Southeast United States during 1994–95: *A Survey Weather and Forecasting 13,* 860-869.

Götz, G. and *Pápainé, Sz.G.,* 1966: Thunderstorm activity in the summer-time period in Hungary (in Hungarian). *Időjárás 70,* 106-116.

Götz, G. and *Pápainé, Sz.G.*, 1967: Thunderstorm activity in the winter-time period in Hungary (in Hungarian). *Időjárás 71,* 302-309.

Héjas, E., 1898*: Thunderstorms in Hungary Based on Observations Between 1871 and 1895* (in Hungarian). Királyi Magyar Természet Tudományi Társulat, Budapest, 174 pp.

Héjas, E., 1909: Space distribution of thunderstorms in Hungary (in Hungarian). *Földrajzi Közlemények 37,* 410-421.

Henz, J., 1974: *Colorado High Plains Thunderstorm Systems - A Radar Synoptic Climatology.* Colorado St. Univ., M.S. Thesis, 82 pp.

Horváth, Á., 2005: Synoptic description of the storm in May 18, 2005 (in Hungarian). *Légkör 50,* No. 3, 12-16.

Horváth, Á. and *Geresdi, I.,* 2000: Severe convective storms and associated phenomena in Hungary. *Atmos. Res. 56,* 127-146.

Horváth, Á., Geresdi, I., Németh, P., and *Dombai, F.*, 2007: The Constitution Day storm in Budapest: Case study of the August 20, 2006 severe storm. *Időjárás 111,* 41-65.

Időjárási Napijelentés (*Daily Weather Reports*), 2003–2007: Országos Meteorológiai Szolgálat, Budapest.

Jaeneke, M., 2001: Radar based climatological studies of the influence of orography on thunderstorm activity in Central Europe. *Proc. 30th International Conference on Radar Meteorology, 12A.5.*

Kuo, J. and *Orville, H. D.,* 1972: Radar climatology of summertime convective clouds in the Black Hills. *J. Appl. Meteorol. 12,* 359-368.

MacKeen, P.L. and *Zhang, J.,* 1999: Convective climatology for Central Arizona during the 1999 Monsoon (http://www.cimms.ou.edu/~heinsel/swconf.html).

Manohar, K. and *Kesarkar, A. P.*, 2003: Climatology of thunderstorm activity over Indian Region: A study of east-west contrast. *Proc. ICAE Conference,* 121-124.

Myers, J., 1964: Preliminary radar climatology of central Pennsylvania. *J. Appl. Meteor. 3*, 421-429.

Ozorai, Z., 1965: Thunderstorm frequency in Budapest-Ferihegy Airport (in Hungarian). *Időjárás 69*, 375-377.

Paiva Pereira, L.G. and *Rutledge, S.A.,* 2003: Convective characteristics over the East Pacific and Southwest Amazon regions: A radar perspective. *EPIC 2001 Workshop,* Boulder, CO, September 15-16, 2003.

Péczely, G. 1957: Grosswetterlagen in Ungarn. Kleinere Veröffentlichungen der Zentralanstalt für Meteorologie, Nr. 30, Budapest.

Raum, O., 1910: Results of the 15-year thunderstorm observation in Hungary between 1896 and 1910 (in Hungarian). *Évkönyvek 40, 2.*

Rigo, T. and *Liasat, M.C.,* 2002: Analysis of convective structures that produce heavy rainfall events in Catalonia (NE of Spain), using meteorological radar. *Proc. ERAD*, 45-48.

Schär, C., Lüthi, D., Beyerle, U., and *Heise, E.,* 1999: The soil-precipitation feedback: A process study with a regional climate model. *J. Climate 12,* 722-741.

Shwehdi, M.H., 2005: Thunderstorm distribution and frequency in Saudi Arabia. *J. Geophys. Eng. 2,* 252-267.

Steiner, M. and *Houze, R.,* 1996: Sensitivity of the estimated monthly convective rain fraction to the choice of Z–R relation. *J. Appl. Meteorol. 36,* 452-462.

Watson, A.I., Lopez, R.E., and *Holle, R.L.,* 1994: Diurnal cloud-to-ground lightning patterns in Arizona during the southwest monsoon. *Mon. Weather Rev. 122,* 1716-1725.

Ziegler, C.L., Lee, J.T., and *Pielke Sr., R.A.,* 1997: Convective initiation at the dryline: A modeling study. *Mon. Weather Rev. 125,* 1001-1026.

IDŐJÁRÁS

Quarterly Journal of the Hungarian Meteorological Service
Vol. 112, No. 1, January–March 2008, pp. 15–31

Attempts to enhance the localization accuracy and to monitor the reliability of the SAFIR HMS lightning localization system

Ferenc Dombai

Hungarian Meteorological Service
P.O. Box 38, H-1525 Budapest, Hungary; E-mail: dombai.f@met.hu

(Manuscript received in final form January 3, 2008)

Abstract—In Hungary, an interferometric lightning localization network named SAFIR HMS was installed in 1998 to follow the total electrical activities of the thunderstorms for nowcasting purposes. In 2006 the real localization precision of SAFIR HMS was heavily investigated. In order to find the source of the gap between the promised and the experienced localization errors, different field measurements and simulation calculations were made. It was found that the random statistical errors of SAFIR HMS are about 0.5–1 degree, but the systematic localization errors could reach about 3–7 degrees in several directions from the detection stations. The badly compensated nonlinearities of the VHF detection sensors are the main sources of these systematic errors. It was found also, that the systematic localization errors could be reduced by reanalyzing of the raw detection data of the SAFIR HMS using the statistical differences of the measured (VHF interferometric) and calculated (from the positions of the return strokes with TOA method) azimuth data. In searching the way of the operational and automatic quality control of the SAFIR HMS, the Flash Backward Calculation (FBC) method have been developed at the Hungarian Meteorological Service (HMS). Using the raw detection data and the processed flash data, the FBC can continuously provide different detection activity and quality measures and detection errors of the SAFIR HMS, which can be fed later into automatic data assimilation processes.

Key-words: SAFIR, lightning localization, radar and lightning, localization error, localization accuracy, correction of localization error, reliability, Hungary

1. Introduction

Many experienced problems and investigations have proved that the reliability and data quality of unmanned and embedded observation system are very critical. The importance of these is even more emphasized in using the so-called intensive observing systems to which the lightning localization system belongs.

Diversely from the conventional observing system, the information provided by intensive observing systems can not be easily proved in real-time, and detection errors can not be easily recognized because of the nature of data (*Dombai*, 2006). Lightning data are not continuous meteorological fields. The existence or the lack of such data depends on the real meteorological situation, but it depends on detection errors as well. The latter strongly depends on the technical reliability and the physical state of the observing system.

In 1998 an interferometric lightning localization network named SAFIR HMS was installed in Hungary to follow the total electrical activities of the thunderstorms with detecting and localizing the intracloud discharges on VHF and cloud to ground flashes on LF frequency bands. For long time period the localization precision of SAFIR HMS was far from the promised values. The evaluation of the real localization precision of SAFIR HMS was heavily investigated in 2006. In order to find the source of the gap between the promised and experienced localization errors, simulation calculations were done to evaluate the impacts of *random statistical* and *systematic* localization errors of the SAFIR HMS system. It was found that the badly compensated nonlinearities of detection sensors are the main sources of systematic localization errors, which could reach at about 3–7 degrees in some directions. The random statistical errors of SAFIR HMS are about 0.5–1 degree after our field measurements. It was found also, that the systematic localization errors could be reduced by reanalyzing the raw detection data of SAFIR HMS after having replaced measured azimuth data by corrected azimuth data calculated statistically after comparing the VHF interferometric return stroke positions and the LF TOA – time of arrivals – return stroke positions of the same flashes. The method of localization error calculations and reanalyzing of the SAFIR HMS raw data are described in Section 2.

In searching the way of the operational and automatic quality control of the SAFIR lightning localization system and the provided data, we have developed the *Flash Backward Calculation* method. Using the raw detection data on flashes arriving from detection station and the processed flash data calculated by the SAFIR CPS (Central Processing System), the FBC can continuously provide different activity and quality measurements, detection errors, etc., to be fed into the automatic processes of data assimilation. The method of FBC is described in Section 3.

2. Localization errors and reanalyzing of the SAFIR HMS data

Since July 1998 the SAFIR HMS lightning localization system has been operated on national basis covering about 250,000 km^2 with 5 VHF/LF interferometric direction finder stations (*Dombai*, 1998). From 2000 the Hungarian Meteorological Service developed and introduced a forecaster's

workstation named HAWK for displaying different kinds of meteorological information in a unified coordinate system. The SAFIR HMS lightning data were also integrated into the HAWK display. From that time HAWK has become the unique displaying tool of lightning data for forecasters. The experiences gained by forecasters in the past years show that the SAFIR HMS data could be unreliable even for long time periods. In these periods, in spite of the fact, that the SAFIR status bars are green, the flashes displayed on HAWK are spatially very badly correlated with the radar or with the satellite data, and sometimes they have strange structures, sometimes not real flashes are displayed, and controversially, there are also severe thunderstorms without any flashes displayed. These cases make our forecasters uncertain, and they have very bad opinion about the reliability of the SAFIR HMS data. The joined display of flash data with radar and satellite data shows very sharply all kind of detection errors. By 2002 the SAFIR HMS was extended by the data of 2 additional sensors from Slovakia, which were giving more redundancy in the detection. In spite of this enhanced ability, the detection efficiency and technical reliability of SAFIR HMS were not enough improved (*Dombai*, 2004). As a consequence, the continuation of the functioning of the SAFIR HMS was seriously questioned in 2004. At this time, a special correction method was developed at the HMS to cut all flashes from the display, which are located outside of radar structures with values above dBZ – reflectivity thresholds (*Fülöp*, 2004) – to avoid the misinterpreting of meteorological situations and the false recognition of thunderstorms in the objective analyzing processes.

In 2005 three neighboring countries – Austria, Slovakia, and Hungary – with an extensive support of Vaisala (SAFIR system provider) started the FLASH cooperation aiming to have joined localization systems with more reliability and more precise localization capability on both VHF band – mainly cloud flashes and LF band – mainly return strokes (*Lojou*, 2005). After the evaluation of the first experiences gained on the course of the FLASH in 2005, two main issues were stated. Firstly, the SAFIR system has not enough tools for the continuous monitoring of the changes in the detection capabilities of sensors and all the system. It is typical that forecasters notify the system malfunctions with missed detection of flashes or situations with some extra detected flashes. Secondly, there is a big gap between the values of localization errors announced by the system providers (*Fig. 1*, left) and the localization errors experienced in the FLASH time period. Several times big localization errors around 10–20 km could be seen on HAWK comparing the flash cell positions to radar or satellite data (*Fig. 2*, right).

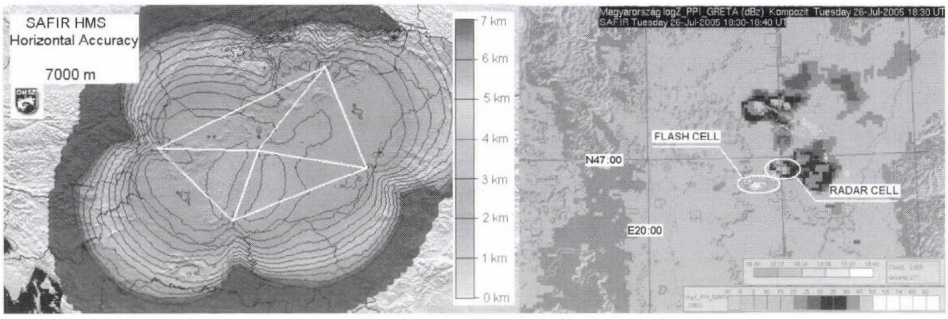


Fig. 1. Localization accuracy calculated by the Vaisala (left) and the localization errors frequently experienced on the HAWK (right – RADAR and SAFIR HMS data on July 26, 2005). The localization error is about 21–22 km.

2.1. Localization error calculations for the SAFIR HMS

The SAFIR HMS is using the goniometric localization method, which means that the position of the VHF sources is determined by crossing points of lines originated from the stations and directed into the measured azimuths. A crossing point needs two lines from two stations. (In practice we have 5 stations, which are giving 10 pairs in result. The selection of appropriate pairs is part of the localization algorithms). The first step in the calculation of the localization error is the calculation of the localization error distribution of the station pairs. Considering the geometrical scheme of crossing lines in *Fig. 2* and the random statistical error of azimuth measurements we may assume, that the possible position of flash will be in the quadrilateral (P_1 P_2 P_3 P_4) which is determined by the crossing points of lines originated from stations into the azimuths modified with mean azimuth errors of stations. The mean error of the localization is assumed to be the square root of the area of this quadrilateral.

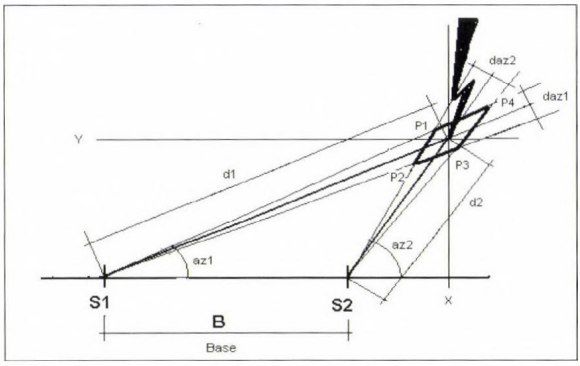


Fig. 2. Geometrical scheme for calculation of the localization error caused by inaccurate azimuth measurements by the SAFIR system.

In the calculation of the localization area we use the *Heron* equations for (P_1 P_2 P_3) triangulation to get the A_1 and for (P_1 P_3 P_4) triangulation to get the A_2 area values:

$$A_1 = \sqrt{s_1(s_1 - a)(s_1 - b)(s_1 - c)} \quad \text{and} \quad A_2 = \sqrt{s_2(s_2 - c)(s_2 - d)(s_2 - e)}, \qquad (1)$$

where

$$s_1 = 0.5(a + b + c) \quad \text{and} \quad s_2 = 0.5(c + d + e),$$

$$a = P_1 P_2, \qquad b = P_2 P_3, \qquad c = P_3 P_1, \qquad d = P_3 P_4, \qquad e = P_4 P_1. \qquad (2)$$

The localization error will be

$$LE = \sqrt{A_1 + A_2}\,. \qquad (3)$$

To get the spatial distribution of localization errors, we need to calculate the localization area values for each grid point $P = (x, y)$ of the covered territory. For the numerical calculation of this we need to know *a, b, c, d, e* values, which are coming from the coordinates of the crossing points P_1, P_2, P_3, P_4. To get these coordinate values around each grid point, first we have to calculate the azimuth values of the lines originated from S_1 and S_2 stations to the crossing points P_1, P_2, P_3, P_4. To calculate these azimuths we need the azimuth of the grid points, which will be corrected with the azimuth errors daz_1, daz_2 later. The grid point azimuths, t_1 and t_2 will be:

$$t_1 = \text{atan}\,(m_1)\,57.3 \quad \text{and} \quad t_2 = \text{atan}\,(m_2)\,57.3, \qquad (4)$$

where

$$m_1 = (y - y_{S1}) / (x - x_{S1}) \quad \text{and} \quad m_2 = (y - y_{S2}) / (x - x_{S2}). \qquad (5)$$

The azimuths of the crossing points, t_{11}, t_{12}, t_{21}, and t_{22}, after correcting with azimuth errors daz_1 and daz_2 will be

$t_{11} = t_1 + daz_1 / 2$ and from S_1 to P_1 and P_4 $\quad t_{12} = t_1 - daz_1 / 2$ from S_1 to P_2 and P_3,

$t_{21} = t_2 + daz_2 / 2$ from S_2 to P_1 and P_2 and $t_{22} = t_2 - daz_2 / 2$ from S_2 to P_3 and P_4. (6)

Now these azimuth values have to be converted into the rise of curve values, m_{ij} for calculating the crossing point coordinates:

$m_{11} = \tan(t_{11}/57.3)$, $m_{12} = \tan(t_{12}/57.3)$, $m_{21} = \tan(t_{21}/57.3)$, $m_{22} = \tan(t_{22}/57.3)$. (7)

Using these rises of curve values we get the coordinate values for crossing points $P_1(x_{11}, y_{11})$, $P_2(x_{21}, y_{21})$, $P_3(x_{22}, y_{22})$, $P_4(x_{12}, y_{12})$.

$$x_{11} = (m_{11}x_{S1} - m_{21}x_{S2} + y_{S2} - y_{S1}) / (m_{11} - m_{21}) \text{ and } y_{11} = m_{11}(x_{11} - x_{S1}) + y_{S1} \text{ for } P_1,$$

$$x_{21} = (m_{12}x_{S1} - m_{21}x_{S2} + y_{S2} - y_{S1}) / (m_{12} - m_{21}) \text{ and } y_{21} = m_{12}(x_{21} - x_{S1}) + y_{S1} \text{ for } P_2,$$

$$x_{22} = (m_{12}x_{S1} - m_{22}x_{S2} + y_{S2} - y_{S1}) / (m_{12} - m_{22}) \text{ and } y_{22} = m_{12}(x_{22} - x_{S1}) + y_{S1} \text{ for } P_3,$$

$$x_{12} = (m_{11}x_{S1} - m_{22}x_{S2} + y_{S2} - y_{S1}) / (m_{11} - m_{22}) \text{ and } y_{12} = m_{11}(x_{12} - x_{S1}) + y_{S1} \text{ for } P_4. \quad (8)$$

At last we get *a, b, c, d, e* values using the coordinate values from above:

$$a = \sqrt{(x_{11} - x_{21})^2 (y_{11} - y_{21})^2},$$
$$b = \sqrt{(x_{21} - x_{22})^2 (y_{21} - y_{22})^2},$$
$$c = \sqrt{(x_{22} - x_{11})^2 (y_{22} - y_{11})^2},$$
$$d = \sqrt{(x_{22} - x_{12})^2 (y_{22} - y_{12})^2},$$
$$e = \sqrt{(x_{11} - x_{12})^2 (y_{11} - y_{12})^2}. \quad (9)$$

In practice, to avoid the extreme localization errors caused by the very low azimuth differences between the crossing lines and by the large distances used in the localization algorithms, limitations are used for these parameters. *Fig. 3* shows the results of azimuth error calculations using the station pair with 160 km base line, and 1 and 2 azimuth errors. The minimum allowed azimuth difference was 10, and the maximum allowed distance was 260 km.

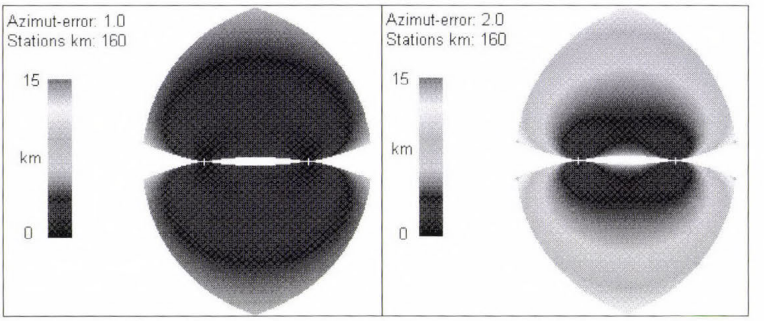


Fig. 3. Structures of localization accuracy of the station pair with 160 km baseline with azimuth errors 1.0° (left) and 2.0° (right). The maximum distance is 260 km and the minimum difference is 10° in azimuth from station1 and from station2.

In *Fig. 3* we can see that the promised localization accuracy of less than 5 km of the SAFIR HMS can be reached only if the azimuth errors are less than

1 degree at each station. If the azimuth errors are larger, the localization error will raise sharply up to 15 km or even more. By analyzing the localization errors calculated with different azimuth errors and baselines, we get that localization errors experienced on HAWK could be answered by supposing some 3–7 degrees variations of azimuth errors, which are far from the expected values.

In order to know the magnitude of the real values of azimuth errors and to evaluate the random statistical and the systematic part of these errors, several field measurements and analyses of raw detection data were done at the central station of the SAFIR HMS, Bugyi. The random statistical part of azimuth errors was evaluated by using fixed VHF sources and the systematic part by using azimuth differences between the detected azimuth by the SAFIR HMS and the calculated azimuth from the GPS coordinates of VHF sources. *Fig. 4* shows the results of field measurements.

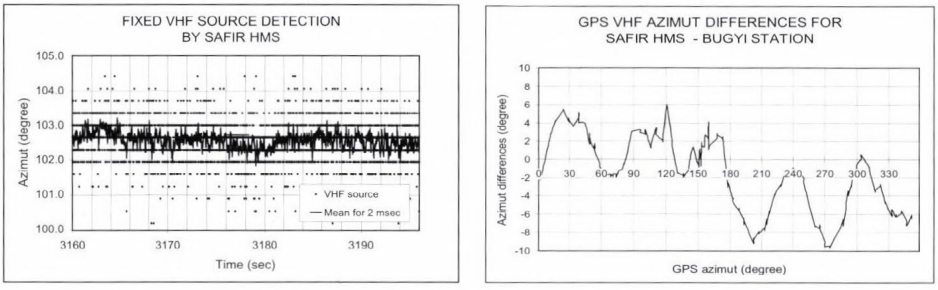


Fig. 4. Results of field measurements for azimuth errors of SAFIR HMS at Bugyi station. Left: random statistical errors – fix source measured on March 17, 2006, right: systematic errors – GPS-VHF azimuth differences around the station measured on June 22, 2006.

From *Fig. 4* left, we can see that the random statistical part of azimuth error is close to the promised values. In this case the dispersion is about 0.6 degree. But from *Fig. 4* right, we can see very large values for the systematic azimuth errors, which are varying from –8 to +5 degrees at Bugyi station. These values are in similar magnitudes to those found in the simulation calculations.

In the period of FLASH we have got a printed report from the Vaisala on the analysis of VHF performances of stations, which were made after the summer period of 2005 (*Lojou*, 2005). In this report VHF/LF coherence was calculated for return strokes using VHF interferometric azimuth and calculated azimuth from LF TOA (time of arrivals) positions. The TOA methods are not used in operational SAFIR 3000 systems, but these stations provide LF data with time resolutions suitable for TOA method. If we suppose that VHF and LF radiations of return strokes are coming from the same positions, then the azimuth values from LF TOA positions can be used as reference positions of VHF sources. Knowing the nature of real flashes it is rather strong hypothesis, but statistically it also seems to be proved. It needs more investigations, because

the TOA methods also have specific localization errors (*Hidayat* and *Ishii*, 1996). From this report we took the azimuth differences and calculated the difference curves shown in *Fig. 5* using spline interpolations. In *Fig. 5* we can see almost the same behavior of the systematic azimuth errors of SAFIR HMS as it was measured by us and shown in *Fig. 4*.

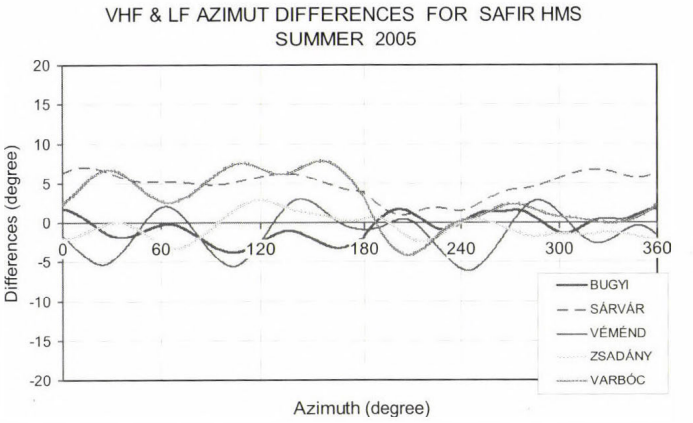


Fig. 5. Azimuth difference curves for all SAFIR HMS stations in the summer period of 2005. (The mean differences in the 0–360 azimuth are calculated between the interferometric VHF and the TOA LF positions of the same return strokes.)

The evaluation of the impact of the big systematic azimuth errors of stations is difficult and needs computer analysis. To do this we have developed a simulation program based on the method described in the previous section. We used the real geometry of the SAFIR HMS with all station pairs and triangulation parameters of localization, and we did azimuth corrections at each station with values of azimuth differences taken from the VAISALA report (*Lojou*, 2005). The calculations are going for each grid point of the covered territory with 2 km resolutions. The results of this simulation are shown in *Fig. 6*.

The localization errors were calculated with the so-called closer pair and mean methods. In the closer pair method a location point is calculated using azimuth values measured by stations, which are at minimum distance from the grid points. This method is used by the SAFIR HMS central processing. In this case the station pair indexes are calculated also marking the station pair providing the given location point. In the mean method a mean location point is calculated from all possible station pair azimuths. In this case a station pair number is calculated also, showing the number of pairs used for the mean position calculation.

Fig. 6 shows that the closer pair method gives much bigger and more inhomogeneous localization error regions than the mean method. Very big

variances of this error changing from region to region can be seen on this maps, and there are very big jumps in these values in nearby regions, where the index of station pair determines the location point changes. In some regions the location error is almost zero, while in other regions these errors exceed 25 km. The inhomogeneous location error regions and these jumps give answer to the experienced phenomena of SAFIR HMS location problems. The deformed asymmetrical location error fields caused by the continuously changing systematic errors of stations in azimuth can be also seen on the location error maps.

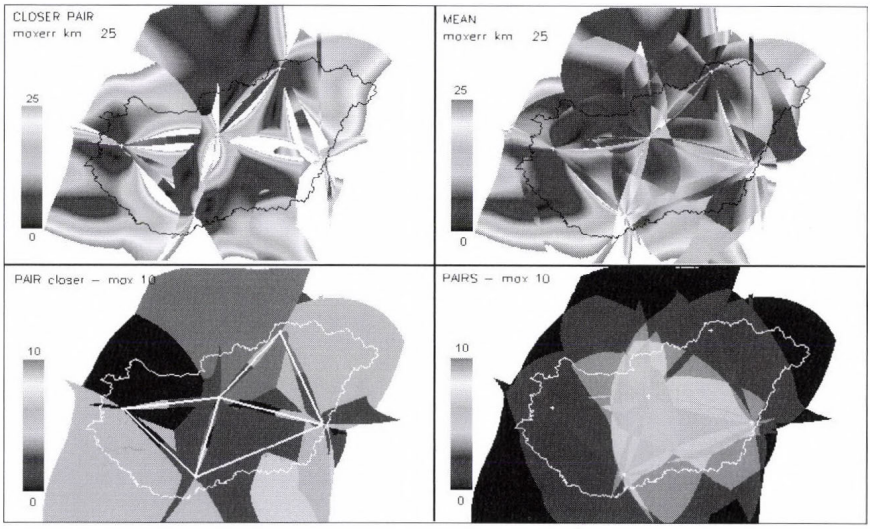


Fig. 6. Localization errors using the azimuth error curves of the SAFIR HMS stations. Closer pair – errors calculated with azimuths 'measured' by closer stations; pair – indexes of station pairs used in the closer pair calculation; mean – errors calculated with azimuths 'measured' by all of the stations; pairs – number of station pairs used in the mean calculations.

2.2. Correction of systematic azimuth errors and reanalyzing of the SAFIR HMS raw data

The fact, that the systematic error can be considered constant in time, gives possibility to develop a method for compensating its impact on the localization data of SAFIR. We know that the correct solution is to create exact azimuth correction tables and load them into stations to compensate the site errors and the nonlinearity of phase measurements in real time processes. We have started to do this, but we have long time data series of lightning locations from which the impact of systematic location errors also needs to be filtered out. At the HMS we have developed a method for reanalyzing the time series of the SAFIR HMS raw data. For this reanalysis we used the two main type

of archived SAFIR data files. We used the so-called B$ archive files containing the VHF and LF detection data provided by the SAFIR stations and the so-called T$ archive files containing data on all localized intracloud flashes and return strokes.

The main steps of this reanalysis are the followings: By the analysis of B$ raw data files of SAFIR with DAM analyzing tool of Vaisala we can derive the azimuth difference curves of the VHF and LF locations. Using these curves we can calculate azimuth correction tables for each station, and using these correction tables we replace all the reported azimuth values by corrected ones in the raw SAFIR data files. At last the localization processes will be run again with the same triangulation but with modified north alignment values to provide us the corrected T$ localization data files. The impact of this reanalysis is illustrated in *Fig. 7*, which shows a map of the displacements of location points with directions and distances.

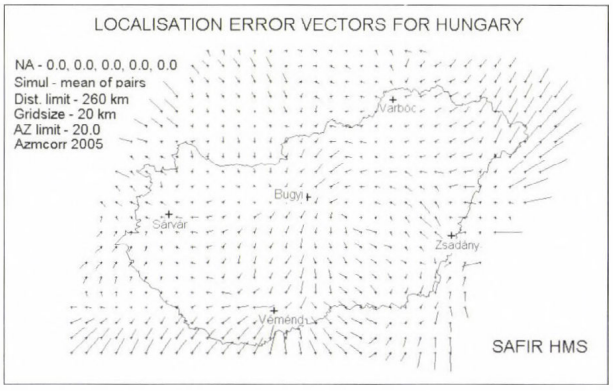


Fig. 7. Displacements of 'gridded flash positions'. Results of the simulation of the SAFIR HMS localization errors using azimuth differences on VHF and LF TOA of the SAFIR HMS stations.

For the validation of the reanalysis of SAFIR HMS data we have used jointly displayed radar and SAFIR HMS localization data precisely aligned in time and space. The time window for the SAFIR HMS data was +5 /–5 minutes around the time stamps of our national radar composites. The reanalysis has been done for the most severe thunderstorms in the summer period of 2005.

Fig. 8 clearly shows that the reanalysis gives better correlated SAFIR HMS data with radar data. The flash cell structure has changed slightly and has been placed into the radar data covered regions near to the radar cells. This joint display after the reanalysis shows better correlated SAFIR HMS and radar data in general for the cases of 18 thunderstorm days of 2005. The reanalysis of the statistical characteristics of the azimuth differences also shows better localization accuracy (*Table 1*).

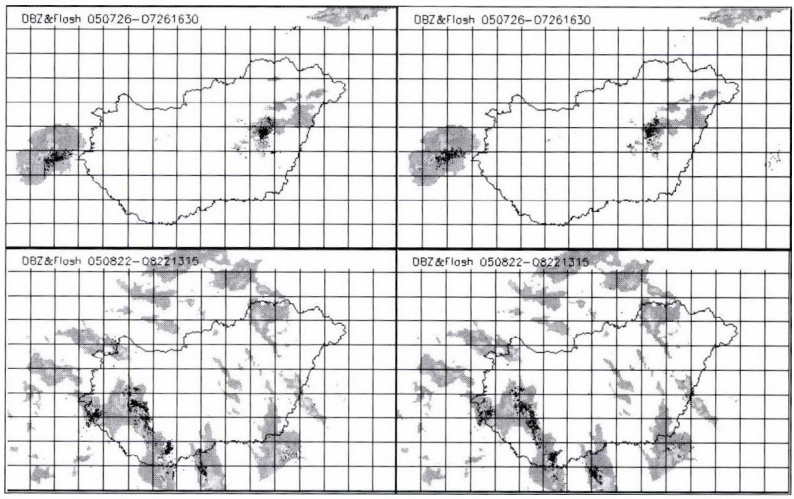


Fig. 8. Results of the reanalysis of SAFIR HMS data using azimuth differences curve of stations – jointly displayed SAFIR HMS location and radar reflectivity data on July 26, 2005 (above) and on August 22, 2005 (below). The original images are on the left, the reanalyzed ones are on the right. The grid size is 50 km.

Table 1. Statistical characteristics of the differences between VHF and LF TOA azimuths before and after reanalyzing the raw data of the SAFIR HMS in 2005

	Bugyi	**Sárvár**	**Véménd**	**Zsadány**	**Varbóc**
Before reanalyzing					
Mean	-0.54	4.54	-1.29	-0.53	2.67
Dispersion	1.40	1.72	2.41	1.29	3.17
Variances	1.97	2.95	5.83	1.66	10.02
Region	4.92	6.33	8.79	5.63	11.60
Minimum	-3.52	0.70	-5.98	-3.16	-3.87
Maximum	1.41	7.03	2.81	2.46	7.73
After reanalyzing					
Mean	-0.16	0.84	-0.37	-0.04	0.10
Dispersion	0.66	0.83	1.10	0.55	0.57
Variances	0.44	0.69	1.21	0.30	0.33
Region	3.16	3.52	4.57	2.81	2.46
Minimum	-2.11	-0.70	-2.46	-1.41	-1.05
Maximum	1.05	2.81	2.11	1.41	1.41

The proposed correction method was applied for the correction of SAFIR HMS data on August 20, 2006. In the evening of this date, a very heavy thunderstorm was developed and moved through Hungary causing serious injuries and death at Budapest. Examining the jointly displayed radar and SAFIR HMS data on the HAWK system we noticed almost 50 km position errors in the southeast part of Hungary. After analyzing the azimuth differences

of VHF and LF TOA, we found very big azimuth errors for Zsadány station, which was caused by a big dephasing of a dipole pair (*Fig. 9*). After correcting the azimuth values of each VHF sources in the raw SAFIR HMS B$ file and making the processed T$ file with locations from the corrected B$, we reanalyzed the radar and SAFIR HMS data (*Fig. 10*).

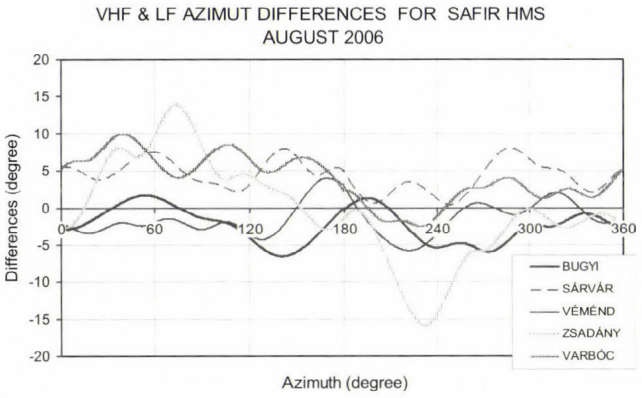


Fig. 9. Azimuth difference curves for all SAFIR HMS stations in August 2006. (The mean differences in the 0–360 azimuth were calculated between the interferometric VHF and the TOA LF positions of the same return strokes.) The azimuth error is very high for Zsadány station, it is about +/–15 degree.

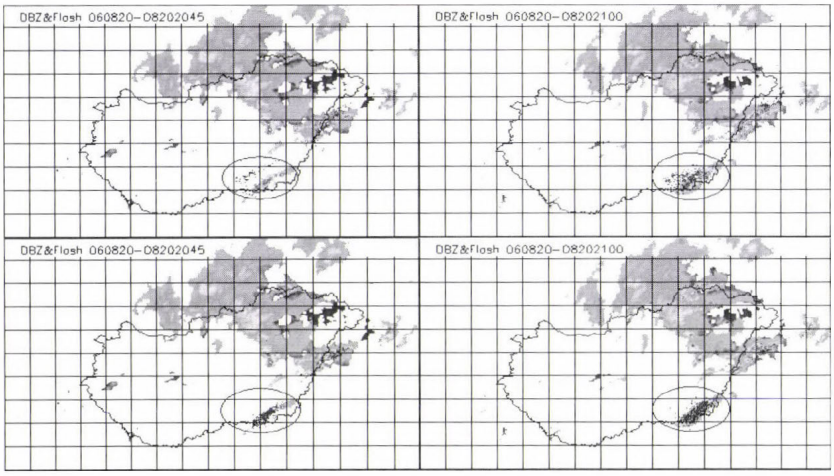


Fig. 10. Results of the reanalysis of SAFIR HMS data using azimuth differences curve of stations – jointly displayed SAFIR HMS location and radar reflectivity data on August 20, 2006, 20:45 UTC (left) and 21:00 UTC (right). The original images are above the reanalyzed ones are below. The grid size is 50 km. The corrected position error was about 50 km at the southeast part of Hungary.

Our correction method is a kind of site error correction method, although, in the focus of the developing was not the compensation of the site dependence of the propagation of the electromagnetic radiation of the flashes but the compensation of the systematic errors of the SAFIR HMS interferometric receivers.

3. *Flash backward calculation*

The basis of the FBC method is that from the data (time, geographical coordinates, amplitude, etc) of *localized flashes* we can derive all the set of the *detection data* (awaited detection time, azimuth, detection level, etc.), which most probably were detected at particular stations. After these calculations we match the calculated detection data with the real detected data for searching pairs between localized flashes and their real detection data at each station. When we have found the origins of localized flashes we mark the real detection data with MF and the calculated detection data with MD at each station. After this matching we can compare the *backwardly* calculated detection data with the *real* detected data for all flashes. In *Fig. 11* we illustrate this calculation method for the VHF sensors of SAFIR HMS.

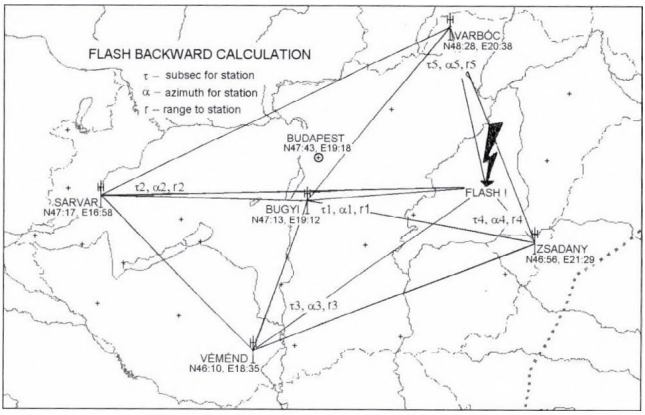


Fig. 11. Geographical positions of the SAFIR HMS stations, and the illustration of the FBC method.

In *Table 2* and *3* we illustrate the FBC results. The FBC was carried out on real flash data from T$ file and on real sensor data from B$ file for a thunderstorm on August 1, 1998. In these tables we show the successfully matched flashes and detections in a second time period. Columns of *Table 2* marked with MD indicate the ordering number of detections and vice versa columns of *Table 3* marked with MF indicate the ordering number of localized flashes.

Table 2. Flash data from T$ file and FBC data for each station with MD (matching number pointing for detections) on August 1, 1998 in the 53,443rd second time period of the day

	Flashes			Hargita				Sárvár				Véménd			
No.	**subs.**	**x**	**y**	**subs.**	**azm.**	**dist.**	**MD**	**subs.**	**azm.**	**dist.**	**MD**	**subs.**	**azm.**	**dist.**	**MD**
1	820	89.2	117.4	824	168	135.9	2	829	206	294.1	0	828	105	264.5	0
2	823	89.6	116.7	827	169	135.8	3	832	207	294.3	0	831	106	264.2	1
3	824	90.4	118.9	828	167	137.6	0	833	206	295.6	1	832	105	266.3	0
4	825	91.1	121.1	829	165	139.4	4	834	204	297.1	0	833	105	268.6	0
5	826	91.3	120.1	830	166	139.1	5	835	205	297.0	0	834	105	268.0	2
6	1477	-0.3	114.4	1479	63	71.8	7	1483	188	209.1	0	1484	53	219.3	0
7	1478	2.1	116.3	1480	66	74.5	0	1485	187	212.1	0	1485	54	221.9	0
8	4017	9.4	129.8	4019	69	89.8	11	4024	180	224.4	0	4024	56	237.1	0
9	8169	66.7	243.3	8176	73	216.9	13	8180	143	335.0	0	8181	63	363.5	0
10	8997	71.2	248.1	9004	74	223.2	14	9008	142	341.6	2	9009	64	369.8	0
11	8998	71.4	245.4	9005	75	220.9	0	9009	144	340.0	0	9010	64	367.3	0
12	9027	9.7	139.6	9030	62	99.0	16	9034	174	229.2	0	9035	54	246.5	0

Remarks for the columns: subs – detection time in 100 us; x, y – coordinate of flashes in km; dist – distance to a flash from a station; MD – matching number pointing for a detection at a station

Table 3. Real sensor data from B$ file with MF (matching number pointing for flashes) on August 1, 1998 in the 53,443rd second time period of the day

	Hargita				Sárvár				Véménd			
No.	**subs.**	**azm.**	**lev.**	**MF**	**subs.**	**azm.**	**lev.**	**MF**	**subs.**	**azm.**	**lev.**	**MF**
1	812	153	101	0	834	182	80	3	832	98	77	2
2	824	161	95	1	9009	134	79	10	833	102	92	5
3	827	162	91	2	0	0	0	0	834	95	82	0
4	828	154	110	4	0	0	0	0	0	0	0	0
5	829	152	105	5	0	0	0	0	0	0	0	0
6	830	160	95	0	0	0	0	0	0	0	0	0
7	1479	40	101	6	0	0	0	0	0	0	0	0
8	1480	59	87	0	0	0	0	0	0	0	0	0
9	1956	31	84	0	0	0	0	0	0	0	0	0
10	2985	44	76	0	0	0	0	0	0	0	0	0
11	4020	54	82	8	0	0	0	0	0	0	0	0
12	4021	56	83	0	0	0	0	0	0	0	0	0
13	8176	64	77	9	0	0	0	0	0	0	0	0
14	9004	64	86	10	0	0	0	0	0	0	0	0
15	9005	69	92	0	0	0	0	0	0	0	0	0
16	9030	49	88	12	0	0	0	0	0	0	0	0

Remarks for the columns: subs – detection time in 100 us; azm – azimut of detected flashes; lev – signal level of detection; MF – matching number pointing for localized flashes

If MD or MF is equal to 0, it indicates that the matching was unsuccessful. When MD is equal to 0 at a station in *Table 2*, it means that the station did not detect that flash, *missed detection.* If MF is equal to 0 at a station in *Table 3*, it means that the station reports without flash, *false detection*. On the course of

FBC using the MD and MF marks we can calculate the differences between calculated and really detected parameters of flashes. Differences in azimuth and timing and relative amplitudes are illustrated in *Table 4.*

Table 4. Differences between the calculated and detected sensor data with MD (matching number) on August 1, 1998 in the 53,443rd second time period of the day

	Flashes			Hargita				Sárvár				Véménd			
No.	**subs.**	**x**	**y**	**subs.**	**azm.**	**lev.**	**MD**	**subs.**	**azm.**	**lev.**	**MD**	**subs.**	**azm.**	**lev.**	**MD**
1	820	89.2	117.4	0	7	0	2	0	0	0	0	0	0	0	0
2	823	89.6	116.7	0	7	0	3	0	0	0	0	-1	8	0	1
3	824	90.4	118.9	0	0	0	0	-1	24	0	1	0	0	0	0
4	825	91.1	121.1	1	11	0	4	0	0	0	0	0	0	0	0
5	826	91.3	120.1	1	14	0	5	0	0	0	0	1	3	0	2
7	1478	2.1	116.3	0	0	0	0	0	0	0	0	0	0	0	0
8	4017	9.4	129.8	-1	15	0	11	0	0	0	0	0	0	0	0
9	8169	66.7	243.3	0	9	0	13	0	0	0	0	0	0	0	0
10	8997	71.2	248.1	0	10	0	14	-1	8	0	2	0	0	0	0
12	9027	9.7	139.6	0	13	0	16	0	0	0	0	0	0	0	0

Remarks for the columns: subs – detection time in 100 us; x, y – coordinate of flashes in km; azm – azimut of detected flashes; lev – signal level of detection; MD – matching number pointing for detection at a station

The FBC method provides us not only the differences of measured and calculated detection parameters for all stations but also the possibility to set up different quality measurements and their ratings for each station or the whole system. The important derived parameters are the followings:

Detection ratio – detection number compared to the possible maximum VHF and LF,

Good detection ratio – proportion of detections associated with flashes at a station,

False detection ratio – proportion of detections without any flashes at a station,

Missed detection ratio – proportion of detections associated with flashes which are missing at a station,

Good station – stations where the *good detection ratio* is bigger than a threshold and the *false detection ratio* is smaller than a threshold,

Azimuth error – difference between detected and calculated azimuths on a flash.

In *Fig. 12* we can see a thunderstorm event on August 1, 1998. At the top, on the left the CC flash activity, on the right the station *VHF detection activities* are shown, at the bottom, on the left the *good detection ratio*, on the right the *false detection ratio* are shown for each station. We can see that two stations

were working with good detection ratio about 80% for all the time of the thunderstorm activity. For other stations this ratio was low, but the distances were high for those stations. When the false detection ratio is high it shows some detection level problems or noisy detection for those stations.

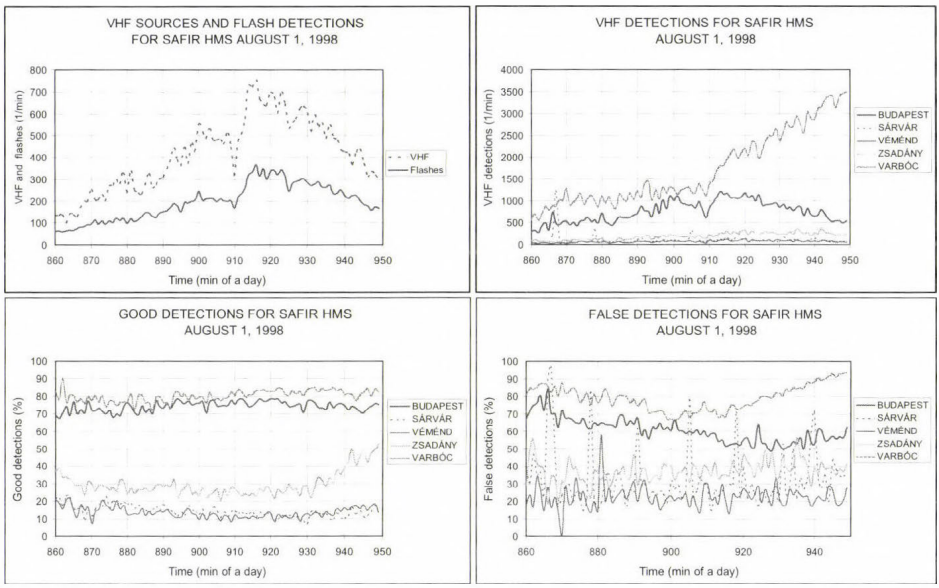


Fig. 12. Quality measurements from FBC results for a severe thunderstorm event on August 1, 1998.

The FBC can be done in real time and the results (azimuth errors, timing problems, detection level problems, etc.) could be displayed or sent to the maintenance team. Also the FBC can be equipped with *alarming levels* for different quality measurements, which could launch some automatic processes to avoid the long time system malfunctions. We hope that the results of our work will be implemented into operational practice soon.

4. Conclusions

- The validation of the real localization accuracy is a very important question of the functioning of the SAFIR HMS system. Now this accuracy is far behind the promises, requirements, and possibilities.
- In this paper it was shown that the reanalysis of raw detection data with corrected azimuth data and the FBC calculation gives possibility to enhance the localization accuracy and reliability of the SAFIR HMS system.

- This reanalysis can help us only if the azimuth differences of VHF and LF TOA positions are derived from sufficiently long time series. The use of short time periods for such reanalysis needs more investigations. It is important, that during the reanalysis the significant changes and settings of station parameters (north alignment, Phi0 parameters, etc.) must be avoided.
- The results of the repeated coherence tests of the VHF and LF TOA azimuth on the corrected raw data files show that the azimuth differences decrease by a magnitude of 2, which means that the azimuth correction tables derived in this way are better to use than the azimuth correction tables provided by the SAFIR system providers.
- The best way to enhance the localization accuracy is to use station and site specific azimuth correction tables loaded into the stations. To get such tables, carefully made field measurements of azimuth responses of stations must be effectuated. We have further plans to carry out such measurements in the near future by using real time RTK GPS and a VHF signal generator.

References

Dombai, F., 1998: Lightning localization network in Hungary (in Hungarian). *Természet Világa (Special edition 1)*, 31–34.

Dombai, F., 2004: On the reliability of the Hungarian SAFIR lightning localization network (in Hungarian). In *Meteorological Scientific Days – Intense Meteorological Observations* (ed.: *Gy. Gyuró* and *J. Nagy*). Országos Meteorológiai Szolgálat, Budapest, 85–96.

Dombai, F., 2006: The importance of advanced operational reliability and readiness monitoring of the SAFIR HMS lightning localization system. *Proceedings of the International Lightning Detection Conference.* Tucson, Arizona, 2006.

Fülöp, A., 2004: Meteorological application of SAFIR lightning localization network data (in Hungarian). *Thesis of degree. Faculty of Meteorology at University of Eötvös Loránd*, Budapest.

Hidayat, S. and *Ishii, M.*, 1996: Error in lightning location by time difference and direction technique–Theory. *Transactions IEE Japan 116-B*, 410–416.

Lojou, J.Y., 2005: Performance evaluation of the FLASH VHF sensors. *Flash Technical Report, Vaisala Inc., Tucson.*

Richard, P. and *Aufrray, G.*, 1985: VHF-UHF interferometric measurements, applications to lightning discharge mapping. *Radio Science 20*, 171–192.

IDŐJÁRÁS

Quarterly Journal of the Hungarian Meteorological Service
Vol. 112, No. 1, January–March 2008, pp. 33–43

Modeling water temperature of Hungarian rice fields

Béla Gombos

Faculty of Agricultural Water and Environmental Management, Tessedik Sámuel College, Szabadság út 1-3, H-5540 Szarvas, Hungary; E-mail: gombos.bela@mvk.tsf.hu

(Manuscript received in final form February 15, 2008)

Abstract—Low temperature during the sensitive phenophases of rice (*Oryza sativa* L.) can cause spikelet sterility. In Hungary this is one of the main weather and climatic risks resulting in yield loss. The thermal characteristics and heat balance of flooding water are very different from that of the air. Therefore, the modifying of water level gives an effective tool for rice growers to reduce cold stress. To help this and also to improve weather-rice models it is essential to predict water temperature from standard meteorological data.

Two empirical models were established based on water temperature measurements in a representative Hungarian rice field during the reproductive and early ripening stages from mid-July till the beginning of September in 2006 (model construction) and 2005 (model verification). Both models proved an efficient and accurate tool in simulating daily minimum, maximum, and average of flooding water temperature. The error in prediction is negligible from a practical point of view, especially if compared to the large differences between the extremes of air and water temperature.

Key-words: temperature, flooding water, rice (*Oryza sativa* L.), empirical model

1. Introduction

Rice (*Oryza sativa* L.) is grown in Hungary on approximately 2000 hectares almost totally under flooded conditions. From the 3–4 leaf stages up to the dough ripening stage continuous water cover is ensured on the field (*Simonné*, 1983). This is the safest way to avoid sub-optimal water supply, which can reduce yield more for rice than for any other cereal crops (*Inthapan* and *Fukai*, 1988). Additionally, a water layer can act effectively in weed control and in thermal control of the fields. Rice growers working at high latitudes (Hungary, North Italy, North Japan, North China, South Australia) consider the water layer as the most important tool to reduce climatic risk caused by extreme temperature in the reproductive phenological phase (*Polgár*, 1961; *Wagner*, 1957; *Simonné*, 1979; *Confalonieri et al.*, 2002; *Shimono et al.*, 2005; *Gunawardena et al.*,

2001). As specific heat capacity of water is much higher than that of air, diurnal temperature amplitudes of flooding water are reduced (*Wagner*, 1966). In the night the flooding water is usually warmer than the air above it, and the benefit of deep water can reach 4 to 6 °C in Hungary (*Gombos*, 2007), 5 °C in Japan (*Shimono et al.*, 2005) and 3.5 to 7 °C in Australia (*Gunawardena et al.*, 2001). During the daytime temperature differences with an opposite sign are typical, which can be as high as 14 °C in some extreme situations (*Dingkuhn at al.*, 1994).

Low temperature in the sensitive phenophases (booting stage, heading, anthesis) can result in significant yield loss due to spikelet sterility. The degree of damage is correlated more with water temperature (*Tw*) than with air temperature (*Ta*) (*Shimono et al.*, 2005; *Roel et al.*, 2005). The rate of development is also determined by water temperature until the growing point of rice is under the water level. Additionally, the temperature of flooding water plays an important role in temperature-dependent soil biochemical transformations. A micrometeorological model able to estimate *Tw* from *Ta* measured by standard meteorological stations (Stevenson screen) could significantly improve the accuracy and reliability of rice simulation models. More research is required to develop models of floodwater temperature and their incorporation into crop simulation models (*Confalonieri et al.*, 2005, 2007; *Cola et al.*, 2007; *Mariani et al.*, 2007). Studies of different kind of water masses provide some theoretical basis and practical information for modeling the effect of floodwater on microclimate of rice fields. However, adaptation of models is problematic, especially because of different vegetation (lack of vegetation, morpho-physiology of the plants), temporary, and spatial scales (*Burba et al.*, 1999; *Jacobs et al.*, 1997; *Gal et al.*, 2003).

Two types of water temperature modeling approaches can be used, namely the deterministic (mechanical) and stochastic (statistical) approaches.

Empirical models based on reliable data can give a good prediction of water temperature, but their weakness is their limited validation. Such models can be used only under circumstances, which characterize the model parameterization. Mechanical models are more sophisticated and more general. They are based on physical equations (energy balance, turbulent transfer processes), but usually contain more or less empirical submodels.

In Hungarian rice fields the main determinants of floodwater temperature (i.e., meteorological conditions, canopy development and structure, irrigation water management) do not show large discrepancies. Therefore, an empirical model could be appropriate for the estimation of the water temperature of most rice fields. Our aim was to create such an empirical model, where the easy availability of input parameters is an important aspect, too.

The importance of such a floodwater temperature model is that it can be built in weather-rice models (simulation model, cold stress model) and be an effective tool for rice growers to calculate water temperature for the next 5–10 days using data of weather forecasts. This information can improve water management, particularly by highlighting the advantages of modifying the water level.

2. *Materials and methods*

2.1. Field measurements

Recently, Hungarian rice production has been concentrated in the south-eastern part of the country, predominantly in large farms in the Körös River Region. Therefore, a rice field of 200 hectares, approximately 1 km distance from the river Hármas-Körös (46°55'N, 20°32'E) was chosen as the study area. This territory is representative of the climatic, soil, and technological conditions of rice growing areas in Hungary. As is common, the field is subdivided into 4 ha (200 × 200 m) units, where independent floodwater level management is possible. One of these plots with a stable and relatively high (25–30 cm) floodwater level with a well developed canopy of cultivar *Bioryza* supplied the basis for our measurements.

Temperature measurements were conducted in 2005 and 2006 from mid-July till the beginning of September during the reproductive and ripening stages of rice. Thermometers were placed near the centre of the plot to minimize the edge effect ("oasis-effect"). In 2005 mini waterproof thermologgers (HOBO Pendant UA-002) registered the water temperature at 5 and 15 cm and the soil temperature at 5 cm under the soil surface in every 20 minutes. In 2006, measurements were extended to the top water layer and to different levels of air. The water temperature at 25 cm and the air temperature at 35, 60, and 85 cm were measured with a thermologger with 4 external sensors (HOBO U12-006). The sampling interval was 5, 10, and 20 minutes in the air, water, and soil, respectively, according to their thermal characteristics.

Data on air temperature at 2 m were measured in a traditional weather shelter (Stevenson screen) at 1 km distance from the flooded rice fields (HOBO U12-006). Additionally, an automatic weather station (Vaisala MAWS-301) near the experiment area (4 km) supplied global radiation, wind, and humidity data.

A detailed data set from 2006 was used to construct the model, while verification was carried out with independent meteorological data from 2005.

2.2. The theoretical base and structure of the model

The energy balance of the water surface can be approximated as:

$$R_n + G + H + LE = 0, \tag{1}$$

where R_n is the net radiation, G is the heat stored in the floodwater and the subsoil, LE is the latent heat flux, and H is the sensible heat flux (*Oke*, 1978).

Heat stored in water (G) can be calculated from the change in mean water temperature:

$$G = c_w d\, \Delta Tw / \Delta t, \tag{2}$$

where ($\Delta Tw/\Delta t$) is the time rate of change in mean water temperature, c_w is the water heat capacity, and d is the water depth.

The flooding water temperature usually reaches its minimum (Tw_{min}) in the morning (t_{min}) and its maximum (Tw_{max}) in the late afternoon hours (t_{max}), i.e., $G > 0$ from t_{min} till t_{max} and $G < 0$ from t_{max} till t_{min} of the next day (*Wagner*, 1966; *Uchijima*, 1976; *Burba et al.*, 1999). These natural time intervals with non-identical length were chosen for the time steps of our model.

The total increase of heat stored in the floodwater during daytime ($G\uparrow$) is the integral of G from t_{min} to t_{max}, and the total decrease of heat during nighttime ($G\downarrow$) is the integral of G (Eq. (2)) from t_{max} to t_{min} on the next day:

$$G\uparrow = c_w d\, \Delta Ti, \tag{3}$$

$$G\downarrow = c_w d\, \Delta Td, \tag{4}$$

where $\Delta Ti = Tw_{max} - Tw_{min}$, $\Delta Td = Tw_{min+1} - Tw_{max}$, and +1 in index means the next day.

The warming process during the daytime and cooling at night have different characteristics. During the daytime, the main driving force of energy balance is the incoming short wave radiation, and the temperature of flooding water decreases downwards from the surface resulting in stabile stratification (*Wagner*, 1966). At night, the long wave radiative cooling at the surface of the water body is the main driving force, and the decrease of water temperature in the top layer increases the water density, which is responsible for the growth of a mixing layer of uniform temperature and density.

A dynamic model was constructed, where daily ΔTi and ΔTd values were empirically estimated and alternately cumulated during the whole study period. This process resulted in calculated time series of minimum and maximum water temperature values. It means, that natural time intervals with non-identical length – according to the sign of G – were the time steps of our model.

The procedure of calculation is as follows:

1. estimating minimum water temperature of Day_1: giving an initial value of $Tw_{min,1}$,
2. calculating daytime increase of water temperature using an empirical relationship with meteorological parameters ($\rightarrow \Delta Ti_n$),
3. calculating maximum water temperature: $Tw_{max,n} = Tw_{min,n} + \Delta Ti_n$,
4. calculating nighttime decrease of Tw using an empirical relationship ($\rightarrow \Delta Td_n$), and
5. calculating minimum water temperature: $Tw_{min,n+1} = Tw_{max,n} + \Delta Td_n$.

The value of n represents the number of day of simulation ($n = 1$: 1st day, $n = N$: final day). Steps from 2 to 5 are to repeat until $n = N$.

An initial water temperature value $Tw_{min,1}$ (or $Tw_{max,1}$) is needed, it have to be given in Step 1.

2.3. *Description of the empirical algorithm*

Our model estimates ΔTi_n and ΔTd_n empirically. Only daily data available from standard meteorological stations were used in calculation of empirical relationships. In cases of both ΔTi_n and ΔTd_n, the water temperature was also used as input to ensure stability of the model due to negative feedback. To do this "warming force" (*WF*) and "cooling force" (*CF*) of the air were checked as possible input variables, as defined in Eqs. (5)–(6).

$$WF_n = Ta_{max,n} - Tw_{min,n}, \tag{5}$$

$$CF_n = Ta_{min,n+1} - Tw_{max,n}, \tag{6}$$

where $Ta_{max,n}$ is the daily maximum air temperature (°C) on Day_n and $Ta_{min,n+1}$ is the daily minimum air temperature (°C) on Day_{n+1}. The physical basis of this assumption is that the sensible heat flux is a linear function of the temperature gradient. This means that the difference between the water and air temperature influences the heat storage term (G) and its integrals ($G\uparrow$ and $G\downarrow$). Consequently, *WF* and *CF* must be in a close linear relationship with ΔTi and ΔTd, respectively. Regression analyses showed that other air temperature parameters (such as average of different periods within a day) used in terms *WF* and *CF* can not improve the model significantly. Therefore, the best choice is to involve Ta_{min} and Ta_{max}, especially because of the easy availability of these data.

The model construction was based on data set from July 20 until August 31, 2006. Water temperature in the medium water level was appropriate to use in model instead of the average temperature of the whole water layer (see details in Section 3)

Two models were constructed. Model 1 (M1) is a very simple one parameter linear regression with input parameters of only *WF* and *CF*, i.e., not more than the knowledge of daily maximum and minimum air temperature is required. Here ΔTi and ΔTd are estimated using the regression equations (Eqs. (7)–(8)):

$$\Delta Ti = 0.323\ WF + 0.73, \tag{7}$$

$$\Delta Td = 0.387\ CF - 0.12. \tag{8}$$

Model 2 (M2) was developed by involving additional parameters into M1. The main criteria for each new input variable were:

- significant improvement ($P = 0.05$) of predicting power of regression,
- availability in standard meteorological data set,
- possibly low correlation with other model parameters,
- simplicity, with clear physical effect on water temperature.

Correlation analyses, stepwise (forward, interactive) regression analysis with Systat 9 statistical software, and applying the above criteria resulted in multilinear regression model:

$$\Delta Ti = 0.135\ RG + 0.133\ WF - 0.46, \tag{9}$$

$$\Delta Td = 0.282\ CF - 0.0473\ RH + 0.195\ w + 3.67, \tag{10}$$

where RG is the daily sum of global radiation (MJ m^{-2}), RH is the daily average of relative air humidity (%), and w is the daily average wind speed (m s^{-1}) at 10 m height.

As expected, the increase of water temperature during daytime (ΔTi) was in strongest correlation with RG, but the temperature difference between air and water (WF) had similar importance.

CF was the most important factor during the cooling period of water. RH is in negative correlation with ΔTd: in case of lower RH values, latent heat loss from water becomes higher. Low RH in daily average usually means strong radiation and higher air temperature at daytime, and so higher ΔTd values can occur because of the increased level of Tw_{max}, too.

Wind speed is not a significant factor in the daytime (Eq. (9)), but an important factor in cooling at night (Eq. (10)). Wind increases both sensible and latent heat fluxes, but in the daytime the direction of these fluxes is opposite. On the contrary, at night the direction of sensible and latent heat flux is usually identical, causing increased heat loss of water layer by windy weather.

2.4. Statistical analyses

The daily water temperature values (mean, minimum, maximum) predicted by our model were compared with the measured values from the rice field. Four complementary statistical criteria were used to compare the predicted (Tp_i) and observed (To_i) values of daily temperature, n being the number of day:

- Coefficient of determination (CD), which indicates whether the model reproduces the trend of measured values or not. Values near 1 are optimal.
- The root mean square error (RMSE):

$$RMSE = \sqrt{\sum \frac{(Tp_i - To_i)^2}{n}}. \tag{11}$$

  This calculation provides the mean difference between predicted and measured values, the smaller the $RMSE$, the better the prediction.
- The modeling efficiency (EF):

$$EF = 1 - \frac{\sum (Tp_i - To_i)^2}{\sum (To_i - \overline{To})^2}. \tag{12}$$

The optimum of this coefficient is 1; if positive, the model is a better predictor than the average of measured values.

- The coefficient of residual mass (*CRM*):

$$CRM = \frac{\sum To_i - \sum Tp_i}{\sum To_i}. \tag{13}$$

Positive coefficient values mean model underestimation, optimum value is 0.

3. Results

The diurnal course of water temperature at different levels and the mean temperature of the whole floodwater layer – the average of August 2006 – is shown in *Fig. 1*. It can be clearly seen that at night (22–06 hours) the temperature is almost the same in each layer. In the evening the isotermia begins to develop first in the upper layer, and the mixed isotherm layer expands downwards. From the morning hours the incoming radiation builds up a well developed thermal gradient and stabile stratification of the flooding water. The mean temperature of the water body (calculated from values of the three levels) is close to the temperature of the medium water level (15 cm). The difference of their maximum values is only approximately 0.2 °C, and the minimum values are almost identical. Therefore, temperature of the medium level seems to be suitable to characterize the whole water layer.

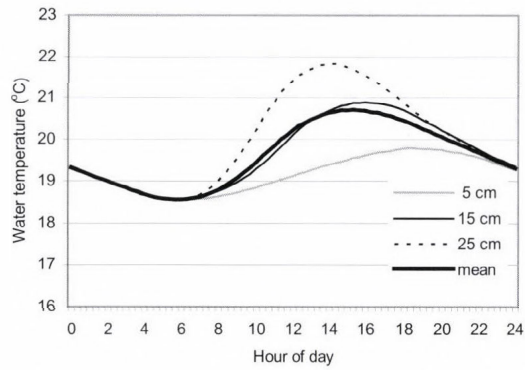


Fig. 1. Average diurnal course of the water temperature at different levels and mean temperature of the whole water layer in August 2006. (Height of the levels are given in centimeters above the soil surface.)

3.1. *Model verification*

In our models the rates were calculated according to empirical relationships described in Eqs. (7)–(10). A parallel calculation of the rates was done to get the course of the minimum and maximum water temperature. Additionally, the averages of minimum and maximum were also determined and included in the verification as daily mean water temperature (Tw_{mean}).

A very good correspondence was found between the simulated and observed values in 2006, especially in case of Model 2 (*Fig. 2*). Model 1 (M1) accounted for 92% and 96% of the variation in minimum and maximum water temperature, respectively. Model 2 (M2) resulted in significantly better predictions than M1 with $CD = 0.98$ both in Tw_{min} and Tw_{max}. The *RMSE* values were reduced to nearly half due to the inclusion of additional input variables into M1 (*Table 1*). The model accuracy is evident in M2, looking at the low values of *RMSE*, at the values of EF close to one and of CRM very close to zero. Against the simplicity of M1, it also resulted in prediction with low error.

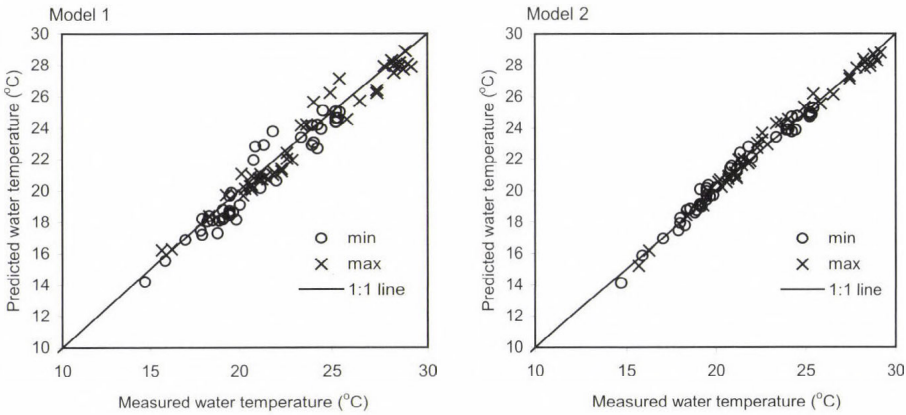


Fig. 2. Comparison of measured and predicted sets of water temperature (minimum, maximum) in 2006 (left: Model 1, right: Model 2).

In 2005, when the validation was based on independent data set, all of the fitting indices show that Model 2 has lost its advantage compared to Model 1. Moreover, in predicting Tw_{min}, M1 became slightly better than M2. Predicting Tw_{max} is the weakest point of our models: $RMSE = 1.31$ (M1) and 1.2 (M2). Almost the same quality of information about mean water temperature is provided by M1 and M2. However, the statistical parameters proved the success of both models.

Table 1. Parameters of model verification

	2006				2005			
	RMSE	***EF***	***CRM***	***CD***	***RMSE***	***EF***	***CRM***	***CD***
Model 1								
Min	0.92	0.90	0.02	0.92	0.83	0.89	0.00	0.91
Max	0.78	0.95	0.01	0.96	1.31	0.81	0.01	0.83
Mean	0.79	0.94	0.01	0.95	0.93	0.87	0.01	0.89
Model 2								
Min	0.44	0.98	-0.00	0.98	1.01	0.84	-0.03	0.89
Max	0.43	0.99	-0.00	0.98	1.20	0.84	-0.01	0.85
Mean	0.41	0.98	-0.00	0.98	0.96	0.87	-0.02	0.90

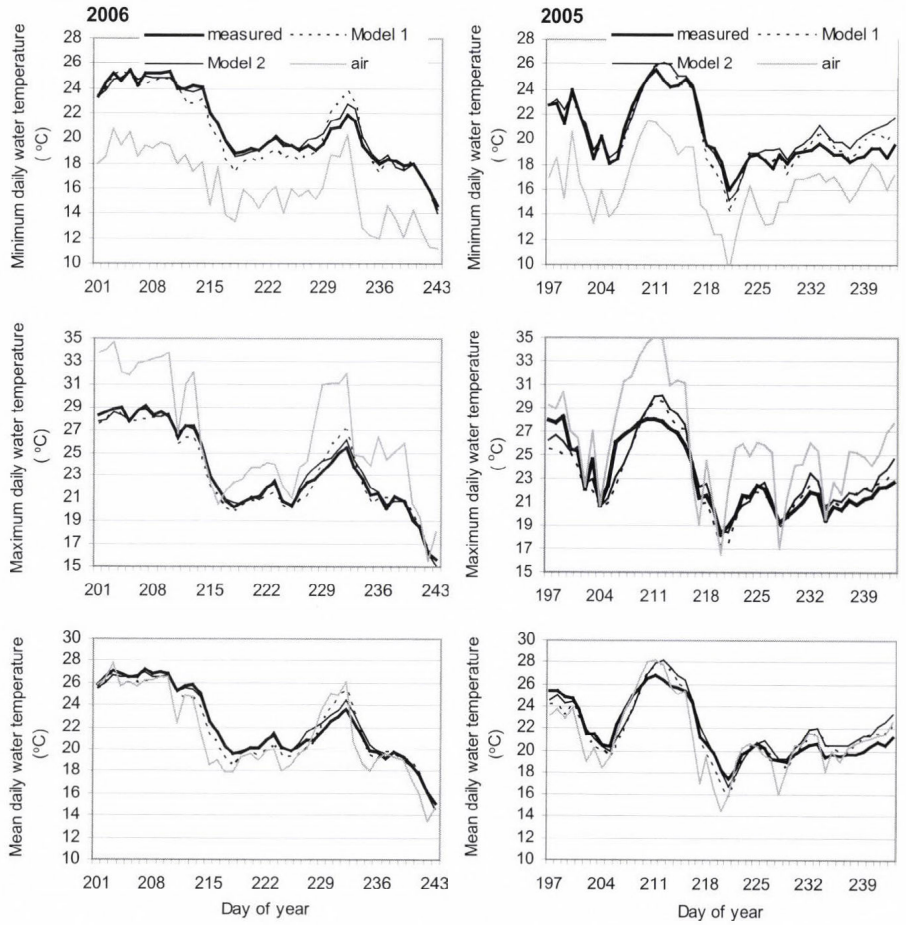


Fig. 3. Results of the modeling daily water temperature (minimum, maximum, mean). Prediction of Model 1 (dotted line) and Model 2 (solid line) compared with measured water (dark line) and air temperature (light line) in 2006 (calibration) and 2005 (verification).

Fig. 3 clearly shows the improved ability of M2 in 2006 to predict the water temperature values (Tw_{min}, Tw_{max}, Tw_{mean}). M1 overestimated these water temperature parameters (especially Tw_{min}) by about 2 °C in the hot, sunny days after an intensive warming period (before August 20). It can be explained by clear, dry, and windy weather conditions, which were not handled properly by M1. The evaporation heat loss due to low *RH* and high windspeed was not captured in the model. A slight under-estimation of Tw_{min} over a longer period can originate from an adverse effect.

In 2005 the highest predicting errors were recorded in Tw_{max}, during a hot, dry period, which occurred suddenly after cool days. The models showed a delayed reaction, then overestimation, similarly to the case in 2006 described above. The moderate warming period at the end of August 2005 (after DOY 235) was more critical for M2 than for M1. Global radiation, air humidity, and wind could not effect the water temperature as expected by Model 2. However, the mean water temperature was persistently lower than the mean air temperature hinting to circumstances different from typical case. It can be expected, that in such situations the more stable stratification of water with higher gradients in the top layer can cause errors in modeling.

4. Conclusions

The thermal characteristics of rice flooding water are very different from that of the air. Therefore, estimating development rate, cold or heat stress, and yield of rice directly from air temperature data can lead to misleading results. Both of our empirical dynamic models proved an efficient and accurate tool in simulating water temperature. The error in prediction is neglible from a practical point of view, especially if compared to the large differences between extremes of air and water temperature. The very simple regression model (Model 1), which needs only daily maximum and minimum air temperature (from standard climate station) as input, is an easy tool for growers to use. It makes it possible to estimate the course of water temperature from the data of weather forecasts, and the results can directly help to make the right decisions for improved water management of paddy fields. The more sophisticated Model 2 provided very accurate predictions in 2006, but did not improve on Model 1 in the independent test period of 2005. Model 2 is recommended as a part of crop simulation models.

Our models in their present form are valid for a deep (20–30 cm) flooding water, and a well developed closed rice canopy under climatic conditions of Hungarian rice growing areas. In any other conditions (water depth, canopy, area), a new calibration of model is required.

References

Burba, G.G., Verma, S.B., and *Kim, J.*, 1999: Surface energy fluxes of *Phragmites australis* in a prairie wetland. *Agr. Forest Meteorol. 94*, 31-51.

Cola, G., Bocchi, S., and *Mariani, L.*, 2007: Modelling of water temperature in flooded rice. *4th International Temperate Rice Conference*. June 25-28, 2007. Novara, Italy, 28-29.

Confalonieri, R., Mariani, L., and *Bocchi, S.*, 2005: Analysis and modelling of water and near water temperatures in flooded rice (*Oryza sativa* L.). *Ecol. Model. 183*, 269-280.

Confalonieri, R., Mariani, L., Facchetti, M., and *Bocchi, S.*, 2002: Analysis of temperature profiles in flooded rice field: Preliminary results. *Int. Rice Res. Notes 27*, 39-40.

Confalonieri, R., Acutis, M., Donatelli, M., Genovese, G., Mariani, L., Gusberti, D., Trevisiol, P., Rodolfi, M., Picco, A.M., Cerrani, I., and *Bellocchi, G.*, 2007: WARM a new model for paddy rice simulations. *4th International Temperate Rice Conference.* June 25-28, 2007. Novara, Italy, 126-127.

Dingkuhn, M., Sow, A., Samb, A., Diack, S., and *Asch, F.*, 1994: Climatic determinants of irrigated rice performance in the Sahel – I. Photothermal and micro-climatic responses of flowering. *Agr. Syst. 48*, 385-410.

Gal, G., Imberger, J., Zohary, T., Antenucci, J., Anis, A., and *Rosenberg, T.*, 2003: Simulating the thermal dynamics of Lake Kinneret. *Ecol. Model. 162*, 69-86.

Gombos, B., 2007: Study of water temperature in flooded rice (in Hungarian). *XIII. Ifjúsági Tudományos Fórum*. Pannon Egyetem Georgikon Mezőgazdaságtudományi Kar, Keszthely, 5 pp.

Gunawardena, T.A., Fukai, S., and *Blamey, F.P.C.*, 2001: Nitrogen decreases deep irrigation efficacy in reducing low temperature damage in rice. In *Proc. of the 10th Australian Agronomy Conference.* Australian Society of Agronomy.

Inthapan, P. and Fukai, S., 1988: Growth and yield of rice cultivars under sprinkler irrigation in south-eastern Queensland. 2. Comparison with maize and grain sorghum under wet and dry conditions. *Aust. J. Exp. Agr. 28*, 243-248.

Jacobs, A.F.G., Jetten, T.H., Lucassen, D.C., Heusinkveld, B.G., and *Nieveen, J.P.*, 1997: Diurnal temperature fluctuations in a natural shallow water body. *Agr. Forest Meteorol. 88*, 269-277.

Mariani, L., Donatelli, M., Confalonieri, R., Acutis, M., and *Cola, G.*, 2007: TRIS_DLL and TRIS_NET: two software components for simulating the floodwater effect on vertical thermal profile in paddy fields. *4th International Temperate Rice Conference.* June 25-28, 2007. Novara, Italy,128-129.

Oke, T.R., 1978: *Boundary Layer Climates*. Methuen&Co., London, 370 pp.

Petrasovits, I., 1958: Thermal effect of rice flooding water with different depth (in Hungarian). *Időjárás 62*, 95-107.

Polgár, S., 1961: Water management of rice fields during cool down at late summertime (in Hungarian). *Debreceni Mezőgazdasági Akadémia Gyakorlati Szaktanácsadója 3*, 43-49.

Roel, A., Mutters, R.J., Eckert, J.W., and *Plant, R.E.*, 2005: Effect of low water temperature on rice yield in California. *Agron. J. 97*, 943-948.

Shimono, H., Hasegawa, T., and *Iwama, K.*, 2002: Response of growth and grain yield in paddy rice to cool water at different growth stages. *Field Crop. Res. 73*, 67-79.

Shimono, H., Hasegawa, T., Moriyama, M., Fujimura, S., and *Nagata, T.*, 2005: Modeling spikelet sterility induced by low temperature in rice. *Agron J. 97*, 1524-1536.

Simonné, K.I., 1979: *Problems of Hungarian Rice Production* (in Hungarian). MÉM Agroinform, Budapest, 36 pp.

Simonné, K.I., 1983: *Rice Production* (in Hungarian). Mezőgazdasági Kiadó, Budapest, 293 pp.

Uchijima, Z., 1976: Microclimate of the rice crop. In *Climate and Rice*. International Rice Research Institute, Manila, Philippines, 115-140.

Wagner, R.., 1957: Climatic data of rice fields in Kopáncs (in Hungarian). *Időjárás 61*, 266-277.

Wagner, R., 1966: The temperature of soil, water and air in Kopáncs (in German). II. *Acta Climatologica VI.* 1-4, 1-51.

IDŐJÁRÁS

Quarterly Journal of the Hungarian Meteorological Service
Vol. 112, No. 1, January–March 2008, pp. 45–60

On the estimation of UV-B radiation over Egypt

S. M. Robaa

Astronomy and Meteorology Department, Faculty of Science, Cairo University, P.O. Box 12613, Giza, Egypt; E-mail: d_robaa@hotmail.com

(Manuscript received in final form November 15, 2006)

Abstract—In this study, four empirical formulae have been established and deduced to estimate UV-B radiation using sunshine duration, n, in cold and hot seasons at four stations that measure global and UV-B solar radiation in Egypt. Another empirical formula has been also deduced to estimate UV-B radiation in cold and hot seasons, at any locations in Egypt. The monthly mean UV-B values have been estimated at each station applying its own formula (*UVB*) and also applying Egypt's formula (UVB_{eg}). The estimated *UVB* and UVB_{eg} values were compared with the corresponding measured values at each station. The agreement between measured and estimated values is remarkable. The percentage errors of *UVB* at each station, (e_1), were always found lower than the corresponding errors of UVB_{eg}, (e_2). It was found that the maximum possible error of estimated values does not exceed 8.0%. The annual mean values of e_1 ranged from – 0.6 to +3.1, while the annual mean values of e_2 ranged from –5.7 to +6.8. It is seen that the Egypt's formula gives precise estimations for UV-B radiation, and it is recommended for use at any locations in Egypt.

The UV-B radiation values have been estimated applying the Egypt's formula at forty selected stations to study the general distribution of UV-B over Egypt. The results revealed that the UV-B radiation depends on the latitude over Egypt. The maximum value of UV-B occurs in June in the southern part of Egypt and ranges from 0.080 to 0.088 MJ m^{-2}, while the minimum value occurs in January in the northern part of Egypt and ranges from 0.020 to 0.044 m^{-2}.

Key-words: global solar radiation, UV-B radiation, sunshine duration; estimation, Egypt

1. Introduction

Ultraviolet solar radiation, UV, either at the edge of the atmosphere or at the earth's surface, accounts for only a small fraction of the total radiation flux. In the outer space, UV radiation accounts for only about 8.73% of the total solar radiation (*Al-Aruri et al.*, 1988), while at any locations on the earth's surface, the UV radiation value depends on the solar zenith angle, atmospheric ozone content, and transparency of the atmosphere (*Kylling et al.*, 2000; *Kirchhoff et*

al., 2002; *Luccini et al.*, 2003). UV radiation wavelength range has been divided into three sub-ranges: UV-A (400–315 nm), UV-B (315–290 nm), and UV-C (290–220 nm). The mentioned lower limit of UV-C (220 nm) is valid only when it is studied in air, but in fact, the wavelength of the shortest wave ultraviolet beams is shorter than 100 nm. The earth's surface receives only UV-A and UV-B, while the UV-C component is removed not only by absorption through the protective ozone layer (O_3) but also because it provides energy for several photoionization processes. UV-B is partially absorbed by the ozone layer, while UV-A is transmitted (*McKenzie et al.*, 1995). The beneficial and damaging effects of UV-A and UV-B radiations on the humans, ecosystem, animals, plants, and materials are many (*Parrish et al.*, 1978; *Biswas*, 1979; *Giese*, 1982). High doses of ultraviolet radiation, especially band B, cause skin diseases, eye cataract, photo-decomposition, degradation of materials, and may also harm crops (*Som*, 1992). Inverse relation is known between the ozone concentration in the atmosphere and the amount of UV reaching the earth's surface. From this point of view, the UV radiation is highly affected by the ozone, which is destroyed by pollutants such as freon refrigerants, spray, and atomic bomb tests (*Elhadidy et al.*, 1990; *Feister* and *Grasnick*, 1992; *Tang et al.*, 1998; *Zerefos et al.*, 2001; *Wuttke et al.*, 2003; *Robaa*, 2005).

Although Egypt is a vast country, the number of its meteorological stations that measure the solar radiation components, especially UV-B radiation, is few (*Fig. 1*). Therefore, the main objective of this paper is to establish a simple model giving precise estimation for UV-B radiation at any locations in Egypt, where there are no measured data of solar radiation components or there are instrumental and other difficulties encountered in measuring components of solar radiation.

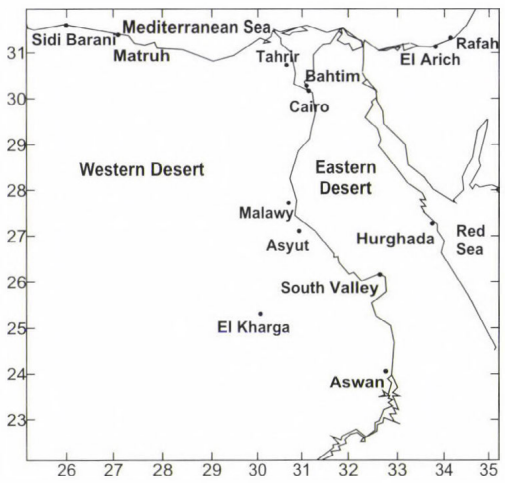


Fig. 1. Radiation network stations in Egypt.

2. *Climate of Egypt*

Egypt lies in north-east Africa. Most of Egypt's terrain is desert, divided into two unequal parts (eastern and western deserts) by the Nile River (*Fig. 1*). The valley and delta of the Nile are the main centers of habitation. The climate of Egypt is characterized by a hot season from March to September and a cold season from October to February. However, the northern winds are a welcome respite and do a good job of keeping the temperatures slightly moderated. The country is characterized by particularly good wind regimes with excellent sites along the Red Sea and Mediterranean coasts. Sites with an annual average of 8–10 m s^{-1} have been identified along the Red Sea coast and about 6.0–6.5 m s^{-1} along the Mediterranean coast. In the coastal regions, average annual temperatures vary from a maximum of 37 °C to a minimum of 14 °C. The most humid area is along the Mediterranean coast, where the average annual rainfall is about 200 mm. Rainfall decreases rapidly towards the south, and in many desert locations it may rain only once in several years. Temperatures vary widely in the inland desert areas, especially in summer, when it may range from 7 °C at night to 43 °C in daytime. During winter, temperatures in the desert fluctuate less dramatically, but they can be as low as 0 °C at night and as high as 18 °C in daytime. The average annual temperature increases moving southward from the Delta in the north to the Sudanese border in the south, where temperatures are similar to those of the open deserts. Throughout the Delta and the northern Nile Valley, there are occasional winter cold spells accompanied by light frost and even snow. In the south part of Egypt, June temperatures can be as low as 10 °C at night and as high as 41 °C in daytime, when the sky is clear. The entire territory enjoys a rather high solar radiation intensity of 1.9–2.6 kWh m^{-2} $year^{-1}$. Further intensity up to about 2.4 kWh m^{-2} $year^{-1}$ is observed when moving from the sea towards the desert.

A phenomenon of Egypt's climate is the hot spring wind that blows across the country. The winds, known to Europeans as the sirocco and to Egyptians as the khamsin, usually arrive in April, but occasionally occur in March and May. The winds form in small but vigorous low-pressure areas in the Isthmus of Suez and sweep across the northern coast of Africa. Unobstructed by geographical features, the winds reach high velocities and carry great quantities of sand and dust from the deserts. These sandstorms, often accompanied by winds of up to 40 m/s, can make temperature to rise as much as 20 °C in two hours. The winds blow intermittently and may continue for days, causing illness in people and animals, harm in crops, and occasionally damages in houses and infrastructure.

3. *Measurements*

The number of stations that measure the solar radiation components in Egypt is still few. Measurements of global solar radiation began in 1960 in Egypt at Tahrir station (see *Fig. 1* and *Table 1*). The ultraviolet radiation has been

measured in Egypt since 1990 at only two meteorological stations of Cairo in the north and Aswan in the south using an Eppley radiometer, which is sensitive to radiation in the wavelength band 290–385 nm (*Salem*, 2000; *Robaa*, 2005). Although, the study of UV-B radiation is very important for the various scientific purposes, it has been measured in Egypt at only four stations (*Fig. 1* and *Table 1*) using the UVB-1 ultraviolet pyranometer. The specifications of the UVB-1 pyranometer are given in *Table 2*.

Table 1. Coordinates of the Egyptian radiation network and the radiation components measured together with the date of commencement of recording

Station	Lat. (N)	Long. (E)	Alt. (m)	Measurements						Date of commencement of records
				G	D	I	S	UV	UV-B	
Sidi-Barrani	31.63	25.40	27	M	M	-	M	-	-	1984
Matruh	31.33	27.22	38	M	M	-	M	-	-	1961
El-Arich	31.08	33.82	32	M	M	-	M	-	-	1980
Rafah	31.22	34.20	73	M	M	M	M	M	M	1994 (2000)
Tahrir	30.65	30.70	16	M	M	-	M	-	-	1960
Bahtim	30.13	31.25	17	M	-	-	M	-	-	1969
Cairo	30.08	31.28	36	M	M	M	M	M	-	1969
Hurghada	27.28	33.75	07	M	M	-	M	-	M	1990 (1994)
Malawy	27.70	30.75	44	M	M	-	-	-	-	1994
Asyut	27.05	31.02	52	M	-	-	M	-	-	1979
El-Kharga	25.45	30.53	78	M	M	-	M	-	-	1964
South Valley	26.16	32.70	77	M	M	-	M	M	M	1994 (2000)
Aswan	23.97	32.78	92	M	M	M	M	M	M	1972 (1998)

The year in brackets indicates the date of commencement of UV-B radiation records. G is the global solar radiation, D is the diffuse solar radiation, I is the direct solar radiation, and S is the sunshine duration. M means existence of measurements.

Table 2. The operating characteristics of the UVB-1 pyranometer

Characteristic	Description
Spectral response	280 to 320 nm
Cosine response	±5% for 0–60 degree solar zenith angle
Sensitivity	1.97 W m^{-2} V^{-1} of total UV-B irradiance
Response time	approximately 0.1 second

The first station is located within the premises of Rafah meteorological station on the extreme northeast boundary of Egypt. It lies in an open landscape of reclaimable desert, about 10 km to the south of the Mediterranean Sea coast. UV-B radiation measurements started at Rafah station in June 2000 and continued till now. The second station is located within the premises of Hurghada meteorological station, about 3 km to the west of the Red Sea coast and 5 kilometers to the north of the town. UV-B radiation measurements started at Hurghada station in January 1994 and continued only thirty three months to

finish in September 1996. The third station is located within the premises of South Valley meteorological station in south Egypt. The measurements of UV-B radiation started at South Valley station in April 2000 and continued till now. The last station is located in south Egypt within the premises of Aswan upper air station, to the west of the Aswan Dam. It is about two kilometers away from the high Dam Lake. UV-B radiation measurements started at Aswan station in August 1998 and continued till now (in addition to UV radiation measurements, which started in 1990). The measuring instruments are fixed on the roof of the building 7 m above the ground level at the four stations. The global solar radiation component is also measured at the above four stations using an Eppley precision spectral pyranometer (Model PSP). The accuracy of the pyaranometers corresponds to the first class according to the World Meteorological Organization classification (*WMO*, 1990). These instruments are calibrated each year against a reference instrument traceable to the World Radiometric Reference (WRR) maintained at Davos, Switzerland (see *WRC*, 1985, 1995). The absolute accuracy of calibration is ±3–4%, (*El-Metwally*, 2004). In the present work, daily values of global and UV-B solar radiation, that were measured through a three years period (2001–2003) at the stations of Rafah, South Valley, and Aswan, and through the period of January 1994–April 1996 at Hurghada station, have been obtained from EMA and used in this study. The monthly means have been calculated and also used in this study.

4. Results and discussion

4.1. Methods of prediction

Sivkov (1964) proposed the original empirical relation to estimate the monthly mean global solar radiation at the latitudes from 35° to 65°N in the form:

$$G = 4.9(n)^{1.31} + 10550(\sin h)^{2.1}, \tag{1}$$

where G and n are the monthly global solar radiation (in cal cm^{-2}) and the monthly sunshine duration, respectively. h is the solar elevation at noon on the 15th day of the month.

Barbaro et al. (1978) modified the above formula to fit 31 Italian stations that were divided into three zones according to their climatological characteristics. The modified formula is

$$G = K(n)^{1.24}(h)^{-0.19} + 10550\sin(h)^{2.1} + 300\sin(h)^3, \tag{2}$$

where K = 8, 9.5, and 11 for zone 1, zone 2, and zone 3, respectively. The computation of G is based on the knowledge of the appropriate zone parameter and long-term averages of sunshine duration and solar elevation.

Eq. (2), which was proposed for high latitudes (35°–65°N), was tested by *Khogali* (1983) for low latitudes (4°–19°N) and has been found applicable with a good degree of accuracy providing that the parameter K is appropriately adjusted.

Furthermore *Robaa* (2003) modified the empirical relation Eq. (2) to estimate global solar radiation in Egypt. In order to improve the obtained results, for prediction purposes, *Robaa* (2003) divided Egypt into five regions most representing the country. The regions are represented by the stations that measure solar radiation. *Table 1* gives a list of these stations and their coordinates in addition to the type of measured radiation at each station and the date of commencement of records. The year has been also divided into cold season (from October to February) and hot season (from March to September). *Robaa* (2003) determined an appropriate regional parameter, K, for the empirical relation Eq. (2) for each region during cold and hot seasons. He found that the modified formula gives precise estimations for global solar radiation at any Egyptian locations, whereas the percentage error was found ranging from –2.4 to +5.9 and having an annual mean value of 1.06 (*Robaa*, 2003). Therefore, the modified formula was recommended for use at any locations in Egypt to estimate the global solar radiation.

On the other hand, a significant correlation between G and UV radiation has been found by *Robaa* (2005) with a correlation coefficient of 0.98, and the standard error was close to zero. The recommended correlation equation has been stated to estimate the values of UV radiation, which can be measured with difficulty at the sites in the zone of Lower Egypt.

Although, the study of UV-B radiation is very important, as mentioned above, the measurements of UV-B radiation are not available at any locations in Egypt except of the four stations of Rafah, Hurghada, South Valley, and Aswan (*Fig. 1* and *Table 1*). Therefore, the main objective of this study is subjected to establish a simple model, which gives precise estimation for UV-B radiation at any Egyptian locations.

In this way, many types of correlations were tried to find out the best fit between the UV-B and global radiation at each station using all available daily measured values of the two parameters through the three years period (2001–2003) for Rafah, South Valley, and Aswan, and through the three years period (1994–1996) for Hurghada. On the other hand, all data of both UV-B and global radiations at the above four stations (3600 records for each parameter) have been used to find out the best fit between the two parameters for the whole territory of Egypt.

A significant positive correlation between the UV-B and global radiation has been found with correlation coefficients ranging between 0.9751 for the whole Egypt and 0.9816 for Aswan, and the standard errors were close to zero for the four stations and whole Egypt (see *Table 3*). The results are illustrated by *Figs. 2a-d* and they were found in the form:

$$UVB = aG + b, \tag{3}$$

where a and b are the regression coefficients which depend on the atmospheric conditions of the location. Data have been processed using an advanced computer program, and the calculated values of a and b for each station and the whole Egypt are given in *Table 3*, beside correlation coefficients, standard errors and the number of used records.

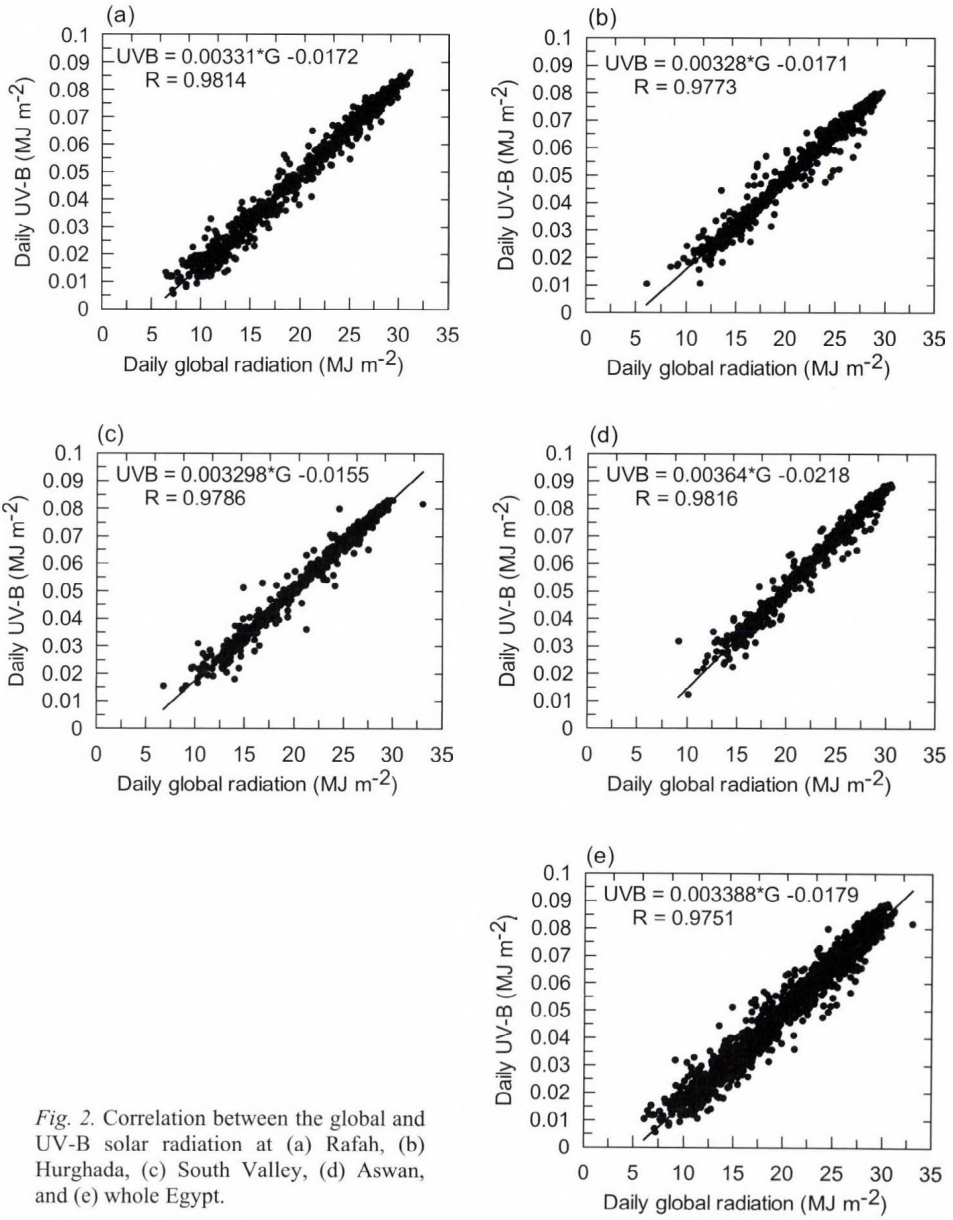


Fig. 2. Correlation between the global and UV-B solar radiation at (a) Rafah, (b) Hurghada, (c) South Valley, (d) Aswan, and (e) whole Egypt.

Table 3. The calculated values of regression coefficients, absolute error and the number of used records at the four stations

Station	Regression coefficients		Correlation coefficient	Standard error	Number of records
	a	*b*			
Rafah	0.003307	-0.017168	0.9814	0.00422	936
Hurghada	0.003283	-0.017026	0.9773	0.00473	730
South Valley	0.003298	-0.015453	0.9786	0.00398	993
Aswan	0.003641	-0.021823	0.9816	0.00395	941
Whole Egypt	0.003388	-0.017924	0.9751	0.02997	3600

From Eqs. (2) and (3) and Table (3), an empirical formula can be proposed to calculate *UVB* at the four stations and the whole Egypt during cold and hot seasons in the following form:

$$UVB = c_1(n)^{1.24}(h)^{-0.19} + c_2 \sin(h)^{2.1} + c_3 \sin(h)^3 + b, \tag{4}$$

where $c_1 = a\,K$, $c_2 = 10550\,a$, and $c_3 = 300\,a$. The calculated values of c_1, c_2, c_3, and b for each station and whole Egypt during cold and hot seasons are given in *Table 4*. The corresponding values of regional parameter K for each station and whole Egypt have been taken from *Robaa* (2003) and given also in *Table 4*. c_1 values change from the cold to hot season at each station, while c_2, c_3, and b take the same values during the two seasons at each station (see *Table 4*).

Wang and *Jianhui* (1996) stated that the impact of ozone depletion on UV radiation at the ground is greater on high latitudes than on middle and low latitudes. Furthermore, effect of the variability of ozone content is relatively low in Egypt (the difference between the highest and lowest monthly ozone values is 10.1% during the period of 1978–2004 (*Robaa* and *Hafez*, 2006)). Therefore, the ozone effect could be neglected in the used empirical formulae.

Table 4. Values of regional parameter K and c_1, c_2, c_3 for each station and whole Egypt during cold and hot seasons

Station	Season	K	c_1	c_2	c_3	b
Rafah	Cold	12.4	0.041007	34.88885	0.9921	-0.017168
	Hot	14.6	0.048282			
Hurghada	Cold	11.5	0.037755	34.63565	0.9849	-0.017026
	Hot	14.5	0.047604			
South Valley	Cold	14.3	0.047161	34.79390	0.9894	-0.015453
	Hot	16.8	0.055406			
Aswan	Cold	13.5	0.049154	38.41255	1.0923	-0.021823
	Hot	16.5	0.060077			
Whole Egypt	Cold	12.8	0.043366	35.74340	1.0164	-0.017924
	Hot	15.5	0.052514			

An empirical formula can be easily deduced for each station and whole Egypt to calculate the monthly mean values of *UVB* during cold and hot seasons as follows:

Rafah's formula:

$$UVB = c_1 (n)^{1.24} (h)^{-0.19} + 34.88885 \sin(h)^{2.1} + 0.9921 \sin(h)^3 - 0.017168, \quad (5)$$

where c_1 value equals to 0.041007 and 0.048282 for cold and hot seasons, respectively.

Hurghada's formula:

$$UVB = c_1 (n)^{1.24} (h)^{-0.19} + 34.63565 \sin(h)^{2.1} + 0.9849 \sin(h)^3 - 0.017026, \quad (6)$$

where c_1 value equals to 0.037755 and 0.047604 for cold and hot seasons, respectively.

South Valley's formula:

$$UVB = c_1 (n)^{1.24} (h)^{-0.19} + 34.79390 \sin(h)^{2.1} + 0.9894 \sin(h)^3 - 0.015453, \quad (7)$$

where c_1 value equals to 0.047161 and 0.055406 for cold and hot seasons, respectively.

Aswan's formula:

$$UVB = c_1 (n)^{1.24} (h)^{-0.19} + 38.41255 \sin(h)^{2.1} + 1.0923 \sin(h)^3 - 0.021823, \quad (8)$$

where c_1 value equals to 0.049154 and 0.060077 for cold and hot seasons, respectively.

Egypt's formula:

$$UVB = c_1 (n)^{1.24} (h)^{-0.19} + 35.74340 \sin(h)^{2.1} + 1.0164 \sin(h)^3 - 0.017924, \quad (9)$$

where c_1 value to equals 0.043366 and 0.052514 for cold and hot seasons, respectively.

4.2. Verification of the deduced empirical formulae

To verify the deduced empirical formulae (Eqs. (5) to (9)), the monthly mean values of *UVB* have been calculated for Rafah, South Valley, and Aswan stations for the two subsequent years 2004 and 2005, and at Hurghada station for the two years of 1994 and 1995 in the cold and hot seasons. The calculated values have been produced for each station using the corresponding measured values of n and applying its deduced empirical formula to give *UVB* and the Egypt's formula (Eq. (9)) to give UVB_{eg}. The values of UVB_{eg} have been calculated at each station to test the validity of the Egypt's formula for estimating *UVB* at any locations in Egypt.

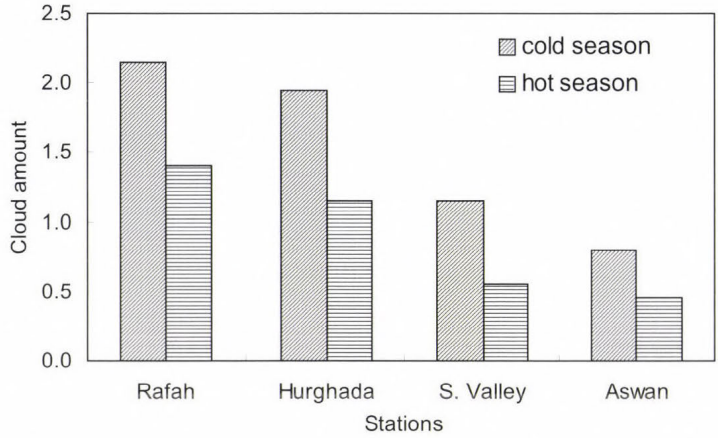


Fig. 3. Cloud amount (in octas) in the hot and cold seasons at the four studied stations (climatological normal value for the period 1975–2004).

The estimated *UVB* and UVB_{eg} values at each station were compared with the corresponding measured values (UVB_m) during the same time period. The results are listed in *Tables 5* and *6*. It can be seen that the estimated values of *UVB* and UVB_{eg} at each station are in a good agreement with the measured values for all months of the year. The percentage errors of *UVB* at each station, e_1, were always found lower than the corresponding errors of UVB_{eg}, e_2 (*Tables 5* and *6*). It was found that the percentage error, e_1, was ranged from –4.0 to +5.7 and from –3.3 to +4.9 during the two years, respectively, while e_2 was ranged from –7.5 to +8.0 and from –7.8 to +7.5 during the two years, respectively. The annual mean values of e_1 were ranged from –0.6 to +2.9 and from –0.3 to +3.1 during the two years, respectively, while the annual mean values of e_2 were ranged from –5.7 to +6.8 and from –5.4 to +5.8 during the two years, respectively (see *Table 7*).

It may be noted that the formula of each station gives precise estimation for UV-B radiation at its own locality with a small overestimation in the cold season (November to February) and underestimation in the remaining months. This is attributed to the higher effect of cloud cover (see *Fig. 3*) and atmospheric water vapor content in the cold season than in the hot and remain seasons. The cloud and atmospheric water vapor content effects are not taken in to the consideration with respect to the estimation formulae. On the other hand, it is to be noted that Eq. (9) of the whole Egypt overestimates the UV-B_{eg} radiation all the year at Rafah and Hurghada, while underestimates it at South Valley and Aswan. This is because Rafah and Hurghada are coast cities and characterized by highest cloud cover (*Fig. 3*) and atmospheric water content during most of the year, especially in the winter season, while South Valley and Aswan are characterized by clear atmosphere and stable weather conditions.

Table 5. Sunshine duration n, solar elevation h, in addition to one year (2004) measured UVB_m (MJ m^{-2}), estimated UVB (applying the station's formula), and UVB_{eg} (applying the Egypt's formula) values of the monthly mean UV-B radiation (MJ m^{-2}) and their percentage errors, e_1 and e_2

Station	Parameter	Jan	Feb	Mar	Apr	May	Jun	Jul	Aug	Sep	Oct	Nov	Dec
Rafah	n	6.4	8.9	9.1	9.4	11	12.2	11.7	11.6	10.5	9.1	8.6	6.8
	h	37.7	45.6	56.1	68.3	78	82.3	80.3	72.4	60.7	49	39.5	35.5
	UVB_m	0.0201	0.0376	0.0518	0.0616	0.0712	0.0782	0.0742	0.0726	0.0618	0.0405	0.0309	0.0203
	UVB	0.0203	0.0381	0.0501	0.0603	0.0703	0.0780	0.0741	0.0712	0.0606	0.0396	0.0309	0.0204
	UVB_{eg}	0.0212	0.0397	0.0531	0.0636	0.0743	0.0824	0.0783	0.0754	0.0643	0.0412	0.0323	0.0213
	e_1	-1.2	-1.4	3.4	2.1	1.2	0.3	0.1	2.0	1.9	2.2	0.0	-0.3
	e_2	-5.4	-5.5	-2.5	-3.3	-4.3	-5.4	-5.5	-3.8	-4.1	-1.9	-4.5	-4.7
Hurghada													
	n	8.1	9.2	10	10.6	11.1	12.3	12	11.7	10.6	9.6	9	8.1
	h	41.5	49.4	59.9	72.1	81.8	86.1	81.1	76.2	64.5	52.8	43.3	39.2
	UVB_m	0.0290	0.0418	0.0572	0.0687	0.0716	0.0789	0.0764	0.0725	0.0647	0.0437	0.0346	0.0277
	UVB	0.0278	0.0402	0.0562	0.0669	0.0709	0.0779	0.0748	0.0722	0.0628	0.0419	0.0330	0.0261
	UVB_{eg}	0.0312	0.0443	0.0603	0.0714	0.0756	0.0832	0.0800	0.0773	0.0673	0.0463	0.0369	0.0295
	e_1	4.1	3.9	1.7	2.6	1.0	1.2	2.1	0.4	2.9	4.0	4.5	5.7
	e_2	-7.5	-5.9	-5.4	-3.9	-5.6	-5.5	-4.7	-6.6	-4.0	-6.0	-6.8	-6.4
South Valley													
	n	9.5	9.9	10.2	10.7	11.2	12.4	12.2	11.8	10.7	9.8	9.1	8.4
	h	42.6	50.6	61	73.3	82.9	87.2	82	77.3	65.7	53.9	44.5	40.5
	UVB_m	0.0401	0.0499	0.065	0.0772	0.081	0.088	0.0812	0.08	0.0719	0.0507	0.0398	0.0331
	UVB	0.0409	0.0507	0.0650	0.0751	0.0790	0.0866	0.0840	0.0810	0.0714	0.0505	0.0410	0.0344
	UVB_{eg}	0.0381	0.0482	0.0621	0.0724	0.0763	0.0837	0.0811	0.0781	0.0685	0.0480	0.0383	0.0317
	e_1	-1.9	-1.6	0.0	2.7	2.5	1.6	-3.5	-1.2	0.7	0.4	-2.9	-4.0
	e_2	5.0	3.4	4.5	6.2	5.8	4.8	0.1	2.4	4.7	5.4	3.7	4.1
Aswan													
	n	10	10.2	10.4	10.8	11.5	12.6	12.4	12	10.8	10	9.2	9
	h	44.3	52.5	63	75	83.8	87.8	83.8	78.7	68.9	57.6	47.6	42.6
	UVB_m	0.0440	0.0542	0.0695	0.0796	0.0844	0.0920	0.0894	0.0864	0.0767	0.0554	0.0433	0.0375
	UVB	0.0442	0.0544	0.0695	0.0795	0.0842	0.0919	0.0894	0.0862	0.0765	0.0548	0.0436	0.0379
	UVB_{eg}	0.0416	0.0511	0.0643	0.0736	0.0779	0.0847	0.0823	0.0795	0.0708	0.0516	0.0412	0.0359
	e_1	-0.4	-0.3	0.0	0.2	0.2	0.1	0.0	0.2	0.2	1.0	-0.6	-1.0
	e_2	5.5	5.7	7.4	7.6	7.8	7.9	7.9	8.0	7.7	6.9	4.8	4.3

Table 6. The same as in Table 5 but for the year 2005

Station	Parameter	Jan	Feb	Mar	Apr	May	Jun	Jul	Aug	Sep	Oct	Nov	Dec
Rafah	n	6.5	8.6	8.8	10.1	11.1	12	11.9	11.4	10.2	9.4	7.9	6.6
	h	37.7	45.6	56.1	68.3	78	82.3	80.3	72.4	60.7	49	39.5	35.5
	UVB_m	0.0204	0.0366	0.0498	0.0646	0.0721	0.0777	0.0764	0.0704	0.0595	0.0418	0.0277	0.0192
	UVB	0.0207	0.0369	0.0487	0.0635	0.0708	0.0771	0.0750	0.0702	0.0593	0.0408	0.0281	0.0196
	UVB_{eg}	0.0216	0.0384	0.0516	0.0670	0.0748	0.0814	0.0793	0.0743	0.0628	0.0425	0.0293	0.0204
	e_1	-1.7	-1.0	2.2	1.8	1.9	0.8	1.8	0.2	0.4	2.3	-1.4	-1.9
	e_2	-5.9	-5.0	-3.6	-3.8	-3.7	-4.8	-3.9	-5.6	-5.5	-1.8	-5.8	-6.3
Hurghada													
	n	8.6	8.5	9.5	10.2	11.3	12	11.9	11.8	10.7	10.1	9.9	9
	h	41.5	49.4	59.9	72.1	81.8	86.1	81.1	76.2	64.5	52.8	43.3	39.2
	UVB_m	0.0312	0.0391	0.0548	0.0668	0.0738	0.0773	0.0758	0.0744	0.0653	0.0458	0.0382	0.0310
	UVB	0.0297	0.0377	0.0539	0.0651	0.0718	0.0766	0.0743	0.0727	0.0633	0.0438	0.0365	0.0295
	UVB_{eg}	0.0333	0.0414	0.0578	0.0694	0.0766	0.0818	0.0795	0.0778	0.0678	0.0484	0.0409	0.0334
	e_1	4.9	3.7	1.6	2.5	2.8	1.0	1.9	2.3	3.1	4.3	4.6	4.7
	e_2	-6.9	-5.8	-5.4	-4.0	-3.7	-5.7	-4.8	-4.5	-3.8	-5.8	-7.0	-7.8
South Valley													
	n	8.8	8.9	9.9	10.4	11.8	12.6	12.4	12.2	10.9	10.1	9.5	8.3
	h	42.6	50.6	61	73.3	82.9	87.2	82	77.3	65.7	53.9	44.5	40.5
	UVB_m	0.0369	0.0456	0.0632	0.0736	0.0831	0.0881	0.0881	0.0845	0.073	0.0524	0.0419	0.0329
	UVB	0.0377	0.0464	0.0634	0.0736	0.0821	0.0876	0.0851	0.0831	0.0724	0.0518	0.0427	0.0340
	UVB_{eg}	0.0350	0.0441	0.0605	0.0709	0.0792	0.0847	0.0821	0.0801	0.0695	0.0493	0.0401	0.0313
	e_1	-2.2	-1.9	-0.3	0.0	1.2	0.5	3.5	1.7	0.8	1.1	-2.1	-3.3
	e_2	5.1	3.3	4.3	3.6	4.6	3.8	6.8	5.2	4.8	5.9	4.3	4.8
Aswan													
	n	9.6	9.8	10.2	10.9	12	12.8	12.6	12.4	11	10.7	10.1	9.1
	h	44.3	52.5	63	75	83.8	87.8	83.8	78.7	68.9	57.6	47.6	42.6
	UVB_m	0.0417	0.0520	0.0683	0.0804	0.0875	0.0931	0.0915	0.0888	0.0786	0.0579	0.0471	0.0373
	UVB	0.0422	0.0525	0.0684	0.0800	0.0871	0.0931	0.0905	0.0885	0.0777	0.0582	0.0480	0.0384
	UVB_{eg}	0.0398	0.0494	0.0633	0.0751	0.0815	0.0873	0.0849	0.0821	0.0738	0.0545	0.0451	0.0363
	e_1	-1.2	-0.9	-0.1	0.5	0.5	0.0	1.1	0.3	1.1	-0.5	-1.8	-2.9
	e_2	4.5	4.9	7.3	6.6	6.9	6.2	7.2	7.5	6.1	5.8	4.3	2.5

Therefore, it could be concluded that, as it was expected, the above Egypt's formula (Eq. (9)) is valid to compute the UV-B solar radiation with high accuracy during cold and hot months at any locations in Egypt. This is due to the modified formulae characterized by simplicity and independence of meteorological parameters, which in turn precisely estimates UV-B radiation at any localitions in Egypt during all months.

Table 7. Annual mean values of UVB_m, UVB, UVB_{eg}, e_1, and e_2 at the four stations

Parameter	El-Arish		Hurghada		S. Valley		Aswan	
	2003	**2004**	**2003**	**2004**	**2003**	**2004**	**2003**	**2004**
UVB_m	0.0517	0.0514	0.0556	0.0561	0.0632	0.0636	0.0677	0.0687
UVB	0.0512	0.0509	0.0542	0.0546	0.0633	0.0633	0.0677	0.0687
UVB_{eg}	0.0539	0.0536	0.0586	0.0590	0.0605	0.0606	0.0629	0.0644
e_1	0.8	0.5	2.9	3.1	-0.6	-0.1	0.0	-0.3
e_2	-4.2	-4.6	-5.7	-5.4	4.2	4.7	6.8	5.8

4.3. UV-B radiation distribution over Egypt

The monthly mean of measured n values at forty selected stations have been taken from the Egyptian Meteorological Authority and used in this study to calculate the corresponding UVB values at these stations applying the Egypt's formulae (Eq. (9)). The stations have been chosen to cover the whole territory of Egypt. The results of calculated UV-B radiation values have been plotted on relevant charts (*Figs. 4* and *5*). The charts have been carried out by using the SURFER program with the interpolation technique of minimum curvature.

These charts (*Figs. 4* and *5*) have been analyzed and discussed. The main climatic features of UV-B radiation over Egypt are given below:

- The distribution of UV-B over Egypt depends on the latitude, where its intensity tends to increase in the southward and decrease in the northward direction in Egypt. The monthly mean values of UV-B radiation ranges from the highest value of 0.088 MJ m^{-2} at the southern part of Egypt in June, to the lowest value of 0.02 MJ m^{-2} at the northern part of Egypt in January.
- In Egypt the highest values of UV-B radiation occur in June, when its values range from 0.080 in the north to 0.088 MJ m^{-2} in the southwest part of Egypt.
- In Egypt the lowest values of UV-B radiation occur in January, when its values range from 0.020 in the north to 0.044 MJ m^{-2} in the southwest part of Egypt.

- There is a marked difference between the intensity of UV-B radiation at the northern and southern parts of Egypt, especially in the winter months (namely in January, the difference is 0.02 MJ m^{-2}), while this difference decreases gradually to take its minimum in the summer months (namely in June, the difference is 0.008 MJ m^{-2}).

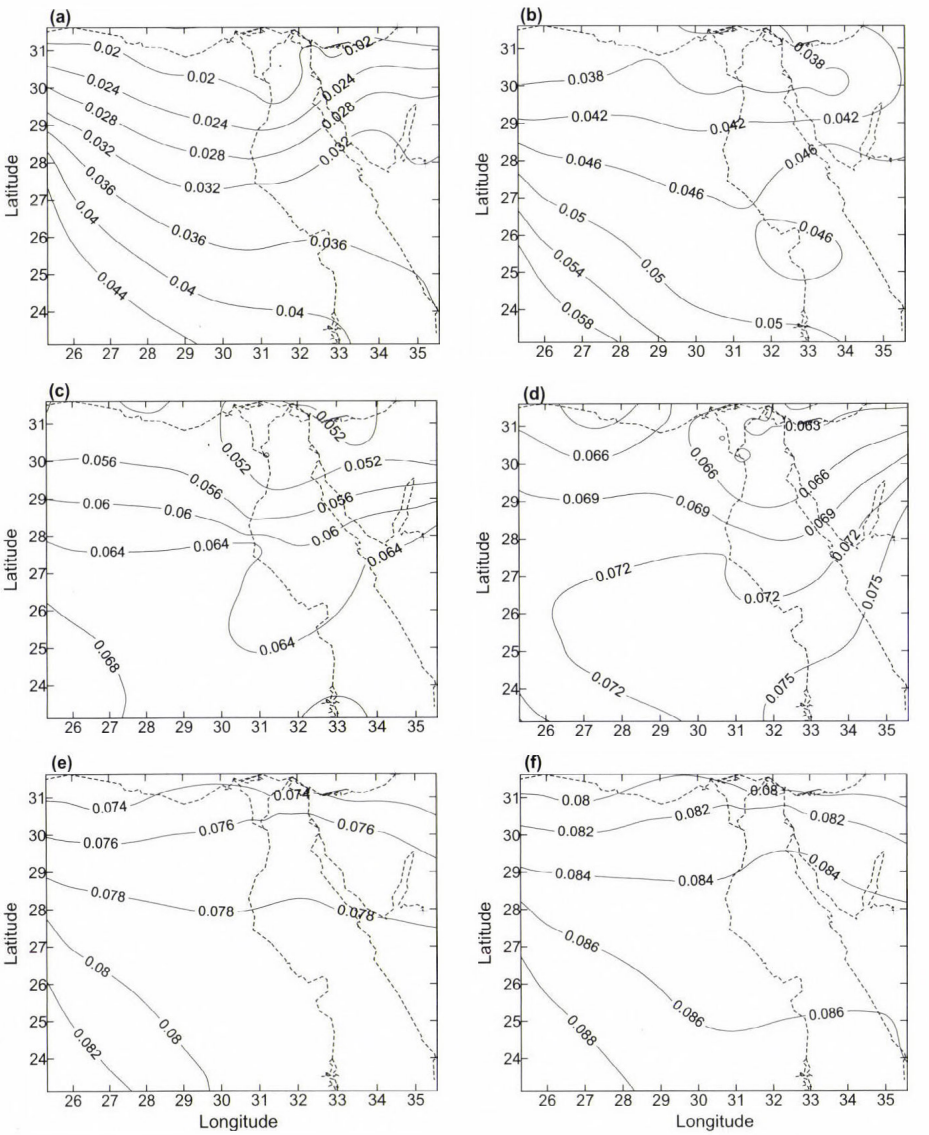


Fig. 4. The calculated UV-B values over Egypt during the months (a) January, (b) February, (c) March, (d) April, (e) May, and (f) June.

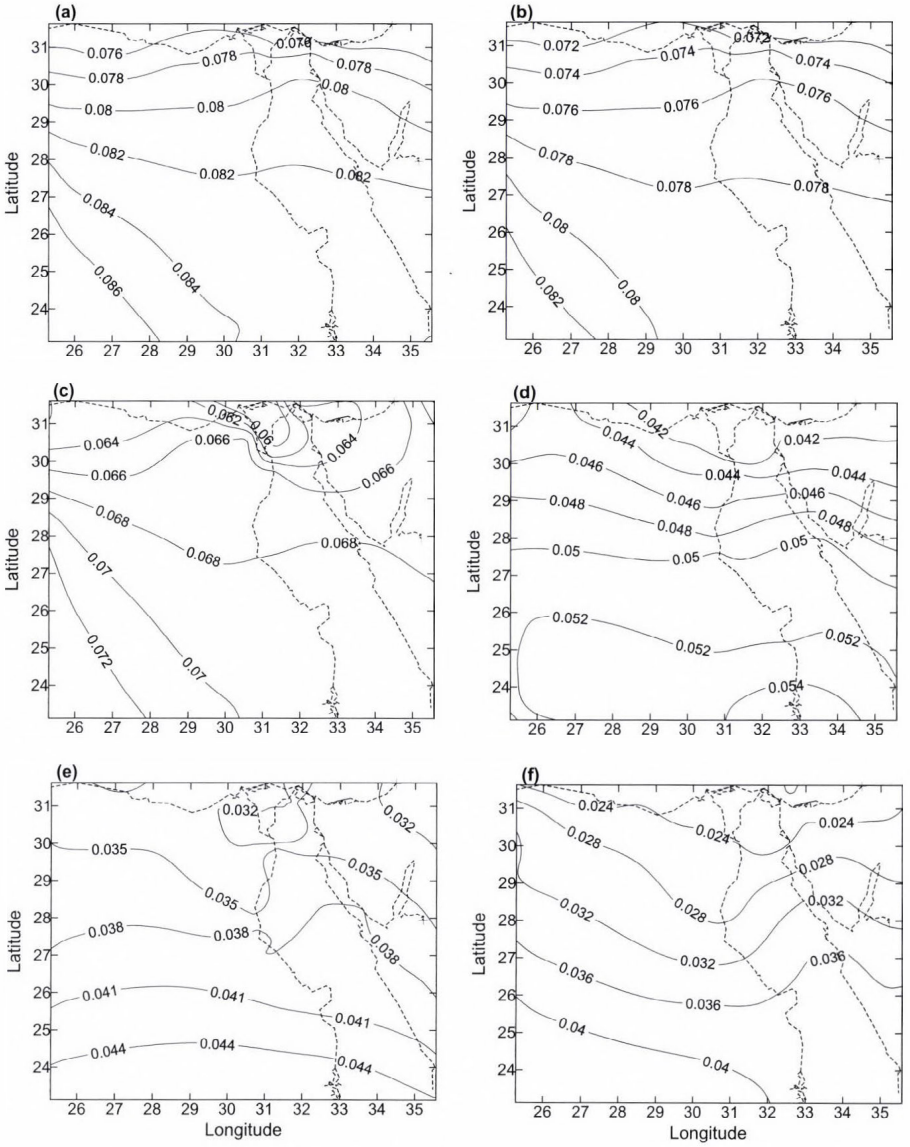


Fig. 5. The same as in Fig. 4 but for the months (a) July, (b) August, (c) September, (d) October, (e) November, and (f) December.

References

Al-Aruri, S., Rasas, M., Al-Jamal, K., and *Shaban, N.,* 1988: An assessment of global ultraviolet radiation in the range (0.290-385 μm) in Kuwait. *Sol. Energy 41*, 159-162.

Barbaro, S., Coppolino, S., Leone, C., and *Sinagra, E.*, 1978: Global solar radiation in Italy. *Sol. Energy 20*, 431-435.

Biswas, A.K., 1979: *The Ozone Layer*. Vol. 4. Pergamon Press, Oxford.

Elhadidy, M.A., Abdel-Nabi, D.Y., and *Kruss P.D.*, 1990: Ultraviolet solar radiation at Dhahran, Saudi Arabia. *Sol. Energy 44*, 315-319.

El-Metwally, M., 2004: Simple new methods to estimate global solar radiation based on meteorological data in Egypt. *Atmos. Res. 69*, 217–239.

Feister, U. and *Grasnick, K.H.*, 1992: Solar UV radiation measurements at Potsdam (52°22′N, 31°5′E). *Sol. Energy 49*, 541-548.

Giese, A.C., 1982: *Living with our Suns' Ultraviolet Rays*. Plenum Press, New York.

Khogali, A., 1983: Solar radiation over Sudan-comparison of measured and predicted data. *Sol. Energy 31*, 45-53.

Kirchhoff, V.W., Silva, A., and *Pinheiro, K.*, 2002: Wavelength dependence of aerosol optical thickness in the UV-B band. *Geophys. Res. Lett. 29*, 1620, doi:10.1029/2001.

Kylling, A., Dahlback A., and *Mayer, B.*, 2000. The effect of clouds and surface albedo on UV irradiances at a high latitude site. *Geophys. Res. Lett. 27*, 1411-1414.

Luccini, E., Cede, A., and *Piacentini, R.D.*, 2003: Effect of clouds on UV and total irradiance at Paradise Bay, Antarctic Peninsula, from a summer 2000 campaign. *Theor. Appl. Climatol. 75*, 105-116.

McKenzie, R.L., Blumthaler M., Booth, C.R., Diaz, S.B., Frederick, J.E., Ito, T., Madronich, S., and *Seckmeyer, G.*, 1995: Surface ultraviolet radiation. In *Scientific Assessment of Ozone Depletion*. WMO Global Ozone Research and Monitoring Project Report No. 37, 9, 1-9. 22.

Parrish, J.A., Rox Arderson, R., Urbach, F., and *Pitts, D.*, 1978: *UV-A*. Plenum Press, New York.

Robaa, S.M., 2003: On the estimation of global and diffuse solar radiation over Egypt. *Mausam 54*, 17-35.

Robaa, S.M., 2005: A study of ultraviolet solar radiation at Cairo urban area, Egypt. *Idojaras 109*, 123-138.

Robaa, S.M. and *Hafez, Y.Y.*, 2006: Study the teleconection between the variations of total ozone values over Egypt and climatic indices NAO and SOI. *J. Environ. Sci. 4*, 70-85.

Salem, A.I., 2000: Analysis and correlation of ultraviolet solar radiation from routine meteorological measurements over Egypt. *Mausam 51*, 275-280.

Sivkov, S.I., 1964. To the methods of computing possible radiation in Italy. *Trans. Main Geophys. Obs.* 160.

Som, A.K., 1992: Solar UV-B radiation measurements over Bahrain. *Renew. Energ. 2*, 93-98.

Tang, X., Madronich, S., Wallington, T., and *Calamari, D.*, 1998: Changes in tropospheric composition and air quality. *J. Photoch. Photobio. B. 46*, 83-95.

Wang, G. and *Jianhui, B.*, 1996: Variation in trend of UV radiation in Beijing district. *First Stratospheric Processes and Their Role in Climate*. Melbourne, Australia, 2-6 Dec 1996, Vol. II, WCRP-99 WMO/TD-NO. 814.

WMO, 1990: *Guide to Meteorological Observations Methods*. Tn-8, Geneva, Switzerland, Chapter 9. WMO Secretariat, 925–932.

WRC, 1985: Sixth international pyreheliometer comparison (IPC VI), 1-18 October. *Working Report,* No. 137, Davos, Switzerland.

WRC, 1995: International pyreheliometer comparison (IPC VII), 25 September-13 October. *Working Report,* No. 188, Davos, Switzerland.

Wuttke, S., Verdebout, J., and *Seckmeyer, G.*, 2003: An improved algorithm for satellite derived UV radiation. *Photochem. Photobiol.* 77, 52-57.

Zerefos, C.S., Balis, D., Tzortziou, M., Bais, A., Tourpali, K., Meleti, C., Bernhard, G., and *Herman, J.*, 2001: A note on the interannual variation of UV-B erythemal doses and solar irradiance from ground – based and satellite observations. *Ann. Geophys. 19*, 115-120.

BOOK REVIEW

Geoffrey K. Vallis: **Atmospheric and Oceanic Fluid Dynamics: Fundamentals and Large-scale Circulation**. Cambridge University Press, 2006, 745 pages, 16 chapters.

Geoffrey K. Vallis condensed his great teaching experience into the textbook on atmospheric and oceanic dynamics. The material is divided into four major parts: (i) fundamentals of geophysical fluid dynamics, (ii) instabilities, wave-mean flow interaction, and turbulence, (iii) large-scale atmospheric, and (iv) large-scale oceanic circulation.

The introductory part, starting from classical concepts of fluid dynamics and thermodynamics, studies the effects of rotation and stratification, shallow water, geostrophic and quasi-geostrophic flow systems, vorticity and potential vorticity, as well as the Rossby waves. The second part guides the reader through barotropic and baroclinic instability, wave-mean flow interaction, theory of incompressible and geostrophic turbulence. Moreover, this part is closed with discussion of turbulent diffusion and eddy transport. The third part is focused on large scale atmospheric circulation: the overturning circulation (Hadley and Ferrel cells), zonally averaged mid-latitude atmospheric circulation, and planetary waves. The subject of the closing part is the wind- and buoyancy-driven as well as simultaneous wind- and buoyancy-driven ocean circulation. Each chapter was designed to form self-contained unit.

The text was written to satisfy the requirements of graduate courses, and it is readable. The basic material was supplemented with parts which contain advanced mathematical derivations, which may be omitted on first reading, and discuss modern research topics. The chapters end with very useful notes, including a short biography of the scientists who have made major contributions to the studied fields, list of further reading, and set of unsolved problems. The author appeals to the readers to post their own problem solutions and to extend the currently very poor set of solutions published on the web site associated with the book. All the figures, many in color, the errata, and the ongoing discussion may be downloaded from the web site.

The book represents a comprehensive survey on the theory of geophysical fluid dynamics, large-scale atmospheric and oceanic dynamics combining needs of graduate students and researchers too. It has the potential to become the standard reference for modern topics of the atmospheric and oceanic dynamics including climate systems.

Á. Bordás

GUIDE FOR AUTHORS OF *IDŐJÁRÁS*

The purpose of the journal is to publish papers in any field of meteorology and atmosphere related scientific areas. These may be

- research papers on new results of scientific investigations,
- critical review articles summarizing the current state of art of a certain topic,
- short contributions dealing with a particular question.

Some issues contain "News" and "Book review", therefore, such contributions are also welcome. The papers must be in American English and should be checked by a native speaker if necessary.

Authors are requested to send their manuscripts to

Editor-in Chief of IDŐJÁRÁS
P.O. Box 39, H-1675 Budapest, Hungary

in three identical printed copies including all illustrations. Papers will then be reviewed normally by two independent referees, who remain unidentified for the author(s). The Editor-in-Chief will inform the author(s) whether or not the paper is acceptable for publication, and what modifications, if any, are necessary.

Please, follow the order given below when typing manuscripts.

Title part: should consist of the title, the name(s) of the author(s), their affiliation(s) including full postal and e-mail address(es). In case of more than one author, the corresponding author must be identified.

Abstract: should contain the purpose, the applied data and methods as well as the basic conclusion(s) of the paper.

Key-words: must be included (from 5 to 10) to help to classify the topic.

Text: has to be typed in single spacing with wide margins on one side of an A4 size white paper. Use of S.I. units are expected, and the use of negative exponent is preferred to fractional sign. Mathematical formulae are expected to be as simple as possible and numbered in parentheses at the right margin.

All publications cited in the text should be presented in a *list of references*, arranged in alphabetical order. For an article: name(s) of author(s) in Italics, year, title of article, name of journal, volume, number (the latter two in Italics) and pages. E.g., *Nathan, K.K.,* 1986: A note on the relationship between photo-synthetically active radiation and cloud amount. *Időjárás 90,* 10-13. For a book: name(s) of author(s), year, title of the book (all in Italics except the year), publisher and place of publication. E.g., *Junge, C.E.,* 1963: *Air Chemistry and Radioactivity*. Academic Press, New York and London. Reference in the text should contain the name(s) of the author(s) in Italics and year of publication. E.g., in the case of one author: *Miller* (1989); in the case of two authors: *Gamov* and *Cleveland* (1973); and if there are more than two authors: *Smith et al.* (1990). If the name of the author cannot be fitted into the text: *(Miller,* 1989); etc. When referring papers published in the same year by the same author, letters a, b, c, etc. should follow the year of publication.

Tables should be marked by Arabic numbers and printed in separate sheets with their numbers and legends given below them. Avoid too lengthy or complicated tables, or tables duplicating results given in other form in the manuscript (e.g., graphs)

Figures should also be marked with Arabic numbers and printed in black and white in camera-ready form in separate sheets with their numbers and captions given below them. TIF, GIF or BMP formats should be used for electronic artwork submission.

The text should be submitted both in manuscript and in electronic form, the latter in e-mail or CD. MS Word format is preferred.

Reprints: authors receive 30 reprints free of charge. Additional reprints may be ordered at the authors' expense when sending back the proofs to the Editorial Office.

More information for authors is available: antal.e@met.hu

Published by the Hungarian Meteorological Service

Budapest, Hungary

INDEX: 26 361

HU ISSN 0324-6329

IDŐJÁRÁS

QUARTERLY JOURNAL
OF THE HUNGARIAN METEOROLOGICAL SERVICE

CONTENTS

Kornelia Imre and *Agnes Molnár:* Hygroscopic behavior of Central European atmospheric background aerosol particles in summer..... 63

Veronika Groma, János Osán, Szabina Török, Florian Meirer, Christina Streli, Peter Wobrauschek and *Gerald Falkenberg:* Trace element analysis of airport related aerosols using SR-TXRF..... 83

Roland Steib, Krisztina Labancz, Zita Ferenczi and *Bálint Alföldy:* Airport (Budapest Ferihegy – Hungary) air quality analysis using the EDMS modeling system. Part I. Model development and testing..... 99

Tamás Weidinger, Györgyi Baranka and *Árpád Bordás:* Comparison study in mixing height determination for dispersion models..... 113

László Dióssy: The influence of global climate change on air and soil temperatures in maize canopy..... 125

****

http://www.met.hu/Journal-Idojaras.php

VOL. 112 * NO. 2 * APRIL – JUNE 2008

IDŐJÁRÁS

Quarterly Journal of the Hungarian Meteorological Service

Editor-in-Chief
LÁSZLÓ BOZÓ

Executive Editor
MARGIT ANTAL

EDITORIAL BOARD

AMBRÓZY, P. (Budapest, Hungary)
ANTAL, E. (Budapest, Hungary)
BARTHOLY, J. (Budapest, Hungary)
BATCHVAROVA, E. (Sofia, Bulgaria)
BRIMBLECOMBE, P. (Norwich, U.K.)
CZELNAI, R. (Dörgicse, Hungary)
DÉVÉNYI, D. (Boulder, CO, U.S.A.)
DUNKEL, Z. (Budapest, Hungary)
FISHER, B. (Reading, U.K.)
GELEYN, J.-Fr. (Toulouse, France)
GERESDI, I. (Pécs, Hungary)
GÖTZ, G. (Budapest, Hungary)
HANTEL, M. (Vienna, Austria)
HASZPRA, L. (Budapest, Hungary)
HORÁNYI, A. (Budapest, Hungary)
HORVÁTH, Á. (Siófok, Hungary)
HORVÁTH, L. (Budapest, Hungary)
HUNKÁR, M. (Keszthely, Hungary)
MAJOR, G. (Budapest, Hungary)
MÉSZÁROS, E. (Veszprém, Hungary)
MIKA, J. (Budapest, Hungary)
MERSICH, I. (Budapest, Hungary)
MÖLLER, D. (Berlin, Germany)
NEUWIRTH, F. (Vienna, Austria)
PAP, J.M. (Greenbelt, MD, U.S.A.)
PINTO, J. (R. Triangle Park, NC, U.S.A)
PRÁGER, T. (Budapest, Hungary)
PROBÁLD, F. (Budapest, Hungary)
RADNÓTI, G. (Budapest, Hungary)
S. BURÁNSZKI, M. (Budapest, Hungary)
SZALAI, S. (Budapest, Hungary)
SZEIDL, L. (Budapest, Hungary)
TAR, K. (Debrecen, Hungary)
TÄNCZER, T. (Budapest, Hungary)
TOTH, Z. (Camp Springs, MD, U.S.A.)
VALI, G. (Laramie, WY, U.S.A.)
VARGA-HASZONITS, Z. (Moson-magyaróvár, Hungary)
WEIDINGER, T. (Budapest, Hungary)

Editorial Office: Gilice tér 39, H-1182 Budapest, Hungary
P.O. Box 39, H-1675 Budapest, Hungary
E-mail: bozo.l@met.hu or antal.e@met.hu
Fax: (36-1) 346-4809

Indexed and abstracted in Science Citation Index Expanded™ and Journal Citation Reports/Science Edition
Covered in the abstract and citation database SCOPUS®

Subscription by

mail: IDŐJÁRÁS, P.O. Box 39, H-1675 Budapest, Hungary;
E-mail: kenderesy.k@met.hu or antal.e@met.hu

IDŐJÁRÁS

Quarterly Journal of the Hungarian Meteorological Service
Vol. 112, No. 2, April–June 2008, pp. 63–82

Hygroscopic behavior of Central European atmospheric background aerosol particles in summer

Kornelia Imre[1] and **Agnes Molnár**[2*]

[1]*Department of Earth and Environmental Sciences, University of Pannonia, P.O. Box 158, H-8201 Veszprém, Hungary; E-mail: kornelia@almos.uni-pannon.hu*

[2]*Air Chemistry Group, Hungarian Academy of Sciences, P.O. Box 158, H-8201 Veszprém, Hungary; E-mail: amolnar@almos.uni-pannon.hu*

(Manuscript received in final form March 7, 2008)

Abstract—The hygroscopic properties of size selected regional background aerosol were studied in 8 size ranges, from 62.5 nm to 16 μm. The mass of the aerosol samples was measured gravimetrically under controlled relative humidity (*RH*). The data showed important variation of the mass growth (*GM*) as a function of the size. In the fine mode, the highest growth was found at 86% *RH* in the smallest particle size range ($GM = 2.2$), while the lowest was found in the 0.25–0.50 μm size interval ($GM = 1.4$). In the coarse mode, the highest growth was found in the 1–4 μm ($GM = 2.1$) range. Based on the inorganic ion content of the samples, the water uptake of model aerosol (determined by the Aerosol Inorganics Model (AIM)) was also calculated; and the measured and calculated mass growth rates were compared. We found that fine range particles absorb less water than the modeled aerosol. In the coarse mode, the measured mass growth rate was often higher than the value calculated. Our results showed that in the fine mode the water deficiency (difference between measured and calculated water concentrations) is the function of the total carbon concentration (*TC*) of the samples (e.g., at 86% *RH*, 1 μg m^{-3} *TC* surplus results in a 2.86 μg m^{-3} decrease of water concentration). On the basis of mass growth factors, particle diameter growth rates (*G*) were derived. At K-puszta, *G* varied between 1.10 and 1.50 at 86% *RH*. Finally, the power-law function was fitted to both the measured (γ_m) and calculated (γ_c) data. With the application of multi-linear regression, we found that the fine mode γ_m can be estimated by the γ_c and the *TC* concentration, conversely to the coarse mode.

Key-words: aerosol particles, water uptake, organic and inorganic composition, size distribution

*Corresponding author

1. Introduction

The physical and chemical nature of aerosol particles is crucial to the control of the radiation budget of the Earth through direct scattering and absorption of the incoming solar radiation. Aerosol particles affect the structure and radiative properties of clouds by determining the number of cloud condensation nuclei. Besides the wavelength, the magnitude of scattered and absorbed radiation is the function of the particle size and chemical composition. Due to water-soluble components, the size of the particles is affected significantly by the ambient relative humidity. Their hygroscopic behavior is determined by the inorganic, as well as organic, species. Although the organic fraction of the particles is rather high, our knowledge on their effects on aerosol hygroscopicity is still limited (*Sjogren et al.*, 2007). Organic compounds can alter the hygroscopic growth by influencing the number of soluble ions available (Raoult's law) and by lowering the surface tension (Kelvin effect) (e.g., *Mircea et al.*, 2002, 2005).

Hygroscopic particle growth has been widely studied for 50 years. It was first measured by *Junge* at the beginning of 1950 (*Warneck*, 1999). *Winkler* and *Junge* (1972) and *Hänel* (1976) applied gravimetric method, while *Mészáros* (1971) studied the hygroscopic behavior of continental aerosol particles by means of optical microscopy. The results of these early studies already showed that hygroscopic growth of aerosol particles was smaller than that of pure salts. Also, the growth curves for continental aerosols were smoother than those of pure salts. Recently, hygroscopic and non-hygroscopic fractions of atmospheric aerosol were generally studied by Tandem Differential Mobility Analyzer (TDMA) systems (e.g., *McMurry* and *Stolzenburg,* 1989; *Svenningsson et al.,* 1994; *Swietlicki et al.,* 2000; *Ferron et al.*, 2005).

In numerous works, the hygroscopic properties of the individual inorganic salts (*Lee* and *Hsu*, 1998, 2000; *Gysel et al.*, 2002), organic compounds, and mixtures of the organic and inorganic particles (*Hämeri et al.*, 1998; *Chan et al.*, 1997; *Hansson et al.*, 1998; *Virkkula et al.*, 1999; *Sjogren et al.*, 2007) were studied. *Cruz* and *Pandis* (1997) concluded that pure dicarboxylic acids acted as CCN. *Mircea et al.* (2002, 2005) pointed out that the water-soluble fraction of aerosol particles influenced the surface tension of the droplets (particles). In several papers the effect of the organic cover of the particles (e.g., *Andrews* and *Larson*, 1993; *Pósfai et al.*, 2004) was studied.

Regarding the role of the organic species in aerosol hygroscopicity, different results and opinions have been published. On one hand, some authors proposed that organic compounds could be considered inactive in particle water uptake (e.g., *Pitchford* and *McMurry*, 1994; *Busch et al.*, 2002). However, more studies reported on how organic species modify the aerosol hygroscopicity (e.g., *Saxena et al.*, 1995; *Dick et al.*, 2000; *Cruz* and *Pandis*, 2000; *Choi* and *Chan*, 2002). *Saxena et al.* (1995) found that hygroscopic properties were affected by the aerosol type and origin: at a non-urban location the organic fraction

enhanced, while at an urban location organic matter reduced the water uptake of inorganic atmospheric aerosol. *Zhou et al.* (2001) proposed that more hygroscopic particles are most likely representative of the aged continental aerosol, while nearly hydrophobic particles originate from nearby combustion sources.

The aim of this work is to contribute to the understanding of the hygroscopic properties of atmospheric aerosol. In this study three problems are considered:

- Determination of hygroscopic growth of ambient aerosol particles with respect to their size distribution.
- Estimation of the effect of organic compounds on hygroscopicity.
- Modeling the hygroscopic growth of the particles as the function of their size and chemical composition.

2. Experimental

In the summer of 2001 and 2002, 13 size-selected ambient aerosol samples were taken at K-puszta station ($\varphi = 46.99°$, $\lambda = 19.55°$, 125 m a.s.l.), Hungary. The sampling site belongs to the GAW and EMEP monitoring networks. It is located on a forest clearing on the Great Hungarian Plain about 70 km south-east from Budapest. The closest town (Kecskemét) is 15 km SE of the station. Since this site is relatively far from direct anthropogenic sources, K-puszta is considered to be a regional background air pollution monitoring station. The representativeness of aerosol measurements at this station is discussed in detail by *Geresdi et al.* (2006).

The air was sampled by a 9-stage Berner impactor (*Berner*, 1984) at a height of 10 m, in order to avoid the direct impact of the surrounding sandy soil. The lower cut-off diameters of the impactor stages are 0.0625, 0.125, 0.25, 0.5, 1, 2, 4, 8, 16 μm at a sampling rate of 31.3 l min^{-1}. The aerosol particles were captured on Al-foils. In the summer of 2001, five samples (from July 27 to August 16) were collected. In 2002 (from June 28 to July 24) the number of samples was eight (sampling details are in *Table 1*). For the sake of reliable mass measurements, the duration of the sampling varied between 3–7 days.

In our experiments, the gravimetric method was applied for the determination of the mass change of aerosol particles due to their water uptake. Mass measurements were carried out by means of a Sartorius microbalance (detection limit is 10 μg), which was placed into an isolated chamber. The relative humidity of the chamber was controlled by saturated solutions of different salts ($Mg(NO_3)_2 \cdot 6\ H_2O$ (51%); NH_4NO_3 (64%); NaCl (76%); NH_4Cl (80%); KCl (86%)), as well as silica gel. The relative humidity was precisely measured by a hygrograph, which was calibrated in a climate chamber at the Hungarian Meteorological Service.

To validate this gravimetric method, the water uptake of ammonium sulfate measured gravimetrically, as well as determined on the basis of thermodynamic approach (using the Aerosol Inorganics Model (AIM) (*Clegg et al.*, 1998)) is summarized. The vaporized solution of ammonium sulfate was dried at $RH < 30\%$, then the dry mass (2.06 mmol) and the mass change (water uptake) were measured at the above mentioned *RH*s. As it is well known, the deliquescence relative humidity of ammonium sulfate is around 80% *RH*. Below this *RH*, both the calculated and measured water mass were zero. At 80, 86, and 90% *RH*s, the calculated water-uptake was 7.9, 10.7, and 14.4 mmol, respectively, while in the case of gravimetric analysis the corresponding values were 7.9, 10.5, and 14.5 mmol, respectively. We concluded that the data from gravimetric analysis are in good agreement with calculated values.

Table 1. Sampling details

Sample number	Sampling date	Air volume (m^3)
S1	July 27–July 31, 2001	163.5
S2	Aug 04–Aug 07, 2001	152.3
S3	Aug 08–Aug 10, 2001	112.4
S4	Aug 11–Aug 13, 2001	113.0
S5	Aug 14–Aug 16, 2001	112.2
S6	June 28–July 04 *d*, 2002	172.4
S7	June 28–July 05 *n*, 2002	122.8
S8	July 05–July 11 *d*, 2002	183.6
S9	July 05–July 12 *n*, 2002	106.4
S10	July 12–July 18 *d*, 2002	187.9
S11	July 12–July 19 *n*, 2002	113.2
S12	July 19–July 24 *d*, 2002	162.6
S13	July 19–July 24 *n*, 2002	79.4

Note: *d* and *n* denote daytime and nighttime sampling, respectively

In this study the following protocol was applied.

Before sampling: The mass of unloaded Al-foils was measured under low relative humidity (30%). The impactor substrates were generally kept in the chamber for more than 48 hours in order to reach thermodynamic equilibrium. After weighting, the Al-foils were packed and stored separately until sampling.

Sampling: The pre-weighted Al-foils were placed into the Berner impactor. After sampling, the Al-foils were carefully packed separately and were stored frozen until further processing and analysis.

After sampling: The dry mass, as well as the mass change of size-selected aerosol (as the function of relative humidity) were measured. The samples were kept at a given relative humidity for more than 48 hours in

order to reach equilibrium with their surroundings. The total aerosol mass collected on the impactor substrates was in the range of 50–780 μg. The standard deviation of parallel mass measurements was generally below 10%, as shown in *Table 2*.

Table 2. Dry mass (average ± standard deviation) of aerosol samples

Sample number	Particle mean diameter (μm)							
	0.088	**0.18**	**0.35**	**0.71**	**1.4**	**2.8**	**5.7**	**11.3**
S1	53±7	230±14	730±42	683±15	150±3	227±15	157±7	130±3
S2	100±11	273±12	640±30	473±6	75±7	197±6	278±12	83±6
S3	210±21	370±17	690±30	427±15	103±7	307±14	370±26	323±7
S4	240±5	305±7	520±28	505±7	390±8	195±7	210±4	70±7
S5	160±3	293±12	780±16	613±21	197±7	280±6	307±15	273±6
S6	103±15	363±10	647±6	467±6	137±6	367±6	363±6	313±6
S7	80±12	195±6	493±21	413±15	170±6	333±6	270±15	333±15
S8	40±20	227±6	547±12	740±10	123±6	230±12	223±12	220±6
S9	58±6	137±12	587±12	573±6	183±6	193±10	233±6	133±6
S10	77±21	223±10	807±10	750±6	187±12	307±10	327±6	290±20
S11	27±6	97±20	447±23	573±12	183±6	227±6	217±21	153±6
S12	75±12	183±6	557±25	547±11	180±17	127±87	177±12	125±6
S13	29±6	51±6	260±6	287±12	170±6	107±6	150±10	90±6

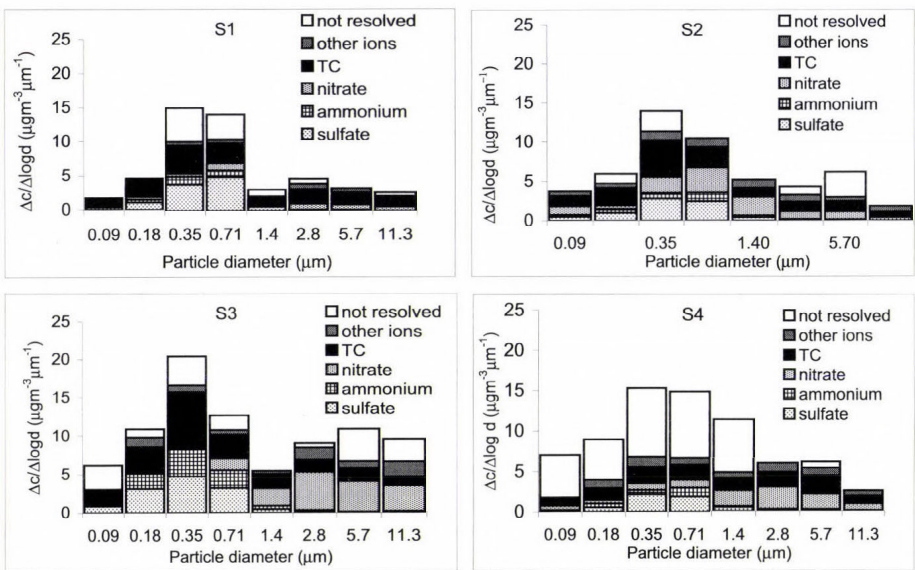
Finally: The chemical composition of the impactor samples was determined. Al-foils were cut into four parts. One part was used for total carbon analysis; the second part was extracted in water to dissolve water-soluble inorganic ions. (The rest of the samples were reserved for further analysis.) The extraction of the samples was performed in 2 ml high purity (MilliQ) water. Then the extracts were filtered through a membrane filter (Millipore, 0.22 μm) in order to remove non-dissolved particles suspended in the solution. The concentrations of inorganic ions (ammonium, potassium, sodium, calcium, magnesium, chloride, sulfate, and nitrate) were determined by capillary electrophoresis and ion chromatography. The detection limits of the inorganic ion concentrations (at a signal-to-noise ratio of 3) were <100 μg l^{-1} for both capillary electrophoresis (details in *Temesi et al.,* 2001) and ion chromatography. The TC concentration of the aerosol samples was measured as carbon dioxide by the catalytic combustion method in oxygen at 680 °C, using the Astro Model 2100 TOC solid-analyzer. The calibration solution was potassium hydrogen phthalate and the detection limit of carbon measurement was 2 μgC (at a signal-to-noise ratio of 3).

3. *Results and discussion*

3.1. Dry mass size distribution and chemical composition

In *Fig. 1*, the size and chemical distribution of dry aerosol particles is presented. During the sampling period the average total dry mass concentration was 17.4 μg m^{-3}, with a standard deviation of 4.5 μg m^{-3} (marked as std. in the following text). The aerosol mass size distribution was generally bimodal. The majority of the dry mass a ccumulated in the fine size range with 62% (std. 6%) of the total mass found in PM_1. This high fraction indicates the importance of aged aerosol over this site. In several cases (see *Fig. 1*), a relatively high aerosol mass was measured in particles with diameter smaller than 0.1 μm, which is probably due to new particle production.

In *Fig. 1* the concentrations of the main chemical components (sulfate, nitrate, ammonium, and total carbon (*TC*)) are also shown. The total mean sulfate concentration was 2.9 μg m^{-3} (std. 1.2 μg m^{-3}), almost 90% of this component accumulated in PM_1, mostly in the range of 0.25–1.0 μm. The size distribution of ammonium was similar to sulfate, while nitrate was detected mainly in the coarse mode. Other ions (chloride, sodium, calcium, potassium, and magnesium) were also analyzed in the samples, and the sum of their concentration is shown in *Fig. 1* under "other ions". Average total carbon concentration amounted to 4.4 μg m^{-3} (std. 1.5 μg m^{-3}), around 60% of which was measured in the fine fraction, with the highest concentration in the range of 0.25–0.50 μm. It should be mentioned that carbonaceous compounds generally dominate the chemical composition of $PM_{0.1}$.



→

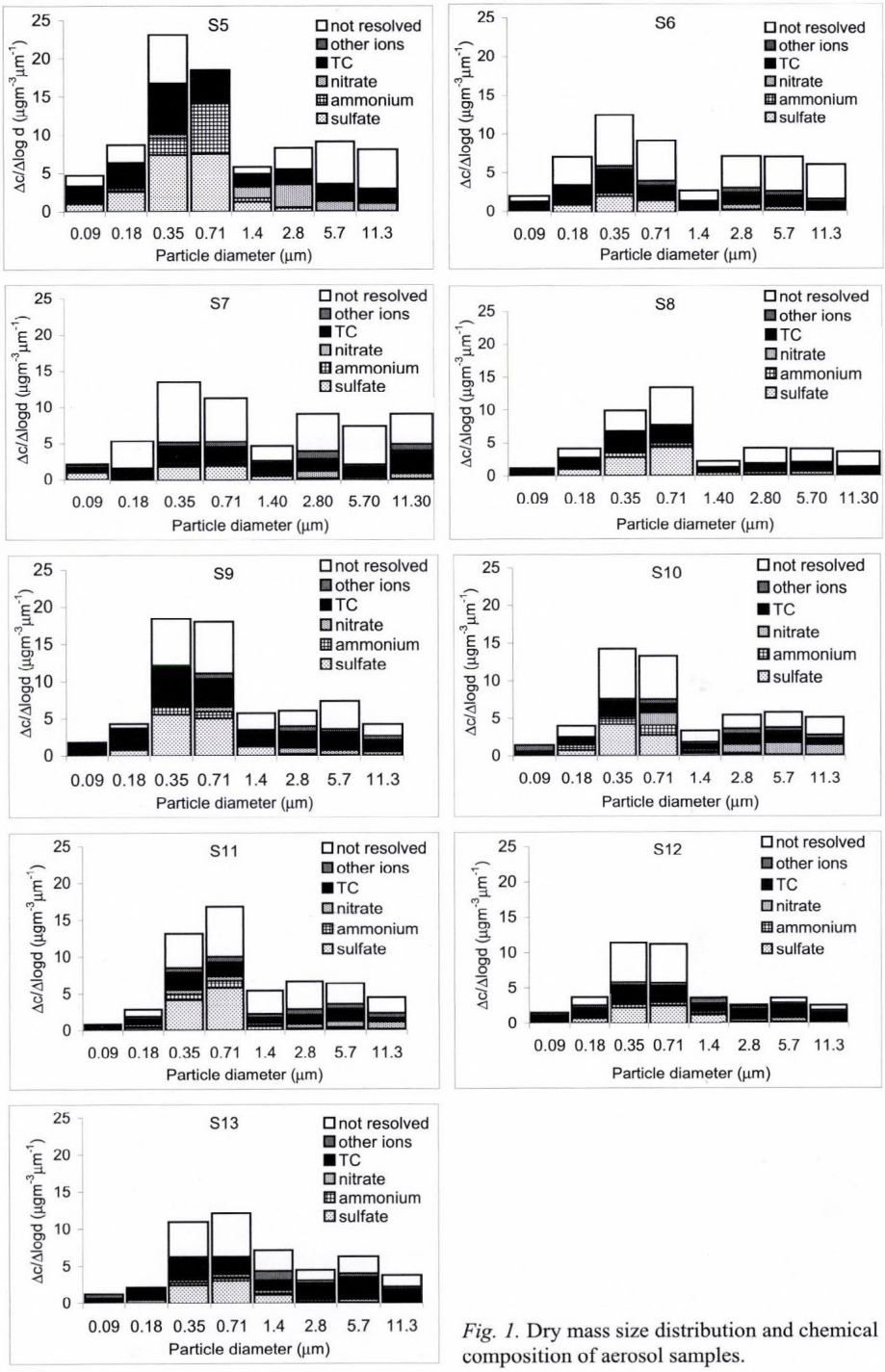


Fig. 1. Dry mass size distribution and chemical composition of aerosol samples.

3.2. *Measured and calculated mass growth*

Due to the hygroscopic behavior of atmospheric aerosol particles, the mass of the aerosol samples increased with increasing relative humidity. In *Fig. 2* the change in mass size distribution due to water absorption is presented for 4 selected samples. Generally, the mass change of the fine particles became significant above 80–86% *RH*, which is higher than the deliquescence *RH* of the most important inorganic salts. This is similar to results published earlier (e.g., *Winkler* and *Junge*, 1972; *Hänel*, 1976; *Hämeri et al.*, 1998; *Chan et al.*, 1997; *Hansson et al.*, 1998; *Virkkula et al.*, 1999; *Sjogren et al.*, 2007). The measured mass growth factors ($GM = M/M_{dry}$) at 86% relative humidity are presented in *Table 3* in the columns denoted by "m" (measured). The data (both in *Fig. 2* and *Table 3*) show important variations of the mass growth as a function of the size. Below 1 μm, the highest growth was found in the smallest particle size range (average: 2.2). Meanwhile, the lowest values were obtained in the 0.25–0.50 μm size interval (average 1.4). It should be noted that the low hygroscopic mass growth rate occurred with high total carbon concentration. In the coarse mode ($1 < d < 16$ μm), the highest growth was found in the range of 1–4 μm (average 2.1). More than 30 years ago *Mészáros* (1971) reported that hygroscopicity of the large and giant particles ($d > 0.4$ μm) decreased with increasing size. Our results differ from this data, probably due to the significant change in inorganic (mainly ammonium sulfate) salt concentrations over this time period (*Mészáros* and *Horváth*, 1984).

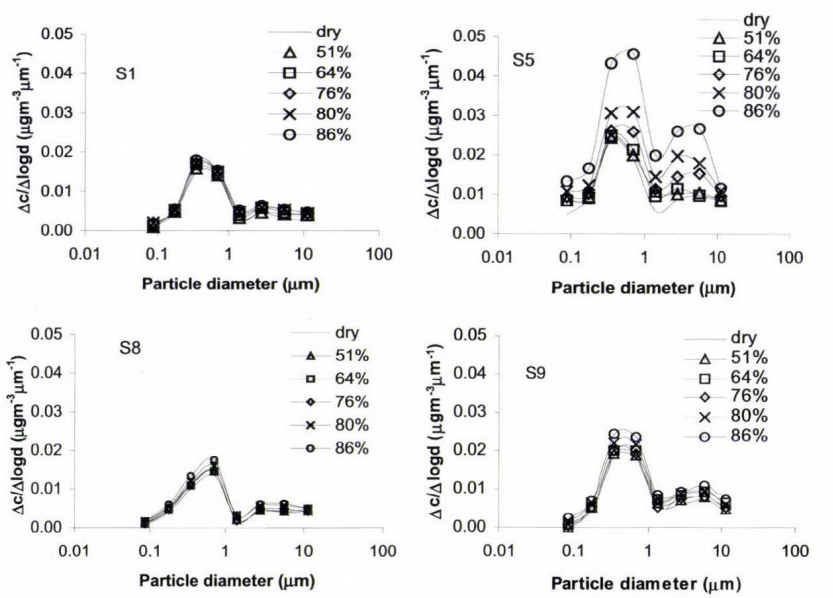


Fig. 2. Change in mass size distribution as the function of relative humidity.

On the basis of inorganic constituents, the mass growth of the particles in different size ranges was calculated by means of the AIM (*Clegg et al.,* 1998). This model gives the water uptake of a model aerosol (composed of inorganic ions: sulfate, nitrate, chloride, ammonium, potassium, sodium, calcium, and hydrogen) as the function of relative humidity. In the calculation we used the ion concentrations (except hydrogen) that were determined analytically in the size selected aerosol samples. The hydrogen concentration was calculated from the ion balance. We have to note that this model gives information on the Raoult-term, while the curvature effect of the particles is not involved. However, considering the aerosol size range evaluated in this work, this latter effect could only be important in the case of the first impactor stages (size range: 0.0625–0.125 μm) (*Maßling et al.*, 2003; *Ferron et al.*, 2005).

Table 3. Mass growth of particles at 86% *RH* (* denotes: data are not available)

Sample number	Particle mean diameter (μm)															
	0.088		0.18		0.35		0.71		1.4		2.8		5.7		11.3	
	m	c	m	c	m	c	m	c	m	c	m	c	m	c	m	c
S1	2.0	2.3	1.6	1.8	1.5	1.7	1.4	2.2	2.7	1.5	1.5	2.2	1.7	2.1	1.8	2.0
S2	1.9	3.6	1.2	1.7	1.3	2.1	1.9	2.7	5.4	7.1	5.3	5.5	*	*	5.2	5.9
S3	2.0	1.4	1.7	1.7	1.1	1.6	4.6	11.1	*	*	2.4	2.8	*	*	2.3	2.7
S4	1.1	1.6	1.1	1.5	1.2	1.7	1.5	1.7	1.7	2.0	1.4	4.5	1.5	2.9	1.4	3.8
S5	2.3	8.2	1.4	1.8	1.3	2.7	1.7	3.0	2.5	2.4	2.4	9.2	2.0	1.6	1.3	1.5
S6	1.1	1.3	1.1	1.4	1.1	1.4	1.1	1.4	1.2	1.3	1.2	1.1	1.1	1.1	1.0	1.0
S7	1.0	2.3	1.0	1.1	1.1	1.4	1.2	1.5	1.0	1.4	1.2	1.0	1.0	1.0	1.1	1.1
S8	2.4	2.5	1.5	2.0	1.3	2.1	1.3	2.3	1.4	2.0	1.5	1.2	1.5	1.1	1.4	1.1
S9	*	*	1.6	1.7	1.3	2.2	1.3	2.1	1.4	2.1	1.6	1.1	1.5	1.1	1.7	1.2
S10	5.9	3.2	2.2	*	2.0	3.0	*	2.4	2.8	1.7	3.2	1.4	2.4	1.1	1.7	1.1
S11	*	3.7	3.8	1.8	2.0	3.2	1.9	3.4	2.0	1.7	1.9	1.7	1.8	*	2.2	1.5
S12	2.4	3.4	1.2	2.3	1.1	2.4	1.2	2.6	1.5	3.4	2.5	1.4	1.4	1.4	1.6	1.3
S13	*	*	2.4	6.0	1.2	1.7	1.3	1.2	1.3	*	1.6	*	1.5	*	1.4	*
Average	**2.2**	**3.1**	**1.7**	**2.1**	**1.4**	**2.1**	**1.7**	**2.9**	**2.1**	**2.4**	**2.1**	**2.8**	**1.6**	**1.5**	**1.8**	**2.0**
σ	1.4	1.9	0.8	1.3	0.3	0.6	1.0	2.6	1.2	1.7	1.1	2.5	0.4	0.6	1.1	1.5

The "calculated" hygroscopic mass growth of the samples was estimated by the addition of measured aerosol dry mass and modeled water uptake (AIM calculations from the inorganic content of the samples) at different relative humidities. In *Table 3*, the calculated results of hygroscopic mass growth of model aerosol at 86% *RH* are presented in columns denoted by "c". The calculated mass growth rate shows a similar size distribution as the measured values (see the average mass growth data). However, in the fine size range the measured mass growth factors are generally lower (20–40%) than the calculated

ones. This indicates that the ambient aerosol is less hygroscopic than the model particles, probably due to their carbonaceous constituents. In the coarse mode, mainly above 2 μm, the mass growth measured is often higher than the value calculated. The ratio of measured and calculated mass growth varies within a rather broad range (26–232%). It is possible that other hygroscopic material besides inorganic salts can also be present in these particles that are not taken into account in the AIM model.

The role of carbonaceous compounds in the control of the hygroscopicity of the particles could be studied, if the difference between measured and calculated water concentration (water deficiency) is related to the total carbon concentration (*TC*) of the samples. In *Fig. 3* the water deficiency at different relative humidities, both for fine (d <1 μm) and coarse (d >1 μm) particles, is presented as the function of *TC* concentration. In the fine mode, a statistically significant relationship was found (probability level >95%) between the parameters. The data show that *TC* significantly affects the water-uptake of the particles. In other words, a higher *TC* concentration results in higher water deficiency. Moreover, besides *TC* concentration, the deficiency of water-uptake of the particles is also affected by the relative humidity. Our results indicate that the higher the relative humidity, the more significant the water deficiency. Regarding linear regression equations (see in *Fig. 3*) at 51%, 64%, 76%, 80%, and 86% *RH*, a 1 μg m^{-3} surplus in *TC* concentration results in a 0.75 μg m^{-3}, 1.20 μg m^{-3}, 1.67 μg m^{-3}, 2.08 μg m^{-3}, and 2.86 μg m^{-3} decrease in the absorbed water mass concentration, respectively. Finally, we have to note that no statistically significant relationship was found between *TC* and water deficiency in the coarse mode, as shown in *Fig. 3*.

The results of laboratory and field studies indicated that organic matter can influence the water uptake of the particles. In laboratory experiments, small carboxylic and multi-functional acids enhanced the water uptake of mixed particles (*Cruz* and *Pandis*, 2000; *Choi* and *Chan*, 2002; *Prenni et al.*, 2003). Field measurements also showed that organic species in aerosol particles can contribute to water absorption (*Dick et al.*, 2000; *Saxena et al.*, 1995). On the other hand, *Choi* and *Chan* (2002), *Cruz* and *Pandis* (2000), and *Saxena et al.*, (1995) reported that mainly in urban environments the organic fraction can reduce the water uptake of the inorganic compounds. Differences in the hygroscopic behavior between urban and non-urban particles are thought to be the result of aerosol ageing processes and the presence of polar organic species (*Alfarra et al.*, 2004; *Aklilu et al.*, 2006). Our results showed, however, that even in the regional background air, the carbonaceous content of the particles could significantly diminish the water absorption of the inorganic fraction.

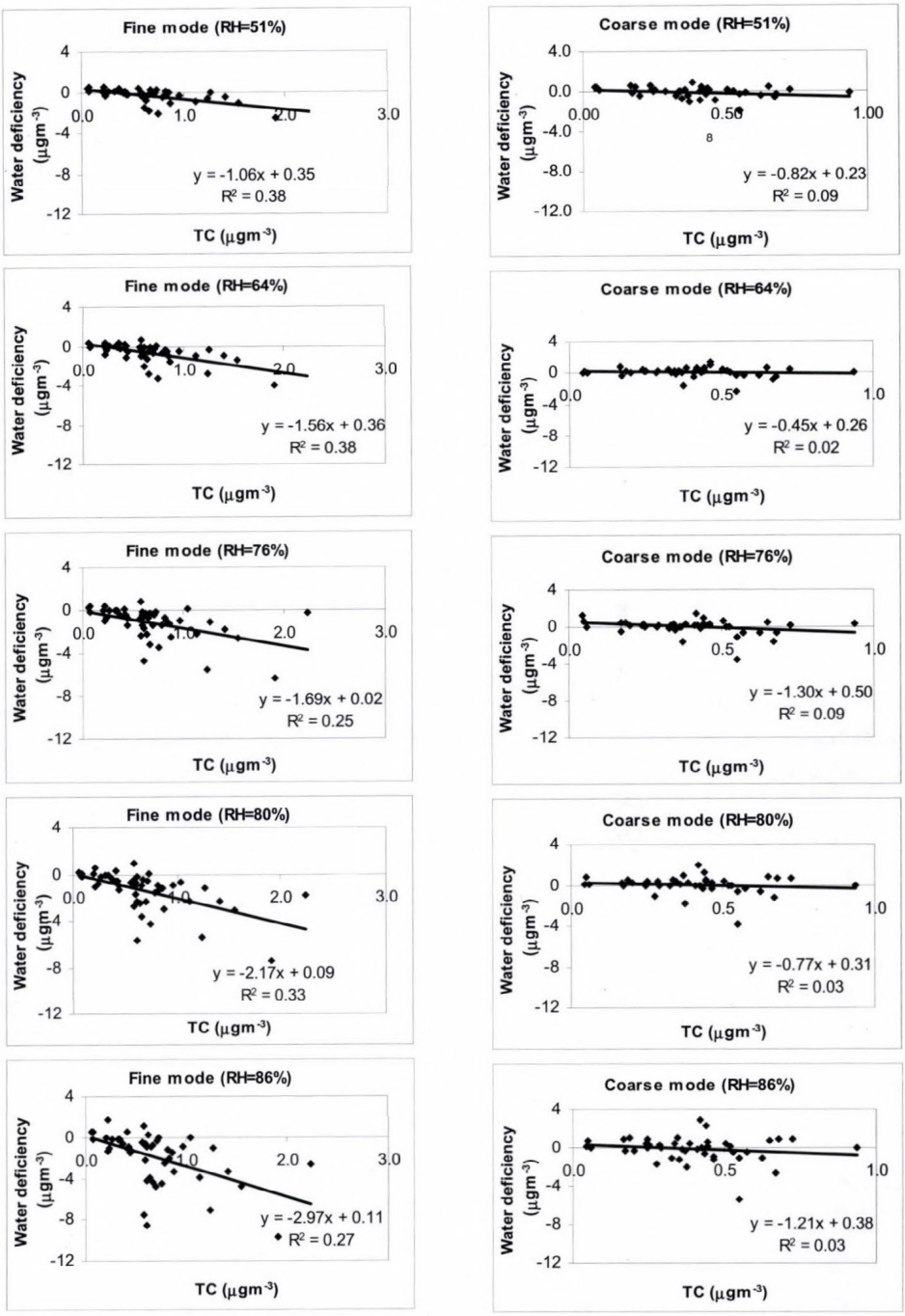


Fig. 3. Water deficiency as the function of total carbon concentration and relative humidity.

3.3. Growth in particle size

In order to compare our results to the hygroscopic growth factors published in the literature, the measured and calculated mass growth was converted into particle growth. Mass growth (GM) and particle size growth (G) factors are defined as:

$$GM_{RH} = \frac{M_{RH}}{M_{dry}} \quad \text{and} \quad G_{RH} = \frac{d_{RH}}{d_{dry}}, \tag{1}$$

where M and d denote the particle mass and particle diameter at a given RH compared to the dry values, respectively. In the calculation, the geometric mean aerodynamic diameter of each impactor stage was considered as the characteristic size of the particles. The conversion of mass growth to particle growth is possible if we consider that:

$$GM_{RH} = \frac{\rho_{RH}}{\rho_{dry}} \cdot \frac{d_{RH}^3}{d_{dry}^3} = \frac{\rho_{RH}}{\rho_{dry}} \cdot G_{RH}^3 . \tag{2}$$

Unfortunately, the estimation of the dry particle density (ρ_{dry}) as well as the particle density at a given relative humidity (ρ_{RH}) is rather uncertain. Concerning dry particle density, few data can be found and these data usually correspond to a certain particle size (e.g., *Stein et al.,* 1994). Stein and co-workers applied TDMA to determine the particle densities. They found that dry particle density for particles smaller than 0.236 μm is in the range of 1.74–1.78 g cm^{-3} within an uncertainty of 4%. In this work 1.76 g cm^{-3} dry particle density was used, which is close to the density of ammonium sulfate (e.g., *Sjogren et al.,* 2007).

To estimate the change in particle density due to water-uptake, further consideration is necessary. Although the absorbed water mass is directly measured, the consideration of the change in particle volume is not evident since the volumes of dry particle and water are not simply additive. However, several workers in the field generally assumed this additivity (e.g., *Hitzenberger et al.,* 1999; *Ferron et al.,* 2005). We also applied this assumption in further calculations:

$$\frac{\rho_{RH}}{\rho_{dry}} = \frac{M_{RH} \cdot \rho_{water}}{M_{dry} \cdot \rho_{water} + M_{water} \cdot \rho_{dry}} . \tag{3}$$

In *Fig. 4a* the size distributions of particle growth (G) are presented at 51%, 76%, and 86% RHs. According to these data, in the range of 0.125–0.500 μm, G

is characterized by a local minimum at all *RH*s. These particle growth factors can be compared to the data published by different authors. At low *RH* (50–55%) in marine air (*Maßling et al.*, 2003; *Zhou et al.*, 2001), the particle growth was more important than in the case of our samples. Data from AEROSOL99 – INDOEX (*Maßling et al.*, 2003) and Arctic Ocean Expedition (*Zhou et al.*, 2001) projects show increasing growth rates (G = 1.20–1.27 and 1.13–1.17, respectively) in the ranges of 50–250 nm and 50–165 nm, respectively. In approximately the same size range we obtained smaller growth rates (1.04–1.23), which decreased with the increasing particle size. At 70–76% *RH* we could draw similar conclusions as before: at K-puszta the aerosol particles were less hygroscopic ($G_{(76\%)}$ = 1.06–1.28) than the marine aerosol (AEROSOL99 – INDOEX (*Maßling et al.*, 2003), $G_{(75\%)}$ = 1.36–1.46 and 1.18–1.20 for more and less hygroscopic particles, respectively; also for the Arctic Ocean Expedition (*Zhou et al.*, 2001), $G_{(70\%)}$=1.23–1.29).

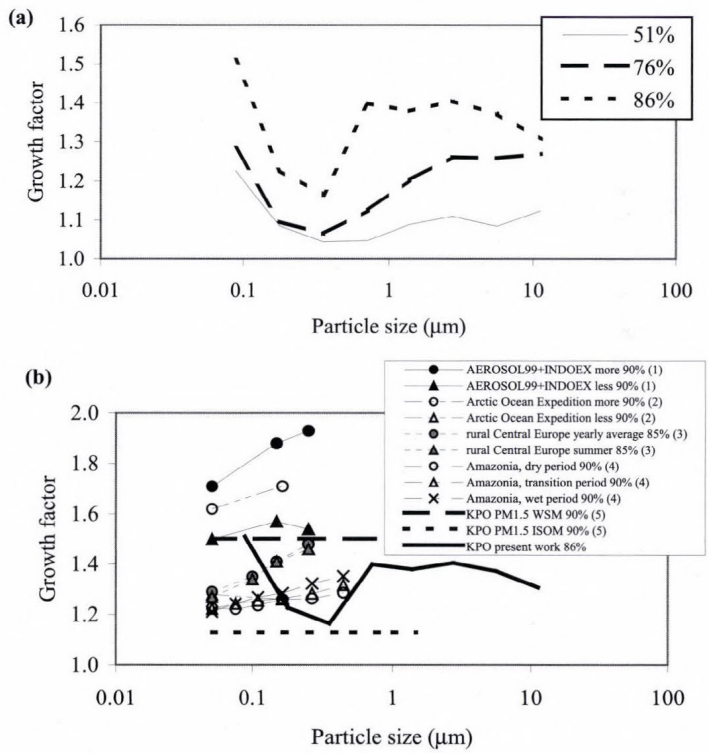


Fig. 4. Hygroscopic growth of aerosol particles as the function of the size. (a) At K-puszta, at 51%, 76%, and 86% *RH*. (b) Comparison of rural and background data at 86–90% *RH*. The referred publications are: (1) *Maßling et al.*, 2003; (2) *Zhou et al.*, 2001; (3) *Ferron et al.*, 2005; (4) *Rissler et al.*, 2006; (5) *Gysel et al.*, 2004.

In *Fig. 4b*, the size distribution of the growth factor at 85–90% relative humidity is presented. Along with our results, hygroscopic growth rates published by different authors are also plotted. These data also show that marine (oceanic) aerosol is more hygroscopic than the particles from the continental air. The growth factor of continental aerosol ranges between 1.13 and 1.50. These (lower and upper) limits correspond to the growth rate of ISOM (isolated water-soluble atmospheric humic matter, which is the less hydrophilic water soluble organic matter) and WSM (water soluble inorganic and organic matter) constituents of the aerosol sampled at K-puszta ($PM_{1.5}$; *Gysel et al.*, 2004). It is interesting to note that all growth rates referring to continental aerosol can be found in this range independently from the particle size and the sampling site. In studying our data we found that, between 125 and 500 nm, the hygroscopicity of the particles is rather similar to ISOM. This indirectly indicates that atmospheric humic matter may dominate in the chemical composition of these particles. On the other hand, in the smaller and larger fine particles (62.5–125 nm and 0.5–1.0 μm) water-soluble compounds (both inorganic and organic) are the most important constituents.

3.4. Modeling of size selected particle growth as a function of relative humidity

Consideration of the hygroscopic growth of aerosol particles in different processes (e.g., radiative forcing estimations) is very important. For the sake of simplicity and consistency, model functions describing the hygroscopic behavior of the aerosol particles are introduced. Particle growth G is generally and simply estimated as the function of relative humidity (RH in percentage). In this work we applied the following power-law function approach frequently proposed (e.g., *Zhou et al.*, 2001):

$$G(RH) = 10^{a} \cdot \left(\frac{1 - RH}{100}\right)^{-\gamma}. \tag{4}$$

In *Table 4* the summary of the fitted γ exponent and 10^{a} parameters are given for the measured, as well as calculated data sets. The growth rate is mostly governed by γ, since 10^{a} varies around 1. It can be seen that if γ is close to zero, the hygroscopicity of the particles is weak. The results in *Table 4* show that the measured particle growth (γexponent) strongly depends on the particle size. The obvious reason for this variation is the difference in chemical composition of the particles, which is indicated by the different γ values of aerosol particles with similar sizes. During the AEROSOL99 – INDOEX project (*Maßling et al.*, 2003), the mean value of the exponent was 0.230, 0.257, and 0.269 in the cases of 50 nm, 150 nm, and 250 nm sized particles, respectively. Meanwhile, *Zhou et al* (2001) published γ values of 0.201 ($d = 50$ nm) and 0.228 ($d = 165$ nm). *Gysel et al.* (2004) found that the mean γ exponent of ISOM and WSM in $PM_{1.5}$ was

0.064 and 0.196, respectively. The exponents obtained from our samples are within these latter two values, similarly to the particle growth rates (see above). Note that in the case of ammonium sulfate, the value of γ is 0.218 (*Sjogren et al.*, 2007).

Table 4. Parameters of power-law functions in different particle sizes for both measured and calculated data sets

Geometric particle diameter (μm)	Measured		Calculated	
	gamma	10^c	gamma	10^c
0.088	0.185	1.02	0.273	0.92
0.18	0.096	0.98	0.164	0.93
0.35	0.078	0.97	0.206	0.93
0.71	0.182	0.91	0.268	0.90
1.4	0.178	0.95	0.205	0.96
2.8	0.201	0.94	0.192	0.96
5.7	0.196	0.93	0.092	0.99
11.3	0.147	0.98	0.140	0.96

In *Fig. 5* the size dependence of "measured" particle growth – estimated by power-law fit – at 86% *RH* is presented. In the fine size range, particles in the smallest size interval (0.0625–0.125 μm) were found to be the most hygroscopic ($G_{(86\%)} \approx 1.5$). This size range was followed by the less hygroscopic particles in the 0.125–0.50 μm interval ($G_{(86\%)} = 1.10$–1.20), where γexponents were closest to zero (see also *Table 4*). The particles in the remaining size intervals showed similar hygroscopicity; their growth rate varied between 1.30 and 1.40. In *Table 4* the γ parameter is also given for the "calculated" data sets; and these data (at 86% RH) are plotted in *Fig. 5*.

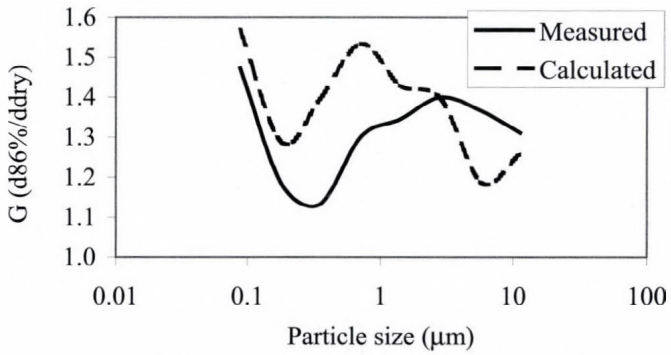


Fig. 5. Measured and calculated growth rate (86% *RH*) as the function of the size.

The size distribution of the "calculated" growth factor shows similarities to the "measured" values; however, in the fine size range the "calculated" growth factors are consistently higher than the "measured" ones. In the coarse mode, no similarities were found. Above 2.8 μm, the "measured" particle growth was underestimated by the growth rates "calculated". As it was mentioned before, it indicates that more compounds – other than those analyzed – can significantly contribute to the hygroscopic growth of the coarse particles. In the fine mode, the best agreement between "calculated" and "measured" data is found in stage 1 (smallest particles), while above this size the difference is rather high. It is supposed that this alteration can be attributed to the effect of carbonaceous compounds, which have the highest concentration in these size ranges (see *Fig. 1*).

One can suppose that the γ exponent is mainly controlled by the chemical composition of the particles. (Note: the curvature effect of the aerosol particles plays an important role only under 100 nm (*Maßling et al.*, 2003; *Ferron et al.*, 2005)). If we suppose that we have information on the concentration of all the important chemical compounds that are responsible for the control of hygroscopic growth, then we can assume that the measured γ exponent (γ_m in the following) can be estimated by the inorganic ion and total carbon concentrations of the aerosol particles. Further, we can presume that:

- The hygroscopic behavior of the inorganic compounds is well estimated by the AIM model. This means that the "calculated" γ exponent (denoted by γ_c in the following) correctly described the water uptake of inorganic ions.
- The hygroscopic effect of carbonaceous compounds can be estimated by the *TC* concentration.

If we accept the above assumptions, then γ_m could be estimated as the function of the γ_c and the *TC* concentration. As a first approximation, the linear function of two variables is considered:

$$\gamma_m = m_1 \cdot \gamma_c + m_2 \cdot TC + b. \tag{5}$$

The calculation is based on a multilinear approach, where m_1 and m_2 are coefficients, parameter b could be considered as the hygroscopic effect of other constituents that are not determined. The statistical significance (at the probability level of 99%) is checked by F-distribution. The results show a statistically significant relationship among the parameters considered, both for particles in fine (d<1 μm) and coarse (d>1 μm) mode. The multilinear regression equations are:

$$\text{fine mode: } \gamma_m = 0.78 \cdot \gamma_c - 0.07 \cdot TC + 0.01, \tag{6}$$

$$\text{coarse mode: } \gamma_m = 0.58 \cdot \gamma_c - 0.12 \cdot TC + 0.13. \tag{7}$$

According to the equations, γ_m is in positive relationship with γ_c, while *TC* has a negative effect on the measured hygroscopic growth, as expected. The results indicate that in the fine mode γ_m can be estimated by the inorganic γ_c and the total carbon concentration, since the unknown constituents (*b*) do not play an important role (<10%) in the control of γ_m. On the other hand, in spite of the statistical relationship for coarse mode aerosol, the same conclusion cannot be drawn because of the high contribution of non-defined compounds (the share of *b* is >70%).

4. Conclusions

The hygroscopic properties of size-selected atmospheric aerosol particles were studied in 8 size intervals ranging from 62.5 nm to 16 μm at K-puszta, Hungary. Our results showed that:

1. In the fine size range ($d \leq 1$ μm):
    a. The absorbed water concentration strongly depends on the particle size, which is the consequence of differences in the chemical composition.
    b. Growth factors (both *GM* and *G*) peak in the smallest size interval, while they reach a local minimum in the range of 250–500 nm.
    c. Total carbon concentration has an important effect on the water uptake of inorganic ions. In regional background air, *TC* lowers the hygroscopicity of the particles at all *RH*s. This diminishing effect increases with increasing *RH*.
    d. The measured particle growth can be estimated by the inorganic ion and *TC* concentrations.

2. In the coarse mode (d >1 μm):
    a. The absorbed water concentration only slightly depends on the particle size.
    b. Measured growth factors (mainly above 2 μm) are underestimated by the calculated growth rates. This indicates that, in addition to the compounds analyzed in the samples, other hygroscopic constituents play an important role in the water uptake of the particles.
    c. Total carbon concentration has no statistically significant effect on the water uptake of inorganic ions.
    d. The measured particle growth cannot be estimated by the inorganic ion and the *TC* concentrations because of the important contribution of the non-determined components.

Acknowledgements—The authors are thankful for the useful comments and advices of *E. Mészáros*. The authors are also indebted to *P. Hajós* and *K. Horváth* for their help in ion chromatography. This work was supported by the National Scientific Research Fund (OTKA, project numbers: T047222 and TS049845) and by the National Program for Research and Development (NKFP, project number 3/2005). The research was done in the frame of ESF COST 633 program.

References

Aklilu, Y., Mozurkewicha, M., Prenni, A.J., Kreidenweis, S.M., Alfarra, M.R., Allan, J.D., Anlauf, K., Brook, J., Leaitch, W.R., Sharma, S., Boudries, H., Worsnop, D.R., 2006: Hygroscopicity of particles at two rural, urban influenced sites during Pacific 2001: Comparison with estimates of water uptake from particle composition. *Atmos. Environ. 40*, 2650–2661.

Alfarra, M.R., Coe, H., Allan, J.D., Bower, K.N., Boudries, H., Canagaratna, M.R., Jimenez, J.L., Jayne, J.T., Garforth, A., Li, S-M., Worsnop, D.R., 2004: Characterization of urban and rural organic particulate in the Lower Fraser Valley using two aerodyne aerosol mass spectrometers. *Atmos. Environ. 38*, 5745–5758.

Andrews, E., Larson, S.M., 1993: Effect of surfactant layers on the size changes of aerosol particles as a function of relative humidity. *Environ. Sci. Technol. 27*, 857-865.

Berner, A., 1984: Design principles of the AERAS low pressure impactor. In *Aerosols* (eds.: *B.Y.H Liu, D.Y.H Pui, H.J. Fissan*). Elsevier, Amsterdam.

Busch, B., Kandler, K., Schutz L., Neusüß, C., 2002: Hygroscopic properties and water-soluble volume fraction of atmospheric particles in the diameter range from 50nm to 3.8 μm during LACE 98. *J. Geophys. Res. 107*, D21, 8119, doi:10.1029/2000JD000228.

Chan, C.K., Kwok, C.S., Chow, A.H.L., 1997: Water activity of mixed organic and inorganic aerosols. *J. Aerosol Sci. 28*, S77-78.

Choi, M.Y., Chan, C.K., 2002: The effects of organic species on the hygroscopic behaviors of inorganic aerosols. *Environ. Sci. Technol. 36*, 2422–2428.

Clegg, S.L., Brimblecombe, P., Wexler, A.S., 1998: Thermodynamic modelling of aqueous aerosols containing electrolytes and dissolved organic compounds. *J. Phys. Chem. 102A*, 2155-2171. http://mae.ucdavis.edu/wexler/aim

Cruz, C.N., Pandis, S.N., 1997: A study of the ability of pure secondary organic aerosol to act as cloud condensation nuclei. *Atmos. Environ. 31*, 2205-2214

Cruz, C.N., Pandis, S.N., 2000: Deliquescence and hygroscopic growth of mixed inorganic–organic atmospheric aerosol. *Environ. Sci. Technol. 34*, 4313–4319.

Dick, W.D., Saxena, P., McMurry, P.H., 2000: Estimation of water uptake by organic compounds in submicron aerosols measured during the southeastern aerosol and visibility study. *J. Geophys. Res. 105*, 1471–1479.

Ferron, G.A., Karg, E., Busch, B., Heyder, J., 2005: Ambient particles at an urban, semi-urban and rural site in Central Europe: hygroscopic properties. *Atmos. Environ. 39*, 343–352.

Geresdi, I., Mészáros, E., Molnár, A., 2006: The effect of chemical composition and size distribution of aerosol particles on droplet formation and albedo of stratocumulus clouds. *Atmos. Environ. 40*, 1845-1855.

Gysel, M., Weingartner, E., Baltensperger, U., 2002: Hygroscopicity of aerosol particles at low temperatures. 2. Theoretical and experimental hygroscopic properties of laboratory generated aerosols. *Environ. Sci. Technol. 36*, 63-68.

Gysel, M., Weingartner, E., Nyeki, S., Paulsen, D., Baltensperger, U., Galambos, I., Kiss, G., 2004: Hygroscopic properties of water-soluble matter and humic-like organics in atmospheric fine aerosol. *Atmos. Chem. Phys. 4*, 35–50.

Hämeri, K., Charlson, R.J., Hansson, H-C., Jacobson, M., 1998: Hygroscopic properties of ammonium sulfate aerosol particles mixed with slightly soluble organic compound. *J. Aerosol Sci. 29*, S587-583.

Hänel, G., 1976: The properties of atmospheric aerosol particles as function of the relative humidity at thermodynamic equilibrium with the surrounding moist air. *Adv. Geophys. 19*, 73-188.

Hansson, H.C., Rood, M.J., Koloutsou-Vakakis, S., Hämeri, K., Orisini, D., Wiedensohler, A., 1998: NaCl aerosol particle hygroscopicity dependence on mixing with organic compounds. *J. Atmos. Chem. 31*, 312-346.

Hitzenberger, R., Berner, A., Giebl, H., Kromp, R., Larson, S.M., Rouc, A., Koch, A., Marischka, S., Puxbaum, H., 1999: Contribution of carbonaceous material to cloud condensation nuclei concentrations in European background (Mt. Sonnblick) and urban (Vienna) aerosols. *Atmos. Environ. 33,* 2647-2659.

Lee, C.T., Hsu, W.C., 1998: A novel method to measure aerosol water mass. *J. Aerosol Sci. 29*, 827–837.

Lee, C.T. and *Hsu, W.C.,* 2000: The measurement of liquid water mass associated with collected hygroscopic particles. *J. Aerosol Sci. 31*, 189–197.

Maßling, A., Wiedensohler, A., Busch, B., Neusüß, C., Quinn, P., Bates, T., Covert, D., 2003: Hygroscopic properties of different aerosol types over the Atlantic and Indian Oceans. *Atmos. Chem. Phys. 3,* 1377–1397.

McMurry, P.H., Stolzenburg, M.R., 1989: On the sensitivity of particle-size to relative humidity for Los Angeles aerosols. *Atmos. Environ. 23,* 497–507.

Mészáros, A., 1971: On the variation of the size distribution of large and giant atmospheric particles as a function of the relative humidity. *Tellus 23,* 436-440.

Mészáros, E., Horváth, L., 1984: Concentration and dry deposition of atmospheric sulfur and nitrogen compound in Hungary. *Atmos. Environ. 18,* 1725-1730.

Mircea, M., Facchini, M.C., Decesari, S., Fuzzi, S., Charlson, R.J., 2002: The influence of the organic aerosol component on CCN supersaturation spectra for different aerosol types. *Tellus 54B,* 74-81.

Mircea, M., Facchini, M.C., Decesari, S., Cavalli, F., Emblico, L., Fuzzi, S., Vestin, A., Rissler, J., Swietlicki, E., Frank, G., Andreae, M.O., Maenhaut, W., Rudich, Y., Artaxo, P., 2005: Importance of the organic aerosol fraction for modeling aerosol hygroscopic growth and activation: a case study in the Amazon Basin. *Atmos. Chem. Phys. 5*, 3111–3126.

Pitchford, M.L., McMurry, P.H., 1994: Relationship between measured water vapor growth and chemistry of atmospheric aerosol for Grand Canyon, Arizona, in winter 1990. *Atmos. Environ. 28*, 827-839.

Pósfai, M., Gelencsér, A., Simonics, R., Arato, K., Li, J., Hobbs, P.V., Busek, P.R., 2004: Atmospheric tar balls: particles from biomass and biofuel burning. *J. Geophys. Res. 109,* doi:10.1029/1003JD004169.

Prenni, A.J., De Mott, P.J., Kreidenweis, S.M., 2003: Water uptake of internally mixed particles containing ammonium sulphate and dicarboxylic acids. *Atmos. Environ. 37,* 4243–4251.

Rissler, J., Vestin, A., Swietlicki, E., Fisch, G., Zhou, J., Artaxo, P., Andreae, M.O., 2006: Size distribution and hygroscopic properties of aerosol particles from dry-season biomass burning in Amazonia. *Atmos. Chem. Phys. 6*, 471–491.

Saxena, P., Hildemann, L.M., McMurry, P.H., and *Seinfeld, J.H.,* 1995: Organics alter hygroscopic behavior of atmospheric particles. *J. Geophys. Res. 100,* D9, 18755-18770.

Sjogren, S., Gysel, M., Weingartner, E., Baltensperger, U., Cubison, M.J., Coe, H., Zardini, A.A., Marcolli, C., Krieger, U.K., Peter, T., 2007: Hygroscopic growth and water uptake kinetics of two-phase aerosol particles consisting of ammonium sulfate, adipic and humic acid mixtures. *J. Aerosol Sci. 38,* 157-171.

Stein, S.W., Turpin, B.J., Cai, X., Huang, P.-F., McMurry, P.H., 1994: Measurements of relative humidity-dependent bounce and density for atmospheric particles using the DMA-impactor technique. *Atmos. Environ. 28,* 9-1746.

Svenningsson, I.B., Hansonn, H.C., Wiedersohler, A., Noone, K.J., Ogren, J., Hallberg, A., Colvile, R., 1994: Hygroscopic growth of aerosol particles and its influence on nucleation scavenging in cloud: Experimental results from Kleiner Feldberg. *J. Atmos. Chem. 19,* 129-152.

Swietlicki, E., Zhou, J., Covert, D.S., Hämeri, K., Busch, B., Väkeva, M., Dusek, U., Berg, O.H., Wiedensohler, A., Aalto, P., Mkela, J., Martinsson, B.G., Papaspiropoulos, G., Mentes, B., Frank, G., Stratmann, F., 2000: Hygroscopic properties of aerosol particles in the north-eastern Atlantic during ACE-2. *Tellus 52B,* 201–227.

Temesi, D., Molnár, A., Mészáros, E., Feczkó, T., Gelencsér, A., Kiss, G., Krivácsy, Z., 2001: Size resolved chemical mass balance of aerosol particles over rural Hungary. *Atmos. Environ. 35,* 4347-4355.

Virkkula, A., Dingenen, R.V., Raes, F., Hjorth, J., 1999: Hygroscopic properties of aerosol formed by oxidation of limonene, a-pinene, and b-pinene. *J. Geophys. Res. 104,* D3, 3569-3579.

Warneck, P., 1999: *Chemistry of the Natural Atmosphere.* Academic Press, San Diego, San Francisco, New York, Boston, London, Sydney, Tokyo.

Winkler, P., Junge, C.E., 1972: The growth of atmospheric aerosol particles a function of the relative humidity, Part I. Method and measurements at different locations. *J. Recherche Atmospherique 6,* 617-638.

Zhou, J., Swietlicki, E., Berg, O.H., Aalto, P.P., Hämeri, K., Nilsson, E.D., Leck, C., 2001: Hygroscopic properties of aerosol particles over the central Arctic Ocean during summer. *J. Geophys. Res. 106,* 32111-32123.

IDŐJÁRÁS

Quarterly Journal of the Hungarian Meteorological Service
Vol. 112, No. 2, April–June 2008, pp. 83–97

Trace element analysis of airport related aerosols using SR-TXRF

Veronika Groma[1]*, János Osán[1], Szabina Török[1], Florian Meirer[2], Christina Streli[2], Peter Wobrauschek[2] and Gerald Falkenberg[3]

[1]*KFKI Atomic Energy Research Institute,*
P.O. Box 49, H-1525 Budapest, Hungary; E-mail: groma@sunsev.kfki.hu
[2]*Atominstitut der österreichischen Universitäten,*
Stadionallee 2, TU Wien, A-1020 Vienna, Austria
[3]*Hamburger Synchrotronstrahlungslabor (HASYLAB) at*
Deutsches Elektronen-Synchrotron (DESY), Notkestr. 85, 22607 Hamburg, Germany

(Manuscript received in final form May 5, 2008)

Abstract—Air quality issues of international airports are becoming more and more important due to the dynamic growth of air traffic. Fine particulate matter ($PM_{2.5}$) originating from emissions of aircrafts, ground handling vehicles, passenger related cars, and point sources is the most critical pollutant in airport areas. The sources have large temporal and spatial variation. In order to correlate the elemental composition of fine particulate matter in different size fractions to airport related sources, special instrumentation and analytical technique need to be used. A novel combination of cascade impactor sampling and total reflection X-ray flourescence (TXRF) analysis employing synchrotron radiation is presented in this paper. The method allows quantitative determination of ultra-trace amounts (pg m^{-3}) of most elements from samples collected for less than 20 min, while retaining the full size resolution of the impactor. Size-fractioned aerosol samples were collected on silicon wafers using a 7-stage May cascade impactor, close to the runway and next to the aircraft stands at Budapest Ferihegy Airport. The comparison of the size distribution of the elemental concentrations for different locations could allow us to differentiate between end-of-pipe and other emission sources. Typical elements coming from combustion processes (Zn, Pb), aircraft related emissions (Cu), as well as road salting processes (Cl) could be determined. Elements connected to crustal erosion and resuspension (Fe, Ti, Ca) had maximum concentration in the micrometer size fractions (1–4 μm). The combination of May impactor sampling and TXRF analysis described in this paper has a potential to be used in industrial/traffic processes where the time scale of the event is similar to the typical sampling durations, even using laboratory scale equipments.

Key-words: airport, air quality, fine particulate matter, trace elements, TXRF, synchrotron radiation

* Corresponding author

1. Introduction

Airport air pollution is coming to be more and more remarkable, since it shows one of the most dynamic growth in the transport sector. Large international airports operate monitoring systems (*Farias* and *ApSimon*, 2006; *Unal et al.*, 2005; *Schürmann et al.*, 2007) for continuous controlling of classical air pollutants (CO, NO_X, SO_2, O_3, PM_{10}, and $PM_{2.5}$). The statistical analyses of these long time series show that the most important pollutants which have the largest contribution to urban air quality are the nitrogen-oxides, since limiting value exceedence occurs only in NO_X concentration values (*Farias* and *ApSimon*, 2006). Whereas, measurement campaigns performed at Budapest Ferihegy International Airport during the year of 2006 show that limiting value exceedence can be detected only in particulate matter (PM_{10}) concentrations, and the only component which show higher values than downtown and suburban areas at Budapest is the fine fraction of particulate matter ($PM_{2.5}$ – particles with aerodynamic diameter smaller than 2.5 μm) (*Groma et al.*, 2007). Additionally, recent publications show that $PM_{2.5}$ causes more severe health effects than coarse particles (*Kampa* and *Castanas*, 2008).

$PM_{2.5}$ monitoring measurements were carried out using a Tapered Element Oscillating Microbalance System (TEOM) (http://www.thermo.com/eThermo/CMA/PDFs/Product/productPDF_2006.pdf) next to the runway (see *Fig. 1*), where the main particle emission sources are the starting, landing, and taxiing aircrafts, in addition to the background, since other traffic sources are far from the measurement site. Since we could determine correlation between aircrafts and $PM_{2.5}$ concentration values, it is obvious that aerosol originating from emissions of aircraft is detectable (*Bozó et al.*, 2006).

Airport related particles originate from aircraft end-of-pipe emission and erosion (brake, concrete, and tire). Moreover, not only aircrafts but also emissions of ground supporting vehicles, point sources, and passenger related cars have to be taken into account. Also, resuspension of crustal particles is a significant source. Since the most polluted sites were found to be the handling and terminal areas (apron) – where human activity is the most remarkable –, measurements capable of source apportionment are needed. Multi-element chemical analysis is one of the most adequate tools for deriving fingerprints of different sources of fine particulate matter. Also, the opportunity of short sampling time is needed, because the duration of an aircraft landing and taxiing nearby parking places is approximately 1 to 3 minutes, while touch down takes a few seconds. For this reason, development of a multielemental analytical technique for aerosol samples allowing very high temporal resolution is required, since compounds in gas phase can be measured with time resolution as low as 1 minute. This would allow a time-resolved correlation between pollutant gases and the composition of primary and secondary aerosols.

Methods allowing the analysis of individual aerosol particles on-line or from samples collected during very short time are useful for source apportionment studies. The recently developed aerosol mass spectrometers (AMS) now have the opportunity to be able to measure the size and the chemical composition of individual particles with a very high time resolution (*Takegawa et al.*, 2006), and can also be used as a monitoring instrument. The combination of time-resolved aerosol collector and computer-controlled electron probe microanalysis (CC-EPMA) of a few thousand individual particles can allow a 10 min time resolution (*Laskin et al.*, 2003). Using the AMS or CC-EPMA methods only the major chemical composition can be specified, from which the different particle types (mineral dust, sulfate, nitrate, organic) can be differentiated. Although this kind of information can be very attractive for studies of airport-related aerosols, the minor or trace elemental composition of aerosols in different size fractions is an important fingerprint of the airport related sources. The latter can be addressed by bulk trace elemental analysis of size-resolved aerosol samples collected for very short time. The aimed high size resolution as well as time resolution results in sample masses less than a microgram, which requires a very sensitive analytical method.

Total reflection X-ray fluorescence spectrometry using high flux synchrotron radiation (SR-TXRF) provides several great advantages for aerosol characterization. Because of the natural collimation of the incident beam, the high intensity of the fluorescence radiation and the low spectral background, SR-TXRF allows a non-destructive detection of trace and ultra-trace atmospheric concentrations (ng m^{-3}, pg m^{-3}) of most elements in size fractionated aerosol. Quantification and standardization of the TXRF technique is straight-forward compared to EPMA or AMS.

Recent investigations present many studies about aerosol measurement methods which have high time resolution and low detection limits. These developments are usually based on size fractionated aerosol sampling combined with TXRF analyses. Results show that they are capable for determination of specific elements, source identification, and fingerprint analysis based on samples collected within hours (*Dudzinska-Huczuk* and *Bolalek*, 2007; *Lammel et al.,* 2007). Whereas, a great disadvantage of these methods lies in the necessity of a pretreatment of the sample carriers used in TXRF analysis in some cases (*John et al.*, 2001). Moreover, higher time and size resolution is needed to study atmospheric processes having characteristic times in the range of hours (*Lammel et al.*, 2007). Since our aim was to study even shorter environmental processes, we needed to develop a method which has better time resolution characteristics. Since the risk of contamination is higher at lower amounts (ng) of samples, the applied technique should be devoid of this problem. Sampling with May impactor combined with SR-TXRF seemed to be a good alternative, since this technique does not need any pretreatment of

samples, and also non-destructive, which allows one to perform further analysis on the collected aerosols.

The aim of this study is (i) to introduce an aerosol analysis method which has potential to use in industrial/traffic processes where the time scale of the event is similar to the typical sampling duration, and (ii) to present its suitability for trace element analysis of airport related aerosols.

2. *Materials and methods*

2.1. Sampling

Aerosol samples were collected in the inside area of Budapest Ferihegy Airport. The airport is located 15 km south-east from the city center of Budapest. A highway with approximately 50,000 cars day^{-1} traffic is located 2 km far from the airport area. The potential measurement sites inside the airport were limited, because movements at the airport area were strictly regulated. Hence, it was not possible to go closer to the runway than 150 meters. To overcome the security problems and reduce influence of road transfer, measurements were performed near the runway and next to terminal buildings (apron) (see *Fig. 1*).

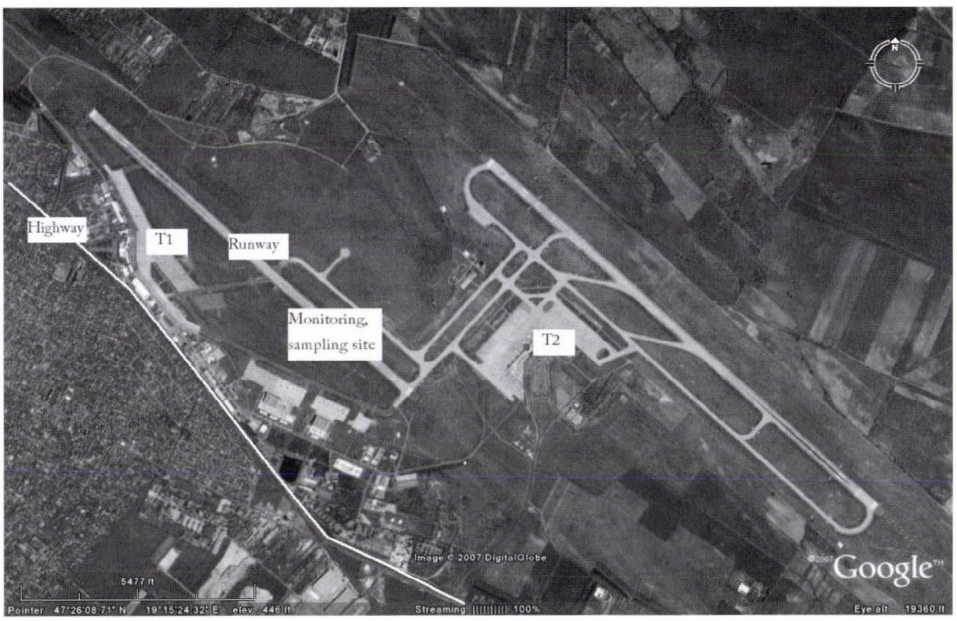


Fig. 1. Measurement sites at Budapest Ferihegy Airport.

First, samples were collected on 20×20 mm^2 silicon wafers using a 7-stage May cascade impactor (*May*, 1975). The May impactor has aerodynamic cut-off diameters of 16, 8, 4, 2, 1, 0.5, 0.25 μm for stages 1–7, respectively, at 20 l min^{-1} sampling flow rate. The sampling duration took 1 (for stage 7), 5 (for stage 6), 10 (for stage 5), and 20 minutes (for stage 4) to obtain the best loading of particles on the impacted strips. Since in this study we aim to investigate the fine aerosol fraction only, aerosol collection was performed only for the above specified four stages (4 to 7). The May impactor has an impacting slit at each stage, and thus the aerosols collected on a silicon substrate show a pattern of a thin line with approximate dimensions of 20 mm × 0.3 mm. To be able to calculate concentration values for each trace element, an internal standard, a Cr strip with a known mass was placed on the Si wafers exactly at the same position as particles from the air sample, prior to collection of particulate matter on the Si carriers. Two sample sets were collected on January 12, 2006 at the runway and Terminal 2 (high traffic: 8 aircraft movements during sampling time), and one at Terminal 1 (low traffic: 1 aircraft movement during sampling time) on January 15, 2006 (hereafter, T2 and T1, respectively). The last sampling day was a Sunday with much lower traffic in the city of Budapest.

Ionic compounds were measured in order to obtain daytime and nighttime averages of sulfate concentrations in $PM_{2.5}$, samples were collected on 1 μm pore-size Teflon filters for 12 h at the terraces of terminal buildings. The cyclone used for the fine aerosol sampling had a cut-off diameter of 2.5 μm at 10 l min^{-1} flow rate. The total sampled air volume was approximately 7 m^3 for all samples. The 12-hour average concentrations of sulfate were measured using ion chromatography (IC), after leaching the filter samples in water.

2.2. Multielemental analysis

Measurements were performed at HASYLAB Beamline L using a total-reflection X-ray fluorescence vacuum chamber (*Streli et al.*, 2005). An automatic sample loader (*Meirer et al.*, 2006) was installed to establish the opportunity to measure 8 samples consecutively without the necessity to close the beam shutter and open the vacuum chamber, resulting significant time saving during the beam time. A special sample holder was used to mount the 20×20 mm^2 Si wafer pieces with the aerosol samples collected in strip form. The synchrotron radiation energy was adjusted to 18.4 keV by means of the NiC multilayer monochromator. The SR beam had a vertical dimension of 1.4 mm and a horizontal dimension of 0.2 mm.

A Vortex Radiant Silicon Drift Detector (SDD) in use was equipped with a special collimator with a 1.5 mm wide slit made of Mo, in order to fit to the geometry of the impacted aerosol samples. As X-ray photons emerging from the total 20 mm length of the aerosol strip could not be detected using the SDD applied, the homogeneity of the aerosol deposition was tested. For the test scans,

the sample strip and the collimator slit was perpendicular to the X-ray beam, therefore, only 1.4 mm section of the sample strip was excited. The vertical scans were performed by moving the sample–detector system relative to the position of the beam using a stepping motor. The step size was set to 1 mm, and the individual spectra were collected for 3 s. Measurements with the new collimator resulted in excellent reproducibility of the individual scan steps. The interpretation is clearly a shielding of the off-lier contaminants as the slit prevented their detection and the geometry of the detector collimator fit to the sample. The measurements aiming the determination of the elemental concentrations were carried out applying the SR beam parallel to the sample strip. The position of the sample strip was determined using vertical scans with 0.2 mm step size. Individual spectra were collected at the strip positions for 100 s. The net characteristic X-ray intensities of the elements were calculated by evaluating the spectra by non-linear least-squares fitting using the AXIL program (*Vekemans et al.*, 1994). In order to calculate the relative sensitivity curve of the setup, 30 nl of a multielement standard solution (11355 Multi Element Standard IV, Merck) containing 1 ng of each element was pipetted onto a Si wafer and measured by SR-TXRF.

3. Results and discussion

3.1. Sample homogeneity

Samples were collected directly on Si wafers containing 5.75 ng Cr in a 300 μm wide strip in the middle centerline of the wafers. As the geometry of the Cr strip was chosen to be similar to that of the deposited aerosol particles, Cr could be efficiently used as internal standard for the SR-TXRF measurements. The standards were provided by the Research Institute for Technical Physics and Materials Science (Budapest, Hungary) (*Watjen et al.*, 2000). The important issue is to make sure that the measured 6 mm sections of the aerosol strip are representative for the total length and thus for the calculation of the total mass deposited here. Only if this is proven, the extrapolation from the mass calculated for 6 mm to the total mass deposition is permitted. The total mass deposited represents the aerosol concentration (ng m^{-3}) in the collected air volume. For this purpose 18 mm of the existing 20 mm strips were measured successively by scanning 3 × 6 mm along the strip. Results shown in *Fig. 2* demonstrate that the Fe intensities normalized to ring current vary within 10% relative standard deviation during the three scans, supporting the proposed extrapolation.

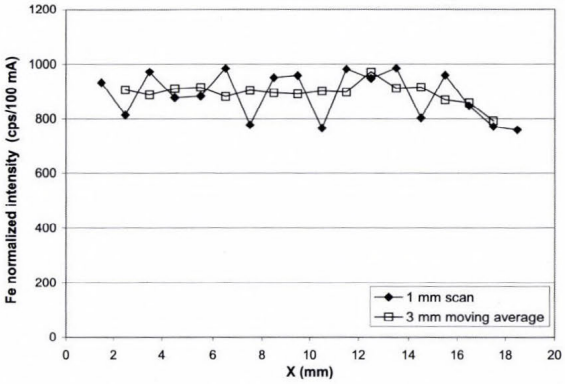


Fig. 2. Results of homogeneity test of impacted aerosol strip.

3.2. Elemental analyses

Long term measurement data showed slight differences between PM_{10} and $PM_{2.5}$ concentrations (*Groma et al.*, 2007). For this reason size fractioned aerosol analyses were only done on the smaller sized particles (0.25–4 μm aerodynamic diameter). Also, larger particles occur in smaller number concentration (particles m^{-3}) naturally, requiring longer sampling time, which does not make any sense on the time-scale of aircraft movements. May impactor sample collection combined with SR-TXRF analysis has the opportunity to calculate elemental concentrations from extremely small sampling volumes. Detection limits achieved for 20-minute sampling time are ranging from ng m^{-3} for the light elements (Al, Si) to pg m^{-3} for the medium *Z* elements like Rb and Sr in the present matrix (see *Table 1*). The detection limits were calculated for 100 s measuring live time and 100 mA ring current.

Table 1. Detection limits for each element detected in aerosol particles collected at airport sites

Element	Detection limit (pg m^{-3})
S	451.3
Cl	282.8
K	107.9
Ca	68.3
Ti	39.9
Cr	23.4
Fe	13.3
Cu	4.6
Zn	3.4
Se	2.4
Br	2.3
Sr	3.6
Pb	5.8

The concentrations of the elements in the samples were calculated based on SR-TXRF spectra collected for 100 s, using the Cr strip as internal standard. A typical spectrum is presented in *Fig. 3*.

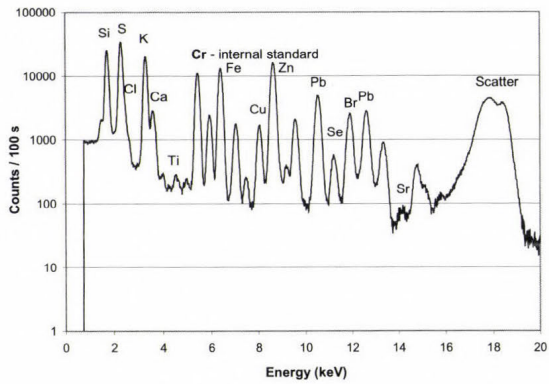


Fig. 3. Typical SR-TXRF spectrum of an aerosol sample collected at the airport, 0.5–1 μm size fraction.

The SR-TXRF measurement results of airport related aerosols sampled by May impactor are presented in *Fig. 4*. Since aerosols were collected in 4 different size fractions at 3 different sites, measurement results for 12 samples are presented here. Each diagram is relevant for one of the elements studied (S, Cl, K, Ca, Ti, Fe, Cu, Zn, Se, Br, Sr, Pb). Each column is relevant for a measurement site: runway, T2 – high traffic (85%) and T1 – low traffic (15%), respectively. Size distribution of concentrations for a specific element is presented within the columns. Diagrams are scaled to the maximum values of the different elements. Measurement results shown in *Fig. 4a–l* confirm facts which were previously expected for typical suburban areas, besides results which show specialties of airport related aerosols. Aerosols originate from long range transport, city plume, and local sources. Local sources show large variability in the airport, since aircrafts, ground supporting vehicles, and also passenger cars have to be taken into account. The emission characteristics are all different, some of them are well known, but some – especially aircraft related – particulates chemical composition is still unknown.

Onsite measurements were recently performed by NASA to improve air quality emission inventories (*Aviation Particle Emissions Workshop*, 2004). These results are very well detailed, but the instrumentation requirement is huge, and no trace element composition analysis can be performed. It follows that the combination of impactor sampling and SR-TXRF analysis presented in this paper provides complementary information.

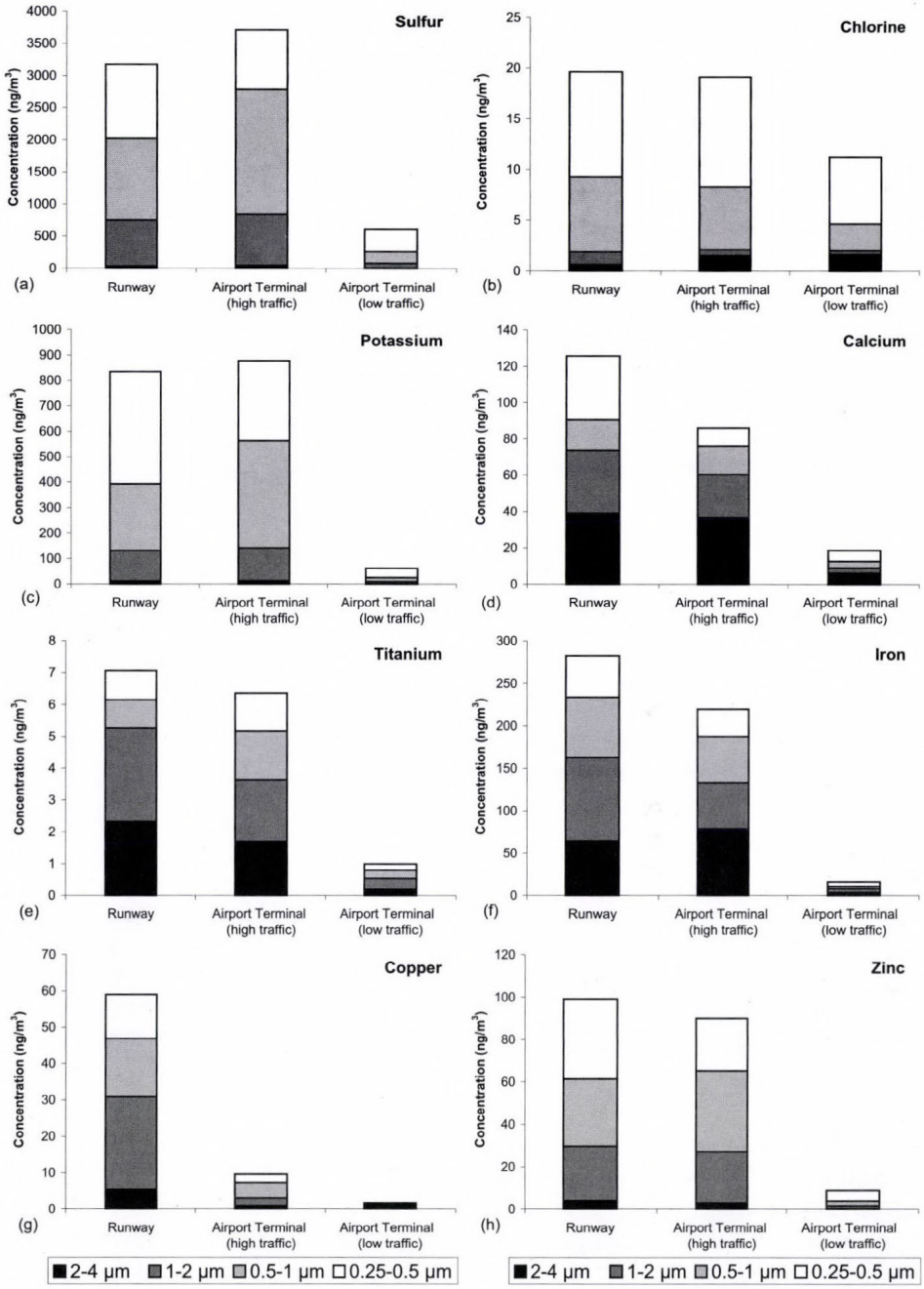


Fig. 4. Size distribution of elemental concentrations at different sites.

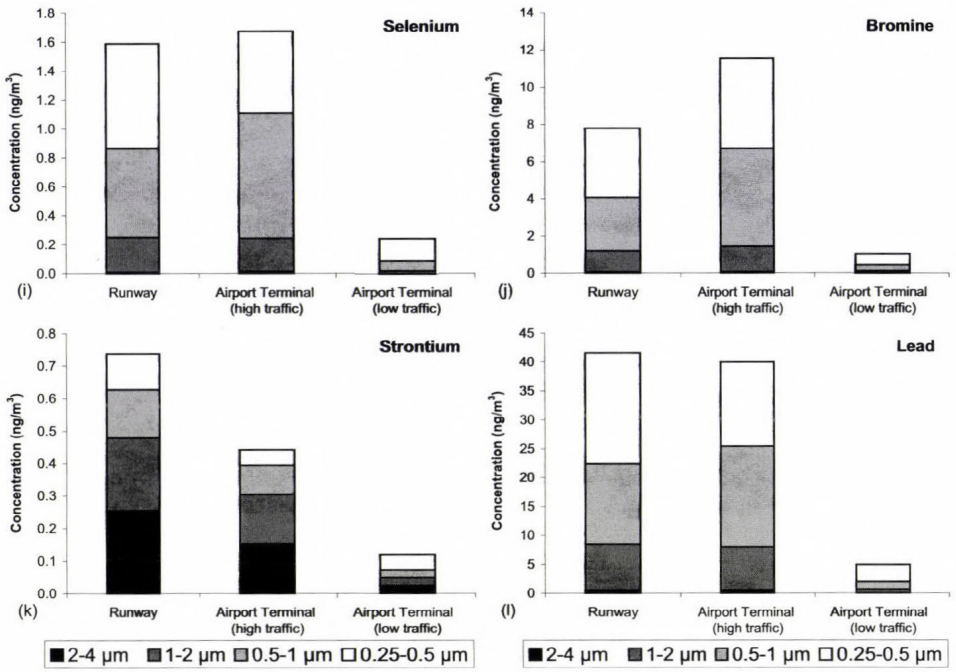


Fig. 4 (continued). Size distribution of elemental concentrations at different sites.

Not only combustion processes, but also resuspension, erosion, and formation of secondary aerosols (which can be classified in typical size fractions) contribute to the ambient particulate concentration. Therefore, measurement results can be discussed in 3 different aspects: (i) size distribution, (ii) magnitude of concentration values at different sites, and (iii) typical elements at different sites. It is obvious to see that concentrations of all elements measured at runway and terminal building with larger traffic (T2) are much higher than values at the other terminal with lower traffic (T1). This is due to the different number of air as well as ground vehicle movements around the sampling sites. Sample collections at the runway and T2 (just after each other) were done during one of the largest aircraft traffic peaks (around 1 p.m.), while sampling at T1 was performed during really small number of vehicle movements. Airport traffic does not only mean the movements of aircrafts, but also ground supporting and passenger cars which both show correlation with aircraft movements. To be able to determine the origin of the aerosol, samples collected at different sites need to be compared. Since the source properties at terminal buildings are complex (large temporal and spatial variation), it is not possible to determine the origin of particles from their chemical composition.

Results from terminal building compared to results from the runway allow one to differentiate between the sources.

It is well-known that sulfate is dominant in smaller size fractions. According to *Kerminen et al.* (2004), the size distribution of sulfate shows a maximum at around 0.3 μm for rural and around 0.7 μm for urban aerosols, based on measurements at several European sites. Previous studies of Hungarian background aerosol have even revealed that the preferred modal diameter of sulfate compounds is smaller in the summer than in the winter (*Mészáros et al.*, 1997). As it can be seen in Fig. 4a, the shape of the size distribution is similar to that observed by impactor sampling and IC measurements reported in the literature (*Kerminen et al.*, 2004; *Mészáros et al.*, 1997). The highest sulfur concentration obtained by SR-TXRF is in the 0.5–1 μm fraction at the runway and at T2, and in the 0.25–0.5 μm fraction at T1. It means that the size distribution of sulfur has a more rural characteristic for low traffic conditions, and more urban at sites influenced by high traffic.

Significant amount of Cl was found to be present in the largest size fraction studied (2–4 μm). Besides long-range transport of sea salt, chlorine also originates from the salt used for preventing ice formation on roads during winter time. The SR-TXRF results are in accordance with this, since the decrease of the traffic intensity at the airport has less influence on the concentrations of Cl than other elements (see *Fig. 4b*).

Ca, Fe, and Ti show similar size distribution at the three locations (see *Figs. 4d, 4e, 4f*). Also, the total concentration values of these elements have similar ratio among the three sites. This means that the source of particles containing these elements must be the same. Since these elements dominate in larger particulates, one can say that they probably originate from resuspension (by movements of vehicles and the blowing effect of the aircraft engine).

Zinc and lead (see *Figs. 4h, 4l*) are usually connected to combustion processes in the engine (*Tesseraux*, 2004). Traffic related particles containing these elements usually occur in fine aerosols, which is in good agreement with our results. Because concentration values of these elements show similar magnitudes: high at high traffic periods and low at the time of low traffic, but no significant difference could be seen at the runway and T2, one can say that particulates containing these elements should originate from the airport related ground supporting vechicles as well as from the city traffic, transported to airport area.

Significant differences between apron and runway areas are in copper concentration values (see *Fig. 4g*). Copper rich particles probably originate from aircraft brake pad erosion. No other studies have been done connected to the erosion during aircraft landing, which means further investigations are needed to be done on this subject.

High concentration values of potassium usually occur near wood-burning emission sources which cannot be found inside, but probably somewhere

outside, near the airport area. This is confirmed by the fact that sulfur has a really similar size distribution to potassium (see *Figs. 4a, 4c*), which is also connected to wood-burning processes in previous studies (*Osán et al.*, 2002).

Since strontium is chemical substituting element for calcium, the size distribution and Sr/Ca ratio at different sampling sites should be the same. Although Sr was found to be present at sub-ng m^{-3} concentration levels (see *Figs. 4k* and *4d*), the present measurement results confirm these assumptions. This very good correlation between Sr and Ca concentrations in all size ranges clearly shows the suitability of SR-TXRF for trace element analysis of aerosol samples.

Selenium and bromine rich particles were found to be dominant in the submicrometer size fractions (see *Figs. 4i, 4j*), therefore, these trace elements can be connected to the combusted fuels used either in air or in ground traffic. The detection of this small quantity in these small size-fractions confirms the fact that this method opens up new opportunities in aerosol analysis research.

3.3. Comparison of IC and SR-TXRF measurements

Since the sulfate content of the $PM_{2.5}$ aerosol at the airport could be measured by IC from 12-hour filter sampling on the same day, it is worth to compare the results obtained by the two techniques. SR-TXRF sulfate concentrations were calculated from stoichiometry based on the sum of the sulfur concentrations for the size fractions in the 0.25–2 μm range.

$PM_{2.5}$ sampling on Teflon filters was done on T2 terminal building during both days, when aerosol collection was performed with the May impactor. Since a large air volume is needed for the IC analyses, the samples were collected for 12 hours. Because the meteorological and traffic conditions are not stationary, it is not trivial to compare the results of these samples with those from SR-TXRF analyses, which are samples collected for much shorter time. *Table 2* shows the results of sulfate concentrations obtained by ion chromatography and SR-TXRF.

Comparing IC and SR-TXRF measurement results for samples originating from the same site during a larger airport traffic volume period shows similar values (less than 20% difference). Also, SR-TXRF results at the runway are in the same magnitude of the ones mentioned above. However, sulfate concentration of aerosol particles collected for 12 hours and analyzed by IC is higher than those measured by SR-TXRF, which should be explained by the fact that a significant sulfate mass can be present in ultrafine particles smaller than 0.25 μm. Also, the short time May impactor sample collection was not performed during the highest traffic period (inside and outside the airport). This also confirms the fact, that long range transport is one of the most important sources of aerosols containing sulfate, besides the local emission and formation effects. To study the contribution of these processes further measurements are needed.

The use of the recently developed ambient ion monitor (http:// www.urgcorp.com/systems/pdf/9000.pdf) that allows IC measurements of ionic compounds in $PM_{2.5}$ at a time resolution of 15 minutes would lead to a more accurate comparison between IC and SR-TXRF results. However, this new IC system is still not capable for providing size-fractionated information.

Table 2. Differences in sulfate concentrations analyzed by IC and SR-TXRF

Sampling site, method	**Runway SR-TXRF**	**T2, SR-TXRF**	**T2, IC**
Concentration (ng m^{-3})	9,500	11,100	13,500

4. Summary and conclusion

Aerosol collection with May impactor combined with the SR-TXRF analytical method could be efficiently used to study atmospheric processes on the time scale of minutes. The sampling and trace element analysis were performed at airport sites near sources which show high spatial and temporal variability. Measurements and trace element analysis at airport sites with such high size resolution have never been done before. We could determine typical aircraft originated particles from these extremely small sampling volumes.

Since the concentration of $PM_{2.5}$ found to be the most critical at airport sites, the aim of our measurements was to determine the airport related aerosol particles. Typical elements of combustion processes like zinc and lead could be determined as well as special, aircraft related particles, namely high copper concentrations were detected near the runway, which is due to aircraft brake erosion. Size fractioned sampling allowed us to sort out particles from not airport related combustion processes, since, for example, due to resuspension, typical aerosols in larger size fractions (Ca, Fe, Ti) can be shown. Also, from the comparison of concentration magnitudes at different sites, we could identify elements originating from wood burning processes like potassium and sulfur, which are connected to atmospheric transport.

Low detection limits (in the range of pg m^{-3}) could be achieved from 20 minutes sampling time thanks to the excellent properties of synchrotron radiation. This short time collection allows to study temporal variation of elemental concentrations in size-fractioned aerosols. SR-TXRF measurements have proven the fact that the most important elements occur in concentrations above detection limits. By choosing the most adequate size and time resolution to that samples, the method prospects to use laboratory TXRF instrumentation also. The aim of our further developments is to establish an instrumentation using the above performed methods which can be used in monitoring measurements.

Acknowledgements—This work was supported by the Jedlik Ányos Programme of the National Office for Research and Technology through contract No. 3/019/2005 and by the European Community - Research Infrastructure Action under the FP6 "Structuring the European Research Area" Programme (through the Integrated Infrastructure Initiative "Integrating Activity on Synchrotron and Free Electron Laser Science") Contract RII3-CT-2004-506008.

The support of the Hungarian Scientific Research Fund (OTKA T049581) and the Austrian–Hungarian Action Foundation (62öu10) are also appreciated. The authors would like to thank the staff of Budapest Airport Zrt. for their help during sampling at the airport.

References

Aviation Particle Emissions Workshop, 2004: Proceedings of a conference sponsored by the Ultra-Efficient Engine Technology (UEET) Project under the Vehicle Systems Program (VSP) of the National Aeronautics and Space Administration (NASA). Cleveland, Ohio, November 18-19, 2004. National Aeronautics and Space Administration, Glenn Research Center, NASA/CP—2004-213398.

Bozó, L., Czitrovszky, A., Alföldy, B., Osán, J., Groma, V., Ferenczi, Z., Labancz, K., Nagy, A., Steib, R., Kalocsainé, M., Récsei, I., Polay, P., 2006: Environmental monitoring system of airport traffic (in Hungarian). Progress report of the Ányos Jedlik Project No. 3/019/2005, October 2006, AEKI-SKL-2006-204-01-01-0. KFKI, Budapest.

Dudzinska-Huczuk, B., Bolalek, J., 2007: Particulate selenium in the Baltic Sea atmosphere. *Water Air Soil Poll. 179*, 29–41.

Farias, F., ApSimon, H., 2006: Relative contributions from traffic and aircraft NO_x emissions to exposure in West London. *Environ. Modell. Softw. 21*, 477–485.

Groma, V., Alföldy, B., Osán, J., Kugler, S., Kalocsai, M., 2007: Impact of the airport related traffic on the urban particulate pollution. *Proceeding of European Aerosol Conference*. 9-14 Sept. 2007, Salzburg, Austria.

John, A.C., Kuhlbusch, T.A.J., Fissan, H., Schmidt, K.-G., 2001: Size-fractioned sampling and chemical analysis by total-reflection X-ray flourescence spectrometry of PM_x in ambient air and emissions. *Spectrochim. Acta B, 56*, 2137–2146.

Kampa, M., Castanas, E., 2008: Human health effects of air pollution. *Environ. Pollut. 151*, 362–367.

Kerminen, V.-M., Hillamo, R., Teinilä, K., Pakkanen, T., Allegrini, I., Sparapani, R., 2004: Ion balances of size-resolved tropospheric aerosol samples: implications for the acidity and atmospheric processing of aerosols. *Atmos. Environ. 35*, 5255–5265.

Lammel, G., Baumgardner, D.G., Fittschen, U.E.A., Peschel, B., 2007: Evolution of anthropogenic aerosols in the coastal town of Salina Cruz, Mexico: Part III size-segregated elemental composition analysed by total-reflection X-ray fluorescence spectrometry. *Int. J. Environ. An. Ch. 87*, 659–672.

Laskin, A., Iedema, M.J., Cowin, J.P., 2003: Time-Resolved Aerosol Collector for CCSEM/EDX Single Particle Analysis. *Aerosol Sci. Tech. 37*, 246–260.

May, K.R., 1975: An "ultimate" cascade impactor for aerosol assessment. *J. Aerosol Sci. 6*, 413–416.

Meirer, F., Streli, C., Wobrauschek, P., Zoeger, N., Jokubonis, C., Pepponi, G., Falkenberg, G., Osan, J., Torok, S., Groma, V., Fittschen, U., Broekaert, J., Mihucz, V.G., Zaray, G., Czech, V., Hofstaetter, J., Roschger, P., Simon, R., 2006: Recent results of the ATI X-Ray group with SR-TXRF, *XRF Newsletter*.

Mészáros, E., Barcza, T., Gelencsér, A., Hlavay, J., Kiss, G., Krivácsy, Z., Molnár, A., Polyák, K., 1997: Size distributions of inorganic and organic species in the atmospheric aerosol in Hungary. *J. Aerosol Sci. 28*, 1163–1175.

Osán, J., Alföldy, B., Török, S., Van Grieken, R., 2002: Characterisation of wood combustion particles using electron probe microanalysis. *Atmos. Environ. 36*, 2207–2214.

Schürmann, G., Schäfer, K., Jahn, C., Hoffmann, H., Bauerfeind, M., Fleuti, E., Rappenglück, B., 2007: The impact of NO_x, CO and VOC emissions on the air quality of Zurich airport. *Atmos. Environ. 41*, 103–118.

Streli, C., Pepponi, G., Wobrauschek, P., Jokubonis, C., Falkenberg, G., Zaray, G., 2005: A new SR-TXRF vacuum chamber for ultra-trace analysis at HASYLAB, Beamline L. *X-Ray Spectrom. 34*, 451–455.

Takegawa, N., Miyakawa, T., Kondo, Y., Jimenez, J.L., Zhang, Q., Worsnop, D.R., Fukuda, M., 2006: Seasonal and diurnal variations of submicron organic aerosol in Tokyo observed using the Aerodyne aerosol mass spectrometer. *J. Geophys. Res.-Atmos. 111*, Art. No. D11206.

Tesseraux, I., 2004: Risk factors of jet fuel combustion products. *Toxicology Letters 149*, 295–300.

Unal, A., Hu, Y., Chang, M.E., Odman, M.T., Russell, A.G., 2005: Airport related emissions and impacts on air quality: Application to the Atlanta International Airport. *Atmos. Environ. 39*, 5787–5798.

Vekemans, B., Janssens, K., Vincze, L., Adams, F., Van Espen, P., 1994: Analysis of X-ray spectra by iterative least squares (AXIL): New developments. *X-Ray Spectrom. 23*, 278–285.

Watjen, U., Bárson,y I., Dücső, C., 2000: A Novel Micro-Structured Reference Material for Ion and X-Ray Microbeam Analysis. *Mikrochim. Acta 132*, 521–525.

IDŐJÁRÁS

Quarterly Journal of the Hungarian Meteorological Service
Vol. 112, No. 2, April–June 2008, pp. 99–112

Airport (Budapest Ferihegy – Hungary) air quality analysis using the EDMS modeling system. Part I. Model development and testing

Roland Steib[1], **Krisztina Labancz**[1], **Zita Ferenczi**[1] and **Bálint Alföldy**[2]

[1]*Hungarian Meteorological Service, P.O. Box 39, H-1675 Budapest, Hungary*
[2]*Hungarian Academy of Sciences KFKI Atomic Energy Research Institute, P.O. Box 49, H-1525 Budapest, Hungary*
E-mails: steib.r@met.hu, ferenczi.z@met.hu, labancz.k@met.hu, alfi@sunserv.kfki.hu

(Manuscript received in final form May 5, 2008)

Abstract—This paper presents an application of the EDMS dispersion modeling system to airport air quality calculations. The EDMS system is a combined emissions and dispersion model which can be used to produce an inventory of emissions generated at Budapest Ferihegy Airport, as well as to calculate pollutant concentrations on and around the airport. Calculated yearly average NO_x and CO concentration distributions over the area of the airport are presented. Calculated hourly average NO_x and CO concentration values are compared with observed air pollution concentrations and meteorological data, which were measured during three measurement campaigns held in the area of Budapest Ferihegy Airport.

Key-words: airport air quality, dispersion modeling, EDMS modeling system

1. Introduction

Aviation has experienced rapid expansion as the world economy has grown, and this has produced a number of major environmental challenges (*Britter*, 2007). As the contribution to urban air pollution from road emissions is steadily reducing in cities of European countries, other emission sources are becoming comparatively more relevant. The contribution to air pollution levels from emissions produced by the operation of airports located close to cities is one example in this respect. This phenomenon is accentuated due to urban settlement dynamics resulting in increases in the number of people exposed either living or working around these facilities and expansion wishes of airport operators to cope with forecasted increases in air traffic demand.

There are a number of widely used operational atmospheric dispersion models applied to airports (*Barrett* and *Britter*, 2007). In the early 2000's, a model intercomparison was executed in the framework of the Project for the Sustainable Development of Heathrow (*Department for Transport, U.K.*, 2006). Three models addressing local air quality at airports were compared with monitored air quality data and each other: (i) ADMS-Airport, based on the ADMS-Urban, a quasi-Gaussian dispersion model nested within a trajectory model (*Carruthers et al.*, 1994, 2007); (ii) LASPORT, based on the LASAT Lagrangian dispersion model (*Janicke et al.*, 2007); (iii) EDMS, based on the AERMOD quasi-Gaussian regulatory-type dispersion model (*CSSI, Inc.*, 2004). Apart from this study, in 2005 the EUROCONTROL initiated the ALAQS project to develop a European methodology and model (ALAQS-AV) to assess aviation's contribution to the degradation of the local air quality in surroundings of airports (*EUROCONTROL*, 2005).

Budapest Ferihegy Airport is not one of the internationally registered busiest airports, but the volume expanding of its traffic requires to be aware of its impact on air quality. By the recommendation of EEA (European Environment Agency), in case an airport has more than 100 thousands LTO cycles (landing, take-off, and taxi) per year, the airport becomes an important air pollution source in the national balance. The traffic at the airport is near to this limit. Especially in the summer period a large number of charter flights can increase the traffic significantly.

In 2005, a new project started to determine the air pollution situation at Budapest Ferihegy Airport, combining the results of measurements and model calculations. Airport related particles originate from aircraft emissions and erosion (brake and tire), moreover, emissions of ground supporting vehicles, point sources, and passanger related cars as well as resuspension of particles had to be taken into account. In the joint research work, the EDMS air quality modeling system was adapted and developed at the Hungarian Meteorological Service (HMS), while three measurement campaigns were performed on the area of Budapest Ferihegy Airport by the Hungarian Research Institute of Physics. The EDMS model system was chosen on the base of studies presented by recent investigations, because the AERMOD dispersion model has been earlier adapted at the HMS including a newly developed terrain preprocessor. During the measuring campaigns, concentration of numerous air pollutants were detected including usual pollutants as nitrogen oxides and carbon-monoxide, as well as rarely observed pollutants as tire and soot, which are characteristic of air traffic. Multi-element chemical analysis were done with high size resolution for deriving fingerprints of different sources of airport related particles.

This paper presents the first results of the EDMS modeling system, compared to the measured data during three short time measuring campaigns. Section 2 describes the model and its required input data, in Section 3 the modeled yearly averages of the concentration of NO_x and CO are presented, and Section 4 presents the comparison of the modeled and observed NO_x and CO data.

2. *The EDMS modeling system*

2.1. The EDMS model

The EDMS (Emissions and Dispersion Modeling System) has been considered a preferred model for airport air quality analysis. The modeling system EDMS was developed in the mid-1980s as a complex source microcomputer model designed to assess the air quality impacts of proposed airport development projects. EDMS is a combined emissions and dispersion model for assessing air quality at the airports. The model is used to produce an inventory of emissions generated by sources on and around the airport or air base, and to calculate pollutant concentrations in these environments. The policy statement is intended to ensure consistency and quality of analysis performed to assess the air quality impacts of airport emission sources for purposes of complying with the National Environmental Policy Act.

The previous version of EDMS (Version 3.23) used CALINE3 and PAL2 models for atmospheric dispersion. In the first quarter of 2001, CALINE3 and PAL2 were replaced by AERMOD quasi-Gaussian dispersion model and its supporting weather and terrain processors, AERMET and AERMAP in Version 4.0 of EDMS. AERMOD has better characterization of the planetary boundary layer (*Steib*, 2006) and allows dispersion to be accomplished using continuous functions rather than with discrete stability classes that do not change with height. In the convective boundary layer a good approximation to the probability density function (PDF) is the superposition of two Gaussian distributions (*Baerentsen* and *Berkowicz*, 1984; *Weil*, 1988), so instead of a Gaussian distribution for both the horizontal and vertical directions, AERMOD uses a bi-Gaussian probability density function, p_w, to characterize the dispersion in the vertical direction (*Cimorelli et al.*, 2004):

$$p_w = \frac{\lambda_1}{\sqrt{2\pi}\sigma_{w1}} \exp\left(-\frac{(w-\overline{w_1})^2}{2\sigma_{w1}^2}\right) + \frac{\lambda_2}{\sqrt{2\pi}\sigma_{w2}} \exp\left(-\frac{(w-\overline{w_1})^2}{2\sigma_{w1}^2}\right), \qquad (1)$$

where λ_1 and λ_2 are weighting coefficients for the two distributions with $\lambda_1 + \lambda_2 = 1$ (the subscripts 1 and 2 refer to the updraft and downdraft distributions, respectively). The parameters of the probability density function (w_1, w_2, σ_{w1}, σ_{w2}, λ_1, λ_2) are functions of σ_w (the "total" or overall root mean square of vertical turbulent velocity). AERMOD also incorporates a new, simple method to model flow and dispersion in complex terrain.

The EDMS version used for this study is EDMS Version 4.5. The model can calculate emission inventories for the following pollutants: CO, NO_x, SO_x, total hydrocarbons (THC), non-methane hydrocarbons (NMHC), volatile organic compounds (VOC), $PM_{2.5}$, and PM_{10}.

At the HMS, the AERMOD model system was adapted first (*Steib* and *Labancz*, 2005). Because of the input data file formats required for AERMET and AERMAP are not available at HMS, new pre-processors were developed for preparing the input files for the dispersion model. The MM5 numerical weather prediction model analysis files are used as meteorological input of AERMOD. After successful setting up of AERMOD, the adaptation of EDMS was not too difficult work. The input files needed for AERMOD were generated by the EDMS model, then AERMOD was run on another computer because of the large memory needs of the dispersion model. *Fig. 1* shows the architecture of the EDMS modeling system.

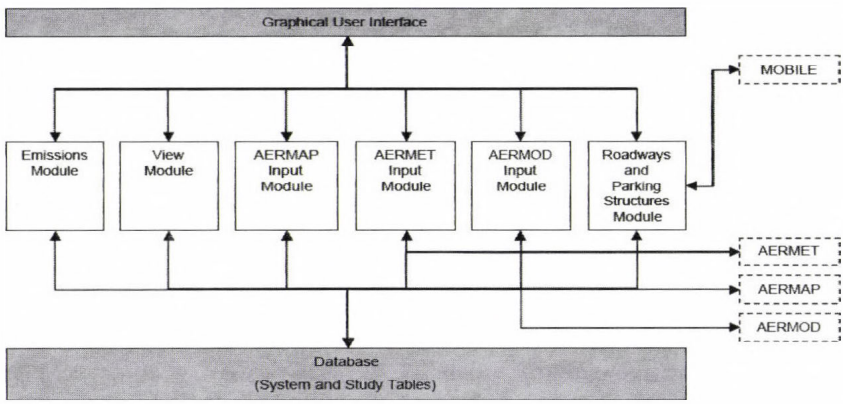


Fig. 1. EDMS system architecture and components.

2.2. EDMS input required

EDMS generates input files for use with the AERMOD dispersion model. Since EDMS is a model specifically developed for use at airports, the inputs relate directly to the placement of aircraft and other source activity and movement on the airport. Data input includes:

1) Creation and specification of
   - runways,
   - queues,
   - taxiways,
   - buildings, and
   - gates.
2) Emission data of
   - aircraft activity,
   - ground support equipment,
   - on-road vehicles,

- parking facilities,
- stationary sources, and
- training fires.

Aircraft activity is expressed in landing-takeoff (LTO) cycles. Each LTO consists of taxiing, queuing, takeoff, climb out, approach, and landing. There is no provision to specify arrival numbers and departure numbers independently of each other. EDMS contains default aircraft-specific data relating to the emissions:

1) Times in mode (TIMs) are the durations per LTO cycle that an aircraft spends in each of the four modes of aircraft operation. Takeoff, climb out, approach, and landing mode TIMs are aircraft-specific in EDMS.
2) Ground support equipments (GSE) are made to be based on aircraft type with an operating time associated with each aircraft LTO cycle.
3) Aircrafts are assigned to an unlimited number of taxiways and runways.
4) Engine emission factors are aircraft-specific.

2.3. Emission data

The dispersion model calculates concentrations for 1 hour periods, and all source types can vary hour by hour in their activity or strength. Therefore, EDMS uses operational profiles which are based on the concept of peak activity. A peak hour, day, or month is defined as that at which the most or maximum activity occurs. Peak activity is represented by a proportional factor of 1 (signifying maximum activity).

In our study three categories are defined for the aircrafts – light, medium, heavy – in accordance with the International Civil Aviation Organization (ICAO) scheme. Each category is represented by the aircraft-type most frequently operated at Ferihegy Airport (Socata Tampico – light, Boeing 737 – medium, Boeing 767 – heavy). All aircrafts are replaced by the appropriate defined aircraft with its default specific data. Hourly, daily, and monthly operational profiles are also calculated for the three defined aircrafts. *Table 1* presents the number of aircrafts used in our work. One third part of all three aircraft types used the gates at Terminal 1 and the other two thirds used the gates at Terminal 2. We calculated with a taxi time of 12 minutes for every aircraft.

Table 1. Representative aircraft types and the number of their LTO cycles

Aircraft		LTO cycles during the year 2006
Boeing 737	– medium	57,594
Socata Tampico	– light	3,769
Boeing 767	– heavy	2,112

Emissions are generated by ground support vehicles and auxiliary power units (APUs) while the aircraft is parked at the gate. GSE emissions are obtained from EPA's NONROAD model and are dependent on the age, fuel, horsepower, and load factor applied to the engine. APUs are most often on-board generators that provide electrical power to the aircraft while its engines are shut down. Like GSE, APU emissions generated per LTO cycle are the product of the emission factor and the operating time, and multiplied by the number of applicable aircraft LTO cycles. In case of B737 and B767 the default APUs were used. In case of the other aircrafts (light aircrafts) APUs were not used. The GSE was also set to the default values of the different aircraft types.

In our work, two parking facilities were used next to the two terminals. The model was run using the number of 300,000 vehicles at Terminal 1 and 350,000 vehicles at Terminal 2, in a year. The average speed of vehicles traveling in the parking facility is one of the parameters necessary to determine the emission factors for the movement of the vehicles using MOBILE5a, MOBILE5b, or MOBILE6.2 models. The default fleet mix (types, fuels and ages of vehicles), the speed (10 mph) in the parking facility and the distance (250 m) traveled in lot were set to the default values. The latter is an estimate for the average distance a vehicle travels between entry and exit.

In order to take into account the motor vehicle activity on roadways at and near the airport, it is necessary to use as many traffic count results as possible. The default fleet mix and the speed (56 km h^{-1}) of the vehicles were set to the default values. *Table 2* shows the traffic count data used in our study. Traffic count and the calculations for the whole year was made for 2006.

Table 2. Number of vehicles using the roads in a year near to the airport. Based on traffic count data of 2006

Road	Number of vehicles/year
Preparatory phase of the Motorway 4 (Gyömrői street)	12,469,212
Bypass of the Motorway 4 near Vecsés	6,258,924
Road to Terminal 2	5,763,492
Road between Terminal 1 and Terminal 2	1,200,000

The general methodology for calculating emissions from stationary sources considers the amount of fuel or substance consumed. In the modeling we used the three main stationary sources at the airport. Each of these sources have a stack height of 40 meters and a stack inside diameter of 1.9 meters. *Fig. 2* shows the aerial map of Budapest Ferihegy Airport. The stationary sources, terminals, major roads, monitoring sites, and main ways inside the airport can be seen on the map.

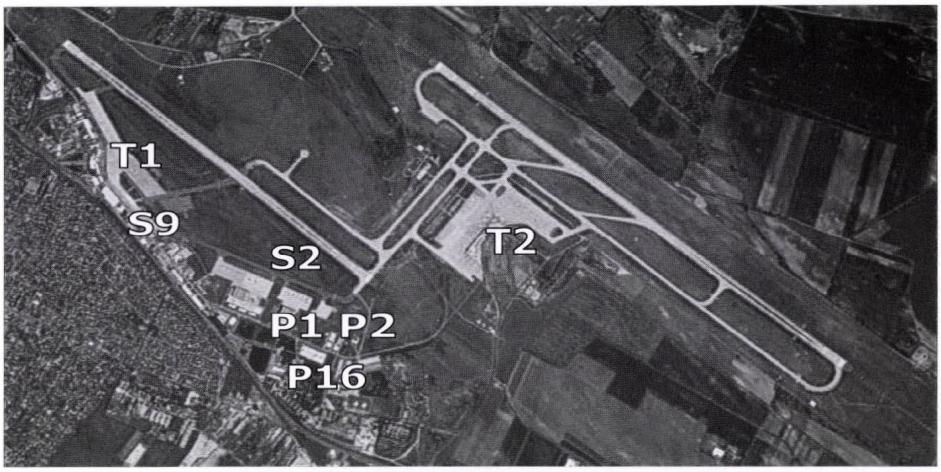


Fig. 2. Aerial map of Budapest Ferihegy Airport. P1, P2, P16: stationary sources; T1, T2: terminals; S2, S9: monitoring sites.

3. Results

Locations at which concentrations are estimated are known as receptors. EDMS allows to consider the placement of receptors in Cartesian or polar coordinate system with the ability to also specify the height of the receptors. In the modeling domain, a Cartesian receptor network was used with different resolutions. Near the main emission sources we used a receptor network with higher resolution (100 m), elsewhere a receptor network with lower resolution (500 m).

Two test runs were made with the EDMS modeling system. The urban ambient NO_x and CO concentrations were not used in the calculations. The EDMS system makes calculation for a whole year cycle using the consecutive modeled meteorological analysis fields and the calculated hourly emission data. The calculated hourly concentration values of the pollutants are then averaged over the year. In the first run we calculated the yearly average NO_x concentration in the receptor points at a height of 1.8 m, based on the meteorological and emission data of the year 2006, in the second run the yearly average CO concentration was calculated in the same way. *Figs. 3* and *4* show the calculated concentrations for NO_x and CO, respectively. In the figures, black solid lines indicate the runways, black dashed lines are taxiways, white solid lines are the main routes next to the airport, and white poligons indicate the two terminals. The numbers at the two axes present the distance in meters from the center (the 0-point) of the figure. The whole area is about 9×8 km^2.

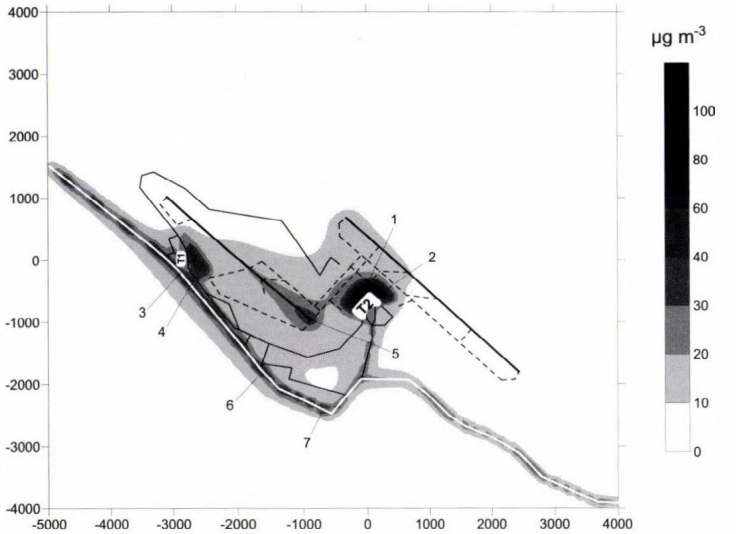


Fig. 3. Yearly average NO_x concentration distribution at Ferihegy Airport, calculated for 2006. Units at the axes are meters.

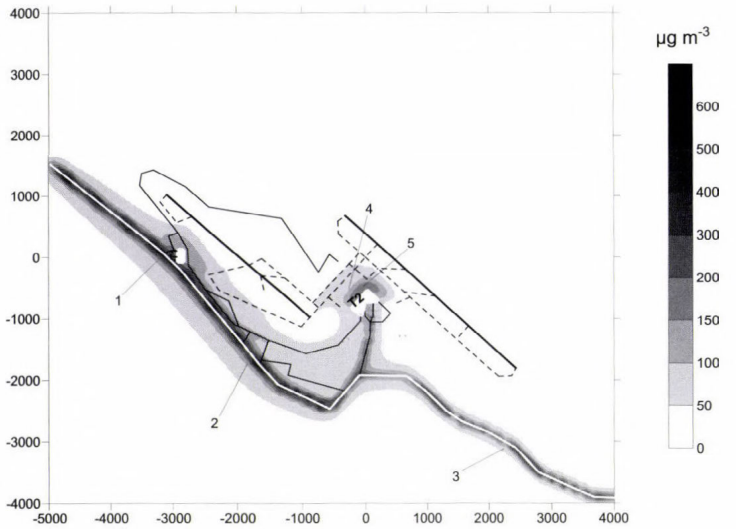


Fig. 4. Yearly average CO concentration distribution at Ferihegy Airport, calculated for 2006. Units at the axes are meters.

Meteorological and emission input data files were constructed on the basis of data, which were observed and calculated for the year of 2006. The pre-processor part of the model makes emission calculations of the different sources

using the input data. After that the dispersion calculations are made. The aim of our modeling work was to determine the concentration distribution of different pollutants near the airport. The main emitted pollutants near the airport are NO_x, CO, PM_{10}, and $PM_{2.5}$. A weakness of the model is that PM emission data is not available for all aircraft engines, thus, we focused on the NO_x and CO concentrations near the airport.

The model calculated the yearly average concentrations at the receptor points. The resolution of the receptor network, used in the model, was not uniform. At the places, where greater emissions occurred, a 100 m receptor network resolution was used. At places, where the emissions are negligible (especially near the edges of the modeling domain), a 500 m receptor network resolution was used. The centre point of the modeling domain is the same as the 0-point of the airport. The geographical coordinates of this point are the following: 47°26'N, 19°15'E. The place of a receptor point is represented with two coordinates. The first coordinate (x-coordinate) shows the distance of the receptor point from the 0-point in east-west direction. In case of positive x-coordinate the receptor point lies east of the 0-point, in case of negative x-coordinate it lies west of the 0-point. The second coordinate (y-coordinate) shows the distance of the receptor point from the 0-point in north-south direction. In case of positive y-coordinate the receptor point lies north of the 0-point, in case of negative y-coordinate it lies south of the 0-point.

Fig. 3 shows the yearly average of the NO_x concentration distribution near the surface of the modeling domain. *Table* 3 presents the receptor points, for which the highest concentrations were found by the model calculations. The place with maximum NO_x concentration can be found at Terminal 2, near the gates (receptor points 1 and 2), with a value of about 100 $\mu g/m^3$. The second highest NO_x concentration values (about 80 $\mu g\ m^{-3}$) can be found near Terminal 1 (points 3 and 4). Because the aircraft traffic is about 25% of the whole traffic at Terminal 1, the concentration values at Terminal 1 are not so high as near Terminal 2. Another maximum place in the NO_x concentration distribution can be found near the starting point of the main runway (receptor point 5). This phenomenon is not strange because the average wind direction near the airport is northwest, so the aircrafts mostly begin the take off cycle from this point (at a specific wind speed value the aircrafts should take off and landing in the direction from where the wind blows). The NO_x emission of the aircraft engines is highest during take off phase, so it is not surprising that the mentioned local maximum place can be found near the most used starting point of the runways. The third place, where the NO_x pollution is significant (about 75 $\mu g\ m^{-3}$) can be found near the motorway No. 4, which runs near the airport (points 6 and 7). This fact is not surprising as the main source of the NO_x pollution is the road traffic. Our calculations show, that in the area of the airport, NO_x emissions of the aircrafts and the vehicles running in the airport and the neighboring motorways give equivalent contributions to the concentration in the ambient air.

Table 3. Locations of the highest yearly average NO_x concentration values

Receptor point	Location	Concentration (μg m^{-3})
1	Terminal 2	102.36
2	Terminal 2	100.93
3	Terminal 1	81.49
4	Terminal 1	81.27
5	Strating point of the runway	92.55
6	Motorway	78.67
7	Motorway	75.79

Fig. 4 shows the yearly average CO concentration distribution near the surface of the modeling domain. *Table 4* presents the receptor points, for which the highest concentrations were found by the model calculations. The first 20 maximum CO concentration values can be found near the motorway No. 4 (receptor points 1, 2, and 3). Concentration values of this 20 receptor points are between 500 and 700 μg m^{-3}. The CO pollution is also significant next to the gates at Terminal 2 (points 4 and 5). The concentration values are here about 200 μg m^{-3}. According to the model calculations, the contribution of the aircrafts to the local ambient CO concentration level is significantly less than the contribution of the ground vehicle traffic.

Table 4. Locations of the highest yearly average CO concentration values

Receptor point	Location	Concentration (μg m^{-3})
1	Motorway	725.48
2	Motorway	711.48
3	Motorway	508.05
4	Terminal 2	211.48
5	Terminal 2	197.25

We can see that in both cases the maximum concentrations are near the gates of Terminal 1 and 2. The maximum yearly NO_x concentrations are about 100 μg m^{-3}, the maximum yearly CO concentrations are about 700 μg m^{-3}. For the maximum concentrations near the gates the GSE and the APUs are responsible. From the emission inventory table of the model it can be seen that GSE and APUs produce the highest CO emissions in the modeling domain. Although the total NO_x emission of the aircrafts and roadways is higher than the NO_x emission of GSE and APUs, aircrafts and vehicles emit the pollutants in a much bigger area. In *Fig. 3* it is visible that in case of NO_x, the vehicles (motorway No. 4) and the moving aircrafts (especially near the starting points, because of the higher NO_x emission in take-off mode) have significant influence in the concentration distribution.

4. Comparison with measurements

In 2006, three measurement campaigns were held to determine the air pollution situation in the area of Budapest Ferihegy Airport. During the measurement campaigns, concentration of numerous air pollutants were detected including common pollutants as nitrogen oxides, carbon-monoxide, and particulate matter, as well as rarely observed pollutants as tire debris and soot particles, which are characteristic of air traffic. The campaigns were performed by the Hungarian Academy of Sciences KFKI Atomic Energy Research Institute. CO, NO, NO_2, SO_2, O_3 and particle mass concentrations were detected in every 2 minutes using gas monitoring equipments (Environnement SA and Airpointer system) and TEOM PM monitor by Thermo. In this study we use hourly averaged NO_x and CO concentrations, measured simultaneously during the second campaign at two places: (i) station 2 was located near ground level, approximately 50 m southwest of the take-off point of one of the runways, and (ii) station 9 was located near ground level, approximately 50 m southwest of the main taxiway to Terminal 1 (see *Fig. 2*).

As the sources at airports show large temporal and spatial variation, and so far we can use observed data measured during short time campaigns, in this first stage of model development we aimed to get a first survey of our results. For this purpose, diurnal variation of hourly averaged concentration values were compared with the modeled values in the period of May 31–June 2, 2006. Based on the results of the measurement campaigns, air pollutant concentrations are going to be monitored continuously at the airport. Thus, in the near future, we plan to make a real validation using the continuously observed data series.

The meteorological situation on the three days of the examined measuring period was rather varied due to the cold front, which crossed Hungary. The sky was generally broken with few hours of sunshine, and showers formed from time to time. There was strong northwest wind with stormy gusts in many places. The maximum temperature was far below the long-time average, 10–17 °C was measured daytime.

There are many papers dealing with the air pollution situation at the airports (*Henry et al.*, 2002; *Yu et al.*, 2004; *Carslaw et al.*, 2006). As the aim of these studies was mainly to detect and quantify aircraft and other on-airport contributions to the ambient air pollution level, they worked with yearly averages of longer data series. Because of the short measuring period, we tried to take a preliminary picture on the temporary pollution situation using hourly averages. *Fig. 5* shows the results of the model calculations for hourly NO_x concentrations compared with the observed data, at stations 2 and 9, during the examined period. The modeled values are increased compared with the ambient NO_x concentration measured at K-puszta (48°58'N, 19°33'E) background monitoring station. The course and order of the modeled and observed data series are very similar, and in most cases, the peaks can be found at the same

time at both measuring sites. This result shows good promise for that we will be able to determine the time and value of the highest peaks of NO_x concentration at both sites.

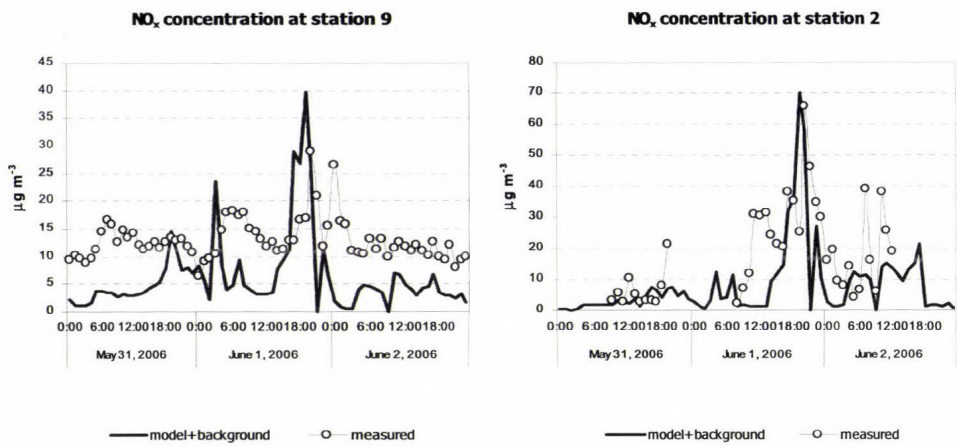


Fig. 5. Comparison of the modeled and measured hourly averages of NO_x concentration at station 2 and 9, during May 31–June 2, 2006.

In case of CO the situation is more complicated. Similarly to NO_x, the modeled CO concentrations were increased compared with the ambient values measured at Hegyhátsál (46°57'N, 16°39'E) background monitoring station. In spite of this, the measured hourly CO concentration values were approximately 100–150 µg m^{-3} higher than the modeled values, and the peaks did not show the same coincidence as in the case of NO_x. The possible reason lies in the buoyant behavior of aircraft plume dilution (*Henry et al.*, 2006), as well as in the fact, which was recognized at other airports: compared with ground vehicle traffic, aircraft do not seem to be a significant source near the airport, at least in terms of producing high concentrations (*Yu et al.*, 2004). CO concentration measured at the area of the airport depends on the wind direction and the CO concentration values in the city, which located in upwind direction from the Budapest Ferihegy Airport. Wind can transport considerable CO pollution from the city, and this effect was not taken into account in the EDMS calculations. It can be assumed, that the missing concentration must be arrived from the areas of Budapest. The wind direction in the examined time period was west, northwest, this fact confirms the previous assumption. This situation must be examined in detail in the near future.

5. *Conclusions*

In this study we presented two model runs using the EDMS airport air quality modeling system. In the first model run the yearly average concentration distribution of NO_x was calculated for the area of the Budapest Ferihegy Airport, based on the calculated hourly concentration values. We saw that the most polluted area was near the gates caused by the emissions of the ground support equipments. Other polluted areas were the starting point of the main runway (effect of the starting aircrafts) and motorway No. 4 (effect of the ground vehicles). In the second run the yearly average concentration distribution of CO was calculated. In this case we could find the most polluted area along motorway No. 4 (effect of the ground traffic). Another polluted area was found near the gates (effect of the ground support equipment). The calculations show, that in the area of the airport, NO_x emissions of the aircrafts and the vehicles running in the airport and the neighboring motorways give equivalent contributions to the concentration in the ambient air, while the contribution of the aircrafts to the local ambient CO concentration level is significantly less than the that of the ground vehicle traffic.

There are three main points which will be further studied in the future. Firstly, we would like to increase the accuracy of our modeling results, mainly in the field of emission input values specific for Budapest Ferihegy Airport. Secondly, as air pollutant concentrations are going to be monitored continuously at the airport, we plan to make a real validation using the measured data series. Finally, the model will be used for calculating the concentration distribution of PM. The main problem is the PM emission data, which is not available for Socata Tampico engines. To solve these problems a lot of measuring work should be completed at and around the airport.

Fortunately, Ferihegy Airport is located in the southeast edge of Budapest, while the prevailing wind direction is northwest. This situation affects the contamination relations advantageously in Budapest. In connection with these work we would like to determine the critical meteorological situations, when high concentration values can be measured next to the terminals.

The sources at airports have large temporal and spatial variation, and concentrations were only measured during short time campaigns. Based on the results of the measurement campaigns, air pollutant concentrations are going to be monitored continuously at the airport. Thus, in the near future, we plan to make a real validation using the continuously observed long time data series.

Acknowledgments—Long-term monitoring of atmospheric carbon monoxide mixing ratio in Hungary is carried out by NOAA ESRL GMD Carbon Cycle and Greenhouse Gases Group (Boulder, Colorado, U.S.A.). The authors thanks them and *Dr. László Haszpra* for making the data available for this study. This paper is supported by the NKFP-JÁP 3/019/2005 National Research Program.

References

Baerentsen, J.H. and *Berkowicy, R.*, 1984: Monte Carlo simulation of plume dispersion in the convective boundary layer. *Atmos. Environ. 18*, 701-712.

Barrett, S. and *Britter, R.*, 2007: A simple approach for rapid operational air quality modelling at airports. *Proceedings of the 11th International Conference on Harmonisation within Atmospheric Dispersion Modelling for Regulatory Purposes.* Cambridge, 2-5 July 2007, 35-361.

Britter, R.E., 2007: The implications of variability of national and regional air quality regulations on the modelling of airport air quality within global aviation/environment models. *Proceedings of the 11th International Conference on Harmonisation within Atmospheric Dispersion Modelling for Regulatory Purposes.* Cambridge, 2-5 July 2007, 335-339.

Carruthers, D., Holroyd, R., Hunt, J.C.R., Weng, W., Robins, A., Apsley, D., Thomson, D., Smith, F., 1994: UK-ADMS: a new approach to modelling dispersion in the earth's atmospheric boundary layer. *J. Wind Eng. Ind. Aerod. 52*, 139-153.

Carruthers, D., McHugh, C., Jackson, M., Johnson, K., 2007: Developments in ADMS-Airport to take account of near field dispersion and applications to the Heathrow Airport. *Proceedings of the 11th International Conference on Harmonisation within Atmospheric Dispersion Modelling for Regulatory Purposes.* Cambridge, 2-5 July 2007, 346-350.

Carslaw, D.C., Beevers, S.D., Ropkins, K., Bell, M.C., 2006: Detecting and quantifying aircraft and other on-airport contributions to ambient nitrogen oxides in the vicinity of a large international airport. *Atmos. Environ. 40*, 5424-5434.

Cimorelli, A.J., Perry, S.G., Venkatram, A., Weil, J.C., Paine, R.J., Wilson, R.B., Lee, R.F., Petersand, W.D., Brode, R.W., Paumier, J.O., 2004: AERMOD: Description of model formulation (EPA-454/R-03-004). US Environmental Protection Agency.

CSSI, Inc., 2004: Emissions and Dispersion Modeling System (EDMS) User's Manual. Prepared for: Federal Aviation Administration Office of Environment and Energy. Washington, DC. FAA-AEE-04-02.

Department for Transport, July 2006: Project for the Sustainable Development of Heathrow – Air Quality Technical Report. www.dft.gov.uk/pgr/aviation

EUROCONTROL Experimental Centre, 2005: Zurich airport 2004: A comparison of modelled and measured air quality. *EEC/SEE/005/017.*

Henry, R.C., Chang, Y.S., Spiegelman, C.H., 2002: Locating nearby sources of air pollution by nonparametric regression of atmospheric concentrations on wind direction. *Atmos. Environ. 36*, 2237-2244.

Janicke, U., Fleuti, E., Fuller, I., 2007: LASPORT – a model system for airport-related source systems based on a Lagrangian particle model. *Proceedings of the 11th International Conference on Harmonisation within Atmospheric Dispersion Modelling for Regulatory Purposes.* Cambridge, 2-5 July 2007, 352-356.

Steib, R. and *Labancz, K.*, 2005: Regulatory modeling in Hungary – the AERMOD model. Part I. Description and application. *Időjárás 109*, 157-172.

Steib, R., 2006: Regulatory modeling in Hungary – the AERMOD model. Part II. Sensitivity of the model and case studies. *Időjárás 110*, 15-33.

U.S. EPA, 2002: User's guide for the AMS/EPA regulatory model – AERMOD. Research Triangle Park, North Carolina.

Weil, I.C., 1988: Dispersion in the convective boundary layer. *Lectures on Air Pollution Modeling* Venkatram, A. and Wyngaard, J.C., American Meteorological Society, 167-227.

Yu, K.N., Cheung, Y.P., Cheung, T., Henry, R.C., 2004: Identifying the impact of large urban airports on local air quality by nonparametric regression. *Atmos. Environ. 38*, 4501-4507.

IDŐJÁRÁS

Quarterly Journal of the Hungarian Meteorological Service
Vol. 112, No. 2, April–June 2008, pp. 113–123

Comparison study in mixing height determination for dispersion models

Tamás Weidinger[1], **Györgyi Baranka**[2] and **Árpád Bordás**[1,3]

[1]*Department of Meteorology, Eötvös Loránd University,*
P.O. Box 32, H-1518 Budapest, Hungary; E-mail: weidi@ludens.elte.hu
[2]*Hungarian Meteorological Service,*
P.O. Box 39, H-1675 Budapest, Hungary; E-mail: baranka.gy@met.hu
[3]*University Centre for Meteorology and Environmental Modelling,*
University of Novi Sad, Trg D. Obradovića 5, 21000 Novi Sad, Serbia;
E-mail: abordas@uns.ns.ac.yu

(Manuscript received in final form June 4, 2008)

Abstract–Hungarian Transmission Standards were updated with the goal of standardising and improving methods for the calculation of meteorological parameters used as inputs in air quality dispersion models. New methods for determining mixing height are recommended by COST 710. For stable and mechanically dominated unstable atmospheric boundary layers, the formula for determining mixing height requires friction velocity, Monin-Obukhov length and Coriolis parameter. For convective boundary layers, a simple prognostic model based on the determination of initial temperature profile, surface momentum and sensible heat fluxes is used. Statistical comparisons among (i) new and (ii) former Hungarian Standards, (iii) AERMOD, (iv) some methods suggested by COST 710 as well as (v) mixing height calculation from radiosonde measurements were performed. Hourly values of mixing height were calculated based on standard meteorological measurements using the different approaches given above for a one-year dataset (1996). Model results for the new Hungarian Standards are in good agreement with radiosonde measurements; the best fit was obtained during periods of a growing convective layer. The growth rate of the mixing layer height is found to be sensitive to the potential temperature gradient above the convective layer.

1. Introduction

In new Hungarian Transmission Standards one chapter deals with the mixing height determination among (i) definitions of meteorological parameters, (ii) description of meteorological measurements at near-surface layer and in the atmospheric boundary layer, (iii) calculation of dynamical parameters of the surface layer, (iv) wind speed, direction and temperature profile and (v) determination of air pollutant dispersion parameters.

Based on hourly standard meteorological measurements, parameterizations (i) of the global radiation and the radiation budget components and (ii) the surface energy budget components (sensible (H) and latent heat (LE) fluxes) were developed using the Penman-Monteith methodology (*De Bruin*, 1983; *Holtslag* and *Van Ulden*, 1983; *Ács*, 1994; *Lagzi et al.*, 2006). Modified Pristley-Taylor parameter was used on the basis of meteorological and agroclimatological information (*Szász* and *Tőkei*, 1997; *Fodor*, 2007). Surface layer parameters, such as friction velocity (u_*), dynamic temperature (T_*), and Monin-Obukhov length (L) were calculated from wind speed (u) and sensible heat flux (H) using Monin-Obukhov similarity theory knowing the roughness length and displacement height (*Weidinger et al.*, 2000; *Ács* and *Kovács*, 2001).

Sources of mixing layer height calculations were (i) formal Hungarian Standards (*Fekete et al.*, 1983; *Szepesi et al.*, 1995, 2005), (ii) the U.S. EPA's AERMOD modeling system (*Cimorelli et al.*, 1998; *Hall et al.*, 2000; *Steib*, 2005; *Steib* and *Labancz*, 2005, *Bozó et al.*, 2006), (iii) results of COST 710 program "Harmonization in the preprocessing of meteorological data for dispersion models" (*Fisher et al.*, 1998) and (iv) the method of *Matyasovszky* and *Weidinger* (1998) using radiosonde measurements.

2. *Mixing height calculation methods to be introduced as New Hungarian Transmission Standards*

2.1. Stable boundary layer

In case of a stable boundary layer three options were applied. If regular upper air measurements were available during the night (at 00:00 UTC), (i) the Richardson number method was used:

$$h = Ri_c \frac{(\Delta u)^2}{\beta \cdot \Delta \Theta_v}, \tag{1}$$

where h is the mixing height, Δu is the difference of wind speed, $\Delta \Theta_v$ is the difference of virtual potential temperature, Ri_c is the critical Richardson number, β is a stability parameter, rate of gravity acceleration and the average temperature of mixing height ($\beta = g/T$). The critical Richardson number was 0.25. (ii) Determination of the top of temperature inversion (h_T) and the level of the local wind maximum (h_u) based on the inflection point of temperature and wind speed and the smaller value ($h = \min(h_T, h_u)$) for the mixing height was chosen.

If upper-air meteorological measurements were not available, then the nocturnal mixing height was parameterised by using (iii) similarity theory (*Zilitinkevich et al.*, 2001; *Zilitinkevich* and *Baklanov*, 2002). Knowing the limitation of the calculation of stable boundary layer height (*Zilitinkevich et al.*,

2007) a traditional form (*Zilitinkevich*, 1972) was used, based on COST 710 (*Fisher et al.*, 1998):

$$h = c \cdot \sqrt{\frac{u_* \cdot L}{f}}, \tag{2}$$

where h is the mixing height (m), u_* is the friction velocity (m s^{-1}), L is the Monin-Obukhov length (m), f is the Coriolis parameter (s^{-1}) and c constant is 0.35.

2.2. Convective boundary layer

In the convective boundary layer a prognostic model derived from simplified formulae of continuity and thermodynamic equations was applied. The increase of mixing layer height caused by thermal turbulence is described by the following differential equation (*Batchvarova* and *Gryning*, 1991):

$$\frac{\partial h}{\partial t} = (1 + 2A)\frac{(-u_* \cdot T_*)}{\gamma_{\Theta_v} \cdot h} + 2B\frac{u_*^3}{\gamma_{\Theta_v} \cdot \beta \cdot h^2}, \tag{3}$$

where h is the mixing layer height, A, B are constants: $A = 0.2$ and $B = 2.5$; $\gamma_{\Theta_v} = \frac{\partial \Theta_v}{\partial z}$ is the virtual potential temperature gradient above the mixing layer, and β is the stability parameter. The first term on the right side of Eq. (3) describes the effect of thermal part of turbulence and the second term describes the mechanical part of the turbulence, which is negligible in most cases.

There is an analytic solution to Eq. (3):

$$\Delta t = t_2 - t_1 = \frac{1}{C^3}\left[\frac{1}{2}(C \cdot h + D)^2 - 2D \cdot (C \cdot h + D) + D^2 \cdot \ln(C \cdot h + D)\right]_{h_1}^{h_2}, \tag{4}$$

where

$$C = \frac{(1 + 2A) \cdot (-u_* \cdot T_*)}{\gamma_{\Theta_v}}, \qquad D = \frac{2B \cdot u_*^3}{\gamma_{\Theta_v} \cdot \beta},$$

h_1 is the height of mixing layer (m) at t_1 starting point of time, h_2 is the height of mixing layer (m) at t_2 given point of time. The mixing height was obtained by iteration using appropriate hourly time step (Δt) as the frequency of the surface synoptic measurements.

Values for two crucial parameters γ_{Θ_v} and $\Delta\Theta$ are needed in this method. γ_{Θ_v} is the virtual potential temperature gradient above the mixing layer determined by radiosonde measurements (γ_{Θ_v}) taking into consideration critical

values of the virtual potential temperature jump at the top of the growing mixed layer ($\Delta\Theta_{vm}$) by Eq. (5) (*Fisher et al.*, 1998):

$$\gamma_{\Theta_v} = \frac{(1+2A)\cdot h - \kappa \cdot B \cdot L}{A \cdot h^2 - \kappa \cdot B \cdot L \cdot h} \cdot \Delta\Theta_{vm} \cdot \tag{5}$$

The growth rate of the mixing layer depends on the value of the virtual potential temperature gradient (γ_{Θ_v}) above the mixing layer. Near surface virtual potential temperature gradient (γ_{Θ_v}) – based on the 00:00 UTC radiosonde measurement – in the stable boundary layer (strong inversion in early morning) has been often underestimated. In this case the virtual potential temperature jump ($\Delta\Theta_{vm}$) has been also underestimated (*Baranka et al.*, 2007).

3. Results

Hourly synoptic meteorological data set as well as 00:00 and 12:00 UTC radiosonde measurements for 1996 from Budapest were used in the development and testing of the new method for calculating the mixing layer height.

3.1. Night time stable stratification

Mixing heights determined from the inflection points of temperature (h_T) and wind (h_u) profiles from the radiosonde measurements ($h = \min(h_T, h_u)$), and from similarity theory (namely Eq. (2)) are very similar during moderate and strong wind speeds ($u(10\text{ m}) > 2\text{ m s}^{-1}$), while in the case of low wind speed the friction velocity ($u*$) is near zero so the estimation of mixing height is uncertain, so a constant value should be used (*Fig. 1*).

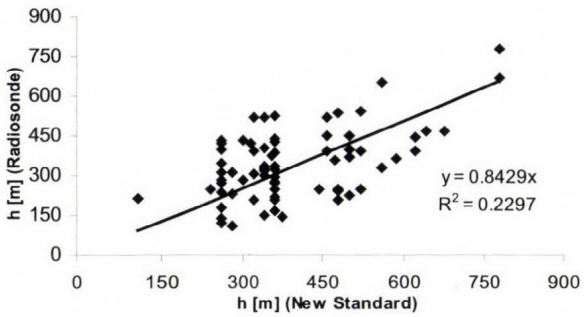


Fig. 1. Mixing height estimation based on radiosonde measurements along with temperature and wind speed, inflection points and similarity theory (New Standard) when the wind speed is higher than 2 m s^{-1} (Budapest, Apr 01, 1996 – Dec 31, 1996, 00:00 UTC).

3.2. *Virtual potential temperature jump above the convective mixing layer*

The behaviour of $\Delta\Theta_{vm}$ and γ_{Θ_v} was investigated using 12:00 UTC radiosonde measurements in the convective cases. The mixing layer height (h) was determined as one of the inflection points of temperature profile.

The critical temperature gradient $\left(\gamma = -\frac{\partial T}{\partial z}\right)$ for (i) the whole mixing layer was > 0.95 °C/100 m and in the upper sublayer it was > 0.8 °C/100 m based on the use of parcel method (*Matyasovszky* and *Weidinger*, 1998).

If the parcel method had not worked (the mechanically driven turbulence, advection, fronts, etc.) the first inflection point of temperature profile was chosen as the mixing height. Of course the mixing height is lower or equal than the cloud base.

In *Fig. 2* the annual course of the virtual potential temperature gradient under (*Fig. 2a*) and above the mixing height (*Fig. 2b*) and the virtual potential temperature jump (*Fig. 2c*) are presented on the basis of radiosonde measurements in Budapest in 1996.

In every month there are few unusable data for determining the mixing layer height by parcel method. Sometimes the virtual potential temperature gradients are very large in the mixing layer (*Fig. 2a*). Incidences of large negative virtual potential temperature gradients and also large positive virtual potential gradients are characteristic of the winter half year. Monthly average virtual potential temperature gradients approach zero in each month. Highest values of monthly average virtual potential temperature gradient above the PBL are formed in summer.

As *Fig. 2b* shows, the virtual potential temperature gradients above the mixing layer are always positive ($\gamma_{\Theta_v} > 0$). Large positive gradients occur in the winter period, with typical values between 0 and 2 °C/100 m. In every season extremely low and high values can be found. However, the monthly averages are larger during the winter than during the summer period. The variability of γ_Θ shows that: the values beneath the mixing height are small, while they are higher above the boundary layer in the free troposphere.

The virtual potential temperature jump ($\Delta\Theta_{vm}$) was also calculated. $\Delta\Theta_{vm}$ is defined as the virtual potential temperature difference in the thin layer (0.1 h) above the top of mixing layer calculated from 12:00 UTC measurements (*Fig. 2c*). The magnitude of $\Delta\Theta_{vm}$ values is between 0.1 °C and 3 °C.

In cases of unstable stratification for each hour the virtual potential temperature jump ($\Delta\Theta_{vm}$) was also calculated by using Eq. (4) during the growth phase of the convective mixing layer. The mixing height was determined by an iterative process. In every time step Eqs. (4) and (5) were solved, and at the same time, the value for γ_{Θ_v} was increased by the actual jump in Θ_{vm}.

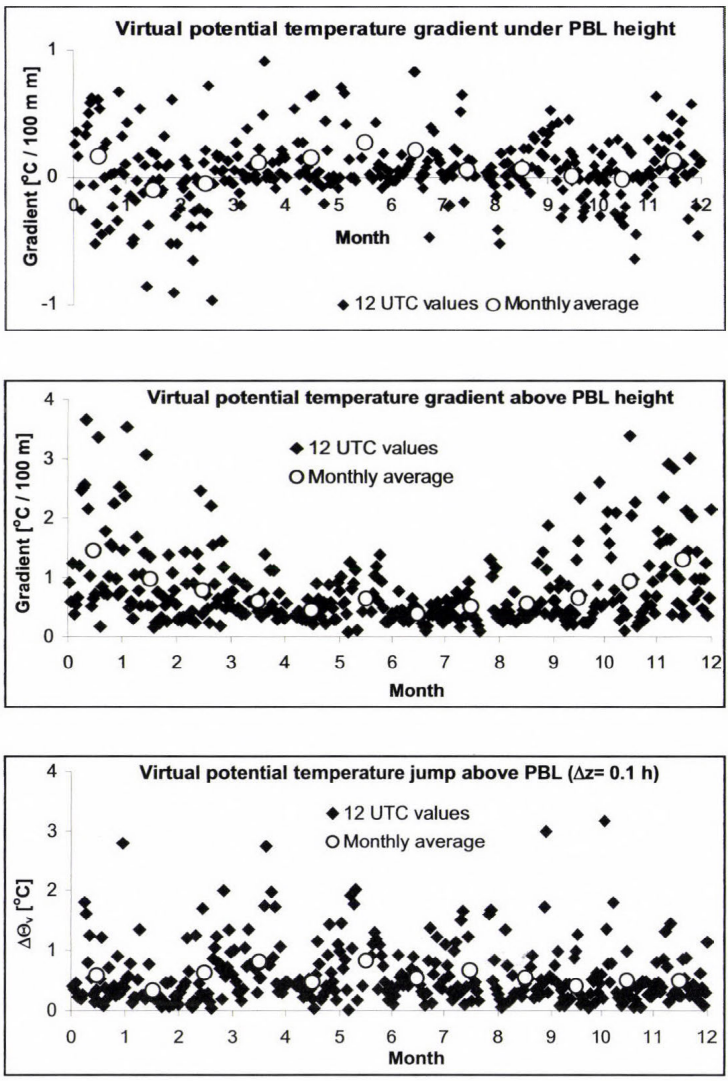


Fig. 2. Time series of the virtual potential temperature gradient under and above mixing height and virtual potential temperature jump above the mixing height in the $\Delta z = 0.1$ h deep layer.

Fig. 3 shows the hourly mixing height values on dependence of $\Delta\Theta_{vm}$ in July (a) and in December (b). High values of $\Delta\Theta_{vm}$ were found around the typical average mixing height for the given season. It means that the increasing rate of mixing height is more intensive in the case of small $\Delta\Theta_{vm}$.

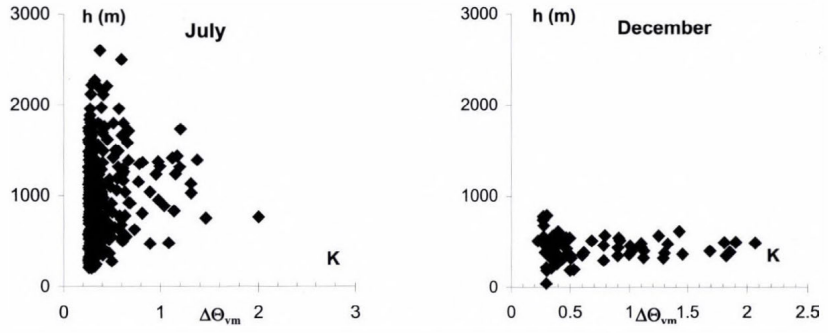


Fig. 3. Hourly values of mixing height (h) against virtual potential temperature jump in July and December of 1996.

The small virtual potential temperature jumps occur at the beginning of the convective growth phase and cases of the well developed mixing height and the larger values of $\Delta\Theta_{vm}$ came from the cases of the moderate mixing heights. The growth rate of the mixing layer $\left(\frac{\partial h}{\partial t}\right)$ is indirectly proportional to the virtual potential temperature jump ($\Delta\Theta_{vm}$).

According to results of numerical experiments, new values of $\Delta\Theta_{vm}$ should be introduced (for lower limit and the upper limit) to check the growth of mixing layer. The new values of potential temperature jump are modified in the following way:

$$\Delta\Theta_{v_m}^{new} = 0.25\ ^{\circ}\mathrm{C}, \quad \text{if} \quad \Delta\Theta_{vm} < 0.25\ ^{\circ}\mathrm{C},$$

$$\Delta\Theta_{v_m}^{new} = 2.25\ ^{\circ}\mathrm{C}, \quad \text{if} \quad \Delta\Theta_{vm} > 2.25\ ^{\circ}\mathrm{C}.$$

The new (corrected) $\gamma_{\Theta_v}^{new}$ is calculated from the Eq. (5).

3.3. Sensitivity analyses of growth of the convective mixing layer height

A sensitivity analysis was carried out to estimate the uncertainty of measurements of meteorological parameters used to determine friction velocity (u_*), virtual potential temperature gradient (γ_{Θ_v}) and dynamical temperature (T_*).

Friction velocity values were modified by ±10% and ±30% during the evaluation the mixing height shown in *Fig. 4*. The example (July 08, 1996) was chosen from the occasional days characterized by quite high insolation. The basic model was developed over a surface covered by grass, and an increase of 30% in u_* over a grass covered surface which is typical over an urban surface

was used and which provides good agreement with radiosonde measurement at Budapest.

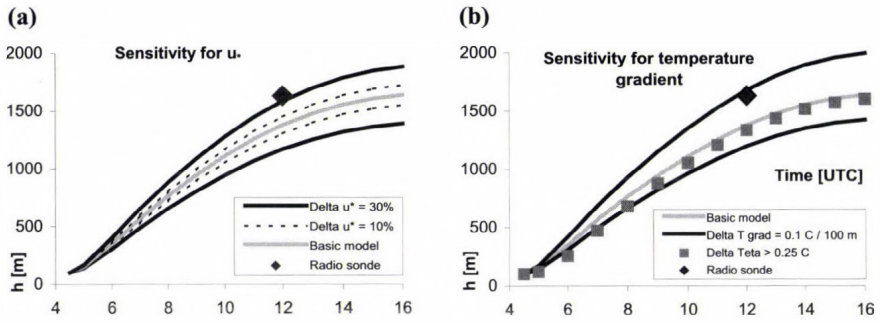


Fig. 4. Sensitivity for u_* (a) and virtual potential temperature gradient (γ_{Θ_v}) above the mixing layer (b) during the growth phase of the convective boundary layer.

The effect of uncertainty in temperature gradient, $\gamma = -\frac{\partial T}{\partial z}$ (or in virtual potential temperature gradient, $\gamma_{\Theta_v} = \frac{\partial \Theta_v}{\partial z}$) above the mixing layer for the calculation of the evaluation of mixing layer height (h) was also examined. The range of uncertainty of temperature gradient (γ) was $\pm$ 0.1 °C/100 m. Mixing layer heights increase more rapidly with larger temperature gradients (smaller virtual potential gradient) than with smaller temperature gradients (larger virtual potential gradient). In this case application of critical values of virtual potential temperature jump has no effect on mixing height. In this case study two mixing height values determined by 12:00 UTC radiosonde data fell within the uncertainty interval of the basic model.

3.4. Comparison study for mixing layer height calculation methods

For validation of mixing height models an intercomparison was carried out using different model formulations. An individual case study of one two-day period from the summer of 1996 is shown in *Fig. 5*. As can be seen from *Fig. 5*, the New Standard method is in good agreement with radiosonde measurements. The methods suggested by COST 710 and the Old Standard method underestimated the mixing layer height measured by radiosonde for about 8 hours during the day on July 15, 1996, otherwise they are also generally in good agreement with the radiosonde measurements. AERMOD generally overpredicted the radiosonde data and showed much poorer agreement with the data than the other three approaches.

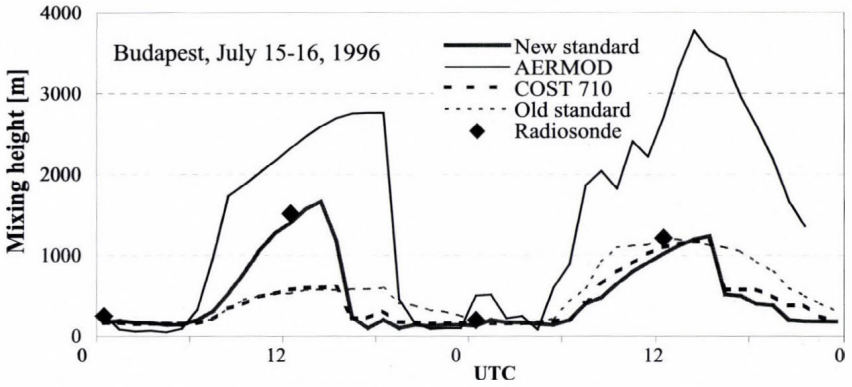


Fig. 5. Evolution and dissolution of mixing layer as computed by different methods.

For each season a statistical study was carried out to establish the characteristics of the four different model approaches comparison with the calculated mixing layer height from the radiosonde data set. *Table 1* gives a summary of results obtained for the summer months at 00:00, 06:00, 12:00, and 18:00 UTC.

The average values and the variances of different models show that there is good agreement between mean values of New Standard and radiosonde measurements at 12:00 UTC. However the New Standard calculated much smaller average values at 00:00 UTC than in the radiosonde data. Mixing height determination in the stable stratification from the inflection points of temperature (h_T) and wind (h_u) profiles from the radiosonde measurements in the case of low wind speed ($u(10\text{ m}) \leq 2\text{ m s}^{-1}$) is uncertain, the mixing heights are often overestimated.

Table 1. Mean values and variances of the mixing height (m) determined by different methodologies at Budapest in summer 1996

	1996 summer season							
	00:00 UTC		**06:00 UTC**		**12:00 UTC**		**18:00 UTC**	
	Mean	**St. dev.**	**Mean**	**St. dev.**	**Mean**	**St. dev.**	**Mean**	**St. dev.**
New standard	153	127	239	155	1349	536	303	597
AERMOD	322	424	451	421	1918	445	453	416
COST 710	140	105	334	660	698	633	284	228
Formal standard	241	73	263	230	1098	494	413	500
Radiosonde	404*	303	-	-	1313	450	-	-

*From top of the temperature inversion (h_T) and from the level of the local wind maximum (h_u) ($h = \min(h_T, h_u)$).

4. Conclusions

In the past years the new meteorological pre-processor for use in transmission models was designed and standardised. The most important part of transmission models is the calculation of the mixing height based on radiosonde and standard meteorological measurements. In the stable case the mixing height was determined using a diagnostic approach, in convective case using prognostic equation. Sensitivity analysis and comparison with other meteorological pre-processors (such as AERMOD, COST 710 recommendations) were done. The new model showed the most acceptable results compared to other mixing height calculation methods.

The advantages of new one-dimensional (1D) mixing layer height calculation model are summarized below:

- Model uses Monin-Obukhov similarity theory to describe the structure of boundary layer.
- Model results provide good agreement with radiosonde data.
- Fundamental input parameters are the potential temperature gradient above the convective layer.
- Growth rate of the mixing height is sensitive to surface fluxes.
- 1D model is easy to use.

Acknowledgements—The work was partly supported by the National Research and Innovation Program (NKFP/088/2004 and 6-00028/2005) and the International Visegrád Found. Special thanks for *Tamás Práger*, *Robert Mészáros,* and *Richárd Kovács* from Department of Meteorology Eötvös Loránd University and *Roland Steib* from Hungarian Meteorological Service for the collaboration in the field of development of meteorological pre-processors for environmental modeling.

References

Ács, F., 1994: A coupled soil–vegetation scheme: description, parameters, validation, and sensitivity studies. *J. Appl. Meteor. 33*, 268–284.

Ács, F. and *Kovács, M.*, 2001: The surface aerodynamic transfer parameterization method SAPA: description and performance analyses. *Időjárás 105*, 165–182.

Baranka, Gy., Weidinger, T., and *Bordás, Á.*, 2007: Analysis of the Hungarian Transmission Standards in mixing heighr determination. *7th Annual Meeting of the European Meteorological Society.* San Lorenzo del El Escorial, Spain, 1-5 October, 2007, EMS2007-A-00395.

Batchvarova, E. and *Gryning, S.E.*, 1991: Applied model for the growth of the daytime mixed layer. *Bound.-Lay. Meteorol. 56*, 261–274.

Bozó, L., Labancz, K., and *Steib, R.*, 2006: Estimation of environmental potential level using dynamical model approach for 2010 in Hungary (in Hungarian). In *Meteorological Scientific Days — Climate Dynamic Researches for Establishment of the Investigation for Estimation of Regional Scale Climate Change* (ed.: *T. Weidinger*). Országos Meteorológiai Szolgálat, Budapest, 207–215.

Cimorelli, A.J., Perry, S.G., Venkatram, A., Weil, J.C., Paine, R.J., Wilson, R.B., Lee, R.F., and *Peters, W.D.*, 1998: AERMOD – Description of Model Formulation. *Version 98315 (AERMOD and*

AERMET) and 98022 (AERMAP)/EPA Document. Posted on EPA Web site. http://www.epa.gov.scram001.

De Bruin, H.A.R., 1983: A model for the Priestley–Taylor parameter *α*. *J. Clim. Appl. Meteorol.* 22, 572–578.

Fekete, K., Popovics, M., and *Szepesi, D.*, 1983: *Guide to Estimate the Transmission of Air Pollutants* (in Hungarian). Országos Meteorológiai Szolgálat Hivatalos Kiadványai LV, Budapest.

Fisher, B., Erbrink, J., Jeannet, P., Joffre, S., Morselli, M., Pechinger, U., Seibert, P., and *Thomson, D.* (eds.), 1998: Harmonisation in the preprocessing of meteorological data for atmospheric dispersion models COST Action 710 Final Report. *EC-DG Science, Research and Development, EUR 18195 EN*, Luxembourg.

Fodor, N., 2007: 4M – Software for Modelling and Analysing Cropping Systems. *J. Univers. Comput. Sci. 12*, No. 9, 1196–1207.

Hall, D.J., Spanton, A.M., Dunkerley, F., Bennett, M., and *Griffiths, R.F.*, 2000: A rewiew of dispersion model inter-comparison studies using ISC, R91, AERMOD and ADMS. *R&D Technical Report P353*, Environment Agency.

Holtslag, A.A.M. and *Van Ulden, A.P.*, 1983: A simple scheme for daytime estimates of the surface fluxes from routine weather data. *J. Clim. Appl. Meteorol. 22*, 517–529.

Lagzi, I., Mészáros, R., Ács, F., Tomlin, A.S., Haszpra, L., and *Turányi, T.*, 2006: Description and evaluation of a coupled Eulerian transport-exchange model. Part I. Model development. *Időjárás 110*, 349–364.

Matyasovszky, I. and *Weidinger, T.*, 1998: Characterizing air pollution potential over Budapest using macrocirculation types. *Időjárás 102*, 219–237.

Steib, R., 2005: Regulatory modeling activity in Hungary. I. In *Advances in Air Pollution Modeling for Environmental Security* (eds.: *I. Faragó, K. Georgiev*, and *Á. Havasi*). Springer, 337–347.

Steib, R. and *Labanc, K.*, 2005: Regulatory modeling in Hungary – the AERMOD model. Part I. Description and application. *Időjárás 109*, 157–172.

Szász, G. and *Tőkei, L.*, 1997: Meteorology for agronomists, horticulturists and foresters (in Hungarian). Mezőgazda Kiadó, Budapest.

Szepesi, D., Fekete, K.E., and *Gyenes, L.*, 1995: Regulatory models for environmental impact in Hungary. *Int. J. Environ. Pollut. 5*, 497–507.

Szepesi, D., Fekete, K., Büki, R., Koncsos, L., and *Kovács, E*, 2005: Development of regulatory transmission modeling in Hungary. *Időjárás 109*, 257–279.

Weidinger, T., Pinto, J., and *Horváth, L.*, 2000: Effects of uncertainties in universal functions, roughness length, and displacement height on the calculation of surface layer fluxes. *Meteorol. Z. 9*, No. 3, 139–154.

Zilitinkevich, S., 1972: On the determination of the height of the Ekman boundary layer. *Bound.-Lay. Meteorol. 3*, 141-145.

Zilitinkevich, S., Baklanov, A., Roost, J., Smedman, A.S., Lykosov, V., and *Calanca, P.*, 2001: Diagnostic and prognostic equations for the dept of the stably stratified Ekman boundary layer. *Danish Meteorological Institute, Scientific Report 01-05*, Copenhagen, Denmark.

Zilitinkevich, S. and *Baklanov, A.*, 2002: Calculation of the height of the stable boundary layer in practical applications. *Bound.-Lay. Meteorol. 105*, 389–409.

Zilitinkevich, S., Esau, I., and *Baklanov, A.*, 2007: Further comments on the equilibrium height of neutral and stable planetary boundary layers. *Q. J. Roy. Meteor. Soc. 133*, 265-271.

IDŐJÁRÁS

Quarterly Journal of the Hungarian Meteorological Service
Vol. 112, No. 2, April–June 2008, pp. 125–139

The influence of global climate change on air and soil temperatures in maize canopy

László Dióssy

Ministry of Environment and Water,
P.O. Box 351, H-1394 Budapest, Hungary; E-mail: diossy@mail.kvvm.hu

(Manuscript received in final form March 7, 2008)

Abstract—On the basis of the climate scenarios downscaled to Hungary from the IPCC Report (*IPCC*, 2007) by *Bartholy et al.* (2007), we performed sensitivity analyses on air temperature in maize canopy. We created the scenario for 2071–2100 by using *Goudriaan*'s (1977) simulation model (Crop Microclimate Simulation Model, CMSM). We selected eight scenarios including the control (1961–1990), one of them examined the changes of the past decade, another one did the impacts of the doubled atmospheric CO_2 concentration. The remaining five scenarios contained different degrees of warming-up beside the doubled atmospheric CO_2 concentration as it follows: scenarios with +3.8, +4.8, +6.0, and two ones with +9.0 °C; the latter two differed only in the quantity of precipitation. Each approach increased the air temperature in maize canopy depending on the degree of warming-up. The changes already occurring in the environmental factors in the past decade increased the air temperature at cob level by 0.6 °C. The presence of plant canopy, however, mitigated the degree of warming-up, likely owing to the shadowing effect of the canopy. We should not ignore the fact that the compensating effect of the canopy depends on the canopy structure determined by the humidity supply. The analysis results made available local level information for the potential users that can provide apparent help in the preparation for the mitigation of adverse impacts of the expected changes.

Key-words: simulation model, air temperature, maize canopy

1. Introduction

Nowadays a lot of Hungarian and foreign studies have been elaborated on the impacts of global warming, as well as one of its cause, the increasing level of the atmospheric CO_2 concentration in the plant physiological processes (*Mihailovic* and *Eitzinger*, 2007; *Mera et al.*, 2006; *Anda* and *Kocsis*, 2007, etc.). The climate scenarios with doubled atmospheric CO_2 concentration attempt to give a picture on the expected changes at different levels (from global to local)

and for periods differing by plant species. The literature interprets doubling of ambient CO_2 concentration as two different values and, therefore, two different time of occurrence. According to the standard interpretation, the doubled ambient CO_2 concentration is 560 ppm, namely the double of the 280 ppm of the period before the industrial revolution. Its realization is expected between 2050 and 2060 as a function of the international CO_2 emission reduction agreements, the innovations in technology and energetics, as well as the world economy's growth. Another interpretation considers 760 ppm, the twofold of the current atmospheric CO_2 level (~380 ppm) as target function; the different scenarios take its expected occurrence time to about 2100 or later (*IPCC*, 2007); as well as in the case of very successful stabilization measures, this level would not be reached in the foreseeable future (see stabilization scenarios of 560 and 680 ppm of the IPCC Report).

The scenarios approximate to the expected temperature with different limit values due to the uncertainty thereof. Global warming is expected to be between 1.1 and 6.4 °C to 2070–2100 in the latest IPCC Report (*IPCC*, 2007). According to *Mika* (2006), a multiplicator of 1.4 should be applied for the Hungarian counterpart; it refers to the higher sensitivity of the Carpathian Basin to the weather changes. In the case of precipitation forecasts the results of the individual GCM runs are very different, on occasion even the signs of the changes differ. Because of the uncertainty exceeding the temperatures in the precipitation forecasts, we laid stress on analyzing the changes in air temperature but not ignoring the changes in precipitation. We applied the scenarios containing the most probable precipitation forecasts for Hungary.

It is not incidental that air temperature is one of the most frequently examined elements of microclimate in researches on plants' environment. Its paramount importance is provided by the fact that ambient air temperature determines the intensity of all physiological processes through influencing biochemical reactions (*Tanner,* 1963; *Graeser et al.,* 1987; *Jacobs et al.,* 1992), based on the temperature optimum curve. Former canopy microclimate observations showed that the air temperatures within plant canopies are different from the temperatures measured on the meteorological station under standard conditions (*Long et al.,* 1964; *Geiger,* 1965; *Jones,* 1983). Observations on maize canopy temperature were synthesized in 1983 by *Warrington* and *Kanemasu* (1983).

With spreading the problem of global warming, it is probable that forecasting the canopy air temperature and the changes thereof will come to the fore again at researches on plants' physiological processes. The aim of our examination was to present the expected changes based on various scenarios in canopy air temperature from the elements of maize microclimate forecast to the area of Keszthely. Topicality of our research was grounded by the appearance of the latest climate scenarios published in IPCC Report (*IPCC*, 2007), and its scenarios downscaled to Hungary's larger regions (*Bartholy et al.,* 2007). The purpose of our analysis was to describe the modifications of these "larger" changes occurring at microclimatic level.

2. *Material and method*

The input data and parameters of the model are derived from the Agrometeorological Research Station at Keszthely (46°44'N; 17°14'E; 114.2 m a. s. l). The input meteorological elements were observed by the local automatic climate station equipped with an Eppley pyranometer, too. Similarly to the meteorological inputs, we used the principle of analogy in the case of the input plant data of the given scenario. As input plant data we looked for data measured in July that was analogous with the weather to be simulated, where the data on maize and soil moisture were the same or almost the same as the values of the year to be simulated. For this we had an about 30-year data series for medium early maturity maize.

The model inputs are site- and plant-specific values (plant height, leaf density in different layers), soil characteristics, and hourly meteorological data (air temperature, global radiation, relative humidity, soil temperatures). The latter data were transformed from the standard measurement levels to the reference levels required by the model. The leaf area and its density were measured in the field on 10 sample plants weekly, using an LI-3000A type leaf area meter.

The soil moisture content in the upper 1 m was also measured in the field with thermo-gravimetric method at 10 cm intervals every 10 days. The actual soil water content was expressed in terms of soil water potential. The physical properties of the Ramann type brown forest soil (heat capacity, heat conductivity, etc.) were determined at the beginning of the investigations. More details on plant and other data samples can be seen in the publication of *Anda* (2006).

The base of the model assumption is the calculation of energy balance in maize canopy after the radiation reflection and transmission processes (*Goudriaan*, 1977; *Goudriaan* and *van Laar*, 1994):

$$0 = R_n - M - Q_H - \lambda E, \tag{1}$$

where R_n is the canopy net radiation (W m^{-2}), M is the metabolic storage (W m^{-2}), Q_H is the sensible heat flux (W m^{-2}), λE is the latent heat flux (W m^{-2}), and λ is the evaporation heat (kJ kg^{-1}).

The sensible heat flux (Q_{Hi}) in the ith layer is:

$$Q_{Hi} = \rho c_p \frac{T_{ci} - T_{ai}}{r_{aHi}}, \tag{2}$$

where T_{ai} is the air temperature in the ith layer (K), T_{ci} is the canopy temperature in the ith layer (K), r_{aHi} is the aerodynamic resistance for sensible heat transfer in the i layer (s m^{-1}), ρ is the air density (kg m^{-3}), and c_p is the specific heat of air (J kg^{-1} K^{-1}).

The latent heat flux (λE_i) in the ith layer can be calculated as follows:

$$\lambda E_i = \rho c_p \{e_s(T_{ci}) - e_i\} / [\gamma(r_{awi} + r_{ci})], \tag{3}$$

where $e_s(T_{ci}) - e_i$ is the difference between the saturation vapor concentration at the plant temperature and the actual vapor concentration ($m^3\ m^{-3}$), r_{awi} is the aerodynamic resistance for water vapor transfer in the ith layer ($s\ m^{-1}$), r_{ci} is the crop resistance in the ith layer ($s\ m^{-1}$), and γ is the psychrometric constant ($0.5\ g\ m^{-3}\ K^{-1}$).

After calculating the sensible and latent heat, the air temperature (T_{ai}) in the ith layer was estimated as:

$$T_{a,i} = T_{a,i-1} + Q_{Hi} R_i / \rho c_p, \tag{4}$$

where R_i is the value characteristic of resistance in the ith layer ($s\ m^{-1}$) when $i=1$ and ($T_{a,i-1}$) is the air temperature for the reference level.

For evaluating the results of the model runs we used paired t-test that was performed by the free version of *STATA 5.0* (1996) program package. The process reduces the two-sample t-test to one-sample test, since there is no possibility of repetition (so of calculation of standard deviation) at the model runs. The test compares the mean value of the sample to an expected mean value. According to the null hypothesis, if the mean value of differences is 0 then the two samples are statistically the same. If the mean value of differences is not 0 then the two samples are significantly different. The significance level was fixed at 5% in the course of the process.

Before applying the Goudriaan model in the present work, the validation of air temperature was carried out locally by *Anda et al.* (2001). The observed air temperature used in the validation of the model was collected in a maize field. To validate the model, the root mean square deviation (*RMSD*) of a number of pairs (n) of simulated (S) and observed (O) elements was applied:

$$RMSD = \left\{ \left[\Sigma (O - S)^2 \right] / n \right\}^{0.5}. \tag{5}$$

The RMSD is one of the best overall measures of model performance (*Willmott*, 1982). More details can be seen in the publication of *Anda* (2006).

2.1. The applied scenarios

The meteorological basis (the control or *first scenario*) of the further scenarios was provided by the mean values of years 1961–1990 measured at Keszthely (*Table 1*), similarly to the reference period of the *IPCC* (2007) scenarios. At the

control run we used the CO_2 concentration measurements performed at Keszthely Agrometeorological Station in the 1980s, as well as the background atmospheric concentration values (1961–1990) from K-puszta and Hegyhátsál (*Dunkel*, 1985; *Haszpra*, 2007) in order to determine the input CO_2 concentration. Finally, we determined the CO_2 concentration of the basic run as 340 ppm. For comparison, *Haszpra* (2007) fixed the Hungarian value for 1981 as 343 ppm.

Table 1. Markings and abbreviations of scenarios used in our investigation. (All meteorological changes refer to the local conditions in July at Keszthely, Hungary.)

Applied scenario	Scenario number	Scenario marking in the figures	Scenario marking in the table of statistical results
Average July data, 1961–1990	1	1961–1990	A
Average data, 1997–2006	2	1997–2006	B
Doubled CO_2 concentration (1961–1990)	3	1961–1990 $2 \times CO_2$	C
Hungarian downscaled values of the B2 SRES scenario*. Precipitation depression: 15% (*Bartholy et al.*, 1997)	4	1961–1990 +3.8 °C	D
Hungarian downscaled values of the A2 SRES scenario*. Precipitation depression: 25% (*Bartholy et al.*, 1997)	5	1961–1990 +4.8 °C	E
6 °C air temperature rise, 25% decrease in precipitation*	6	1961–1990 +6.0 °C	F
9 °C air temperature rise, 10% decrease in precipitation*	7	1961–1990 +9 °C/1	G
9 °C air temperature rise, 30% decrease in precipitation*	8	1961–1990 +9 °C/2	H

*Scenario with doubled CO_2 concentration

The *second scenario* is to represent the changes in the recent past on the basis of the data of the decade between 1997 and 2006. According to the last climate normal, at Keszthely in summer the air temperature is significantly higher by 0.6 °C than the monthly average of all July months in the 1901–2000 data series (*Kocsis* and *Anda*, 2006a). Though it cannot be statistically justified, the accumulated amount of precipitation of July has decreased by about 10–15% at Keszthely (*Kocsis* and *Anda*, 2005, 2006b). We estimated the background CO_2 concentration to be 380 ppm.

The *third scenario* is to represent the impacts of the rising ambient CO_2 concentration in quantitative terms. Therefore, we doubled only the CO_2 gas concentration out of the input data of basic run (760 ppm), and the meteorological inputs remained the same. With this we localized the date of the expected change to 2070–2100.

In the further scenarios – besides doubling the current CO_2 level (760 ppm) –, we gradually increased the air temperature values compared to the basic run (1961–1990), and together with this we also modified the precipitation amount. The *fourth scenario*, based on the B2 scenario (*Nakićenović* and *Swart*, 2000), also applied by the recent IPCC Report (*IPCC*, 2007) contained the summer values pertaining to the Keszthely meteorological elements elaborated and mapped for Hungary by *Bartholy et al.* (2007), and made a forecast to the period of 2070–2100. In this scenario the summer average air temperature at Keszthely will be risen by 3.8 °C, together with an about 15% decrease in precipitation. The *fifth scenario* used the summer data according to the A2 SRES scenario (*Nakićenović* and *Swart*, 2000), downscaled to Hungary by the above-mentioned method, which calculated stronger warming than the former one (+4.8 °C). There is a 25% decrease in the precipitation amount associated to this temperature rise. We note here, that standard deviation is rather high in both scenarios (±15%); this implies strong uncertainty.

In the *sixth scenario* we increased the average air temperature by 6.0 °C, together with 25% decrease in precipitation. This 6 °C rise is close to the upper limit (6.4 °C) of changes related to the annual global mean temperature in the IPCC Fourth Assessment Report (*IPCC*, 2007). However, summer temperature changes can be stronger in Hungary than the global mean warming (*Mika*, 2006). Keeping this in view, in the last two scenarios we presumed a further increase in the warming-up, by involving the product of the 1.4 times higher temperature rise (6.4 °C) pertaining to Hungary (9 °C). Since we knew the uncertainty of precipitation forecasts, we associated two types of precipitation supply to these +9 °C projections: the *seventh scenario* assumed almost no change in precipitation (–10%), while the *eighth scenario* calculated more significant drying (30% precipitation decrease). The comparison of these latter two scenarios later provided opportunity to quantify the impacts of the different precipitation supplies on the plants. Markings of the individual scenarios are summarized in *Table 1*.

3. Results and discussion

The observations on air temperature in maize canopy are of importance since C_4 plants are less sensitive to the changes in the environmental elements than C_3 plants, their radiation and temperature reactions given to global warming showed as being significant (*Mera et al.*, 2006).

In all the scenarios the increased surrounding temperature has increased the canopy air temperature at the cob level, where plant physiological processes are most intensive. The degrees of the warming-up within canopy at cob level were not significantly different by the sun angle (*Fig. 1*), though at the warmer scenarios (from the *fourth scenario*) the peak of maximum temperatures tendentiously occur one hour later, at 3 p.m. instead of 2 p.m.

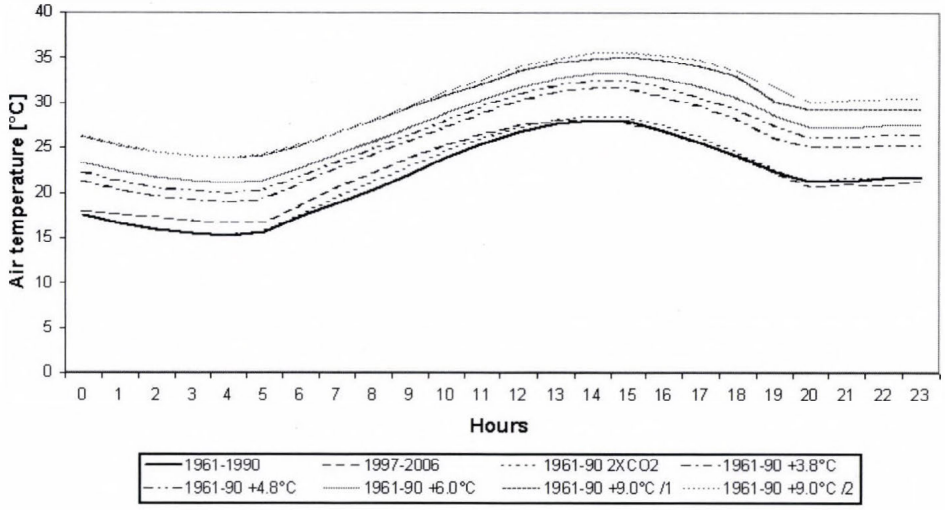


Fig. 1. Air temperature course within maize canopy at cob level, on an average day in July, Keszthely. The height of the simulation is 1 m above the soil surface.

Keszthely was affected by the global warming in the past decade as regards the canopy inside air temperature. During the comparison the temperature rise at the cob level followed the rise of the ambient air temperature compared to the 1961–1990 climate normal serving as basis in many researches; the increase was 0.6 °C compared to the average of the 1961–1990 years on an average day in July. The change is significant at high level (*Table 2*).

Doubling the atmospheric CO_2 concentration [the single input parameter out of the inputs of the basic run (1961–1990)] has significantly increased (by 0.3 °C) the canopy air temperature at the cob level; this indicated the stimulating effect on the pores by the higher CO_2 concentration on the movements of stomata. Stimulation of the closure of stomata controls the transpiration (and also the CO_2 gain), and this energy may emerge as surplus at other energy consuming processes, for example one of the components of sensible heat. According to *Fulco* and *Asseng* (2006), a 50% rise in CO_2 level would compensate the impacts of a 2 °C warming-up and 15% decrease in precipitation amount as the result of the effects on stomata. The authors also noted that the impact is not linear, so, for example, it is not suitable to compensate the impacts of a 4 °C warming-up deriving from a 100% rise in CO_2 level.

The comparison among the first and third scenarios and the results of runs of IPCC origin shows, that the connection of warming-up and doubling the CO_2 concentration together interacted in a way inducing a "milder" change in canopy air temperature. This corresponds with the former experience of *Prasad et al.* (2006).

Table 2. Basic data of statistical analyses relating to the differences of the daily average air temperatures at the cob level. Bold letters highlight *p* values of the t-test, which represent significant difference at level of at least 5%. At the compared scenarios bold and italic letters are used for the basic run

Scenario pairs	Average temperature [°C]	Calculated *p* value of t-test	Standard error
A = basic	21.7		
B	22.2	**0.0025**	0.169
C	21.9	**0.0001**	0.062
D	25.3	**0.0000**	0.038
E	26.3	**0.0000**	0.060
F	27.3	**0.0000**	0.096
G	29.5	**0.0000**	0.147
H	29.9	**0.0000**	0.149
G = basic	29.5		
H	29.9	**0.0000**	0.086
D = basic	25.3		
E	26.3	**0.0000**	0.040
F = basic	27.3		
G	29.5	**0.0000**	0.092
H	29.9	**0.0000**	0.057

At scenarios simulating the change downscaled to Hungary (A2 and B2 scenarios), the degree of warming-up within the canopy fell from the growth level of surrounding air temperature used regarding the warming-up; the conclusion is that the presence of the canopy slightly compensates the warming-up. The compensation degrees were the same at both scenarios (0.2 °C). The degrees of change of the canopy air temperature given to the outer environmental force were of similar tendencies at both scenarios of IPCC origin, but regarding the magnitude, they followed the temperature changes simulated in the warming-up being significantly different from each other. This means that the absolute values of warming-up were different in the two scenarios, only the degrees of change compared to the control values were the same. Warming-up of the canopy of A2 scenario significantly exceeded the value of B2 scenario.

In the case of the last two increased global warming scenarios, the compensating effect of maize canopy on the air temperature at cob level endured, however, it strongly depended on the soil moisture level. Assuming less decrease in precipitation (–10%), the presence of the canopy could mitigate the 9 °C ambient warming-up by 1.2 °C. This is likely owing to the stronger shadowing effect of larger green surface, which could be developed as a result of the better water supply. If we connect the warming-up of the above-mentioned degree with a more significant decrease in precipitation, and we analyze it assuming the presence of a lesser shadowing green surface together

with this (plant-analogy), the compensating effect is immediately halved, to about 0.7 °C.

Warming-up within the canopy results in a statistically justifiable change in all scenarios (see *Table 2*).

The temperature simulation of the model (air temperature above soil, soil temperature) extends from 50 cm below surface to the height of 3 m above soil surface (*Fig. 2*).

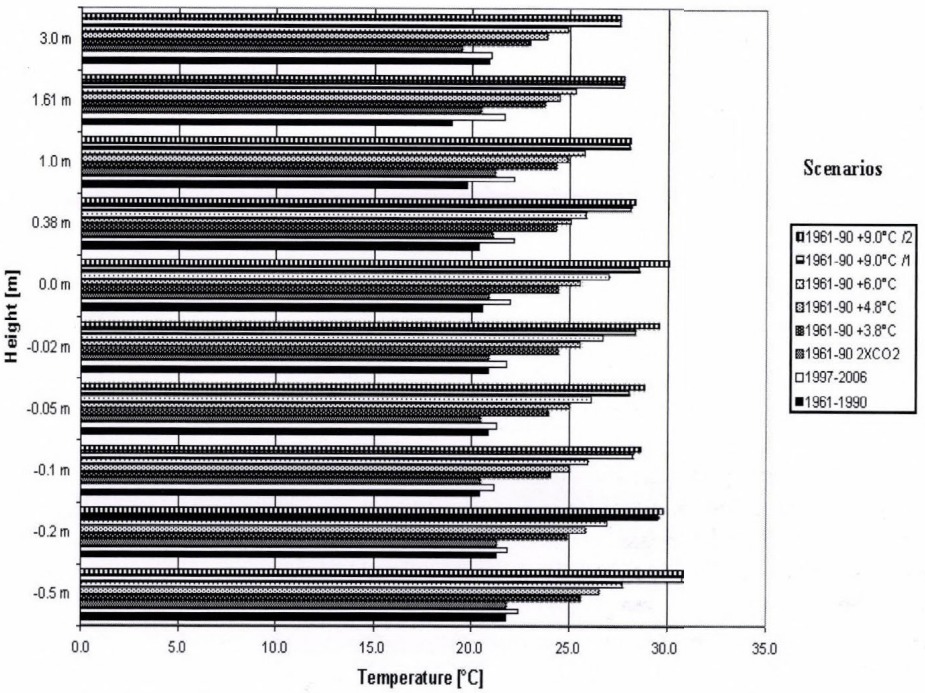


Fig. 2. Estimated air and soil temperature values in case of different climatic scenarios and different levels, at low solar angles (at 9 a.m.).

The levels representing soil temperatures with negative sign (2, 5, 10, 20, and 50 cm) correspond with the locations of soil temperature measurements applied at standard meteorological observations. At 9 a.m. the slightly higher soil temperatures of the deeper layers can be seen at each scenario. The temperature of the air layer above the canopy between 1.8–2.0 m (3 m) determined to low solar position – in accordance with former observations – is cooler above each treatment than the value calculated to the canopy level of 1.6 m.

Except for the scenario assuming the doubled CO_2 level with unchanged air temperature, the temperature of the air is a bit warmer in the layer closest to the soil, and further to the upper layers in the canopy it is slightly decreasing.

Exclusively at the doubled CO_2 level in the morning, the air temperature at cob level and above canopy has increased by a couple of tenths °C compared to the layer close to the soil, and has only decreased above 3 m of the canopy. It refers to the fact that at doubling the CO_2 concentration the energy balance has been modified, and a larger part of the energy balance has remained in the canopy and a smaller part has been transferred to the air above the plant stand. Scenarios with increased air temperature and doubled atmospheric CO_2 concentration transferred more energy to the ambient air above the canopy.

We also illustrate the changes of air and soil temperatures through another vertical profile with different grouping, where the individual scenarios form a category on the vertical axis of the figure (*Fig. 3*). In this case we can follow the expected temperatures of the scenarios one by one, from the depth of 50 cm in the soil up to 3 m in the air. The highest point above soil surface exceeds the top point of the canopy by 1–1.2 m. Ordering of the scenarios occurred by the increasing degree of warming-up, it is well reflected by the length of the columns of the graph. As we go up with the scenarios simulating larger and larger warming-up, warmer and warmer plant canopy develops in terms of soil and air in the morning.

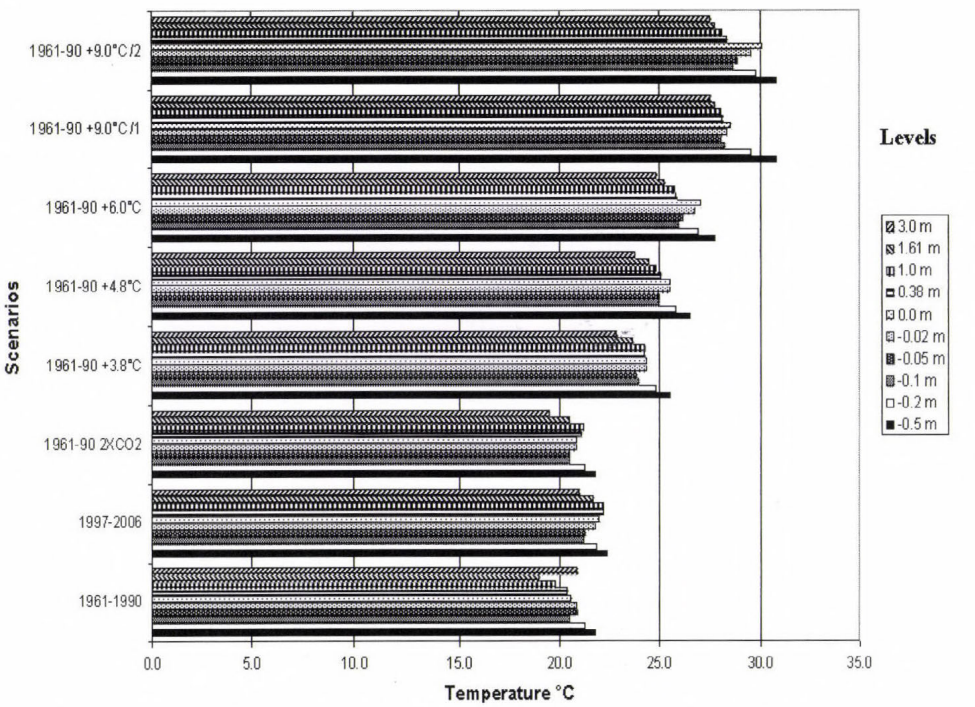


Fig. 3. Estimated air temperature and soil temperature values in case of different climatic scenarios and different levels, at low solar angles (at 9 a.m.).

At high insulation the temperature differences between the different levels are increasing both in the soil and air (*Fig. 4*). As a result of the intensive radiation, the temperature of the soil layers close to the surface are rising quicker than that of the deeper layers. The warmest level is the soil surface. At the warming-up simulation of above 4.8 °C, the soil temperature of the layer of 2 cm reaches or exceeds 30 °C at least. It should be noted that the presented soil temperature is within the canopy, so it is exposed to the shadowing effect of the plants, therefore, it can not be considered as extremely high.

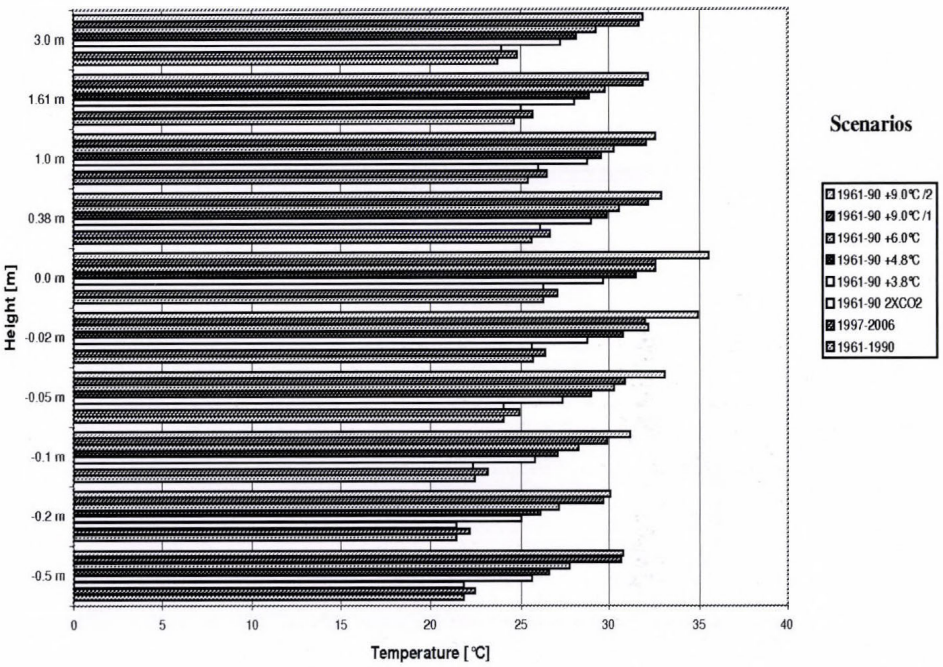


Fig. 4. Expected air and soil temperatures at high solar incoming radiation (at 12 a.m.) at Keszthely. The levels of soil temperature are marked with negative sign. 0.0 m means soil surface.

Similarly to the differences of soil and air temperatures presented at low solar angle by scenarios, the warmer or cooler statuses of canopies of scenarios representing different warming-up levels can also be well seen in the presentation containing high incoming solar radiation (*Fig. 5*). The cooler status of the scenarios with only doubled CO_2 concentration compared to the other scenarios has also remained at the high incoming radiation level.

In the simulations, at noon the frequency of events reaching and exceeding 30 °C has increased. At the run representing the warming-up forecast of 9 °C, the temperature of the entire canopy – both below and above soil surface – exceeds 30 °C, which is far higher than the desired optimal temperature for maize, 23 °C.

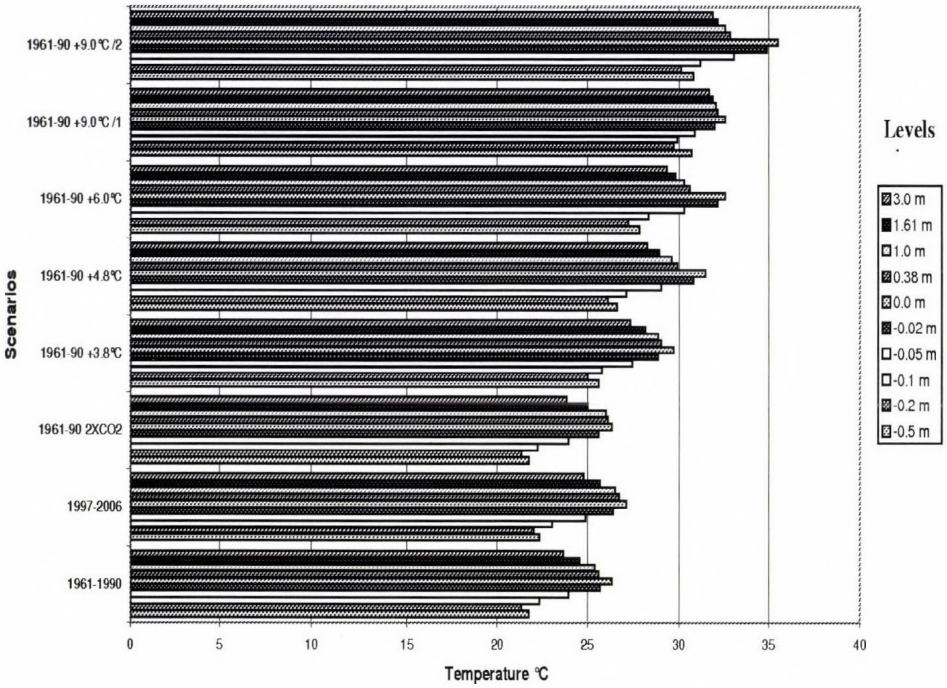


Fig. 5. Estimated air and soil temperature values in case of different climatic scenarios and different levels, at high solar radiation (12 a.m.).

3.1. Development of carbon assimilation

In the Julies of the past decade, both the unit green surface area and the CO_2 assimilation capacity per unit soil surface rose by about 7% in maize (*Table 3*). An increased atmospheric CO_2 concentration itself would enhance the CO_2 assimilation of canopy by about 40%.

In B2 run the entire canopy carbon assimilation above leaf and soil showed an increase compared to the control scenario at both levels, at leaf level the rise was higher, by 24.7%, while the unit value at the soil (canopy level) was lower, by 13.8%. In the case of A2 scenario, the assimilation change was positive only at the leaves, and this value was lower about 10% (14.4%) than the determined value of B2 scenario. The development trend of the average July carbon assimilation per unit soil surface at canopy level was of different direction and degree than it occurred in the case of leaves; the depression of 9.4% compared to the July averages of 1961–1990 emerging at A2 scenario provides a good characterization thereof. In our scenarios simulating a warming-up over 6 °C, the carbon assimilation of both the leaves and the entire canopy has decreased compared to the control run. The depression occurring in the assimilation of leaves has especially emerged at the scenario representing a warming-up of 9 °C,

associated with stronger water deficit. The very strong decrease emerging in carbon assimilation determined to the canopies (soil surface) and exceeding leaves is considerable, which is almost 50% at a scenario simulating a monthly average warming-up of 6 °C; it is 62.5% at runs containing a warming-up of 9 °C, with a decrease in precipitation of 10%; and it is 95.3% in the case of applying a water deficit of 30%.

Table 3. Daily average of carbon assimilation in kg related to unit leaf [m^2] and soil surface area [m^2] during July, at Keszthely. *The values in % represent the differences in photosynthesis of scenarios compared to control run

Scenario/ (kg CO_2 m^{-2})	**1961–1990**	**1997–2006**	**Basic 2×CO_2**	**B2**	**A2**	**+6 °C**	**+9 °C/1**	**+9 °C/2**
CO_2 assimilation per unit leaf area in kg	1.35	1.45	2.02	1.73	1.56	1.32	1.32	1.03
*Change in % to control run	0.0	7.14	39.76	24.68	14.43	–2.25	–2.25	–26.89
CO_2 assimilation per unit soil surface in kg	3.78	4.05	5.66	4.34	3.44	2.38	1.98	1.34
*Change in % to control run	0.0	6.90	39.83	13.79	–9.42	–45.45	–62.50	–95.31

4. Conclusions

The canopy air temperature in each scenario has significantly warmed at high probability level compared to the basic run. In the past decade its degree was 0.6 °C compared to the 1961–1990 period. Warming-up of the canopy changed proportionally to the increase in ambient air temperature. According to the investigations of *Lobell* and *Field* (2007), warming-up of plant stands would expectedly have an adverse impact on plant species belonging to various plant physiological groups, so on C_4 maize.

Comparison of the different runs shows that the change of either the air temperature or the atmospheric CO_2 concentration itself will not result in appropriate outcome, since these factors may strengthen or suppress each other's effects. In accordance with this, the different precipitation supplies of the last two scenarios (7th and 8th) caused significant difference in the canopy air temperatures. We should be cautious because of the significantly different reactions regarding canopy air temperature at both runs containing air temperature increase of 9 °C compared to warming-up of 6 °C.

Our own investigations confirmed the former statement of *Prasad et al.* (2006), that the impact of the increased atmospheric CO_2 gas concentration, which enhances the intensity of photosynthesis cannot be always realized due to

the accompanying warmer plant and air temperature, so it is not expedient to calculate with the emergence of monthly average summer warming-up of above 6 °C at Keszthely; this positive effect is associated to one of the causes of global warming, the higher CO_2 concentration.

These scenarios – opposite to the data on global warming – could even provide insight into the issue of weather and CO_2 concentration changes and plant reactions for the local farmers. Local level information could provide apparent help for the local farmers in the preparation for defending against the adverse effects of the expected changes.

References

Anda, A., 2006: Modeling maize response to climate modification in Hungary. *Commun. Biometry Crop Sci. 1* (2), 90-98.

Anda, A. and *Kocsis, T.*, 2007: Evaluation of the influence of climatic changes on maize energy consumption in Hungary. GSB. *The Eur. J. Plant Sci. and Biotech. 1, 200-205.*

Anda, A., Lőke, Zs., and *Burucs, Z.*, 2001: Microclimate of irrigated and non irrigated maize (in Hungarian). *Növénytermelés 50*, 249-260.

Bartholy, J., Pongrácz, R., and *Gelybó, Gy.*, 2007: Regional climate change in Hungary for 2071-2100. *Applied Ecol. and Environ. Res. 5,* 1-17.

Dunkel, Z., 1985: Vertical profiles of CO_2 in maize canopy (in Hungarian). *Beszámolók az 1982-ben végzett tud. kutatásokról*. Országos Meteorológiai Szolgálat, Budapest, 82-97.

Fulco, L. and *Asseng, S.*, 2006: Climate change impacts on wheat production in a Mediterranean environment in Western Australia. *Agr. Syst. 90,* 159-179.

Geiger, R., 1965: *The Climate Near the Ground*. Harvard Univ. Press, Harvard, Mass.

Graeser, E.A., Verma, S.B., and *Rosenberg, N.J.*, 1987: Within canopy temperature patterns of sorghum at two row spacings. *Agr. Forest Meteorol. 41,* 187-205.

Goudriaan, J., 1977: *Crop Micrometeorology: A Simulation Study*. Simulation Monographs. Pudoc, Wageningen.

Goudriaan, J., and *van Laar, H.H.*, 1994: *Modelling Potential Crop Growth Processes*. Kluwer Academic Publishers, Dordrecht-Boston-London, 238 pp.

Haszpra, L., 2007: 25 years history of CO_2 measurements in Hungary (in Hungarian). *Légkör 52*, No.1, 4-7.

IPCC, 2007: Climate Change 2007: The Physical Science Basis. Contribution of Working Group I to the Fourth Assessment Report of the Intergovernmental Panel on Climate Change [*Solomon, S., D. Qin, M. Manning, Z. Chen, M. Marquis, K.B. Averyt, M. Tignor* and *H.L. Miller* (eds.)]. Cambridge University Press, Cambridge, United Kingdom and New York, NY, USA, 996 pp. Available: http://www.ipcc.ch/pdf/assessment-report/ar4/wg1/ar4-wg1-frontmatter.pdf

Jacobs, A.F.G., van Boxel, J.H., and *Shaw, R.H.*, 1992: Horizontal and vertical distribution of air temperature in a vegetation canopy. *Neth. J. Agr. Sci. 40*, 359-372.

Jones, H.G., 1983: *Plants and Microclimate*. Cambridge University Press. Cambridge-London-New York-New Rochelle-Melbourne-Sydney, 323 pp.

Kocsis, T. and *Anda, A.*, 2005: Tendency in yearly precipitation sums at Keszthely as a result of 130 year observation (in Hungarian). *Légkör 50,* 2, 16-20.

Kocsis, T. and *Anda, A.*, 2006a: The air temperature at Keszthely in 20th century (in Hungarian). *Légkör 51,* 1, 21-24.

Kocsis, T. and *Anda, A.*, 2006b: The precipitation at Keszthely by investigating long time series (in Hungarian). *J. Central Eur. Agric. 7,* 699-708.

Lobell, D.B. and *Field, C.B.*, 2007: Global scale climate–crop yield relationships and the impacts of recent warming. *Environ. Res. Letters 2,* 14-21.

Long, I.F., Monteith, J.L., Penman, H.L., Szeicz, G., 1964: The plant and its environment. *Meteorol. Rundsch. 17*, 97-101.

Mera, R.J., Niyogi, D., Buol, G.S., Wilkerson, G.G., and *Semazzi, F.H.M.*, 2006: Potential individual versus simultaneous climate change effects on soybean (C3) and maize (C4) crops: An agrotechnology model based study. *Global Planet. Change 54*, 163-182.

Mihailovic, D.T. and *Eitzinger, J.,* 2007: Modelling temperatures of crop environment *Ecol. Model. 202,* 465-475.

Mika, J., 2006: Preparation of climatic scenarios by using statistical methods (in Hungarian). *Theses of DSc Degree,* Hungarian Academie of Sciences, Budapest, 143 pp.

Nakićenović, N. and *Swart, R.* (eds.), 2000: *Special Report on Emissions Scenarios. A Special Report of Working Group III of the Intergovernmental Panel on Climate Change.* Cambridge University Press, Cambridge, United Kingdom and New York, NY, USA, 599 pp.

Prasad, P.V.V., Boote, K.J., Allen, L.H. Jr., 2006: Adverse high temperature effects on pollen viability, seed-set, seed yield and harvest index of grain-sorghum are more severe at elevated carbon dioxide due to higher tissue temperatures. *Agr. Forest Meteorol. 139*, 237-251.

STATA 5.0, 1996: Stata Corporation LP Texas, USA. Available online: www.stata.com

Tanner, C.B., 1963: Plant temperatures. *Agron. J. 55*, 210-214.

Warrington, I.J. and *Kanemasu, E.T.*, 1983: Corn growth response to temperature and photoperiod. *Agron. J. 75*, 749-75.

Willmott, C.J., 1982: Some comments on the evaluation of model performance. *B. Am. Meteorol. Soc.*, 1309-1313.

GUIDE FOR AUTHORS OF *IDŐJÁRÁS*

The purpose of the journal is to publish papers in any field of meteorology and atmosphere related scientific areas. These may be

- research papers on new results of scientific investigations,
- critical review articles summarizing the current state of art of a certain topic,
- short contributions dealing with a particular question.

Some issues contain "News" and "Book review", therefore, such contributions are also welcome. The papers must be in American English and should be checked by a native speaker if necessary.

Authors are requested to send their manuscripts to

Editor-in Chief of IDŐJÁRÁS

P.O. Box 39, H-1675 Budapest, Hungary

in three identical printed copies including all illustrations. Papers will then be reviewed normally by two independent referees, who remain unidentified for the author(s). The Editor-in-Chief will inform the author(s) whether or not the paper is acceptable for publication, and what modifications, if any, are necessary.

Please, follow the order given below when typing manuscripts.

Title part: should consist of the title, the name(s) of the author(s), their affiliation(s) including full postal and e-mail address(es). In case of more than one author, the corresponding author must be identified.

Abstract: should contain the purpose, the applied data and methods as well as the basic conclusion(s) of the paper.

Key-words: must be included (from 5 to 10) to help to classify the topic.

Text: has to be typed in single spacing with wide margins on one side of an A4 size white paper. Use of S.I. units are expected, and the use of negative exponent is preferred to fractional sign. Mathematical formulae are expected to be as simple as possible and numbered in parentheses at the right margin.

All publications cited in the text should be presented in a *list of references*, arranged in alphabetical order. For an article: name(s) of author(s) in Italics, year, title of article, name of journal, volume, number (the latter two in Italics) and pages. E.g., *Nathan, K.K.*, 1986: A note on the relationship between photo-synthetically active radiation and cloud amount. *Időjárás 90,* 10-13. For a book: name(s) of author(s), year, title of the book (all in Italics except the year), publisher and place of publication. E.g., *Junge, C.E.*, 1963: *Air Chemistry and Radioactivity*. Academic Press, New York and London. Reference in the text should contain the name(s) of the author(s) in Italics and year of publication. E.g., in the case of one author: *Miller* (1989); in the case of two authors: *Gamov* and *Cleveland* (1973); and if there are more than two authors: *Smith et al.* (1990). If the name of the author cannot be fitted into the text: *(Miller,* 1989); etc. When referring papers published in the same year by the same author, letters a, b, c, etc. should follow the year of publication.

Tables should be marked by Arabic numbers and printed in separate sheets with their numbers and legends given below them. Avoid too lengthy or complicated tables, or tables duplicating results given in other form in the manuscript (e.g., graphs)

Figures should also be marked with Arabic numbers and printed in black and white in camera-ready form in separate sheets with their numbers and captions given below them. TIF, GIF or BMP formats should be used for electronic artwork submission.

The text should be submitted both in manuscript and in electronic form, the latter in e-mail or CD. MS Word format is preferred.

Reprints: authors receive 30 reprints free of charge. Additional reprints may be ordered at the authors' expense when sending back the proofs to the Editorial Office.

More information for authors is available: antal.e@met.hu

Published by the Hungarian Meteorological Service

Budapest, Hungary

INDEX: 26 361

HU ISSN 0324-6329

IDŐJÁRÁS

QUARTERLY JOURNAL
OF THE HUNGARIAN METEOROLOGICAL SERVICE

Special Issue: Workshop on Regional Climate Modeling

Guest Editors: **Tomas Halenka and Daniela Jacob**
Local Organizer: **András Horányi**

CONTENTS

Preface I
Editorial III

Daniela Jacob, Lola Kotova, Philip Lorenz, Christopher Moseley and *Susanne Pfeifer:* Regional climate modeling activities in relation to the CLAVIER project 141

Gabriella Csima and *András Horányi:* Validation of the ALADIN-Climate regional climate model at the Hungarian Meteorological Service 155

Michel Déqué and *Samuel Somot:* Analysis of heavy precipitation for France using high resolution ALADIN RCM simulations 179

Petr Skalák, Petr Štipánek and *Aleš Farda:* Validation of ALADIN-Climate/CZ for present climate (1961-1990) over the Czech Republic 191

Gabriella Szépszó and *András Horányi:* Transient simulation of the REMO regional climate model and its evaluation over Hungary 203

Csaba Torma, Judit Bartholy, Rita Pongrácz, Zoltán Barcza, Erika Coppola and *Filippo Giorgi:* Adaptation of the RegCM3 climate model for the Carpathian Basin .. 233

Judit Bartholy, Rita Pongrácz, Györgyi Gelybó and *Péter Szabó:* Analysis of expected climate change in the Carpathian Basin using the PRUDENCE results 249

Gabriella Szépszó: Regional change of climate extremes over Hungary based on different regional climate models of the PRUDENCE project 265

Bernd C. Krüger, E. Katragkou, I. Tegoulias, P. Zanis, D. Melas, E. Coppola, S. Rauscher, P. Huszar and *T. Halenka:* Regional photochemical model calculations for Europe concerning ozone levels in a changing climate 285

Book review 301

****

http://www.met.hu/Journal-Idojaras.php

VOL. 112 * NO. 3 – 4 * JULY – DECEMBER 2008

IDŐJÁRÁS

Quarterly Journal of the Hungarian Meteorological Service

Editor-in-Chief
LÁSZLÓ BOZÓ

Executive Editor
MARGIT ANTAL

EDITORIAL BOARD

AMBRÓZY, P. (Budapest, Hungary)
ANTAL, E. (Budapest, Hungary)
BARTHOLY, J. (Budapest, Hungary)
BATCHVAROVA, E. (Sofia, Bulgaria)
BRIMBLECOMBE, P. (Norwich, U.K.)
CZELNAI, R. (Dörgicse, Hungary)
DÉVÉNYI, D. (Boulder, CO, U.S.A.)
DUNKEL, Z. (Budapest, Hungary)
FISHER, B. (Reading, U.K.)
GELEYN, J.-Fr. (Toulouse, France)
GERESDI, I. (Pécs, Hungary)
GÖTZ, G. (Budapest, Hungary)
HANTEL, M. (Vienna, Austria)
HASZPRA, L. (Budapest, Hungary)
HORÁNYI, A. (Budapest, Hungary)
HORVÁTH, Á. (Siófok, Hungary)
HORVÁTH, L. (Budapest, Hungary)
HUNKÁR, M. (Keszthely, Hungary)
MAJOR, G. (Budapest, Hungary)
MÉSZÁROS, E. (Veszprém, Hungary)
MIKA, J. (Budapest, Hungary)
MERSICH, I. (Budapest, Hungary)
MÖLLER, D. (Berlin, Germany)
NEUWIRTH, F. (Vienna, Austria)
PAP, J.M. (Greenbelt, MD, U.S.A.)
PINTO, J. (R. Triangle Park, NC, U.S.A)
PRÁGER, T. (Budapest, Hungary)
PROBÁLD, F. (Budapest, Hungary)
RADNÓTI, G. (Budapest, Hungary)
S. BURÁNSZKI, M. (Budapest, Hungary)
SZALAI, S. (Budapest, Hungary)
SZEIDL, L. (Budapest, Hungary)
TAR, K. (Debrecen, Hungary)
TÄNCZER, T. (Budapest, Hungary)
TOTH, Z. (Camp Springs, MD, U.S.A.)
VALI, G. (Laramie, WY, U.S.A.)
VARGA-HASZONITS, Z. (Moson-magyaróvár, Hungary)
WEIDINGER, T. (Budapest, Hungary)

Editorial Office: Gilice tér 39, H-1182 Budapest, Hungary
P.O. Box 39, H-1675 Budapest, Hungary
E-mail: bozo.l@met.hu or *antal.e@met.hu*
Fax: (36-1) 346-4809

Indexed and abstracted in Science Citation Index Expanded™ and Journal Citation Reports/Science Edition
Covered in the abstract and citation database SCOPUS®

Subscription by
mail: IDŐJÁRÁS, P.O. Box 39, H-1675 Budapest, Hungary
E-mail: kenderesy.k@met.hu or *antal.e@met.hu*

IDŐJÁRÁS

Quarterly Journal of the Hungarian Meteorological Service
Vol. 112, No. 3–4, July–December 2008

Preface

Climate models in general and regional climate models (RCM) in particular are essential tools for the exploration of the future change of the global and regional climate. Their role is continuously increasing all over the world and inevitably in Europe. In the recent past several international projects (most of them supported by the European Commission) were initiated with the main objectives to provide quantitative estimates for the expected climate change in Europe. It is now more and more recognized that the impact of the climate change can only be investigated based on the results of climate models. In the last few years more and more activities in this field were also carried out in Central and Eastern Europe (CEE). Another important boost was given to these developments: the successful application and acceptance of the CECILIA (www.cecilia-eu.org) and CLAVIER (www.clavier-eu.org) projects in the 6th Framework Programme of the European Commission. These collaborations are not "only" dealing with the quantification of the regional climate change (together with the related uncertainties) based on regional climate models, but also studying the impact of the foreseen change on agriculture, tourism, air pollution, etc.

The first important event in the field of regional climate modeling in Central and Eastern Europe took place in Prague, at the end of 2004, when Charles University organized a regional climate modeling gathering ("Workshop on Regional Climate Modeling and Mini-Symposium on Climate Change in Europe"). This meeting can be considered as an important milestone for building those teams, which were later assembled under the umbrella of the CECILIA and CLAVIER projects. Later on in the course of the above-mentioned two projects, the CLAVIER project initiated another workshop on regional climate modeling with the primary aim to discuss key scientific issues on regional climate modeling (model development, validation, and application) and, furthermore, to strengthen the cooperation between the CECILIA and CLAVIER projects. This latter event was held at the headquarters of the Hungarian Meteorological Service in Budapest at February 4–6, 2008. It was attended by approximately 50 scientists from 11 countries (mostly from the CECILIA and CLAVIER partners). The presentations of the workshop were put to the homepage of the Hungarian Meteorological Service (http://www.met.hu/seminars/rcm2008.php) after the meeting. Moreover, it was decided that a Special Issue of the Quarterly Journal of the Hungarian Meteorological Service (IDŐJÁRÁS) would be compiled from the peer reviewed scientific papers of the workshop. It is our great pleasure to present this Special Issue of IDŐJÁRÁS not only for those, who are working in the field of regional climate

modeling, but also for those, who are dealing with the impact assessment of climate change over the Central and Eastern European territory. We are convinced that the further research and development activities in the field of regional climate modeling are essential for the reliable estimates of the climate change over Central and Eastern Europe, and we hope that this Special Issue can be a modest contribution to this challenge with its 9 scientific articles (and two introductory project descriptions) in this volume. It is furthermore anticipated that this issue will also help to promote the further cooperation between the CECILIA and CLAVIER_EU projects.

We are extremely grateful to all the authors, who contributed to this edition of IDŐJÁRÁS and also for the dedicated reviewers significantly helping to improve the scientific content of this thematic Special Issue.

László Bozó
Editor-in-Chief

András Horányi
Local Organizer of the RCM workshop

Editorial

Regional climate modeling activities in CECILIA project

Introduction

Although the broad response of global climate to increased greenhouse gas concentrations is well established, many unknowns remain in the regional details of projections of future climate change. The floods and droughts, which occurred in recent summers in the Central and Eastern European (CEE) region, highlight the importance of the hydrologic cycle and water management in Elbe and Danube river catchments in response to the occurrence of precipitation extremes. In summer of 2002, the Czech Republic experienced some of its worst floods in history with the Vltava river inundating Prague causing severe and widespread damage. The 2003 heat wave, one of the severest heat waves on record in Central and Western Europe causing both human losses (Kysely, 2004) and extensive damage to human activities and natural ecosystems, demonstrated the importance of the health impacts of extreme conditions that could also lead to considerable changes in air quality, both regionally and in major urban centers. The possibility of changes in the frequency and intensity of these extreme events is one of the most dreaded manifestations of anthropogenic climate change. A number of studies have linked the occurrence of the extreme events to anthropogenic forcings (Beniston and Stephenson, 2004; Schär et al., 2004; Pal et al., 2004; Meehl et al., 2004; Meehl and Tebaldi, 2004). Impacts on agriculture and forestry affecting the economy of countries in the region are extensively studied as well (Menzel et al., 2006; Menzel et al., 2003; Hafner, 2003; Gobron et al., 2005).

While coupled atmosphere-ocean general circulation models (AOGCMs) provide basic information on the development of the climate change, their horizontal resolution is still too coarse to describe in detail processes affecting extreme events at the regional scale (Gates et al., 1996). In order to regionally enhance the AOGCM information, a number of regionalization techniques have been developed (Giorgi et al., 2001). One of them is the use of limited area regional climate models (RCMs) nested in driving fields from reanalysis or GCMs similarly as previously done in numerical weather prediction for decades (Giorgi and Mearns, 1999). The main advantage of this method is that it can reach with the same or even less computational resources horizontal grid intervals of a few tens of km, and thus, RCMs can provide improved simulation of extreme events (e.g., Huntingford et al., 2003; Frei et al., 2003). During the last decade, RCMs have been increasingly used to examine climate variations at scales that are not resolved by global models. To the extent that they produce realistic climate simulations, such models can be powerful tools in the study of regional climate impacts.

Thus, the aim of the EC FP6 project CECILIA (Central and Eastern Europe Climate Change Impact and Vulnerability Assessment) is to go into these regional details assessing the impact of climate change at the regional to local scale for Central and Eastern Europe using very high resolution simulations in order to capture the effects of the complex terrain of the region. In this region the need for very high resolution studies is particularly important. The region is characterized by the northern flanks of the Alps, the long arc of the Carpathians, and smaller mountain chains and highlands in the Czech Republic, Slovakia, Romania, and Bulgaria that significantly affect the local climate conditions. A resolution sufficient to capture the effects of such topographical and associated land-use features is necessary. Therefore, the central internal

objectives of CECILIA are to improve regional climate scenarios and their localization for climate impacts models, and comparing these results against the results of previous and ongoing projects to assess the added value of dynamical downscaling at very fine scales. The proposed research will benefit greatly from the results of previous and ongoing EC projects, like:

- *"Modeling the Impact of Climate Extremes (MICE)";*
- *"Statistical and Regional Dynamical Downscaling of Extremes for European regions (STARDEX)";*
- *"Prediction of Regional scenarios and Uncertainties for Defining EuropeaN Climate change risks and Effects" (PRUDENCE);*
- *"ENSEMBLE-based Predictions of Climate Changes and their Impacts" (ENSEMBLES).*

The goals will be achieved mainly using very high resolution RCMs run locally for individual targeted areas. As for climate change scenario projections, the production of two time slices are realised covering years 2020–2050 and 2070–2100, with 1961–1990 as a reference period. Weather pattern changes as well as changes of extreme events appearance are addressed within the project as they affect the important sectors of the economies and welfare of individual countries in the CEE region. To address the uncertainties, the results of previous or ongoing projects (PRUDENCE, ENSEMBLES) will be evaluated and used in CECILIA. The selected applications of the outputs are supposed toward water resources and management, agriculture, forestry, air quality and health. The objectives will be achieved through the following specific tasks:

- *To collect, assess, and make available for first local impact studies the scenarios and climate simulations produced in previous relevant projects, especially PRUDENCE, STARTDEX, MICE, and ENSEMBLES, where available (WP1, see Giorgi and Coppola, 2007);*
- *To adapt and develop very high resolution RCMs for the region (10 km grid spacing) and perform regional time-slice nested runs driven by ERA-40 data (Uppala et al., 2004) and by GCMs for selected GHG change scenarios (WP2);*
- *To verify the model results, compare RCM and statistical downscaling results, analyze and develop the methods for verification, particularly at local scales, to provide the scenarios (WP3);*
- *To estimate the effect of global climate change on extreme events in the region, including the assessment of the added value of high-resolution for the simulation of the relevant processes and feedbacks. To evaluate uncertainties in regional projections by comparing results from previous projects (WP4);*
- *To assess (using high resolution downscaling results) the impacts of climate change on the hydrological cycle and water resources over selected catchments; the effects of climate change on the Black Sea (WP5);*
- *To study (based on the high resolution downscaling results) the impacts of climate change on agriculture and forestry, carbon cycle and selected species (WP6);*
- *To study (based on the high resolution downscaling results) the impacts of climate change on health and air quality (photochemistry of air pollution, aerosols) (WP7).*

The main goal of the CECILIA project is to integrate results from different previous and ongoing modeling activities and approaches to provide the basis for very high resolution climate

change impact and vulnerability assessment in important human activity sectors and natural ecosystems. It is prohibitive to cover within the STREP (Specific Targeted Research Project) all the sectors in their complexity, so that our analysis is limited on some key areas of specific interest to the CEE regions. Nevertheless, the scope of the project is big enough and highly multidisciplinary, which required quite big team. The consortium comprises 16 partner institutions (see Table 1) that bring together a wide range of inter-disciplinary expertise and experience in the areas of climate change modeling, statistical analysis, climate change impact assessment, as well as anthropogenic and biogenic pollutant emissions. Reflecting the shared and overlapping expertise and interests of the partners, most of the work packages involve contributions from several partners, under the direction of a lead partner. As the targeted area is Central and Eastern Europe the substantial part of participant institutes comes from this area (10–12, depending on the political or geographical point of view), complemented by selected partners from western part of EU to add necessary access to experience, know-how, and data for working on the project.

Table 1. List of partners in project CECILIA

Partner name	*Partner short name*	*Country*
Charles University, Prague	*CUNI*	*Czech Rep.*
The Abdus Salam ICTP, Trieste	*ICTP*	*Italy*
Météo-France, Toulouse	*CNRM*	*France*
Danish Meteorological Institute, Copenhagen	*DMI*	*Denmark*
Aristotle University of Thessaloniki	*AUTH*	*Greece*
Czech Hydrometeorological Institute, Prague	*CHMI*	*Czech Rep.*
Institute of Atmospheric Physics, Prague	*IAP*	*Czech Rep.*
Swiss Federal Institute of Technology Zurich	*ETH*	*Switzerland*
University of Natural Resources and Applied Life Sciences, Vienna	*BOKU*	*Austria*
National Meteorological Administration, Bucharest	*NMA*	*Romania*
National Institute of Meteorology and Hydrology, Sofia	*NIMH*	*Bulgaria*
National Institute of Hydrology and Water Management, Bucharest	*NIHWM*	*Romania*
Hungarian Meteorological Service, Budapest	*OMSZ*	*Hungary*
Forest Research Institute, Zvolen	*FRI*	*Slovakia*
Warsaw University of Technology, Warsaw	*WUT*	*Poland*
Eötvös Loránd University, Budapest	*ELU*	*Hungary*

CECILIA RCMs and simulation strategy

One of the commonly used RCMs in the targeted region is the model RegCM distributed freely from ICTP. The model was originally developed by Giorgi et al. (1993a,b) and later augmented as described by Giorgi and Mearns (1999), Pal et al. (2000), and Pal et al. (2007). The dynamical core of the RegCM is equivalent to the hydrostatic version of the NCAR/Pennsylvania State University mesoscale model MM5. Surface processes are represented via the Biosphere-Atmosphere Transfer Scheme (BATS – Dickinson et al., 1993) and boundary layer physics is formulated following a non-local vertical diffusion scheme (Giorgi et al., 1993a). Resolvable scale precipitation is represented

via the scheme of Pal et al. (2000), which includes a prognostic equation for cloud water and allows for fractional grid box cloudiness, accretion, and re-evaporation of falling precipitation. Convective precipitation is represented using a mass flux convective scheme (Giorgi et al., 1993b), while radiative transfer is computed using the radiation package of the NCAR Community Climate Model, version CCM3 (Giorgi et al., 1999). This scheme describes the effect of different greenhouse gases, cloud water, cloud ice, and atmospheric aerosols. Cloud radiation is calculated in terms of cloud fractional cover and cloud water content, and the fraction of cloud ice is diagnosed by the scheme as a function of temperature. For more details on the use of the model see Elguindi et al. (2006). The model has been already applied in targeted regions, e.g., by Halenka et al. (2006) and Busuioc et al. (2006).

Another RCM has been used recently, starting from an operational NWP model used in several national meteorological services in the targeted domain. This is the ALADIN-Climate model, and first experiences from its development can be found in Huth et al. (2003). Originally, the limited-area prediction model ALADIN has been developed by the international team headed by Météo-France, and modification for RCM purposes started in 2001 in cooperation with CHMI in Prague. ALADIN is a fully three-dimensional baroclinic system of primitive equations using a two-time-level semi-Lagrangian semi-implicit numerical integration scheme and digital filter initialization. For the description of the model and its parameterizations, refer, e.g., to Bubnová et al. (1994) and Váňa (1998). The physical parameterizations package comprises gravity wave drag parameterization, implicit horizontal diffusion computed in spectral space (fourth order and increasing with height), vertical diffusion and planetary boundary layer parameterization, constant analyzed sea surface temperature and amount of sea-ice, an improved version of the ISBA (Interaction Soil Biosphere Atmosphere) scheme, including an explicit parameterization of soil freezing (prognostic variables in ISBA: surface temperature, mean soil temperature, interception water content, superficial soil water content, total liquid soil water content, total frozen soil water content), simple parameterization of snow cover, soil characteristics (texture, depth) that are point-dependent, vegetation characteristics that are point- and month-dependent, simplified radiation scheme called at every time step, mass flux convection scheme including the entrainment profile, specific humidity as a solely prognostic variable: no storage of condensate; evaporation of falling rain; treatment of the ice-phase, and a sophisticated diagnostic cloud (and cloud content) method used for radiative transfer calculations. For running the ALADIN model in a climate mode, a few modifications had to be made, which include mainly changes in lower boundary condition specifications and availability of restart.

Another way to increase resolution is to use GCM with a variable horizontal resolution, e.g., model ARPEGE (Déqué and Piedelievre, 1995; Déqué et al., 1998), an approach that, however, requires even larger computational resources than RCMs. Basically, there is close connection in modeling activities of the CECILIA project to the project ENSEMBLES, where all the three models mentioned above are used as well, both for climate change projections and model inter-comparison and validation. Since the field of regional climate prediction is still evolving, the skill of RCMs in simulating climate variability has not been extensively evaluated. This is planned within the framework of the project ENSEMBLES for simulations at 50 and 25 km resolution driven by ERA-40 reanalyses. As part of the ENSEMBLES project, transient scenario runs of one hundred year length (1950–2050, some even longer) are also planned under different greenhouse gases (GHG) and aerosol forcings. In CECILIA, a detailed analysis and use of the results of the project ENSEMBLES is planned for focused initial impact studies in our target region (WP1 and starting stage of WP4,5,6,7). However, next to this initial phase, the main objective of this proposal is to adapt the RCMs used for ENSEMBLES (ALADIN-Climate and RegCM) for very high resolution

(grid spacing of 10 km) simulations over selected sub-domains, which will provide additional information related to the complex terrain of the region. The assessment of the role of significant but previously not resolved topographical features and land use patterns will be provided in these experiments as well as the evaluation of the sensitivity of the simulations to the choice and size of the model domain. Furthermore, for the CECILIA project, last 50 years of present century was run by the ARPEGE (CNRM) and RegCM@25km (ICTP) to provide driving fields for ALADIN-Climate and RegCM families partners, respectively, in end-of-century time slice.

In addition, there is statistical downscaling involved in the project (Busuioc et al., 2006; Huth, 2002, 2005) both for comparison and localization of the model results. The availability of different methodologies giving often different results implies that a full assessment of the uncertainties in regional climate change simulation may require the use of multiple techniques (as proposed in this project). The CECILIA project is also going to provide insights on the validation and relative merits of statistical and dynamical downscaling, in particular as applied to provide local climate information.

The higher resolution enables not only more detailed description of the topography and land use, but it allows to introduce new processes, as interactive interaction of climate change and air quality, subgrid effects, etc. The preliminary results show the promising benefits of very high resolution towards the use in impact studies. More detailed analysis of results, which is clearly beyond the purpose of this introduction, is either already done or it is planned in the near future within the project. Moreover, development of new features in the parameterization of high resolution physics in the models is expected. Adjustment of large scale precipitation parameterization has been mentioned already as improving the precipitation results significantly in very high resolution. Exploration of the possible improvements of high resolution regional climate modeling by testing new parameterization schemes better adapted to this resolution is another objective of modeling activities within the project.

Previous results show the possibility of the changes of statistical distribution of climate parameters in our targeted domain. Despite the relative agreement of climate-change scenarios concerning the changes in extremes over this region, a significant uncertainty remains with regard to their exact magnitude and the attribution of the causes for these changes. Some studies have highlighted the role of large-scale circulation changes, but land-atmosphere interactions are clearly of key relevance as well. Moreover, certain aspects central to this issue are often not well represented in GCMs (land surface heterogeneity, complex topography, convection), or even in RCMs. Very high-resolution simulations could help investigating some of these open questions and yield more accurate estimates of future changes in extreme weather events over the targeted regions.

The basic objective of modeling activities in CECILIA project is to produce simulations on targeted domains for a past period (1961–1990) driven by ERA-40 reanalysis used for validation of the models, as well as for a reference period (1961–1990) and scenario time slices (2021–2050 and 2071–2100) based on ENSEMBLES 6FP EC IP A1B GCM simulations. Two models have been supposed to be used as source of driving fields over six target areas, ALADIN-Climate family using stretched climate change transient run by ARPEGE-Climate for ENSEMBLES project, RegCM family using RegCM transient ENSEMBLES run for whole Europe in 25 km resolution driven by transient run of ECHAM5. While the stretched ARPEGE run provides reasonable resolution in targeted regions for direct application of 10 km resolution RCM, the difference between 10 km resolution of RegCM and the resolution of other common global models is too large, that is why the double-nesting using 25 km RegCM run as an intermediate step is necessary. Some of the results already achieved are discussed in papers within this Special Issue of IDŐJÁRÁS.

References

Beniston, M. and Stephenson, D.B., 2004: Extreme climatic events and their evolution under changing climatic conditions. Global Planet. Change 44, 1-9.

Bubnová, R., Hello, G., Bénard, P., and Geleyn, J.-F., 1994: Integration of the fully compressible equations with orography in the framework of the ARPEGE/ALADIN NWP. Meteorol. zpr. 47, 69-76.

Busuioc, A, Giorgi, F., Bi, X., and Ionita, M., 2006: Comparison of regional climate model and statistical downscaling simulations of different winter precipitation change scenarios over Romania. Theor. Appl. Climatol. 86, 101-123.

Déqué, M. and Piedelievre, J.P., 1995: High-Resolution climate simulation over Europe. Clim. Dynam. 11, 321-339.

Déqué, M., Marquet, P., and Jones, R.G., 1998: Simulation of climate change over Europe using a global variable resolution general circulation model. Clim. Dynam. 14,173-189.

Dickinson, R., Henderson-Sellers, A., and Kennedy, P.J., 1993: Biosphere-Atmosphere Transfer Scheme (BATS) version 1E as coupled to the NCAR community climate model. NCAR Technical Report TN-387+STR, 72 pp.

Elguindi, N., Bi, X., Giorgi, F., Nagarajan, B., Pal, J., Solmon, F., Rauscher, S., and Zakey, A., 2006: RegCM Version 3.1 User's Guide. PWCG Abdus Salam ICTP.

Frei, C., Christensen, J.H., Deque, M., Jacob, D., Jones, R.G., and Vidale, P.L., 2003: Daily precipitation statistics in regional climate models: Evaluation and intercomparison for the European Alps. J. Geophys. Res. 108 (D3), 4124.

Gates, W.L., Henderson-Sellers, A., Boer, G.J., Folland, C.K., Kitoh, A., McAvaney, B.J., Semazzi, F., Smith, N., Weaver, A.J., and Zeng, Q.-C., 1996: Climate models – Evaluation. In Climate Change 1995: The Science of Climate Change (ed.: J.T. Houghton et al.). Cambridge Univ. Press, New York, 229–284.

Giorgi, F. and Mearns, L.O., 1999: Introduction to special section: regional climate modeling revisited. J. Geophys. Res. 104, 6,335–6,352

Giorgi, F. and Coppola, E., 2007: European climate-change oscillation (ECO). Geophys. Res. Lett. 34, L21703, doi:10.1029/2007GL031223.

Giorgi, F., Marinucci, M.R., and Bates, G.T., 1993a: Development of a second generation regional climate model (RegCM2). Part I: Boundary layer and radiative transfer processes. Mon. Weather Rev. 121, 2794-2813.

Giorgi, F., Marinucci, M.R., Bates, G.T., and DeCanio, G., 1993b: Development of a second generation regional climate model (RegCM2). Part II: Convective processes and assimilation of lateral boundary conditions. Mon. Weather Rev. 121, 2814-2832.

Giorgi, F., Huang, Y., Nishizawa, K., and Fu, C., 1999: A seasonal cycle simulation over eastern Asia and its sensitivity to radiative transfer and surface processes. J. Geophys. Res. 104, 6403-6423.

Giorgi, F., Hewitson, B., Christensen, J., Hulme, M., von Storch, H., Whetton, P., Jones, R., Mearns, L., and Fu, C., 2001: Regional climate information – evaluation and projections. In Climate Change 2001: The Scientific Basis (eds.: J.T. Houghton, Y. Ding, D.J. Griggs, M. Noguer, P.J. van der Linden, Dai, X., K. Maskell, C.A. Johnson). Cambridge University Press, Cambridge, 583-638.

Giorgi, F., Huang, Y., Nishizawa, K., and Fu, C., 1999: A seasonal cycle simulation over eastern Asia and its sensitivity to radiative transfer and surface processes. J. Geophys. Res. 104, 6403-6423.

Gobron, N., Pinty, B., Melin, F., Taberner, M., Verstraete, M.M., Belward, A., Lavergne, T., and Widlowski, J.L., 2005: The state of vegetation in Europe following the 2003 drought. Int. J. Remote Sens. 26, 2013-2020.

Hafner, S., 2003: Trends in maize, rice and wheat yields for 188 nations over the past 40 years: a prevalence of linear growth. Agr. Ecosyst. Environ. 97, 275-283.

Halenka, T., Kalvová, J., Chládová, Z., Demeterová, A., Zemánková, K., and Belda, M., 2006: On the capability of RegCM to capture extremes in long term regional climate simulation – comparison with the observations for Czech Republic. Theor. Appl. Climatol. 86, 125-145.

Huntingford, C., Jones, R.G., Prudhomme, C., Lamb, R., Gash, J.H.C., and Jones, D.A., 2003: Regional climate-model predictions of extreme rainfall for a changing climate. Q. J. Roy. Meteor. Soc. 129, 1607-1621.

Huth, R., 2002: Statistical downscaling of daily temperature in central Europe. J. Climate 15, 1731-1742.

Huth, R., 2005: Downscaling of humidity variables: A search for suitable predictors and predictands. Int. J. Climatol. 25, 243-250.

Huth, R., Kyselý, J., and Dubrovský, M., 2003: Simulation of surface air temperature by GCMs, statistical downscaling and weather generator: Higher-order statistical moments. Studia geoph. geod. 47, 203-216.

Huth, R., Mládek, R., Metelka, L., Sedlák, P., Huthová, Z., Kliegrová, S., Kyselý, J., Pokorná, L., Janoušek, M. and Halenka, T., 2003: On the integrability of limited-area numerical weather prediction model ALADIN over extended time periods. Studia geoph. geod. 47, 863-873.

Kysely, J., 2004: Mortality and displacedmortality during heat waves in the Czech Republic. Int. J. Biometeorol. 49, 91-97.

Meehl, G.A. and Tebaldi, C., 2004: More intense, more frequent and longer lasting heat waves in the 21st century. Science 305, 994-997.

Meehl, G.A., Tebaldi, C., and Nychka, D., 2004: Changes in frost days in simulations of 21st century climate. Clim. Dynam. 23, 495-511.

Menzel, A., Jakobi, G., Ahas, R., Scheifinger, H., and Estrella, N., 2003:Variations of the climatological growing season (1951-2000) in Germany compared with other countries. Int. J. Climatol. 23, 793-812.

Menzel, A., Sparks, T.H., Estrella, N., Koch, E., Aasa, A., Ahas, R., Alm-Kubler, K., Bissolli, P., Braslavska, O., Briede, A., Chmielewski, F.M., Crepinsek, Z., Curnel, Y., Dahl, A., Defila, C., Donnelly, A., Filella, Y., Jatczak, K., Mage, F., Mestre, A., Nordli, O., Penuelas, J., Pirinen, P., Remišova, V., Scheifinger, H., Striz, M., Susnik, A., vanVliet, A.J.H., Wielgolaski, F.-E., Zach, S., and Zust, A., 2006: European phonological response to climate change matches the warming pattern. Glob. Change Biol. 12, 1969-1976.

Pal, J.S., Giorgi, F., and Bi, X., 2004: Consistency of recent European summer precipitation trends and extremes with future regional climate projections. Geophys. Res. Lett. 31, L13202, doi:10.1029/2004GL019836.

Pal, J.S., Small, E.E., and Eltahir, E.A., 2000: Simulation of regional-scale water and energy budgets: Representation of subgrid cloud and precipitation processes within RegCM. J. Geophys. Res. 105, 29579-29594.

Pal, J.S., Giorgi, F., Bi, X., Elguindi, N., Solmon, F., Gao, X., Rauscher, S.A., Francisco, R., Zakey, A., Winter, J., Ashfaq, M., Syed, F.S., Bell, J.L., Diffenbaugh, N.S., Karmacharya, J., Konaré, A., Martinez, D., da Rocha, R.P., Sloan, L.C., and Steiner, A.L., 2007: Regional Climate Modeling for the Developing World: The ICTP RegCM3 and RegCNET. B. Am. Meteorol. Soc. 88, 1395–1409.

Schär, C., Vidale, P.L., Luthi, D., Frei, C., Haberli, C., Liniger, M.A., and Appenzeller, C., 2004: The role of increasing temperature variability in European summer heat waves. Nature 427, 332-336.

Uppala, S., Kallberg, P., Hernandez, A., Saarinen, S., Fiorino, M., Li, X., Onogi, K., Sokka, N., Andrae, U., and Da Costa Bechtold, V., 2004: ERA-40: ECMWF 45-year reanalysis of the global atmosphere and surface conditions 1957-2002. ECMWF Newsletter 101, 2-21.

Váňa, F., 1998: Physical parameterizations in the ALADIN model (in Czech). Meteorol. zpr. 51, 33-44.

Tomas Halenka

Guest Editor on behalf of the CECILIA project

Short overview of the CLAVIER project

Herewith I would like to give a short overview of the CLAVIER project. The project is founded by the European Commission's 6th Framework Programme as a Specific Targeted Research Project under the thematic sub-priority "Global Change and Ecosystems". CLAVIER has a duration of three years (until the end of August, 2009) with the coordination of the Max Planck Institute of Meteorology.

The overall aim of CLAVIER is to provide contribution in order to successfully cope with ongoing challenges in Central and Eastern Europe (CEE) through the economic and political transition, continuing vulnerability to environmental hazards and longer term impacts of global climate changes. We focus on three CEE countries – Hungary, Romania, and Bulgaria and address the following scientific goals:

- *Investigation of ongoing and future climate changes and their associated uncertainties in Central and Eastern European Countries (CEEC);*
- *Analyses of possible impact of climate changes in CEEC on weather pattern and extremes, air pollution, human health, natural ecosystems, forestry, agriculture, and infrastructure as well as water resources;*
- *Evaluation of the economic impacts of climate changes on CEEC economies, concentrating on four economic sectors, which are agriculture, tourism, energy supply, and the public sector.*

We wish to achieve our goals through investigation of the links between climate change and its impact on weather pattern and air pollution, extreme events, water resources, as well as on natural ecosystems, infrastructure, and human health. As a result, the impact of climate changes on economics of the countries mentioned above is evaluated.

The first step is to provide reliable climate evaluation scenarios of the first half of the 21st century for impact researches from CEE. Three different regional models are used in the project to form a small ensemble. An article related to regional modeling activity of the CLAVIER project is presented later in this issue.

A crucial part of the project is the establishment of an effective interface between the climate modeling and climate impact assessment communities. This interface is realized by dynamical and statistical techniques. Dynamic modeling and adaptation at very fine scales (3 to 1 km grid spacing) provide an input for the case studies in the field of hydrology and agriculture, and the multi-scale simulations are used to investigate model resolution suited for representation of meteorological and climate extreme events. Statistical downscaling techniques are applied for directly derived parameters of weather and climate extremes as well as climate impact parameters in the fields of ecosystems, health, infrastructure, and economics.

Analyses of possible impact of climate changes in CEE on weather pattern and extremes, air pollution, human health, natural ecosystems, forestry, agriculture, infrastructure, and water resources stretches through several work packages.

Within CLAVIER we not only analyze weather regimes for the region of CEE, but study their future changes and implication to air pollution levels. While the methodology of the work on characterization of the current regional climate is based on a synoptic-climatological approach, classification methods are applied to complete statistics of weather regimes for climate scenarios. As a result, composite meteorological datasets are calculated and will be used in a regional scale air pollution model.

It is generally expected within the climate research community that the extreme events will increase under climate change conditions, they will occur more often and will become more intense. Here we analyze past and future trends of extreme events in CEE based on existing regional climate model simulations. Special emphasis is put on the summer drying problem, which is a systematic bias in the simulation of today's mean climate and is typical for many regional models. We also focus on the potential impacts of extreme events on forestry and water management as well as soil and agriculture.

One of the main aims of the project is the production of future hydrological and agricultural scenarios. This includes the investigation of changes in the hydrological regime of various catchments, the estimation of changes in riverine flood characteristics, as well as the estimation of the long-term evaporation rates from large lakes. An analysis of changes in water stress for crops and changes in low water conditions is taken into account.

Various methods are developed and integrated within the project to reveal the spatial-dependent interrelationship between the climate/weather parameters and the impact processes. Here we consider the following impact case studies: grassland, roads, heat waves, buildings (roof), and ragweed.

The knowledge gained through the scientific goals mentioned above builds the basis for evaluation of the economic impacts of climate change on national economies. Four sectors are of particular interest – agriculture, tourism, energy supply, and the public sector. Furthermore, ten case studies for selected regions in Hungary, Bulgaria, and Romania are identified. As a result, the overall macroeconomic relevance of the studied phenomena is drawn.

A substantial part of the project is in close contacts with a wide range of user groups from CEE countries, who will benefit from our results. CLAVIER closely cooperates with the EU projects ENSEMBLES and CECILIA.

Please visit the project web-site to learn more about CLAVIER: www.clavier-eu.org.

Daniela Jacob

Guest Editor on behalf of the CLAVIER project

IDŐJÁRÁS

Quarterly Journal of the Hungarian Meteorological Service
Vol. 112, No. 3–4, July–December 2008, pp. 141–153

Regional climate modeling activities in relation to the CLAVIER project

Daniela Jacob*, Lola Kotova, Philip Lorenz, Christopher Moseley and **Susanne Pfeifer**

Max Planck Institute for Meteorology,
Bundesstrasse 53, D-20146 Hamburg, Germany

(Manuscript received in final form November 13, 2008)

Abstract—Observational records show that the global climate is changing and these changes are visible in the Central and Eastern European Countries (CEEC). Certainly negative impacts of climate change will involve significant economic losses in several regions of Europe, while others may bring health or welfare problems somewhere else. Within the EU funded project CLAVIER (Climate ChAnge and Variability: Impact on Central and Eastern EuRope) three representative CEEC are studied in detail: Hungary, Romania, and Bulgaria. Researchers from 6 countries and different disciplines identify linkages between climate change and its impact on weather patterns with consequences on air pollution, extreme events, and water resources. Furthermore, an evaluation of the economic impact on agriculture, tourism, energy supply, and public sector will be conducted. CLAVIER focuses on ongoing and future climate changes in CEEC using measurements and existing regional scenarios to determine possible developments of the climate and to address related uncertainties. Three regional climate models are used to simulate the climate evolution in CEEC for the period 1951 to 2050, the future regional climate projection being the first half of the 21st century. The issue of climate change uncertainties is addressed through the multi-model and multi-scenario ensemble approach. As a result, CLAVIER establishes a large data base, tools, and methodologies, which contribute to reasonable planning for a successful development of society and economy in CEEC under climate change conditions. Current regional climate projections show a strong warming and drying during the summer months, which seems partly due to a systematic error in model simulations. Detailed validation of the CLAVIER simulations, which goes much beyond this paper, is needed, and the results have to be related to possible climate changes projected for the region in future simulations.

Key-words: climate, climate change signal, regional climate change, regional climate modeling, validation, Central and Eastern Europe, temperature, precipitation

* Corresponding author, E-mail: Daniela.Jacob@zmaw.de

1. Introduction

The nations in Central and Eastern Europe (CEE) face triple challenges of the ongoing economic and political transition, continuing vulnerability to environmental hazards, and longer term impacts of global climate change. Domestic development of market economies and democratic institutions is taking place in the context of complying the rules of these international bodies. At the same time, vulnerability to natural and human environmental hazards knows no boundaries in time and space. Examples include a series of extreme floods hitting the Tisza basin in the period of 1998–2001, the catastrophic dam failure such as the Baia Mare gold mine dam failure in Romania which resulted in cyanide pollution of the Lapus-Somes-Tisza-Danube rivers (January 2000; Relief Web, 2000), a number of other flood events such as the Labe/Elbe and Danube rivers (August 2002), a sequence of mostly flash flood disasters throughout Romania in 2005, plus the ongoing menace of air pollution, drought, deforestation, land slides, and soil erosion. In addition to these challenges, long term global climate change may offer opportunities as well as threats to environment, resources, and national well-being amidst the on-going stresses of transition and capricious environmental forces (most of it citation from Climate change in Central and Eastern Europe: Introduction, GeoJournal 57, 2002, 113–115).

It is urgently needed to address the ongoing and future climatic changes and possible consequences in CEEC.

Therefore, CLAVIER addresses the following three scientific goals:

1. Investigation of ongoing and future climate changes and their associated uncertainties in CEEC.
2. Analyses of possible impact of climate changes in CEEC on weather pattern and extremes, air pollution, human health, natural ecosystems, forestry, agriculture and infrastructure as well as water resources.
3. Evaluation of the economic impacts of climate changes on CEEC economies, concentrating on four economic sectors, which are the agriculture, tourism, energy supply, and public sector.

Objective 1 is to provide reliable climate evolution scenarios of the first half period of the 21st century for impacts research in the CEEC region. The issue of climate change uncertainties is particularly addressed. This objective will be achieved through assembling and assessment of existing climate scenarios for the region, the validation and improvement of the regional climate models, the performance of regional climate change simulations, and the detailed assessment of the associated uncertainties.

The evaluation of the economic impacts will be based on representative case study regions located in the three CLAVIER countries Hungary, Bulgaria, and Romania shown in *Fig. 1*.

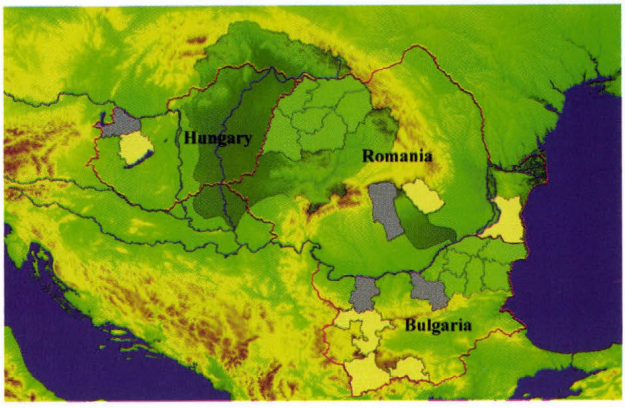


Fig. 1. CLAVIER case study regions for economic impact assessment (cyan: hydrological/water management; green: agriculture; gray: energy; yellow: tourism).

Table 1. List of CLAVIER project partners

Participant name	**Participant short name**	**Country**
Max-Planck-Institute for Meteorology, Hamburg	MPI-M	Germany
Hungarian Meteorological Service, Budapest	OMSZ	Hungary
University of Graz/Wegener Centre, Graz	WegCenter	Austria
Centre National de la Recherche Scientifique, Paris	CNRS	France
Joanneum Research, Graz	JR	Austria
VITUKI Environmental Protection and Water Management Institute, Budapest	VITUKI	Hungary
Budapest University of Technology and Economics, Faculty of Civil Engineering, Department of Hydraulic and Water Resources Engineering, Budapest	BME	Hungary
Env-In-Cent Consulting Ltd., Budapest	EiC	Hungary
National Institute of Meteorology and Hydrology, Sofia	NIMH	Bulgaria
University of National and World Economy, Sofia	UNWE	Bulgaria
National Institute of Hydrology and Water Management, Bucharest	INHGA	Romania
University of Cluj, Cluj	UBB	Romania
The Institute of Geography of the Romanian Academy, Bucharest	IG	Romania

To meet the project goals CLAVIER is split into a number of scientific objectives, for which work is carried out within 7 work packages. Researchers (*Table 1*) from 6 countries and different disciplines identify linkages between climate change and its impact on weather patterns with consequences on air pollution, extreme events, and water resources. A large effort is related to the first objective and includes modeling efforts on different scales, with different models, carried out by several partners. This paper will shortly introduce the modeling activities within CLAVIER, which will be presented in more detail in several other papers within this issue (*Szépszó* and *Horányi*, 2008). Here the

focus will be on simulations from the regional climate model used at the Max Planck Institute for Meteorology. In addition, some general information about regional climate change in Europe, which has been achieved through regional downscaling of global IPCC AR4 simulations with the regional climate model REMO, will be presented. These simulations built the basis for more detailed investigations and first climate change assessments within CLAVIER.

2. The climate in the region

A whole suite of studies shows that the climate is already changing and various impacts are visible throughout the world (*McCarthy et al.*, 2001; *Voigt el al.*, 2004). The impacts on natural ecosystems and human health may be serious in the emerging but vulnerable regions in Europe, especially in CEEC. In Europe, 64% of all catastrophic events since 1980 are directly attributed to weather and climate extremes, and climate change projections show even an increasing likelihood of extreme weather events (i.e., *Voigt et al.*, 2004). The average annual length of the growing season in Europe has increased by about 10 days in the recent four decades and is projected to increase further in the future (*Voigt et al.*, 2004). As the annual air temperature increases in Europe, regional differences show that the temperature increase leads to warmer winters in the northeast part of Europe, while the southern part might face even warmer summers. Results from the PRUDENCE project (www.prudence.dmi.dk) show also a clear trend in annual precipitation, with a small increase in the North and a clear decrease in the southern regions of Europe, mainly in summer.

These results also point to the uncertainties, which are still included in climate change projections in CEE. A special model feature, that is typical for many regional climate models (RCMs) and to a less extent is visible in some general circulation models (GCMs), is the too dry and too warm simulation of climate over CEE during the summer (RAACS project; *Machenhauer et al.*, 1998). Their studies showed that this bias could not be explained by systematic errors in the large scale general circulation. In the MERCURE project (http://www.pa.op.dlr.de/climate/mercure.html), a follow-up of a RAACS, a major task was to understand and reduce or eliminate this model error, referred to as the summer drying problem (SDP). Here the Danube catchment was considered where the SDP is prominent. A major conclusion in MERCURE was that for three of five of the participating models, systematic errors in the dynamics appear which cause the SDP (*Hagemann et al.*, 2004). In the fourth RCM, deficiencies in the land surface parameterizations were mainly responsible for its SDP; while the fifth does not have a SDP. (This RCM is not a limited area model but a global model with a stretched grid that had a high resolution over Europe.) As the SDP seems to be related to the dynamics in several models, it was speculated that deficient features in the dynamic part of

the fourth and fifth RCM may also exist, which are only overlaid by systematic errors in the surface parameterizations of these two models. Although the SDP was allocated to the representation of the dynamics in the RCMs, an exact cause of the problem was not found nor could it be eliminated. Following studies in the PRUDENCE project (*Christensen* and *Christensen*, 2007; *Jacob et al.*, 2007) have shown that the SDP still exists in 8 of 10 participating RCMs (*Hagemann* and *Jacob*, 2007). The ninth RCM is the stretched GCM mentioned before, and in the tenth RCM large overestimation of precipitation over the Danube catchment throughout most parts of the year might compensate any tendencies of erroneous drying of the area in its climate simulation. A summer warm bias (compared to CRU data: http://www.cru.uea.ac.uk/) over the Danube catchment is present for all 10 RCMs (*Hagemann* and *Jacob*, 2007). The SDP is a systematic bias in the simulation of today's mean climate, and several questions concerning their influence on extremes like floods, droughts, and their interaction with land use changes arise from it if the quality of current and future climate simulations is considered.

The summer drying problem is still an open issue strongly influencing the uncertainty related to climate change projections in CEEC. This issue as well as other factors determining the uncertainty in climate change projections will, therefore, be addressed within CLAVIER taking into account results from past and ongoing climate change investigations, like PRUDENCE and ENSEMBLES.

Within CLAVIER linkage between climate change and its impact on water resources is investigated. Ongoing and future climate changes are influencing the hydrological cycle and its variability as shown in many studies (e.g., *Hagemann* and *Jacob*, 2007; *Vidale et al.*, 2007). CEECs are especially exposed to changes in means and extremes of the hydrological cycle, e.g., changes in the water level of Lake Balaton or heavy precipitation events in the mountains of the Carpathian Range, which frequently lead to flash floods. Also the central and lower Danube basin ranks high on the world list of catchments exposed to flooding. Many of the streams have trans-boundary character what underlines the necessity to tackle these questions in a regional manner. The governments are planning measures to improve flood safety across CEE, and these efforts should be supported by reliable assessment of climate change induced modifications of flood hazard and flood risk.

Many regions of CEEC are surprisingly dry on the European scale; those are frequently exposed to droughts of short and long term (*Sharov* and *Koleva*, 1994). *Tran et al.* (2002) analyzed the relationship between atmospheric synoptic conditions over Europe and droughts in Bulgaria. *Szilagyi* and *Vorosmarty* (1997) analyzed the extreme groundwater depletion in the region along the central Danube. A clear connection between the atmospheric pattern and droughts is presented; however, Bulgarian droughts are influenced by even more features, thus many open questions have to be addressed. *Tran et al.* (2002) ask for more studies focusing on the impact of changes in atmospheric synoptic conditions and precipitation over the region. CLAVIER will address

this issue and contribute to an improvement in the prediction of droughts in CEEC as well as to the investment of preparedness actions.

3. CLAVIER simulations

The issue of climate change uncertainties will be addressed through the multi-model and multi-scenario ensemble approach considering the three steps of the scenario production chain: greenhouse gas emission, climate scenario with coarse resolution global coupled climate model, and regionally-oriented high spatio-temporal resolution climate scenario. The regional climate models used within CLAVIER are REMO from MPI-M (*Jacob*, 2001), used in Version 5.7 by MPI-M and version 5.0 by the Hungarian Meteorological Service, and the LMDZ model, developed at CNRS in Paris (*Hourdin et al.*, 2006). The former is a limited-area model and the latter is a variable-grid atmospheric general circulation model with zoom over CEE. Data from two global climate models are used to drive and initialize the regional models. All three models use the ECHAM5/MPI-OM simulations performed for the 4th IPCC assessment report with a horizontal resolution of T63 (*Roeckner et al.*, 2006). In addition, the LMDZ model will be forced by boundary data with 2 to 3 degree resolution from the IPSL global model. For the greenhouse gas emission, the scenario is based on the IPCC A1B scenario mainly; additional simulations with the B2 scenario are available for the LMDZ model. Therefore, an ensemble of climate change simulations allows an advanced analysis of uncertainties.

The three regional climate models are used to simulate the climate evolution in CEE for the period 1951 to 2050, the future regional climate projection being the first half of the 21st century. The spatial resolution is around 20 km for most of the simulations, which are currently analyzed. A high resolution (10 km) transient scenario simulation with REMO5.7 is planned on the inner domain shown in *Fig. 2*, covering the CLAVIER target area. The regional modeling activities are carried out in four steps:

Assembling and assessment of existing climate scenarios for the region:
Several climate change simulations exist for CEEC carried out either in context of the IPCC report or within European projects, i.e., PRUDENCE, ENSEMBLES. These simulations are, however, not sufficient for advanced impact studies, due to either the too low spatial-temporal resolution, or the partial spatial coverage of our domain of interest.

Validation and adjustment of regional climate models:
Both regional models REMO and LMDZ, need to be adapted for the region. In particular, the elimination of the SDP is envisaged. Model parameters will be adjusted in order to break down the summer anticyclone blocking situation, which seems to be too persistent in this region.

Climate change simulations:
Once the regional models are validated, climate change simulations will be run from 1951 to 2050 at about 20 km and 10 km horizontal resolutions. The 20 km simulations are directly driven by the global model data, whereas the 10 km simulation will be performed in a two step double nesting approach, i.e., using the coarser regional model simulation results to initialize and drive the high resolution regional model simulation on 10 km.

Uncertainty due to internal variability of regional climate:
To further investigate the issue of regional climate change uncertainties, a new technique for quantification of the uncertainties related to model internal variability is being introduced within CLAVIER. A physical consistent perturbation technique of the lateral boundary data as well as the surface boundary data (as for example orography, albedo, or sea surface temperature) has been developed. Therefore, several RCM simulations can be carried out for one given set of forcing data (like global reanalysis data or global climate model output). The simulations are sensitive to the slightly perturbed data at the lateral and lower boundaries, and the differences between the individual runs can be attributed to internal variability. This technique is in a first step tested for single decades. In a second step the developed perturbation method will be applied for longer time periods in order to create an ensemble of simulations with one RCM (in this case REMO) for one forcing data set (in this case ECHAM5/MPI-OM). The results of this ensemble will be analyzed in order to quantify the uncertainty related to model internal variability. This approach is complementary to the multi-model and multi-scenario ensemble approach.



Fig. 2. Model simulation domain for the 0.22° (~25km horizontal resolution) domain. Inner box shows the CLAVIER target region.

4. Climate change in Europe

Within the last years, new global climate change simulations have been produced and published in the IPCC AR4 process. They have also been used for regional downscaling activities, which now provide new regional climate change signals, which are consistent with IPCC AR4 information. As an example, the horizontal pattern of possible climate change signals are shown using REMO5.7 results. Prior to the CLAVIER activities and in context of IPCC AR4, REMO was nested into the global climate model ECHAM5/MPI-OM developed and used at MPI-M. This means that at the lateral boundaries of the regional model domain, air masses are advected into the domain as they are calculated in the global model. Inside the regional model domain they are modulated through the influence of local and regional characteristics. Here REMO was used on a 50 km horizontal grid size for Europe, to analyze different developments of the climate change signals in different regions of Europe assuming an A1B scenario. All members of the ensemble of the A1B scenario, one A2 and one B1 scenario have been downscaled using the MPI-M modeling chain: ECHAM5/MPIOM and REMO5.7. Here only results from one A1B member (Nr. 1) are shown. A more detailed description and analyses of the climate signal are in preparation.

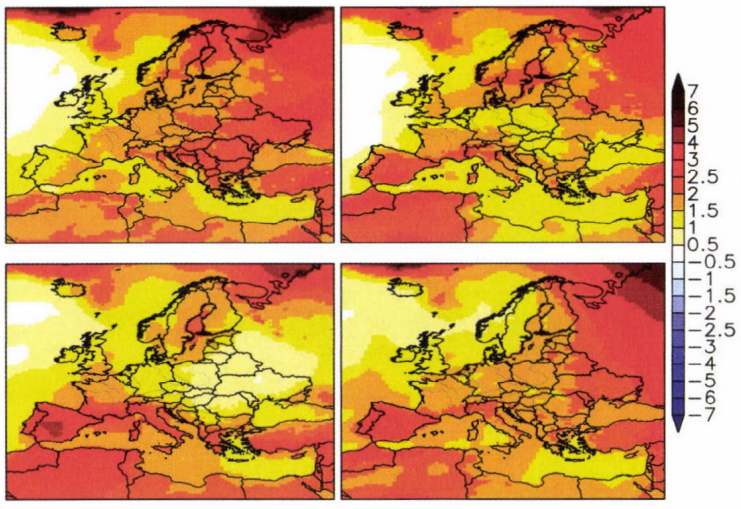


Fig. 3. Differences in the seasonal mean 2m air temperature [°C] around 2050 compared to the reference period 1961–1990. Winter (upper left), spring (upper right), summer (lower left) and fall (lower right).

Fig. 3 shows the change in 2m air temperature for Europe, which is regionally very different. Until 2040–2050 an increase in summer temperatures (*Fig. 3*, lower left) of more that 2.5 °C compared to 1961–1990 is calculated for

the south part of France, Spain, and Portugal, while in most parts of Central Europe less than 1 °C increase is projected. In winter (*Fig. 3*, upper left) the simulated increase in temperatures is about 1.5 °C to 2 °C and covers an area from Scandinavia to the Mediterranean. Only in those regions, which are directly influenced by air masses from the Atlantic Ocean, like Great Britain, Portugal, and parts of Spain, a less strong increase is simulated.

The changes until 2100 are displayed in *Fig. 4*. Here a strong warming of more than 3 °C for the entire European region is visible in summer and winter seasons.

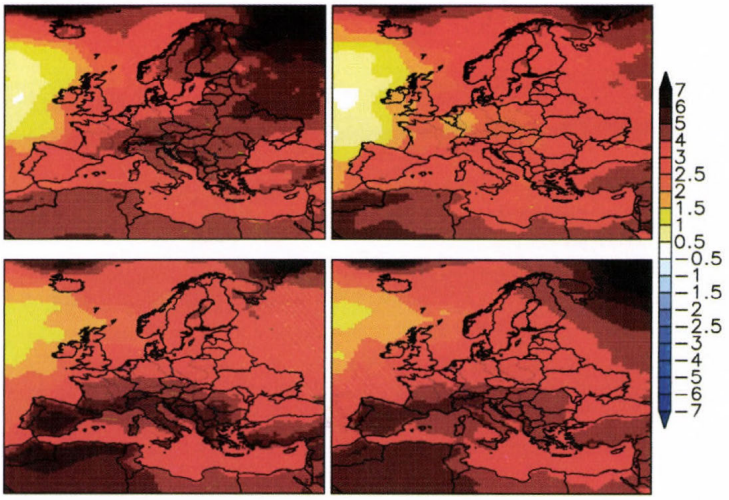


Fig. 4. Differences in the seasonal mean 2m air temperature [°C] around 2100 compared to the reference period 1961–1990. Winter (upper left), spring (upper right), summer (lower left) and fall (lower right).

At the same time, changes in precipitation pattern are projected. Until the middle of this century (~2050, *Fig. 5*) a clear decreasing trend of about 50% and more is calculated for the Mediterranean region in all seasons. Scandinavia might face more precipitation than today, especially in winter. During summer months precipitation seems to decrease with more than 30% in Great Britain. These changes are most likely related to an extension of the Azores High, which stretched further northeast into parts of Western Europe. The simulated pattern changes are developing further until 2100 (*Fig. 6*), with precipitation decreases in summer up to the southern part of Scandinavia.

For the CLAVIER region (as well as for the entire Europe) a strong warming is projected, which needs to be considered in view of the well-known SDP. Associated with the warming, a dividing line between areas with precipitation increase and decrease is calculated. The position of this line is still very difficult to project and its location can vary with emission scenarios or

models under consideration. Therefore, CLAVIER emphasizes model validations and aims to analyze the robustness of the climate change signals from different simulations in the CLAVIER region.

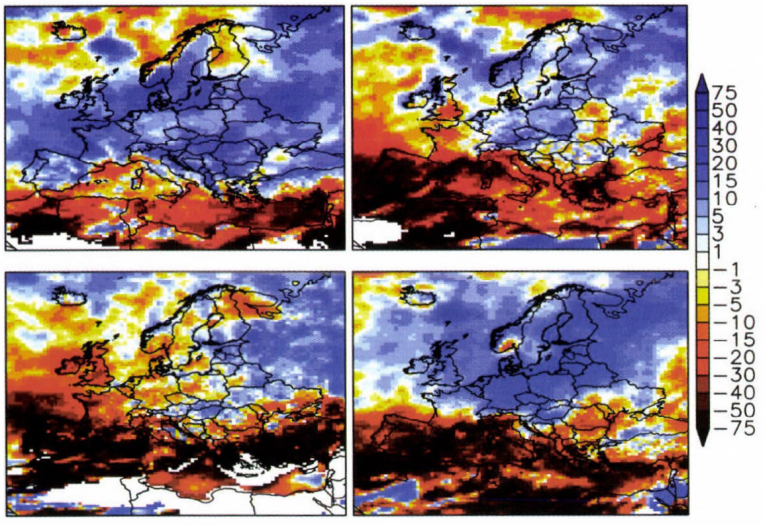


Fig. 5. Differences in the seasonal precipitation [%] around 2050 compared to the reference period 1961–1990. Winter (upper left), spring (upper right), summer (lower left) and fall (lower right).

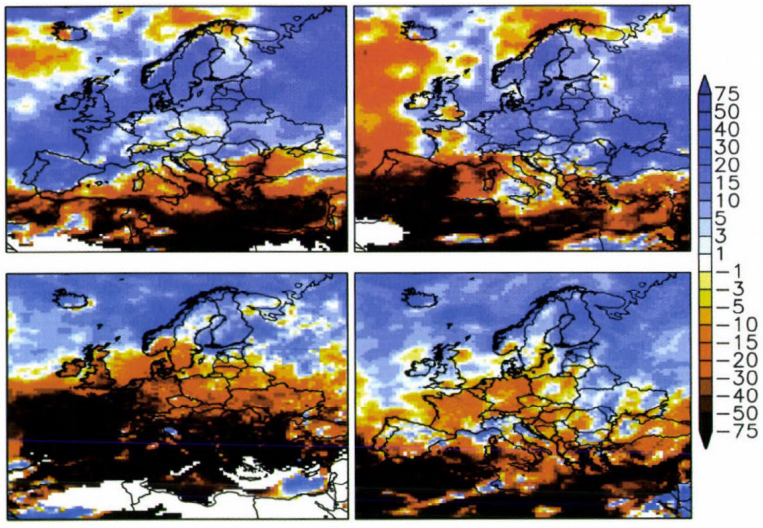


Fig. 6. Differences in the seasonal precipitation [%] around 2100 compared to the reference period 1961–1990. Winter (upper left), spring (upper right), summer (lower left) and fall (lower right).

5. *Validation of model performance in the CEEC region*

The CLAVIER project is still ongoing, therefore, results of the model validation will be shown exemplarily for the MPI-M REMO5.7 simulations. Similar work is done for the LMDZ model and for the REMO5.0 simulations done at the Hungarian Meteorological Service.

To assess how well the REMO model is suited to simulate the climate in Central and Eastern Europe, a validation based on a REMO simulation with a horizontal resolution of 0.22° driven by ECMWF ERA-40 reanalysis data has been performed. Initializing and forcing the regional model with reanalysis data ensures that the model results represent the real observed climate in the best possible way. These kinds of model simulations are thus well suited for a detailed comparison to meteorological observations. The model domain is shown in *Fig. 2*, where the small inner box denotes the area used for the evaluation. The model simulation covers the whole ERA-40 period from 1958 to 2001. For the analysis, seasonal mean values of simulated temperature and precipitation for a 20-year period from 1960 to 1979 have been compared to observed values. The observational dataset used was a gridded dataset of daily temperature and precipitation provided by the ENSEMBLES project (*Haylock et al.*, 2007).

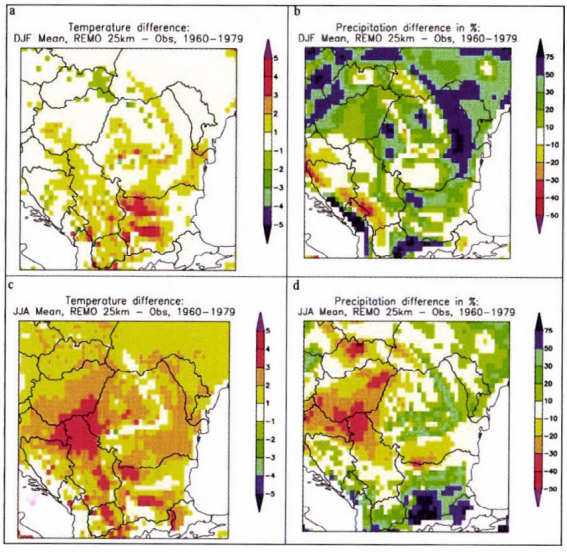


Fig. 7. Difference between REMO-ERA-40 simulation and ENSEMBLES observations for temperature [°C] (a, c) and precipitation [%] (b, d), for winter (upper panels) and summer (lower panels).

Fig. 7 shows the deviations between simulated and observed 20 year mean winter and summer temperature and precipitation. For temperature (*Fig. 7a, c*) a warm bias of the model can be seen, which is larger in summer than in winter,

and which is typical for the above mentioned summer drying problem. Associated with the summer warm bias there is a dry bias shown in *Fig. 7d*. The summer dry bias is prevalent in the lower regions, whereas precipitation in higher elevations is overestimated by the model (e.g., over the Carpathians and the mountain areas of Pirin, Rila, and Rhodopes in Bulgaria). Winter precipitation seems to be overestimated by the model in most regions (*Fig. 7b*). Part of the differences in winter precipitation, especially in mountainous areas might be related to a systematic underestimation of snow in the observational dataset, which is known as undercatch the measuring gauge, and which can be as large as 30 to 50% of the actual solid precipitation (e.g., *Frei* and *Schär*, 1998; *Fassnacht*, 2004). The warm bias and the underestimation of summer precipitation by the model are a substantial part of ongoing model development in the CLAVIER project.

6. Conclusions

The validation of the REMO model for the Central and Eastern European region revealed that the summer drying problem known from previous modeling studies like MERCURE and PRUDENCE is still present in actual REMO simulations. The knowledge of such model biases is indispensable for the assessment of climate change impacts. The CLAVIER strategy to deal with the known model deficiency is firstly to examine the possible reasons for the SDP in detail in order to improve the responsible part of the model physics/dynamics. Secondly, existing biases have to be communicated to the users of the climate model data and solutions have to be provided to cope with the known uncertainties. This is especially important in a multidisciplinary climate change impact assessment project, like CLAVIER. For the CLAVIER project this means that the climate change information are provided as 'delta change approach', i.e., only changes of climatic variables are considered, not the absolute values calculated by the model. This approach is based on the assumption that model biases do not change under climate change conditions. In case that absolute values are inevitable, e.g., for the calibration of impact models, a bias correction based on observational data will be performed. Currently, the climate change simulations are in progress and first results are analyzed and distributed to CLAVIER partners.

Acknowledgments—We acknowledge the climate dataset from the EU-FP6 project ENSEMBLES (http://www.ensembles-eu.org) and the data providers in the ECA&D project (http://eca.knmi.nl). We also thank *Holger Göttel* for providing Figs. 3 to 6.

References

Christensen, J.H and *Christensen, O.B.*, 2007: A summary of the PRUDENCE model projections of changes in European climate by the end of this century. *Climatic Change 81,* 7-30, doi 10.1007/s10584-006-9210-7.

Fassnacht, S.R., 2004: Estimatoin of alter-shielded gauge snowfall undercatch, snowpack sublimation, and blowing snow transport at six sites in the coterminous USA. *Hydrol. Process. 18*, 3481-3492.

Frei, C. and *Schär, C.,* 1998: A precipitation climatology of the Alps from high-resolution rain18 gauge observations. *Int. J. Climatol. 18*, 873-900.

Hagemann, S. and *Jacob, D.,* 2007: Gradient in the climate change signal of European discharge predicted by a multi-model ensemble. *Climatic Change 81,* 309-327, doi 10.1007/s10584-006-9225-0.

Hagemann, S., Machenhauer, B., Jones, R., Christensen, O.B., Déqué, M., Jacob D., and *Vidale, P.L.,* 2004: Evaluation of water and energy budgets in regional climate models applied over Europe. *Clim. Dynam. 23*, 547-567.

Haylock, M.R., Hofstra, N., Klein Tank, A.M.G., Klok, E.J., Jones, P.D., and *New, M.*, 2007: A European daily high-resolution gridded dataset of surface temperature and precipitation. *J. Geophys. Res. 113*, D20119, doi:10.1029/2008JD010201, 2008.

Hourdin, F., Musat, I., Bony, S., Braconnot, P., Codron, F. ,Dufresne, J-L., Fairhead, L., Filiberti, M-A., Friedlingstein, P., Grandpeix, J-Y., Krinner, G., LeVan, P., Li, Z-X., and *Lotta, F.,* 2006: The LMDZ4 general circulation model: climate performance and sensitivity to parametrized physics with emphasis on tropical convection. *Clim. Dynam. 27*, 787-813.

Jacob, D., 2001: A note to the simulation of the annual and inter-annual variability of the water budget over the Baltic Sea drainage basin. *Meteorol. Atmos. Phys. 77,* Issue 1-4, 61-73.

Jacob, D., Bärring, L., Christensen, O.B., Christensen, J.H., Hagemann, S., Hirschi, M., Kjellström, E., Lenderink, G., Rockel, B., Schär, C., Seneviratne, S.I., Somot, S., van Ulden, A., and *van den Hurk, B.,* 2007: An inter-comparison of regional climate models for Europe: Design of the experiments and model performance. *Climatic Change 81*, 31-52. doi 10.1007/s10584-006-9213-4.

Machenhauer, B., Windelband, M., Botzet, M., Christensen, J.H., Déqué, M., Jones, R.G., Ruti, P.M., and *Visconti, G.,* 1998: Validation and analysis of regional present-day climate and climate change simulations over Europe. Max Planck Institute for Meteorology, *Rep. 275*, Hamburg, Germany.

McCarthy, J.J., Canziani, O.F., Leary, N.A., Dokken, D.J., and *White, K.S.,* 2001: *Climate Change* 2001: Working Group II: Impacts, adaptation and vulnerability. Cambridge University Press, Cambridge, UK.

Roeckner, E., Lautenschlager, M., and *Schneider, H.,* 2006: IPCC-AR4 MPI-ECHAM5_T63L31 MPI-OM_GR1.5L40 SRESA1B run no.3: Atmosphere 6 HOUR values MPImet/MaD Germany. World Data Center for Climate. doi: 10.1594/WDCC/EH5-T63L31_OM-GR1.5L40_A1B_3_6H.

Sharov, V. and *K. Koleva*, 1994: Droughts in Bulgaria. *Final Project Report, VI- 19/91*, Institute of Meteorology and Hydrology of Sofia, Bulgaria.

Szilagyi, J. and *Vorosmarty, C.J.,* 1997: Water-balance modeling in a changing environment: reductions in unconfined aquifer levels in the area between the Danube and Tisza rivers in Hungary. *J. of Hydrology and Hydromechanics 45,* 348-364.

Szépszó, G. and *Horányi, A.*, 2008: Transient simulation of the REMO regional climate model and its evaluation over Hungary. *Időjárás 112*, 203-231.

Tran, L., Knight, C.G., and *Wesner, V.,* 2002: Drought in Bulgaria and atmospheric synoptic conditions over Europe. *GeoJournal 57*, 149-157.

Vidale P.L., Lüthi, D., Wegmann, R.., and *Schär, C.,* 2007: Variability of European climate in a heterogeneous multi-model ensemble. *Climatic Change 81*, 209-232, doi: 10.1007/s10584-006-9218-z.

Voigt, T., van Minnen, J., Erhard, M., Zebisch, M., Viner, D., and *Koelenmeijer, R.,* 2004: Impacts of Europe's changing climate – an indicator-based assessment. European Environmental Agency *Rep. 2,* Copenhagen, Denmark.

IDŐJÁRÁS

Quarterly Journal of the Hungarian Meteorological Service
Vol. 112, No. 3–4, July–December 2008, pp. 155–177

Validation of the ALADIN-Climate regional climate model at the Hungarian Meteorological Service

Gabriella Csima* and **András Horányi**

Hungarian Meteorological Service,
P.O. Box 38, H-1525 Budapest, Hungary
E-mails: csima.g@met.hu; horanyi.a@met.hu

(Manuscript received in final form October 28, 2008)

Abstract—Regional climate models are popular and efficient tools for the assessment of the regional aspects of the past and future climate. The application of such models is indispensable for the provision of climate simulations over a smaller region, such as Hungary. The ALADIN-Climate regional climate model was adapted by the Hungarian Meteorological Service in order to derive a regional climate model which can be used efficiently for climate change simulations over Hungary. In this paper three different recent past (1961–2000) regional climate simulations are examined and evaluated: the ERA-40-driven 10 km and 25 km resolution simulations and the ARPEGE-driven 10 km resolution simulation. Based on these investigations, the strengths and weaknesses of the simulations are analyzed in detail in order to understand the behavior and reliability of the ALADIN-Climate model for the past climate. Also, some examination regarding the sensitivity of the model with respect to the domain size and resolution was undertaken. It was demonstrated to what extent the model is capable of simulating the statistical characteristics of the climate for a 30-year period. The results obtained suggest: (1) the ALADIN-Climate model driven by ERA-40 "perfect" lateral boundaries is colder and wetter than reality for the period of 1961–1990, (2) the integration driven by the ARPEGE model slightly improved the results and, furthermore, (3) provided added value to the global model's results. Additionally it was found that (4) the 25 km simulation on a larger domain provided better results than the 10 km one using a smaller domain, which can be attributed to the fact that 10 km domain is overly small. The results also (5) justify the application of the ALADIN-Climate model for climate change scenario experiments for Hungary.

Key-words: regional climate modeling, ALADIN-Climate model, dynamical downscaling

* Corresponding author

1. Introduction

The demand for more spatially and temporally detailed weather and climate information is continuously increasing. This requirement, together with the increased availability of computer power, led to the application of more highly resolved models from the nowcasting to the climate ranges. As far as climate modeling is concerned, global and regional climate models are widely used for the simulation of the past and the future evolution of the climate system. There are three tools that have been successfully applied to bridge the gap between the low resolution global climate models and the regional and local characteristics: variable-resolution global models, statistical downscaling, and dynamical downscaling with regional climate models (RCMs). The first method allows the production of higher resolution climate information without too much additional investment in computer power with respect to the "usual" global simulations (*Brankovic* and *Gregory*, 2001; *May* and *Roeckner*, 2001; *Duffy et al.*, 2003; *Coppola* and *Giorgi*, 2005). Statistical downscaling consists of establishing statistical relationships between large scale (global) parameters as predictors and regional (local) parameters as predictands. These relationships are then applied to the global model outputs (*Kattenberg et al.*, 1996; *Hewitson* and *Crane*, 1996; *Wilby et al.*, 2004) and results in information on a regional scale. RCMs, as limited area models, cover only a portion of the planet, typically a continental or even smaller domain (*Giorgi* and *Mearns*, 1991; *McGregor*, 1997; *Giorgi* and *Mearns*, 1999; *Wang et al.*, 2004). They require lateral boundary conditions (LBCs) obtained from "observations", such as atmospheric analyses (*Uppala et al.*, 2005), or global simulations. The principal reason for performing regional simulations is to successfully simulate such regional characteristics which are "out of the reach" of the global models, therefore, providing added value through more precise representation of the different surface features, the application of the higher resolution dynamics and improved physical parameterizations.

The ALADIN limited area numerical weather prediction model (*Horányi et al.*, 1996; *Horányi et al.*, 2006) has been developed through an international cooperation and is one of the widely used limited area models in Europe. The ALADIN spectral model family is a very useful tool not only for short range weather prediction, but also for climate range simulations because of its particularly high computational efficiency. Firstly, the original short range version of the model was studied in order to check whether any spurious accumulation of systematic errors (biases) could be detected for longer integrations – it was found not to be the case (*Janisková*, 1994). Later the ALADIN-Climate model had been created by merging the physical parameterization package of the ARPEGE-Climat global climate model and the dynamics of the ALADIN model. This model was successfully adapted by the Hungarian Meteorological Service in 2005, and it has been used for

various climate experiments. Within that framework some shorter time range (3–5 years) experiments have been carried out in order to establish the most appropriate model version, the model domain, the horizontal resolution, and the spin-up time before committing to the first longer time period experiments. This first long-term experiment (1958–2000) has been performed by the Hungarian *National Climate Dynamics Programme* (*www.met.hu/palyazat/nkfp_klima2005.php*), and the second one, at a higher horizontal resolution, within the framework of the *CECILIA* (*Central and Eastern Europe Climate Change Impact and Vulnerability Assessment*) project (*www.cecilia-eu.org*).

In Section 2 a brief description of the ALADIN-Climate model is given. Section 3 introduces the model experiments, the evaluation methods, and the observational data used in the present work. Results are presented in Section 4 and the conclusions are drawn in Section 5.

2. The ALADIN-Climate model

The ALADIN-Climate model has been created with the combination of the ALADIN model's dynamics and the ARPEGE-Climat global model's physics. The ARPEGE-Climat global model has been constructed with the relevant modifications of the physical parameterization package of the ARPEGE/IFS global model (*Courtier et al.*, 1991). The ALADIN model is a spectral limited area model developed for short-range regional weather forecasting (*Horányi et al.*, 1996). Likewise the "mother" system of the ALADIN model is ARPEGE/IFS, the ALADIN-Climate's one is ARPEGE-Climat.

For the sake of completeness it has to be mentioned here that in most applications of the ALADIN model the initial and lateral boundary conditions are obtained by interpolation from the ARPEGE analysis and forecast fields. Horizontally, the model domain represents a rectangular area with uniform spacing between the grid points in both horizontal directions. Usually the tangent version of the Lambert conformal projection is used. The vertical coordinate system is a pressure-based hybrid-eta – terrain-following near the ground and converging towards a pressure-type system close to the model top (*Simmons* and *Burridge*, 1981). The model dynamics are based on the non-linear hydrostatic primitive equations. The time integration of the model includes a semi-implicit treatment of fast-propagating waves combined with the application of a semi-Lagrangian advection scheme. All of this allows a significantly larger time step to be used due to the weakened numerical stability criteria obtained in the two-time-level semi-implicit semi-Lagrangian scheme. The large scale meteorological information is imposed on the inner model solution by a classical relaxation scheme (*Davies*, 1976). With the application of an additional relaxation zone, the method is also capable of damping the artificial reflection

and transmission of small scale waves on the boundaries of the domain of interest. Model prognostic variables are zonal and meridional wind components, temperature, specific humidity, and surface pressure.

The physical parameterization package of the ALADIN-Climate model largely corresponds to the physics of the ARPEGE-Climat global model. It uses the Fouquart and Morcrette radiation scheme (FMR), which follows the concept of *Morcrette* (1989) and is based on the ECMWF model including the effects of the greenhouse gases and direct effects of aerosols based on Tegen monthly climatology. As for the land-scheme, the ALADIN-Climate model applies the ISBA (*Interaction of Soil Biosphere Atmosphere*) scheme (*Noilhan* and *Planton*, 1989), which involves four soil temperature layers without a deep relaxation, two soil moisture layers, and a single layer snow model with variable albedo and density based on *Douville et al.* (1995). The deep convection scheme follows *Bougeault* (1985), but unlike the short range version of the model, it excludes the entrainment and detrainment profiles from the description of convective precipitation processes. *Ricard* and *Royer*'s scheme (1993) is used for cloudiness and *Smith*'s scheme (1990) for large scale precipitation.

3. Experiments and evaluation

The basic objective of the recent work is to understand and assess the behavior of the ALADIN-Climate model regarding its ability to represent the climate of the recent past. Without such thorough testing the model cannot be used for providing climate simulations for the future (although the validation information based on the simulations of the past cannot be directly and explicitly applied for the "bias correction" of the scenario integrations). For this kind of evaluation, the most common approach is to integrate the model over a recent, sufficiently long period (e.g., 40 years) using "perfect" lateral boundary conditions, such as the ERA-40 dataset derived at ECMWF (*Uppala et al.*, 2005). It is noted here that the ERA-40 data are certainly not perfect in every sense – they have their own deficiencies as well (*Simmons et al.*, 2004; *Hagemann et al.*, 2005). However, they do provide one of the best estimates of the past and present climate. Furthermore, during the ERA-40-driven model integrations (due to the differences between the derivation of the ERA-40 data and the internal dynamics and physics of the ALADIN-Climate model) some unbalances might occur, arising from the boundary conditions. Nevertheless, in spite of these deficiencies, the ALADIN-Climate model integration driven by the ERA-40 data is considered to be a reliable solution for the application of the model in reproducing the recent past climate over our domain of interest.

Two model domains and resolutions were defined: a larger domain with 25 km horizontal resolution and a smaller one with 10 km resolution, both with 31 vertical levels. The domains and their orography are shown in *Fig. 1*. Both

domains were used for model integrations between 1958 and 2000, where the first three years were considered as the spin-up period, therefore, the results were evaluated only for the period 1961–2000. The smaller 10 km resolution domain was used to assess the impact of the resolution increase and domain changes as compared to the coarser resolution and larger domain integrations. A third simulation was carried out with the smaller domain for the period of 1960–1990. This integration was driven by the ARPEGE-Climat model. It is noted here that the ARPEGE-Climat boundary conditions are in much better physical and dynamical consistency with the ALADIN-Climate model, than the ERA-40 data. The ARPEGE-Climat model has a variable resolution being around 50 km over Southern Europe, decreasing to 300 km at the antipode (*Table 1*).

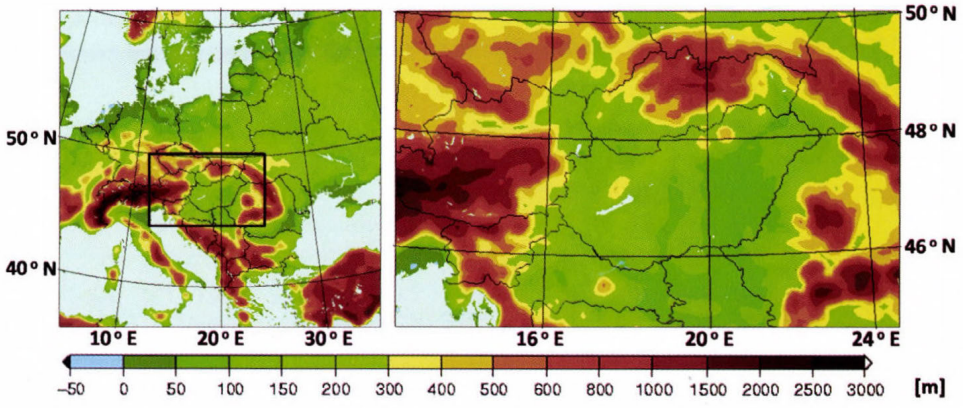


Fig. 1. The ALADIN-Climate model domain and orography for the 25 km (left) and 10 km (right) integrations.

The drawback in applying the ARPEGE-Climat model as lateral boundary condition is that it is also a simulation, which might have biases with respect to the real climate. Therefore, it is worth checking how the "perfect, but inconsistent" and the "simulated, but consistent" boundary conditions compare for the same limited area model integration. Two factors should be kept in mind while considering the length of the spin-up period for the ALADIN-Climate simulations driven by the ARPEGE-Climat model: the global lateral boundary conditions are already in good dynamical and physical balance; and there are similarities (in terms of dynamical core and physical parameterizations) between the global and limited area models. Therefore, the spin-up period for this integration was shorter than was the case for the ERA-40 run. In practice, this means that for the 1960–1990 integrations just the first year was considered as spin-up time and the 1961–1990 classical reference period was used for the evaluation. In spite of the difference in spin-up periods, it is believed that the different model simulations are fully comparable.

Table 1. Basic characteristics of the different integrations analyzed

Short name referred to in this paper	Domain	Horizontal resolution (km)	Vertical levels	Timestep (minutes)	Initial and lateral boundary conditions
ALADERA_25	lat: 35.8 – 59.3°N lon: 4.8 – 44.1°E	25	31	15	ERA-40
ALADERA_10	lat: 44.6 – 50.0°N lon: 12.4 – 25.2°E	10	31	6	ERA-40
ALADARP	lat: 44.6 – 50.0°N lon: 12.4 – 25.2°E	10	31	6	ARPEGE-Climat
ARPEGE	global model	50	31	30	–

During the evaluation the different integrations are inter-compared to each other and also compared to different observational datasets (*Table 2*). These observational data comprise both the widely used *Climatic Research Unit* (CRU) dataset (*New et al.*, 2000; *Mitchell* and *Jones*, 2005) and the *Hungarian gridded dataset* (HUGRID). The CRU data (*www.cru.uea.ac.uk*, produced by the University of East Anglia) were applied at a resolution of 10 arc minutes (CRU10, *Mitchell et al.*, 2004). HUGRID was created at the Hungarian Meteorological Service by the Meteorological Interpolation based on Surface Homogenized Data Basis (MISH) method (*Szentimrey et al.*, 2005), which was developed for the spatial interpolation of different conventional meteorological observations. These data are available for the Hungarian territory with 0.1 degree latitude-longitude resolution.

Table 2. Characteristics of the different observational data used

	Domain	Resolution
CRU10	lat: 34.0 – 72.0°N lon: 11.0°W – 32.0°E	10 arc minutes
HUGRID	lat: 45.7 – 48.6°N lon: 16.0 – 23.0°E	0.1 degree

It is important to note that for the production of the ARPEGE-Climat model driving fields for the ALADIN-Climate model, an interpolation has been done from the global resolution to the resolution of the ALADIN-Climate model (10 km). This interpolation is performed on anomaly values, where explicitly the differences between the ARPEGE-Climat model and the surface climatic values (for instance orography, albedo, emissivity, land-sea mask, etc.) of the global model are considered. After interpolation to the target grid (in this case to 10 km), the interpolated anomaly values are added to the higher resolution surface climatic values provided for the regional climate model. Based on this method, the information of the coarse resolution (50 km) global model (projected to the

regional one) also reflects high-resolution surface properties, such as higher mountains or the areas around big lakes, for example.

The evaluations are carried out through the assessment of deviations from the observations, and additionally, systematic errors and root mean square errors (RMSE) are computed. With reference to RMSE it is already anticipated here that the RCMs cannot be expected to simulate the time series of annual or seasonal means if the driving data are given by global climate model – and not a re-analysis database – since the global models are unable to provide information on individual years. The global and regional climate models are expected to simulate only the long term inter-annual variability and the average behavior of the climate system on a longer time scale (30–40 years). Consequently, it is not expected that results in terms of RMSE, the frequency distributions of the parameters or the temporal evolution charts, would be as good as those from the ERA-40-driven cases. It is also noted that the 2D-map evaluations (patterns) are computed over the domain of the 10 km resolution model, and all the other evaluations (tables, time evolution and frequency distribution figures) are made on the Hungarian territory.

4. Results

4.1. 2m temperature

It can be clearly seen (*Fig. 2*) that the models have systematic underestimation with respect to the CRU10 dataset. This temperature underestimation is generally 1–3 °C in the ERA40-driven cases (ALADERA_25 and ALADERA_10) and around 1 °C in the ARPEGE-driven (ALADARP) case and in the ARPEGE-Climat (ARPEGE) global model itself.

Looking at the results in detail, the simulations are always closer to the observations in the area of the Carpathian Basin – which is a relatively flat terrain – than in the higher mountains. Additionally, for the 10 km simulations the biggest systematic errors arise near to the model boundaries. The errors in the Alpine region are considerable in all simulations. This is attributed not only to the impact of the model boundaries (though the error is largest in the case of the 10 km simulations, where the model boundaries are near to the high mountains) but also to the orography mis-representation within both the models and the observational data sets.

Focusing only on the basin area, particularly over Hungary, the global and the ARPEGE-driven simulations are the closest to the observations – the underestimation remains under 1 °C over the largest part of the Hungarian territory. On the other hand, slight overestimation seems to occur in the eastern part of the basin, on the Great Hungarian Plain (see *Fig. 3*, where the eastern part of Hungary is zoomed and another color palette is used). This characteristic feature of the global model, as can be seen later, remains the same in the different

seasons, i.e., the ARPEGE global model is relatively warm in the Great Hungarian Plain, compared to the observations. Surprisingly, the results of the ERA-40-driven simulations are rather different from each other; the higher resolution results are more biased in general, particularly near the edges of the high resolution model domain but also over Hungary, where the underestimation is more conspicuous for the 10 km simulation. The difference between the two simulations is around 1 °C in the Hungarian territory.

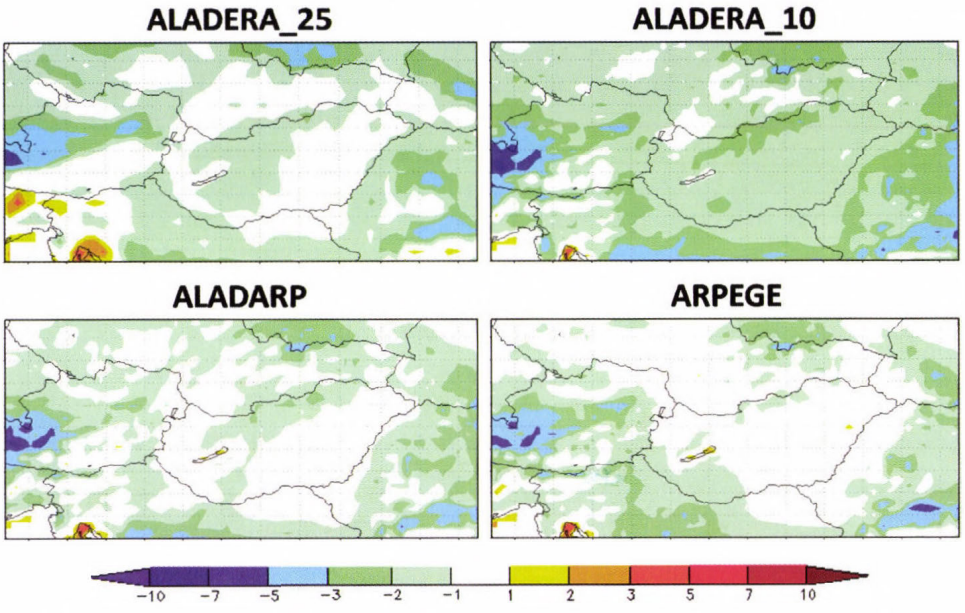


Fig. 2. Difference of annual mean temperatures (model simulation – CRU10 [°C]) for the period of 1961–1990 for ALADERA_25, ALADERA_10, ALADARP, and ARPEGE.

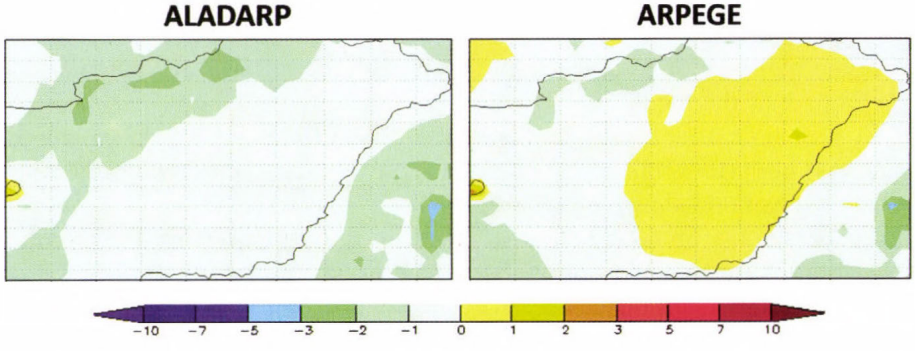


Fig. 3. Difference of annual mean temperatures in the case of ALADARP and ARPEGE (model simulation – CRU10 [°C]) for the period of 1961–1990 – zoomed over the eastern part of Hungary.

Regarding the seasonal mean temperature difference fields (*Fig. 4*) in general, the simulations are colder than the observations in the transitional seasons (spring and autumn), and are, with some exceptions, rather near to the observations in summer and winter. The systematic underestimation exceeds 5 °C in some mountainous regions and even 7–10 °C in the Alps during the transitional seasons.

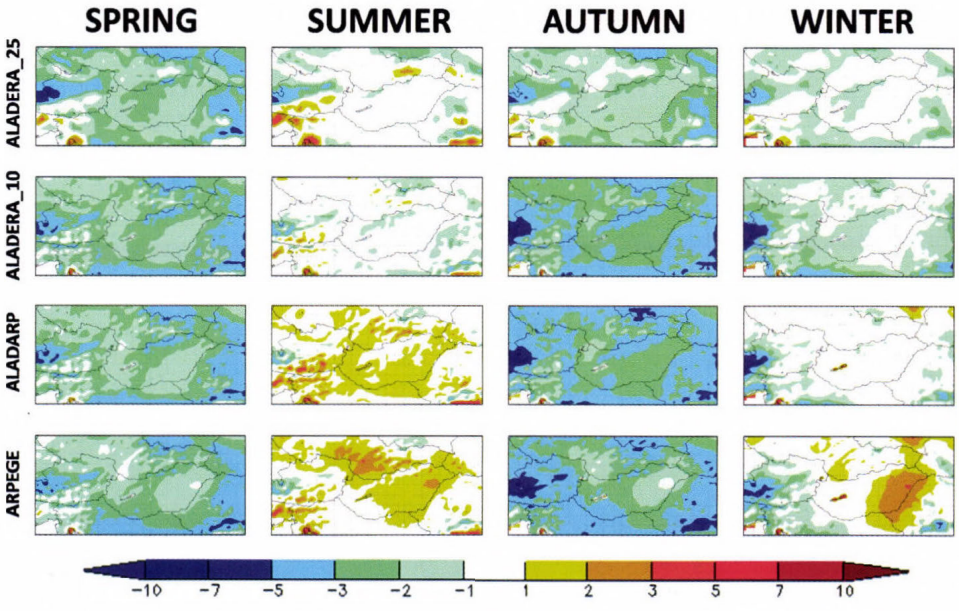


Fig. 4. Difference of seasonal mean temperatures (model simulation – CRU10) [°C]) for the period of 1961–1990 (from the top to the bottom: ALADERA_25, ALADERA_10, ALADARP and ARPEGE).

Probably due to the deficiencies of the observation datasets in the high mountains and the negative impact of the model boundaries, as in the annual case, the estimations are always closer to the observations in the fairly flat Carpathian Basin, than in the higher mountainous areas. Moreover, the biggest errors occur again near to the model boundaries in the 10 km simulations. Curiously, in the case of the ARPEGE-Climat global model (which does not suffer from any lateral boundary problem), similar large errors can also be seen at the edges of the 10 km domain, mainly in the high mountains. This is probably due to the inaccurate description of the orography.

Concentrating only on the basin area, all of the simulations give similar results in spring: the underestimation of temperature is higher than the annual systematic error; it is between 1 and 2 °C on the plains and 2–3 °C in the hills. The 25 km simulation in autumn shows relatively similar results to spring but, unexpectedly, the 10 km simulations have an even bigger negative bias. These

significant underestimations in the transitional seasons cause a slight annual negative bias in the majority of the model versions examined, even if the other seasons show positive biases. The ERA-40 forced versions are fairly unbiased during the summer – the underestimation exceeds 1 °C only in the Hungarian mountains. However, 1–2 °C overestimation can be seen in the ARPEGE and ALADARP integrations. Due to this summer overestimation, the ARPEGE-driven case and the global model have smaller annual systematic errors (almost unbiased) than the ERA-40-driven versions. While the ERA-40-driven versions are closer to the observations in summer than in winter, the ALADARP is almost perfectly unbiased in winter, and it has a relatively big overestimation in summer. The disagreement between the ARPEGE-driven ALADIN-Climate model and its driving model is largest in the coldest season. While the regional model has practically no bias, the systematic errors of the ARPEGE-Climat model exceed 2–3 °C in the eastern part of Hungary. If the difference maps of the ARPEGE-Climat model are studied more carefully, it can be seen that it has relatively large systematic errors throughout the year; however, these biases have different signs (as will be shown later, where the systematic errors are quantified) and compensate for each other during the year resulting in a rather good annual performance (*Fig. 2*). On the other hand, the "always relatively warmer" Great Hungarian Plain in the driving model decreases the bias of the model over the domain in spring and autumn, and increases it, by about 2–3 °C, in summer and even more in winter.

The systematic errors given in *Table 3* objectively quantify the evaluations based on *Figs. 2–4* for the Hungarian area. Annually, the ERA-40-driven model versions have bigger systematic errors than the global and the ARPEGE-driven ones. As mentioned above, the smallest annual bias can be found in the ARPEGE-Climat model. Although it has the coarsest horizontal resolution and the systematic errors are relatively large in every season, the biases with different signs compensate each other. The ERA-40-driven cases are better, particularly during the summer. Surprisingly, the performances of the two ERA-40 simulations are rather different in terms of bias especially in autumn, when the ALADERA_10 simulations are systematically worse than those of the ALADERA_25. The global model has a bias one order of magnitude larger than that of the driven ALADIN-Climate version for winter. As indicated earlier, the global model, throughout the year, simulates the temperature field of the Great Hungarian plain with a much larger warm bias than in other areas of the domain. This is also true when compared to the other model versions. These relatively large positive errors during summer and winter in the eastern part of Hungary cause bigger biases for the ARPEGE than in the case of ALADARP. Though it can be expected that the limited area model improves the simulations of the global model by the coupling, it is not certain that the desired "added value" is the only answer for this significant difference. While the size of the errors is bigger in the transitional seasons in all of the model cases examined, the

differences between the simulations are much larger in summer and winter; on the other hand, the models are very close to each other in spring and autumn.

The results of the models compared against CRU10 are similar to those against the Hungarian gridded dataset. The small differences can be explained by the different resolution of the two observational datasets. The differences between the two datasets are particularly emphasized in the mountainous areas, where the temperatures are lower in the HUGRID data. Consequently, when the models have negative systematic errors compared to the CRU10 dataset, the absolute values of the errors are slightly decreased with respect to the HUGRID data.

Table 3. Systematic errors of annual and seasonal simulated temperature fields against the CRU10 and the HUGRID data in the case of ALADERA_25, ALADERA_10, ALADARP, and ARPEGE experiments, in the area of Hungary for the period of 1961–1990

Temperature bias [°C]	Annual	Spring	Summer	Autumn	Winter
ALADERA_25 – CRU10	–1.05	–1.99	–0.25	–1.61	–0.66
ALADERA_10 – CRU10	–1.50	–2.12	–0.60	–2.66	–0.88
ALADARP – CRU10	–0.80	–2.01	1.06	–2.69	0.11
ARPEGE – CRU10	–0.37	–1.91	1.29	–2.27	1.11
ALADERA_25 – HUGRID	–0.89	–1.84	–0.13	–1.14	–0.36
ALADERA_10 – HUGRID	–1.41	–2.05	–0.56	–2.28	–0.72
ALADARP – HUGRID	–0.72	–1.94	1.10	–2.31	0.27
ARPEGE – HUGRID	–0.29	–1.83	1.32	–1.89	1.27

Table 4. Root mean square errors of annual and seasonal simulated temperature fields against the CRU10 and the HUGRID data in the case of ALADERA_25, ALADERA_10, ALADARP, and ARPEGE experiments, in the area of Hungary for the period of 1961–1990

Temperature RMSE [°C]	Annual	Spring	Summer	Autumn	Winter
ALADERA_25 – CRU10	1.12	2.05	0.80	1.71	1.71
ALADERA_10 – CRU10	1.55	2.17	0.89	2.71	1.26
ALADARP – CRU10	1.15	2.34	1.80	3.22	2.33
ARPEGE – CRU10	1.06	2.26	1.85	2.95	2.74
ALADERA_25 – HU	0.97	1.90	0.78	1.26	1.01
ALADERA_10 – HU	1.46	2.09	0.83	2.33	1.17
ALADARP – HU	1.13	2.31	1.82	2.95	2.37
ARPEGE – HU	1.08	2.23	1.89	2.72	2.82

In order to get a deeper insight into the behavior of the regional climate simulations, it is not sufficient to focus only on the systematic errors, since large errors of opposite sign may compensate each other resulting in a perfectly unbiased – though far from accurate – model. For instance, within the ALADERA_25 and ALADERA_10 simulations, underestimation (negative bias) occurs in every

season and, therefore, the annual bias is a relatively large negative value. On the other hand, for ALADARP the bias is changing its sign across the seasons resulting in a smaller annual bias value. Indeed, if the root mean square errors (RMSE, *Table 4*) are examined, then (for instance) the ALADERA_25 and the ALADARP annual values are rather near to each other, in spite of the fact that the bias characteristics were better for ALADARP.

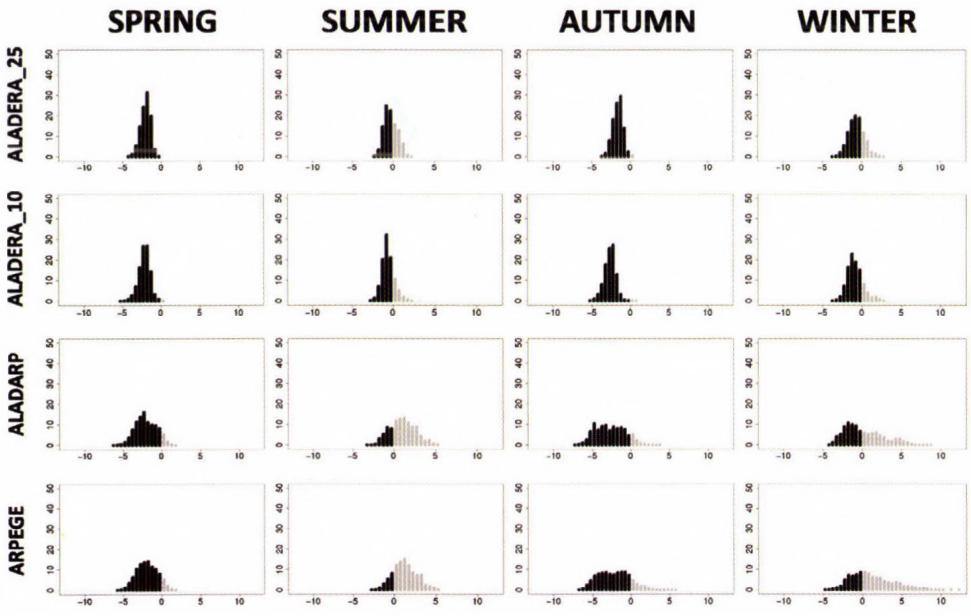


Fig. 5. Frequency distribution of seasonal temperature differences with respect to CRU10 data for ALADERA_25, ALADERA_10, ALADARP, and ARPEGE simulations. X axis: temperature difference [°C] in the range of [–10, +10]. Y axis: frequency [%] in the range of [0, 50] (gray: positive bias, black: negative bias).

Fig. 5 shows the relative frequency distributions of the seasonal temperature systematic errors, specifically, the distribution of the different amplitudes of the systematic errors, measured year by year and gridpoint by gridpoint in the different seasons. These plots indicate the amount of the positive (gray) and negative (black) biases during the 30 years in the different seasons. For these kinds of diagrams the bias is optimal if the histograms are symmetric around the zero line (the total area of the gray and black columns are the same). In those model cases, where the graph of the distribution function of the frequency is relatively narrow and high, and naturally the peak is not too far from the zero x coordinate, the RMSE is reasonably low. Where the graph is wide and low, even if the area of the positive and negative biases are the same (that is the bias of the whole period is close to zero), the RMSE is considerably high.

These kinds of charts are based on the year by year biases. The global model driven cases (and the global models themselves) are not expected to simulate the time evolution of the atmosphere during the examined period (see explanation above). Therefore, unsurprisingly, the range of the differences is much wider in the case of ALADARP and ARPEGE, than that in the ERA-40-driven cases.

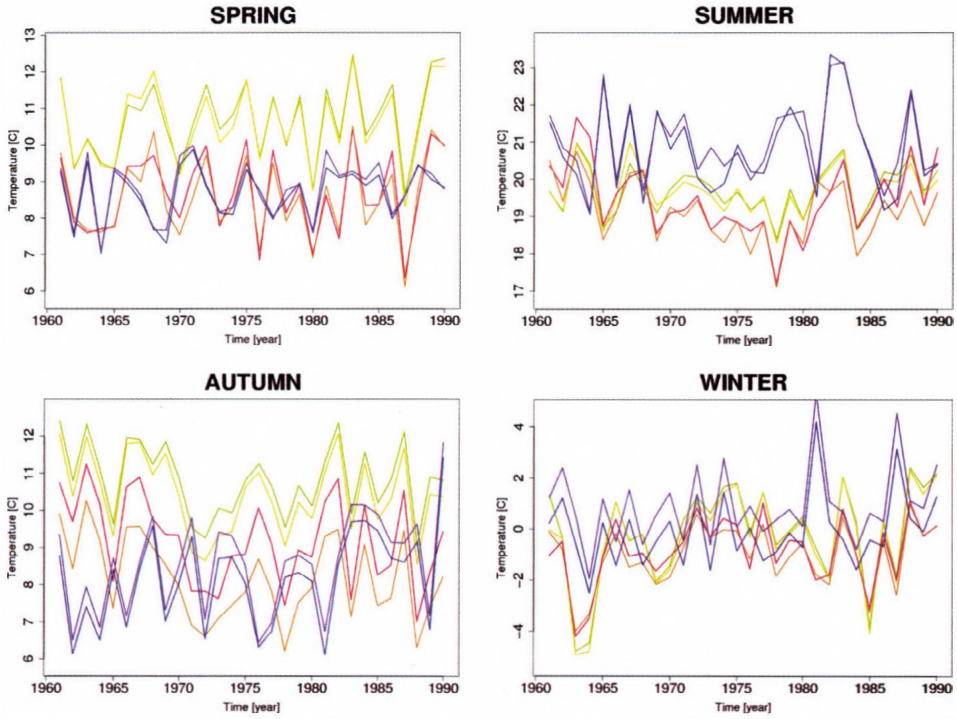


Fig. 6. Temporal evolution of the seasonal mean temperature of the examined models and observational data (CRU10: light green; HUGRID: yellow; ALADERA_25: red; ALADERA_10: orange; ALADARP: blue; ARPEGE: purple).

Correspondingly, studying the temporal evolution of the mean temperature during the 30 years examined (*Fig. 6*), the main variability features for the ERA-40-driven cases (red, orange) are naturally in good agreement with the observations (yellow and green). On the other hand, for the ARPEGE and ARPEGE-driven ALADIN-Climate (purple and blue, respectively) simulations of the variability characteristics can be evaluated only by considering the entire 30 years without any direct links to the individual years. This arises from the fact that only the global external forcing, and not the initial conditions, constrains the limited area model simulation; consequently the climate adaptation process is realized over a longer time scale.

For spring and autumn, all models underestimate the temperature in the entire period of 1961–1990. As the average distances between the different models and the observations are comparable, the models have roughly similar bias and RMSE values. On the other hand, while ARPEGE and ALADARP overestimate, the ERA-40-driven simulations underestimate the summer temperature throughout most of the years and, as in the transitional seasons, the model biases have essentially the same sign during the entire period. Therefore, smaller bias seems to indicate smaller RMSE (and vice versa) in all of the seasons except for winter. In the coldest season the ALADARP values are situated randomly under or over the observations, therefore, the systematic error is small in spite of the fact that the difference in errors between individual years can even exceed 5 °C, providing a large RMSE.

Summarizing the results for the temperature, it can be said that annually and in winter the systematic errors of the ARPEGE-driven ALADIN-Climate model seem to be lower than the reanalysis-driven models' errors. However, the results are comparable in the transitional seasons, and the ERA-40-driven versions have smaller biases than the other models in summer. As far as the RMSE and the year-by-year variability characteristics are concerned, the correlation between the ERA-40-driven cases and the observed data are obviously higher than is the case between the observations and ARPEGE or ALADARP. This fact corresponds to our initial expectations, indicating that the global model and the limited area model driven by the global one are unable to simulate the time series of annual or seasonal means. Subsequently, the frequency distributions are reasonably high and narrow in the cases of the ERA-40-driven simulations (low RMSE), and rather low and wide in the case of the ARPEGE and ALADARP ones (high RMSE).

4.2. Precipitation

From hereinafter only the ALADERA_25, ALADERA_10, and ALADARP simulations are evaluated.

Looking at the annual relative differences (the deviations between the simulations and the observations normalized by the corresponding values of the observational data), generally a 10–50% overestimation can be seen in the Carpathian Basin for all of the models investigated (*Fig. 7*). The systematic errors are much larger outside the basin, especially for the ALADERA_10 simulation. There is also an underestimation pattern appearing in the south-western part of the domain for every experiment, which is more pronounced within the high resolution model versions. The biggest errors are near to the model boundaries indicating spurious precipitation patterns originating from the lateral boundaries: it is especially true for the two 10 km integrations. Moreover, the lower resolution ALADIN-Climate model, due to the smaller biases at the edges of the visualization domain (which are not the physical boundaries in that

case), has the smallest spatial variability in terms of model bias. The best simulation for the Carpathian Basin is the ARPEGE-driven one, which obviously indicates the importance of the proper dynamical and physical balance between the coupling and coupled models. The systematic error in the southwest part of Hungary is around zero, and basically, with some small exceptions, the errors remain under 30% throughout Hungary. A patchy picture can be seen in the results of ALADERA_25, which shows slightly worse results than ALADARP, but considerably better than the high resolution ERA-40-driven run. Although the largest systematic errors can be seen in the ALADERA_10 simulation, the errors are rather small in the southwest part of the Carpathian Basin. All of this means that the resolution increase for the ERA-40-driven models does not automatically improve the performance of the simulation. It might be attributed to the difference between the resolutions of the driving and the driven models. The increase in resolution is causing more discrepancy through the lateral boundaries and furthermore the proximity of the boundaries (which are situated over mountainous regions), which might cause unrealistic precipitation fields near to them.

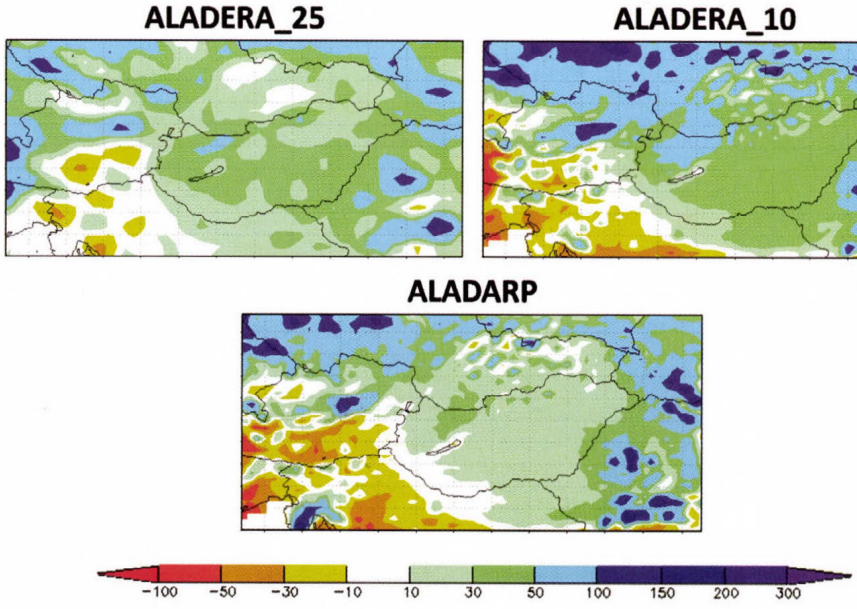


Fig. 7. Relative difference of annual mean precipitation for the period of 1961–1990 for ALADERA_25, ALADERA_10, and ALADARP (model simulation – CRU10)/CRU10 [%]).

Regarding the seasonal features in general, spring and summer are more humid than the observations in all of the simulations, and a relatively variable pattern with locally significant over- and underestimations can be seen during

autumn and winter. While the relative difference of precipitation is around zero in winter in the Carpathian Basin, very extreme positive and negative values can be seen outside the basin, near the model boundaries. The autumn features are extremely different and the best results (as for the annual situation) are in the low resolution model case. The ALADERA_10 and ALADARP simulations are rather similar, except for summer, when the ARPEGE-driven integration performs significantly better than the ERA-40-driven one. It can also be seen that all of the models (even ALADERA_25) have very variable results outside the Carpathian Basin. Inside the Basin, all simulations give similar results in spring with a general significant overestimation pattern. This positive bias is also typical for the summer for all of the models. However, there is a significant difference between the worst version (ALADERA_10) and the best one (ALADARP). During the autumn very low bias (overestimation) can be seen in the Carpathian Basin in the 25 km resolution ERA-40-driven model. The other two models have larger negative systematic errors all across the domain. Regarding the winter season, while the ALADERA_25 results are rather similar to its autumn ones, the maps of the ALADERA_10 and ALADARP models have very different features. While the models underestimate the precipitation in the southwest and overestimate it along the other parts of the domain edges, the bias in the majority part of Hungary remains reasonably good. The biggest differences between the two model results are the (positive) extremes in the eastern part of the domain.

As far as the bias values are concerned, *Table 5* reflects the Hungarian situation as can be also derived from *Figs. 7* and *8*. These values help to quantify those small differences, which are otherwise difficult to interpret subjectively.

Table 5. Systematic errors of annual and seasonal simulated precipitation fields against the CRU10 and the HUGRID data in the case of ALADERA_25, ALADERA_10, and ALADARP experiments in the area of Hungary for the period of 1961–1990

Precipitation bias [mm/months]	Annual	Spring	Summer	Autumn	Winter
ALADERA_25 – CRU10	15.31	31.11	22.06	3.56	4.50
ALADERA_10 – CRU10	18.72	33.36	49.91	–8.53	0.14
ALADARP – CRU10	9.33	31.72	15.12	–10.20	0.83
ALADERA_25 – HUGRID	15.60	30.34	23.35	4.76	4.55
ALADERA_10 – HUGRID	18.69	32.14	50.96	–7.43	–0.26
ALADARP – HUGRID	9.30	30.49	16.17	–9.11	0.44

Taking into account the fact that the global models and the global model driven simulations are able to simulate only the long term inter-annual variability, as in the case of temperature, a short review of the results of the RMSE, the frequency distribution and temporal evolution charts of precipitation is given below.

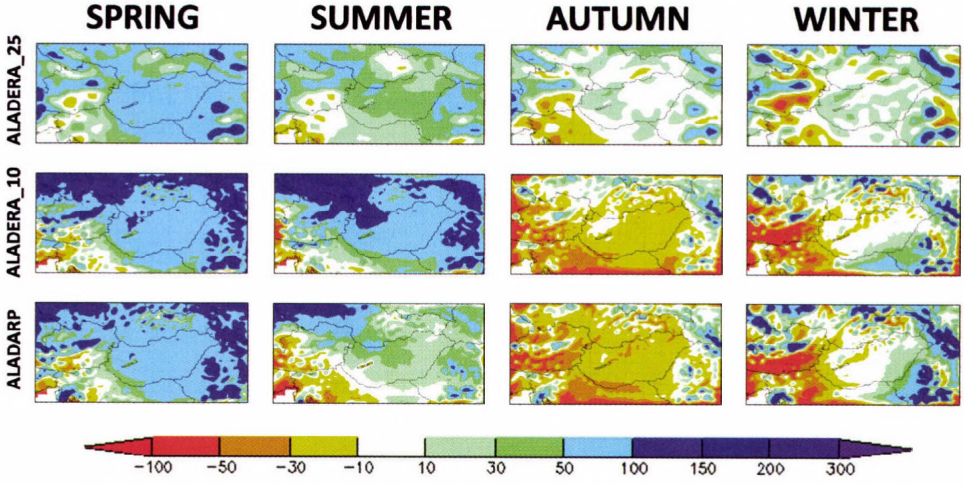


Fig. 8. Relative difference of seasonal mean precipitation for the period of 1961–1990 (model simulation – CRU10)/CRU10 [%]) (from top to the bottom: ALADERA_25, ALADERA_10, and ALADARP, respectively).

Table 6. Root mean square errors of annual and seasonal precipitation against the CRU10 and the HUGRID data in the case of ALADERA_25, ALADERA_10, and ALADARP experiments in the area of Hungary for the period of 1961–1990

Precipitation RMSE [mm/months]	**Annual**	**Spring**	**Summer**	**Autumn**	**Winter**
ALADERA_25 – CRU10	18.00	34.23	30.80	13.54	9.99
ALADERA_10 – CRU10	20.91	35.61	54.10	14.72	11.22
ALADARP – CRU10	15.58	37.12	35.58	22.09	18.25
ALADERA_25 – HUGRID	18.54	33.91	32.23	14.05	10.65
ALADERA_10 – HUGRID	21.19	34.68	55.57	14.81	12.78
ALADARP – HUGRID	16.39	36.36	37.04	22.75	19.89

As already explained and demonstrated for temperature, the small bias may not indicate small RMSE values due to the possible cancellation effects arising from the bias computations. In order to illustrate this feature for precipitation as well, the winter values of ALADARP and ALADERA_25 are considered. While the ALADARP experiment possesses a rather small bias value (0.83), the ALADERA_25 is characterized by a larger one (4.5). On the other hand the RMSE of ALADERA_25 is significantly lower (9.99) than in the case of ALADARP (18.25). Essentially, small bias corresponds to large RMSE (*Table 6*) and vice versa. That is because the ALADERA_25 integration has significant systematic overestimation – which is present for a large part of the domain in the majority of the years and in basically all the seasons –, but it does not manifest

itself in big RMSE values because the overestimation values are not too big. In contrast, ALADARP results have very small systematic error, but significant RMSE values, at the same time, because there are significant errors of different signs across the domain and throughout the different seasons during the period studied.

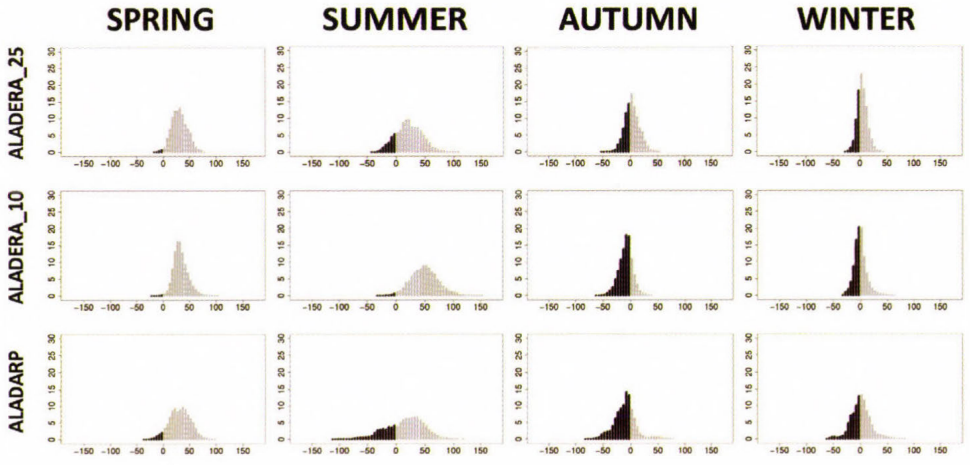


Fig. 9. The frequency distribution of seasonal precipitation differences with respect to CRU10 data for ALADERA_25, ALADERA_10 and ALADARP. X axis: difference of precipitation [mm] in the range of [–150, +150]. Y axis: frequency [%] in the range of [0, 30] (black: negative bias, gray: positive bias).

The same issue can be also seen, while looking at the frequency distribution of seasonal precipitation differences (*Fig. 9*). The two histograms for ALADERA_25 and ALADARP in winter are rather different: narrow, high, and asymmetric for ALADERA_25 and lower, wider, and more symmetric for ALADARP. There is an annual variation of the frequency distribution in every experiment; the histograms are relatively high and narrow in winter and low and wide in summer. This fact confirms that the general predictability of precipitation is much higher in winter than in summer. Although, the histogram of ALADARP is slightly lower and wider than the ALADERA_10's one in the warmest season, its RMSE remains smaller than that of the ALADERA_10. This is because the systematic errors of ALADARP are around zero and the errors are not extremely big, and in the case of ALADERA_10 the absolute errors are rather high and they are mostly realized in overestimations.

Regarding the seasonal mean precipitation variation (*Fig. 10*), it can be seen that, as expected, the two kinds of observations (CRU10 and HUGRID in green and yellow) run together. Also the trends of the ERA-40-driven cases (red, orange) are similar to the observational ones. Particularly, the maximum and minimum values are roughly at the same places, although the correlation,

particularly during summer, is not as good as was the case for temperature. As ALADARP cannot represent the observed series of year (see Sect. 3), the behavior of the ALADARP simulation (blue) is rather different to the ERA-40-driven cases. During spring, all models overestimate the precipitation for every year of the period 1961–1990. For summer, the picture is more chaotic: the high resolution ERA-40-driven results are relatively far from the observations, while the lower resolution version is closer to reality. Nevertheless, the two curves are still basically parallel. In autumn the ERA-40-driven versions have some bias – the low resolution model overestimates and the high resolution one underestimates the precipitation. However, the differences are smaller than in spring and summer, hence the RMSE and bias values are lower. The correspondence between the different experiments and the observations is best during winter. This fact is also apparent on the rather high and narrow (i.e. small errors) distribution functions in that season (*Fig. 9*).

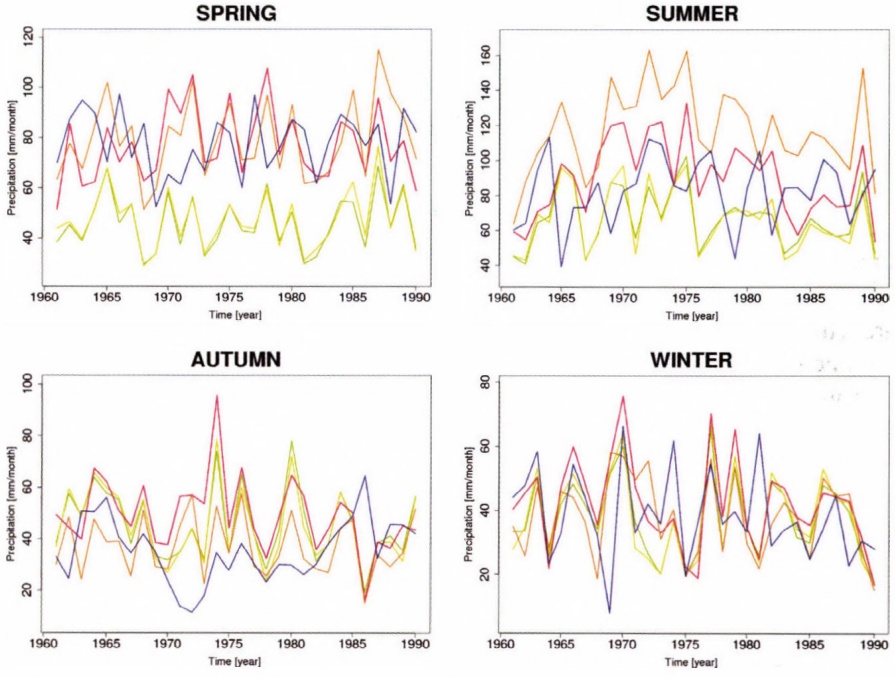


Fig. 10. The temporal evolution of the seasonal mean precipitation of the examined models and observational data (CRU10: light green; HUGRID: yellow; ALADERA_25: red; ALADERA_10: orange; ALADARP: blue).

In summary, the results of the simulated precipitation over the Carpathian Basin show that ALADARP is the best annually and in the extreme seasons. Regarding the RMSE and the inter-annual characteristics, the correlation

between the ERA-40-driven cases and the observed data is unsurprisingly higher than is the case for the ARPEGE-driven simulation. On the other hand, the low resolution ERA-40-driven case (ALADERA_25) has better verification characteristics than that of the high resolution re-analysis-driven case (ALADERA_10).

5. Conclusions

The aim of this paper was to give a comprehensive analysis of temperature and precipitation fields of the ALADIN-Climate model "family" integrated at the Hungarian Meteorological Service. Four different kinds of simulation have been investigated in the case of temperature, and three in the case of precipitation. These simulations are the 25 km resolution ALADIN-Climate (LBC: ERA-40), the 10 km resolution ALADIN-Climate (LBC: ERA-40), the 10 km resolution ALADIN-Climate (LBC: ARPEGE-Climat) and, only in the case of temperature, the ARPEGE-Climat model. It was considered essential to explore the behavior of the available climate models for the recent past, since valuable information can be expected from the simulations of the future only if the main characteristics of the models are well known and its strengths and weaknesses are explored. This statement is true in spite of the well-known fact that the error characteristics for the past might not have any relation with those for the scenario runs. Moreover, it is also generally accepted that changes in the future are computed with respect to the same model simulations for the past. This technique implicitly assumes that the same error characteristics occur in the past as for the future (this fact cannot be verified and most probably is not true), hence the difference between the absolute fields automatically neglects those errors.

It was largely illustrated that the global climate models, and those regional climate models that are driven by global models, are not expected to simulate the time series of annual or seasonal means (only the long term inter-annual variability), since the global models do not provide any information on real years. Nevertheless, it is expected from all of the model versions that the average behavior of the atmosphere is reasonably well simulated for a longer time period (typically 30 years).

The figures and tables in this paper illustrated that the ARPEGE-driven version and even the driving model, in general, give better results in the Carpathian Basin for the whole period (1961–1990), than the ERA-40-driven versions. These results are certainly due to the much better physical and dynamical consistency between the ALADIN-Climate and ARPEGE-Climat models than between the limited area model and the ERA-40 data. Moreover, the coupled ALADARP gives better results than its mother model (the ARPEGE-Climat global model), providing the anticipated "added value" by the application of the higher resolution regional climate model.

The examination and comparison of the two "observation-driven" cases helps to draw some conclusions about the sensitivity of the simulations with respect to the domain size and resolution. The realization, that the lower resolution model (in a bigger domain) gives better results than the higher resolution one (in a smaller domain), points to the fact that the domain of the 10 km resolution model is too small, and the errors appearing at the edges of the model domain have a strong effect on the simulation of the inner area as well.

Finally, based on all of these results, we are tempted to conclude that the results of the ARPEGE-driven regional model – even in this small domain – might be used for making reasonably good projections for the future. If this "climate shift" or "climate transformation" of the investigated regional model is fairly comparable to other models known from different projects (e.g., ENSEMBLES (*ensembles-eu.metoffice.com*), PRUDENCE (*prudence.dmi.dk*), etc.) in low resolution, then this provides some reassurance that the model examined will probably provide reliable results and can be used in the future at higher resolution as well.

The future work will concentrate both on the issue of the optimal domain size and resolution for the Central-European climate simulations and on the scenario runs together with their evaluations for the determination of climate scenarios for the Hungarian territory.

Acknowledgements—The authors are very grateful to all of the colleagues of the international ALADIN cooperation for the development of the ALADIN model. Special thanks are given to *Michel Déqué* and *Samuel Somot* for their constant support and guidance, while adapting the ALADIN-Climate model and later for answering questions during the experimentation. The fruitful discussions with the members of the Division for Numerical Modeling and Climate Dynamics of the Hungarian Meteorological Service and all of their valuable help are highly appreciated. The adaptation and first experiments with the ALADIN-Climate model in Hungary were undertaken by *Helga Tóth* and *Andrea Lőrincz*: the authors are indebted to them for all of their work related to the ALADIN-Climate model. Many thanks for *Gábor Radnóti* for useful comments on parts of the manuscript, which helped significantly on the general understanding of the capabilities of the regional climate models. Special thanks are due for the careful revision work of *Tamás Práger*, which significantly contributed to the improvements of the manuscript. The other reviewer's comments were also appreciated and helped while revising the paper. Many thanks for *Karl Kitchen* for the significant improvement of the English of the manuscript. This work was supported by the European Commission's 6th Framework Programme in the framework of CECILIA project (contract number 037005), the Hungarian National Office for Research and Technology (NKFP, grant No. 3A/082/2004), and the János Bolyai Research Scholarship of the Hungarian Academy of Science.

References

Bougeault, P., 1985: A simple parameterization of the large-scale effects of cumulus convection. *Mon. Weather Rev. 113*, 2108-2121.

Brankovic, T. and *Gregory, D.*, 2001: Impact of horizontal resolution on seasonal integrations. *Clim. Dynam. 18*, 123-143.

Coppola, E. and *Giorgi, G.*, 2005: Climate change in tropical regions from high-resolution time slice AGCM experiments. *Q. J. Roy. Meteor. Soc. 131*, 3123-3145.

Courtier, Ph., Freydier, C., Geleyn, J.-F., Rabier, F., and *Rochas, M.*, 1991: The ARPEGE project at Météo-France. In *Proc. ECMWF Workshop on Numerical Methods in Atmospheric Modelling*. 9-13 Sept 1991. *Vol. 2*, 193-231.

Davies, H.C., 1976: A lateral boundary formulation for multi level prediction models. *Q. J. Roy. Meteor. Soc.102*, 405-418.

Douville, H., Royer, J.-F., and *Mahfouf, J.-F.*, 1995: A new snow parametrization for the Météo-France climate model. Part I: Validation in stand-alone experiments. *Clim. Dynam. 12*, 21-35.

Duffy, P.B., Govindasamy, B., Iorio, J.P., Milovich, J., Sperber, K.R., Taylor, K.E., Wehner, M.F., and *Thompson S.L.*, 2003: High-resolution simulations of global climate. Part 1: Present climate. *Clim. Dynam. 21*, 371-390.

Giorgi, F. and *Mearns, L.O.*, 1991: Approaches to regional climate change simulation: A review. *Rev. Geophys. 29*, 191-216.

Giorgi, F. and *Mearns, L.O.*, 1999: Introduction to special section: Regional climate modelling revisited. *J. Geophys. Res. 104* (D6), 6335-6352.

Hagemann, S., Arpe, L., and *Bengtsson, L.*, 2005: Validation of the hydrological cycle of ERA40. *ERA-40 Project Report Series,* 24, Reading, UK.

Hewitson, B.C. and *Crane, R.G.*, 1996: Climate downscaling: Techniques and application. *Climate Res. 7*, 85-95.

Horányi, A., Ihász I., and *Radnóti, G.*, 1996: ARPEGE/ALADIN: A numerical weather predicition model for Central-Europe with the participation of the Hungarian Meteorological Service. *Időjárás 100*, 277-300.

Horányi A., S. Kertész, L. Kullmann, and *G. Radnóti*, 2006: The ARPEGE/ALADIN mesoscale numerical modeling system and its application at the Hungarian Meteorological Service. *Időjárás 110*, 203-227.

Janisková, M., 1994: Study of the systematic errors in ALADIN associated to the physical part of the model. *Note ALADIN n°7*, CNRM, Météo-France, 82 pp.

Kattenberg, A., Giorgi, F., Grassl, H., Meehl, G.A., Mitchell, J.F.B., Stouffer, R.J., Tokioka, T., Weaver, A.J., and *Mitchell, T.M.L.*, 1996: *Climate Models*. Projections of future climate. In *Climate Change* 1995: The science of climate change. Second assessment report of the IPCC: Contribution of WG1 (eds.: *J.F. Houghton, G. Meira, B.A. Callander, N. Harris, A. Kattenberg, K. Maskell*). Cambridge University Press, 285-357.

McGregor, J.L., 1997: Regional climate modelling. *Meteorol. Atmos. Phys. 63*, 105-117.

Mitchell, T.D., Carter, T.R., Jones, P.D., Hulme, M., and *New, M.*, 2004: A comprehensive set of high-resolution grids of monthly climate for Europe and the globe: the observed record (1901-2000) and 16 scenarios (2001-2100). *Working Paper 55*. Tyndall Centre for Climate Change Research, University of East Anglia, Norwich, UK.

Mitchell, T.D. and *Jones, P.D.*, 2005: An improved method of constructing a database of monthly climate observations and associated high-resolution grids. *Int. J. Climatol.* 25, 693-712.

May, W. and *Roeckner, E.*, 2001: A time-slice experiment with the ECHAM4 AGCM at high resolution: The impact of horizontal resolution on annual mean climate change. *Clim. Dynam. 17*, 407-420.

Morcrette, J.-J., 1989: Description of the Radiation Scheme in the ECMWF Model. *Technical Memorandum*, 165, ECMWF, 26 pp.

New, M., Hulme, M., and *Jones, P.D.*, 2000: Representing twentieth century space-time climate variability. Part 2: development of 1901–96 monthly grids of terrestrial surface climate. *J. Clim. 13*, 2217-2238.

Noilhan, J. and *Planton, S.*, 1989: A simple parametrization of land surface processes for meteorological models'. *Mon. Weather Rev. 117*, 536-549.

Ricard, J.-L. and *Royer, J.-F.*, 1993: A statistical cloud scheme for use in a AGCM. *Ann. Geophysicae 11*, 1095-1115.

Simmons, A.J. and *Burridge, D.M.*, 1981: An energy and angular-momentum conserving finite-difference scheme and hybrid vertical coordinates. *Mon. Weaather Rev. 109*, 758-766.

Simmons, A.J., Jones, P.D., and *da Costa Bechtold, V.*, 2004: Comparison of trends and variability in CRU, ERA-40 and NCEP/NCAR analysis of monthly-mean surface air temperatures. *ERA-40 Project Report Series 18. R*eading, UK, ECMWF Re-Analysis Project. 38p.

Smith, R.N.B., 1990: A scheme for predicting layer clouds and their water content in a general circulation model. *Q. J. Roy. Meteor. Soc. 116*, 435-460.

Szentimrey, T., Bihari, Z., and *Szalai, S.*, 2005: Meteorological Interpolation based on Surface Homogenized Data Basis (MISH). *Geophys. Res. Abstracts 7*, 2005.

Uppala, S.M., Kållberg, P.W., Simmons, A.J., Andrae, U., da Costa Bechtold, V., Fiorino, M., Gibson, J.K., Haseler, J., Hernandez, A., Kelly, G.A., Li, X., Onogi, K., Saarinen, S., Sokka, N., Allan, R.P., Andersson, E., Arpe, K., Balmaseda, M.A., Beljaars, A.C.M., van de Berg, L., Bidlot, J., Bormann, N., Caires, S., Chevallier, F., Dethof, A., Dragosavac, M., Fisher, M., Fuentes, M., Hagemann, S., Hólm, E., Hoskins, B.J., Isaksen, L., Janssen, P.A.E.M., Jenne, R., McNally, A.P., Mahfouf, J.-F., Morcrette, J.-J., Rayner, N.A., Saunders, R.W., Simon, P., Sterl, A., Trenberth, K.E., Untch, A., Vasiljevic, D., Viterbo, P., and *Woollen, J.*, 2005: The ERA-40 re-analysis. *Q. J. Roy. Meteor. Soc. 131*, 2961-3012.

Wang, Y., Leung, L.R., McGregor, J.L., Lee, D.K., Wang, W.C., Ding, Y., and *Kimura, F.*, 2004: Regional climate modeling: Progress, challenges, and prospects. *J. Meteor. Soc. Japan 82*, 1599-1628.

Wilby, R.L., Charles, S.P., Zorita, E., Timbal, B., Whetton, P., and *Mearns, L.O.*, 2004: *Guidelines for Use of Climate Scenarios Developed from Statistical Downscaling Methods.* IPCC Data Distribution Centre, University of East Anglia, U.K., 27pp.

IDŐJÁRÁS

Quarterly Journal of the Hungarian Meteorological Service
Vol. 112, No. 3–4, July–December 2008, pp. 179–190

Analysis of heavy precipitation for France using high resolution ALADIN RCM simulations

Michel Déqué and **Samuel Somot**

Météo-France CNRM, CNRS/GAME,
42 avenue Coriolis, 31057 Toulouse, France; E-mail: deque@meteo.fr

(Manuscript received in final form October 24, 2008)

Abstract—A high resolution version of ALADIN over France is analyzed here in 30-year ERA-40-driven simulations. It is demonstrated that a resolution of 12 km improves some features of the mean precipitation field with respect to the same version at 50 km resolution. This version improves also the representation of precipitation upper quantiles in summer by producing less high precipitation rates.

Key-words: extreme events, precipitation, regional climate modeling, horizontal resolution, France

1. Introduction

Successful reproduction of large-scale features of climate, such as pole-to-equator gradient or location of main subtropical anticyclones from a set of equations, is a great challenge of numerical modeling. The average public, however, is little concerned. Similarly, predicting a global warming of 2 °C if carbon dioxide concentration doubles is little informative for the scientific impact community. The simulation of features at the scale of human activities, like the geographical distribution of precipitation over a country, is much more interesting for decision makers.

Regional climate modeling is thus an important issue. Climate simulation with a purely local model is not possible, except in idealized experiments, since the atmosphere has no borders. The first climate models were global or at least hemispheric (*Kasahara* and *Washington*, 1967; *Manabe et al.*, 1965). With increasing computer resources in the last decades, modelers have refined more and more the resolution of the general circulation models (GCMs). Increasing horizontal resolution corresponds to two categories of needs:

1) allowing a more accurate discretization of the Navier-Stokes equations which cannot be solved analytically; this also applies for vertical or time resolution: the higher the resolution, the closer the discretized solution to the exact solution,
2) enabling a better representation of surface forcing and, as a consequence, the meso- and synoptic scales.

In case 1) the minimum resolution seems to be 300 km, but further increases modify only to a limited extent the large-scale atmospheric circulation (*Sperber et al.*, 1994). This explains why during a quarter of century, GCMs have been run at that resolution. In case 2) there is no mesh size limit, since the scales of the forcing extend up to 1 km (mountain) and even to 1 mm (canopy).

Limited area climate models appeared some 25 years after the GCMs (*Giorgi*, 1990). An additional reason for the need of higher resolution in the 1990s was the availability of atmospheric reanalyses at typically 100 km resolution (ERA-40, *Uppala et al.*, 2005). Indeed, one can use regional climate models (RCMs) at high resolution as intelligent "interpolators" to produce data in area where observations are scarce or doubtful. Another recent and practical reason for higher horizontal resolution is the need by hydrologists for climate simulations taking into account surface elevation in the best possible agreement with their drainage basin. In a pioneer study, *Christensen et al.* (1998) showed that a LAM at high resolution (20 km) was able to produce intense local precipitation events which were not grid point storms.

The ALADIN model is a limited area version of the ARPEGE-IFS forecast system. It has been used in numerical weather prediction by a wide community since the 1990s (*Bubnova et al.*, 1995) and more recently in regional climate modeling (*Radu et al.*, 2008; *Farda et al.*, 2008). In the framework of the CECILIA European project presented in this special issue, ALADIN has been used at 10 km resolution over three domains, Czech Republic, Hungary, and Bulgaria. In the present study, we analyze a similar experiment with ALADIN covering a domain over France, with special emphasis on extreme precipitation. Although this study is not formally part of the CECILIA project, it has permitted to explore and extend the capacities of ALADIN to simulate climate at high resolution.

In this paper we want to investigate whether the ARPEGE-climate physical parameterizations, which has been developed for spatial scales between 50 km and 300 km, are still valid at higher resolution. In addition, we wish to verify if the increase in resolution can produce some details, which make the model closer to observation. We do not analyze the temperature field because:

- due to the small size of the integration domain, temperature is largely controlled by advection from the lateral boundary conditions,
- the small-scale details are easy to mimic by simple surface elevation correction (the maps of mean screen level temperature present strong similarities with the pattern of the orography map).

Simulating precipitation is a harder challenge, and the present paper will address this field, with a special attention to heavy daily precipitation.

The paper is organized as follows: in Section 2, we present the experiments and validation data. In Section 3, we validate seasonal mean precipitation. In Section 4, we examine the probability distribution function of daily precipitation, and we focus on its tail in Section 5. Then we conclude in Section 6.

2. Experiments and data

ALADIN is a limited area model issued from the ARPEGE-IFS software developed at Météo-France and ECMWF. Proper references have been given in the previous section. More specifically, here we use version 4.6 of the climate model which is based on cycle 24 of ARPEGE-IFS. Two model discretizations are used here: one with 50 km resolution, the other with 12 km resolution. The two integration domains have the same center, which is also the center of the Lambert projection (2°E, 47°N). The relaxation-free area is shown in *Fig. 1* (solid line for the 12 km resolution, dashed line for the 50 km resolution). The higher resolution domain is larger than the lower resolution one, because the relaxation zone is narrower (8 grid points on each side in both cases).

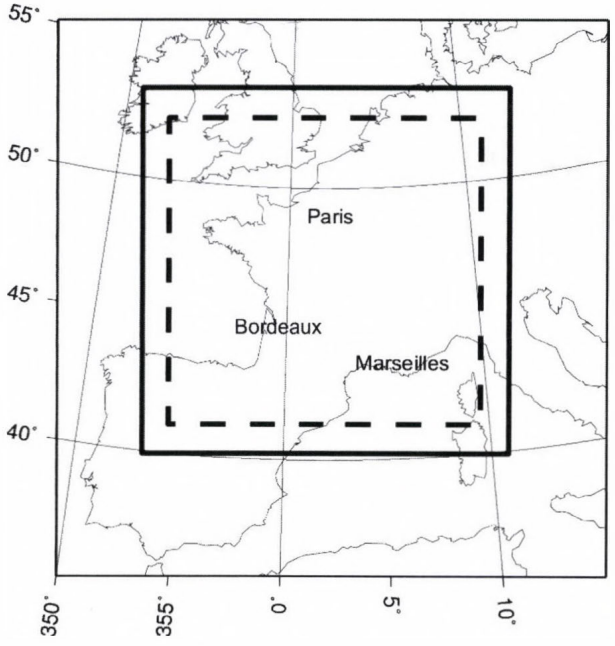


Fig. 1. Integration domain of the two ALADIN versions where no Davies relaxation is applied (i.e., without the 8 rows at each border): FR12 (solid) and FR50 (dashed).

The total number of grid points is 50 by 50 for the 50 km version, referred to as FR50 in the following and 150 by 150 for the 12 km version, referred to as FR12 in the following. There are 31 vertical levels in both cases, and the time step is 15 min for FR50 and 10 min for FR12. Except for mesh size and time step, the two versions have exactly the same physical parameterizations described in *Radu et al.* (2008).

A 41-year simulation has been carried out with each model (1960–2000). The 6-hourly lateral forcing is ERA-40 reanalysis (*Uppala et al.*, 2005). We examine here only 30 years (1971–2000) of both simulations. We have at disposal a high resolution (8 km grid) reanalysis over France since 1971 (*Quintana-Segui et al.*, 2008). Such a dataset, named SAFRAN, is essential to evaluate the added value of 12 km resolution versus 50 km resolution (*Déqué* and *Somot*, 2008). It has been obtained by optimal interpolation of all climatological stations over France, so the true resolution (distance between two actual observations) is rather 30 km on average. In a numerical model, the true resolution is also coarser than the mesh size, because of numerical diffusion. We have also used raw observations from three rain-gauge series to validate the SAFRAN series (see Section 4).

In order to make an easy comparison between three different resolutions, first we have selected the land grid points of FR50, which are located in the French metropolitan territory. Then, for FR12 and SAFRAN, each land grid point is associated to the nearest neighbor in the FR50 restricted grid. All FR50 grid points which have less than 12 neighbors in FR12 or less than 20 neighbors in SAFRAN are eliminated. Finally, we retain, for each FR50 remaining point 12 neighbors for FR12 and 20 neighbors with SAFRAN. We have thus 166 boxes containing each 1 point of FR50 grid, 12 points of FR12 grid, and 20 points of SAFRAN grid. These numbers of 12 and 20 are a trade-off to keep the maximum number of boxes with the maximum of points inside: if we had imposed more points in the boxes, we would have got less boxes. This selection avoids sampling artifacts in coastal or border regions by ensuring equi-populated boxes. Indeed, the variance of box-averages decreases with the size of the box, and we could get higher extremes with small-populated boxes.

3. Seasonal mean precipitation

Let us first consider 30-year averages for each season. *Fig. 2* shows the precipitation distribution over France in summer (JJA) for SAFRAN, FR50, and FR12. The model is too wet, but reproduces the main geographical contrasts, and increasing resolution does not increase precipitation (a feature often observed in ARPEGE GCM). The model precipitation rates are too large over high mountains (Alps and Pyrenees). One can see that the pattern of Massif Central precipitation (just south to the center of France) is improved by higher resolution (unrealistic double maximum in FR50).

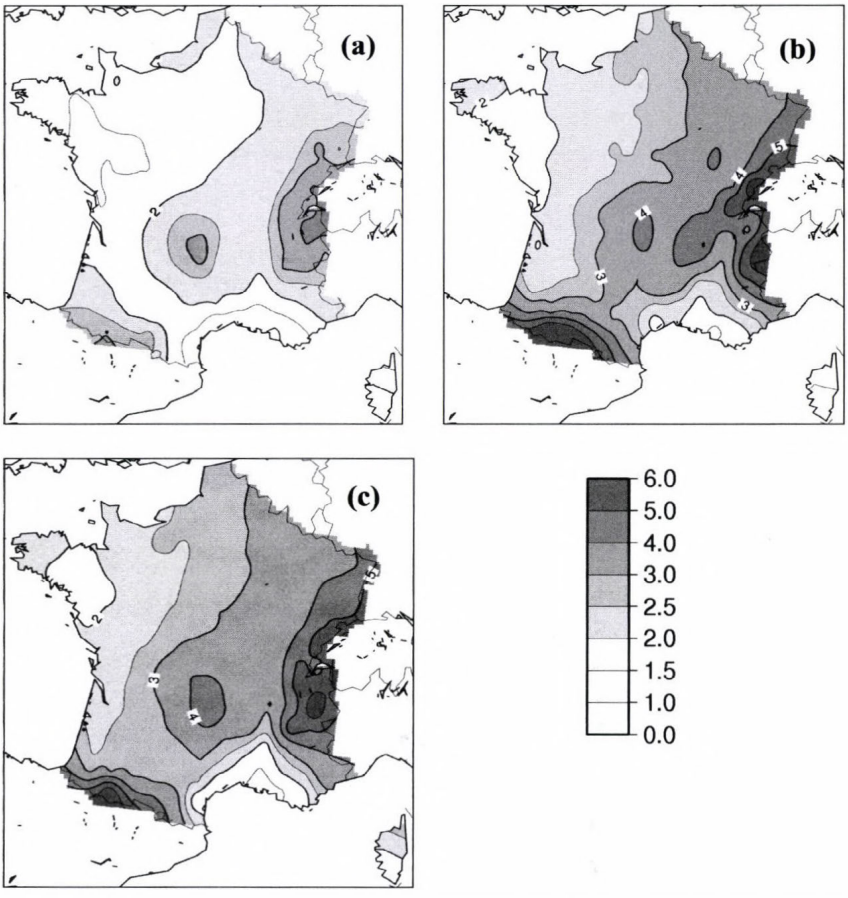


Fig. 2. Mean summer precipitation for SAFRAN (a), FR50 (b) and FR12 (c). Contours: 1, 1.5, 2, 2.5, 3, 4, 5 and 6 mm/day.

To make the comparison more accurate, precipitation is averaged in each box (see previous section for definition of the 166 boxes), and root mean square error (RMSE) is calculated for each season with respect to SAFRAN. *Table 1* shows the results. In each season, the higher resolution is superior to the lower one. The improvement is not spectacular, but systematic.

Table 1. Root mean square error of precipitation (mm/day) over France for seasonal means with the two ALADINs versions calculated on 50 km × 50 km averages.

	DJF	**MAM**	**JJA**	**SON**
FR50	0.72	1.37	1.32	0.76
FR12	0.65	1.24	1.16	0.59

4. Precipitation probability density functions

In order to evaluate the precipitation probability density function (pdf), quantile-quantile (q-q) diagrams of ALADIN and SAFRAN versus observation are plotted for three French cities. Paris is representative of the climate of the northern half of France. In the southern half, due to the presence of Massif Central mountains and Mediterranean sea, two climates are observed: Bordeaux is representative of the oceanic climate, whereas Marseilles is representative of the Mediterranean climate. In fact, Bordeaux and Paris climates are not so different, but there is a latitudinal and continental gradient at a time between the two cities. The location of the three cities is indicated in *Fig. 1*.

We consider here daily precipitation over 30 years. Each calendar season is analyzed separately. The quantile resolution is 1/1000 (probabilities between 0.1 and 99.9%). Three methods have been used to evaluate the quantiles in the boxes.

- Method 1 consists of averaging precipitation in each of the 3 boxes closest to the 3 cities, as we did in last section for RMSE over whole France. This method favors the extremes in FR50, because no spatial averaging is performed before sorting daily precipitation.
- Method 2 consists of computing quantiles for each model grid point, whatever the resolution. Then the quantiles are averaged for all grid points of a given box. This allows a fairer comparison between two resolutions, because no preliminary damping of high resolution data is applied before sorting.
- Method 3 consists of sorting the daily precipitation data of all points inside a box (pooling). This allows a better sampling of higher quantiles in high resolution data.

For FR50, the three methods are identical, because there is only one grid point per box. This is also the case with observations: we have a single time series for each city. In order to better capture the differences between the three methods, let us use the following notations:
R_{ijk} is precipitation for box i (i = 1,3 for the closest box to Paris, Bordeaux, and Marseilles), grid point j (j = 1,20 for SAFRAN grid, j = 1,12 for FR12 grid, and j = 1 for FRA50 grid), and day k (k takes about 2700 values depending on the season). A^x means averaging for index x ($x = j$ or k) and S^x means sorting with respect to index x.

- Method 1 computes $S^k(Aj(R_{ijk}))$.
- Method 2 computes $A^j(Sk(R_{ijk}))$.
- Method 3 computes $S^{jk}(R_{ijk})$.

From statistical point of view, methods 2 and 3 evaluate the same quantity, provided that each box is homogeneous. Method 3 is more accurate, in particular for extreme values, whereas Method 2 allows to calculate a confidence interval

with some hypotheses. For our three cities, Methods 2 and 3 give similar results, whereas Method 1 provides systematically less precipitation rates, because of spacial averaging of wet and dry grid points.

Fig. 3 shows the q-q plots for DJF and JJA obtained by Method 3. For the three locations, SAFRAN provides a pdf in good agreement with raw station data (except for Paris JJA beyond 99% quantile). This indicates that the SAFRAN interpolation algorithm is not detrimental to high precipitation events. FR12 provides systematically less precipitation than FR50, whatever the quantile. Both models are generally below the diagonal of the diagram, indicating less precipitation than observed, except for summer precipitation below 5 mm/day, where both models exaggerate the quantities.

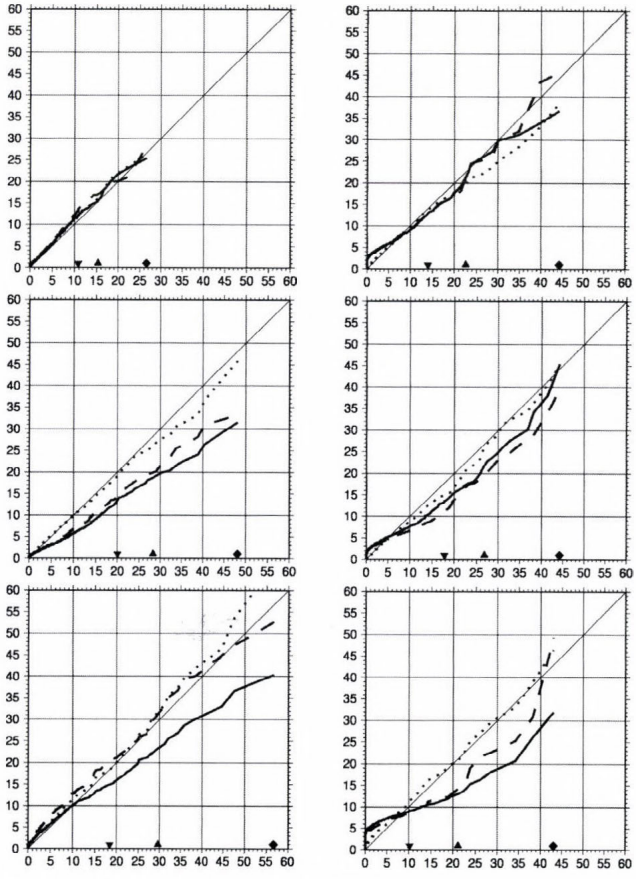


Fig. 3. Quantile-quantile plots of winter (left) and summer (right) daily precipitation (mm/day). Observed quantiles are sorted along the x-axis and model/analysis quantiles are sorted along the y-axis. Solid line corresponds to FR12, dashed line to FR50, and dotted line to SAFRAN. Top panels correspond to Paris, medium panels to Bordeaux, and bottom panels to Marseilles. The 99.9%, 99%, and 97.5% observed quantiles are indicated along the x-axis by a diamond, a triangle, and an inverted triangle, respectively.

From this first analysis, it appears that we can rely upon SAFRAN data for precipitation pdf, that FR12 and FR50 behave similarly for Paris and Bordeaux, but FR12 is worse than FR50 for Marseilles.

5. *Heavy precipitation events*

In order to make a more systematic comparison over France without inflating the paper with maps, we must use a quality criterion. The ranked probability score (*RPS*, *Epstein*, 1969) is well adapted to pdf comparison for variables like precipitation. It is widely used in probability forecast evaluation. It is simply based on the euclidean distance between the cumulated density functions (cdf) for a set of thresholds t_i, $i = 1, n$:

$$RPS = \sum_{i=1}^{n} [\mathrm{Prob}(MOD < t_i) - \mathrm{Prob}(REF < t_i)]^2 , \quad (1)$$

where *MOD* is FR12 or FR50 daily precipitation and *REF* is SAFRAN precipitation. Generally, the thresholds t_i are chosen to sample the pdf in a homogeneous way by taking the quantiles of a climatological distribution. Here we want to measure the fit of the tail of the distribution, so we selected the quantiles above 95% from the SAFRAN pdf (n = 49). The *RPS* is a dimensionless quantity and can be averaged for France, as the *MSE* in Section 3. However, a squared difference between two quantities close to each other (order of magnitude 0.95–1.00 each) produces small values, and we multiplied this score by 10^4 to handle quantities with order of magnitude 1. With this scaling, an *RPS* of 1 corresponds to a departure of 0.01 (e.g., 98% versus 99%) between ALADIN and SAFRAN cdf. *Table 2* shows *RPS* for each season. The 3 aggregation methods have been used to calculate the pdf. Methods 2 and 3 give similar *RPS*, which are smaller than those of Method 1. However, the conclusion is the same, whatever the method: FR12 has a better pdf tail than FR50, except in winter.

Table 2. Ranked probability scores for the tail of precipitation pdf (dimensionless units multiplied by 10^4) over France per season and with the 3 aggregation methods

	Method 1		**Method 2**		**Method 3**	
	FR50	**FR12**	**FR50**	**FR12**	**FR50**	**FR12**
DJF	1.88	2.50	1.65	2.34	1.56	2.16
MAM	3.15	1.44	2.18	1.13	2.04	1.16
JJA	1.73	0.66	1.39	0.64	1.35	0.66
SON	1.37	1.06	1.22	1.03	1.20	1.00

Fig. 4 helps to localize the weaknesses of the model pdf. It shows the ratio of the 99.9% quantiles between ALADIN and SAFRAN. The return period corresponding to this quantile is about 10 years, because one year contains about 90 days per season, so 10 years corresponds to 1000 values and thus to a probability of 0.1%. In winter, the behaviors of FR12 and FR50 are similar: the model overestimates the return value in the center of the country and underestimates it in the rest of the country. Contrary to the RPS results (which take into account all quantiles between 95% and 99.9%), there is no evidence that FR12 is worse than FR50. In particular, the underestimation by 30% in the southeast is improved by increasing resolution. In summer, the superiority of FR12 is obvious. FR50 produces return values in excess by 50% with respect to SAFRAN in some part of the country. However, FR12 is still too weak in the Mediterranean region.

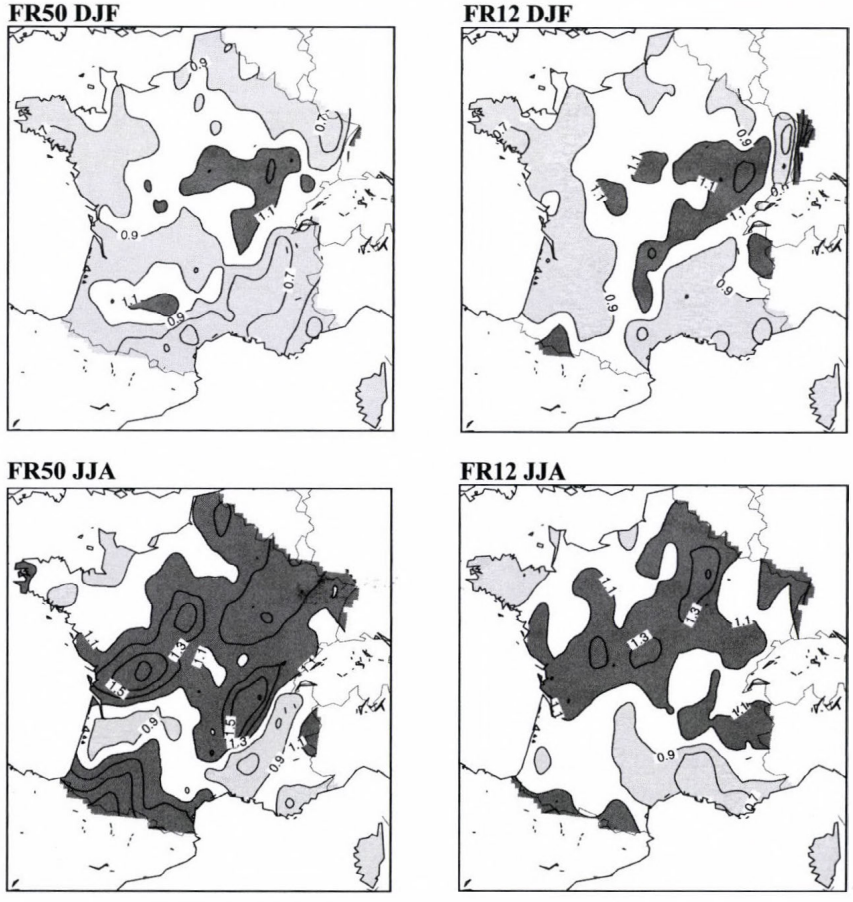


Fig. 4. Ratio of the 99.9% quantiles FRA50 over SAFRAN (left) and FRA12 over SAFRAN (right) in winter (top) and summer (bottom). The contour interval is 0.2, values over 1.1 are dense shaded, and values below 0.9 are light shaded.

We also computed the absolute maximum of precipitation of individual grid points by pooling all seasons (not shown). This 30-year maximum is about 50 mm/day over most of France for SAFRAN and ALADIN, but in the Cevennes region (southeast), it reaches 260, 144, and 108 mm/day for SAFRAN, FR12 and FR50, respectively. The highest events occur in autumn. The accurate representation of this kind of event is out of scope of ALADIN-climate.

6. Conclusion

The above results show that ALADIN is able to simulate the seasonal mean precipitation field and the tail of the probability distribution function (from one month to ten years return periods). For most quality criteria, the 12 km resolution version of ALADIN is superior to the 50 km one. The relatively small size of the domain (about 1200 km for the relaxation-free area) is not too detrimental to the simulation over the country, since no spurious strong precipitation stripes have been found over France. However, this small size does not allow the RCM to produce its own climate: we are here in a typical numerical downscaling exercise.

In the validation process of extreme precipitations, we used an alternative strategy by not considering a model grid point as a spatial average of observations, but by considering that a sample of grid points represents statistically a sample of observations. SAFRAN data are not really a series of observations, but the result of optimal interpolations. Using raw rain-gauge data over France is more complex, because the density is one observation per 10 km in some areas and one observation per 100 km in other areas. In *Déqué* (2007), such a comparison is performed with a 50 km resolution RCM.

Two important points are not addressed in this study. The first one is the space and time distributions of the highest precipitation extremes. As shown in previous section, the distribution is not uniform over France and the highest events are observed in the southeastern part in Autumn. The ALADIN-climate model, which is based on hydrostatic equations (in our climate version) with a full parameterization of convection, is not able to reproduce them quantitatively. To our knowledge, only 2-1 km resolution non-hydrostatic models like Meso-NH (*Ducrocq et al.*, 2008) can produce them explicitly. However, a recent study performed in the French project CYPRIM suggests that coarser resolution models like ARPEGE or ALADIN can produce strong rainy events (with respect to model quantiles) at a reasonable frequency. When the non-hydrostatic model Meso-NH is driven by ARPEGE during these events, it produces large amounts of rainfall (above 200 mm/day). This shows that one can use ARPEGE or ALADIN precipitation as a proxy of severe events with a proper statistical postprocessing (*Déqué*, 2007).

The second point is the added value of high resolution. The fact, that the probability distribution is improved in FR12, is not a proof that the spatial distribution of the 12–50 km scale structures is improved. In *Déqué* and *Somot* (2008) we show, that the spatial correlation of FR12 versus SAFRAN inside each 50 km box is significantly better than the correlation of FR50 interpolated onto the FR12 grid.

The perspective of this study is to extend the extreme precipitation analysis to CECILIA domains (Czech Republic, Hungary, Bulgaria, and Romania), where high resolution daily precipitation observations will be available soon. We plan to run the same scenarios (IPCC-A1B 2021–2050 and 2071–2100) with FR12 as in CECILIA. PRUDENCE simulations (*Christensen* and *Christensen*, 2007) at 50 km resolution suggest that the upper quantiles should increase in a warmer climate. As we have illustrated here that 12 km resolution ALADIN has a generally better representation of precipitation extremes than FR50, it is worth checking that the upper quantiles increase as a response of global warming is still valid at 12 km resolution.

Ackowledgements—This work was partly supported by European Commission FP-6 project CECILIA (GOCE-CT-2006-037005) and by French program ANR-MEDUP. The authors would like to thank *A. Horányi* for organizing the excellent workshop in Budapest, 2008. They are grateful to the two anonymous referees who suggested large improvements with respect to the first extended abstract.

References

Bubnova, R., Hello, G., Bénard, P., and *Geleyn, J.F.,* 1995: Integration of the fully elastic equations cast in the hydrostatic pressure terrain-following coordinate in the framework of ARPEGE/ALADIN NWP system. *Mon. Weather Rev. 123*, 515-535.

Christensen, O.B., Christensen, J.H., Machenhauer, B., and *Botzet, M.*, 1998: Very high-resolution regional climate simulations over Scandinavia-present climate. *J. Climate 11*, 3204–3229.

Christensen, J.H. and *Christensen, O.B.*, 2007: A summary of the PRUDENCE model projections of changes in European climate by the end of this century. *Climatic Change 81*, 7-30.

Déqué, M., 2007: Frequency of precipitation and temperature extremes over France in an anthropogenic scenario: Model results and statistical correction according to observed values. *Global Planet. Change 57*, 16-26.

Déqué, M. and *Somot, S.*, 2008: Added value of high resolution for ALADIN Regional Climate Model. *Research Activities in Atmospheric and Oceanic Modelling 38*, 5.2-5.2.

Ducrocq, V., Nuissier, O., Ricard, D., Lebeaupin, C., and *Thouvenin, T.*, 2008: A numerical study of three catastrophic precipitating events over Western Mediterranean region (Southern France). Part II: Mesoscale triggering and stationarity factors. *Q. J. Roy. Meteor. Soc. 134*, 131-145.

Epstein, E.S., 1969: A scoring system for probability forecasts of ranked categories. *J. Appl. Meteorol. 8*, 985-987.

Farda, A., Déqué, M., Somot, S., Horányi, A., Spiridonov, V., and *Toth, H.*, 2008: The ALADIN model as regional climate model for Central and Eastern Europe. *Stud. Geophys. Geod.* (under revision).

Giorgi, F., 1990: Simulation of regional climate using a limited area model nested in a general circulation model. *J. Climate 3*, 941-963.

Kasahara, A. and *Washington, W.M.*, 1967: NCAR global general circulation model. *Mon. Weather Rev. 95*, 389-402.

Manabe, S., Smagorinsky, J., and *Strickler, R.F.,* 1965: Simulated climatology of a general circulation model with a hydrological cycle. *Mon. Weather Rev. 93*, 769-798.

Quintana-Segui, P., Le Moigne, P., Durand, Y., Martin, E., Habets, F., Baillon, M., Canellas, C., Franchisteguy, L., and *Morel, S.,* 2008: Analysis of near-surface atmospheric variables: validation of the SAFRAN analysis over France. *J. Appl. Meteorol. Clim. 47*, 92–107.

Radu, R., Somot, S., and *Déqué, M.,* 2008: Spectral nudging in a spectral regional climate model. *Tellus 60A,* 898-910. doi: 10.1111/j.1600-0870.2008.00341.x

Sperber, K.R., Hameed, S., Potter, G.L., and *Boyle, J.S.,* 1994: Simulation of the northern summer monsoon in the ECMWF model: Sensitivity to horizontal resolution. *Mon. Weather Rev. 122*, 2461-2481.

Uppala, S.M., Kållberg, P.W., Simmons, A.J., Andrae, U., Da Costa Bechtold, V., Fiorino, M., Gibson, J.K., Haseler, J., Hernandez, A., Kelly, G.A., Li, X., Onogi, K., Saarinen, S., Sokka, N., Allan, R.P., Andersson, E., Arpe, K., Balmaseda, M.A., Beljaars, A.C.M., Van De Berg, L., Bidlot, J., Bormann, N., Caires, S., Chevallier, F., Dethof, A., Dragosavac, M., Fisher, M., Fuentes, M., Hagemann, S., Holm, E., Hoskins, B.J., Isaksen, L., Janssen, P.A.E.M., Jenne, R., Mcnally, A.P., Mahfouf, J.F., Morcrette, J.J., Rayner, N.A., Saunders, R.W., Simon, P., Sterl, A., Trenberth, K.E., Untch, A., Vasiljevic, D., Viterbo, P., and *Woollen, J.,* 2005: The ERA-40 re-analysis. *Q. J. Roy. Meteor. Soc. 131*, 2961-3012.

IDŐJÁRÁS

Quarterly Journal of the Hungarian Meteorological Service
Vol. 112, No. 3–4, July–December 2008, pp. 191–201

Validation of ALADIN-Climate/CZ for present climate (1961–1990) over the Czech Republic

Petr Skalák[1]*, **Petr Štěpánek**[2] and **Aleš Farda**[1]

[1]*Czech Hydrometeorological Institute,*
Na Šabatce 17, 14306, Prague, Czech Republic

[2]*Czech Hydrometeorological Institute,*
Regional office Brno, Kroftova 43, 61667, Brno, Czech Republic

(Manuscript received in final form September 4, 2008)

Abstract—Two present-time climate simulations performed with a regional climate model ALADIN-Climate/CZ in the framework of the EU FP6 project CECILIA were investigated to assess the model's ability to reproduce the main patterns of 2-meter temperature and precipitation in the orographically complicated region of Central Europe. To allow a direct comparison of high-resolution model outputs with the station data over the territory of the Czech Republic, a new gridded dataset with the same 10 km resolution was created. The obtained results of the first evaluation dealing with the model's performance during the control period 1961–1990 are presented here. In term of mean values, the model driven by the ERA-40 re-analyses is in better accordance with the observed data than when it is forced by the global circulation model ARPEGE-Climat. The selected characteristics based on daily maximum and minimum temperatures and sum of precipitation are very similar in both simulations. Although the evaluation has revealed weaknesses originating either from the model itself or driving data, the overall performance of the model is reasonably good in both simulations.

Key-words: regional climate modeling, validation, temperature, precipitation, gridding, ALADIN, Czech Republic

1. Introduction

Regional climate models (RCMs) are the state-of-the-art tools employed for downscaling information from the coarse resolution global circulation models (GCMs) on a local scale. With their increasing popularity for climate change

* Corresponding author, E-mail: skalak@chmi.cz

studies, it is important to assess the reliability of the information provided by RCMs. Validation of RCMs outputs is based on their comparison with a reference dataset, e.g., re-analysis fields or observed data. It is made much easier when the observed data is available on the same regular grid as the model. Real station observations are irregularly spatially distributed and, therefore, first they must be interpolated into a regular grid. There are already several existing gridded datasets of observations. Many of them have got either shorter time span or cover only a limited region, however. Those ones covering major parts of Europe and having the records at least for the period 1961–2000 are rather at coarse spatial resolution (~50 km). The best currently available European gridded dataset was prepared as a part of the ENSEMBLES project, and it contains high resolution (~25 km) daily data for precipitation and minimum, maximum, and mean temperatures for the period 1950–2006 (*Haylock et al.*, 2008).

The Czech Hydrometeorological Institute (CHMI) is a member of the international consortium developing and using the limited area model ALADIN for weather prediction. At the beginning of the 2000s the tests showed the model's capability to be run for a longer period and adapted for climate research purposes (*Huth et al.*, 2004). The further work has led to development of a regional climate model that is now designated as ALADIN-Climate/CZ. Unlike many other contemporary RCMs, ALADIN-Climate/CZ is a spectral model based on a semi-implicit semi-Lagrangian scheme as described in *Temperton* and *Staniforth* (1987). Physical computations are performed in the conventional grid space, however. The set of parameterizations is briefly described below. The model uses a convection scheme designed according to *Bougeault* (1985), a simple diagnostic cloudiness scheme together with large-scale precipitation parameterization (including evaporation of droplets), and the newly improved version of ACRANEB radiation scheme described in *Ritter* and *Geleyn* (1992). More detailed description of the model and its set of physical parameterizations can be found, e.g., in *Gerard* (2001) or *Farda* (2008). We would like to stress here that ALADIN-Climate/CZ is a different model than the RCM ALADIN-Climat developed at the Centre National de Recherches Météorologiques (CNRM) of Météo-France and employed also in other countries of the ALADIN consortium (*Spiridonov et al.*, 2005). Although both models share the same dynamical core and basic principles and formulations, they differ significantly in their physical parameterization packages. Physical parameterizations of the CNRM's ALADIN-Climat model are derived directly from those used in GCM ARPEGE-Climat 4 (*Déqué*, 2007), while those of the CHMI's ALADIN-Climate/CZ arises from parameterizations in the ALADIN numerical weather prediction version CY28T3 that was in operational use at CHMI in the years 2003 and 2004.

2. *Experiment setups*

Two simulations of present climate conditions were performed with ALADIN-Climate/CZ over the Central European domain in resolution of 10 km. These runs used either perfect lateral boundary conditions (LBCs) represented by the ECMWF ERA-40 re-analyses (*Uppala et al.*, 2005) or LBCs coming from a driving model planned to be taken for scenario runs (GCM ARPEGE-Climat in our case). While forcing by the GCM ARPEGE-Climat could be done directly due to the ARPEGE-Climat's high horizontal resolution (~50 km over Central Europe), a double nesting technique was applied to enable RCM ALADIN with 10 km grid to be driven by the ERA-40 re-analyses with coarse resolution. The ALADIN 50 km grid integration forced by the ERA-40 re-analyses (originally coming from the EC FP6 ENSEMBLES project) was taken to drive the model at 10 km resolution over the smaller Central European domain. The sea surface temperature fields came either directly from the ERA-40 re-analyses (ERA-40 experiment) or from the atmosphere-ocean GCM ARPEGE/OPA data (ARPEGE-Climat experiment). A brief summary of both experiments' setups is in *Table 1*. The whole integration domain and illustration of the model's orography are presented in *Fig. 1*.

Table 1. Model setup for the experiments

Experiment designation	**ERA-40**	**ARPEGE-Climat**
Integration domain size (lat. × lon.)	74 × 148 points	
Horizontal resolution	10 km	
Vertical resolution	43 levels	
Time step	450 s	
Integration period	Jan 1, 1960 – Dec 31, 2000	Jan 1, 1960 – Dec 31, 2000
Input data	ERA-40 re-analyses*	GCM ARPEGE-Climat

* by nesting through the ALADIN 50 km resolution integration

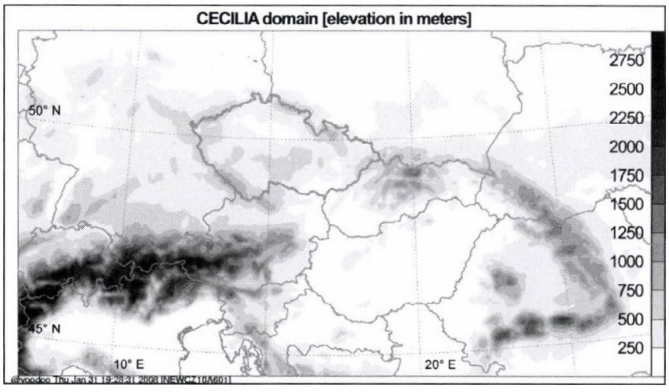


Fig. 1. Orography over the Central European model's integration domain.

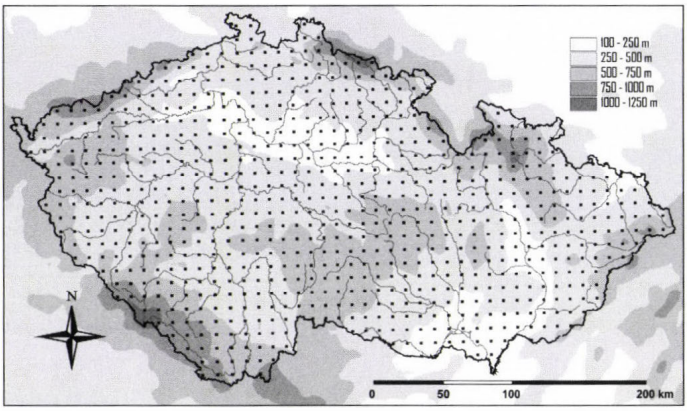


Fig. 2. Grid points and orography of the model in the Czech Republic. Elevation is in meters.

3. Data and methodology

For validation of the model results against the station data over the territory of the Czech Republic, a new gridded dataset of comparable spatial, 10 km resolution was created. It is based on the records stored in the CHMI climatological database. The daily data of four meteorological parameters (precipitation, mean, maximum, and minimum temperatures) from 302 stations measuring 2-meter temperature and 787 stations measuring precipitation were taken and recalculated to the model's grid (*Fig. 2*). The station data were at first reduced to the altitude of a selected grid point by applying a local linear regression and then the reduced values were interpolated to a position of the grid point. The inverse distance weighting was selected as the interpolation method. The weight parameter was set as $1/d$ in case of temperature and $1/d^3$ for precipitation, where the variable stands for d distance. In addition, when interpolating, a trimmed mean was applied for the temperature characteristics, thus excluding the values smaller than the 20th percentile and larger than the 80th percentile from the data of the input of every interpolation step. The gridding as well as quality control and homogenization of the input station data were done by the ProClimDB application (*Štěpánek*, 2008).

4. Results

Some of our very preliminary results obtained by a comparison of the model outputs to the newly created gridded dataset of station observations are presented here. We focused only on the territory of the Czech Republic. The reference period used for this study is 1961–1990.

Table 2 shows the basic statistics of the biases between model and station data. Long-term seasonal means of 2-meter temperature and sums of precipitation (expressed in millimeters per day) are included for both experiments. A column containing mean values refers to an average regional bias calculated from 789 grid points over the Czech Republic, while maximum and minimum values represent an extreme bias belonging to one particular grid point of the total.

Table 2. Regional average and extremes of seasonal biases (model versus gridded station dataset) of 2-meter temperature and precipitation fields over the Czech Republic in the period 1961–1990. The model experiments are designated according their LBCs. (DJF = winter, MAM = spring, JJA = summer, and SON = autumn)

Season	Dataset	2-meter temperature (°C)			Precipitation (mm/day)		
		minimum	mean	maximum	minimum	mean	maximum
DJF	ERA-40	–1.8	0.1	1.4	–2.6	0.2	4.1
	ARPEGE	–1.8	0.5	1.8	–1.8	0.7	5.7
MAM	ERA-40	–2.4	–0.9	0.5	–1.3	0.3	3.8
	ARPEGE	–2.8	–1.2	0.1	–0.6	0.9	5.3
JJA	ERA-40	–1.5	0.2	1.9	–0.6	0.6	3.2
	ARPEGE	–0.5	0.9	2.6	–0.7	0.7	3.2
SON	ERA-40	–1.3	0.4	1.9	–1.9	0.0	2.8
	ARPEGE	–2.8	–1.1	0.3	–1.6	0.2	4.1

In term of mean values, the model driven by ERA-40 captures well the 2-meter temperature in winter, summer, and autumn with positive biases less than 0.5 °C. In spring it exhibits a more pronounced cold bias (–0.9 °C), however. The latter can be also detected when GCM ARPEGE-Climat is used as a source of the driving data. The ARPEGE-Climat experiment also exhibits another significant cold bias in autumn (–1.1 °C) which is not corresponding to the warm bias (+0.4 °C) in the ERA-40 experiment. The positive biases, larger than those in the ERA-40 experiment, dominate in the ARPEGE-Climat experiment in winter and summer. The range of the seasonal biases among the grid points on the territory of the Czech Republic is similar in both experiments in all seasons. The high individual seasonal biases, whose extreme values are listed in *Table 2*, are mainly due to the remaining differences between the real and model orography.

Precipitation is corresponding well to the station data in autumn, otherwise in other seasons the model is more humid in both experiments than stations. The highest seasonal bias in the ERA-40 experiment is detected in summer (+0.6 mm/day), while in the ARPEGE-Climat experiment it is in spring (+0.9 mm/day). The seasonal biases in the ERA-40 experiment are always smaller than in the ARPEGE-Climat experiment. The range of the seasonal biases among the grid points on the territory of the Czech Republic is a little larger when the model is driven by the GCM ARPEGE-Climat.

In *Table 3* percentiles of daily mean temperature for each of 12 months in the year are presented. These were calculated as an spatial average from the percentile values computed in the grid points within the studied area. The percentile in a single grid point was derived from the series of daily mean temperatures over the whole period 1961–1990 for each particular month.

Table 3. Percentiles of 2-meter temperature derived from the daily data in individual months in the period 1961–1990 and averaged over the Czech Republic in the model experiments (designated according their LBCs), compared with the gridded station dataset

Percentile	Dataset	Jan	Feb	Mar	Apr	May	Jun	Jul	Aug	Sep	Oct	Nov	Dec
1st	ERA-40	-11.7	-9.2	-6.8	-0.4	3.9	8.6	11.3	10.4	7.0	1.2	-5.2	-9.1
1st	ARPEGE	-12.9	-9.5	-5.9	-3.4	4.2	9.3	11.8	12.6	5.8	-4.1	-7.8	-11.2
1st	Stations	-17.4	-13.7	-9.6	-0.9	3.2	7.5	10.1	9.5	5.4	-0.2	-7.4	-13.8
5th	ERA-40	-8.6	-7.0	-4.1	0.8	6.3	10.2	12.4	11.9	8.6	2.8	-3.2	-6.9
5th	ARPEGE	-10.3	-6.9	-3.5	-1.0	5.8	10.9	13.1	13.9	7.2	-0.8	-5.3	-7.7
5th	Stations	-12.6	-9.5	-5.1	1.0	5.8	9.4	11.4	10.9	7.2	1.8	-4.1	-9.7
25th	ERA-40	-4.2	-3.3	-0.4	3.5	9.5	12.9	15.1	14.4	11.4	6.1	0.0	-3.4
25th	ARPEGE	-5.7	-2.0	-0.2	2.4	8.7	13.7	15.2	16.1	10.2	2.8	-1.7	-3.0
25th	Stations	-5.7	-3.9	-0.3	4.1	9.4	12.5	14.1	13.7	10.2	5.2	0.1	-3.7
50th	ERA-40	-2.0	-1.0	1.5	5.5	12.0	15.0	17.2	16.5	13.5	8.5	2.3	-1.3
50th	ARPEGE	-2.6	0.6	1.9	4.8	11.2	16.1	17.0	17.8	12.8	5.8	1.1	-0.6
50th	Stations	-1.9	-0.5	2.5	6.9	12.1	15.3	16.6	16.1	12.6	7.9	2.6	-0.7
75th	ERA-40	0.0	0.8	3.4	7.8	14.3	17.2	19.2	18.7	15.7	10.8	4.8	0.9
75th	ARPEGE	-0.4	2.7	4.0	7.1	14.0	18.2	18.8	19.5	15.1	8.7	4.2	1.7
75th	Stations	0.7	1.7	5.3	9.9	14.9	17.9	19.3	18.6	15.1	10.6	5.3	1.8
95th	ERA-40	2.9	3.2	6.3	11.4	17.5	19.8	21.8	21.5	18.5	14.0	8.4	4.2
95th	ARPEGE	2.3	5.7	7.0	10.2	17.4	20.8	21.6	22.2	18.9	12.6	8.1	5.2
95th	Stations	4.1	5.1	9.6	14.1	18.3	21.4	22.4	22.0	18.4	14.1	9.2	6.3
99th	ERA-40	4.7	5.1	8.1	13.6	18.9	21.1	23.6	23.1	20.3	15.8	10.8	6.8
99th	ARPEGE	4.2	7.9	8.8	12.2	19.0	22.7	23.6	24.1	21.9	15.5	10.5	7.5
99th	Stations	6.3	7.8	12.2	17.0	20.6	23.2	24.3	24.0	20.6	16.1	11.5	8.7

The p-% percentiles of 2-meter temperature for p = 1 and p = 5 (p = 95 and p = 99) are smaller (larger) in the gridded station dataset than in the model experiments in most cases. A certain exception from above can be found in the ARPEGE-Climat experiment in April, October, and November, when the 1st and 5th percentiles are smaller than in the gridded station dataset, in April and October even significantly (more than 2 °C). Similar exception can be detected in the ARPEGE-Climat experiment in February, August, and September when the 90th and 95th percentiles are larger in the model than station observations, although the differences are rather small (on about several tenths of °C). The

mean values of the 2-meter temperature distribution (between the 25th and 75th percentiles) in the ERA-40 experiment are usually closer to those in the gridded station dataset except for March, September, and December when the ARPEGE-Climat experiment is in better accordance. The ARPEGE-Climat experiment also captures the lower end of the 2-meter temperature distribution (represented here by the 1st and 5th percentiles) better in winter and September. For higher end of the 2-meter temperature distribution (represented here by the 95th and 99th percentiles), the ARPEGE-Climat shows better accordance than the ERA-40 experiment approximately in half of the cases.

Tables 4 and *5* present the long-term spatial means in the occurrence of days with daily maximum (TMA) or minimum (TMI) air temperature and sum of precipitation (PR) over (or under) a defined threshold.

Table 4. Long-term (1961–1990) average of seasonal and annual numbers of tropical (TMA ≥ 30 °C), warm (TMA ≥ 25 °C), ice (TMA < 0 °C), arctic (TMA ≤ –10 °C) and frost (TMI < 0 °C) days averaged over the Czech Republic in the model experiments (designated according their LBCs), compared with the gridded station dataset. (DJF = winter, MAM = spring, JJA = summer, and SON = autumn)

Season	Dataset	Number of days (TMA and TMI in °C)				
		TMA ≥ 30	TMA ≥ 25	TMA < 0	TMA ≤ –10	TMI < 0
DJF	ERA-40	0.0	0.0	30.6	0.2	80.9
	ARPEGE	0.0	0.0	29.7	0.6	75.8
	Stations	0.0	0.0	33.2	1.2	73.3
MAM	ERA-40	0.0	0.2	2.3	0.0	39.7
	ARPEGE	0.1	0.3	2.1	0.0	40.0
	Stations	0.1	2.5	2.8	0.0	28.8
JJA	ERA-40	1.2	12.2	0.0	0.0	0.0
	ARPEGE	1.4	13.5	0.0	0.0	0.0
	Stations	4.2	26.5	0.0	0.0	0.1
SON	ERA-40	0.1	2.3	1.6	0.0	19.9
	ARPEGE	0.3	1.9	4.6	0.0	28.6
	Stations	0.2	2.7	2.8	0.0	20.9
YEAR	ERA-40	1.4	14.7	34.5	0.2	140.4
	ARPEGE	1.7	15.7	36.4	0.6	144.5
	Stations	4.4	31.7	38.9	1.2	123.0

In winter the numbers of ice (TMA < 0 °C) and frost (TMI < 0 °C) days are well corresponding to the observed data in both experiments, but the occurrence of arctic (TMA ≤ –10 °C) days is slightly underestimated. In spring the number of frost days is overestimated in both experiments, while the warm events characterized by the number of warm (TMA ≥ 25 °C) days are underestimated. The latter is also valid for the occurrence of warm events in summer. In autumn

the number of warm days is slightly lower in both experiments than in the observed data. The cold events are represented well in the ERA-40 experiment in autumn, but they are overestimated in the ARPEGE-Climat experiment, especially considering frost days. In term of annual numbers, good agreement between the experiments and observed data occurs only in the number of ice days, otherwise the model underestimates the occurrence of tropical (TMA ≥ 30°C), warm, and arctic days, and also, it gives higher than observed numbers of frost days. When the model experiments are compared to each other, significant differences are detected mainly in the autumn occurrence of ice and frost days, which are more often in the ARPEGE-Climat experiment, otherwise the performance of the model in both experiments is the same or very similar.

Table 5. Long-term (1961–1990) average of seasonal and annual numbers of rainy days (with daily amount exceeding given threshold) averaged over the Czech Republic in the model experiments (designated according their LBCs), compared with the gridded station. (DJF = winter, MAM = spring, JJA = summer, and SON = autumn)

Season	Dataset	Number of days (PR in mm)				
		PR > 0	PR > 1	PR > 5	PR > 10	PR > 20
DJF	ERA-40	55.4	25.2	8.4	3.1	0.6
	ARPEGE	56.7	29.5	11.2	4.6	1.1
	Stations	45.1	26.2	7.7	2.2	0.3
MAM	ERA-40	66.5	36.7	10.4	3.7	0.8
	ARPEGE	72.2	41.7	13.7	5.9	1.6
	Stations	43.3	27.6	10.2	3.9	0.8
JJA	ERA-40	71.2	50.6	15.7	6.4	2.1
	ARPEGE	75.2	53.7	16.5	6.7	2.2
	Stations	44.7	31.5	15.0	7.2	2.1
SON	ERA-40	49.0	23.1	8.0	3.5	1.0
	ARPEGE	54.8	26.5	9.2	3.8	0.9
	Stations	40.0	24.3	9.2	3.6	0.7
YEAR	ERA-40	242.2	135.7	42.5	16.6	4.5
	ARPEGE	258.9	151.4	50.6	21.0	5.8
	Stations	173.0	109.6	42.1	17.0	3.9

The number of days with precipitation (PR > 0) is always overestimated on 20–70% in the model experiments in all seasons. The ERA-40 experiment captures the seasonal and annual number of days with precipitation over 5, 10, and 20 well, while the ARPEGE-Climat experiment well simulates the occurrence of these precipitation events only in summer and autumn and otherwise it overestimates them. In winter and autumn seasonal number of days with precipitation over 1 mm are close to the observed data in both experiments, while in other seasons they are overestimated by the model. When the model

experiments are compared to each other, in the ERA-40 experiment the number of precipitation days are less than in the ARPEGE-Climat experiment and in better accordance with the observed data in most cases.

5. Discussion

Our primary interest was to study the model's performance over a small target region. Therefore, we have not chosen the common available pan-European gridded datasets for model's validation because they offer rather coarse resolution and low density of input information (station data) from which they were created. Instead we took the advantage of the access to the observation data in its best available quality in the studied region, created a new gridded dataset of station observations corresponding to the RCM ALADIN grid at 10 km horizontal resolution in the CECILIA project climate simulations and compared the model's results with it.

As for seasonal mean values, the model is generally in a good accordance with the observed data, although some weaknesses have been identified as well. The spring cold bias of 2-meter temperature detected in both experiments indicates that its origin is rather in the regional model itself than the driving fields. The similar pattern in its extent covering large parts of Central and Eastern Europe, has been already found in the previous, coarse resolution experiments and it has been associated with a snow accumulation over the winter season and consecutive prolonged snow melting during the spring (*Farda et al.*, 2007). On the other hand, the autumn cold bias in the ARPEGE-Climat experiment not corresponding to the positive bias in the ERA-40 experiment is perhaps a consequence of a stronger zonal flow in the driving GCM.

The warm (cold) biases can be also identified in the shift of the mean values of the 2-meter temperature distribution (between the 25th and 75th percentiles) in the model experiments toward warmer (or colder) values, while the same shift is usually found only in one end of the temperature distribution (*Table 3*). When considering the data from *Tables 3* and *4* it appears, that the positive (negative) biases in 2-meter temperature are not usually associated with the significantly increased number of warm (cold) extreme events defined on the base of daily maximum temperature in the model experiments. Certain exception from the above mentioned phenomenon is the reduced number of warm days in spring and arctic days in winter in the model experiments. The spring cold bias is also well expressed in the increased number of frost days.

Positive precipitation biases can be linked with the tendency of the model "to precipitate" more often than in the station measurements (*Table 5*). In all seasons the increased number of rainy days could be attributed to more frequent occurrence of drizzling or little rain with daily precipitation sums ≤ 1 mm (≤ 5 mm in spring and summer).

Although some biases of precipitation and 2-meter temperature in the model experiments can be linked with other phenomena and their sources can be identified either in the regional model or the driving data, further analysis is still needed to confirm these hypotheses.

The studied area is rather small compared to the regions on which the RCMs are often validated, e.g., PRUDENCE project regions. Due to the local variability of climate conditions mainly with the altitude in the selected area, further improvement of the results of the model validation could be achieved by performing the analysis in the sub-regions defined according to the altitude or climate classifications.

6. Conclusions

The presented results of the first evaluation of the historic run experiments performed with the RCM ALADIN-Climate/CZ confirm the findings of previous studies made with the model with coarse resolution, see e.g., *Farda et al.* (2007). The model is capable to capture the main features of the 2-meter temperature and precipitation fields in the region of Central Europe, and it is working well even over smaller areas with a rather complex orography represented here by the territory of the Czech Republic. The overall performance is better when the model is driven by the ERA-40 re-analyses, especially in terms of mean values, however, the results obtained with the model forced by the GCM ARPEGE-Climat are very satisfactory as well. The increased differences between the model driven by GCM and the observed data are mainly due to the use of less perfect driving data than the re-analyses. Nevertheless, some weaknesses and problems in simulating 2-meter temperature and precipitation detected in this study can be attributed directly to the model. It is the spring cold bias caused by winter snow accumulation and later prolonged snow melting in spring of the model or the tendency, to generate more precipitation than in the reality. Although the mean values vary between the described experiments, the analysis of selected characteristics based on daily maximum and minimum temperatures and sums of precipitation have revealed that the model experiments provide results which may differ from the observations, but they are similar when compared to each other.

To validate the model under the high resolution of 10 km, the gridded dataset of the station observations has been created. It is planned to broaden the dataset to cover the region of the common CECILIA target area (CECILIA project: http://www.cecilia-eu.org). Before that, a more detailed investigation of the gridding technique and its affect on the quality of the final dataset is necessary to be carried out, however.

Acknowledgments—The present work was supported by the European Commission under the Contract No. 037005. The ERA-40 re-analysis data used in the study were provided by the European Centre for Medium-Range Weather Forecast. The authors would like to thank *A. Horányi* at the Hungarian Meteorological Service for organizing the regional climate modeling workshop in Budapest in February 2008.

References

Bougeault, P., 1985: A simple parameterization of the large-scale effects of cumulus convection. *Mon. Weather Rev. 113*, 2108-2121.

Déqué, M., 2007: Frequency of precipitation and temperature extremes over France in an anthropogenic scenario: model results and statistical correction according to observed values. *Global Planet. Change 57*, 16-26.

Farda, A., 2008: Dynamical downscaling of Air Temperature in the Central Europe. *PhD. Thesis* (in Czech with extended abstract in English). Faculty of Mathematics and Physics, Charles University in Prague.

Farda, A., Štěpánek, P., Halenka, T., Skalák, P., and *Belda, M.*, 2007: Model ALADIN in climate mode forced with ERA-40 reanalysis (coarse resolution experiment). *Meteorol. J. 10*, 123-130.

Gerard, L., 2001: Physical parameterizations in ARPÉGE-ALADIN operational model. *ALADIN Documentation*, Météo-France, 130 pp.

Haylock, M.R., Hofstra, N., Klein Tank, A.M.G., Klok, E.J., Jones, P.D., and *New, M.*, 2008: A European daily high-resolution gridded dataset of surface temperature and precipitation for 1950–2006. *J. Geophys. Res.* (accepted).

Huth, R., Kyselý, J., Pokorná, L., Farda, A., Mládek, R., Kliegrová, S., and *Metelka, L.*, 2004: One month-long integrations of the ALADIN model in the climate mode: effect of selected parameters (in Czech). *Meteorol. Bull. 57*, 41-46.

Ritter, B., and *Geleyn, J.-F.*, 1992: A comprehensive radiation scheme for numerical weather prediction models with potential applications in climate simulations. *Mon. Weather Rev. 120*, 303-325.

Spiridonov, V., Déqué, M., and *Somot, S.*, 2005: ALADIN-Climate: from the origins to present date. *ALADIN Newsletter 29*, 89-92.

Štěpánek, P., 2008: ProClimDB – software for processing climatological datasets. Czech Hydrometeorological Institute, http://www.climahom.eu.

Temperton, C., and *Staniforth, A.*, 1987: An efficient two-time-tevel semi-Lagrangian semi-implicit integration scheme. *Q. J. Roy. Meteorol. Soc. 113*, 1025-1039.

Uppala, S.M., Kållberg, P.W., Simmons, A.J., Andrae, U., da Costa Bechtold, V., Fiorino, M., Gibson, J.K., Haseler, J., Hernandez, A., Kelly, G.A., Li, X., Onogi, K., Saarinen, S., Sokka, N., Allan, R.P., Andersson, E., Arpe, K., Balmaseda, M.A., Beljaars, A.C.M., van de Berg, L., Bidlot, J., Bormann, N., Caires, S., Chevallier, F., Dethof, A., Dragosavac, M., Fisher, M., Fuentes, M., Hagemann, S., Holm, E., Hoskins, B.J., Isaksen, L., Janssen, P.A.E.M., Jenne, R., McNally, A.P., Mahfouf, J.-F., Morcrette, J.-J., Rayner, N.A., Saunders, R.W., Simon, P., Sterl, A., Trenberth, K.E., Untch, A., Vasiljevic, D., Viterbo, P., and *Woollen, J.*, 2005: The ERA-40 re-analysis. *Q. J. Roy. Meteor. Soc. 131*, 2961-3012.

IDŐJÁRÁS

Quarterly Journal of the Hungarian Meteorological Service
Vol. 112, No. 3–4, July–December 2008, pp. 203–231

Transient simulation of the REMO regional climate model and its evaluation over Hungary

Gabriella Szépszó* and **András Horányi**

Hungarian Meteorological Service,
P.O. Box 38, H-1525 Budapest, Hungary
E-mails: szepszo.g@met.hu, horanyi.a@met.hu

(Manuscript received in final form October 28, 2008)

Abstract—A couple of years ago the REMO model originally developed by the Max Planck Institute for Meteorology (MPI-M) in Hamburg was adapted at the Hungarian Meteorological Service with the aim to become an essential tool for providing realistic regional climate estimations for the next few decades particularly for the area of the Carpathian Basin. This area of interest is especially important considering the fact that one of the largest uncertainties in climate projections can be found over the Carpathian Basin, as it had already been identified by former large international climate projects. Various versions of the REMO model have already been tested all over the world for different geographical domains, however, recently further validations and tests have been started also at the Hungarian Meteorological Service in the framework of the CLAVIER EU project. The article is dealing with the 100-year transient simulation of REMO5.0 model for the period 1951–2050. The lateral boundary conditions for the domain covering continental Europe with 25 km horizontal resolution were provided by the ECHAM5/MPI-OM global atmosphere-ocean general circulation model with the use of A1B SRES scenario for the future. On the one hand, present article is dedicated to summarize in detail the validation results of the experiment for the past climate, and on the other hand, to introduce the preliminary climate change estimations based on REMO results for the future. Special emphasis is put on evaluating the performance of the REMO model for the Carpathian Basin in general and for Hungary in particular.

Key-words: regional climate modeling, transient simulation, REMO model, subjective and objective evaluation

1. Introduction

The Earth's climate system is defined (*GARP,* 1975) as being composed of the atmosphere, hydrosphere, cryosphere, land surface, and biosphere, together with their complicated and two-way interactions as further important ingredients,

* Corresponding author

playing crucial role in the understanding and determination of the climate. It is generally accepted that the only scientifically sound way to understand the behavior of this complex system and, furthermore, estimate its future evolution is provided by its numerical modeling. In the last half century, more and more sophisticated models were developed in order to describe the individual components of the system and also to take into account the highly non-linear links and feedbacks between these subsystems.

Due to the rapid scientific, technical, and algorithmic evolution of the models and the available enhanced computer power, the horizontal resolution of the global general circulation models developed and exploited by the largest world climate centers reaches nowadays the 100 km range. These models are continuously improving (for instance they possess rather complex physical parameterization schemes), and recently they are providing solid basis and realistic projections for the synoptic scale characteristics of the climate, however, they are at the moment largely insufficient for detailed regional scale estimations. These global projections are not capable to yield detailed and reliable information, e.g., about the summer precipitation over the Carpathian Basin, because their spatial resolution is still far too low to account for such regional phenomena, and on top of it all their ability to describe properly the surface characteristics (typically and most importantly the orography for instance, but other surface features as lakes can be also mentioned) of the area of interest is still limited.

Currently there are three main methods (referred to as regionalization techniques or downscaling methods) for getting improved information about regional climate, and climate change based on the results of the global climate model systems: the application of high and variable resolution general circulation models (*Cubasch et al.*, 1995; *Déqué* and *Piedelievre*, 1995), the use of high resolution limited area regional climate models (*Giorgi* and *Bates*, 1989), and statistical downscaling (*Wilby et al.*, 1998). The first two methods belong to the dynamically-based techniques, where the global results are dynamically refined for obtaining smaller scale climate details. The statistical downscaling procedures are using statistical relations between the global and regional climatic characteristics described for the past and assuming their applicability for the future as well. Hereafter the employment of regional models will be considered and illustrated with the help of the REMO regional climate model.

The limited area models have already been widely and successfully used in the weather forecast for many decades. Their employment for climate "prediction" purposes was arisen in the late 1980s. The first climate simulation with a regional climate model (RCM), which was developed on the basis of a short-range weather forecasting model, was carried out by Giorgi and Bates (1989). The RCM was nested into a global climate simulation, which provided the initial and lateral boundary conditions for the experiment. The following

issues regarding this nested modeling approach were investigated in the first experiments:

- Whether the long integration is not accompanied by accumulation of error characteristics in time (one can imagine that even small systematic errors during a climate simulation might accumulate in such a way that destroy the signal otherwise provided by the model);
- Whether the regional model is able to reproduce realistically those synoptic scale features of the climate, which are specified by the lateral boundary conditions;
- Whether the regional model reflects accurately the regional climate statistics.

The experiments supplied positive results, so green light was given for the wide-range employment of limited area models in climate simulations. All this had revolutionary consequences, because the use of regional models really provides an effective way to investigate in the fullest detail the regional aspects of the global climate change due to their finer resolution, better representation of the surface characteristics (topography, land-sea mask, albedo, etc.), and mesoscale processes. Since that time new and new generations of regional climate models were developed and applied: some of them were originated from weather forecasting models, while others were developed based on global counterparts (i.e., global climate models). The aforementioned questions investigated in the pioneering work of Giorgi and Bates are still important issues before starting any meaningful model validation experiments and/or climate change simulations.

Naturally, the validation of regional climate models for the past climate is a crucial ingredient of the work with RCMs. This is coming from the consideration that hopes for successful climate scenario projections can be only considered if the models are already reasonably capable to simulate the past climate. (Certainly this issue is not that straightforward due to the fact, that successful past simulations do not ensure directly that a changing future climate will be also well simulated; the reverse is also true, i.e., bias in the past simulations does not mean that for the future the same bias will surely occur.) In the last decade several international projects have been initiated and then realized in order to explore the strengths and weaknesses of the regional climate models, i.e., what the model parameters are, which can be predicted with larger confidence, and what the regions are, where the climatic characteristics are sufficiently well-described in the simulations. For instance, in the framework of the RAACS project (Regionalization of Anthropogenic Climate Change Simulations; *Machenhauer et al.,* 1998) it was recognized that many regional climate models simulate too dry and too warm summer climate over Central and Eastern Europe for the second half of the 20th century. Later on, in the MERCURE project (Modeling European Regional Climate: Understanding and Reducing Errors) an important objective was to understand and reduce this

model bias referred to as summer drying problem (*Hagemann et al.,* 2004). The investigations of the PRUDENCE project (Prediction of Regional scenarios and Uncertainties for Defining European Climate change risks and Effects, *Christensen*, 2005) focused on the comprehensive validation of simulations of ten regional models (using a horizontal resolution of about 50 km) for the period of 1961–1990. The results have shown that the summer warm bias still exists in the majority of the participating RCMs, therefore, unfortunately no model developments in between improved the situation substantially (*Hagemann* and *Jacob*, 2007).

Meanwhile, in order to satisfy the increasing demands, the models are also applied to realize climate change simulations in spite of the known model deficiencies. Therefore, in the ongoing and future works the issues related to the summer drying problem and other model deficiencies should be addressed in an extended perspective, and the following additional questions should be discussed and answered: what is the influence (if any) of the systematic past biases on the climate change signals, what is the relative size of the bias with respect to the real climate change signals, can the differences between the climate change signals of the various models be originated from their different bias characteristics (*Jacob et al.,* 2007)?

As it was indicated above, the summer drying problem is still an open and acute issue strongly influencing the uncertainty of the climate change projections for the Central and Eastern European region. This particular issue together with other aspects related to the uncertainties in climate change projections are addressed within the CLAVIER EU project (Climate ChAnge and Variability: Impact on Central and Eastern EuRope, http://www.clavier-eu.org). In the framework of this project, the LMDZ model (developed by the Institut Pierre Simon Laplace in Paris) and two versions of the REMO model (developed by the Max Planck Institute in Hamburg) were considered in order to provide a small ensemble of regional simulations for the area of interest (mainly the territories of Bulgaria, Hungary, and Romania). Firstly, the models were integrated for a past period (1961–2000) with the use of ERA-40 re-analyses (*Simmons* and *Gibson*, 2000) as lateral boundary conditions in order to explore the main characteristics of the models' behavior in case of "quasi-perfect" driving. It is noted here that the present article does not discuss the results of these "reference" simulations, however, a lot of results were already introduced and reported earlier (see for instance at *Szépszó,* 2008). It was decided that the succeeding climate change simulations are going to focus on the near past and future in a transient manner, therefore, the different REMO-versions (REMO5.7 at the Max Planck Institute in Hamburg and REMO5.0 at the Hungarian Meteorological Service) and the LMDZ model are integrated for the period between 1951 and 2050 using relatively high (10 and 25 km) horizontal resolution. (Hereafter the results of REMO5.0 simulation on 25 km resolution will be introduced and discussed in detail.) The large scale forcings for the

regional models are provided by the global fields of the ECHAM5/MPI-OM coupled atmosphere-ocean general circulation model, and in the case of the LMDZ regional model the simulation was repeated with the use of driving fields from its global counterpart. The regional models were forced only with the A1B SRES emission scenario, which is considered as a "realistic" estimate for the evolution of the greenhouse gas concentrations until the end of the 21st century (*Nakicenovic et al.,* 2000). Nevertheless, it is remarked here that basically until 2050 there is no real difference even between the most optimistic emission scenario and the most pessimistic one compared to the natural climate variability and uncertainties in the RCMs.

After this introduction a brief overview is given about the most important characteristics of the ECHAM5/MPI-OM coupled model system and REMO5.0 regional climate model adapted at the Hungarian Meteorological Service. Section 3 deals with the description of the accomplished simulation together with the thorough analysis of the validation results over Europe with special emphasis on the Hungarian territory. The results for the future are also detailed in the same section providing preliminary climate change estimations. In Section 4 several open issues are addressed and discussed together with those major conclusions, which could be drawn based on the results of the transient simulation.

2. The applied models

The ECHAM5 (*Roeckner et al.,* 2003) is the current version of the ECHAM models. The ECHAM atmospheric general circulation model has been developed compounding the dynamical part of global weather prediction model of European Centre for Medium-Range Weather Forecasts (therefore, the first part of its name is EC) and a comprehensive parameterization package developed at Max Planck Institute in Hamburg (therefore the abbreviation HAM), which allows the model to be used for climate simulations. The MPI-OM model (*Marsland et al.,* 2003) was developed (also by the MPI-M) based on the HOPE (Hamburg Ocean Primitive Equation) ocean general circulation model and includes also a dynamic-thermodynamic sea-ice submodel.

For the fourth assessment report of the IPCC the coupled ECHAM5/MPI-OM atmosphere-ocean model has been used among other models to provide global climate simulations. The coupled model was run without flux correction at T63 (about 1.875 degree or 200 km) horizontal resolution and 31 vertical levels in the atmosphere, and about 1.5 degree horizontal resolution and 40 vertical layers in the ocean. The model integrations encompass control simulations covering the period 1860–2000 and hundred-year simulations for the future climate from 2001 onwards. For the past climate observed concentrations of CO_2, CH_4, N_2O, CFCs, ozone and sulphate aerosols were taken, while for the 21st century these concentrations were prescribed according

to the three IPCC scenarios B1, A1B, and A2 (note that for our investigations exclusively the A1B scenario results were used).

The REMO regional climate model was developed on the basis of the "Europa Model" (the former numerical weather prediction model of the German Weather Service, *Majewski*, 1991) together with the inclusion of the global atmospheric general circulation model ECHAM4's (*Roeckner et al.,* 1996) physical parameterization package.

REMO (*Jacob* and *Podzun,* 1997) is a gridpoint model and the primitive equations are written in advective form in rotated spherical coordinate system. The phase-errors caused by horizontal discretization are reduced by staggered Arakawa grid (C-type) (*Mesinger* and *Arakawa,* 1976). The prognostic variables of the model are the temperature, horizontal wind-components, specific humidity, and cloud water content on the model levels and the surface pressure. In vertical a hybrid coordinate system is defined (*Simmons* and *Burridge,* 1981). The maximum number of vertical levels in the model is 49 (for our experiments 20 levels were used). At the moment only the hydrostatic model version is available, therefore, the highest possible, plausible resolution of the model is about 10 km. Due to the Eulerian treatment of advection, the longest possible timestep, used at the highest resolution is 45 seconds. For the appropriate treatment of the lateral boundary conditions the model uses the classical Davies' scheme (*Davies,* 1976).

In the REMO version adapted at the Hungarian Meteorological Service (REMO5.0) the description of the thermal and hydrological processes in the soil follows the ECHAM4's schemes: the temporal evolutions of the soil temperature and the soil water content are predicted by solving the diffusion equation using a five-layer model (*Warrilow et al.,* 1986); the vertical diffusion and surface turbulent fluxes are calculated based on the Monin–Obukhov similarity theory (*Monin* and *Obukhov*, 1954); the runoff scheme is based on catchment consideration including sub-grid scale variations of field capacity over inhomogeneous terrain (*Dümenil* and *Todini,* 1992). The parameterization of radiation processes is called every hour during the model integration: the description of short-wave radiation follows the method developed by *Fouquart* and *Bonnell* (1980) in two spectral intervals; for the longwave the model uses the narrow-band model after *Morcrette et al.* (1986) with several modifications for additional greenhouse gases and various types of aerosols. The large scale cloud and precipitation formation are calculated based on the budget equations of total cloud water (including cloud liquid water and cloud ice with a simple diagnostic formulation for the latter one) and water vapor, taking into account sources and sinks due to advective and sub-grid scale moisture transports, condensation of water vapor, precipitation formation by coalescence of cloud droplets and sedimentation of ice crystals, evaporation of cloud water and precipitation in unsaturated air (*Sundquist*, 1978). The parameterization of the moist convection is based on a mass flux scheme (*Tiedtke,* 1989) including three

types of convection, but it contains also several improvements described by *Nordeng* (1994).

The physical parameterization packages of REMO5.0 and ECHAM5 are mainly consistent, since in REMO5.0 the schemes of ECHAM4 were implemented, however, the 5th generation of ECHAM model includes several improvements (e.g., a prognostic equation for cloud ice content instead of the former diagnostic formulation).

3. Investigations for the Carpathian Basin

3.1. Experimental design

The model domain applied at the Hungarian Meteorological Service (OMSZ) covers large part of the continental Europe (*Fig. 1*): it certainly includes the entire Central and Eastern European region of interest with sufficiently large extension towards west (the main direction of flow). Furthermore, care was taken to ensure that the lateral boundaries of the domain are in relatively far distance from the high mountain ranges (especially from the Alps and the Carpathian Mountains). The horizontal resolution of the integration domain is approximately 25 km (exactly 0.22 degree), which allows 2 minutes integration timestep. The global fields were coupled to the limited area with 6-hour temporal frequency.

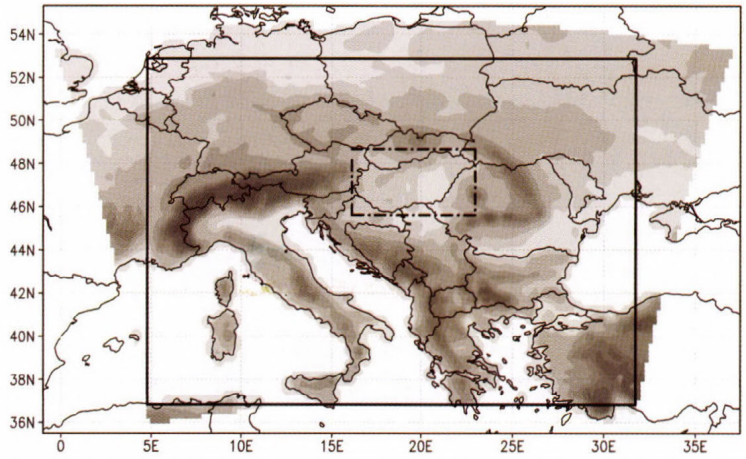


Fig. 1. Orography of the REMO domain used for the long transient climate change simulation (1951–2050). The domain consists of 101×81 gridpoints and its horizontal resolution is approximately 25 km (exactly 0.22 degree). The large (solid) rectangle represents the evaluation domain with respect to the CRU dataset and the small (chained) one indicates the verification area with respect to the Hungarian gridded dataset.

First of all, the performance of the model is validated with respect to various "observational" data in order to understand the model's behavior for the past, which is considered as valuable information for evaluating the simulations for the future. For that purpose the model results are verified for the period of 1961–1990 with the 10-minute (approximately 20 km) version of CRU database (*Mitchell et al.,* 2004) for the European region and with the gridded (0.1 degree resolution) Hungarian observational dataset over Hungary. The application of the latter dataset is justified by the suspicion that the CRU database might not be sufficiently precise over our main area of interest (i.e., Hungary), because of the less local data used for its constitution. The gridded Hungarian dataset (hereafter referred to as HUGRID) is based on Hungarian surface measurements post-processed by the so-called MISH (Meteorological Interpolation based on Surface Homogenized Data Basis) special interpolation technique (*Szentimrey* and *Bihari*, 2005), where the irregularly distributed observations are interpolated to a 0.1-degree resolution latitude-longitude grid covering Hungary using also climatic information based on long observational time series.

The evaluation is concentrating on the differences between the model results and the observational data for two main parameters: 2-meter mean temperature and precipitation amount. Besides the departure and standard deviation fields (the latter ones are not shown in the article) visualized at monthly, seasonal, and annual scale, also several objective statistical characteristics (e.g., mean error, root mean square error) are calculated focusing on the region of our interest (Hungary).

3.2. Validation results for the past climate

Regarding the general flavor of the results, having a look at the annual departure fields of mean temperature and precipitation, as a basic conclusion one can say, while the model provides quite realistic temperature distributions almost everywhere in the domain, it results too high precipitation amounts over large part of the area. (So the model is rather correct in temperature, but at the same time too wet.)

Temperature

Generally speaking, the annual temperature differences between the model results and the (CRU) observations (*Fig. 2*) are rather small (indicating rather perfect simulation), remaining under 1 °C over the major part of the domain, which is especially true for our region of main interest (over Hungary). Exceptions can be noticed over the Alpine region and southeast from the Carpathian Basin: whilst in the elevated points the model underestimates the annual mean temperature, over the southeastern region it predicts too warm climate for the reference period 1961–1990 (it can be remarked that even at that "critical" areas the errors do not exceed 3 °C).

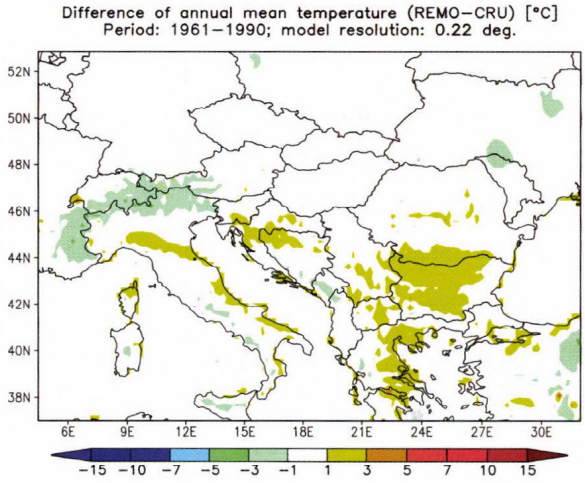


Fig. 2. Difference (in °C) of the annual mean (2-meter) temperature between the model results and the 10-minute resolution CRU dataset for the period of 1961–1990. The intercomparison was carried out on the 0.22 degree resolution re-rotated model grid.

Comparing the mean temperature in the regional model and the driving ECHAM5/MPI-OM global model (*Fig. 3*), it can be generally pinpointed (as anticipated), that the similar large scale features of both models are refined in terms of spatial details by the regional model. It can be clearly seen that due to the more exact description of orography and land-sea mask, the REMO model reflects the temperature patterns of the higher mountains (e.g., the Alps, the Carpathians, and the Dinaric Alps) and the land-sea "contours" (see Apennine Peninsula for instance) more realistically than the global one.

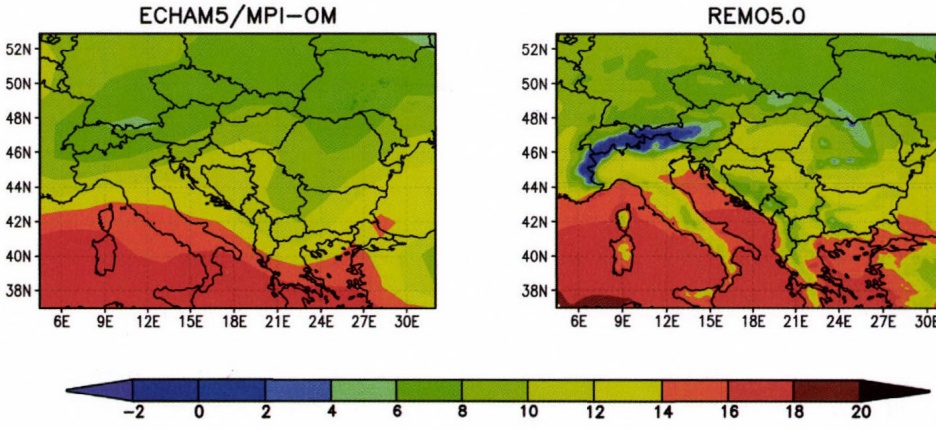


Fig. 3. The annual mean (2-meter) temperature (in °C) in the results of ECHAM5/MPI-OM global model and ECHAM5/MPI-OM-driven REMO5.0 regional model for 1961–1990. The maps indicate the original model resolutions.

Looking at the seasonal details (*Fig. 4*), the main characteristics of the annual pattern are still visible (underestimation at the Alps and overestimation over Bulgaria). The best seasons are autumn and spring (with slight preference towards spring) in terms of deviations from the CRU data. The behavior of the model for the main seasons (winter and summer) is quite different: in winter mostly overestimation can be seen except some mountainous (the Alpine region) and coastal (around the Mediterranean Sea) regions; in summer the model domain is decomposed into two parts: underestimation on the North and overestimation over the South.

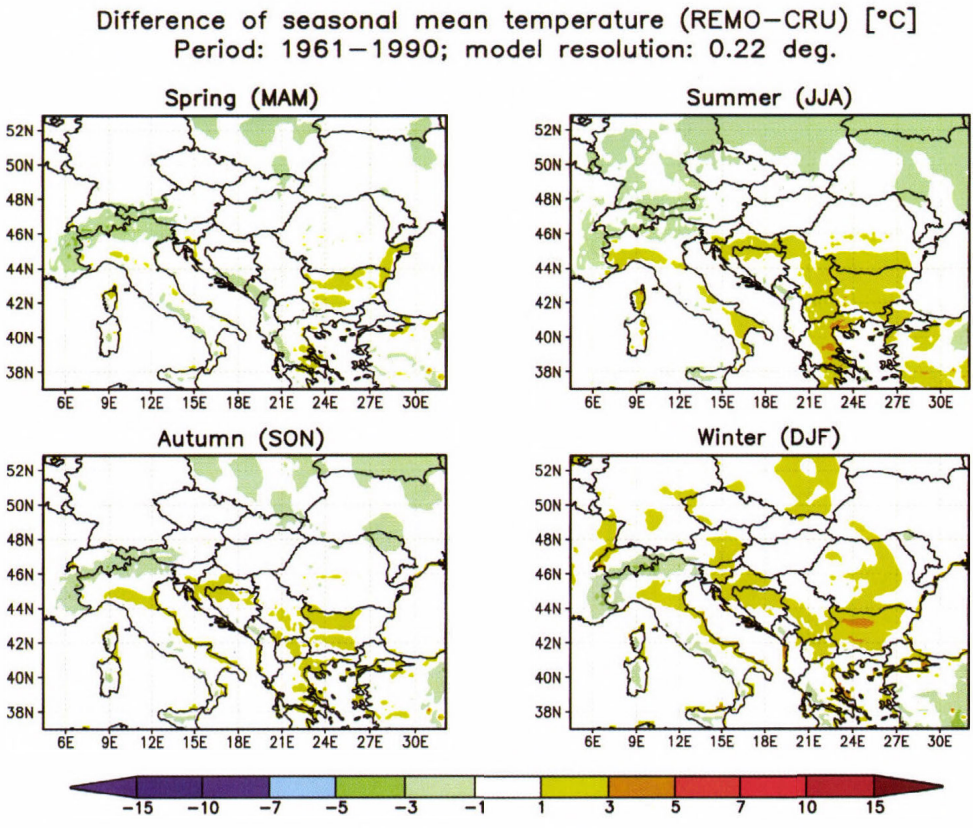


Fig. 4. Difference (in °C) of the seasonal mean (2-meter) temperature between the model results and the 10-minute resolution CRU dataset for the period of 1961–1990 The intercomparison was carried out on the 0.22 degree resolution re-rotated model grid.

The monthly figures (not shown) bring some additional details: the temperature fields of REMO are especially warm during December and January (especially South of the Carpathian Basin), whereas for April and May the smallest bias can be noticed. The winter overestimation is gradually reduced towards the coming spring months. The leading errors during the summer are in August,

when both positive and negative areas can be concluded (the above-mentioned bimodal pattern between the northern and southern part of the domain).

Focusing on the performance of REMO5.0 over Hungary and concentrating on objective scores it can be seen, that the annual mean temperature simulated by the model is almost perfect with respect to the CRU-dataset (*Table 1*): its annual bias is –0.01 °C. Seasonally the simulations are mainly too cool (the only exception is the winter period, when a slight positive bias can be seen), but the errors never reach the 0.5 °C. In spite of the best performance in spring for the entire domain (see above), this season is the worst in terms of bias with respect to CRU over Hungary. The best simulations over Hungary occur in summer as it is also confirmed by the root mean square error values (*Table 2*). The differences (biases) are a bit larger if the validation is realized against the Hungarian gridded observational dataset (but they are still modest remaining mainly under 0.5 °C). It is interesting to see that although the magnitude of the biases with respect to the CRU and HUGRID are similarly small, for the CRU rather the underestimation, while for the Hungarian dataset rather the overestimation is typical. (This means that although the differences between the CRU and Hungarian datasets are small, due to the small bias values this slight deviation might cause different direction of the bias.) The density functions for the differences (not shown) provide some additional insight into the distribution of the seasonal errors with respect to the Hungarian observations: the bias range covers the –1.5 – +1.5 °C interval in general, however, in particular the errors occur mostly between –1 and 1 °C all over the year.

Table 1. The annual and seasonal differences (biases) between the REMO5.0 simulation and the different reference (CRU and HUGRID) datasets, and the ECHAM5/MPI-OM global model averaged over Hungary for 2-meter temperature and precipitation. The values are valid for the period of 1961–1990

	Mean differences (biases)									
	Mean 2-meter temperature [°C]					**Precipitation [mm/month]**				
	Annual	**MAM**	**JJA**	**SON**	**DJF**	**Annual**	**MAM**	**JJA**	**SON**	**DJF**
REMO-CRU	–0.01	–0.43	–0.05	–0.11	0.26	7.68	16.81	–1.94	7.50	8.07
REMO-HU	0.21	–0.22	0.14	0.44	0.52	8.05	16.07	–0.62	8.70	8.42
REMO-ECHAM	0.92	0.83	1.16	1.12	0.55	8.36	6.43	21.28	7.19	–1.52

The mean difference between the (regional) REMO and the (global) ECHAM5/MPI-OM models (*Table 1*) shows that the temperature prediction of REMO is warmer than that of the global one. This departure is the lowest in winter, however, it is always only around 1 °C. In spite of the fact, that the biases between the two models are larger than those between the models and the observations, the root mean square values indicate that the inter-annual variability between the models is more similar than it is the case between the models and the observations. This is somehow understandable, because in the

temporal trends the boundary conditions are important "constraints" for the regional model and most probably the models are unable to simulate the inter-annual variability with sufficient preciseness. For any case generally it can be concluded, that over Hungary the results of REMO model are slightly cooler than the CRU observations, however, the regional model is still warmer compared to the global driving fields (so the global model is even cooler). It was the case also at the simulation driven by ERA-40 data (i.e., the regional results were warmer than the global ones), so it seems that the REMO model introduces a systematic heating effect into the large scale fields, however, in the re-analyses-driven case REMO overheated the temperature fields with respect to the observations.

Table 2. Root mean square errors between annual and seasonal results of REMO5.0 simulation and the different reference datasets (CRU and HUGRID), and the ECHAM5/MPI-OM global model averaged over Hungary for 2-meter temperature and precipitation. The values are valid for the period of 1961–1990

	Root mean square error									
	Mean 2-meter temperature [°C]					**Precipitation [mm/month]**				
	Annual	**MAM**	**JJA**	**SON**	**DJF**	**Annual**	**MAM**	**JJA**	**SON**	**DJF**
REMO-CRU	1.15	1.67	1.30	1.43	2.49	16.63	28.57	29.96	23.63	18.87
REMO-HU	1.14	1.60	1.28	1.53	2.50	17.57	28.37	31.52	25.29	20.37
REMO-ECHAM	1.07	1.04	1.31	1.33	1.02	10.35	13.85	25.06	14.59	10.84

Precipitation

As far as the relative differences of the annual precipitation fields are concerned (*Fig. 5*), besides the general wet characteristics, the orographic features can be immediately noticed: around the highest peaks in Europe (the Swiss, Italian, and Austrian ranges of the Alps) the precipitation overestimation is the strongest (exceeding even 200 percent of the observed values). It is noted that the exact location of this overestimation is not over the mountain peaks, but rather over the slopes. The situation is qualitatively similar for the Carpathian ridge, however, the overestimation is much less pronounced (its magnitude remains "only" between 50 and 100 percent). Curiously, opposite tendencies can be detected in other elevated parts of Europe, like the Adriatic side of the Alps, the Dinaric Alps, the Apennines, or the southern ranges of the Carpathians: the underestimation varies between 10 and 50 percent. As far as Hungary is concerned, also here the too much humidity is dominant (as it is the case for almost all along the domain): the model predicts more precipitation (mainly with 10–50 percent) than the observed annual mean (but the situation is not as bad as at some other parts of the domain).

Comparing the mean precipitation in the regional (REMO) and the global driving (ECHAM5/MPI-OM) model (*Fig. 6*), the situation is (not surprisingly)

similar to that of for the temperature: the large scale features are regionally refined by REMO most particularly over the mountain ranges. Generally speaking, the regional model is significantly more humid than the global one, especially over the highest mountains and in the vicinity of the northern boundary of the integration domain. This latter feature might caused by some "unbalances" between the global and regional fields, while the mountainous humid behavior might stem from the fact that the resolution of the regional model is meaningfully higher, resulting in more precipitation than it is the case for the coarser resolution global model.

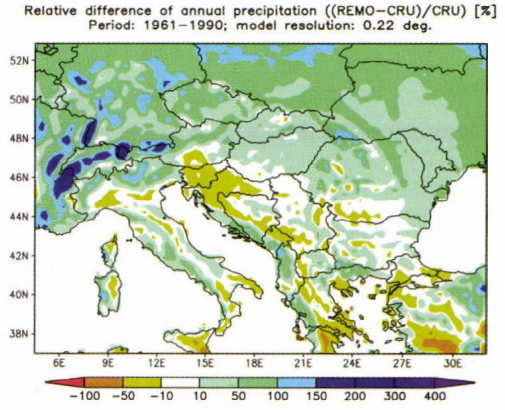


Fig. 5. Relative difference (in percentage) of the annual precipitation between the model results and the 10-minute resolution CRU dataset (reference: CRU dataset) for the period of 1961–1990. The intercomparison was carried out on the 0.22 degree resolution re-rotated model grid.

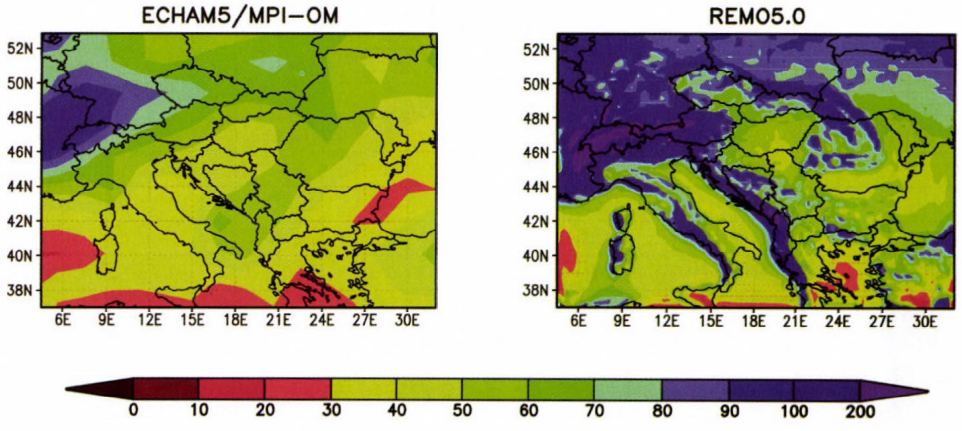


Fig. 6. The annual mean precipitation (in mm/month) in the results of ECHAM5/MPI-OM global model and REMO5.0 regional model for 1961–1990. The maps indicate the original model resolutions.

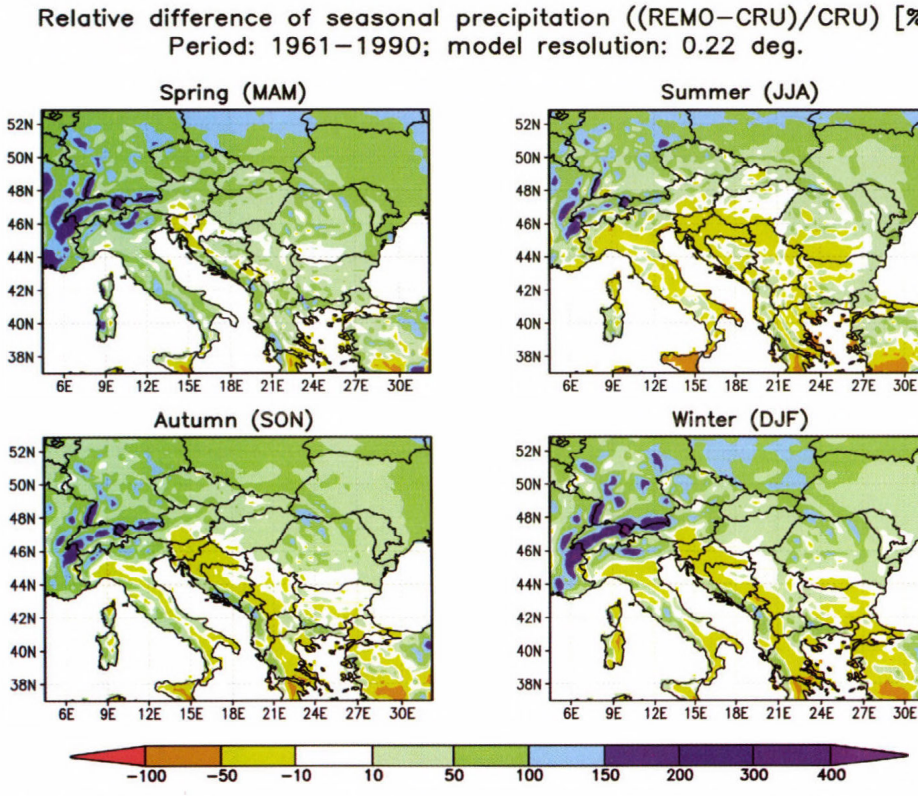


Fig. 7. Relative difference (in %) of the seasonal precipitation between the model results and the 10-minute resolution CRU dataset (reference: CRU dataset) for the period of 1961–1990. The intercomparison was carried out on the 0.22 degree resolution re-rotated model grid.

Investigating the seasonal relative differences between the model results and the CRU-dataset (*Fig. 7*), it can be said, that the seasonal distributions of the departure fields are basically similar to the annual case with some small differences. In spring the overestimation is really dominant, with some very few spotty regions (near to the coastal areas, especially at the Adriatic Sea) with underestimation. On the contrary, in summer while at the northern part of the domain overestimation is dominant, the drying in the model at the South is rather extended. In autumn both the positive errors in the North and the negative errors in the South are decreased (the latter is with respect to the summer situation), whilst in winter the magnitude of overestimation over the Alpine region and the northern part of the domain is strengthened to a "dramatic" level exceeding even 100–200% again. These figures (maybe except the spring one, but especially the summer one) indicate that the Carpathian Basin is situated in an "intermediate" zone, which separates the areas characterized by overestimation over the North and the regions of underestimation over the South. This fact is in

agreement with former studies (e.g., PRUDENCE, *Déqué et al.,* 2007, *Jacob et al.,* 2007), where the northerly wet regions and the southerly dry ones are split around the Carpathian Basin, anticipating the serious difficulties for the provision of reliable precipitation estimates for the Carpathian Basin in general and for Hungary in particular. Otherwise, the simulation for Hungary is fairly satisfactory (especially in summer): the departures from the observations generally remain mainly between 10 and 50% (both in positive and negative orientation, however, the positive ones are dominating especially in spring).

The departure fields for the monthly precipitation amounts (not shown) largely support the conclusions of the seasonal results, namely, that the REMO model overestimates the precipitation over the northern part of the region (especially in winter and spring); and underestimates over the southern part of the continent (especially in summer). The largest negative anomalies can be found in June, August, September, and December and the strongest overestimations occur from January to April.

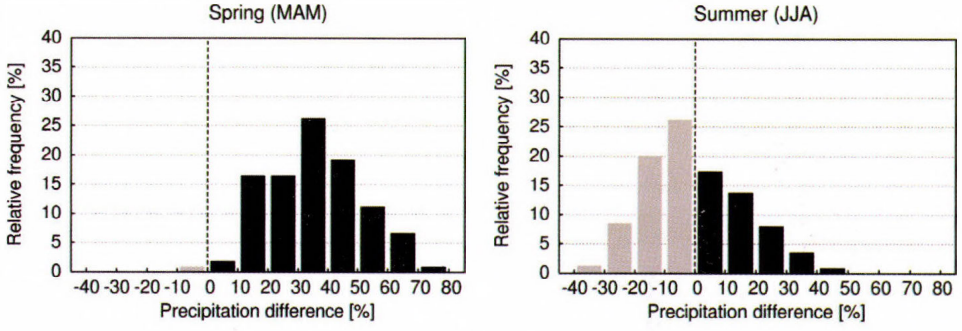


Fig. 8. Discrete density function (in percentage) of the seasonal relative departures (in percentage) for precipitation between the model results and the gridded Hungarian dataset over Hungary for the period of 1961–1990. The dashed line represents the value of 0 percent separating the ranges of over- and underestimation.

Examining the model's behavior over Hungary in terms of objective scores (*Table 1*) one can conclude, that REMO predicts too humid climate (except for summer, when a slight underestimation is exists) for the past compared both to the CRU and the Hungarian gridded observational datasets: the departure is about 8 mm/month on annual scale (contrary to temperature, the error characteristics for the comparison to the two datasets are rather similar). The largest (positive) errors are produced in spring with around 17 mm/month. Basically, the error density functions (*Fig. 8*) confirm these findings, together with some additional information regarding the range and frequency of the model inaccuracies over Hungary. One can easily notice (comparing the above referred maps and histograms), that the span of the over- and underestimation ranges is narrower over Hungary than at the other parts of the integration

domain: it varies between 0 and 80% for the overestimation and 0 and 40% for the underestimation. In spring the abovementioned large positive bias with approximately 16 mm/month means 10–70% overestimation. The particularly low error in summer (seen from the bias values over Hungary) is due to the compensation between the over- and underestimated regions of the country (i.e., the almost symmetric arrangement of the histograms).

Looking at the mean annual difference between the precipitation results of the regional and the global model (*Table 1*), a positive deviation can be found with similar magnitude as it is the case with respect to the observations. But carefully scrutinizing the seasonal departures, some other characteristics can be also noticed: the regional model is more humid than the driving global model (as already mentioned above) with a maximum in summer, when the departure exceeds 20 mm/month. The best correspondence between the global and regional results is in winter, when the global model is slightly wetter (the difference is around 2 mm/month). The relatively lower values of the root mean square departures between the two simulated results (*Table 2*) point to the higher variability of errors with respect to the observations, i.e., in the simulated cases the regional results deviate quite systematically (positively) from the global ones, while compared to the observations, the positive and negative errors rather compensate each other as the lower bias values indicate.

Generally it can be concluded, that over Hungary the REMO model is wetter than the global driving fields, which results in too humid features compared to the various observational datasets.

3.3. Preliminary climate change signals over Hungary

The present part of the article is dedicated to introduce what kind of near future changes can be expected over Hungary according to the results of the transient model simulations (the global and the regional one), whose validations were detailed in the previous subsection. The ensuing evaluation is based on the transient integration considering the "classical" reference period (1961–1990) for the past and the period of 2021–2050 for the future. Therefore, the described changes hereafter are always considered with respect to the model reference (the changes with respect to the observations are not discussed). This approach has the advantage that in case of equal model biases for the past and future periods, the subtraction of the future and past values diminishes those biases in the climate change signals (it is a rather commonly accepted approach in spite of its possible weaknesses, therefore, it was also adapted to our use). The forthcoming evaluation is concentrating on the two basic parameters already investigated above: 2-meter mean temperature and precipitation amount.

Temperature

The main and general orientation of the temperature change is quite clear (see *Figs. 9* and *10*): for the period of 2021–2050 an overall temperature increase is

projected (either for annual or seasonal means). Nevertheless, some special features can be noticed between the global and regional results and also in terms of temporal (seasonal) and spatial details.

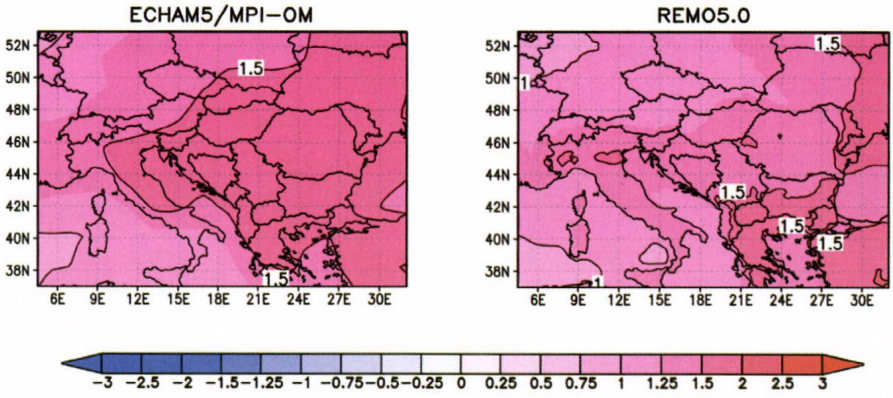


Fig. 9. Change (in °C) of the annual mean (2-meter) temperature projected by the global ECHAM5/MPI-OM coupled model system and by REMO5.0 for the period of 2021–2050 with respect to the period of 1961–1990.

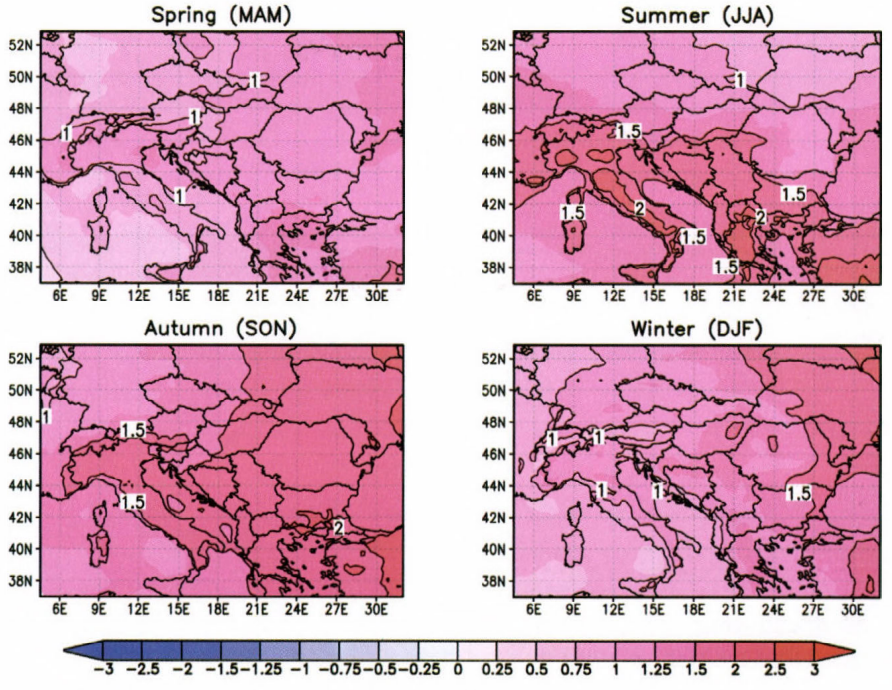


Fig. 10. Change (in °C) of the seasonal mean (2-meter) temperature projected by REMO5.0 for the period of 2021–2050 with respect to the period of 1961–1990.

First, looking at the "driving" global fields (first panel of *Fig. 9*), it can be seen, that the annual temperature change of a given location is mainly affected by its distance from the ocean, i.e., the warming is more intensive inside the continent (especially over Hungary). This characteristic appears also in the seasonal results except for summer (not shown), when the signal is rather influenced by the latitudinal position of the point: over the southern part of Europe the temperature change exceeds the 2 °C, while over the northern (cooler) part of the continent, the increase remains between 1 and 1.5 °C (in other words the warming will be stronger in the South than in the North during the summer). Regarding the regional results, similarly to the global ones, annual and generally seasonal east-west gradient of change can be noticed (right panel of *Fig. 9* and *Fig. 10*), while at the summer also a north-south gradient appears. As far as the magnitude of the increase is concerned it can be pinpointed, that for the REMO model slightly lower temperature growth can be seen than it is the case for ECHAM. The difference between the two simulations is more spectacular, especially during the summer and autumn, when the regional model projects 1–2 °C change over Hungary, whereas the global model covers the interval of 1.75–2.5 °C (note that this conclusion can be also easily seen quantitatively in *Table 3*).

Table 3. Annual and seasonal change and standard deviation of the annual mean (2-meter) temperature (in °C) and precipitation (in percentage) over Hungary projected by REMO5.0 and ECHAM5/MPI-OM for the period of 2021–2050 with respect to the period of 1961–1990. The latter panel of table represents the annual and seasonal mean differences between REMO 5.0 and ECHAM5/MPI-OM for the period of 2021–2050 (in °C for temperature and mm/month for precipitation).

	Target: 2021–2050, reference: 1961–1990									
	REMO					**ECHAM**				
Change	**Annual**	**MAM**	**JJA**	**SON**	**DJF**	**Annual**	**MAM**	**JJA**	**SON**	**DJF**
Temperature	1.35	1.08	1.35	1.58	1.34	1.73	1.33	1.91	2.07	1.51
Precipitation	–0.91	–7.10	–4.83	2.98	7.24	–3.61	–6.17	–15.30	0.32	5.32
Standard deviation	**Annual**	**MAM**	**JJA**	**SON**	**DJF**	**Annual**	**MAM**	**JJA**	**SON**	**DJF**
Temperature	1.01	1.20	1.33	1.54	1.60	1.08	1.23	1.59	1.67	1.70
Precipitation	17.33	21.10	28.96	32.81	28.22	20.23	30.48	40.71	39.57	32.97
REMO–ECHAM	**Annual**	**MAM**	**JJA**	**SON**	**DJF**					
Temperature	0.54	0.58	0.60	0.64	0.37					
Precipitation	9.63	5.51	24.76	8.81	–0.81					

Concentrating uniquely on the changes over Hungary (*Table 3*), REMO indicates, that the temperature will increase with approximately 1.4 °C in annual mean, and with 1.1, 1.4, 1.6, 1.3 °C in spring, summer, autumn, and winter, respectively. It is interesting to see that this warming is not an obviously temporally linear process, i.e., there is quite significant inter-annual variability

considering both the annual (*Fig. 11*) and seasonal (*Fig. 12*) trends. All this implies, that although the general trend shows temperature increase, this does not mean that all the forthcoming years will be warmer than the reference (even at the second part of the projected period there might be years with near-reference or even below-reference values). Nevertheless, it seems that the signal for temperature is rather robust based on the REMO simulations. It is also noted here that one has to be careful with the interpretation of the annual behavior of the model, because although it is expected that the 30-year averages are correctly reflected by the model, it does not mean that the inter-annual variability is also properly addressed.

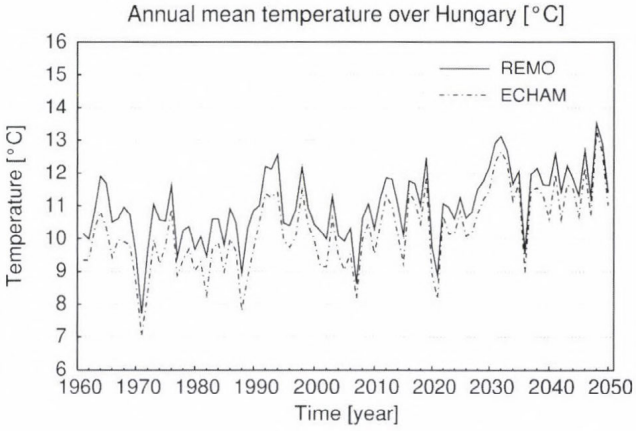


Fig. 11. The annual mean (2-meter) temperature in the results of ECHAM5/MPI-OM global model (chained curve) and ECHAM5/MPI-OM-driven REMO5.0 regional model (solid curve) focused on Hungary for the period 1961–2050.

Certainly besides the relative changes, it is also fascinating to look at the absolute values. According to these (not shown), the main "initial" structure of the temperature fields over Hungary will be conserved at every season (north-south gradient with higher values in the southern regions), however, the temperature values are shifted with 1 °C towards the higher ones. Comparing again the global and regional results for the evolution of the annual mean temperature (*Fig. 11*), it is visible that the difference between the two models is diminishing in the course of time (and it was also quantitatively confirmed by the values regarding the mean deviation between the regional and global fields in *Tables 2* and *3*), because during the reference period the difference between the two models is around 1 °C, then for the future this departure decreases to approximately 0.5 °C (almost vanishing by the end of the integration period) over Hungary. However, the "trend" within the single 30-year periods should be interpreted with special care, because of the fact that the mean signal projected by the regional climate model can not be "split" for individual years.

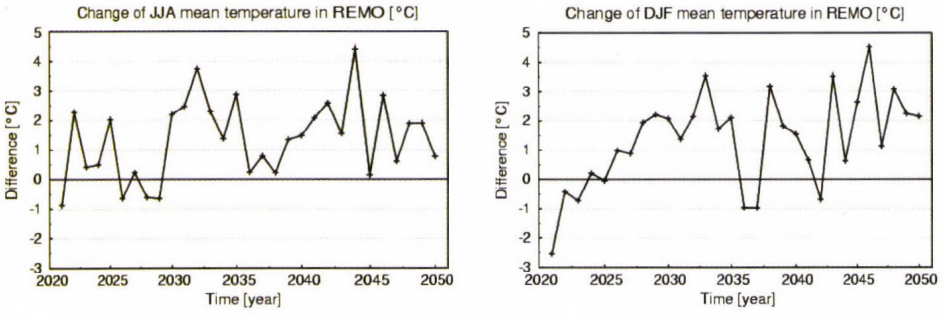


Fig. 12. Evolution of the seasonal (2-meter) temperature change over Hungary projected by REMO5.0 for the period of 2021–2050 with respect to the period of 1961–1990 (left: summer, right: winter).

Precipitation

Regarding the annual precipitation amount, only small changes are projected for the 2021–2050 period by the global and regional models (*Fig. 13*): the precipitation reduction is a bit more characteristic for the entire domain, however, the changes are around –10 and 10 percent in average and maximum –20% in certain regions. As far as the geographical distribution is concerned, at the northern regions of Europe and for the areas being relatively far from the Atlantic-ocean precipitation increase is projected, while over the southern part of the continent and over the Carpathian Basin slight drying can be expected.

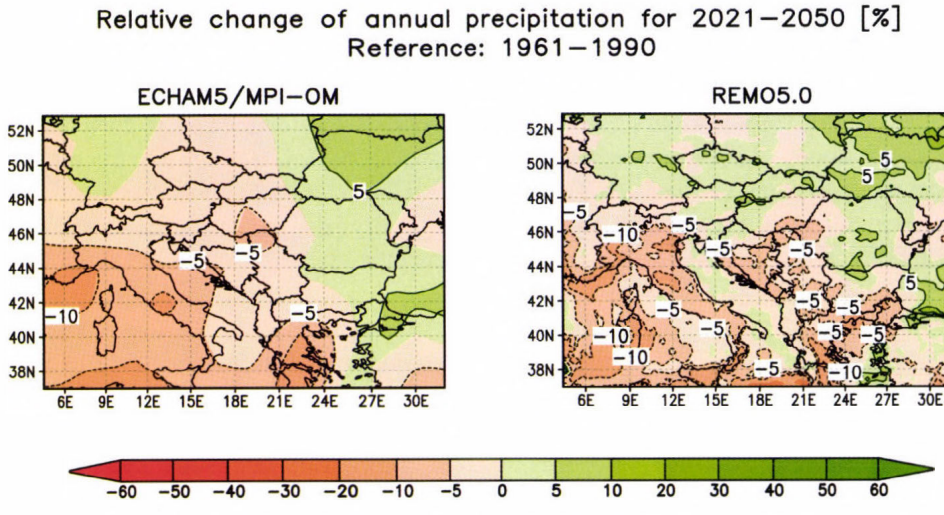


Fig. 13. Relative change (in percentage) of the annual mean precipitation projected by the global ECHAM5/MPI-OM coupled model system and by REMO5.0 for the period of 2021–2050 with respect to the period of 1961–1990.

The global and regional results are in good agreement with each other, however, there are also some differences, e.g., north from Hungary the global model projects drying for the future, whereas REMO renders rather increasing precipitation (this can be probably explained by better description of the mountain ranges over Slovakia and Czech Republic by the regional model).

The seasonal details of the precipitation change are far more interesting than that of the annual ones: there is a large seasonal variability, and therefore, the projected seasonal absolute precipitation values rearrange the whole annual precipitation distribution of the Central European region. Generally speaking, in spring and summer (*Fig. 14*) the precipitation will be reduced for the middle part of the 21st century. Nevertheless, there are also some exceptions: e.g., Northeastern Europe, the highly elevated orographic features like the ranges of Carpathians, where rather increasing precipitation can be foreseen. In autumn the increase will be more overwhelming, especially over the northern part of the domain, while in the South and Southwest rather some drying will take place. Winter is characterized by rather uniform increasing pattern almost all over the domain.

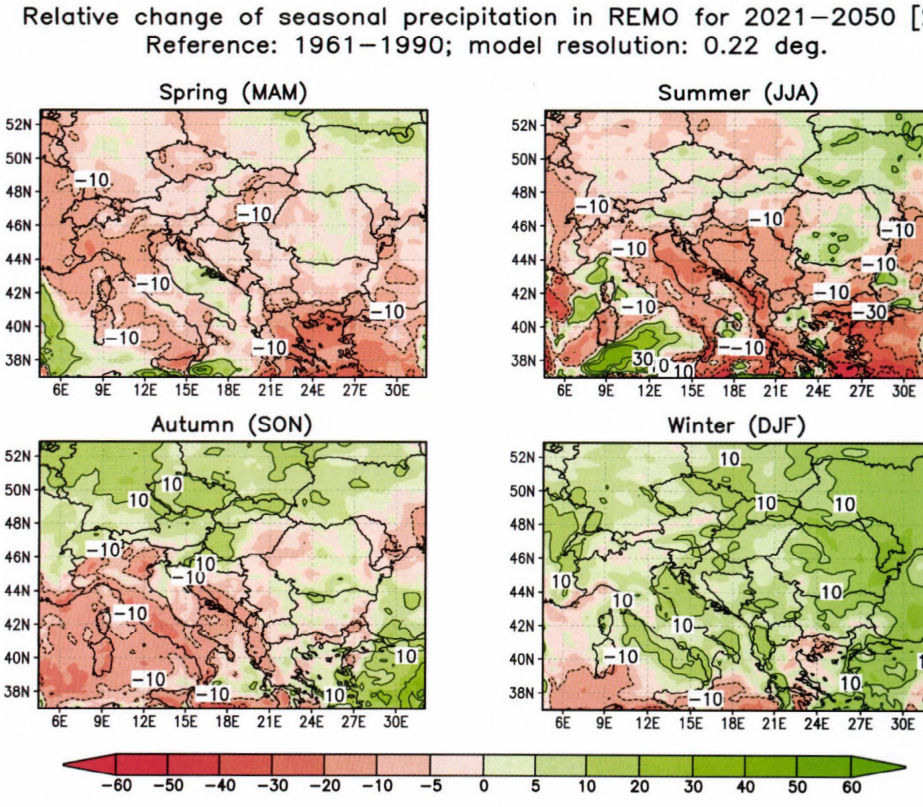


Fig. 14. Relative change (in percentage) of the seasonal mean precipitation projected by REMO5.0 for the period of 2021–2050 with respect to the period of 1961–1990.

The overall magnitude of the likely decrease is slightly larger than the expected increase: in summer the reduction in the global results (not shown) reaches even the 30–50% over the southernmost regions, whilst in winter the increase remains below 20 percent (at that point one also has to consider, that the amount of the winter precipitation is less than the summer one, so the summer "drying" in terms of absolute values will be stronger than the winter growth). Examining the regional results (*Fig. 14*) one can generally say, that the main characteristics of the changes projected by the REMO model is consistent with the results of the ECHAM5/MPI-OM model system, however, a slightly moderate drying is projected for summer over Southern Europe (it reaches only 20–40% over the southern regions) and at the same time (i.e., in summer) the regional results indicate some increase over the highly elevated part of the continent due to its better representation of the regional topographical details.

Furthermore, scrutinizing the REMO results just particularly over Hungary (*Table 3*) it seems, that the relative changes are –7.1, –4.8, 3, and 7.2% in spring, summer, autumn, and winter, respectively, resulting an annual 0.9 percent decrease. These values indicate, that on the one hand, the relative reduction is larger in spring than in summer, and on the other hand, in autumn the precipitation enhancement over the western part of the country and the opposite tendency in East produce an increase in average over Hungary. These findings are rather interesting considering the fact, that recently the most precipitation is falling during the summer and the least one during the winter. The projected changes anticipate that this twofold pattern will significantly change in the future with a more uniform precipitation distribution over Central Europe in general and for Hungary in particular. The inter-annual precipitation changes (*Fig. 15* and *16*) indicate even more fascinating features than it was the case for the temperature: even for those seasons, when the sign of change is rather clear there are lots of years, when the precipitation amount is just the opposite as it would be anticipated by the general average trend (for instance in spring, when the strongest negative change can be concluded, there are several years, when the precipitation is above the reference mean or in winter, when the highest increasing tendency can be seen, there are plenty of years with below average precipitation amounts). All this indicates and proves that an "unusual" season does not provide any direct hint towards the tendencies of the climate change. The abovementioned inter-annual variability is valid not only for the regional model, but it can be noticed also in the global fields (*Fig. 15*). The general temporal evolution of the annual mean precipitation is quite similar in the two models for the past and for the future as well, however, the differences between the global and regional simulated results show an increasing tendency coming from the past towards the future (the opposite trend was found for the temperature).

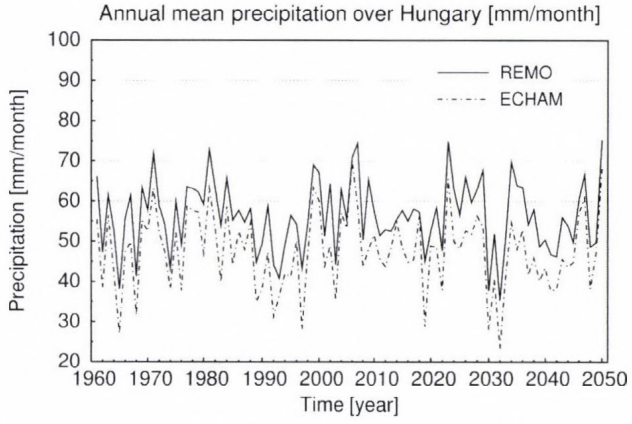


Fig. 15. The annual mean precipitation in the results of ECHAM5/MPI-OM global model (chained curve) and ECHAM5/MPI-OM-driven REMO5.0 regional model (solid curve) focused on Hungary for the period 1961–2050.

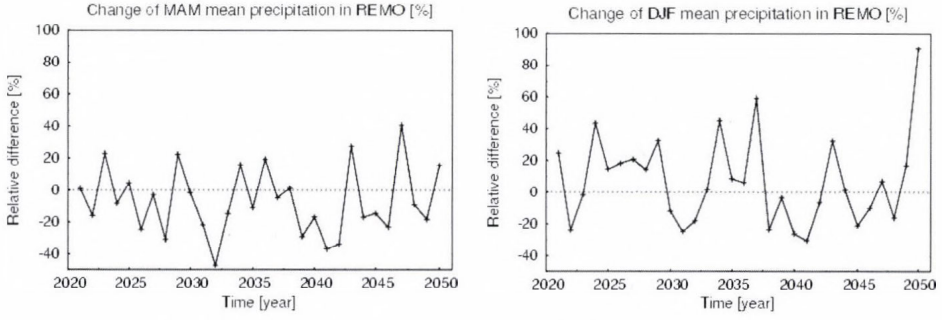


Fig. 16. Evolution of the relative seasonal precipitation change over Hungary projected by REMO5.0 for the period of 2021–2050 with respect to the period of 1961–1990 (left: spring, right: winter).

In the case of precipitation, the absolute precipitation amounts are important information in order to understand the exact quantitative characteristics of the expected changes. For instance, a relative 10 percent change might have rather different consequences for wet and dry regions (because the respective absolute amounts might significantly differ form each other). Comparing the seasonal fields for the reference (past) and for the future over Hungary (not shown), one can conclude, that the basic spatial distribution of the precipitation field will remain unchanged: the minimum values can be found over the Great Hungarian Plain, and the precipitation amount is increasing towards the northern and western parts of the country. The decrease in spring is valid for the entire country, however, the most significant one will be over the area between the Danube and Tisza rivers, where the seasonal mean is

approximately 55–60 mm/month in the reference, and the more than 10% decrease results in 50–55 mm/month for the future. In summer when the precipitation amount is higher than in spring, besides the general reduction some increase can be expected over the northern (elevated) regions – here the precipitation is enhanced to around 80–100 mm/month in average. The autumn tendencies are rather interesting: over the western part of Hungary increase is foreseen, whereas in the East precipitation decrease can be expected, all this results in the slight average enhancement (3%) as mentioned above and can be read from *Table 3*. This spatial distribution is a very crucial issue, because these tendencies might have even dramatic consequences: namely the reduction will be realized over an area where the rainfall is anyway occasionally missing (and it is the case also in summer and autumn over the southern part of Hungary), therefore, the number of drought events might increase in the future. In winter the 0–10% precipitation increase means around 5 mm/month extra precipitation almost everywhere in the domain (most probably considering the simultaneous change of temperature, this precipitation would fall in the form of rain).

4. Summary, conclusions, discussion, and future plans

In this article an overview was given about the validation of the REMO regional climate model and about the main characteristics of the expected climate change over Hungary based on the transient simulation of the model. According to former results of large international cooperations, the regional climate models in general and REMO in particular have a characteristic feature in the summer and autumn months over the Danube catchment area: namely it predicts too warm and dry climate for that region.

The main motivation for the validation of the REMO5.0 simulation was on the one hand, to explore the weaknesses and strengths of the model over Hungary for a longer past period, and on the other hand, to check whether the summer drying problem also appears in the model version adapted in 2004 at the Hungarian Meteorological Service. A long transient climate change simulation was carried out for the hundred-year period of 1951–2050. The model domain covers almost the entire continental Europe with 0.22 degree horizontal and 20 levels vertical resolution, and the lateral boundary forcings were provided by the ECHAM5/MPI-OM coupled atmosphere-ocean model system. For the future part of the integration, the A1B SRES scenario was applied for the global model in order to describe the greenhouse gas and aerosol emissions.

Generally it can be said (based on the subjective and objective verifications achieved for the time being), that the results just partly confirm the conclusions of the former studies: although the REMO model indeed overestimates the temperature over the southeastern part of the continent, over the other parts of the Danube catchment and particularly in Hungary its temperature prediction is quite reliable not only annually, but seasonally as well; furthermore, the

precipitation patterns are mostly characterized by overestimation: the underestimation is restricted to the Adriatic coasts, whereas over the rest of the domain (including also Hungary) the overestimation is typical. Consequently, one can simply say that the model simulation for the recent past is cooler and more humid than it was anticipated based on earlier results.

Nevertheless, the temperature differences between the simulated and observed fields are quite convincing and encouraging from the point of view, that the REMO5.0 will provide realistic temperature projections also for the future. However, it has to be mentioned that even perfect past simulation does not guarantee that the future projection will be equally perfect (and the reverse is also true – maybe in lesser extent –, i.e., erroneous past simulation is not surely accompanied by wrong climate projection). Nevertheless, it is believed that the *real* model developments (based on the understanding and improvement of the inaccurately described physical processes) can essentially contribute to the enhancements of the regional climate models. In the case of precipitation the results proved to be too humid over the major part of the continent, however, in Hungary the magnitude of the errors is much lower reaching a rather satisfactory level. This humid characteristic can be caught not only in the context of the differences between model results and observations, but also in the inter-comparison of the global and regional fields: REMO5.0 simulates a moister past climate than it was originally in the forcing ECHAM-fields. It is especially noticeable over the highly elevated parts of Europe (like the Alps, the Carpathians, the Dinaric Alps) and it is believed as a straight consequence of the finer horizontal resolution of the regional model. (The resolution ratio between the two models is not even negligible: the REMO5.0 has approximately 8.5 times finer resolution than it is the case for ECHAM5/MPI-OM.) Furthermore, the regional model gives unrealistically high precipitation in the vicinity of the northern boundary. This feature is not unknown for regional climate models, where spurious precipitation patterns appear near to the model boundaries. These phenomena are usually explained by the inconsistency between the RCM's internal circulation and the lateral boundary forcings. It might be still the case for REMO in spite of the fact that the physical parameterization packages of the RCM and the GCM are quite similar. One possibility to check whether the strange features are really caused by this incompatibility and reduce it would be the application of two-way nesting technique (*Lorenz* and *Jacob*, 2008), when not only the large scale processes constraint the regional model, but also the small scale processes supply feedback to the global model through more realistic two-way lateral boundary interactions. Besides implementing the global and regional models at the same location, the only disadvantage of the method is its enormous computer resources, because it requires the simultaneous execution of the regional and global models with continuous interactions between them (and this constraint makes impossible to apply the method at the Hungarian Meteorological Service).

As far as the climate change part of the simulation is concerned, it can be pinpointed with rather large confidence, that by the middle of the 21st century, the mean temperature over Hungary will increase with about 1–2 °C in every season, with the smallest values (1.1 °C) in spring and largest ones (1.6 °C) in autumn. These outcomes are in good agreement with the results of the other regional climate model (the ALADIN-Climate model, *Csima*, 2008) adapted at the Hungarian Meteorological Service. The precipitation changes can not be specified so unambiguously: the annual change is a non-significant decrease with around 1 (!) percent, but among the seasons large differences can be experienced. In the first half of the year, i.e., in spring and summer, some reduction can be expected (with larger relative percentage in spring), then it is followed by precipitation increase in autumn and especially in winter. The precipitation surplus in autumn is valid only in spatial average, the details indicate, that over the western part of Hungary some increase, whereas over the eastern (anyway dryer) side of the country rather some decrease is anticipated. This latter fact might induce, that the drought and extremely dry years in the East might mean serious threats for the agriculture. For any case, it is mentioned here that one has to be careful, while interpreting such regional details, because the 25 km resolution of REMO is still on the limit for making such conclusions possible (certainly it would be desirable in the future to realize higher resolution experiments to check the aforementioned regional details). On the other hand, the simulation for the past indicated that the REMO model is capable for providing small scale details for instance for the wind speed, where the most important climatological wind characteristics of Hungary were successfully reflected by the model (not shown).

Basically, all these findings are more or less in good consistency with the tendencies obtained in the PRUDENCE project, which justifies the higher level of temperature change in Hungary than the global average as well as the similar intra-annual distribution of future precipitation (*Christensen*, 2005). (It is strongly emphasized here that these are certainly very qualitative statements due to the fact that the PRUDENCE experimentations were preformed with different SRES scenarios, and moreover, with different lateral boundary forcings in certain cases and for a time slice over the very end of the 21st century.) Besides the concrete projections, another main conclusion of the PRUDENCE project was that Central and Eastern Europe is a very "uncertain" region from the modeling point of view, because the simulations based on different regional climate models result in quite deviating projections (especially for temporal distribution of precipitation). More particularly, Hungary is situated in an "intermediate" zone, between the northern regions anticipated more humid in the future and the southern ones expected drier in the future (this also calls for more regional simulations with different RCMs for our region of interest).

Finally, it has to be remarked that the results introduced in this article are still preliminary ones and they are based only on one (the REMO) model. It

provides very useful hints for applicability of the model for the Carpathian Basin, and moreover, also gives high resolution estimations for the future climate change over the region, which are the first such realizations in Hungary. Nevertheless, in order to draw more reliable and robust conclusions on the one hand, even more sophisticated analysis of the results are necessary, and on the other hand, comparisons to other models' results are indispensable in order to objectively quantify the uncertainties in the projections. For that purpose the results of ALADIN-Climate model (for the time slice of 2021–2050) with the use of the same A1B scenario in the framework of the CECILIA project (Central and Eastern Europe Climate Change Impact and Vulnerability Assessment, http://www.cecilia-eu.org) are going to provide a good basis at the Hungarian Meteorological Service, and the RCMs adapted at the Eötvös Loránd University (PRECIS and RegCM models) will provide further comparable projections, too.

Acknowledgements—The authors are very grateful to the colleagues of the Max Planck Institute for Meteorology for introducing Gabriella Szépszó into the details of the REMO model. Special thanks go to *Susanne Pfeifer* and *Ralf Podzun*, who are always prepared to discuss the arising questions. The fruitful discussions with the members of the Division for Numerical Modeling and Climate Dynamics of Hungarian Meteorological Service and all their valuable helps are highly appreciated. This work was supported by the European Commission's 6th Framework Programme in the framework of CLAVIER project (contract number 037013), the Hungarian National Office for Research and Technology (NKFP, grant No. 3A/082/2004), and the János Bolyai Research Scholarship of the Hungarian Academy of Science.

References

Christensen, J.H., 2005: Prediction of Regional scenarios and Uncertainties for Defining European Climate change risks and Effects. *Final Report.* Danish Meteorological Institute, Copenhagen. http://prudence.dmi.dk/public/publications/PRUDENCE%20Final%20report.pdf

Csima, G., 2008: Validation of the ALADIN-CLIMATE regional climate model at the HMS. *Geophys. Res. Abstracts 10,* 1607-7962/gra/EGU2008-A-07728, European Geosciences Union General Assembly 2008, Vienna, Austria.

Cubasch, U., Waszkewitz, J., Hegerl, G., and *Perlwitz, J.,* 1995: Regional climate changes as simulated in time-slice experiments. *Climatic Change 31,* 273–304.

Davies, H.C., 1976: A lateral boundary formulation for multi-level prediction models. *Q. J. Roy. Meteor. Soc. 102,* 405–418.

Déqué, M., and *Piedelievre, J.P.,* 1995: High resolution climate simulation over Europe. *Clim. Dynam. 11,* 321–339.

Déqué, M., Rowell, D.P., Lüthi, D., Giorgi, F., Christensen, J.H., Rockel, B., Jacob, D., Kjellström, E., de Castro, M., and *van den Hurk, B.,* 2007: An intercomparison of regional climate simulations for Europe: assessing uncertainties in model projections. *Climatic Change (PRUDENCE Special Issue) 81,* 53–70.

Dümenil, L. and *Todini, E.,* 1992: A rainfall-runoff scheme for use in the Hamburg climate model. In *Advances in Theoretical Hydrology, A Tribute to James Dooge* (ed.: *J.P. O'Kane*). *European Geophysical Society Series on Hydrological Sciences 1.* Elsevier Press Amsterdam, 129–157.

Fouquart, Y. and *Bonnel, B.,* 1980: Computation of solar heating of the Earth's atmosphere: A new parameterization. *Beitr. Phys. Atmos. 53, 35–62.*

GARP, 1975: *The Physical Basis of Climate and Climate Modeling. Report of the International Study Conference in Stockholm, Global Atmospheric Research Program (GARP) 16.* World Meteorological Organization, Geneva, Switzerland, 265 pp.

Giorgi, F. and *Bates, G.*, 1989: The climatological skill of a regional model over complex terrain. *Mon. Weather Rev. 117,* 2325–2347.

Hagemann, S. and *Jacob, D.*, 2007: Gradient in the climate change signal of European discharge predicted by a multi-model ensemble. *Climatic Change (PRUDENCE Special Issue) 81, Supplement 1, 309–327.*

Hagemann, S., Machenhauer, B., Jones, R., Christensen, O.B., Déqué, M., Jacob, D., and *Vidale, P.L., 2004:* Evaluation of water and energy budgets in regional climate models applied over Europe. *Clim. Dynam. 23,* 547–567.

Jacob, D., Bärring, L., Christensen, O.B., Christensen, J.H., Hagemann, S., Hirschi, M., Kjellström, E., Lenderink, G., Rockel, B., Schär, C., Seneviratne, S.I., Somot, S., van Ulden, A., and *van den Hurk, B.*, 2007: An inter-comparison of regional climate models for Europe: Design of the experiments and model performance. *Climatic Change (PRUDENCE Special Issue) 81,* Supplement 1, 31–52.

Jacob, D. and *Podzun, R.*, 1997: Sensitivity studies with the regional climate model REMO. *Meteorol. Atmos. Phys. 63,* 119–129.

Lorenz, P. and *Jacob, D.*, 2008: Can two-way nesting improve a regional climate model simulation? *Geophys. Res. Abstracts 10,* 1607-7962/gra/EGU2008-A-11025, European Geosciences Union General Assembly 2008, Vienna, Austria.

Machenhauer, B., Windelband, M., Botzet, M., Christensen, J.H., Déqué, M., Jones, R.G., Ruti, P.M., and *Visconti, G.*, 1998: Validation and analysis of regional present-day climate and climate change simulations over Europe. *Report No. 275,* Max Planck Institute for Meteorology Hamburg, Germany.

Majewski, M., 1991: The Europa Modell of the Deutscher Wetterdienst. *ECMWF Seminar of Numerical Methods in Atmospheric Models II,* ECMWF, 147–191.

Marsland, S.J., Haak, H., Jungclaus, J.H., Latif, M., and *Röske, F.*, 2003: The Max Planck Institute global ocean/sea-ice model with orthogonal curvilinear coordinates. *Ocean Model. 5,* 91–127.

Mesinger, F. and *Arakawa, A.*, 1976: Numerical methods used in atmospheric models. *GARP Publications Series 17,* 1.

Mitchell, T.D., Carter, T.R., Jones, Ph.D., Hulme, M., and *New, M.*, 2004: A comprehensive set of climate scenarios for Europe and the globe. *Tyndall Centre Working Paper 55.*

Monin, A.S. and *Obukhov, A.M.*, 1954: Basic laws of turbulent mixing in the ground layer of the atmosphere. *Doklady Akademii Nauk SSSR Trudy Instituta Geofiziki 151,* 163–187.

Morcrette, J.-J., Smith, L., and *Fouquart, Y.*, 1986: Pressure and temperature dependence of the absorption in longwave radiation parameterizations. *Beitr. Phys. Atmos. 59,* 455–469.

Nakicenovic, N., Alcamo, J., Davis, G., de Vries, B., Fenhann, J., Gaffin, S., Gregory, K., Grübler, A., Jung, T.Y., Kram, T., La Rovere, E.L., Michaelis, L., Mori, S., Morita, T., Pepper, W., Pitcher, H., Price, L., Raihi, K., Roehrl, A., Rogner, H.-H., Sankovski, A., Schlesinger, M., Shukla, P., Smith, S., Swart, R., van Rooijen, S., Victor, N., and *Dadi, Z.*, 2000: *IPCC Special Report on Emissions Scenarios.* Cambridge University Press, Cambridge.

Nordeng, T.E., 1994: Extended versions of the convective parametrization scheme at ECMWF and their impact on the mean and transient activity of the model in the tropics. ECMWF Research Department. *Technical Memorandum No. 206,* European Centre for Medium Range Weather Forecasts, Reading, UK.

Roeckner, E., Arpe, K., Bengtsson, L., Christoph, M., Claussen, M., Dümenil, L., Esch, M., Giorgetta, M., Schlese, U., and *Schulzweida, U.*, 1996: The atmospheric general circulation model ECHAM-4: Model description and simulation of present-day climate. *Report No. 18,* Max Planck Institute for Meteorology, Hamburg, Germany.

Roeckner, E., Bäuml, G., Bonaventura, L., Brokopf, R., Esch, M., Giorgetta, M., Hagemann, S., Kirchner, I., Kornblueh, L., Manzini, E., Rhodin, A., Schlese, U., Schulzweida, U., and *Tompkins, A.*, 2003: The atmospheric general circulation model ECHAM5. Part I: Model description. *Report No. 349,* Max Planck Institute for Meteorology, Hamburg, Germany.

Simmons, A.J. and *Burridge, D.M.*, 1981: An energy and angular-momentum conserving vertical finite-difference scheme and hybrid vertical coordinates. *Mon. Weather Rev. 109,* 758–766.

Simmons, A.J. and *Gibson, J.K.*, 2000: The ERA-40 Project Plan. *ERA-40 Project Report Series*, 1.

Sundquist, H., 1978: A parameterization scheme for non-convective condensation including prediction of cloud water content. *Q. J. Roy. Meteor. Soc. 104,* 677–690.

Szentimrey, T. and *Bihari, Z.*, 2007: Mathematical background of the spatialinterpolation methods and the software MISH (Meteorological Interpolationbased on Surface Homogenized Data Basis). Proceedings of the Conference on Spatial Interpolation in Climatology and Meteorology (eds.: *S. Szalai, Z. Bihari, T. Szentimrey* and *M. Lakatos*) 2007, COST Office, Luxemburg, ISBN 92-898-0033-X, pp.17-28.

Szépszó, G., 2008: Validation of the REMO regional climate model over the Carpathian Basin. *Poster, European Geosciences Union General Assembly 2008*, Vienna, Austria.
http://clavier-eu.org/clavier/?q=system/files/szepszo-2008-EGUViennaPoster.pdf

Tiedtke, M., 1989: A comprehensive mass flux scheme for cumulus parameterization in large scale models. *Mon. Weather Rev. 117,* 1779–1800.

Warrilow, D.A., Sangster, A.B., and *Slingo, A.,* 1986: Modeling of land surface processes and their influence on European climate. *Technical Note DCTN 38,* Dynamical Climatology Branch, United Kingdom Meteorological Office.

Wilby, R.L., Wigley, T.M.L., Conway, D., Jones, P.D., Hewitson, B.C., Main, J., and *Wilks, D.S.,* 1998: Statistical downscaling of General Circulation Model Output: A Comparison of Methods. *Water Resour. Res. 34,* 2995–3008.

IDŐJÁRÁS

Quarterly Journal of the Hungarian Meteorological Service
Vol. 112, No. 3–4, July–December 2008, pp. 233–247

Adaptation of the RegCM3 climate model for the Carpathian Basin

Csaba Torma[1], **Judit Bartholy**[1], **Rita Pongrácz**[1], **Zoltán Barcza**[1], **Erika Coppola**[2] and **Filippo Giorgi**[2]

[1]*Department of Meteorology, Eötvös Loránd University, P.O. Box 32, H-1518, Budapest, Hungary; E-mail: csabi_t@hotmail.com*
[2]*Earth System Physics Section, Abdus Salam International Centre for Theoretical Physics, Trieste, Italy*

(Manuscript received in final form October 21, 2008)

Abstract—Sensitivity experiments of present day climate (1961–1970) using the well-known regional climate model RegCM3 are analyzed over a complex topography domain covering the Carpathian Basin and its surroundings. The horizontal resolution of the model experiments is 10 km, the highest so far used with the RegCM modeling framework. When RegCM3 is run with the original settings used for coarser resolutions, highly unrealistic precipitation values are found in the selected domain, namely a large overprediction of precipitation. In order to reduce this large precipitation bias, we adjusted some of the parameters in the precipitation parameterization and compared results with the original model set up. Annual and seasonal average temperature and precipitation over different sub-regions of the domain are intercompared across the model versions and compared to observational datasets. The results show that the performance of the modified model is considerably better for the Carpathian Basin, especially for annual and seasonal precipitation, which show small biases with the new parameter setting. Our study indicates that some model parameters may have to be suitably modified to use the RegCM at very high resolutions.

Key-words: regional climate model, temperature, precipitation, Carpathian Basin, model validation

1. Introduction

The Fourth Assessment Report of the Intergovernmental Panel on Climate Change (*IPCC*, 2007) suggests changes in regional climate conditions in the 21st century, such as increasing winter precipitation and decreasing summer precipitation over Central Europe. Moreover, studies with different greenhouse gas emission scenarios show that Europe is one of the Earth's most sensitive

regions to global warming (*Giorgi*, 2006). These results are obtained using global climate models (GCM), which are typically run at low spatial resolutions (200–300 km). The main goal of the global model simulations is to capture the effects of large scale processes on the climate system, including land-ocean-atmosphere and sometimes biosphere feedbacks.

One technique that can be use to obtain finer scale climate change information at the regional scale is the use of nested regional climate models (RCM) (*Giorgi* and *Mearns*, 1999). RCMs can focus on specific regions using fine spatial resolutions of the order of 10–50 km, and they are run using as initial and lateral boundary conditions the output from GCM simulations. In the frame of the PRUDENCE project (European Union 5th Framework Program), several RCM simulations of present day (1961–1990) and future (2071–2100) climate were carried out for the entire European continent using 50 km horizontal resolution (*Christensen*, 2005). Based on the 1961–1990 reference period, both the simulated temperature and precipitation values in the PRUDENCE models exhibited substantial biases over the Carpathian Basin, particularly in summer, when they exceeded 2.5 °C and 25%, respectively (*Jacob et al.*, 2007).

As part of the project CECILIA (Central and Eastern Europe Climate Change Impact and Vulnerability Assessment; *Halenka*, 2007) we plan to use the regional climate model RegCM3 originally developed by *Giorgi et al.* (1993a,b) and further modified as described by *Pal et al.* (2007) to produce climate change scenarios over Hungary and the surrounding regions at very high resolution, 10 km. This is to date the highest resolution used within the RegCM3 model framework, and therefore, an important first step in the project is the evaluation of the model performance at this resolution. We here present preliminary results from such an analysis.

We carried out two sets of 10-year simulations with the model over a domain covering our region of interest. First, the standard model set up was adopted, which has been mostly used for resolutions of the order of 30–50 km. After the results from this run showed significant biases in the model simulation, we modified some model parameters to improve the model biases and repeated the simulation. These changes are justified by the fact that 10 km is a resolution at which the assumption underlying standard physics schemes (e.g., convection) may be expected to loose validity, and thus the model may need to be recalibrated. Both simulations are driven at the lateral boundaries by analyses of observations. In this paper we intercompare the two simulations and discuss the model sensitivity to these parameter changes, with a focus on seasonal and annual temperature and precipitation. In the next section we begin with a description of the model and experiment design.

2. *Model description and experiment design*

2.1. Description of RegCM

In order to simulate the climate of the Carpathian Basin, the latest version of RegCM (RegCM3) and a modified version of RegCM3 are used for the reference period 1961–1990. This model was originally developed by *Giorgi et al.* (1993a,b), and then modified, improved and discussed by *Giorgi* and *Mearns* (1999), *Giorgi et al.* (2003), and *Pal et al.* (2007). The dynamical core of the RegCM3 is fundamentally equivalent to the hydrostatic version of the National Center for Atmospheric Research (NCAR) and the Pennsylvania State University joint mesoscale model MM5 (*Grell et al.,* 1994). Surface processes are represented in the model via the Biosphere-Atmosphere Transfer Scheme, BATS (*Dickinson et al.,* 1993). The non-local vertical diffusion scheme of *Holtslag et al.* (1990) is used to calculate the boundary layer physics. Additionally, the physics parameterization is mostly based on the comprehensive radiative transfer package of the NCAR Community Climate Model, the latest version CCM3 (*Kiehl et al.,* 1996). Fraction of cloud ice is diagnosed by the scheme as a function of temperature, and solar radiative transfer is calculated with δ–Eddington approach (*Lenoble*, 1993). The cloud radiation is calculated in a function of cloud fractional cover, cloud effective droplet radius, and cloud liquid water content. The mass flux cumulus cloud scheme of *Grell* (1993) is used to represent the convective precipitation with two closures as an option: *Arakawa* and *Schubert* (1974) and *Fritsch* and *Chappell* (1980). The resolvable scale precipitation is represented via the scheme of *Pal et al.* (2000). This scheme includes a prognostic equation for cloud water and allows determining the subgrid-scale variability of clouds.

2.2. RegCM experiments for the Carpathian Basin

All RCM experiments are initialized on January 1, 1960 and integrated until December 31, 1970, the first year (1960) serves as the spin-up period of the model. The model domain covers 120 × 100 grid points at 10 km grid spacing and centered over Hungary (*Fig. 1*). The domain includes the Carpathian Basin and surrounding areas. The main topographical features of the domain, such as the Carpathians enclosing the basin in the east, the Alps to the west, the Dinari mountains to the south, and a small fraction of the Adriatic sea are also represented.

The topography of the terrain is quite complex, especially at the boundaries, which can cause significant fine-scale variations in weather and climate. The RegCM can be run with initial and lateral boundary conditions (ICBC) from global analysis datasets, the output of a GCM or the output of a previous RegCM simulation. In our experiments the ICBCs are interpolated at

6-hourly intervals from the 45-year reanalysis datasets (ERA-40) of the European Centre for Medium-Range Weather Forecasts (ECMWF). We carefully selected the appropriate setting through various sensitivity experiments, for instance, we changed the number of vertical levels (14, 18, and 23). Although the ECMWF's numerical weather forecast model applies 91 vertical levels (*ECMWF*, 2007), this is not the case in the regional climate models, where usually only 15–30 vertical levels are used (e.g., *Jacob et al.*, 2007). Furthermore, we made test runs with different convective schemes, different type of lateral boundary conditions (sponge, linear, and exponential), and different resolutions (with and without double nesting), and the settings for the 30-year experiments have been selected on the base of the preliminary results of these test runs. Since we are specifically interested in precipitation and temperature in high spatial resolution to validate present-day climate simulation, we used the gridded climatological data provided by the Climatic Research Unit (CRU) of the University of East Anglia (CRU TS 1.2 dataset; *Mitchell* and *Jones,* 2005) for the comparisons.

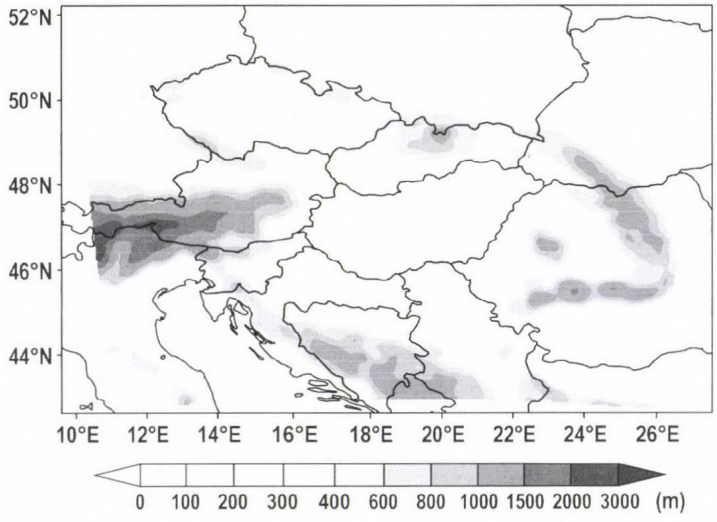


Fig. 1. Model domain and topography (m) for the simulations (10 km grid spacing).

2.3. Adjustment of RegCM parameters

As discussed below, the standard verison of RegCM3 substantially overestimated precipitation over the whole domain, except for the southeastern part of the Alps. In order to decrease precipitation the following parameters were changed: the cloud-to-rain autoconversion rate was decreased from 0.0005 to 0.00025, the raindrop evaporation rate coefficient was increased from $0.2 \cdot 10^{-4}$

to $1.0 \cdot 10^{-3}$ (kg m^{-2} s^{-1})$^{-1/2}$ s^{-1}, the raindrop accretion rate was decreased from 6 to 3 m^3 kg s. Note that all these parameters appear in the resolvable scale precipitation scheme (see *Pal et al.,* 2000), they are all quite uncertain, and these changes made agree within bounds found in the literature. This choice was made because at 10 km resolution most precipitation was produced by this scheme even in the summer, probably because the Grell convection scheme is not activated often at high resolution. The final settings of the parameter are based on expert judgement of the model developers (with almost two decades of modeling experience) and several test runs of RegCM3 for the Carpathian Basin. Of course, the ideal optimization process of model parameters would be based on statistical techniques (e.g., Monte-Carlo simulation, Bayes' theorem), however, due to computational constraints it is not possible to fully accomplish this type of calibration process in case of regional climate models. We call the version of RegCM3 with the above listed changes as RegCM Beta. Details of the RegCM3 and RegCM Beta experiments are summarized in *Table 1*. In both simulations the model employs 18 vertical σ–levels reaching up to 70 hPa with time step 30s and the Grell cumulus scheme with the Fritsch-Chappell closure (see *Grell*, 1993).

Table 1. Settings of the simulations including the modified values of the parameterizations

	RegCM3	**RegCM Beta**
Driving field	ERA-40	ERA-40
Number of grid points	120 × 100	120 × 100
Number of vertical levels	18	18
Spin-up	1 year	1 year
Integration time	Jan 01, 1961–Dec 31, 1970	Jan 01, 1961–Dec 31, 1970
Time step	90 s	90 s
Cloud-to-rain autoconversion rate	0.0005	0.0025
Raindrop evaporation rate coefficient	$0.2 \cdot 10^{-4}$ (kg m^{-2} s^{-1})$^{-1/2}$ s^{-1}	$1.0 \cdot 10^{-3}$ (kg m^{-2} s^{-1})$^{-1/2}$ s^{-1}
Raindrop accretion rate	6 m^3 kg s	3 m^3 kg s

3. Results

In this section the results of the 10-year long simulations (1961–1970) are presented and discussed. The results are shown on a smaller fraction of the entire model domain after eliminating the buffer zone (*Fig. 1*). In order to analyze the model performance in simulating temperature and precipitation, spatial averages are calculated. When computing these spatial averages the buffer zone, which consists of 12 grid points in each direction, is neglected. Since in earlier studies (*Bartholy et al.*, 2006) a large overestimation of precipitation and underestimation of temperature were found in summer, for the

standard RegCM, special consideration is given to the summer results. The bias fields presented in the maps are defined as the difference between the simulated (RegCM3 or RegCM Beta) and observed (CRU) datasets. The mean bias value is defined as the spatial average of these differences.

3.1. Temperature

Fig. 2 compares the annual mean 2-meter air temperatures in RegCM3 and RegCM Beta with the CRU data and the driving ERA-40 data. The maps of *Fig. 2* present the annual average of the RegCM data (lower panels), average of CRU data (upper right panel), and average of ERA-40 data (upper left panel). The bias fields between the RegCM and CRU data are presented in *Fig. 3*. The CRU temperature field shows substantial spatial variability with topographically induced fine-scale regional features. The topographic signal related to the mountain chains of the Carpathians and the eastern edge of the Alps is evident in each seasonal and monthly average as well. (The region of the Adriatic Sea is white in all CRU maps due to the fact that CRU data are available only over land).

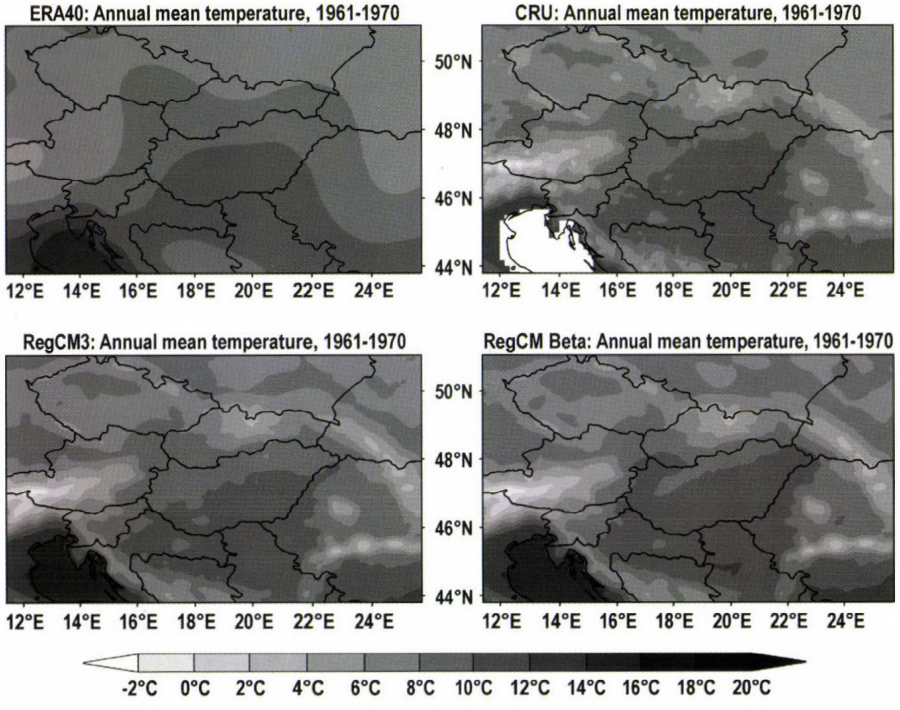


Fig. 2. Spatial distribution of mean annual 2-meter air temperature (°C) averaged over the period 1961–1970. The lower maps corresponds to the result for RegCM3 and RegCM Beta, the upper right map is the annual mean temperature calculated from CRU TS 1.2, and the upper left map is the annual mean temperature calculated from driving data (ERA-40).

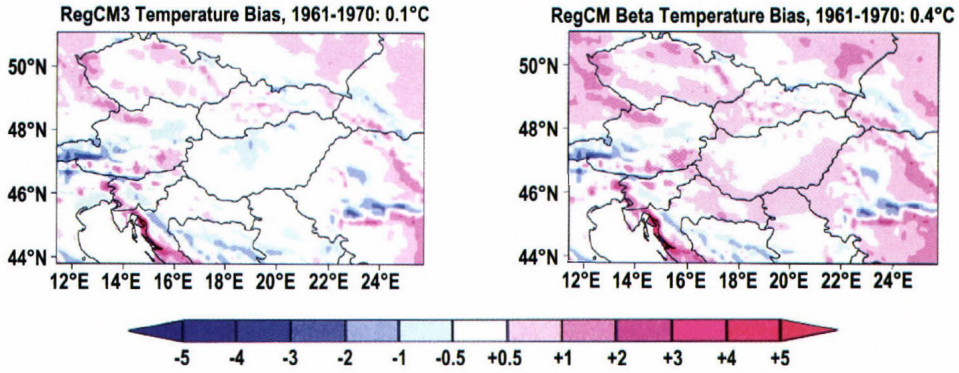


Fig. 3. Spatial distribution of the mean temperature bias (RegCM-CRU, in °C) of RegCM3 and RegCM Beta. The annual average bias field is calculated for the period 1961–1970.

The annual averaged RegCM (both RegCM3 and RegCM Beta) results are very similar to the CRU data. It is clearly shown in *Fig. 2* that the 2-meter air temperature in the annual average is well captured by the regional model (the results were improved a lot compared to the ERA-40 fields), especially, over lowlands. Focusing on Hungary, a very moderate cold bias occurred over the mountainous subregion in the case of the RegCM3 simulation (*Fig. 3*). Complex topography of a domain – such as the surrounding region of Hungary – is always difficult to reproduce for climate models at high resolution (e.g., 10 km) (*Halenka et al.,* 2006). Both simulations show a small warm bias (0.08 °C and 0.36 °C) for the entire domain, the spatially averaged warm bias of the RegCM Beta simulation is a bit higher than the one of the standard RegCM3. The spatial distribution of the bias is very similar in the two simulations. The annual average temperature bias over Hungary is –0.1 °C and 0.45 °C in case of RegCM3 and RegCM Beta, respectively (*Fig. 4*).

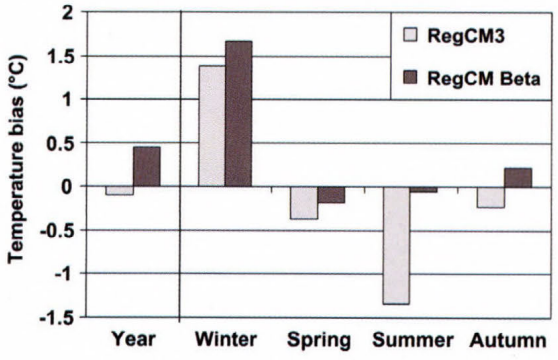


Fig. 4. Annual and seasonal spatial average 2-meter air temperature bias (°C) of RegCM3 and RegCM Beta over Hungary.

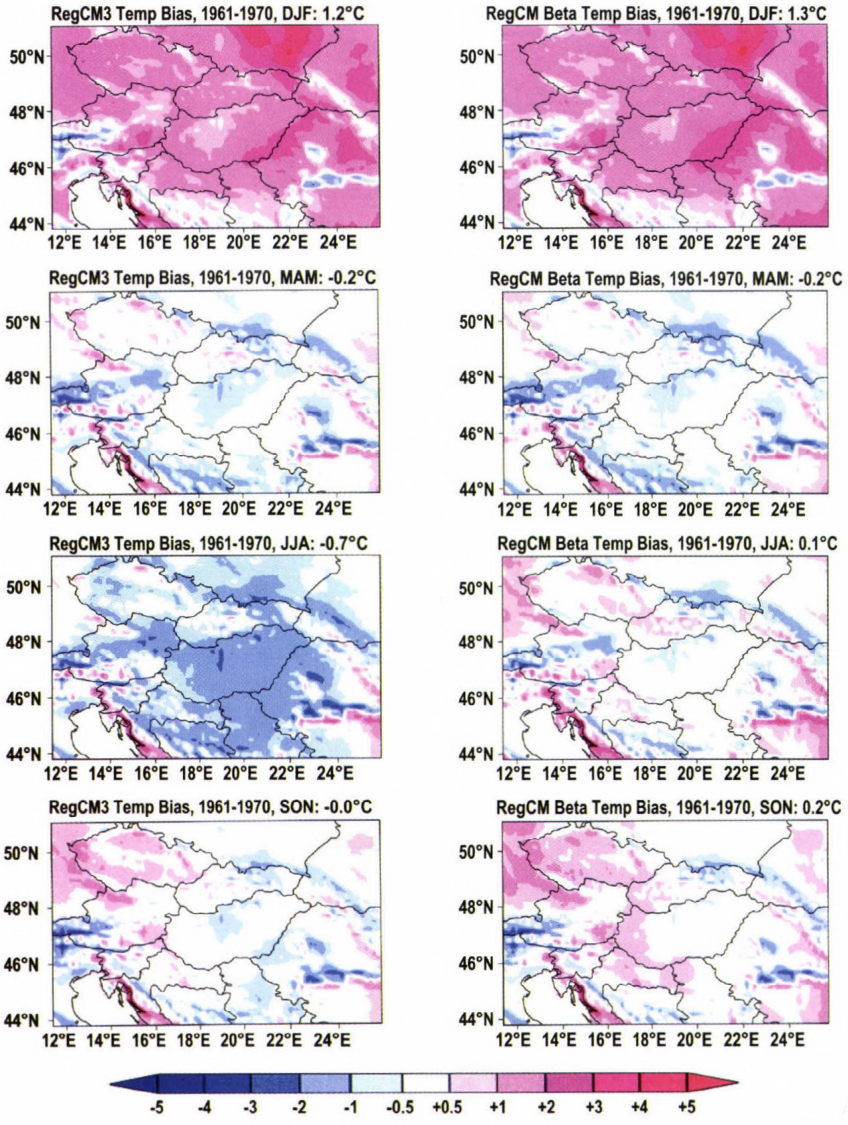


Fig. 5. Spatial distribution of seasonal bias (RegCM-CRU) of 2 meter air temperature (°C) averaged over the period 1961–1970. Maps on the left and on the right represent the RegCM3 and RegCM Beta bias fields, respectively.

The seasonal temperature bias fields are shown in *Fig. 5*. In the transitional seasons, both bias values are relatively small in the entire region (the spatial average is not exceeding 0.23 °C in absolute value) and in Hungary (the spatial average bias is less than 0.37 °C in absolute value), and the results from the RegCM3 and RegCM Beta simulations provide similar structure of the bias

fields. During the summers of 1961–1970 some substantial differences between RegCM3 and RegCM Beta simulated surface air temperature are found. In particular, the RegCM3 results show a dominant cold bias over Hungary (–1.34 °C on spatial average as shown in *Fig. 4*), while in case of the RegCM Beta results the bias does not exceed 0.05 °C in absolute value. This means that only the RegCM Beta simulations reproduced the hottest summer temperature over the Hungarian Great Plains. The largest bias values are found in winter for both simulations, with no improvement found in the RegCM Beta version. The spatial structures of the bias fields are similar, the spatially averaged bias values are 1.22 °C (RegCM3) and 1.32 °C (RegCM Beta) for the entire domain, and 1.38 °C (RegCM3) and 1.67 °C (RegCM Beta) for Hungary (*Fig. 4*).

Summarizing the above results, a cold bias is found in the RegCM3 simulations except in winter, while a small warm bias is found in the RegCM Beta simulation except in spring. *Fig. 5* indicates that RegCM Beta model runs simulate temperature more realistically in summer over the entire domain than RegCM3. Overall, the results of both simulations agree well with the spatial patterns of the annual surface air temperature of the CRU observations. On the basis of the simulated 10 years, the modification made in RegCM3 to RegCM Beta lead to a significant improvement of 2 meter air temperature simulations in summer. This conclusion is also supported by the RMSE values shown in *Table 2* (first two columns).

Table 2. Root mean square error (RMSE) for temperature and for precipitation

RMSE	Temperature (°C)		Precipitation (mm/day)	
	RegCM3	RegCM Beta	RegCM3	RegCM Beta
Winter (DJF)	1.3	1.4	1.2	0.6
Spring (MAM)	0.5	0.5	2.0	0.6
Summer (JJA)	0.9	0.5	2.9	0.6
Autumn (SON)	0.5	0.5	1.0	0.4
Year	0.5	0.6	1.8	0.5

3.2. Precipitation

In this section the precipitation results of RegCM3 and RegCM Beta are discussed and compared to CRU data with a similar approach as in the case of temperature (section 3.1). *Fig. 6* shows the annual mean precipitation; results of the RegCM3 and RegCM Beta can be seen on the left and on the right, respectively. In the case of RegCM3 the bias map is dominated by a dark green color, which means large overestimation of precipitation over the whole domain. The precipitation bias of RegCM3 simulations exceeds 85% on average. This bias is significantly reduced using RegCM Beta to 15%, especially in lowland areas (e.g., in Hungary from 84% to 26%, as shown in *Fig. 7*). The largest bias

occurs over the mountainous subregions in both simulations. The only region where RegCM3 shows lower biases for precipitation is the southeastern edge of the Alps, but this can be attributed to the special effect of this region on precipitation in regional climate simulations.

The annual and seasonal RMSE values of precipitation amounts are shown in *Table 2* (last two columns). As these values suggest, the RegCM Beta simulations resulted in significantly smaller error values, in case of the annual precipitation the RMSE decreased by 73%, while in case of the seasonal precipitation the RMSE decreased by 46%, 71%, 78%, and 58% in winter, spring, summer, and autumn, respectively.

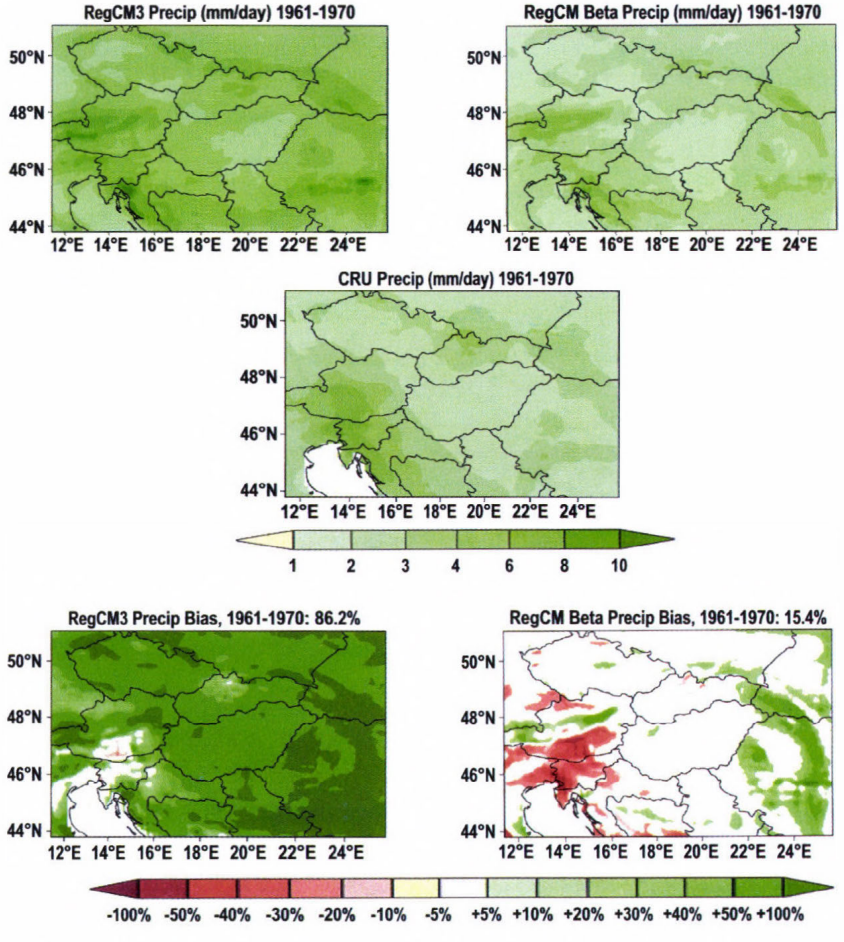


Fig. 6. Spatial distribution of precipitation (mm/day) averaged over the period 1961–1970. The upper maps correspond to the result for RegCM3 and RegCM Beta, the middle map is the annual mean precipitation calculated from CRU TS 1.2, and the lower maps are the bias fields (RegCM-CRU, in %) of RegCM3 and RegCM Beta.

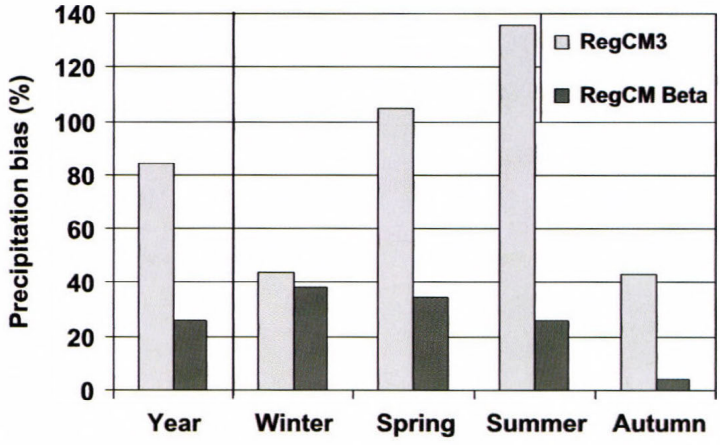


Fig. 7. Annual and seasonal spatial average precipitation bias of RegCM3 and RegCM Beta over Hungary.

Seasonal precipitation bias fields for the 1961–1970 period are shown in *Fig. 8*. Maps on the left represent the spatial structure of the seasonal bias in case of the RegCM3 simulation. These maps are dominated by a large overestimation in the entire domain in all seasons: the bias is 82% in winter, 98% in spring, 108% in summer, and 65% in autumn. For Hungary, these bias values are 44% in winter, 105% in spring, 135% in summer, and 43% in autumn (*Fig. 7*). As a result of the tuning the physical parameterizations in RegCM Beta, the seasonal bias values are reduced significantly, not exceed 47% for seasonal averages over the entire domain (maps shown on the right of *Fig. 8*). The spatial averages of seasonal bias are 47% in winter (38% for Hungary), 26% in spring (35% for Hungary), 7% in summer (26% for Hungary), and –2% in autumn (4% for Hungary).

During summer (JJA) RegCM3 simulates heavy rainfalls over mountainous subregions except in the southeastern edge of the Alps. RegCM3 could not represent well the minimum and maximum rainfall; additional heavy rainfall covers several smaller areas over the southern part of the domain. Observed rainfall was concentrated over high altitudes (Alps and Carpathians), where maximum values of precipitation were about 5 mm/day, but the maximum values of RegCM3 exceeded 10 mm/day. Although in case of the RegCM Beta simulation the precipitation is less intense, and the overall structure and the magnitude of precipitation pattern are reproduced quite well, the mean precipitation fields differ from the CRU datasets in some respects. The simulated precipitation is less than the observed over the southeastern parts of the Alps and over the northern part of Slovakia (mountain Tatra). However, there may exist some uncertainty in observational precipitation data over these high mountains.

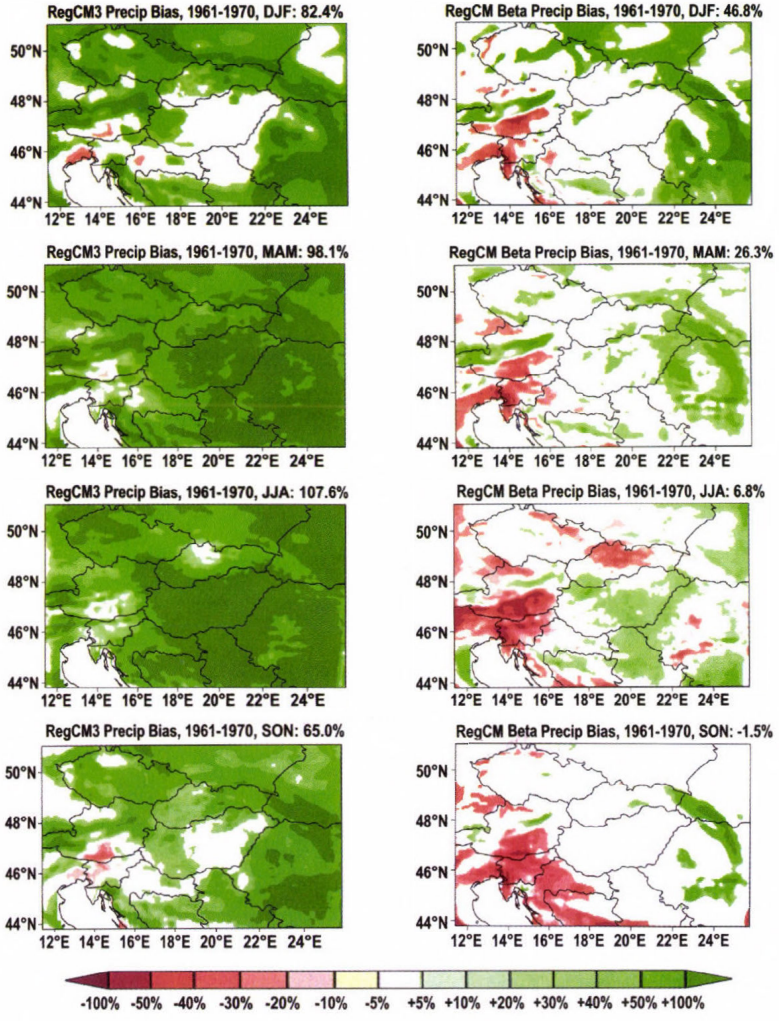


Fig. 8. Spatial distribution of seasonal precipitation bias (RegCM-CRU, in %) averaged over the period 1961–1970. Maps on the left and on the right represent the RegCM3 and RegCM Beta bias fields, respectively.

Summarizing the above results, RegCM3 produced unrealistic precipitation results, with a positive bias exceeding 60% in all season over the entire domain. RegCM Beta simulated the precipitation far more realistically. Thus, the bias was reduced considerably, especially in summer, when the convective parameterization plays an important role in simulating precipitation. Not only the precipitation pattern but also the values themselves agree with the CRU data much more when using RegCM Beta. Although the modifications made to the RegCM3 yield considerably drier simulations, an overestimation of precipitation still exists in some parts of the domain, especially in mountainous regions.

In order to illustrate the ratio of the stratiform and convective precipitation, *Fig. 9* presents an example for June. The maps suggest that both types are considerably reduced to more realistic values in case of RegCM Beta.

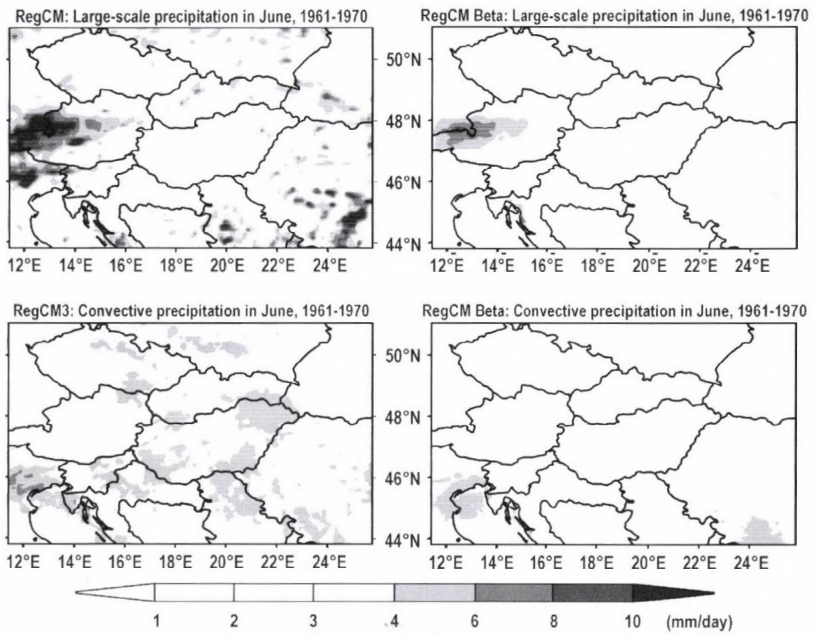


Fig. 9. Monthly mean stratiform (upper maps) and convective (lower maps) precipitation in June, 1961–1970. Maps on the left and on the right represent the RegCM3 and RegCM Beta simulated values, respectively.

4. Conclusions

The regional climate model RegCM3 has been adapted for high resolution simulations over a Central European domain centered around Hungary. The horizontal resolution of the model is 10 km, and decade-long (1961–1970) simulations have been conducted and analyzed. When the original settings of RegCM3 are used, the simulated precipitation pronouncedly exceeds the observed seasonal and annual values, especially in summer and spring. These standard settings have been used for resolutions of 25–50 km and appear not to work properly at resolutions of about 10 km. It is important to note that at the resolution of 10 km the scale separation assumption, underlying the model convection scheme and its interaction with the large scale precipitation scheme, may not be entirely valid. Therefore, a few parameters in the precipitation parameterization scheme were adjusted, namely the cloud-to-rain autoconversion rate, the raindrop evaporation rate, and the raindrop accretion rate, with the aim of reducing precipitation. This modification of physical parameters resulted in a

significant improvement of the precipitation simulation. The overestimation in seasonal precipitation was much reduced, 47% in winter, 26% in spring, 7% in summer, and –2% in autumn for the entire domain. For Hungary, the large positive bias of the summer and spring precipitation found in the standarad RegCM were reduced to 26% and 7%, respectively, leading to a good precipitation simulation. According to these results, the performance of the modified model is considerably better over the entire domain, and especially for Hungary, in the case of precipitation. In case of temperature the positive winter bias (exceeding 1 °C) was not improved in the RegCM Beta version, but the large cold bias of summer temperature was reduced significantly, likely because of the reduced precipitation amounts. In the transition seasons both model experiments reproduced the observational temperature values well with less than 0.5 °C bias.

Our results show that the RegCM simulated precipitation exhibits a substantial sensitivity to horizontal resolution, thus confirming the previous findings of *Giorgi* and *Marinucci* (1996). We stress that the 10 km scale is at the limits of the applicability of cumulus convection schemes, so that the poor performance of the standard RegCM model is not surprising. In particular, we found that at 10 km the Grell convection scheme is not sufficiently activated, so that much of the summer precipitation is produced by the large scale scheme. For this reason, in the RegCM Beta version the parameter adjustment was carried out on the resolvable scale parameterization.

After this adjustment, the RegCM Beta version shows a good performance over the region even at the 10 km resolution and thus, it can be used to simulate future climate conditions (e.g., 2021–2050 and 2071–2100) using the output of coarse resolution GCMs as lateral boundary conditions. These simulations are currently under way in the frame of the CECILIA project and will be reported on in future papers.

Acknowledgements—Research leading to this paper has been supported by the following sources: the Hungarian Academy of Sciences under the program 2006/TKI/246 titled Adaptation to climate change, the Hungarian National Research Development Program under grants NKFP-3A/082/2004 and NKFP-6/079/2005, the Hungarian National Science Research Foundation under grants T-049824, K-67626, and K-69164, the Hungarian Ministry of Environment and Water under the National Climate Strategy Development project, and the CECILIA project of the European Union Nr. 6 program (contract no. GOCE-037005). The authors wish to thank the Physics of Weather and Climate group at the Abdus Salam International Centre of Theoretical Physics (ICTP) for technical support, computational time, and providing data for the simulations.

References

Arakawa, A. and *Schubert, W.H.,* 1974: Interaction of cumulus cloud ensemble with the largescale environment, Part I. *J. Atmos. Sci.,* 31, 674-701.

Bartholy, J., Pongrácz, R., Torma, Cs., and *Hunyady, A.,* 2006: Comparing potential models for projecting regional climate change in the Carpathian Basin. *European Meteorological Society Annual Meeting, Abstracts* 3, EMS2006-A-00519.

Christensen, J.H., 2005: *Prediction of Regional scenarios and Uncertainties for Defining European Climate change risks and Effects. Final Report.* 269p. Danish Meteorological Institute, Copenhagen.

Dickinson, R., Henderson-Sellers, A., and *Kennedy, P.*, 1993: Biosphere-Atmosphere Transfer Scheme (BATS) version 1 as coupled to the NCAR community climate model. *NCAR Technical Note* NCAR/TN-387 + STR, 72p.

ECMWF, 2007: IFS Documentation – Cy31r1. ECMWF, Reading, UK.

Fritsch, J.M. and *Chappell, C.*, 1980: Numerical simulation of convectively driven pressure systems. Part I: Convective parameterization. *J. Atmos. Sci. 37*, 1722-1733.

Giorgi, F., 2006: Climate change hot-spots. *Geophys. Res. Lett. 33*, L08707, doi:10.1029/2006GL025734.

Giorgi, F. and *Marinucci, M.R.*, 1996: An investigation of the sensitivity of simulated precipitation to model resolution and its implications for climate studies. *Mon. Weather Rev. 124*, 148-166.

Giorgi, F. and *Mearns, L.O.*, 1999: Introduction to special section: regional climate modeling revisited. *J. Geophys. Res. 104*, 6335-6352.

Giorgi, F., Francisco, R., and *Pal, J.S.*, 2003: Effects of a subgrid-scale topography and land use scheme on the simulation of surface climate and hidrology. Part 1: Effects of temperature and water vapor disaggregation. *Journal of Hydrometeorology* 4, 317-333.

Giorgi, F., Marinucci, M.R., and *Bates, G.T.*, 1993a: Development of a second generation regional climate model (RegCM2). Part I: Boundary layer and radiative transfer processes. *Mon. Weather Rev. 121*, 2794-2813.

Giorgi, F., Marinucci, M.R., Bates, G.T., and *DeCanio, G.*, 1993b: Development of a second generation regional climate model (RegCM2). Part II: Convective processes and assimilation of lateral boundary conditions. *Mon. Weather Rev. 121*, 2814–2832.

Grell, G., 1993: Prognostic evaluation of assumptions used by cumulus parametrizations. *Mon. Weather Rev. 121*, 764-787.

Grell, G., Dudhia, J., and *Stauffer, D.R.*, 1994: A Description of the fifth generation Penn State/NCAR Mesoscale Model (MM5). *NCAR Technical Note* NCAR/TN-398 + STR, 121p.

Halenka, T., 2007: On the Assessment of Climate Change Impacts in Central and Eastern Europe - EC FP6 Project CECILIA. *Geophys. Res. Abstracts 9*, 10545.

Halenka, T., Kalvova, J., Chladova, Z., Demeterova, A., Zemankova, K., and *Belda, M.*, 2006: On the capability of RegCM to capture extremes in long term regional climate simulation – comparison with the observations for Czech Republic. *Theor. Appl. Climatol. 86*, 125-145. doi:10.1007/s00704-005-0205-5.

Holtslag, A., de Bruiin, E., and *Pan, H.-L.*, 1990: A high resolution air mass transformation model for short-range weather forecasting. *Mon. Weather Rev. 118*, 1561-1575.

IPCC, 2007: *Climate Change 2007: The Physical Science Basis. Contribution of Working Group I to the Fourth Assessment Report of the Intergovernmental Panel on Climate Change*. Edited by *S. Solomon, D. Qin, M. Manning, Z. Chen, M. Marquis, K.B. Averyt, M. Tignor,* and *H.L. Miller*. Cambridge, UK and New York, NY, Cambridge University Press. 996p. (Available online from http://www.ippc.ch)

Jacob, D., Bärring, L., Christensen, O.B., Christensen, J.H., de Castro, M., Déqué, M., Giorgi, F., Hagemann, S., Hirschi, M., Jones, R., Kjellström, E., Lenderink, G., Rockel, B., Sánchez, E., Schär, Ch., Seneviratne, S.I., Somot, S., van Ulden, A., and *van den Hurk, B.*, 2007: An inter-comparison of regional climate models for Europe: Model performance in Present-Day Climate. *Climatic Change 81*, 21-53. doi:10.1007/s10584-006-9213-4.

Kiehl, J., Hack, J., Bonan, G.B., Boville, B., Briegleb, B., Williamson, D., and *Rasch, P.*, 1996: Description of NCAR community climate model (CCM3). *NCAR Technical Note* NCAR/TN-420 + STR, 152p.

Lenoble, J., 1993: *Atmospheric Radiative Transfer*. Deepak, Hampton VA. 532p.

Mitchell, T.D., and *Jones, P.D.*, 2005: An improved method of constructing a database of monthly *climate observations and associated high-resolution grids. Int. J. Climatol. 25, 693-712.*

Pal, J.S., Small, E., and *Eltahir, E.*, 2000: Simulation of regionalscale water and energy budgets: representation of subgrid cloud and precipitation processes within RegCM. *J. Geophys. Res. 105*(29), 567-594.

Pal, J.S., Giorgi, F., Bi, X., Elguindi, N., Solmon, F., Gao, X., Francisco, R., Zakey, A., Winter, J., Ashfaq, M., Syed, F., Bell, J.L., Diffenbaugh, N.S., Karmacharya, J., Konaré, A., Martinez, D., da Rocha, R.P., Sloan, L.C., and *Steiner, A.*, 2007: Regional climate modeling for the developing world: The ICTP RegCM3 and RegCNET. *B. Am. Meteorol. Soc. 88,* 1395-1409.

IDŐJÁRÁS

Quarterly Journal of the Hungarian Meteorological Service
Vol. 112, No. 3–4, July–December 2008, pp. 249–264

Analysis of expected climate change in the Carpathian Basin using the PRUDENCE results

Judit Bartholy, Rita Pongrácz, Györgyi Gelybó and **Péter Szabó**

Department of Meteorology, Eötvös Loránd University
P.O. Box 32, H-1518, Budapest, Hungary
E-mails: bari@ludens.elte.hu, prita@nimbus.elte.hu,
gyoresz@elte.hu, szabpet83@gmail.com

(Manuscript received in final form October 16, 2008)

Abstract—Expected temperature and precipitation changes are analyzed for the Carpathian Basin and, especially, in Hungary, for the 2071-2100 period using outputs of the PRUDENCE project for the A2 and B2 emission scenarios. Different regional climate models (RCMs) of PRUDENCE use 50 km as horizontal spatial resolution, which enables us to estimate the climate change on regional scale. Composite maps of the expected seasonal temperature change and trend analysis of extreme temperature indices suggest that a regional warming trend is evident in the Carpathian Basin. According to the results the largest warming is expected in summer. Negative temperature extremes are projected to decrease while positive extremes tend to increase significantly. The climate simulation results suggest that the expected change of annual total precipitation is not significant in the Carpathian Basin. However, significantly large and opposite trends are expected in different seasons. Seasonal precipitation amount is very likely to increase in winter, and it is expected to decrease in summer, which implies that the annual distribution of precipitation is expected to be restructured. The wettest summer season may become the driest (especially in case of A2 scenario), and the driest winter is expected to be the wettest by the end of the 21st century. The extreme precipitation events are expected to become more intense and more frequent in winter, while a general decrease of extreme precipitation indices is expected in summer.

Key-words: regional climate model, temperature, precipitation, Carpathian Basin, extreme climate index, expected trend

1. Introduction

Spatial resolution of global climate models (GCMs) is inappropriate to describe regional climate processes; therefore, GCM outputs may be misleading to compose regional climate change scenarios for the 21st century (*Mearns et al.*, 2001). In order to determine better estimations for regional climate parameters,

fine resolution regional climate models (RCMs) can be used. RCMs are limited area models nested in GCMs, i.e., the initial and boundary conditions of RCMs are provided by the GCM outputs (*Giorgi*, 1990). Due to computational constrains, the domain of an RCM evidently does not cover the entire globe, and sometimes not even a continent. On the other hand, their horizontal resolution may as fine as 5–10 km. The first project completed in the frame of the European Union V Program is the PRUDENCE (Prediction of Regional scenarios and Uncertainties for Defining EuropeaN Climate change risks and Effects), which involved 21 European research institutes and universities. The primary objectives of PRUDENCE were to provide high resolution (50 km × 50 km) climate change scenarios for Europe for 2071–2100 using dynamical downscaling methods with RCMs (using the reference period 1961–1990), and to explore the uncertainty in these projections (*Christensen et al.*, 2007). Results of the project PRUDENCE are disseminated widely via Internet (http://prudence.dmi.dk) and several other media, and thus, they support socio-economic and policy related decisions.

In the frame of the project PRUDENCE, the following sources of climate uncertainty were studied (*Christensen*, 2005):

- Sampling uncertainty. Simulated climate is considered as an average over 30 years (2071–2100, reference period 1961–1990).
- Regional model uncertainty. RCMs use different techniques to discretize the differential equations and to represent physical processes on sub-grid scales.
- Emission uncertainty. RCM runs used two IPCC-SRES emission scenarios, namely, A2 and B2. 16 experiments from the PRUDENCE simulations considered the A2 scenario, while only 9 of them used the B2 scenario.
- Boundary uncertainty. RCMs were run with boundary conditions from different GCMs. Most of the PRUDENCE simulations used HadAM3H as the driving GCM. Only a few of them used ECHAM4 or ARPEGE (*Déqué et al.*, 2005).

In this paper, the regional climate change projections are summarized for the Carpathian Basin using the outputs of all available PRUDENCE simulations. Results of the expected mean temperature and precipitation change by the end of the 21st century are discussed using composite maps. Furthermore, the expected changes of the extreme climate indices following the guidelines suggested by one of the task groups of a joint WMO-CCl (World Meteorological Organization Commission for Climatology)/CLIVAR (a project of the World Climate Research Programme addressing Climate Variability and Predictability) Working Group formed in 1998 on climate change detection (*Karl et al.,* 1999; *Peterson et al.,* 2002) are also analyzed.

2. Data

Adaptation of RCMs with 10–25 km horizontal resolution is currently proceeding in Hungary, namely, at the Department of Meteorology, Eötvös Loránd University (*Bartholy et al.,* 2006), and at the Hungarian Meteorological Service (*Horányi*, 2006). Results of these RCM experiments are expected within 1–2 years, however, impact studies and end-users need and would like to have access to climate change scenario data much earlier. Also, for the Hungarian National Climate Change Strategy (accepted by the Parliament in March 2008), climate change input data are needed for Hungary. Therefore, in order to fulfill this instant demand with preliminary information, outputs of PRUDENCE simulations (for the 2071–2100 and 1961–1990 periods) are evaluated and offered for the Carpathian Basin. Composite maps of expected temperature and precipitation change cover the Carpathian Basin (45.25°–49.25°N, 13.75°–26.50°E). Since the project PRUDENCE used only two emission scenarios (i.e., A2 and B2), no other scenario is discussed in this paper. In case of the A2 scenario, 16 RCM experiments are used, while in case of B2, only outputs of 8 RCM simulations are available (*Table 1*).

Table 1. List of RCMs with their driving coupled GCMs used in the composite analysis

	Institute	RCM	Driving GCM	Scenario
1	Danish Meteorological Institute	HIRHAM	HadAM3H/HadCM3	A2, B2
2		HIRHAM	ECHAM4/OPYC	A2
3		HIRHAM high res.	HadAM3H/HadCM3	A2
4		HIRHAM extra high res.	HadAM3H/HadCM3	A2
5	Hadley Centre of the UK Met Office	HadRM3P (ensemble/1)	HadAM3P/HadCM3	A2, B2
6		HadRM3P (ensemble/2)	HadAM3P/HadCM3	A2
7	ETH (Eidgenössische Technische Hochschule)	CHRM	HadAM3H/HadCM3	A2
8	GKSS (Gesellschaft für Kernenergieverwertung in Schiffbau und Schiffahrt)	CLM	HadAM3H/HadCM3	A2
9		CLM improved	HadAM3H/HadCM3	A2
10	Max Planck Institute	REMO	HadAM3H/HadCM3	A2
11	Swedish Meteorological and Hydrological Inst.	RCAO	HadAM3H/HadCM3	A2, B2
12		RCAO	ECHAM4/OPYC	B2
13	UCM (Universidad Complutense Madrid)	PROMES	HadAM3H/HadCM3	A2, B2
14	International Centre for Theoretical Physics	RegCM	HadAM3H/HadCM3	A2, B2
15	Norwegian Meteorological Institute	HIRHAM	HadAM3H/HadCM3	A2
16	KNMI (Koninklijk Nederlands Meteorologisch Inst.)	RACMO	HadAM3H/HadCM3	A2
17	Météo-France	ARPEGE	HadAM3H/HadCM3	A2, B2
18		ARPEGE	ARPEGE/OPA	B2

According to the A2 global emission scenario, fertility patterns across regions converge very slowly resulting in continuously increasing world population. Economic development is primarily regionally oriented, per capita economic growth and technological changes are fragmented and slow. The projected CO_2 concentration may reach 850 ppm by the end of the 21st century (*IPCC*, 2007), which is about triple of the pre-industrial concentration level (280 ppm). The global emission scenario B2 describes a world with intermediate population and economic growth, emphasizing local solutions to economic, social, and environmental sustainability. According to the B2 scenario, the projected CO_2 concentration is likely to exceed 600 ppm (*IPCC*, 2007), which is somewhat larger than a double concentration level relative to the pre-industrial CO_2 conditions.

Regional analysis of the detected trend of different extreme climate indices for the Carpathian Basin is discussed by *Bartholy* and *Pongrácz* (2005, 2006, 2007), where the list and definition of the indices can be found also. In this paper, the expected future trends of extreme climate indices are analyzed in the Carpathian Basin using daily temperature and precipitation outputs of four different RCMs run by the (i) Danish Meteorological Institute (DMI), (ii) Abdus Salam International Centre for Theoretical Physics (ICTP) in Trieste, (iii) Royal Meteorological Institute of the Netherlands (Koninklijk Nederlands Meteorologisch Institute, KNMI), and (iv) Swiss Federal Institute of Technology Zurich (Eidgenössische Technische Hochschule Zürich, ETHZ). For all of these simulations the boundary conditions were provided by the HadAM3H/HadCM3 (*Rowell*, 2005) global climate model of the UK Met Office (Table 1). DMI used the HIRHAM4 RCM (*Christensen et al.,* 1996), which has been developed jointly by DMI and the Max-Planck Institute in Hamburg. ICTP used the regional climate model RegCM, which was originally developed by *Giorgi et al.* (1993a, 1993b) and then improved as described by *Giorgi et al.* (1999) and *Pal et al.* (2000). KNMI used the RACMO2 (*Lenderink et al.,* 2003), which combines dynamical core of the HIRLAM Numerical Weather Prediction System with the physical parameterization of the European Centre for Medium-range Weather Forecasting used for the ERA-40 re-analysis project. ETHZ used the Climate High Resolution Model (CHRM) RCM described by *Vidale et al.* (2003). Model performances of the four selected RCMs are analyzed by *Jacob et al.* (2007) using the simulations of the reference period 1961-1990. Besides the A2 scenario experiments, DMI and ICTP accomplished further experiments using the B2 emission scenario.

3. Analysis of the expected regional climate change

Composites of the mean seasonal temperature (daily mean, maximum, and minimum) and precipitation changes are mapped for both A2 and B2 scenarios. The spatial variation of the composite maps are summarized in tables for the

gridpoints located inside Hungary. In order to represent the uncertainty of the composite maps, standard deviations of the RCM model results are also determined and mapped for all seasons.

First, the expected temperature change is discussed, followed by the analysis of the expected precipitation change for the Carpathian Basin.

3.1. Temperature

Fig. 1 presents the expected seasonal temperature change for A2 and B2 scenarios (left and right panel, respectively). Similarly to the global and the European climate change results, larger warming can be expected for A2 scenario in the Carpathian Basin than for B2 scenario. The largest temperature increase is expected in summer, while the smallest increase in spring. The same conclusion can be drawn from *Table 2*, where the intervals of the seasonal temperature increase are summarized for the area of Hungary. The largest warming is expected in summer for both scenarios: in case of the daily mean temperature the interval of the expected increase is 4.5–5.1°C (A2) and 3.7–4.2°C (B2), in case of the daily maximum temperature these intervals are 4.9–5.3°C (A2) and 4.0–4.4 (B2), and in case of the daily minimum temperature these intervals are 4.2–4.8°C (A2) and 3.5–4.0°C (B2). According to the climate projections, the expected increase of mean temperature in summer is between the expected warming of the maximum temperature and that of the minimum temperature. In case of spring, the expected temperature increase inside Hungary is 2.8–3.3°C (for A2 scenario) and 2.3–2.7°C (for B2 scenario).

Fig. 2 summarizes the expected mean seasonal warming for Hungary in case of A2 and B2 scenarios. In general, the expected warming by 2071–2100 is more than 2.4 °C and less than 5.1 °C for all seasons and for both scenarios. Expected temperature changes for the A2 scenario are larger than for the B2 scenarios. The smallest difference is expected in spring (0.6–0.7 °C), and the largest in winter (1.0–1.1 °C). The largest daily mean temperature increase is expected in summer, 4.8 °C (A2) and 4.0 °C (B2). The smallest daily mean temperature increase is expected in spring (3.1 °C and 2.5 °C in case of A2 and B2 scenarios, respectively). Expected increase of the daily maximum temperature exceeds that of the daily minimum temperature by about 0.1–0.6 °C (the largest is in summer), except in winter when the seasonal average daily minimum temperature is projected to increase by 4.1 °C (using the A2 scenario) and 3.0 °C (using the B2 scenario), both of them are 0.1 °C larger than what is projected for the daily maximum temperature increase.

On the basis of seasonal standard deviation fields (*Bartholy et al.,* 2007), the largest uncertainty of the expected temperature change occurs in summer for both emission scenarios.

Similarly to mean temperature, expected seasonal increase of daily maximum and minimum temperatures in the Carpathian Basin was also mapped

(*Bartholy et al.*, 2007). *Fig. 3* compares the projected increases of the winter and summer average daily maximum temperatures for the A2 and B2 scenarios. It can be seen that the spatial structure of the expected warming is similar to that of the expected daily mean temperature increase (*Fig. 1*), but in case of the maximum temperature the projected warming is larger by about 0.1–0.2 °C in winter and 0.3–0.4 °C in summer than in case of the mean temperature.

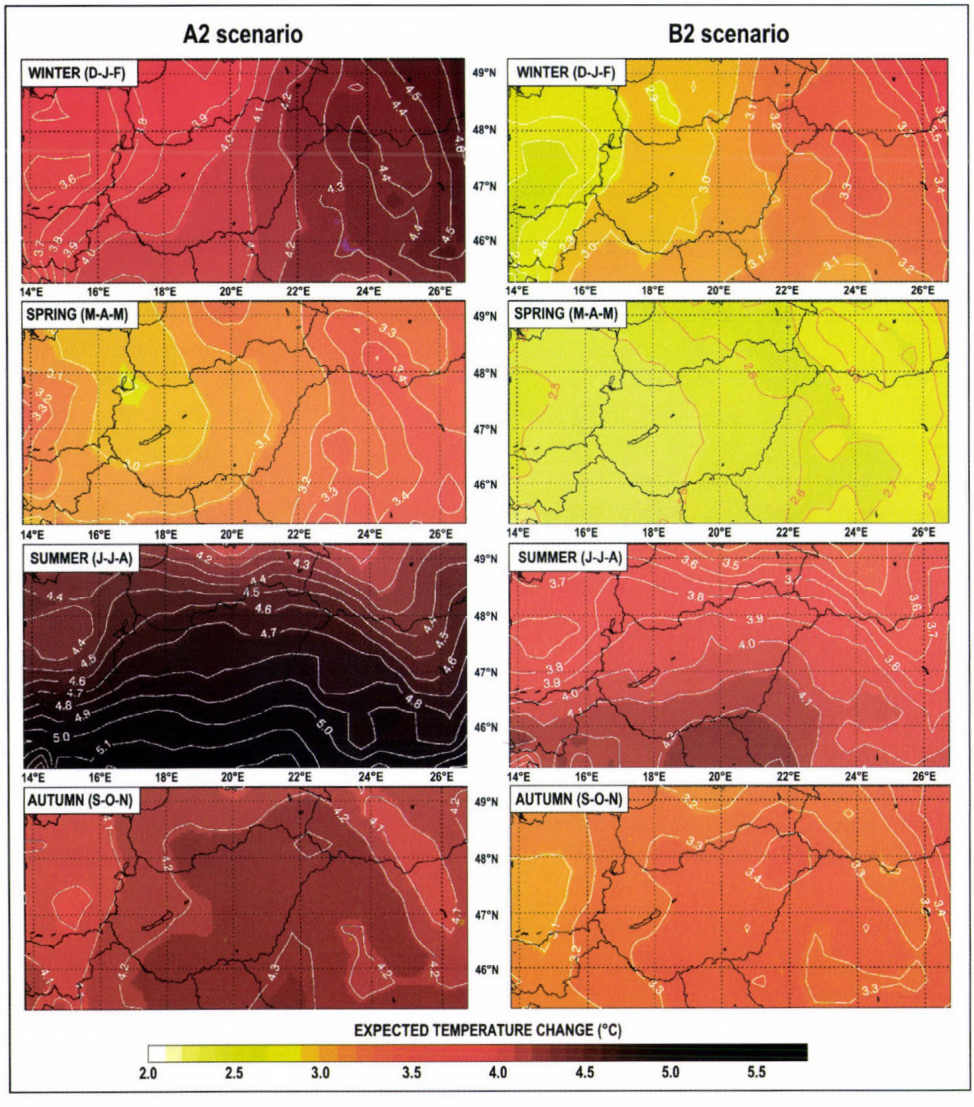


Fig. 1. Seasonal temperature change (°C) expected by 2071–2100 for the Carpathian Basin using the outputs of 16 and 8 RCM simulations in case of A2 and B2 scenarios, respectively (reference period: 1961–1990).

Table 2. Expected increase in mean, maximum, and minimum temperatures (°C) by 2071–2100 for Hungary in case of A2 and B2 scenarios using 16 and 8 RCM simulations, respectively (reference period: 1961–1990)

Temperature	Scenario	Winter (DJF)	Spring (MAM)	Summer (JJA)	Autumn (SON)
Mean	A2	3.7–4.3	2.9–3.2	4.5–5.1	4.1–4.3
	B2	2.9–3.2	2.4–2.7	3.7–4.2	3.2–3.4
Maximum	A2	3.7–4.2	2.8–3.3	4.9–5.3	4.3–4.6
	B2	2.6–3.0	2.4–2.6	4.0–4.4	3.3–3.5
Minimum	A2	3.8–4.6	3.0–3.2	4.2–4.8	4.0–4.2
	B2	2.8–3.5	2.3–2.7	3.5–4.0	3.0–3.2

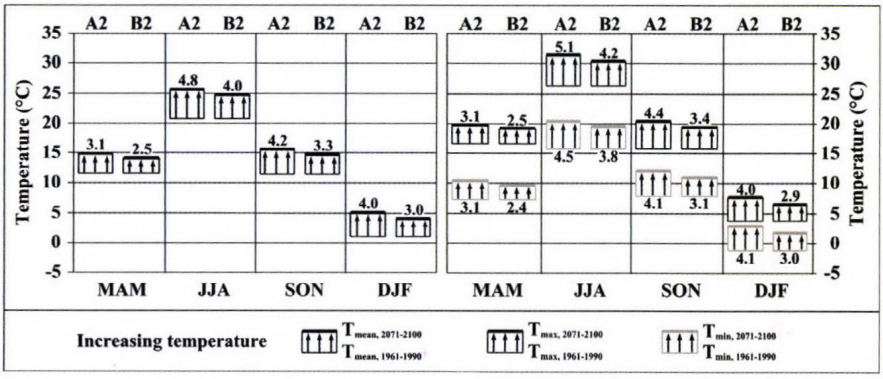


Fig. 2. Expected seasonal increase of daily mean, minimum, and maximum temperatures (°C) for Hungary (temperature values of the reference period 1961–1990 represent the seasonal mean temperature in Budapest).

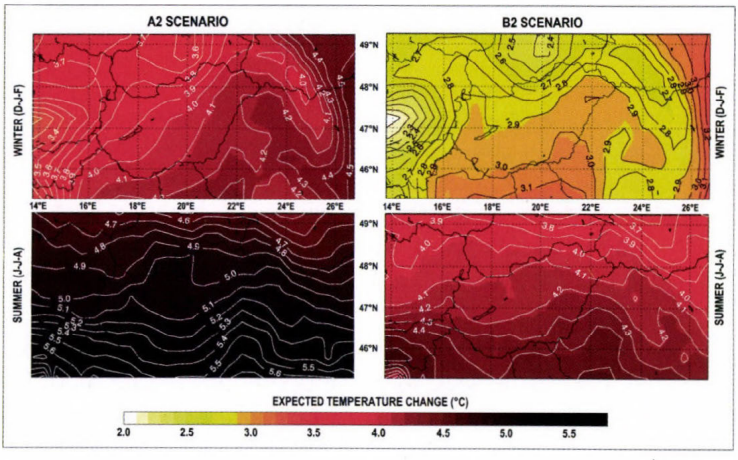


Fig. 3. Expected change of daily maximum temperature (°C) in winter and summer by 2071–2100 for the Carpathian Basin using the outputs of 16 and 8 RCM simulations in case of A2 and B2 scenarios, respectively (reference period: 1961–1990).

The expected trends of the extreme temperature indices are compared in *Fig. 4* for A2 and B2 scenarios using the daily temperature outputs of the regional climate modeling experiments (both for the 1961–1990 and 2071–2100 periods) of four different institutes (i.e., DMI, ICTP, KNMI, and ETHZ). The annual values of the indices are calculated as a spatial average of all the grid points located in Hungary, and then, the expected change is determined. According to the results, negative extremes are expected to decrease, while positive extremes tend to increase significantly. Both imply regional warming in the Carpathian Basin. The largest increase due to this warming trend can be expected in case of extremely hot days (Tx35GE), hot nights (Tn20GT), hot days (Tx30GE), warm nights (Tn90), and warm days (Tx90) by more than 100%. The expected changes are larger in case of the more pessimistic A2 emission scenario than in case of B2, the ratio is about 1–3. The expected warming trends of all the temperature indices are completely consistent with the detected trend in the 1961–2001 period (*Bartholy* and *Pongrácz*, 2006, 2007).

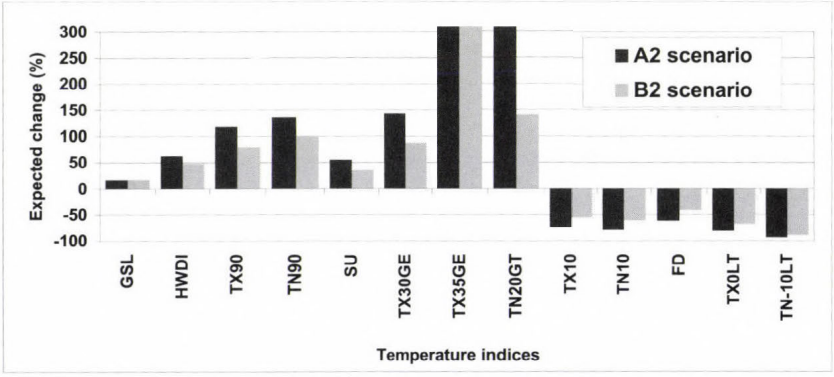


Fig. 4. Expected change of the extreme temperature indices in case of A2 and B2 scenarios (2071–2100) based on the daily outputs of the regional climate models of DMI, ICTP, KNMI, and ETHZ (reference period: 1961–1990).

In order to evaluate the model performance, temperature bias is determined for each RCM output fields using the simulations for the reference period (1961–1990), and the CRU (Climate Research Unit of the University of East Anglia) database (*New et al.*, 1999). In general, the RCM simulations overestimate the temperature in most parts of the Carpathian Basin, however, small underestimation can be seen in the western and northeastern boundary of the selected domain (*Bartholy et al.*, 2007). The largest overestimation can be detected in the southern part of Hungary (1.0–1.5 °C). In the northern part of Transdanubia and the northern part of the Great Plains the temperature is overestimated by 0.5–1.0 °C, while in the northeastern part of the country the overestimation is only 0–0.5 °C.

3.2. *Precipitation*

Similarly to temperature projections, composites of mean seasonal precipitation change and standard deviations are mapped for both A2 and B2 scenarios for the 2071–2100 period. *Fig. 5* presents the expected seasonal precipitation change for A2 and B2 scenarios (left and right panel, respectively) for the Carpathian Basin. The annual precipitation sum is not expected to change significantly in this region (Bartholy et al., 2003), but it is not valid for seasonal precipitation. According to the results shown in Fig. 5, summer precipitation is very likely to decrease (also, slight decrease of autumn precipitation is expected), while winter precipitation is likely to increase considerably (slight increase in spring is also expected).

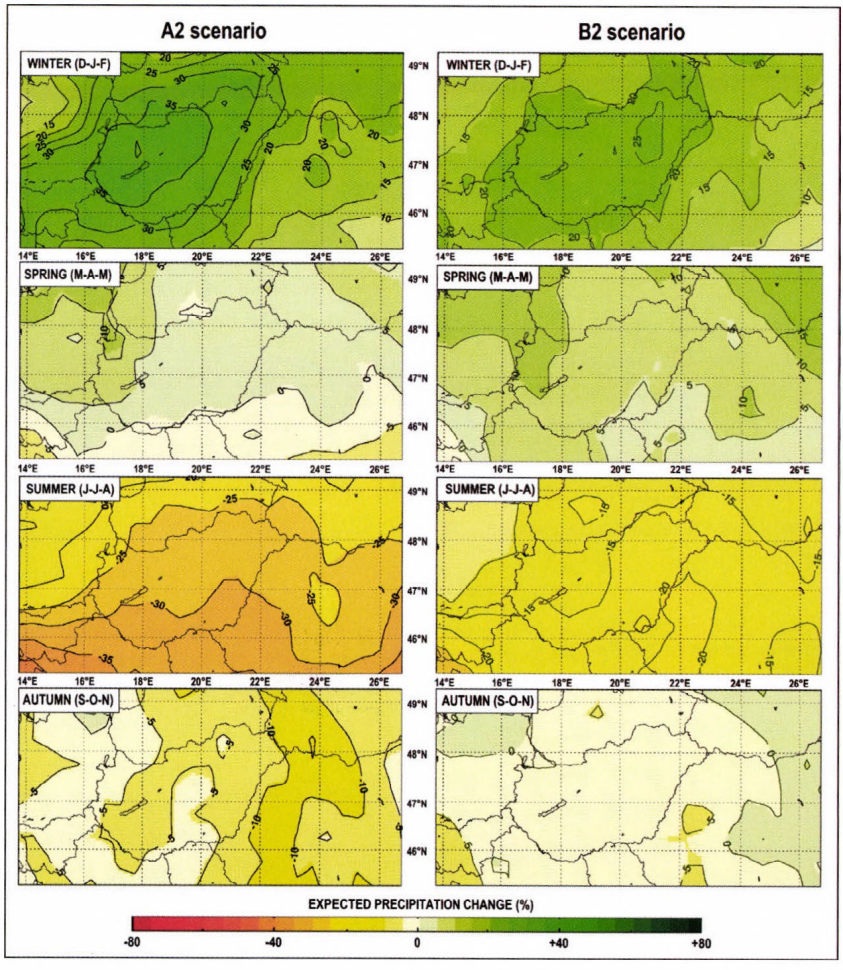


Fig. 5. Seasonal precipitation change (%) expected by 2071–2100 for the Carpathian Basin using the outputs of 16 and 8 RCM simulations in case of A2 and B2 scenarios, respectively (reference period: 1961–1990).

Table 3 summarizes the intervals of seasonal precipitation change for Hungary. In summer, the projected precipitation decrease is 24–33% (A2) and 10–20% (B2). In winter, the expected precipitation increase is 23–37% (A2) and 20–27% (B2). Based on the seasonal standard deviation values (*Bartholy et al.*, 2007), the largest uncertainty of precipitation change is expected in summer, especially, in case of A2 scenario (the standard deviation of the RCM results exceeds 20%).

Table 3. Expected mean precipitation change (%) by 2071–2100 for Hungary in case of A2 and B2 scenarios using 16 and 8 RCM simulations (reference period: 1961–1990)

Scenario	Winter (DJF)	Spring (MAM)	Summer (JJA)	Autumn (SON)
A2	(+23) – (+37)	0 – (+10)	(–24) – (–33)	(–3) – (–10)
B2	(+20) – (+27)	(+3) – (+12)	(–10) – (–20)	(–5) – 0

The expected seasonal change of precipitation for Hungary in case of A2 and B2 scenarios are summarized in *Fig. 6*. Black and grey arrows indicate increase and decrease of precipitation, respectively. According to the reference period 1961–1990, the wettest season was summer, then less precipitation was observed in spring, even less in autumn, and the driest season was winter. If the projections are realized, then the annual distribution of precipitation will be totally restructured, namely, the wettest seasons will be winter and spring (in this order) in cases of both A2 and B2 scenarios. The driest season will be summer in case of A2 scenario, while autumn in case of B2 scenario. On the base of the projections, the annual difference between the seasonal precipitation amounts is expected to decrease significantly (by half) in case of B2 scenario (which implies more similar seasonal amounts), while it is not expected to change in case of A2 scenario (nevertheless, the wettest and driest seasons are completely changed).

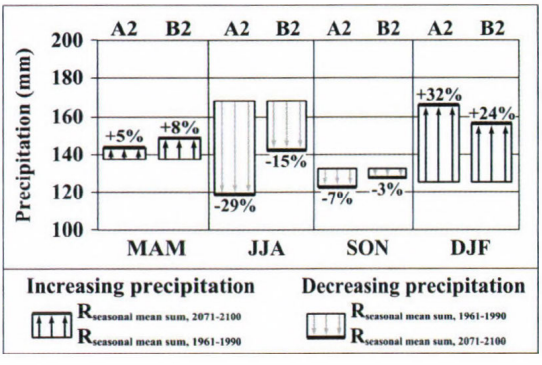


Fig. 6. Expected seasonal change of mean precipitation (mm) for Hungary (increasing or decreasing precipitation is also indicated in %). Precipitation values of the reference period 1961–1990 represent the seasonal mean precipitation amount in Budapest.

Table 4. Expected change of extreme precipitation indices in case of A2 and B2 scenarios (%) (2071–2100) based on the daily outputs of the RCMs of DMI, ICTP, KNMI, and ETHZ (reference period: 1961–1990). In case of the detected trends, signs in parentheses indicate regional mean coefficients being not significant at 95% level.

Precipitation index	A2 scenario			B2 scenario			Detected trend
	Year	January	July	Year	January	July	1976–2001
Rx1 (R_{max})	+17	+29	–2	+13	+23	–5	–
Rx5 ($R_{max,5\ days}$)	+10	+26	–11	+11	+17	–11	+
SDII (R_{year}/RR1)	+10	+16	+13	+7	+12	+1	(+)
R95 ($R_{day} \geq R_{95\%,1961\text{-}90}$)	+7	+60	–30	+14	+35	–22	+
R75 ($R_{day} \geq R_{75\%,1961\text{-}90}$)	–9	+19	–35	+0	+8	–21	+
RR20 ($R_{day} \geq 20$ mm)	+60	+233	+66	+68	+212	–24	+
RR10 ($R_{day} \geq 10$ mm)	+14	+95	–11	+20	+58	–14	+
RR5 ($R_{day} \geq 5$ mm)	–1	+52	–30	+7	+28	–22	(–)
RR1 ($R_{day} \geq 1$ mm)	–10	+19	–31	–2	+6	–19	–
RR0.1 ($R_{day} \geq 0.1$ mm)	–11	+9	–3	–3	+1	–10	–
R95T ($\Sigma R_{day:\ when\ R_{day}>R_{95\%,1961-90}}/R_{total}$)	+16	+27	+9	+14	+23	+0	+

Table 4 summarizes the expected future trends of the extreme precipitation indices determined using the climate simulations of four selected RCMs (i.e., HIRHAM4 of the DMI, RegCM of the ICTP, RACMO2 of the KNMI, and CHRM of the ETHZ) for the 1961–1990 and 2071–2100 periods. Expected changes of annual precipitation indices are generally consistent with the detected trends in the last quarter of the 20th century (*Bartholy* and *Pongrácz*, 2005, 2007). However, the expected regional increase or decrease is usually small (not exceeding 20% in absolute value), except of RR20, the number of very heavy precipitation days. Much larger positive and negative changes are projected in January and July, respectively, on the base of the RCM simulations in case of the A2 and B2 scenarios. These results together with the composite maps shown in Fig. 5 suggest that the climate tends to be wetter in January and drier in July in the Carpathian Basin. Since the projected increases of the RR20, RR10, and R95 (these indices describe very extreme precipitation events) exceed 60% in January in case of A2 scenario, and the expected increases of RR0.1 or RR1 (these indices are not related to extreme precipitation) is 9% and 19%, respectively, the extreme precipitation events are expected to become more

intense and more frequent in January. Similar but smaller changes are expected in case of B2 scenario. Furthermore, drought is projected to become more severe in July by the end of the 21st century, which can be derived from the robust decrease of precipitation indices. The largest decrease rates (exceeding 30%) in July are expected in case of the R75, RR1, RR0.1, RR5, and R95 indices for the A2 scenario. The projected monthly changes are smaller for the B2 scenario.

The expected changes of R95 (number of very wet days) are illustrated in *Fig. 7* using annual and monthly (January and July) changes of grid point values of the extreme climate indices for A2 (upper maps) and B2 (lower maps) scenarios. Blue circles in the maps indicate expected increase, while yellow and red circles imply expected decrease. The size of the circles corresponds to the magnitude of the expected changes. In case of the annual change, the expected increasing rate between 2071–2100 and 1961–1990 in Hungary is about 9% and 18% on average using the A2 and B2 emission scenarios, respectively. Much larger changes are projected in January, namely, +59% and +41% for the country. Opposite changes can be expected in July, the average decrease is expected about 28% (A2) and 23% (B2) for the grid points located in Hungary.

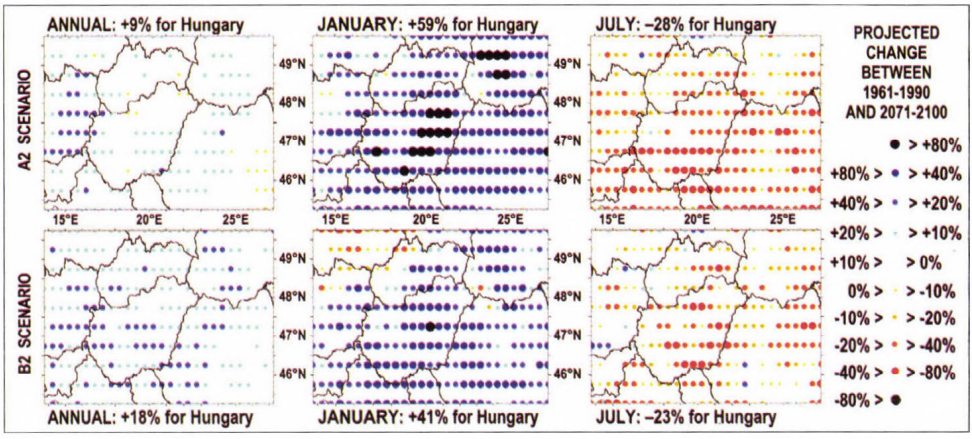


Fig. 7. Expected change of annual and monthly number of very wet days (R95) in case of A2 and B2 scenarios (2071–2100) compared to the reference period (1961–1990). Maps are determined using simulated daily precipitation amounts of the regional climate model of DMI.

In order to evaluate the model performance, precipitation bias is determined for all the RCM output fields using the simulations for the reference period (1961–1990), and the CRU database (*New et al.*, 1999). In general, the RCM simulations overestimate the precipitation in most parts of the Carpathian Basin, however, underestimation can be seen in the southwestern part of the region (*Bartholy et al.*, 2007). In Hungary, the bias is not exceeding 15% in absolute values. The precipitation is slightly underestimated in the western/-

southwestern part of the country, while precipitation in the other large parts (including the entire Great Plains and the eastern part of Transdanubia) is slightly overestimated.

4. Conclusions and discussion

On the basis of the results shown in this paper, the following conclusions can be drawn using the RCM experiment outputs of the PRUDENCE project.

(1) Expected seasonal temperature increase for the Carpathian Basin in case of the A2 scenario is larger than in case of the B2 scenario, which is in good agreement with the expected global and European climate change results (*IPCC*, 2007). The smallest difference between the A2 and B2 scenarios is projected for spring (0.6–0.7 °C), while the largest for winter (1.0–1.1 °C).

(2) The largest daily mean temperature increase is projected for summer, 4.8 °C (A2) and 4.0 °C (B2), while the smallest seasonal warming is expected in spring, 3.1 °C (A2) and 2.5 °C (B2).

(3) The largest increase of maximum and minimum temperatures is expected also in summer for both scenarios. In case of maximum temperature, the intervals of the expected warming are 4.9–5.3 °C (A2) and 4.0–4.4 °C (B2), while in case of minimum temperature, these intervals are 4.2–4.8 °C (A2) and 3.5–4.0 °C (B2). Expected increase of the daily maximum temperature exceeds that of the daily minimum temperature, except in winter.

(4) The extreme temperature indices associated with cold climatic conditions are projected to decrease in the Carpathian Basin by 2071–2100 while the positive extremes tend to increase significantly. The expected changes of the extreme temperature indices are larger in case of the A2 scenario than in case of the B2 scenario.

(5) The annual precipitation sum is not expected to change significantly in this region, but it is not valid for seasonal precipitation sums. Summer precipitation is very likely to decrease, furthermore, slight decrease of autumn precipitation is expected. On the other hand, winter precipitation is likely to increase considerably, and slight increase in spring is also expected.

(6) The projected summer precipitation decrease is 24–33% (A2) and 10–20% (B2), while the expected winter precipitation increase is 23–37% (A2) and 20–27% (B2).

(7) In the reference period (1961–1990), the wettest season was summer, while the driest season was winter. If the projections are realized, then the annual distribution of precipitation will be totally restructured. Namely, the wettest season will be winter in case of both A2 and B2 scenarios. The driest season will be summer in case of A2 scenario, while autumn in case of B2 scenario.

(8) Expected changes (for 2071–2100) of annual precipitation indices are small, but generally consistent with the detected trends in 1976–2001. The projected changes in winter and summer are opposite to each other, which means that large positive and negative changes of monthly precipitation indices are projected in January and July, respectively. Projected increase of very extreme precipitation events exceeds 60% in January, while the expected increases of not extreme precipitation indices do not reach 20%. These results imply that the extreme precipitation events are expected to become more intense and more frequent in January. Furthermore, drought is projected to become more severe and a general decrease of extreme precipitation indices is expected in July.

The analysis discussed in this paper is based on the PRUDENCE simulations, which means that only very few GCMs (mainly HadAM3H/HadCM3, some RCM experiments used ECHAM4/OPYC, and ARPEGE/OPA) are used as driving data of RCMs, which can be considered as limitations of the presented analysis. In an earlier paper (*Bartholy et al.,* 2003), 16 GCM outputs (i.e., ECHAM1, ECHAM3, ECHAM4, HadCM2, UKHI-EQ, UKTR, GFDL-TR, NCAR-DOE, UIUC-EQ, CGCM1-TR, CCC-EQ, BMRC-EQ, CSIRO1-EQ, CSIRO2-EQ, CSIRO-TR, and CCSR-NIES) are analyzed for Hungary in case of A1, A2, B1, and B2 scenarios. The results of the multi-GCM analysis are very similar to most of the findings of the present paper. The quartile range of the expected seasonal temperature change by the end of the 21st century is 3.0–5.5°C in winter, 2.1–3.9°C in spring, 3.0–4.6°C in summer, and 3.0–4.5°C in autumn in case of A2 scenario. The expected temperature increase is smaller for B2 than for A2 scenario. The quartile intervals for the B2 scenario are as follows: 2.0–3.8°C in winter, 1.5–2.5°C in spring, 2.0–3.1°C in summer, and 2.0–3.0°C in autumn. Thus, the projected warming is somewhat smaller than the expected temperature increase of the RCM simulations of PRUDENCE in most of the seasons except winter. However, one must not forget that the horizontal resolution is far more coarse in case of the GCMs (where only 1 or 2 gridpoints represent the entire area of Hungary) than RCMs. For the seasonal precipitation projections the GCM quartile ranges are also considerably smaller, especially, in case of winter and summer (the sign of the projected changes are the same as in the RCM simulations). The GCMs suggest that wetter winters and drier summers are expected by the end of the 21st century (the quartile intervals are (+5%)-(+25%) for A2 and (+2%)-(+15%) for B2 in winter, and (–2%)–(–24%) for A2 and (–2%)–(–15%) for B2 in summer). The projected precipitation changes in spring and autumn are very small (around zero), which also supports the RCM-based results discussed in the present paper.

Acknowledgements—Research leading to this paper has been supported by the following sources: the Hungarian Academy of Sciences under the program 2006/TKI/246 titled Adaptation to climate change, the Hungarian National Research Development Program under grants NKFP-3A/082/2004 and NKFP-6/079/2005, the Hungarian National Sciences Research Foundation under grants T-049824, K-67626, and K-69164, the Hungarian Academy of Science and the Hungarian Prime Minister's

Office under grant 10.025-MeH-IV/3.1/2006, the Hungarian Ministry of Environment and Water under the National Climate Strategy Development project, and the CECILIA project of the European Union Nr. 6 program (contract no. GOCE-037005). Climate change data have been provided through the PRUDENCE data archive, funded by the EU through contract EVK2-CT2001-00132.

References

Bartholy, J. and *Pongrácz, R.*, 2005: Tendencies of extreme climate indices based on daily precipitation in the Carpathian Basin for the 20th century. *Időjárás 109*, 1-20.

Bartholy, J. and *Pongrácz, R.*, 2006: Comparing tendencies of some temperature related extreme indices on global and regional scales. *Időjárás 110*, 35-48.

Bartholy, J. and *Pongrácz, R.*, 2007. Regional analysis of extreme temperature and precipitation indices for the Carpathian Basin from 1946 to 2001. *Global Planet. Change 57*, 83-95. doi:10.1016/j.gloplacha.2006.11.002

Bartholy, J., Pongrácz, R., Matyasovszky, I., and *Schlanger, V.*, 2003: Expected regional variations and changes of mean and extreme climatology of Eastern/Central Europe. *Combined Preprints CD-ROM of the 83rd AMS Annual Meeting*. Paper 4.7, American Meteorological Society. 10p.

Bartholy, J., Pongrácz, R., Torma, Cs., and *Hunyady, A.*, 2006: Regional climate model PRECIS and its adaptation at the Department of Meteorology, Eötvös Loránd University (in Hungarian). In *31. Meteorological Scientific Days – Dynamical climatological research on objective estimation of regional climate change* (ed.: *T. Weidinger*). Hungarian Meteorological Service, Budapest. 99-114.

Bartholy, J., Pongrácz, R., and *Gelybó, Gy.*, 2007: Regional climate change expected in Hungary for 2071-2100. *Applied Ecology and Environmental Research 5*, 1-17.

Christensen, J.H., 2005: Prediction of Regional scenarios and Uncertainties for Defining European Climate change risks and Effects. *Final Report*. 269p. Danish Meteorological Institute, Copenhagen.

Christensen, J.H., Christensen, O.B., Lopez, P., Van Meijgaard, E., and *Botzet, M.*, 1996: The HIRHAM4 Regional Atmospheric Climate Model. *Scientific Report* 96-4, 51p. Copenhagen, DMI.

Christensen, J.H., Carter, T.R., Rummukainen, M., Amanatidis, G., 2007: Evaluating the performance and utility of regional climate models: The PRUDENCE project. *Climatic Change 81*, 1-6. doi:10.1007/s10584-006-9211-6

Déqué, M., Jones, R.G., Wild, M., Giorgi, F., Christensen, J.H., Hassell, D.C., Vidale, P.L., Rockel, B., Jacob, D., Kjellström, E., de Castro, M., Kucharski, F., and *van den Hurk, B.*, 2005: Global high resolution versus Limited Area Model climate change scenarios over Europe: Results from the PRUDENCE project. *Clim. Dynam. 25*, 653-670. doi:10.1007/s00382-005-0052-1.

Giorgi, F., 1990: Simulation of regional climate using a limited area model nested in a general circulation model. *J. Climate 3*, 941-963.

Giorgi, F., Marinucci, M.R., and *Bates, G.T.*, 1993a: Development of a second generation regional climate model (RegCM2). Part I: Boundary layer and radiative transfer processes. *Mon. Weather Rev. 121*, 2794-2813.

Giorgi, F., Marinucci, M.R., Bates, G.T., and *DeCanio, G.*, 1993b: Development of a second generation regional climate model (RegCM2). Part II: Convective processes and assimilation of lateral boundary conditions. *Mon. Weather Rev. 121*, 2814-2832.

Giorgi, F., Huang, Y., Nishizawa, K., and *Fu, C.*, 1999: A seasonal cycle simulation over eastern Asia and its sensitivity to radiative transfer and surface processes. *J. Geophys. Res. 104*, 6403-6423.

Horányi, A., 2006: Dynamical climatological research on regional scales: International and Hungarian review (in Hungarian). In *31. Meteorological Scientific Days – Dynamical climatological research on objective estimation of regional climate change* (ed.: *T. Weidinger*). Hungarian Meteorological Service, Budapest. 62-70.

IPCC, 2007: *Climate Change 2007: The Physical Science Basis. Contribution of Working Group I to the Fourth Assessment Report of the Intergovernmental Panel on Climate Change*. Edited by *S. Solomon, D. Qin, M. Manning, Z. Chen, M. Marquis, K.B. Averyt, M. Tignor*, and *H.L. Miller.*

Cambridge, UK and New York, NY, Cambridge University Press. 996p. (Available online from http://www.ippc.ch)

Jacob, D., Bärring, L., Christensen, O.B., Christensen, J.H., de Castro, M., Déqué, M., Giorgi, F., Hagemann, S., Hirschi, M., Jones, R., Kjellström, E., Lenderink, G., Rockel, B., Sánchez, E., Schär, Ch., Seneviratne, S.I., Somot, S., van Ulden, A., and *van den Hurk, B.,* 2007: An inter-comparison of regional climate models for Europe: Model performance in Present-Day Climate. *Climatic Change 81*, 21-53. doi:10.1007/s10584-006-9213-4

Karl, T.R., Nicholls, N., and *Ghazi, A.,* 1999: Clivar/GCOS/WMO Workshop on Indices and Indicators for Climate Extremes Workshop Summary. *Climatic Change 42*, 3-7.

Lenderink, G., van den Hurk, B., van Meijgaard, E., van Ulden, A., and *Cuijpers, H.,* 2003: Simulation of present-day climate in RACMO2: First results and model development. *KMNI, Technical Report TR-252.*

Mearns, L.O., Hulme, M., Carter, T.R., Leemans, R., Lal, M., and *Whetton, P.H.,* 2001: Climate scenario development. In *Climate Change 2001: The Scientific Basis* (ed.: *J. Houghton et al.*). Intergovernmental Panel on Climate Change, Cambridge University Press, New York.

New, M., Hulme, M., and *Jones, P.,* 1999: Representing twentieth-century space-time climate variability. Part I: Development of a 1961-90 mean monthly terrestrial climatology. *J. Climate 12*, 829-856.

Pal, J.S., Small, E., and *Elthair, E.,* 2000: Simulation of regional scale water and energy budgets: representation of subgrid cloud and precipitation processes within RegCM. *J. Geophys. Res. 105*(29), 567-594.

Peterson, T., Folland, C.K., Gruza, G., Hogg, W., Mokssit, A., and *Plummer, N.,* 2002: Report on the Activities of the Working Group on Climate Change Detection and Related Rapporteurs, 1998-2001. World Meteorological Organisation Rep. WCDMP-47. WMO-TD 1071. 143p. Geneva, Switzerland.

Rowell, D.P., 2005: A scenario of European climate change for the late 21st century: Seasonal means and interannual variability. *Clim. Dynam. 25*, 837-849.

Vidale, P.L., Lüthi, D., Frei, C., Seneviratne, S.I., and *Schar, C.,* 2003: Predictability and uncertainty in a regional climate model. *J. Geophys. Res. 108*(D18), 4586, doi:10.1029/2002JD002810.

IDŐJÁRÁS

Quarterly Journal of the Hungarian Meteorological Service
Vol. 112, No. 3–4, July–December 2008, pp. 265–284

Regional change of climate extremes over Hungary based on different regional climate models of the PRUDENCE project

Gabriella Szépszó

Hungarian Meteorological Service,
P.O. Box 38, H-1525 Budapest, Hungary
E-mail: szepszo.g@met.hu

(Manuscript received in final form October 28, 2008)

Abstract—On the basis of different regional climate model (RCM) outputs of the PRUDENCE project, several precipitation-, temperature-, and wind-related extreme parameters were investigated at the Hungarian Meteorological Service: the occurrence of extreme precipitation events, the rate of frost, summer, hot, and extremely hot days, the number of heat waves, hot and freezing periods, and the frequency of the maximum wind speed exceeding given thresholds. The changes of these extreme events were computed for the period of 2071–2100 with respect to the reference period of 1961–1990 focusing on the Hungarian territory. The chosen regional models, which were driven with the same or similar general circulation models, are using 50 km horizontal resolution and two (A2 and B2) climate change scenarios. The investigations based on several models serve as an excellent opportunity to explore those uncertainties in the projections, which are due to the different regional climate models and different emission scenarios. Besides the abovementioned analysis of the future trends, the results of the reference period were validated with Hungarian (gridded) observational time series. In the paper the evaluation of the regional extreme parameters for the past over the Carpathian Basin is briefly introduced, and the changes of these extreme characteristics are summarized based on the RCM outputs of the PRUDENCE project. The results indicate, that by the end of the 21st century the number of days with precipitation would slightly decrease over Hungary, whereas the frequency of the days with heavy precipitation would expectedly be enhanced. The warm extremes, heat waves, and hot periods will occur more often, which were accompanied by the reducing number of cold extreme events. The occurrence of intensive and stormy winds will likely increase, however, the projected change has very small magnitude.

Key-words: regional climate modeling, PRUDENCE project, extreme indices, uncertainty, regional climate change

1. Introduction

The spatially coarse (recently around 100 km) resolution global models are unable to correctly simulate extreme climate characteristics since their low "coverage" smoothes out the extreme values otherwise present in the atmosphere. Since the raw results of global climate models do not provide sufficient details, regionalization techniques are needed to obtain more information about the regional aspects of the climate change. Additionally to the application of higher or variable resolution general circulation models, two further methods are known for gaining smaller scale information based on the global results: the statistical downscaling (*Wilby et al.,* 1998) and the technique with the use of high-resolution limited area regional climate models (*Giorgi* and *Bates*, 1989). Hereafter the present article is uniquely dealing with results obtained with this dynamical downscaling technique based on regional climate models.

The regional climate models belong to the dynamically-based techniques, which physically refine the raw global results on regional scale. In that case the regional model is focusing only on a selected limited area (e.g., on Europe) with finer horizontal resolution, and the large scale processes are taken into account by the (lower – like sea surface temperature – and lateral boundary) forcings provided by the global results. Due to the higher resolution not only a more precise description of the surface characteristics (e.g., the orography) is possible, but also the dynamical processes accounted by this kind of models are certainly adapting to these more accurate conditions.

In spite of all the advantages coming from the fine resolution, today's regional climate models and their simulations are still exacerbated by multiple deficiencies (which can vary from one model to other one), which are intensively studied by a number of international cooperations initiated in last decade (see e.g., *Jacob et al.,* 2007). Nevertheless, for satisfying the increasing demands the models are also applied to realize climate change simulations parallelly with the model developments. For that reason it is crucial at the design of the experiments for the future to consider not only single, but also several simulations of various models, because only the ensemble approach provides appropriate tool to specify the uncertain (and certain) aspects in the projections.

Inevitably the most important regional climate modeling project, which already gives concrete climate projections for Europe with relatively high resolution, is the PRUDENCE project (Predicting of Regional Scenarios and Uncertainties for Defining European Climate Change Risks and Effects, *Christensen et al.,* 2007). The main scientific objectives of the project were, on the one hand, to provide high-resolution regional climate change projections for the period of 2071–2100 and, on the other hand, to characterize the reliability of the climate change projections, with special emphasis on the distinction of the obtained variabilities coming from the differences between the regional models and the internal variability of the climate system. The results of the project serve

as good basis to the ensemble consideration of climate change, since numerous model simulations were carried out with a range of global and regional climate models. The uncertainties in the projections did not purely come from the differences between the applied climate models (from the dissimilarities of their dynamical core and physical parameterizations), but also the future tendencies were forced by two basically different scenarios (one from the pessimistic and one from the optimistic groups) for greenhouse gas and aerosol emissions. The outcomes and outputs of the regional simulations of the PRUDENCE project have been public since the end of the project, and they have been directly accessible from the project's web page (http://prudence.dmi.dk) since 2006.

Being one of the essential indicators of the climate change, the extreme events and their future tendencies are intensively studied area of the climate researches. In 1997, the workshop on "Indices and Indicators for Climate Extremes" (*Karl et al.*, 1999) and later on the CCl/CLIVAR (World Meteorological Organization – Commission for Climatology/Climate Variability and Predictability) working group of World Meteorological Organization are dedicated to define extreme indices for the different meteorological parameters (mainly for the temperature and precipitation) in order to establish their common use. The STARDEX project (Statistical and Regional dynamical Downscaling of Extremes for European regions; *Goodess,* 2003) was initiated in 2001 to comprehensively evaluate the statistical and dynamical downscaling methods in order to reconstruct the observed past extremes and to construct regional scenarios for the future. In the framework of STARDEX, the past tendencies of several chosen extreme indices were analyzed in detail for Europe based on long observational time-series (e.g., *Haylock* and *Goodess*, 2004), and furthermore, the model simulations of the PRUDENCE project provided a good basis for the intercomparisons with the statistical methods (e.g., *Schmidli et al.,* 2007). The PRUDENCE's model simulations were thoroughly validated (for the mean precipitation, minimum, maximum, and mean temperature) by *Jacob et al.* (2007) for eight geographical regions in Europe. The projections were exhaustively investigated in the context of extremes by *Beniston et al.* (2007), which gave a detailed overview about the change of heat waves, heavy precipitation, drought, wind storms, and storm surges based on several RCMs' simulations; *Schär et al.* (2004) found that the future temperature variability will intensify with the largest degree in Central and Eastern Europe bringing severe consequences to the (increasing) number of heat waves; despite the general summer precipitation reduction and the warming trends projected by the majority of the RCMs over relevant part of the continent; *Christensen* and *Christensen* (2003) showed that there are many regions where enhancing frequency of the large precipitation events can be expected for the future together with more frequent flooding episodes. Particularly for the Carpathian Basin several studies aimed to explore and detect the trends of extreme events in last decades mainly on the basis of observational datasets: the work presented in

Bartholy and *Pongrácz* (2007) was carried out on long time series of Hungarian station data, while by *Lakatos et al.* (2007) already the homogenized time series were analyzed.

Present article is intended to provide an overview about the outcomes of the efforts, which have been made at the Hungarian Meteorological Service in order to estimate the future trends of the extreme events over Hungary based on the results of the regional climate models applied in the PRUDENCE project. The article is structured as follows: in the next section, on the one hand, a limited overview is provided about various sources of the uncertainties in the regional projections of the PRUDENCE project and, on the other hand, a brief description is given about the investigations carried out by the Hungarian Meteorological Service for the Carpathian Basin on the basis of the results of different RCMs. Section 3 considers in detail the projected change of the investigated extreme characteristics of precipitation, temperature, and wind speed; finally, Section 4 discusses the conclusions based on the extreme characteristics presented in the previous section.

2. Methodology of the investigations for Hungary

To achieve the aforementioned objectives in the PRUDENCE project, a hierarchical model system was applied with complex interactions between its components: the large scale circulation was described by coupled atmosphere-ocean models (AOGCMs) through long transient climate change simulations on 300 km horizontal resolution. These AOGCMs provided the atmospheric radiative forcings and the matching sea-surface boundary conditions for the time-slice experiments (covering the "discrete" periods of 1961–1990 and 2071–2100) to be carried out by stand-alone advanced high (150 km) resolution atmospheric general circulation models (AGCMs). Finally, these refined global results served as initial and lateral boundary conditions for the finest resolution regional simulations, which already focused on the European region with 50 km grid spacing. The preference of the relatively far future projection period was motivated by the assumption, that the future signal will be in this manner strong enough to draw robust conclusions on the expected climate change. As far as radiative constraints for the future are concerned, two different SRES emission scenarios (*Nakicenovic et al.,* 2000) were considered in the project: the A2 and B2 ones, which provide pessimistic and optimistic realizations of the emission levels in the 21st century (see *Fig. 1*).

The complex system sketched above takes into account multiple sources of uncertainties (*Christensen et al.,* 2007):

1. The large scale forcings for the higher resolution AGCMs were produced by different AOGCMs;
2. Several AGCMs were used to conduct the higher resolution global runs;

3. The radiative forcings in the future for the global models were described by two greenhouse gas and aerosol emission scenarios;
4. 8 RCMs were integrated to provide regional climate projections for the future.

Therefore, the different kind of uncertainties in the model simulations can be characterized through multiple ensembles of model integrations. Besides analyzing the future tendencies of the extreme precipitation, temperature, and wind events focusing for our region of interest (i.e., Hungary), the present article is dedicated to assess only and uniquely those uncertainties in the projections, which are due to the different regional climate models and different emission scenarios.

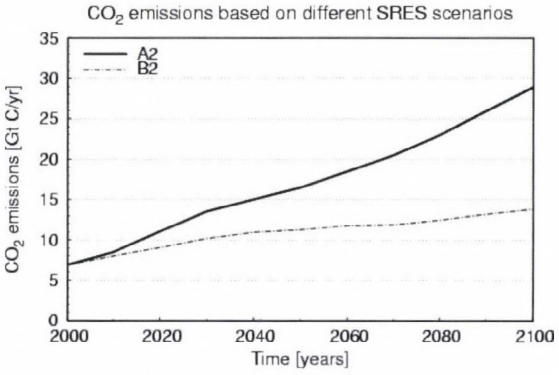


Fig. 1. The total future anthropogenic carbon dioxide emission (in gigatons of C per year) based on two reference scenarios: A2 (solid line) and B2 (chained line). (The diagram was constructed based on the data of *Nakicenovic et al.*, 2000.)

For that purpose daily outputs of five regional climate models applied in the PRUDENCE project were considered for Hungary: the HIRHAM, RegCM, PROMES, RCAO, and HadRM3P models (for additional information about the underlying model simulations see *Table 1*). The reasons for choosing these model simulations were, on the one hand, that for each integration the large scale forcings were provided by the same (or very similar in the case of HadAM3P, which is a successor of the HadAM3H model with few changes in the physical parameterizations) atmospheric general circulation model and, on the other hand, these RCMs were driven with both of the SRES scenarios (A2 and B2) applied in the project.

In the evaluation of the simulated extreme characteristics for the past, some observational time series were also taken into account in order to draw conclusions about the real spatial distribution of the examined parameters and to assess the performance of the models. For that purpose a gridded dataset on 0.1-degree horizontal resolution was applied, which was generated by interpolation based on Hungarian surface observations (*Szentimrey* and *Bihari*, 2007). This

validation was limited to the daily precipitation amount and the daily minimum and maximum temperature.

Table 1. The main characteristics of the model simulations used for the investigations at the Carpathian Basin: the institute being responsible for the experiment, the applied regional model, the employed SRES scenario, and the global model which provided the driving data for the regional climate models

Institute	RCM	Reference	Scenario	Driving data
Danish Meteorological Institute (DMI)	HIRHAM	*Christensen et al.*, 1996	A2, B2	HadAM3H
Hadley Centre	HadRM3P	*Jones et al.*, 1995	A2, B2	HadAM3P
The Abdus Salam International Centre for Theoretical Physics (ICTP)	RegCM	*Giorgi* and *Mearns*, 1999	A2, B2	HadAM3H
Swedish Meteorological and Hydrological Institute (SMHI)	RCAO	*Döscher et al.*, 2002	A2, B2	HadAM3H
Universidad Complutense de Madrid (UCM)	PROMES	*Castro et al.*, 1993	A2, B2	HadAM3H

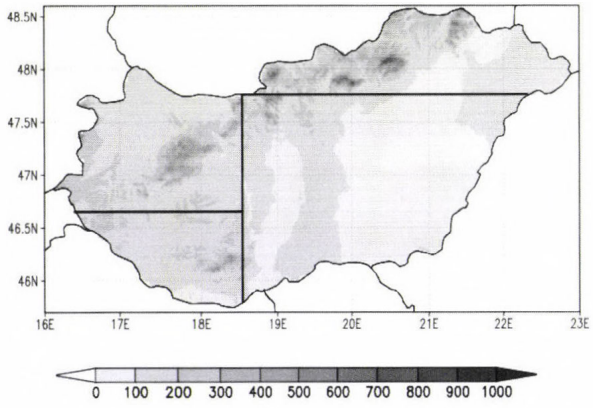


Fig. 2. Orography of the entire domain (i.e., Hungary) and sub-areas (separated with lines) defined for the investigations. (The orography on the map was generated from the data provided by the MISH software on 30-second horizontal resolution.)

In this study the threshold approach is used, i.e., it is examined whether certain fixed thresholds (whose majority was defined based on the recommendations of the WMO-CCl/CLIVAR Working Group) were exceeded or not for given parameters. The investigated changes of the different extreme parameters are always considered with respect to the reference (1961–1990) period of the same model (the changes with respect to the observations are not discussed). The analyses were carried out considering spatial averages not only over the entire country, but also for sub-areas within the country (namely, northeastern, northwestern, southeastern, and southwestern parts of Hungary).

These sub-domains were selected after simple consideration of the geographical and climatic conditions of Hungary (*Fig. 2*). The computations were carried out separately for each gridpoint over Hungary, and the values of figures and tables were obtained by averaging them for the entire country or the regions.

3. Results

Precipitation

Based on the results of the selected RCMs, the changes of the number of days with precipitation, heavy and very heavy precipitation (with daily amount exceeding 0.1, 10, and 20 mm, respectively) were investigated. Comparing the results for the reference period to the observed values it can be generally concluded, that the models mainly overestimate the number of events with small precipitation, while they rather underestimate the occurrence of the days with heavier precipitation; the only exception is the RegCM model, which projects too many events in every category (see *Fig. 3* and *Table 2*). As far as the future trends are concerned, it can be noticed, that for the A2 scenario the frequency of the days with precipitation will probably slightly decrease, however, at the same time some increase can be expected for the occurrences of the extreme precipitations (with the only exception of the Hadley Centre's model, which simulates rather decrease of the heavy precipitation with more than 10 mm daily amount). The former minor reduction proves to be much smaller for the B2 scenario, which is also valid for the days with very heavy precipitation (i.e., for the threshold of 20 mm/day), while in the case of events over the 10 mm daily amount the majority of the models projects slightly larger increase for the more optimistic B2 scenario. Nevertheless, it has to be remarked, that the tendencies concluded above mean very small changes, therefore, the differences between these signals are probably not significant. Therefore, for making sure of the correctness of these qualitative conclusions, the concrete values of the relative changes projected by the different models and the standard deviation between them are also calculated.

Table 3 provides some additional quantitative details to the conclusions mentioned above. Although for the thresholds of 0.1 and 10 mm the mean changes are similar to each other in magnitude (more or less around –10 and 10%, respectively, with some "extreme" values), the standard deviation for the higher threshold is too large compared to the magnitude of the mean change. This fact indicates that for the 10 mm/day threshold the signal is rather "uncertain", so this figure should be interpreted with special care. On the other hand, the situation is "better" for the 20 mm/day threshold (even though the absolute value of the standard deviation is higher than in the 10 mm/day case): the projected change is approximately 45% with a lower level (27%) of standard deviation, which can be interpreted in a way that the increase of heavy precipitation events is rather certain, however, its exact value is more uncertain (between around 5 and 65%).

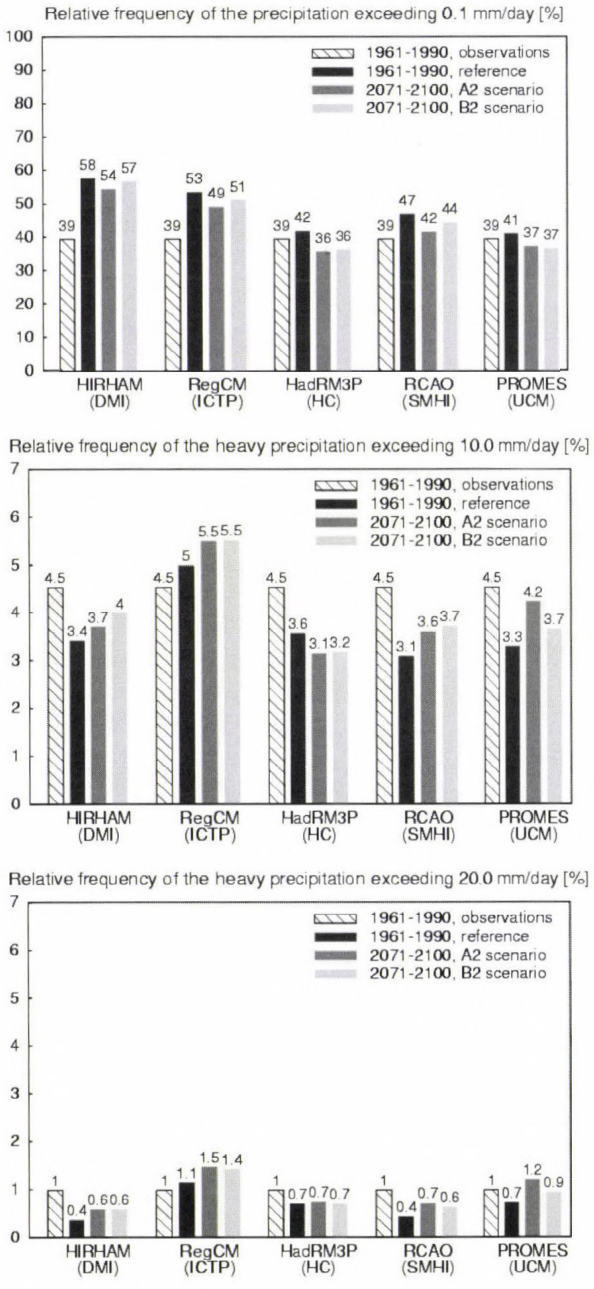


Fig. 3. Relative frequency of the daily precipitation amounts above different thresholds over Hungary. The groups of bars represent the different models, and the first two bars within each group denote the reference period (based on observations for the first one and on model results for the second one), the last two ones refer to the period of 2071–2100 with the use of different SRES scenarios (A2 and B2, respectively).

Table 2. The mean differences (in %) between the frequency of the simulated and observed extreme characteristics (R0.1, R10, R20: precipitation events exceeding 0.1, 10, and 20 mm/day, respectively; TN0: frost days; TX30: hot days) for the period of 1961–1990 over Hungary. The values of "Mean" represent average of these departures (in %)

Model	R0.1	R10	R20	TN0	TX30
HIRHAM	19	–1.1	–0.63	–6	4.1
RegCM	14	0.5	0.12	2	6.7
HadRM3P	3	–0.9	–0.28	1	10.7
RCAO	8	–1.4	–0.54	–14	5.6
PROMES	2	–1.2	–0.26	–5	–0.4
Mean	9	–0.8	–0.32	–4	5.3

Table 3. The changes (in %) of the frequency of different extreme characteristics (V5 and and V10: wind events exceeding 5 and 10 m/s in the maximum) for the period of 2071–2100 with respect to the period of 1961–1990 over Hungary based on different model simulations. The values of "Mean"/"Std. dev." represent average/standard deviation of the changes (in %) computed from the results of the different models. All the values are valid for the A2 SRES scenario

	Precipitation			Temperature				Wind speed	
Model	R0.1	R10	R20	TN0	TX30	Freezing period	Heat wave	V5	V10
HIRHAM	–5.5	8.5	64.3	–62.9	141.6	–54.2	58.2	–3.2	3.7
RegCM	–8.3	10.3	29.0	–67.3	87.6	–27.8	80.9	–	–
HadRM3P	–14.7	–11.9	4.7	–52.1	97.1	–44.4	46.2	4.8	17.9
RCAO	–11.6	16.6	62.4	–69.9	129.0	–62.7	59.1	1.5	31.1
PROMES	–9.5	28.6	65.6	–59.6	260.5	–46.4	196.4	0.2	14.2
Mean	–9.9	10.4	45.2	–62.4	143.2	–47.1	88.1	0.8	16.7
Std. dev.	3.5	14.7	27.3	7.0	69.3	13.0	61.8	3.3	11.3

Temperature

In the case of temperature, the changes of relative frequency for summer, hot, and extremely hot days (defined as days when the maximum temperature exceeds the 25, 30 and 35 °C, respectively) were investigated as "warm" extreme indices, while the tendency of frost days (defined as days when the minimum temperature is below 0 °C) was examined as "cold" extreme taking into account again both the observations and model results. For the warm parameters one can generally conclude, that for each of them frequency increase can be expected by the end of the 21st century, both for entire Hungary and for every sub-region. (Only the results related to hot days over Hungary are presented in *Fig. 4* and *Table 3.*) Although lots of differences can be noticed (e.g., already for the reference period) between the models, it can be generally pinpointed, that:

- The simulations for both scenarios indicate frequency increase of the warm extreme events;
- Between the two scenarios (A2 and B2), the B2 one shows more moderate changes (which is not surprising at all, because the B2 scenario is the more optimistic one, i.e., considering smaller anthropogenic emissions of greenhouse gases and aerosols, see *Fig. 1*);
- The *absolute* increase of the warm and hot days for the future exceeds in general with 10 percent according to the more pessimistic A2 scenario, while in the case of extremely hot days, the absolute increase is more moderate (around 4–8 percent).

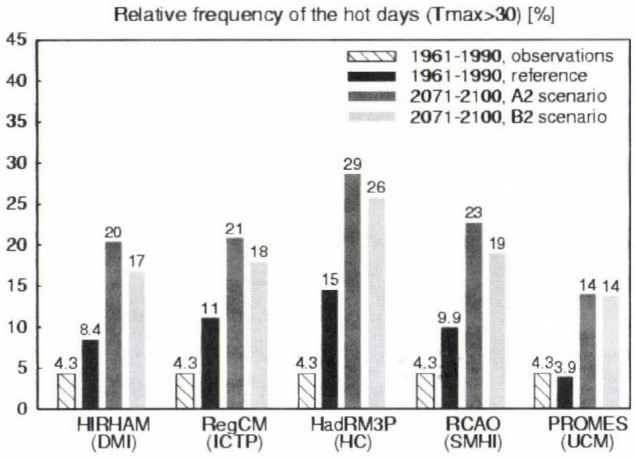


Fig. 4. Relative frequency of hot days over Hungary. The groups of bars represent the different models, and the first two bars within each group denote the reference period (based on observations for the first one and on model results for the second one), the last two ones refer to the period of 2071–2100 with the use of different SRES scenarios (A2 and B2, respectively).

More particularly, regarding the change of the number of hot days over Hungary it can be seen, that the majority of the investigated RCMs significantly overestimates the number of hot days for the past (*Fig. 4* and *Table 2*): the models simulate twice or even three times larger frequency than it was observed with the only exception of the PROMES model, which almost correctly reflects the true conditions (rather with a minor underestimation). In spite of the large uncertainty for the past, the projected positive tendency is obvious for every experiment (as it can be also easily read from *Table 3*). The mean of the signals over the entire country is 143% (i.e., the hot days will occur approximately 2.5 times more frequently in the future than in the past), and the simulated changes range the interval of 97–260%. The upper extreme (260%) is coming from the PROMES results and it is due to the fact that its reference is (correctly) the

lowest among the models, and therefore, the relative increase is the largest (in spite of the fact that the PROMES model provides the lowest absolute change).

For the frost days, the RCMs behave rather differently from each other during the reference period: three of them underestimate the number of the cold extreme events, while the remaining two are rather perfect (with a very-very slight non-significant overestimation) – see *Fig. 5* and *Table 2*. The absolute errors do not have such large magnitude than it was the case for the hot days, due to the anyway more frequent occurrence of the event. The sign of the projected change is opposite with respect to the hot days: by the end of the 21st century, decrease of frost days has to be envisaged according to every experiment. On top of that, considering the very low value of the standard deviation (7%) in *Table 3* it can be stated with large confidence, that the simulated reduction of 60% can be identified as very sharp and convincing projection for the future. All this is valid not only for the A2 scenario, but also for the (more optimistic) B2 one with the restriction that the probable change is lower (about 40%; not shown).

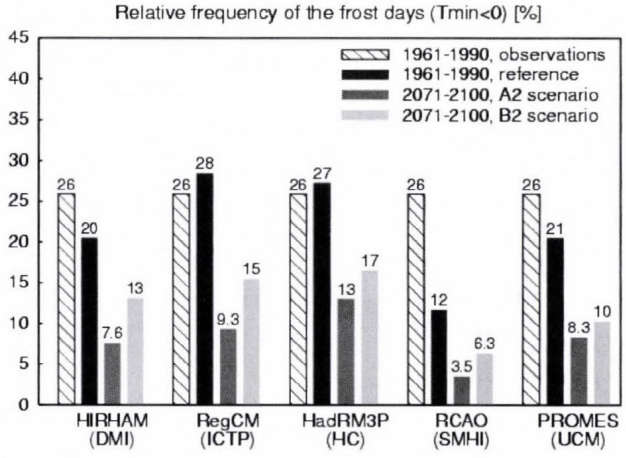


Fig. 5. Relative frequency of frost days over Hungary. The groups of bars represent the different models, and the first two bars within each group denote the reference period (based on observations for the first one and on model results for the second one), the last two ones refer to the period of 2071–2100 with the use of different SRES scenarios (A2 and B2, respectively).

In the case of temperature, not only the tendency of the occurrence of the days with maximum, minimum, and mean temperature exceeding given values, but also their persistence on consecutive days is of interest. For instance, from the aspects of human health the expected frequency of heat waves in future has also great importance, while for the building industry or forestry the changes of freezing periods in winter and hot periods in summer are also meaningful

parameters to be considered. *Fig. 6* provides some information about the simulated frequency of heat waves (defined as periods of at least 3 consecutive days, when the daily mean temperatures exceed 25 °C) over Hungary both for the past (reference) and the future. The results of the five investigated models clearly indicate that the occurrence of this event will increase by the end of the 21st century with slightly different magnitudes for the individual model simulations, but with more than 50 percent in most of the cases for the A2 scenario (see *Table 3*). The mean of the signals projected by the ensemble of RCMs is approximately 88% due to the "outlier" value (196%) simulated again by the PROMES model (however, it has to be mentioned, that the future frequency of the heat waves produced by PROMES is in good agreement with the other models' result, and the reason for the large relative deviation is coming from the significant differences in the reference period.)

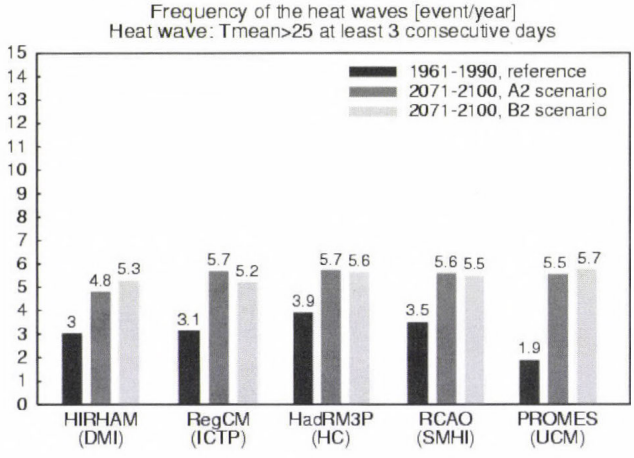


Fig. 6. Frequency of the heat waves over Hungary. The groups of bars represent the different models, and the first bar within each group denotes the reference period, the last two ones refer to the period of 2071–2100 with the use of different SRES scenarios (A2 and B2, respectively).

Regarding the hot periods (defined as periods of at least 3 consecutive days, when the daily maximum temperatures exceed 35 °C), a dramatic level of change is anticipated for the last decades of the 21st century: it will increase from the former 0.5–3 to 2–6 events per year (not shown). It is worth noting, that both in the case of heat waves and hot periods, there are no significant differences between the results for the two emission scenarios.

As far as the freezing periods (defined as periods of at least 3 consecutive days, when the daily minimum temperatures are not higher than 0 °C) are concerned, there is a large uncertainty between the models for the reference period (the

results vary from 4 to 10 events annually – see *Fig. 7*), however, on the contrary, there is a good agreement between them regarding the future trends: the frequency of the freezing periods will uniformly decrease (with approximately 50% in the case of A2 scenario) – with large confidence as it is indicated by the especially low (13%) standard deviation value (*Table 3*). The sign of the change for the B2-case is the same, but its magnitude is smaller: about 30% (not shown).

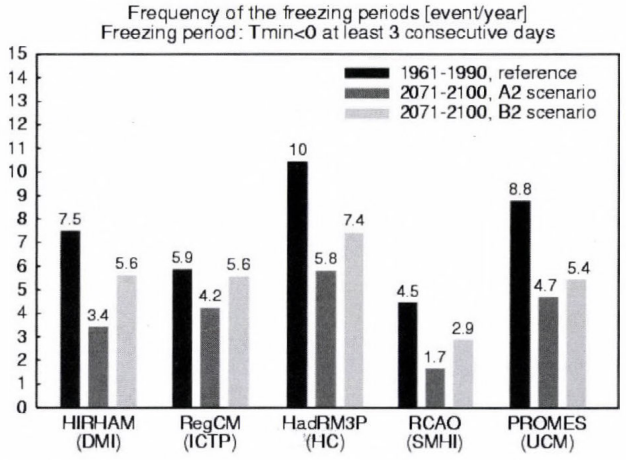


Fig. 7. Frequency of the freezing periods over Hungary. The groups of bars represent the different models, and the first bar within each group denotes the reference period, the last two ones refer to the period of 2071–2100 with the use of different SRES scenarios (A2 and B2, respectively).

It is worthwhile to pay special attention to the behavior of the PROMES model: its temperature simulation for the past seems to be the uniquely correct one compared to the observations in the case of warm values (remember the hot days), whereas in the cold range its performance is rather "ordinary" with some deficiency. Although in the case of persistence characteristics the observed values are not calculated and their occurrence is relatively rare over Hungary, it is rather clear, that less heat waves (and hot periods) are peculiar to the simulation of PROMES model for the past than it was projected by the other models, while the number of freezing periods is rather similar to the others. Another important feature is in that respect, that later (in the future) the model "compensates" its low level of the heat waves in the past: the simulated occurrence is almost the same as it is for the other models – it is not valid either for the hot (extremely hot and warm) days or the hot periods, however, the outstanding large magnitude of the changes leads to the conclusion, that the PROMES model projects much more heated climate conditions by the end of the 21st century than it was typical in the reference period.

Wind speed

The extreme characteristics' investigations for 10-meter wind speed take into account only the results of four regional climate models – the RegCM model is excluded due to the lack of wind data. Before the analyses of model results, maybe it is worthwhile to look at the spatial distribution of the relative frequency of mean wind speed exceeding given thresholds based on observational data (*Fig. 8*): the windiest parts of the country are in the elevated points of the North-Transdanubian regions (north from the Lake Balaton). Higher values occur also at the northwestern boundary of the country, and over the southeastern and northeastern part of the Great Hungarian Plain. (This spatial distribution can be explained by the topographical features of Hungary, namely that the typical northwesterly flow naturally enters the basin through the valley between the Alps and Carpathians, while the eastern part of the basin is under the influence of the mountainous flow blowing from the North Carpathian range.)

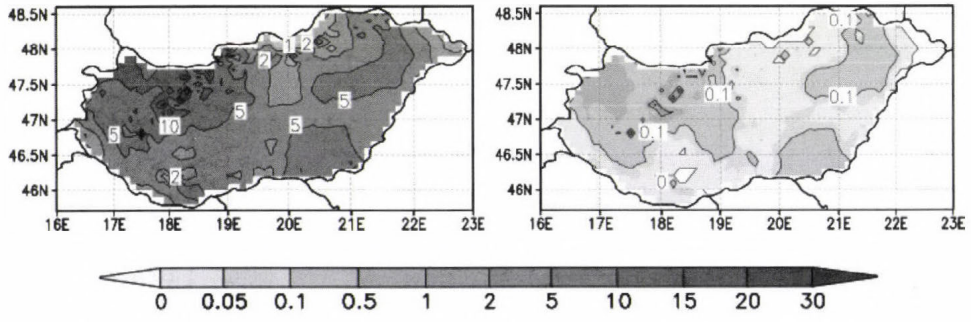


Fig. 8. Relative frequency (in %) of the observed daily mean 10-meter wind speed over Hungary exceeding different thresholds: 5 m/s on the left and 10 m/s on the right. The maps are generated on 0.1-degree horizontal resolution.

As far as the model simulations are concerned, firstly the tendencies for the entire country were examined for the relative frequency of such events, when the daily maximum of 10-meter wind speed exceeds given limit values. The range of investigated thresholds covers the interval between 0 and 20 m/s, however, in *Fig. 9* only the results of 5, 7, 10, and 14 m/s are presented, respectively. It is hard to conclude any significant tendency in the case of the lower daily wind maxima, while in the case of the higher ones, the trends are a bit more easily interpretable (as it is also clearly quantified in *Table 3* for the simulations driven by the A2 SRES scenario). Particularly, for the threshold of 5 m/s the relative changes projected by individual models are very small positive ones (except the HIRHAM model): the mean of the models' ensemble is 0.8%; while the standard deviation between the signals is too large (3.3%) compared to the mean

change. On the contrary, the frequency of the daily wind maxima exceeding the threshold of 10 m/s indicates an increase with generally larger magnitude (16.7% in average) accompanied with a standard deviation (11.3%) remaining under the signal of the relative change. All this just means that the increase of the stronger wind events is rather significant with respect to the uncertain "situation" for the lower thresholds.

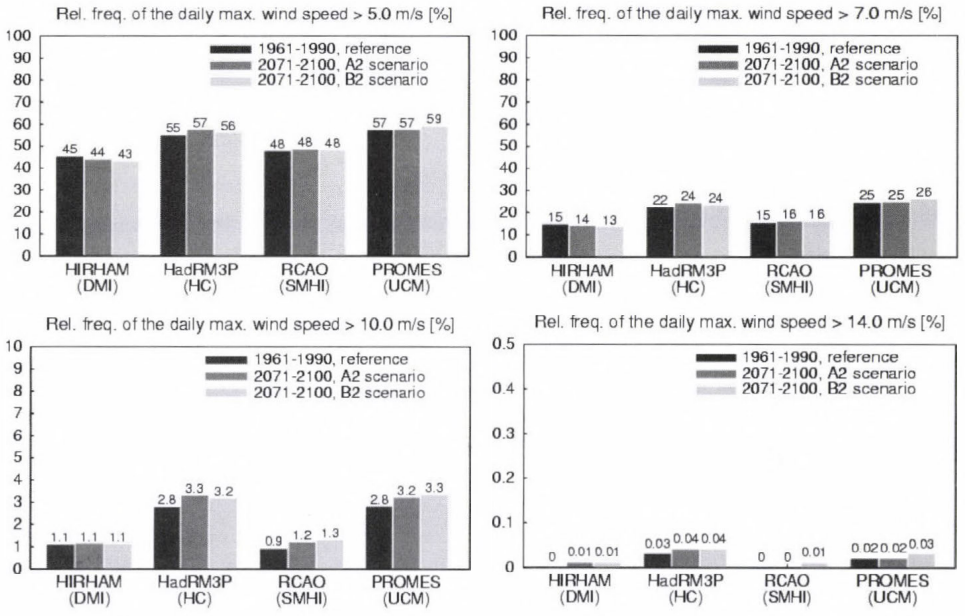


Fig. 9. Relative frequency of the simulated daily maximum 10-meter wind speed over Hungary exceeding different thresholds. The groups of bars represent the different models, and the first bar within each group denotes the reference period, the last two ones refer to the period of 2071–2100 with the use of different SRES scenarios (A2 and B2, respectively).

The separate examination of the results over different geographical regions provides further valuable insight into the future wind patterns. According to the quantitative results for the threshold of 10 m/s (*Table 4*), it can be generally pinpointed, that the more pronounced (and uniformly positive) changes are found over the least windy parts of the country, namely over the northeastern and southwestern regions, where also the standard deviations between the model results are the most "acceptable" (for the northwestern and southeastern parts of Hungary the standard deviations are too large with respect to the magnitude of the signal). This argumentation is not only valid for the ensemble mean, but also for the individual model results with the only exception for the RCAO model (which produces the strongest change besides the northeastern region also at the

southeastern one). Furthermore, it is noteworthy, that the HIRHAM model simulates systematically the lowest degree of change for almost every sub-area (the only exception is the northeastern sub-domain).

Table 4. The changes (in %) of the frequency of the event, that the daily maximum of 10-meter wind speed exceeds 10 m/s, for the period of 2071–2100 with respect to the period of 1961–1990 over different regions (NW: Northwestern, NE: Northeastern, SE: Southeastern, SW: Southwestern Hungary, and HU: entire Hungary) based on different model simulations. The values of "Mean"/"Std. dev." represent average/standard deviation of the changes (in %) computed from the results of the different models. All the numbers indicate the simulation results driven by A2 SRES scenario, except the last column, where the values in the brackets refer to the B2 SRES scenario

Model	NW	NE	SE	SW	HU
HIRHAM	3.5	29.6	–1.2	10.5	3.7 (0.9)
HadRM3P	27.4	30.4	11.4	32.2	17.9 (13.3)
RCAO	24.1	35.9	37.9	27.2	31.1 (42.2)
PROMES	11.8	17.0	12.6	20.6	14.2 (18.5)
Mean	16.7	28.2	15.2	22.6	16.7 (18.7)
Std. dev.	11.1	8.0	16.4	9.4	11.3 (17.3)

The results for the lower threshold values slightly differ from all this, particularly for the 5 m/s (not shown): the average signals have quite similar magnitudes for each region, they do not reach (except for the northeastern part of Hungary) the –1 or 1 percent, while the standard deviation between the simulated changes exceeds the degree of the change in every case. The HIRHAM model is again in noticeable contrast with its counterparts: it is the only model, which projects a decrease of the frequency of the event for each sub-area. This behavior of HIRHAM (i.e., non-significant decrease of the frequency of lower wind maxima and almost negligible increase of the frequency of higher maxima) might indicate that its simulated circulation and mean wind patterns are a bit different from those of the other models.

It is also interesting to see, that in contradiction of the results concluded at the temperature extremes, there are two models (both for lower and higher thresholds of daily maximum), which project larger changes for the more optimistic B2 scenario.

According to all this, it can be generally said, that any tendentious change is rather concluded in the case of higher wind speeds, and according to the results, for the higher thresholds some compensation can be expected between the presently windiest and the less windy parts of Hungary; nevertheless, it should not be forgotten, that these signals are very-very small ones and their significance are doubtful and arguable.

4. Summary, conclusions

In the last years several efforts were carried out world-wide in order to estimate the regional impacts of the global climate change, from which the PRUDENCE project (completed in 2004) provided the first comprehensive projections for the European region. At the Hungarian Meteorological Service the 50 km resolution results of five regional climate models used in the project were analyzed, and the tendencies of precipitation-, temperature-, and wind-related extreme parameters were intensively examined providing a good basis for the preparation of National Climate Strategy of Hungary, which is a guideline for the Hungarian policy makers to define the main track of the adaptation policy to the impacts of the climate change in Hungary. The projected changes of the extreme characteristics were investigated for the period of 2071–2100 with respect to the period of 1961–1990 focusing on the territory of Hungary. The choice of these simulations was mainly motivated by the fact, that these RCMs were driven with both of the SRES scenarios (A2 being a pessimistic one and B2 being an optimistic one). With this type of consideration of model outputs only a part of the uncertainties in the projection can be specified, namely the uncertainties due to the application of different regional climate models and different emission scenarios. However, it has to be underlined, that in the PRUDENCE project much more model simulations were accomplished, which were carried out on the one hand with the use of other RCMs and on the other hand with the use of further driving global models. Therefore, the real spectrum of the uncertainties is surely broader, which fact was also confirmed by recent studies (e.g., in *Déqué et al.,* 2007 it was showed that the variability introduced by the choice of the driving GCM has the largest contribution to the range of uncertainty).

According to the results detailed above it can be generally concluded, that in spite of the fact, that between the individual model simulations there are lots of differences over Hungary, the main tendencies of the future extreme features are characterized rather similarly.

In the case of precipitation it is emphasized, that for the end of the 21st century the reduction of the number of days with precipitation has to be considered, while at the same time the frequency of the days with heavy (and very heavy) precipitation will expectedly increase (and consequently, the number of days with light precipitation will be reduced). These conclusions are valid for both of the applied SRES scenarios with generally more considerable level of the change for the more pessimistic one, however in the case of heavy precipitation over 10 mm daily amount, the B2 scenario provides larger increase. Nevertheless, it has to be mentioned here, that these changes have very small magnitude, therefore, the results have to be taken into account with careful consideration. It would be also useful to examine the seasonal distribution: e.g., in *Pongrácz et al.* (2008) it was concluded, that the precipitation events become more frequent in winter and more seldom in summer over the Carpathian Basin

(based on the results of ETH's (Swiss Federal Institute of Technology) CHRM model, which model's results were not the subject of our study), but what is even more interesting, that the occurrence of extreme precipitation days will be intensified in winter and reduced in summer.

Regarding the temperature extremes, the model results render the increase not only for the individual warm extremes (warm, summer, and hot days), but also the heat waves and hot periods will occur more often. As further consequence of the regional climate change over Hungary, the frequency of frost days and freezing periods will be expectedly reduced. All this (i.e., the decrease of cold and increase of warm extremes) fits well to our view about the mean warming tendencies over Hungary. Additionally, it should be noticed, that compared to the other investigated parameters these temperature signals are quite sharp and convincing ones, it is especially valid for the cold temperature extremes. On the other hand, with regard the persistence characteristics further analyses would be desired, because on the basis of these results there is no information about the tendencies of the duration of heat waves, hot and freezing periods. For instance, since the three as well as the more than three consecutive days exceeding given threshold are considered with equal weight in the present analyses, the future situation with more and longer warm periods can be imagined with the same probability as the situation with more but shorter ones.

As far as the wind events are concerned, no significant changes could be detected in the range of lower and "ordinary" wind speed values, the occurrence of intensive and stormy winds will likely increase, however, the projected change has very small magnitude. An interesting issue is, that while for the temperature extremes the more pessimistic A2 scenario provides more dramatic signals uniformly for every model, in the case of wind, there are several models, where the optimistic B2 one simulates slightly more pronounced changes. Regarding the wind-related investigations it has to be mentioned, that the daily maximum wind speed is not the most appropriate indicator for the extreme storm events. In the background of this fact is, that in the case of the chosen RCMs, this variable was calculated purely based on the 10-meter wind speed without application of any gust parameterization, and this empirical formulation led to the under-representation of strong wind events in the simulations (further details are provided in *Rockel* and *Woth*, 2007).

It has to be mentioned, that the accomplished analyses were based on simple examinations, where it was checked, whether different fixed thresholds for given parameters were exceeded or not. Nevertheless, it is evidenced, that this fixed threshold approach is not satisfactory at every case, e.g., there are regions (gridpoints) and seasons, where and when the given thresholds are not considered as extremes, but "usual" values. For that reason it is planned to continue the analyses on the basis of the percentile approach with the further extensions for seasonal investigations and for several new extreme indices. Finally, as it was indicated by the results, in the case of certain extreme

parameters not only the signals are modest, but also the absolute occurrence of the event. The question is naturally arising, whether these changes are statistically significant or not. The follow-on of the recent work aims to investigate the statistical significance of the obtained results in order to be in the position to have more solid conclusions regarding the future change of the extreme characteristics over Hungary.

The valuable outcomes of PRUDENCE project provide the first regional projections for Europe (for two emission scenarios); PRUDENCE was followed by the ENSEMBLES project, in which the main focus is on the pervasive quantification of the uncertainties originating from different sources in the regional climate simulations. Nevertheless, it is underlined, that these results do not substitute the further application of finer resolution climate simulations and analyses. These investigations are already ongoing in Hungary at the Hungarian Meteorological Service and Eötvös Loránd University with the use of adapted high-resolution regional climate models. Several simulations of four regional climate models (ALADIN-Climate, REMO, PRECIS, and RegCM) are already accomplished or planned to be carried out for the Carpathian Basin on high (25 and 10 km) resolution taking into account different emission scenarios (besides the widely used and rather realistic A1B also the A2 one) and lateral boundary conditions in order to compose a small ensemble, which will serve as a great opportunity to explore the certainties and uncertainties in the model results focusing over our area of interest.

Acknowledgements—The author would like to express special thanks to *András Horányi* for his critical but always objective and motivating help during the preparation of the article. This work was supported by the Hungarian National Office for Research and Technology (NKFP, grant No. 3A/082/2004) and the Hungarian Ministry of Environment and Water via supporting the National Climate Strategy of Hungary. Data have been provided through the PRUDENCE data archive, funded by the European Union through contract EVK2-CT2001-00132.

References

Bartholy, J. and *Pongrácz, R.*, 2007: Regional analysis of extreme temperature and precipitation indices for the Carpathian Basin from 1946 to 2001. *Global Planet. Change 57*, 83-95.

Beniston, M., Stephenson, D.B., Christensen, O.B., Ferro, C.A.T., Frei, C., Goyette, S., Halsnaes, K., Holt, T., Jylhä, K., Koffi, B., Palutikof, J., Schöll, R., Semmler T., and *Woth, K.*, 2007: Future extreme events in European climate: An exploration of regional climate model projections. *Climatic Change (PRUDENCE Special Issue) 81*, 71-95.

Castro, M., Fernández, C., and *Gaertner, M.A.*, 1993: Description of a mesoscale atmospheric numerical model. In *Mathematics, Climate and Environment* (eds.: *J.I. Díaz* and *J.L. Lions*). *Rech. Math. Appl. Ser. Mason*, 230-253.

Christensen, J.H., Carter, T.R., Rummukainen M., and *Amanatidis, G.*, 2007. Evaluating the performance and utility of climate models: the PRUDENCE project. *Climatic Change (PRUDENCE Special Issue) 81*, 1-6.

Christensen, J.H. and *Christensen, O.B.*, 2003: Severe summertime flooding in Europe. *Nature 421*, 805-806.

Christensen, J.H., Christensen, O.B., Lopez, P., van Meijgaard, E., and *Botzet, M.,* 1996: The HIRHAM4 Regional Atmospheric Model. *Scientific Report 96-4,* DMI, Copenhagen, 51 pp.

Déqué, M., Rowell, D.P., Lüthi, D., Giorgi, F., Christensen, J.H., Rockel, B., Jacob, D., Kjellström, E., de Castro, M., and *van den Hurk, B.,* 2007: An intercomparison of regional climate simulations for Europe: assessing uncertainties in model projections. *Climatic Change (PRUDENCE Special Issue) 81,* 53-70.

Döscher, R., Willén, U., Jones, C., Rutgersson, A., Meier, H.E.M., Hansson, U., and *Graham, L.P.,* 2002: The development of the coupled regional ocean-atmosphere model RCAO. *Boreal Env. Res. 7,* 183-192.

Giorgi, F. and *Bates, G.,* 1989: The Climatological Skill of a Regional Model over Complex Terrain. *Mon. Weather Rev. 117,* 2325-2347.

Giorgi, F. and *Mearns, L.O.,* 1999: Introduction to special section: regional climate modeling revisited. *J. Geophys. Res. 104,* 6335-6352.

Goodess, C.M., 2003: STAtistical and Regional dynamical Downscaling of EXtremes for European regions: STARDEX. *The Eggs 6,* available form http://www.the-eggs.org/articles.php?id=37.

Haylock, M.R. and *Goodess, C.M.,* 2004: Interannual variability of European extreme winter rainfall and links with mean large-scale circulation. *Int. J. Climatol. 24,* 759-776.

Jacob, D., Bärring, L., Christensen, O.B., Christensen, J.H., Hagemann, S., Hirschi, M., Kjellström, E., Lenderink, G., Rockel, B., Schär, C., Seneviratne, S.I., Somot, S., van Ulden, A., and *van den Hurk, B.,* 2007: An inter-comparison of regional climate models for Europe: Design of the experiments and model performance. *Climatic Change (PRUDENCE Special Issue) 81,* Supplement 1, 31-52.

Jones, R.G., Murphy, J.M., and *Noguer, M.,* 1995: Simulation of climate change over Europe using a nested regional-climate model I: Assessment of control climate, including sensitivity to location of lateral boundaries. *Q. J. Roy. Meteorol. Soc. 121,* 1413-1449.

Karl, T.R., Nicholls, N., and *Ghazi, A.,* 1999: CLIVAR/GCOS/WMO workshop on indices and indicators for climate extremes: Workshop summary. *Climatic Change 42,* 3-7.

Lakatos, M., Szentimrey, T., Birszki, B., Kövér, Zs., Bihari, Z., and *Szalai, S.,* 2007: Changes of the temperature and precipitation extremes on homogenized data. *Acta Silvatica & Lingaria Hungarica 3,* 87-96.

Nakicenovic, N., Alcamo, J., Davis, G., de Vries, B., Fenhann, J., Gaffin, S., Gregory, K., Grübler, A., Jung, T.Y., Kram, T., La Rovere, E.L., Michaelis, L., Mori, S., Morita, T., Pepper, W., Pitcher, H., Price, L., Raihi, K., Roehrl, A., Rogner, H.-H., Sankovski, A., Schlesinger, M., Shukla, P., Smith, S., Swart, R., van Rooijen, S., Victor, N., and *Dadi, Z.,* 2000: *IPCC Special Report on Emissions Scenarios.* Cambridge University Press, Cambridge.

Pongrácz, R., Bartholy, J., Gelybó, Gy., and *Szabó, P.,* 2008: Detected and expected trends of extreme climate indices for the Carpathian basin. In *Bioclimatology and Natural Hazards* (eds: *K. Strelcova et al.*). Springer, 15-28.

Rockel, B. and *Woth, K.,* 2007: Extremes of near-surface wind speed over Europe and their future changes as estimated from an ensemble of RCM simulations. *Climatic Change (PRUDENCE Special Issue) 81,* 267-280.

Schär, C., Vidale, P.L., Lüthi, D., Frei, C., Häberli, C., Liniger, M.A., and *Appenzeller, C.,* 2004: The role of increasing temperature variability in European summer heatwaves. *Nature 427,* 332-336.

Schmidli, J., Goodess, C.M., Frei, C., Haylock, M.R., Hundecha, Y., Ribalaygua J., and *Schmith, T.,* 2007: Statistical and dynamical downscaling of precipitation: An evaluation and comparison of scenarios for the European Alps. *J. Geophys. Res. 112,* 1-20.

Szentimrey, T. and *Bihari, Z.,* 2007: Mathematical background of the spatialinterpolation methods and the software MISH (Meteorological Interpolationbased on Surface Homogenized Data Basis). Proceedings of the Conference on Spatial Interpolation in Climatology and Meteorology (eds.: *S. Szalai, Z. Bihari, T. Szentimrey* and *M. Lakatos*) 2007, COST Office, Luxemburg, ISBN 92-898-0033-X, pp.17-28.

Wilby, R.L., Wigley, T.M.L., Conway, D., Jones, P.D., Hewitson, B.C., Main, J., and *Wilks, D.S.,* 1998: Statistical downscaling of general circulation model output: A comparison of methods. *Water Resour. Res. 34,* 2995-3008.

IDŐJÁRÁS

Quarterly Journal of the Hungarian Meteorological Service
Vol. 112, No. 3–4, July–December 2008, pp. 285–300

Regional photochemical model calculations for Europe concerning ozone levels in a changing climate

B. C. Krüger[1*], E. Katragkou[2], I. Tegoulias[3], P. Zanis[3], D. Melas[2], E. Coppola[4], S. Rauscher[4], P. Huszar[5] and T. Halenka[5]

[1]*Institute of Meteorology (BOKU-Met), University of Natural Resources and Applied Life Sciences, Peter-Jordan-Str. 82, A-1190 Vienna, Austria*

[2]*Laboratory of Atmospheric Physics, Aristotle University of Thessaloniki (AUTH), Greece*

[3]*Department of Meteorology and Climatology, Aristotle University of Thessaloniki, Greece*

[4]*Earth System Physics Section, The Abdus Salam International Centre for Theoretical Physics (ICTP), Trieste, Italy*

[5]*Department of Meteorology and Environmental Protection, Charles University (CUNI), Prague, Czech Republic*

(Manuscript received in final form October 14, 2008)

Abstract—Regional photochemical model calculations were performed for three decadal time periods: 1991–2000, 2041–2050, and 2091–2100 under changing climate conditions for Europe. While the climatic conditions changed between the decades, all other input fields of the chemical model were held constant in order to separate climate effects from others. In particular, model results for summer ozone concentrations were investigated. These show increasing ozone values in response to higher temperatures and net radiation associated with increases in anthropogenic greenhouse gases. The increase of ozone is stronger in the second half of the 21st century than in the first half. In the course of the whole century, the average summer ozone maxima will rise by several ppbv over most parts of Europe with the highest change in the northwest of the continent. This increase suggests more frequent concentrations above legal thresholds in the future and is partly caused by higher emissions of biogenic hydrocarbons in the model calculation.

Key-words: photochemical transport model, tropospheric ozone, climate change, CECILIA project, ozone threshold level

1. Introduction

High ozone levels above legal thresholds affecting human health as well as vegetation are of primary interest in air quality research. Several factors affect

* Corresponding author; E-mail: bernd.krueger@boku.ac.at

ozone concentration, including the availability of ozone precursors, namely nitrogen oxides and volatile hydrocarbons, which are to a large fraction of anthropogenic origin. In addition, ozone formation is favored under certain meteorological conditions. Therefore, the question arises, what influence climate change will have in the future on the potential of ozone formation. Ozone concentration is in part controlled by the global background level formed by the long-range transport of pollutants and the exchange of air masses between the troposphere and stratosphere as the main mechanisms. However, over populated areas, anthropogenic emissions on local and regional scales often lead to high ozone concentration levels. Therefore, projections for future burdens of ozone should be made on a regional scale, at least.

Recently, there have been several studies with regional model calculations for Europe concerning air pollution under changing climate conditions. For example, *Meleux et al.* (2007) investigated summer ozone amounts over Europe with a 50 km resolution model by comparing two time slices of 30 years each, namely 1961–1990 and 2071–2100. *Forkel* and *Knoche* (2007) used a nested regional climate-chemistry model with a highest spatial resolution of 20 km over central Europe and compared the two time slices of 1991–2000 and 2030–2039. *Hedegaard et al.* (2008) had a resolution of 150 km in their model and inspected three decades (1990s, 2040s, and 2090s) for the Northern Hemisphere. In all of these studies, the anthropogenic emissions were kept unchanged for the future projections, so that their focus was on the effects of changing meteorological conditions. This approach is also applied in the present study.

This work was carried out within the European FP6 project CECILIA (Central and Eastern Europe Climate Change Impact and Vulnerability Assessment, http://www.cecilia-eu.org/). In this project, regional climate simulations with high spatial resolution are carried out for the target area. In addition, impact studies concerning hydrology, agriculture and forestry, as well as air quality are performed. For the latter, the model runs described in this study will be used to provide boundary concentrations for photochemical model calculations with 10 km resolution in smaller regional grids within the target area of this project. Three decadal time slices, namely 1991–2000, 2041–2050, and 2091–2100 were calculated.

It is not the purpose of this study to predict exact levels of air quality of the future until the year 2100, as there are too many unknown parameters such as the amount and composition of future anthropogenic emissions of air pollutants due to progress in technology as well as changes in land use. The latter is important, since it affects the distribution and amount of biogenic and anthropogenic emissions, and it is subject of man-made changes as well as of feedbacks from climate change. Similar to the studies by the other authors mentioned above, this study was performed to investigate the effect of climate change on ozone concentrations under the assumption that all parameters affecting air quality, except for the meteorological data, are kept unchanged.

2. *Description of the models and input data*

2.1. RegCM and CAMx

Meteorological input files for the photochemical model were taken from a transient climate run with the hydrostatic RegCM3 model (*Pal et al.*, 2007) performed at ICTP, that was driven at the lateral boundaries by the global ECHAM5 model under forcing from the SRES-A1B IPCC greenhouse gas scenario (*Nakicenovic et al.*, 2000) for the future projections. The spatial resolution of the model was 25 km × 25 km. A part of these calculations was performed for the EU-FP6 project ENSEMBLES (http://ensembles-eu.metoffice.com/).

The Comprehensive Air quality Model with eXtensions (CAMx), which is available at http://www.camx.com, from ENVIRON International Corporation (Novato, California) is an Eulerian photochemical dispersion model that allows for regional integrated "one-atmosphere" assessments of gaseous and particulate air pollution. Model version 4.40 was used (*ENVIRON*, 2006). The chemistry mechanism invoked was an extended Carbon Bond version 4 mechanism (*Gery et al.*, 1989). This mechanism includes 117 reactions – 11 of which are photolytic – and up to 67 species (37 state gases, up to 18 state particulates and 12 radicals).

The spatial resolution of the CAMx model grid was 50 km × 50 km and the domain had 94 × 102 grid cells. The domain's vertical profile contained 12 layers with varying thicknesses, extending up to 450 hPa. The 25 km RegCM results were upscaled to this resolution by averaging. The domains of the two models were the same. The grid covered most of Europe and parts of northern Africa as it may be seen in the figures, which display the whole domain. Time resolution of meteorological input was 6 hours, the emission input as well as the output of the photochemical model had a resolution of one hour.

The RegCM output was transformed to the format required by CAMx by a pre-processor program. Some of the fields could be taken directly like wind direction, wind speed, and temperature, while others had to be calculated analytically. The vertical diffusion coefficient needed by CAMx to model the vertical transport was calculated following the method by *O'Brian* (1970). In the pre-processing step, the biogenic emissions of isoprene and monoterpenes were calculated following *Guenther et al.* (1993) with respect to the actual meteorological fields of the day from RegCM. Also the temporal disaggregation of the anthropogenic emissions was performed in the preprocessing.

Although chemical transport models usually need a relatively small spin-up time of a few days for initialization, we calculated the full year prior to the decades considered (i.e., 1990, 2040, and 2090). In addition, we ran the period from 1990 to 2001 with RegCM fields driven by the ERA-40 reanalysis (*Uppala et al.*, 2005) for the validation of the model system. The comparison of the ERA-40 run with measurements and with the control run showed a reasonable agreement and will be described in a separate study.

2.2. *Emissions*

Anthropogenic emissions used in this study are based on the UNECE/EMEP database (http://webdab.emep.int/) for European emissions (*Vestreng et al.*, 2005) for the year 2000. The "expert emissions" are derived from the national totals reported by the individual countries and have been completed and corrected/substituted for the use of dispersion modeling. These data comprise the annual sums of the emissions of NO_x, CO, non-methane hydrocarbons, SO_2, NH_3, fine particles (<2.5 μm), and coarse particles (2.5 μm to 10 μm) on a 50 km × 50 km grid. 11 sectors of anthropogenic activity are distinguished.

For the Pannonean countries Austria, Czech Republic, Hungary, and Slovakia, the EMEP data for the year 2000 are downscaled to a spatial resolution of 5 km × 5 km. An emission inventory for theses countries from the year 1995 (*Winiwarter* and *Zueger*, 1996) is used as database for the spatial distribution of the emissions within the 50 km × 50 km EMEP grid cells.

For every sector the emission model applies different distributions for the month, day of the week, and hour of the day for temporal disaggregation. The disaggregation factors are taken from the inventory by *Winiwarter* and *Zueger* (1996). They are available for the Pannonean countries. For all other countries the disaggregation data for Austria have been used.

The emissions from the inventories must be splitted sector specifically into the speciation of the chemical compounds that corresponds to the chemical mechanisms of the photochemical model. In the case of NO_x it is assumed in all sectors of anthropogenic emissions, that 10% are NO_2 and 90% are NO (in molar percentages). The emissions of non-methane hydrocarbons are disaggregated in accordance with the needs of the chemical mechanism CBM-IV (*Gery et al.*, 1989). This results in specific emissions of the following species, given in CBM-IV notation: PAR (alcane groups), ETH (ethene), OLE (alcene groups), TOL and XYL (aromatics of different reactivity), FORM (formaldehyde), and ALD2 (aldehydes, ketones). The emissions of $PM_{2.5}$ were splitted into organic aerosol (POA), elementary carbon (PEC), and remaining aerosol following the split suggested in the EMEP model (*Simpson et al.*, 2003). In addition, the following species are emitted without chemical disaggregation: CO, SO_2, NH_3, and $PM_{2.5-10}$.

The anthropogenic emissions were not changed between the three decades, although it may be assumed for sure, that changes, mainly in energy supply, both for stationary and mobile sources, will have the most important impact on future air quality. However, there is a large uncertainty about the actual future emissions, even for the next approaching decades, that depends on technical development and energy availability in the future.

2.3. *Other input data*

Regional photochemical transport models need concentrations of trace species prescribed at the lateral boundaries and the top of the model. They have an

influence on the model results when the wind moves air masses from the boundaries into the model. In the calculations described in this study, we assumed clean air conditions at all boundaries, namely 40 ppbv of ozone and very low mixing ratios for all other compounds. This implies that changes of these concentrations in the global background, that may be caused by changes of climate or other conditions, are not covered by this study. In addition, impacts from potential changes in stratosphere/troposphere exchange as well as effects of long range transport of pollutants, which often takes place at tropospheric altitudes above the top of our model grid (*Trickl et al.*, 2003), are not considered here. As stated previously, future changes in land use may also be expected. Such changes might affect atmospheric composition through emissions, including biogenics, and through deposition of compounds. For this parameter also the same data for the present time were used for every decade. The data come along with the preprocessor terrain of the regional mesoscale model MM5 (http://www.mmm.ucar.edu/mm5/). They distinguish 25 land use categories and are based on global data from the United States Geological Survey (USGS).

3. Results

3.1. Daily maxima of ozone in summer

In air quality studies, changes in the daily maximum concentration of ozone are of particular interest, since they allow us to estimate to which extent legal thresholds of ozone may be exceeded in a future climate. At present, following European legislation, the population has to be informed about ozone volume mixing ratios exceeding 90 ppbv. Values above 120 ppbv must lead to further measures.

However, it must be noted that the spatial resolution of the model setup in this study does not allow calculating urban plumes. Instead, only background concentrations are calculated. Therefore, the calculated maxima are expected to be lower than the maxima typically measured. Averaging may also result in lower values than it may be observed in the real world. In the following, seasonal averages of the daily maxima for the decades considered during summer are presented.

Seasonal averages of the daily ozone maxima as calculated for the control decade 1991–2000 for summer (JJA) are displayed in *Fig. 1* (upper left panel). The highest values of more than 60 ppbv are obtained over the Mediterranean Sea. A latitudinal gradient can be observed with the lowest values in the north, and the highest values in the south. In general, this corresponds to the observed behavior of ozone over Europe at the present time.

The upper right panel of *Fig. 1* shows the difference in the decadal average of the daily ozone maxima between the mid-century period and the control run. All differences are small. An increase below 2.5 ppbv can be observed over the

southeast part of Europe, stretching as far west as Italy and southern Germany. For most of the rest of the model domain over Europe, a slight decrease of the ozone maxima occurs. In a belt from southern England along the North Sea coast to southern Scandinavia, this decrease is somewhat stronger, but still below 5 ppbv.

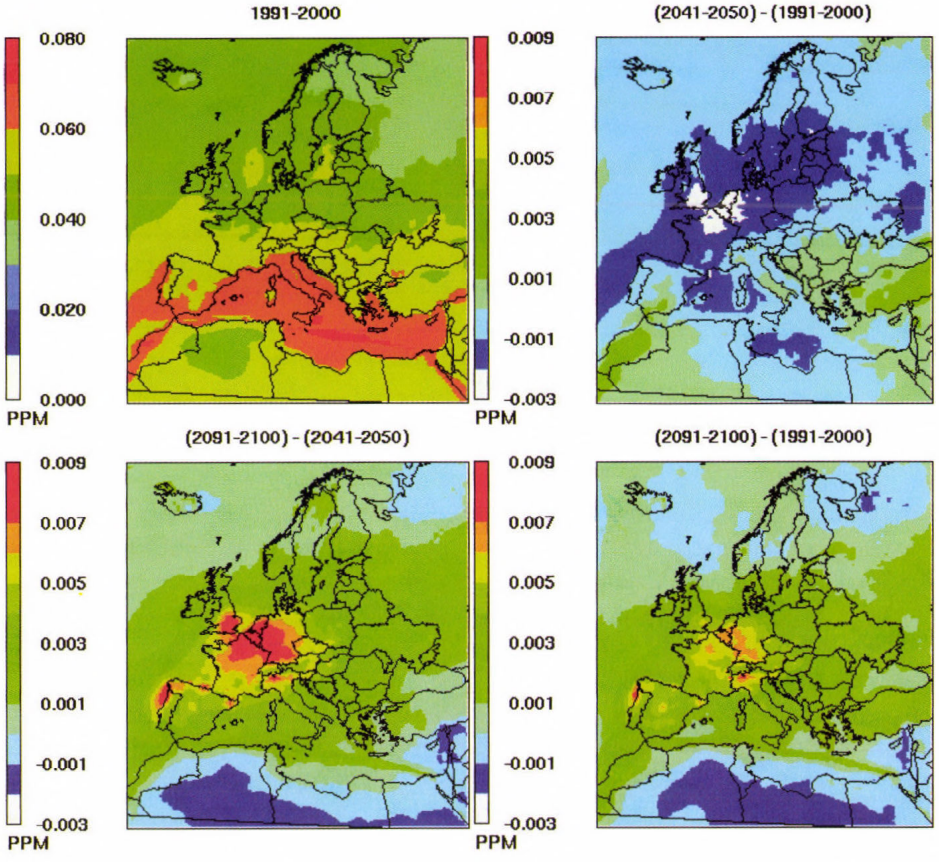


Fig. 1. Average of the daily maxima of ozone volume mixing ratio in summer (JJA) from the control decade 1991–2000 (upper left), and differences of the maximum ozone volume mixing ratios in summer between the calculated decades: first half-century (upper right), second half-century (lower left), and whole century (lower right).

Between the mid-century and end-century decades, a much stronger increase of the ozone maxima occurs. The highest increase is located over southern England, northern France, the Benelux countries, and western Germany reaching about 10 ppbv. However, with the exception of Africa, the eastern Mediterranean, and northern Russia, an increase of ozone is calculated all over the model domain.

The difference between the results of the end-century and control runs showing the development of the ozone maxima within 100 years is displayed in the lower right panel of *Fig. 1*. Due to the stronger increase in the second half of the 21st century, the decrease of ozone in the first half over wide parts of Europe is compensated. The highest change occurs over northern France, Belgium, and western Germany, as well as over the Po valley in Italy. These regions have the highest emissions of ozone precursors at the present time. Since the anthropogenic emissions were not changed between the decades, this emission pattern persists throughout the century.

3.2. Daily maxima of ozone in other seasons

In the other seasons the averaged daily maxima of ozone do not change as strongly as in summer. In spring (MAM) the ozone values increase from the control decade to the end-century decade by about 3 ppbv over most parts of Europe except for Scandinavia and the British Isles, where the increase is lower or even a slight decrease was calculated. The spring increase is of the same amount as in summer, except for those parts of western Europe that show a stronger summer increase. As an illustration, *Fig. 2* displays the change during the whole century in spring and autumn.

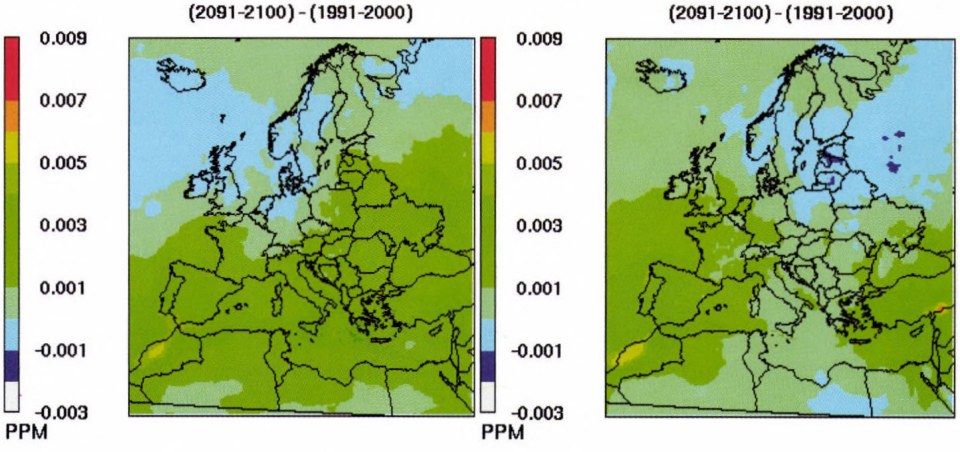


Fig. 2. Differences of the average daily maxima of ozone volume mixing ratio in spring (MAM, left) and autumn (SON, right) during the whole century.

In autumn (SON) the average of the daily ozone maxima decreases over most of Europe in the first half of the 21st century and increases in the second half; each change is approximately 3 ppbv. For the whole century this results in a slightly stronger increase over western Europe than over the central and eastern regions. Winter (DJF) shows the smallest changes. In contrast to the

other seasons, a decrease of ozone occurs in winter in the second half of the century in most land-covered parts of the model domain, while other regions show a small increase between the control decade and the mid-century decade.

Since the highest concentrations of ozone occur in summer causing perturbations of the air quality by exceeding legal thresholds, and since the highest alterations due to climate change in these calculations also occur in summer, in the following only the changes in summer will be further considered in this study.

3.3. AOT40

Accumulated ozone exposure values over a certain threshold (AOT) are common measures for the ozone impact. In this study we compare AOT40 (accumulated ozone over a threshold of 40 ppbv) for the period from April to September, which is considered as a measure for the impact of ozone on forests. The sum of the differences between the hourly mean ozone concentration (in ppb) and 40 ppb for each hour when the concentration exceeds 40 ppb, accumulated between 8:00 and 20:00 hours during the period is calculated. As a long-term objective for the protection of forests, a maximum value of 10000 ppbv h is considered. (*European Communities*, 2002).

The upper left panel of *Fig. 3* shows the average AOT40 data as they were calculated for the control period 1991–2000. Only in northern Europe the long-term objective is not exceeded. The highest values can be found over the Mediterranean Sea. In the first half of the 21st century, AOT 40 goes down over most of Europe, except of the Iberian Peninsula and southeast Europe (upper right panel), while there is a strong increase over most of Europe in the second half of the century (lower left panel). The lower right panel shows that during the whole 21st century, AOT40 values will go up over the whole of Europe with the highest increase over the Iberian Peninsula and the Alps.

Similar results were obtained for other quantities describing the exposure to elevated ozone concentrations like AOT40 (May–July), which is considered as a measure for the exposure of agricultural plants during the growing period, or AOT60, which measures the exposure of humans. Also average ozone concentrations show a small change during the first half of the 21st century and a strong increase in the second half, with stronger increases in the south part of Europe than in the north.

3.4. Temperature

As an indicator for the changing climate, the changes of the temperature in the lowest model level are shown, as they were taken from the RegCM results, which were input data to the photochemical model CAMx. The upper left panel of *Fig. 4* shows the average summer temperature from the control period 1991–2000 with the expected north-south gradient.

The changes in average temperature until the mid-century decade 2041–2050 are less than 1 degree over most of Europe except for the very northern areas as well as southern Spain, Sicily, and southern Greece, where an increase between 1 and 2 degrees occurs, as it is shown in the upper right panel. Over England and northwestern France there is even a decrease of the average temperature. In the second half of the 21st century a much stronger increase occurs, displayed in the lower left panel, amounting to 1 to 2 degrees in northern Europe, up to 3 degrees in Germany and eastern Europe, up to 4 degrees over France and Italy, and even more over the Iberian peninsula.

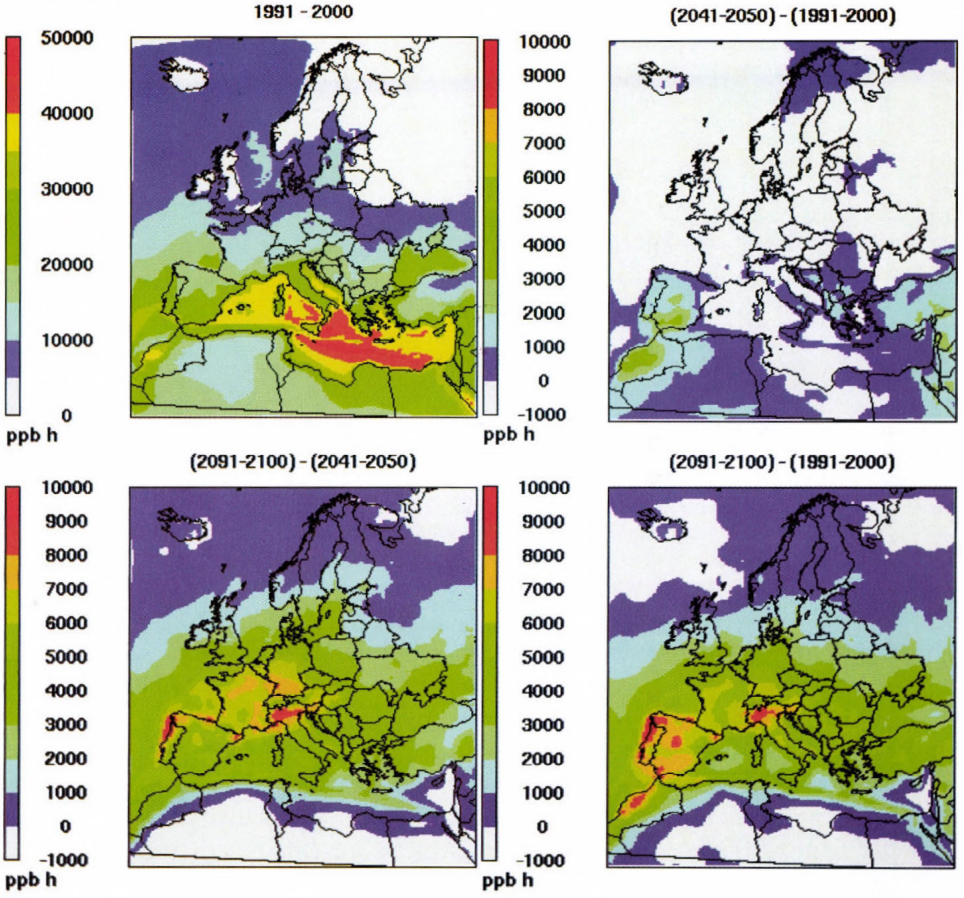


Fig 3. AOT40 (accumulated ozone over a threshold of 40 ppbv) from April to September in the control decade 1991–2000 (upper left), and differences of AOT40 from April to September between the calculated decades: first half-century (upper right), second half-century (lower left), and whole century (lower right).

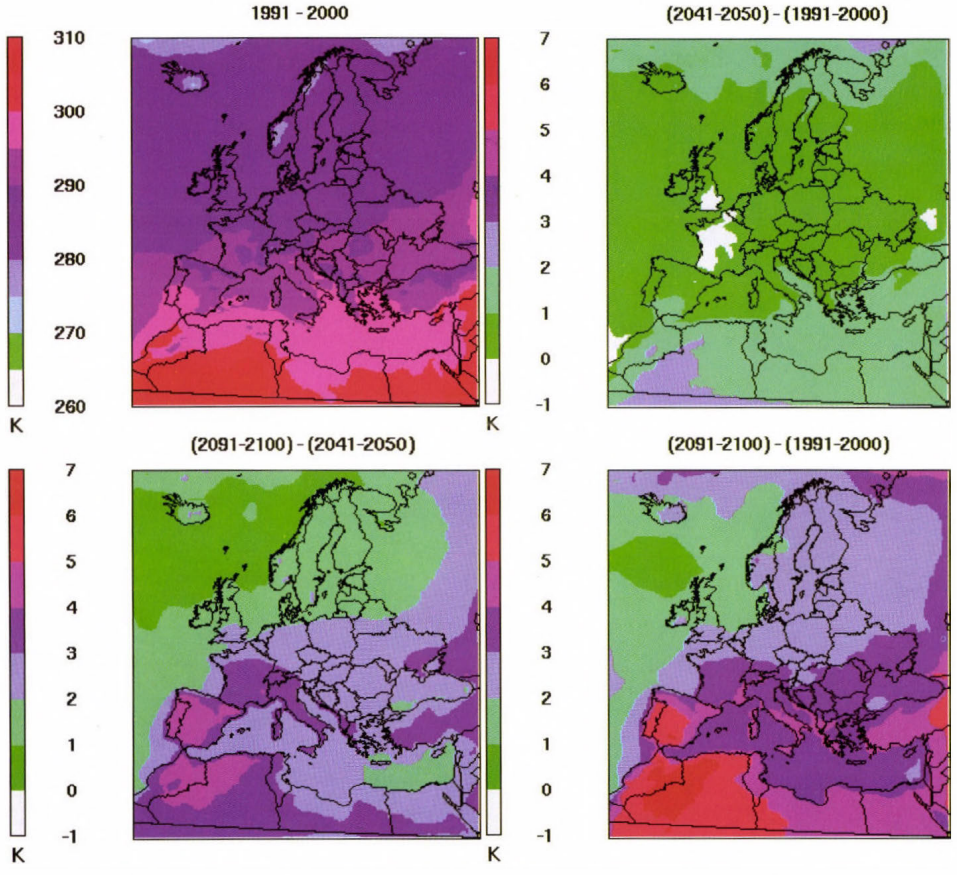


Fig. 4. Average temperature in the lowest model level in summer (JJA) in the control decade 1991–2000 (upper left), and differences of the average temperatures in summer between the calculated decades: first half-century (upper right), second half-century (lower left), and whole century (lower right).

3.5. Cloud optical depth

Besides temperature, photochemical activity is strongly influenced by the amount of radiation, which drives the formation of radicals and enhances the production of biogenic hydrocarbons. These emissions act as precursors in ozone formation along with the anthropogenic emissions of hydrocarbons and nitrogen oxides. In CAMx the photolysis rates are calculated from a look-up table that contains clear sky photolysis rates at various solar zenith angles, altitudes, total ozone columns, values for the surface albedo, and atmospheric turbidity. The effect of clouds is treated based upon the RADM approach (*Chang et al.*, 1987), in which the cloud optical depth is used to scale down the photolysis rates for layers within or below clouds to account for UV attenuation, or to scale up the rates for layers above clouds to account for UV reflection. The

cloud optical depth is calculated by an empirical expression with the preprocessor from the actual cloud water mixing ratio.

As a qualitative measure of the attenuation of radiation, *Fig. 5* shows the average cloud optical depth of the control period (upper left panel) during summer. The highest values in the model domain occur over the Atlantic Ocean, and the lowest values are observed over the Mediterranean Sea. During the first half of the 21st century there is an increase all over Europe. The highest rise occurs over the sea (Atlantic Ocean, North Sea, Baltic Sea), while over southern Europe the increase is small (upper right panel). This increase in the cloud optical depth leads to a reduction in photochemically active radiation.

In the second half of the century the cloud optical depth decreases all over Europe. With the exception of northern Europe, this decrease compensates the increase in the first half (lower right panel). This net effect is that the photochemically active radiation becomes stronger.

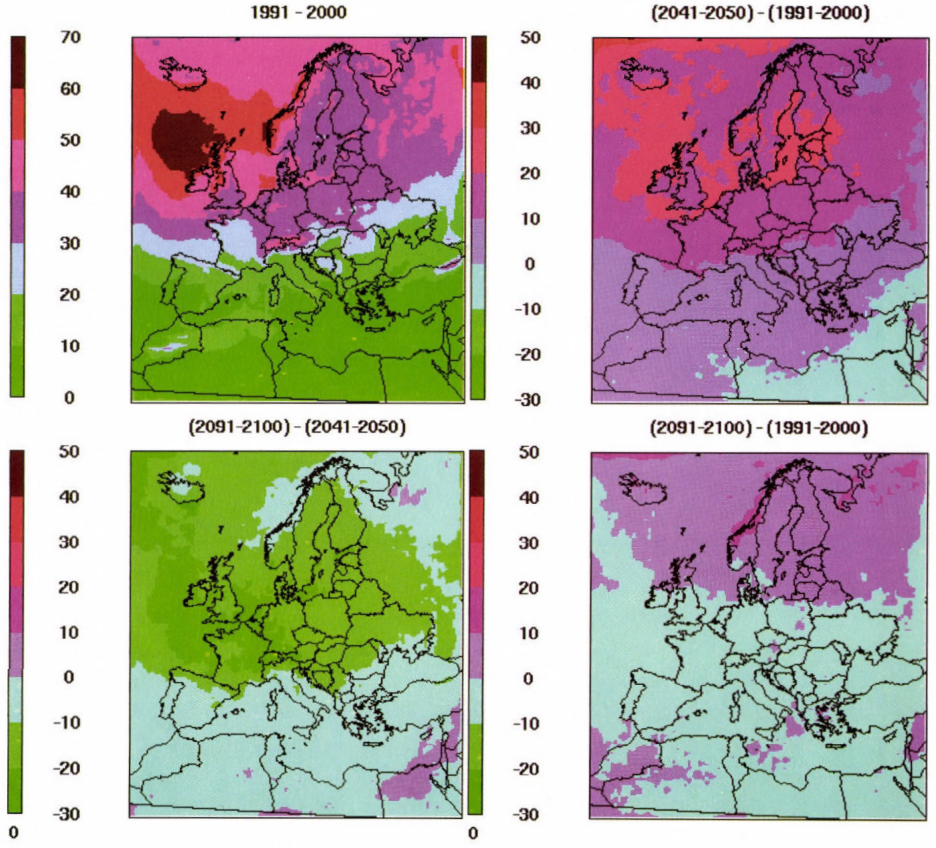


Fig. 5. Average cloud optical depth in the lowest model level in summer (JJA) in the control decade 1991–2000 (upper left), and differences of the average cloud optical depths in summer between the calculated decades: first half-century (upper right), second half-century (lower left), and whole century (lower right).

3.6. *Isoprene*

Higher temperatures and stronger radiation both support the emission of biogenic hydrocarbons. Isoprene and monoterpenes are the only ozone precursors, with changing emissions in the decades calculated in this study. The change of the volume mixing ratio of isoprene is displayed in *Fig. 6*. The upper left panel shows the summer average of isoprene during the control period. Since the lifetime of isoprene amounts to only a few hours or even less, noteworthy concentrations occur over the land areas only. The highest values can be found over Portugal and the Balkan. Until the decade from 2041 to 2050 the values increase slightly over most of the model domain. Even over the sea a small increase is plotted. The increase continues until the end-century decade. During this time span there is a greater increase of the isoprene concentration over the areas that had the highest abundance already.

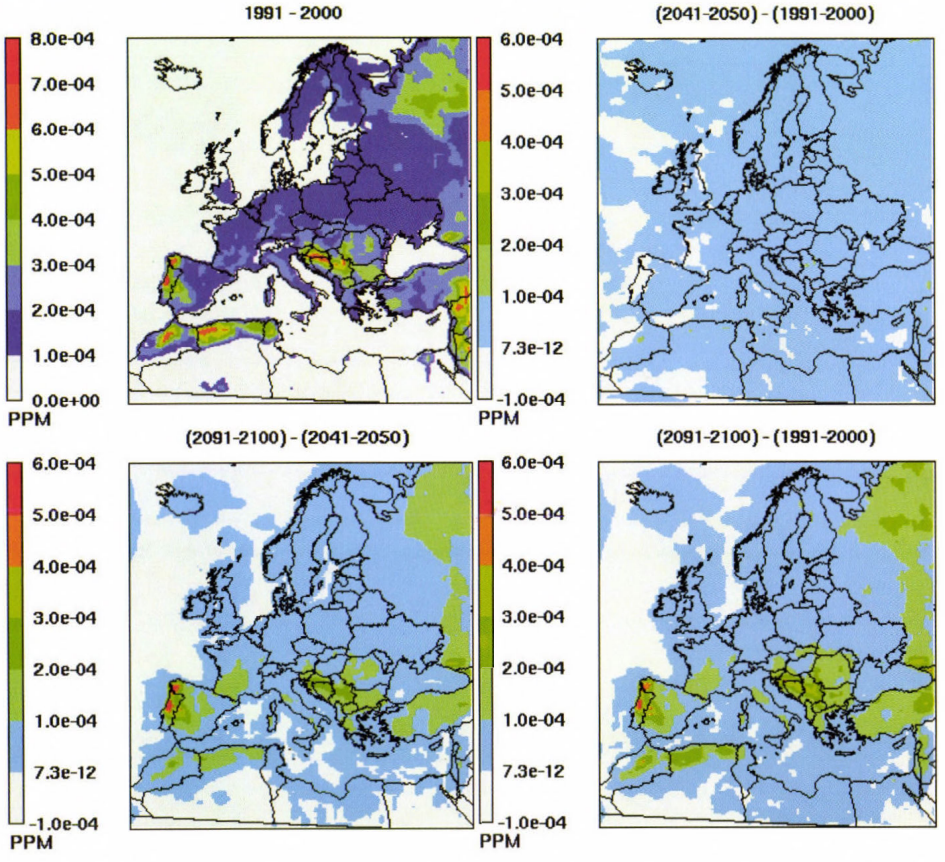


Fig. 6. Average volume mixing ratio of isoprene in the lowest model level in summer (JJA) in the control decade 1991–2000 (upper left), and differences of the average volume mixing ratios in summer between the calculated decades: first half-century (upper right), second half-century (lower left), and whole century (lower right).

4. Discussion

Photochemical model calculations, which are driven by meteorological fields from climate scenario runs with a regional climate model, show an increase of ozone formation concurrent with climate change. In the second half of the 21st century, the increase of the ozone concentration is much stronger than in the first half, coinciding with a larger increase in average temperature and a decrease of the average cloud optical depth.

Since ozone is a secondary pollutant that is formed in the atmosphere, its abundance depends on the availability of sufficient ozone precursors. In addition, the right conditions must be present, including the presence of high temperatures, strong solar radiation, and stagnant winds. Biogenic emissions were the only variable ozone precursors in this study, and their emission in turn depends on temperature and radiation in the model. Therefore, it follows that ozone should increase mostly where the highest increases of temperature and radiation occur.

By comparing the results for the decade 2041–2050 with the control period 1991–2000, the changes projected for the first half of the 21st century can be seen. A small increase of temperature occurs over most parts of Europe. On the other hand, there is also an increase in the cloud optical depth, which, therefore, counteracts ozone formation due to less radiation. This results in only a small increase of the averaged daily maxima of ozone in southeastern Europe, where the effect of temperature change seems to outweigh the effect of radiation. In northern and western Europe the opposite occurs and the average daily maxima of ozone are reduced. Similar results of increasing and decreasing values are obtained for AOT40 (Apr–Sep) as well as for other ozone measures, which are not shown.

In the second half of the 21st century, the temperature increase in the input data is much stronger, and the radiation increases due to a decrease of the cloud optical depth. Therefore the calculated increase of ozone in all parts of Europe is also much stronger in the later half of the 21st century

The highest changes of ozone occur in summer, the season that shows the highest ozone concentrations. Interestingly, these future increases in ozone occur where the highest emissions of ozone precursors are present, not where the highest temperature increases occur. From the increase of the averaged daily maxima of ozone it can be concluded, that the ozone concentration would exceed present legal thresholds in the future more often under the assumptions of unchanged anthropogenic emissions of ozone precursors. The long-term objective for AOT40 (Apr–Sep) of 10000 ppbv h will also not be maintained under these conditions.

An increase of biogenic hydrocarbon emissions caused by higher temperatures and stronger radiation certainly supports ozone formation. However, this effect should be treated with caution, since the meteorological effects also may lead to changes in land use, which in turn affects the intensity of emissions. In addition, there are indications that the production of isoprene by

forest ecosystems may be reduced under conditions of elevated CO_2 concentrations (*Rosenstiel et al.*, 2003, *Monson et al,* 2007), which is the main driving force for the projected climate change. Such feedbacks were not considered in this study and land use patterns were kept constant over all decades.

Furthermore, areas with the strongest increase of biogenic emissions must not be, by all means, the areas with the strongest ozone increase, since NO_x must also be available for ozone formation. For example, the Balkan area shows a strong increase of isoprene until the 2091–2100 decade (*Fig. 6*), while the increase of ozone in that area is not exceptionally strong (*Fig. 1* and *Fig. 3*). *Forkel* and *Knoche* (2007) show similar results for this area and explain them with the lack of NO_x.

The concentration of ozone may also change due to alterations of the patterns of horizontal atmospheric transport within the model domain. Such phenomena have not been investigated in this study. On the other hand, effects of vertical transport were excluded from this study, since constant clean air conditions have been assumed at the top of the model.

The coarse grid resolution of 50 km in the CAMx calculation implies, that this is a study for background concentrations. The highest concentrations of ozone are normally observed within urban plumes, while urban areas, on the other hand, usually show a strong reduction of ozone during nighttime due to destruction by primary emissions of NO. These features are not resolved with the applied model grid. In addition, the 50 km resolution of the used emission inventory causes an instantaneous mixing of emitted ozone precursors. This also prevents the formation of high ozone concentrations as well as local destruction. Therefore, extreme high and low ozone values may not be expected in the model results. Within the project CECILIA, air quality calculation with a higher spatial resolution will be performed at a later stage for smaller model domains.

The results of this study agree well with results from other studies, although they may be compared only qualitatively, since other studies use different greenhouse gas scenarios and different time periods are considered. *Forkel* and *Knoche* (2007) calculated the 2030s-decade as climate projection, and also found an increase of ozone over Europe. *Hedegaard et al.* (2008) performed their calculations for the same decades as in this study, but they used the A2 scenario and a coarser model resolution. However, they did not find the distinction between small changes in the first half and strong changes in the second half of the 21st century that was found in this work. This difference is likely to be caused by the different GCM boundary conditions. *Meleux et al.* (2007) looked at time slices of 30 years, in contrast to 10 years in the other studies. However, their qualitative result is very similar. Nonetheless, the fact, that different models applied under partly different assumptions lead to qualitatively similar results, shows some robustness of the message that the projected climate change would lead to enhanced ozone formation if anthropogenic emissions would be kept unchanged.

5. Summary and conclusions

Regional photochemical model simulations were carried out with the model CAMx. The model domain covered Europe with a spatial resolution of 50 km. Three decades were calculated, namely 1991–2000, 2041–2050, and 2091–2100, driven by a climate change simulation of the model RegCM. These in turn were driven by the global model simulation of the ECHAM5 model under the SRES-A1B-greenhouse gas scenario.

Of the many species calculated by the photochemical model, this study mainly examined ozone concentrations during summer due to its adverse effects on human health and vegetation. Ozone levels are projected to increase over Europe during the 21sth century. The increase will be stronger in the second half of the century; in the first half a decrease in northern parts of Europe is projected.

The projected ozone increase must be attributed to more frequent meteorological conditions that promote ozone formation like high temperature, strong solar radiation, and stagnant flow conditions. In addition, increasing concentration of biogenic hydrocarbons calculated with respect to the meteorological input data, which in turn are dependent on the temperature and the available radiation, may also be a factor in the projected ozone increases.

Acknowledgement—This work has been funded by the European Community's Sixth Framework Programme as part of the project CECILIA (Central and Eastern Europe Climate Change Impact and Vulnerability Assessment) under Contract No. 037005.

References

Chang, J.S., Brost, R.A., Isaksen, I.S.A., Madronich, S., Middleton, P., Stockwell, W.R., and *Walcek, C.J.*, 1987: A three-dimensional Eulerian acid deposition model: Physical concepts and formulation. *J. Geophys. Res. 92*, 14681-14700.

ENVIRON, 2006: *User's Guide to the Comprehensive Air Quality Model with Extensions (CAMx)*, Version 4.40. ENVIRON International Corporation, Novato, CA.

European Communities, 2002: Directive 2002/3/EC of the European Parliament and of the Council of 12 February 2002 relating to ozone in ambient air. *Official J. of the European Communities*, L67/14, EN.

Forkel, R. and *Knoche, R.*, 2007: Nested regional climate-chemistry simulations for central Europe. *C. R. Geoscience 339*, 734-746.

Gery M.W., Whitten G.Z., Killus, J.P., and *Dodge, M.C.*, 1989: A photochemical kinetics mechanism for urban and regional scale computer modelling. *J. Geophys. Res. 94*, 12925-12956.

Guenther, A.B., Zimmermann, P.C., Harley, R., Monson, R.K., and *Fall, R.*, 1993: Isoprene and monoterpene emission rate variability: model evaluations and sensitivity analyses. *J. Geophys. Res. 98*, 12609-12617.

Hedegaard, G.B., Brandt, J., Christensen, J.H., Frohn, L. M., Geels, C., Hansen, M., and *Stendel, M.*, 2008: Impacts of climate change on air pollution levels in the Northern Hemisphere with special focus on Europe and the Arctic. *Atmos. Chem. Phys. Discuss. 8*, 1757-1831.

Meleux, F., Solmon, F., and *Giorgi, F.*, 2007: Increase in summer European ozone amounts due to climate change. *Atmos. Environ. 41*, 7577-7587.

Monson, R., Trahan, N., Rosenstiel, T., Veres, P., Moore, D., Wilkinson, M., Norby, R., Volder, A., Tjoelker, M., Briske, D., Karnosky, D., and *Fall, R.*, 2007: Isoprene emission from terrestrial

ecosystems in response to global change: minding the gap between models and observations. *Philos. T. Roy. Soc.A. 365*, 1677-1695.

Nakicenovic, N., Alcamo, J., Davis, G., de Vries, B., Fenhann, J., Gaffin, S., Gregory, K., Grübler, A., Jung, T., Kram, T., Rovere, E.L., Michaelis, L., Mori, S., Morita, T., Pepper, W., Pitcher, H., Price, L., Riahi, K., Roehrl, A., Rogner, H.-H., Sankovski, A., Schlesinger, M., Shukla, P., Smith, S., Swart, R., van Rooijen, S., Victor, N., and *Dadi, Z.*, 2000: *Special Report on Emission Scenarios*. Cambridge University Press.

O'Brien, J.J., 1970: A note on the Vertical Structure of Eddy Exchange Coefficient in the Planetary Boundary Layer. *J. Atmos. Sci. 27*, 1213-1215.

Pal, J.S., Giorgi, F., Bi, X., Elguindi, N., Solmon, F., Gao, X., Rauscher, S.A., Francisco, R., Zakey, A., Winter, J., Ashfaq, M., Syed, F.S., Bell, J.L., Diffenbaugh, N.S., Karmacharya, J., Konare, A., Martinez, D., da Rocha, R.P., Sloan, L.C., and *Steiner, A.*, 2007: Regional climate modeling for the developing world: The ICTP RegCM3 and RegCNET. *B. Am. Meteorol. Soc. 88*, 1395-1409.

Rosenstiel, T.N., Potosnak, M.J., Griffin, K.L., Fall, R., and *Monson, R.K.*, 2003: Increased CO_2 uncouples growth from isoprene emission in an agriforest ecosystem. *Nature 421*, 256-259.

Simpson, D., Fagerli, H., Jonson, J.E., Tsyro, S., Wind, P., and *Tuovinen, J.-P.*, 2003: Transboundary acidification and eutrophication and ground level ozone in Europe: Unified EMEP Model Description. *EMEP Status Report 1/2003 Part I*, EMEP/MSC-W Report, The Norwegian Meteorological Institute, Oslo, Norway.

Trickl, T., Cooper, O., Eisele, H., James, P., Mücke, R., and *Stohl, A.*, 2003: Intercontinental transport and its influence on the ozone concentrations over central Europe: Three case studies. *J. Geophys. Res. 108*, 8530.

Uppala, S. M., Kållberg, P. W., Simmons, A. J., Andrae, U., da Costa Bechtold, V., Fiorino, M., Gibson, J. K., Haseler, J., Hernandez, A., Kelly, G.A., Li, X., Onogi, K., Saarinen, S., Sokka, N., Allan, R.P., Andersson, E., Arpe, K., Balmaseda, M.A., Beljaars, A.C.M., van de Berg, L., Bidlot, J., Bormann, N., Caires, S., Chevallier, F., Dethof, A., Dragosavac, M., Fisher, M., Fuentes, M., Hagemann, S., Hólm, E., Hoskins, B.J., Isaksen, L., Janssen, P.A.E. M., Jenne, R., McNally, A.P., Mahfouf, J.-F., Morcrette, J.-J., Rayner, N.A., Saunders, R.W., Simon, P., Sterl, A., Trenberth, K.E., Untch, A., Vasiljevic, D., Viterbo, P., and *Woollen, J.* 2005: The ERA-40 re-analysis. *Q. J. Roy. Meteorol. Soc. 131*, 2961-3012.

Vestreng, V., Breivik; K., Adams, M., Wagener, A., Goodwin, J., Rozovskkaya, O., and *Pacyna, J.M.*, 2005: Inventory Review 2005, Emission Data reported to LRTAP Convention and NEC Directive, Initial review of HMs and POPs. *Technical Report* MSC-W 1/2005, ISSN 0804-2446.

Williams, E.J., Parrish, D.D., and *Fehsenfeld, F.C.*, 1987: Determination of NO_x emissions from soils. *J. Geophys. Res. 92*, 2173-2179.

Winiwarter, W. and *Zueger, J.*, 1996: Pannonisches Ozonprojekt, Teilprojekt Emissionen. Endbericht. *Report* OEFZS-A-3817, Austrian Research Center, Seibersdorf.

BOOK REVIEW

C. Gualtieri and *D.T. Mihailović* (eds.): **Fluid Mechanics of Environmental Interfaces**. Taylor and Francis, London, 2008, 348 pages, 11 chapters.

C. Gualtieri and *D.T. Mihailović* assembled an international team of 16 authors with the idea to condense into a textbook an overview of fluid mechanical processes in the environmental interfaces. The book is divided into three parts with an introductory chapter. The introductory chapter, written by *B. Cushman-Roisin* and the editors, focuses on the importance of turbulence and stratification in environmental systems. Furthermore, it touches on the main differences between engineering fluid mechanics, geophysical fluid dynamics, and environmental fluid mechanics.

The first part is dedicated to the processes at atmospheric interfaces. Starting from the theory of atmospheric dispersion and modeling of dispersion of passive substance, the authors guide the reader through the concepts of the modeling of momentum, heat, and mass flux exchange between heterogeneous land surfaces, sea surface, as well as the atmosphere. The part is closed with description of desert dust transport.

Part two is devoted to the fluid mechanical processes at water interfaces. This part reviews the theory and numerical simulation of gas transfer at unshared free surfaces important for water quality in aquatic systems. It also elaborates basic mechanisms, analytical solutions of advective diffusion of air bubbles in turbulent water flows and analyses structure of the bubbly flow.

The final part covers processes at the interfaces between atmosphere or water and biotic systems. Opening with a very detailed description of transport processes and parameterizations in the soil-vegetation-lower atmosphere system, the third part deals with mechanical effects of forest canopy, rigid submerged vegetation in open channels.

Assuming undergraduate knowledge of fluid mechanics and environmental physics, each chapter is written easy to understand. The considerable drawback of the book, which can confuse an inexperienced reader, is the usage of non-uniform formula type by different authors. Unfortunately, the book contains some grayscale contour graphs and low resolution pictures taken from the internet which do not provide necessary information. In contrast, the high resolution full color illustrations are very impressive.

The book represents a very good compilation of modern theoretical and experimental approaches in fluid mechanical processes at environmental interfaces. It is especially useful for students, engineers, and scientists working in the fields of environmental engineering and sciences as well as applied mathematics.

Á. Bordás

IDŐJÁRÁS

VOLUME 112 * 2008

EDITORIAL BOARD

AMBRÓZY, P. (Budapest, Hungary)
ANTAL, E. (Budapest, Hungary)
BARTHOLY, J. (Budapest, Hungary)
BATCHVAROVA, E. (Sofia, Bulgaria)
BRIMBLECOMBE, P. (Norwich, U.K.)
CZELNAI, R. (Dörgicse, Hungary)
DÉVÉNYI, D. (Boulder, CO, U.S.A.)
DUNKEL, Z. (Budapest, Hungary)
FISHER, B. (Reading, U.K.)
GELEYN, J.-Fr. (Toulouse, France)
GERESDI, I. (Pécs, Hungary)
GÖTZ, G. (Budapest, Hungary)
HANTEL, M. (Vienna, Austria)
HASZPRA, L. (Budapest, Hungary)
HORÁNYI, A. (Budapest, Hungary)
HORVÁTH, Á. (Siófok, Hungary)
HORVÁTH, L. (Budapest, Hungary)
HUNKÁR, M. (Keszthely, Hungary)
MAJOR, G. (Budapest, Hungary)
MÉSZÁROS, E. (Veszprém, Hungary)
MIKA, J. (Budapest, Hungary)
MERSICH, I. (Budapest, Hungary)
MÖLLER, D. (Berlin, Germany)
NEUWIRTH, F. (Vienna, Austria)
PAP, J. M. (Greenbelt, MD, U.S.A.)
PINTO, J. (R. Triangle Park, NC, U.S.A.)
PRÁGER, T. (Budapest, Hungary)
PROBÁLD, F. (Budapest, Hungary)
RADNÓTI, G. (Budapest, Hungary)
S. BURÁNSZKI, M. (Budapest, Hungary)
SZALAI, S. (Budapest, Hungary)
SZEIDL, L. (Budapest, Hungary)
TAR, K. (Debrecen, Hungary)
TÄNCZER, T. (Budapest, Hungary)
TOTH, Z. (Camp Springs, MD, U.S.A.)
VALI, G. (Laramie, WY, U.S.A.)
VARGA-HASZONITS, Z. (Mosonmagyaróvár, Hungary)
WEIDINGER, T. (Budapest, Hungary)

Editor-in-Chief
LÁSZLÓ BOZÓ

Executive Editor
MARGIT ANTAL

BUDAPEST, HUNGARY

AUTHOR INDEX

Alföldi, B. (Budapest, Hungary) 99
Ács, F. (Budapest, Hungary) 1
Baranka, Gy. (Budapest, Hungary) 113
Barcza, Z. (Budapest, Hungary) 233
Bartholy, J. (Budapest, Hungary) 233, 249
Bordás, Á. (Novi Sad, Serbia) 113
Coppola, E. (Trieste, Italy) 233, 285
Csima, G. (Budapest, Hungary) 155
Déqué, M. (Toulouse, France) 179
Dióssy, L. (Budapest, Hungary) 125
Dombai, F. (Budapest, Hungary) 15
Falkenberg, G. (Hamburg, Germany) 83
Farda, A. (Prague, Czech Republic) 191
Ferenczi, Z. (Budapest, Hungary) 99
Gelybó, Gy. (Budapest, Hungary) 249
Giorgi, F. (Trieste, Italy) 233
Gombos, B. (Szarvas, Hungary) 33
Groma, V. (Budapest, Hungary) 83
Illenka, T. (Prague, Czech Republic) 285
Horányi, A. (Budapest, Hungary) 155, 203
Horváth, Á. (Siófok, Hungary) 1
Huszar, P. (Prague, Czech Republic) 285
Imre, K. (Veszprém, Hungary) 63
Xob, D. (Hamburg, Germany) 141
Katragkou, E. (Thessaloniki, Greece) 285
Kotova, L. (Hamburg, Germany) 141
Krüger, B.C. (Vienna, Austria) 285
Labancz, K. (Budapest, Hungary) 99
Lorencz, Ph. (Hamburg, Germany) 141
Meirer, F. (Vienna, Austria) 83
Melas, D. (Thessaloniki, Greece) 285
Molnár, A. (Veszprém, Hungary) 63
Mosely, Ch. (Hamburg, Germany) 141
Osán, J. (Budapest, Hungary) 83
Pfeifer, S. (Hamburg, Germany) 141
Pongrácz, R. (Budapest, Hungary) 233, 249
Rauscher, S. (Trieste, Italy) 285
Robaa, S.M. (Giza, Egypt) 45
Seres, T. (Budapest, Hungary) 1
Skalák, P. (Prague, Czech Republic) 191
Somot, S. (Toulouse, France) 179
Steib, R. (Budapest, Hungary) 99
Štěpánek, P. (Brno, Czech Republic) 191
Streli, Ch. (Vienna, Austria) 83
Szabó, P. (Budapest, Hungary) 249
Szépszó, G. (Budapest, Hungary) 203, 265
Tegoulias, I. (Thessalonoki, Greece) 285
Torma, Cs. (Budapest, Hungary) 233
Török, Sz. (Budapest, Hungary) 83
Weidinger, T. (Budapest, Hungary) 113
Wobrauschek, P. (Vienna, Austria) 83
Zanis, P. (Thessalonoki, Greece) 285

TABLE OF CONTENTS
I. Papers

Bartholy, J., Pongrácz, R., Gelybó, Gy. and *Szabó, P.*: Analysis of expected climate change in the Carpathian Basin using the PRUDENCE results 249

Csima, G. and *Horányi, A.*: Validation of the ALADIN-Climate regional climate model at the Hungarian Meteorological Service 155

Déqué, M. and *Somot, S.*: Analysis of heavy precipitation for France using high resolution ALADIN RCM simulations 179

Dióssy, L.: The influence of global climate change on air and soil temperatures in maize canopy 125

Dombai, F.: Attempts to enhance the localization accuracy and to monitor the reliability of the SAFIR HMS lightning localization system 15

Gombos, B.: Modeling water temperature of Hungarian rice fields 33

Groma, V., Osán, J., Török, Sz., Meirer, F., Streli, Ch., Wobrauschek, P. and *Falkenberg, G.*: Trace element analysis of airport related aerosols using SR-TXRF 83

Horváth, Á., Ács, F. and *Seres, A.T.*: Thunderstorm climatology analyses in Hungary using radar observations 1

Imre, K. and *Molnár, A.*: Hygroscopic behavior of Central European atmospheric background aerosol particles in summer . 63

Xob, D., Kotova, L., Lorenz, Ph., Moseley, Ch. and *Pfeifer, S.*: Regional climate modeling activities in relation to the CLAVIER project 141

Krüger, B.C., Katragkou, E., Tegoulias, I., Zanis, P., Melas, D., Coppola, E., Rauscher, S., Huszar, P. and *IIlenka, T.:* Regional photochemical model calculations for Europe concerning ozone levels in a changing climate 285
Robaa, S.M.: On the estimation of UV-B radiation over Egypt 45
Skalák, P., Štěpánek, P. and *Farda, A.:* Validation of ALADIN-Climate/CZ for present climate (1961–1990) over the Czech Republic 191
Steib, R., Labancz, K., Ferenczi, Z. and *Alföldy, B.:* Airport (Budapest Ferihegy – Hungary) air quality analysis using the EDMS modeling system. Part I. Model development and testing 99
Szépszó, G.: Regional change of climate extremes over Hungary based on different regional climate models of the PRUDENCE project 265
Szépszó, G. and *Horányi, A.:* Transient simulation of the REMO regional climate model and its evaluation over Hungary 179
Torma, Cs., Bartholy, J., Pongrácz, R., Barcza, Z., Coppola, E. and *Giorgi, F.:* Adaptation of the RegCM3 climate model for the Carpathian Basin..... 233
Weidinger, T., Baranka, Gy. and *Bordás, Á.:* Comparison study in mixing height determination for dispersion models.... 113

II. Book reviews

Vallis, G.K. 2006: Atmospheric and Oceanic Fluid Dynamics: Fundamentals and Large-scale Circulation (*Á. Bordás*) 61
Gualtieri, C. and *Mihailović, D.T.* (eds.): Fluid Mechanics of Environmental Interfaces (*Á. Bordás*) 301

SUBJECT INDEX

A

aerosol
- particles 63
- size distribution 63
- organic and inorganic composition 63
airport air quality 83, 99
ALADIN 191, 179, 155
ALADIN-Climate model 155

C

canopy, maize 125
Carpathian Basin 249, 233, 155, 203, 265, 141
CECILIA project 249, 179, 233, 155, III
Central and Eastern Europe 141, III, X
circulation
- large scale 61
- atmospheric and oceanic 61
CLAVIER project 203, III, X
climate change 233, 155, 203, 265
- downscaling for Hungary 125
- effect on tropospheric ozone level 285
- scenario 125, 249, 265, 141, III
climate index 249, 141
climate model evaluation 155, 203, 141
climate modeling
- regional 191, 249, 179, 233, 155, 203, 265, 141
climatology 1
composition of aerosol particles 63
correction of localization error 15
crop microclimate 125
Czech Republic 191, III

D

dispersion modeling, local scale 99
downscaling, dynamical 155

E

EDMS modeling system 99
Egypt
- climate 45
- formula for UV-B radiation distribution 45
empirical model 33
environmental interfaces 301
evaluation
- objective 203
- of climate model 203, 141
- subjective 203
expected trend, climate 249

extreme
- climate index 249, 265, 141
- events 179, III
- precipitation 179, III
Europe 285, 141

F

fine particulate matter 83
fluid
- dynamics 61
- mechanics 301
France 179

G

gridding, climate modeling 191

H

horizontal resolution 179
Hungary 1, 15, 33, 125, 63, 83, 99, 249, 155, 203, 265

L

lightning
- localization 15
- radar 15
localization
- accuracy 15
- error correction 15
- lightning 15

M

maize canopy 125
microclimate in crop 125
model
- airport air quality 99
- crop microclimate simulation 125
- dispersion on local scale 99
- empirical 33
- evaluation 155
- for flooding water temperature 33
- regional climate 191, 249, 179, 233, 155, 203, 265, 141, III
- regional photochemical 285
- validation 233, 203

O

objective evaluation 203
organic and inorganic aerosol particles 63
ozone level changes in the troposphere 285

P

particulate matter, fine 83
Péczely-classification 1
precipitation
- in climate modeling 191, 249, 179, 233, 155, 203, 141
PRUDENCE project 249, 179, 233, 155, 265, 141
pyranometer 45

R

radar 1, 15
regional climate modeling 191
reliability 15
REMO model 203
rice (*Oryza sativa* L.) 33

S

SAFIR 15
size distribution of aerosol particles 63
solar radiation
- estimation 45
- Egypt's method 45
subjective evaluation 203
synchrotron radiation 83

T

temperature
- air in maize canopy 125
- in climate modeling 191, 249, 233, 155, 203, 141
- soil 125
- water 33
thunderstorms
- analysis 1
- climatology 1
TITAN-method 1
trace elements 83
transient simulation 203
trend, expected 249, 285
tropospheric ozone 285
TXRF (X-ray) analysis 83

U

uncertainty 265
UV-B radiation 45

W

water
- flooding 33
- temperature 33
- uptake of aerosol particles 63

Y

X-ray fluorescence method (total reflection) 83

GUIDE FOR AUTHORS OF *IDŐJÁRÁS*

The purpose of the journal is to publish papers in any field of meteorology and atmosphere related scientific areas. These may be

- research papers on new results of scientific investigations,
- critical review articles summarizing the current state of art of a certain topic,
- short contributions dealing with a particular question.

Some issues contain "News" and "Book review", therefore, such contributions are also welcome. The papers must be in American English and should be checked by a native speaker if necessary.

Authors are requested to send their manuscripts to

Editor-in Chief of IDŐJÁRÁS

P.O. Box 39, H-1675 Budapest, Hungary

in three identical printed copies including all illustrations. Papers will then be reviewed normally by two independent referees, who remain unidentified for the author(s). The Editor-in-Chief will inform the author(s) whether or not the paper is acceptable for publication, and what modifications, if any, are necessary.

Please, follow the order given below when typing manuscripts.

Title part: should consist of the title, the name(s) of the author(s), their affiliation(s) including full postal and e-mail address(es). In case of more than one author, the corresponding author must be identified.

Abstract: should contain the purpose, the applied data and methods as well as the basic conclusion(s) of the paper.

Key-words: must be included (from 5 to 10) to help to classify the topic.

Text: has to be typed in single spacing with wide margins on one side of an A4 size white paper. Use of S.I. units are expected, and the use of negative exponent is preferred to fractional sign. Mathematical formulae are expected to be as simple as possible and numbered in parentheses at the right margin.

All publications cited in the text should be presented in a *list of references*, arranged in alphabetical order. For an article: name(s) of author(s) in Italics, year, title of article, name of journal, volume, number (the latter two in Italics) and pages. E.g., *Nathan, K.K.,* 1986: A note on the relationship between photo-synthetically active radiation and cloud amount. *Időjárás 90,* 10-13. For a book: name(s) of author(s), year, title of the book (all in Italics except the year), publisher and place of publication. E.g., *Junge, C.E.,* 1963: *Air Chemistry and Radioactivity*. Academic Press, New York and London. Reference in the text should contain the name(s) of the author(s) in Italics and year of publication. E.g., in the case of one author: *Miller* (1989); in the case of two authors: *Gamov* and *Cleveland* (1973); and if there are more than two authors: *Smith et al.* (1990). If the name of the author cannot be fitted into the text: *(Miller,* 1989); etc. When referring papers published in the same year by the same author, letters a, b, c, etc. should follow the year of publication.

Tables should be marked by Arabic numbers and printed in separate sheets with their numbers and legends given below them. Avoid too lengthy or complicated tables, or tables duplicating results given in other form in the manuscript (e.g., graphs)

Figures should also be marked with Arabic numbers and printed in black and white in camera-ready form in separate sheets with their numbers and captions given below them. TIF, GIF or BMP formats should be used for electronic artwork submission.

The text should be submitted both in manuscript and in electronic form, the latter in e-mail or CD. MS Word format is preferred.

Reprints: authors receive 30 reprints free of charge. Additional reprints may be ordered at the authors' expense when sending back the proofs to the Editorial Office.

More information for authors is available: antal.e@met.hu

Published by the Hungarian Meteorological Service

Budapest, Hungary

INDEX: 26 361

HU ISSN 0324-6329